USE OF AN ONLINE ACOUSTIC BACKSCATTER SYSTEM TO MONITOR INDUSTRIAL SLURRY FLOWS

Serish Tanya Hussain

Submitted in accordance with the requirements
for the degree of Doctor of Philosophy

The University of Leeds
School of Chemical and Process Engineering
Next Generation Nuclear CDT

January 2023

The PGR confirms that the work submitted is his/her/their own, except where work which has formed part of jointly authored publications has been included. The contribution of the PGR and the other authors to this work has been explicitly indicated below. The PGR confirms that appropriate credit has been given within the thesis where reference has been made to the work of others.

Chapter 4 is based on the paper: Hussain, S.T., Hunter, T.N., Peakall, J. and Barnes, M. 2020. Utilisation of underwater acoustic backscatter systems to characterise nuclear waste suspensions remotely. *Proceedings of meeting on acoustics, Acoustical Society of America.* **40**(1), pp.1-12. The candidate was responsible for the experiments, analysis, figures, calculations, and writing the paper. Hunter provided supervisory support, Jeff provided feedback and proofreading support, Martyn provided comments, and all authors provided comments on the content of the paper.

Chapter 6 is based on the paper: Hussain, S.T., Hunter, T.N., Peakall, J. and Barnes, M. 2021. Characterising flocculated suspensions with an ultrasonic velocity profiler in backscatter mode. In: *IEEE International Ultrasonics Symposium (IUS), September 2021*. China: IEEE. The candidate was responsible for the experiments, analysis, figures, calculations, and writing the paper. Hunter provided supervisory support, Jeff provided feedback and proofreading support, Martyn provided comments, and all authors provided comments on the content of the paper.

Chapter 7 is based on the paper: Hussain, S.T., Hunter, T.N., Peakall, J. and Barnes, M. 2021. Simultaneous velocity and concentration profiling of nuclear waste suspensions in pipe-flow, using ultrasonic Doppler and backscatter analysis. *Proceedings of meeting on acoustics, Acoustical Society of America.* **150**(4), pp.1-13. The candidate was responsible for the experiments, analysis, figures,

calculations, and writing the paper. Hunter provided supervisory support, Jeff provided feedback and proofreading support, Martyn provided comments, and all authors provided comments on the content of the paper.

Chapter 8 is based on the paper: Hussain, S.T., Hunter, T.N., Peakall, J., Barnes, M. and Rice, H. 2022. Remote analysis of complex mineral suspensions in engineered pipelines: utilising underwater acoustic backscatter systems – 22142. In: *WM Symposia Conference Proceedings, March 2022, Phoenix.* Phoenix: WM Symposia. The candidate was responsible for the experiments, analysis, figures, calculations, and writing the paper. Hunter provided supervisory support, Jeff provided feedback and proofreading support, Martyn provided comments, Rice supports with calculations and comments, and all authors provided comments on the content of the paper.

For my mum

ACKNOWLEDGEMENTS

I would like to thank Timothy Hunter, my primary supervisor, for his support over the last four years. His guidance has been invaluable and his encouragement through the pandemic gave me the determination to get through the PhD. I would also like to thank Jeff Peakall and Hugh Rice for their input and words of wisdom. Jeff was always there to advise, and Hugh provided me with technical support on numerous occasions. I would also like to thank Alex Lockwood and Joe Hartley for their assistance. This research was funded by the ESPRC and Sellafield Ltd. As part of this research, I was able to liaise with Martyn Barnes who has directed me throughout and provided me with a direct link to industry.

I would like to thank all of my friends and colleagues who have supported me along the way and helped me during the last four years. These include Alastair Baker and Chris Bulman. Alastair was always there to lend an ear and has reassured me whenever I needed it. Chris was consistently present not only as a technician but as a friend, his unwavering belief in me and his ability to make me laugh at the end of a long day was always appreciated.

I would especially like to thank all my friends and family who have taken time out of their own lives to read my work when they had no expertise in the subject and were willing to listen to me complain no matter how busy they were. To Yasmin and Aysha who have been my primary proof-readers, I think they will be the most relieved to know that it is finally coming to an end. Thank you for everything, I can’t list all the support you’ve given me when I have doubted myself.

And finally, I would like to thank the people closest to me, who have been so patient and understanding over the last four years. To my brother who has never doubted me, he is the reason I strive to succeed in everything I set my mind to. To my dad who is my biggest supporter, the sense of pride he has in me will forever motivate me to do better. To my mum who has been my one and only role model in life, you’ve shown me that anything is possible if you really try. Without you, I wouldn’t be where I am today. And finally, to my husband who has been my rock.

Thank you for the coffee’s, late night drives and motivational speeches. Your infectious positive outlook has helped me stay optimistic even when I felt uncertain.

- Serish T Hussain

ABSTRACT

Throughout this thesis an acoustic backscatter system was utilised to characterise sediment suspensions in real time. The specific commercial acoustic backscatter system (ABS) used was an ultrasonic velocity profiler (UVP). ABS was used because it is a flexible system with transducers of a small diameter (5-10 mm) which can be used to mount onto smaller pipes (~ 25 mm). The ABS will be used to analyse nuclear waste in transport. The main properties to be analysed are the concentration and velocity which will be used to understand how the nuclear waste moves in transit. Several nuclear simulant suspensions were used throughout this thesis, the most prominent simulants were silica glass bead powders which were dispersed in an aqueous suspension. To calibrate the UVP, silica glass beads suspensions of varying sizes were suspended in a calibration rig and ultrasonic transducers of 2 and 4 MHz frequency with a 2.5 and 5 mm active radius were used to produce acoustic profiles of the suspensions. An additional novel error analysis approach was used in tandem with a detailed calibration method. Once the system was calibrated, silica glass beads of varying concentrations were suspended in a calibration tank and analysed using 2 and 4 MHz ultrasonic transducers which were used *in situ* and in remote configurations to produce acoustic profiles for direct comparison to previous literature. Remote placement of UVP transducers has not been used to analyse homogeneous suspensions of silica glass bead particles. These sedimentation attenuation coefficients were compared to combined attenuation predictions from scattering and viscous losses to determine the accuracy of measured remote data.

After the calibration of the experimental method using silica glass beads, complex mineral suspensions were analysed in the calibration rig. Calcium carbonate ($CaCO_3$) and magnesium hydroxide ($Mg(OH)_2$) mineral suspensions were suspended in the calibration tank and *in situ* and remotely placed ultrasonic transducers were utilised to extract acoustic profiles. Flocculant was used to investigate the capability of the UVP to monitor changes in particle sizing. Sedimentation attenuation coefficients were extracted from non-flocculated and flocculated suspensions for both calcium carbonate and magnesium hydroxide and

compared to understand the effects of flocculation on attenuation. This has not been achieved before using both *in situ* and remotely placed transducers. Measured values were compared to combined predicted attenuation from scattering and viscous losses to determine the accuracy of models for attenuation of flocculating suspensions. Coefficients from the calibration tank compare well to sedimentation attenuation coefficients from previous literature, therefore, data was validated before analysis of complex mineral suspensions. Accuracy of the sedimentation coefficients shows that the UVP is able to monitor changes in concentration as well as particle size for complex mineral suspensions. This can be utilised across industries where complex suspensions have unknown physical properties.

To understand whether this method could be used on small pipelines, the engineered pipe loop was commissioned (with an outer diameter of 0.03 m) and silica glass suspensions were dispersed in the pipe loop. Transducers were mounted in a non-contact configuration on horizontal and vertical pipelines to understand which pipeline arrangement provided the most accurate results. Transducers were mounted at 90 and 135° for novel simultaneous extraction of acoustic profiles and velocity profiles respectively. This has not been achieved in a single experiment before for silica glass beads using this specific UVP. Attenuation coefficients were extracted and compared to combined attenuation predictions and coefficients from previous Chapters.

Complex mineral suspensions were also suspended in the pipe loop and flocculated to show a change in particle size. The UVP was used for novel analysis of non-flocculated and flocculated complex mineral suspensions using remotely placed transducers. Transducers were mounted at 90 and 135° for novel simultaneous extraction of acoustic profiles and velocity profiles respectively. An FBRM was also inserted into the pipeline and utilised as a validation technique for the change in size of the flocculating mineral suspensions. Remote data was comparable to *in situ* data where sedimentation attenuation coefficients were attained accurately using either technique, this is vital for industries like the

nuclear waste sector where suspensions cannot be extracted for analysis. Remote data analysis saves taxpayers money and ensures worker safety.

TABLE OF CONTENTS

LIST OF FIGURES

LIST OF TABLES

FIGURES IN APPENDIX

TABLES IN APPENDIX

NOMENCLATURE

ROMAN SYMBOLS

a	Particle Radius	a
a^t	Transducer Active Radius	m
c	Speed of Sound, Chord Length	$m.s^{-1}$, µm
d	Particle Diameter D_{50} 50^{th} Percentile	µm
D	Pipe Inner Diameter	m
E	Raw Echo Amplitude	Decibel
E_{inst}	Instantaneous Raw Echo Amplitude	Decibel
f	Ultrasonic Frequency, Form Factor, Darcy Friction Factor	MHz, dimensionless, dimensionless
g	Acceleration due to Gravity	$m.s^{-2}$
g	Gain Function	Decibel
G	Range Corrected Echo Amplitude	$Neper.m^{-1}$
k	Wavenumber, Compressibility	m^{-1}.m2.N-1
K^h	Combined Scattering and System Constant	$V.m^{2.5}.kg0^{.5}$
k_s	Backscattering Coefficient	$m.kg^{0.5}$
k_t	Transducer Constant	$V.m^{1.5}$
L	Length	m
M	Solid Phase Concentration	$kg.m^{-3}$
n	Number of Samples	
Q	Volumetric Flow Rate	$m^3.s^{-1}$
r	Distance From Transducer	m
r_f	Transducer Focal Distance	m
r_n	Transducer Near Field Distance	m
T	Temperature	°C
t	Time	s
U	Mean Velocity	$m.s^{-1}$
v	Velocity	$m.s^{-1}$
V	Received Voltage	Volts
$Vinst$	Instantaneous Echo Voltage	Volts

Re	Reynolds Number	

DIMENSIONLESS NUMBERS

Re	Reynolds Number

GREEK SYMBOLS

δ	Viscous Boundary Layer	m
μ	Dynamic Viscosity	$kg.m^{-1}.s^{-1}$
α	Total Attenuation	m^{-1}
α_s	Attenuation due to Solid Phase	m^{-1}
α_w	Attenuation due to Water	m^{-1}
γ	Beam Divergence Angle	°
ε	Roughness Coefficient	Dimensionless
λ	Ultrasonic Wavelength	m
ξ	Sediment Attenuation Constant	$m^2.kg^{-1}$
ρ	Density	$Kg.m^{-3}$
υ	Kinematic Viscosity	$m^2.s^{-1}$
ϕ	Volume Fraction	Dimensionless
χ	Normalised Total Scattering Cross Section	Dimensionless
ψ	Near Field Correction Factor	Dimensionless
ω	Angular Frequency	$rad.s^{-1}$

SUBSCRIPTS, SUPERSCRIPTS, ABBREVIATIONS ACRONYMS

ABS	Acoustic Backscatter System
ACVP	Acoustic Concentration and Velocity Profiler
ADCP	Acoustic Doppler Current Profiler
ADV	Acoustic Doppler Velocimeter
ANN	Artificial Neural Network
b	Bulk Density
CFD	Computational Fluid Dynamics

CLD	Chord Length Distribution
EIT	Electrical Impedance Tomography
EM	Electromagnetic Spectrum
Err	Error Analysis
ERT	Electrical Resistance Tomography
FBRM	Focused Beam Reflectance Measurement
FGMSP	First Generation Magnox Storage Pond
HAST	Highly Active Storage Tank
IAEA	International Atomic Energy Agency
LISST	Laser *In Situ* Scattering and Transmissometer
MRI	Magnetic Resonance Imaging
MSSS	Magnox Swarf Storage Silos
NDA	Nuclear Decommissioning Authority
NDA	Non-Destructive Assay
NIR	Near Infared
NPP	Nuclear Power Plant
OD	Outer Diameter
OBS	Optical Backscattering System
PDA	Photometric Dispersion Analyser
PFCS	Pile Fuel Cladding Silo
PFSP	Pile Fuel Storage Pond
PMMA	Poly(Methyl Methacrylate)
PPE	Personal Protection Equipment
PSD	Particle Size Distribution
PVM	Particle View and Measurement
s	Solid
SSC	Suspended Sediment Concentration
SEM	Scanning Electron Microscope
SEPA	Scottish Environmental Protection Agency
SMART	Specific, Measurable, Achievable, Relevant and Time-based
TEM	Transmission Electron Microscope
TRL	Technology Readiness Level
UARP	Ultrasonic Array Research Platform
UAS	Ultrasonic Attenuation Spectroscopy

UVP	Ultrasonic Velocity Profiler
w	Water
XRD	X-Ray Diffraction
XRF	X-Ray Fluorescence

1. INTRODUCTION

1.1 BACKGROUND

Characterisation of sediment suspensions is a complex process which is vital for industrial processing. A suspension can be characterised physically or chemically where the results of both can vary greatly (Mechtcherine *et al*., 2019). Chemical characterisation will often lead to understanding the chemical composition and chemical structure of a suspension, on the other hand, physical characterisation lends to concentration profiling, particle sizing, velocity profiling etc. Within the scope of this PhD, physical characterisation can provide the necessary information on the physical characteristics of suspensions including viscosity, rheology, and density (Giglio and Sabbatini, 2022). *In situ* characterisation of sediment suspensions requires samples to be taken from the suspension environment which cannot be used for any material which is radioactive or too dangerous to be taken offsite (Biggs *et al*., 2009). For complex suspensions such as these, remote characterisation techniques are required for analysis however, there are not many remote techniques which are capable of concentration profiling (Hunter *et al*., 2011). In this thesis, remote is a non-contact technique which is non-invasive and does not require contact with the suspension or slurry for analysis. This specific thesis focuses on the use of a remote technique for characterisation of nuclear waste suspensions. Particularly in the nuclear industry where samples of any complex suspensions cannot be taken off-site due to contamination risks (Biggs *et al*., 2009).

In this PhD, the remote characterisation is focused on analysis nuclear waste slurries and sludges, specifically a magnesium hydroxide-based sludge with unknown chemical and physical properties (Alderman and Heywood, 2011; Hunter *et al*., 2020). The origin of this waste is from the spent fuel assemblies in the magnox fleet of reactors which were decommissioned due to the detrimental effect of using fuel assemblies composed of magnox; a magnesium non oxidising metal (Gregson *et al*., 2011; Johnson *et al*., 2019). Magnox was not able to maintain its integrity at the high operating temperatures within the plant which led

to loss of stability of the wind scale pile reactor (Hill, 2013). The spent fuel assemblies from these magnox fleet of reactors were decommissioned over time and left in open-air storage ponds. Over time, the spent fuel assemblies have hydrolysed into a magnesium hydroxide-based sludge with unknown properties (Burton, 2002). The plan is to transport this sludge in engineered pipelines to an interim storage or waste treatment plant, this will require remote in-line characterisation of the sludge in transit which is not viable for most techniques in industry (Alderman and Heywood, 2011; Hunter *et al*., 2020).

Remote characterisation techniques can be incredibly useful especially in industries like nuclear where minimal exposure to workers is key to maintaining a safe environment (Mirlean *et al*., 2001). There are a range of remote techniques which have been proven to accurately characterise suspensions, these techniques have been detailed in the literature review. However, for most remote analysis techniques, a sample is required to be taken off site or only the surface is characterised (Sourdeval, *et al*., 2018). One of the most common techniques especially in the marine and defence sector is the use of ultrasonics which are the most practical and applicable technique available from the wide range of methods in industry at the moment. Ultrasonics is the science and application of ultrasonic waves, which are waves above a frequency of the audible human range of 20 kHz (Butler and Sherman, 2016). Ultrasonic acoustics has been used in marine surveying where underwater ultrasonic transducers were used to detect moving sediment on the seabed (Carrera *et al*., 2019). Acoustics is the branch of physics which is concerned with the property of sound whilst ultrasonic transducers are devices which convert electrical energy into ultrasound and vice versa (Butler and Sherman, 2016). From this principle, ultrasonic transducers can be utilised to analyse moving sediment in a tank or a pipe. In this thesis acoustic backscatter systems (ABS) were used where a single ultrasonic transducer or a transducer array acts as transmitter and reciever. When using a single transducer, the wave is reflected or back scattered. ABS have been used extensively in marine or estuarine environments and generally use single frequency transducers (Hunter *et al*., 2012; Rice *et al*., 2014; Bux *et al*., 2015; Tonge *et al*., 2019). The transducers

produce the ultrasound and then detect the echo signal which allows the generation of acoustic profiles. The specific ABS used within this thesis is the ultrasonic velocity profiler (UVP) which is a commercial ABS. The UVP was used in backscatter mode to collect acoustic profiles for attenuation coefficients from voltage data. UVP systems have been used previously in well-mixed tanks to measure attenuation of a variety of suspension environments (Ogasawara *et al.*, 2019).

The main focus of this PhD is the magnox sludge in the open-air ponds which requires characterisation before being transported to a long-term storage facility (Gregson *et al*., 2011). The physical and chemical properties of the sludge have changed over time due to the hydrolysis of the magnox fuel assemblies (Adams *et al*., 2011). Basic physical properties of the sludge such as concentration, velocity and particle sizing need to be monitored in order to safely transport the sludge into long term storage (Alderman and Heywood, 2011; Giglio and Sabbatini, 2022). The use of a remote characterisation system allows a safer, more economically viable technique for the analysis of the sludge. Preventing workers from having direct contact with the material will require less PPE, less precautions and less funding whilst collecting data remotely and in real-time will cut down on analysis time (Mirlean *et al*., 2001).

The set-up in this thesis evolved over time to produce a fully remote characterisation technique. Through the Chapters there were several experimental set-ups used which include the use of a well-mixed tank as well as a pipe loop. Collectively, for all the set-ups used throughout the thesis there were a limited number of nuclear simulants used. The first simulants were spherical glass dispersions which had been used previously by Rice *et al*., (2014), (2015). The scattering-attenuation properties of the spherical glass dispersions can be correlated to theoretically known models which is why they have been used in this thesis (Betteridge *et al*., 2008). Several particle size distributions of these spherical glass beads were used to understand whether the UVP was able to analyse suspensions of varying particle size accurately. Two mineral suspensions

were used, namely calcium carbonate and magnesium hydroxide. Calcium carbonate is a non-hazardous test material with a similar structure to common fine sludges. It has also been used extensively as an analogue for nuclear wastes in experiments (Hunter *et al*., 2020). The other mineral suspension used was a magnesium hydroxide powder which was dispersed in an aqueous suspension. The magnesium hydroxide is a more chemically similar simulant to the Magnox sludge in the Sellafield storage ponds (Hriljac *et al*., 2018).

1.2 Objectives and overview of the thesis

1.2.1 Aims

The main aim of this PhD was to prove that acoustic backscatter systems could be used to analyse sediment suspensions in-line and remotely using a non-contact arrangement (Rice, 2013). This technique has been shown with a nuclear specific focus; however, the use of a remote system can be used in most industries especially in the current global climate (Jung, *et al*., 2021). The ability to protect workers and prevent direct contact limits exposure to any hazardous suspensions whilst analysing and providing data rich results (Ahmed *et al*., 2021). Any solid-liquid suspensions can be analysed using acoustic backscatter systems however, in this thesis the main liquid dispersant was water. Aqueous sediment suspensions are found in all industries including water treatment and the oil and gas sector (Liu *et al*., 2021).

The specific acoustic backscatter system used in this thesis is an ultrasonic velocity profiler which is a commercial system that has been used by previous researchers (Rice *et al.*, 2015). Rice *et al*., (2015) were able to use the UVP to analyse various sediment suspensions and produce acoustic and velocity profiles. In this thesis, the author has gone a step further and illustrated the use of the UVP for complex mineral suspensions which change in particle size and has demonstrated the validity of the technique in an engineered pipe loop where data was collected simultaneously for velocity and acoustic profiling accurately. More specific objectives as well as the scientific novelties are shown below;

- Ensure all Measured Sedimentation Attenuation Coefficients are Accurate.

  To ensure accuracy of results extracted from the UVP, the author conducted error analysis on the raw echo amplitude. The array of echo data was used to determine the minimum and maximum attenuation coefficients. This was only conducted on the linear region of the attenuation profile, where the suspension is homogeneous. The error analysis ensures other researchers that the attenuation coefficients extracted from measured data are accurate and the possible variation from the echo array can be visualised to determine the repeatability of results. This error analysis method was novel in that other researchers have not utilised the array of echo data to determine the variation in voltage, G-function, attenuation and subsequently sedimentation attenuation coefficients.

- Provide Accurate Predictions for Comparison to Measured Data

  To ensure the measured data was accurate, a combined attenuation prediction was used where Betteridge *et al.*, (2008) derivations were used to model scattering losses whilst Urick, (1948) derivations were used to model viscous losses. The combination of both allowed for a combined attenuation prediction which compared well for homogeneous suspensions of glass particles and complex flocculating mineral suspensions. This combined attenuation prediction has not been used in tandem with measured data from the UVP.

- Develop a Non-invasive System for Analysis.

  Both *in situ* and remote (non-invasive) transducers were used to analyse homogeneous silica glass dispersions and flocculating complex mineral suspensions. It was established that the remote transducers were able to provide accurate data which compared well to data from invasive, *in situ* transducers. A non-invasive configuration has not been achieved before for homogeneous glass dispersions with the UVP transducers.

- Ensure the Measured Scattering Cross Section is Accurate.

  To predict scattering, the form function and normalised scattering cross section values were determined experimentally for homogeneous suspensions of glass beads. These were compared to heuristic expressions where values aligned very well. This has not been achieved before for remotely placed transducers. This shows the applicability of non-contact transducers in non-contact environments.

- Monitor a Flocculating System Accurately and Non-invasively.

  Complex mineral suspensions were analysed in non-flocculated and flocculated form where the UVP transducers were used to determine sedimentation attenuation coefficients in the calibration rig. These coefficients could be used to monitor the flocculation process. This was also achieved in line where UVP transdcuers were mounted onto a pipe line non-invasively and simultaneous velocity and acoustic data was extracted. Attenuation coefficients from the in line data could be used to compare non-flocculated and flocculated suspensions of complex mineral suspensions which had not been achieved before. The non-invasive analysis is novel, but the comparison of attenuation coefficients is also novel. Novel comparisons of normalised scattering cross section values were made to predictions which had been conducted by Tonge *et al*., (2021) for homogeneous glass suspensions not complex mineral suspensions.

- Develop an Online Characterisation System which can Provide Simultaneous Data.

  For the development of an online characterisation system, UVP transducers were mounted in a remote configuration on horizontal and vertical pipe lengths. These transducers were utilised to extract raw echo date as well as velocity data simultaneously, from this raw data, attenuation coefficients and velocity profiles were developed An FBRM system was mounted for *in situ* particle sizing, this was the only equipment which was invasive. A flow meter was mounted for flow measurements. This set-up was novel where a single

experiment could yield attenuation coefficients, velocity profiles, Chord Length Distributions (CLD's) and flow data.

1.2.2 Objectives

The objectives in this thesis have been outlines using Specific, Measurable, Achievable, Relevant and Time-based (SMART) actions to outline clear, targeted research goals.

The desired outcome of Chapter 2 is to show that the author has been able to review literature relevant to the specific research goal of this thesis: Use of an Online Acoustic Backscatter System to Monitor Industrial Slurry Flows. This can be measured by the number of relevant techniques covered in the literature review, see the summary in Table 2.1. Although the author has attempted to cover all relevant techniques, there is always the possibility that some techniques have been missed or overlooked. Therefore, the author caveats that although some techniques familiar to the reader have not been included, these were not relevant options for the research goal identified. This has allowed the author to provide a literature review which was achievable in the scope of the PhD. The techniques shown in Table 2.1 are specifically relevant to the research goal, the author has shown this by providing papers which use these techniques for physical characterisation. The literature review was completed across the PhD to allow consideration of techniques which were used throughout the entire study period.

The desired outcome of the Analytical Theory Chapter was to provide a background to the acoustic and pipe loop theoretical expressions and derivations which are used as a foundation for the results produced across Chapters 4-8. The author has been sure to include all relevant literature from Chapter 2 to provide a thorough understanding of the acoustic theory. The author has only included relevant theory which is used for data analysis in this thesis. Inspiration has been taken from other researchers who have published papers detailing new and novel calibration procedures and this thesis has detailed a thorough step-by-step process so readers can follow the theory.

Chapter 4 is the first results Chapter and the desired outcome is the calibration of the UVP transducers with varying active radii and frequency. Sedimentation attenuation coefficients extracted from the transducers with varying active radii and frequency can be directly compared to coefficients from previous literature so the author can show the acoustic system used can provide accurate results. This was achieved using a calibration rig for two sets of silica glass beads with two different particle size distributions. Calibration of the UVP transducers will allow the author to show that the transducers used can provide accurate results for the analysis of slurry flows. This was achieved in the first year of the PhD, results were published by the author, see Hussain *et al*., 2020.

The desired outcome of Chapter 5 was to use the now calibrated UVP transducers in an *in situ* and remote placement to analyse an array of silica glass beads with varying particle size distributions. The sedimentation attenuation coefficients extracted have been used to understand the effect of the particle size on the attenuation of the aqueous suspensions. This outcome is measured by the attenuation coefficients calculated for all four silica glass bead suspensions with particle sizes varying from 36-170 μm. This was achieved by submerging the UVP transducers for *in situ* data and mounting the transducers on the outside of the tank for remote, non-contact data. The *in situ* data can be used to prove that mounting transducers remotely can produce accurate results. Mounting remotely can show that ultrasonic transducers can be used to monitor slurry flows in the nuclear industry safely. This was achieved in the second year of the PhD and all data is shown in Chapter 5.

The desired outcome of Chapter 6 was to be able to extract attenuation coefficients from non-flocculated and flocculated mineral suspensions using UVP transducers in an *in situ* and remote arrangement. This is measured by the sedimentation attenuation coefficients extracted from the mineral suspensions. two mineral suspensions were used in this thesis; calcium carbonate and magnesium hydroxide which are both commercial powders and so, are readily available. As UVP can be used to extraction of sedimentation attenuation

coefficients of non-flocculated and flocculated suspensions, it can also be inferred that the UVP can be used to monitor the flocculation of mineral suspensions via *in situ* or remote methods. As the nuclear waste is often in a sludge form of magnesium hydroxide, accurate results can show that the UVP can be used to monitor the non-flocculated and flocculated suspensions of sludge. Results from this Chapter were published in the authors second paper, see Hussain *et al*., 2021a.

Chapter 7 is the first Chapter where the engineered pipe loop was utilised. The desired outcome of this Chapter was to use the UVP transducers to extract velocity profiles and sedimentation attenuation coefficients from aqueous suspensions running through horizontal and vertical pipe lengths. This is measured by the sedimentation attenuation coefficients extracted and the velocity profiles produced. This was achieved by the planning and systematic installation and engineering of the pipe loop which occurred over the first two years of the PhD. As this PhD has a focus on the nuclear industry and Sellafield is the sponsor of this project. It is relevant to understand that Sellafield are planning to transport their nuclear waste in pipelines. Therefore, having accurate velocity and acoustic profiles from various pipe length is relevant to prove that the system can be used for aqueous suspensions in transit. Results also provide Sellafield with an understanding of which pipe orientation would be ideal for simultaneous transport and analysis of nuclear waste. This work was conducted over the third year of the PhD and published in the authors third paper, see Hussain *et al*., 2021b.

Chapter 8 was the final results Chapter where the experimental set-up was pushed to its limits. Only vertically mounted transducers were used due to the findings in Chapter 8. The desired outcome of this Chapter was to show that the UVP transducers could be used to analyse complex non-flocculated and flocculated mineral suspensions in pipe flow. This was measured by the velocity and acoustic profiles extracted from the system. The flocculation of mineral suspensions had been achieved before in Chapter 6 whilst the pipe loop had been used for analysis of homogeneous suspensions had been achieved in Chapter 7. Therefore, Chapter

8 was an amalgamation of lesson learned through the two previous Chapters. Magnesium hydroxide is the main component of a specific waste sludge at Sellafield and accurate results can be used to prove to Sellafield that acoustics can be used for analysis of complex mineral suspensions with varying particle sizes. This work was conducted over the third year of the PhD and published in the authors fourth paper, see Hussain *et al*., 2022.

Chapter 9 concludes the thesis and provides a summary of the most prominent results from each section of the results. Future work is also covered in Chapter 9. Chapter 10 shows details of all the references used throughout the thesis and finally, Chapter 12 shows the electronic supplementary material which provides more insight into the experiments conducted throughout the thesis.

2. LITERATURE REVIEW

In this literature review the author will cover the background to the nuclear industry to identify the research drive, this covers the specific industry for which this research is focused on and other industries where this research is relevant. The nuclear waste industry is covered in detail including where the nuclear waste originates from and how the waste has formed over the last 80 years or so. The relevance for this waste is highlighted as well as the complexities which come with analysing this type of waste. Nuclear waste analogues used in literature are specified where the analogues can be utilised to demonstrate competency for analysis techniques. As this thesis hinges on the abilities of acoustic methods, a background to ultrasonics is covered. The background on the physics behind acoustic theory and acoustic backscatter systems is covered for a non-specialist scientific audience. There is also a smaller background on ultrasonic spectroscopy which is another common method used for analysis of suspensions.

The author also investigates the range of techniques available for *in situ* physical characterisation specifically for slurries and suspensions. *In situ* characterisation is necessary in the nuclear industry to provide accurate results for characterisation of radioactive suspensions and slurries. Although sampling is not required for *in situ* characterisation, the equipment may need to be mounted to be in contact with the suspension or slurry. This can lead to contamination risks through the instrumentation being exposed to radiation and as a result has a higher risk to workers. Exposure of equipment to the suspensions can also decrease the usability of the equipment over time. Therefore, remotely placed equipment which is not in direct contact with the slurry is investigated here as the ideal characterisation method for the nuclear industry. Remote experiments prevent the contamination of equipment, permits equipment to be taken on and off site and allows workers to characterise radioactive suspensions with no contact with the waste. This technique set-up will prioritise workers health and safety whilst also producing accurate results without the need for additional contamination risk.

A range of *in situ* characterisation techniques will be scrutinised to show why acoustics were selected as the non-contact characterisation method. The techniques investigated will be characterised by their ability to analyse particle size and concentration as these are the main properties to be investigated in this thesis. The author will then look into the use of remote characterisation of suspensions, where the equipment does not require sampling or direct contact with the suspension or slurry. A separate section in this Chapter explores the use of acoustics for characterisation which directly compares the use of ultrasonics for *in situ* measurements in comparison to non-ultrasonic based techniques e.g. microscopy. Acoustics have mainly been utilised in the marine and defence sector for analysing marine life on the seabed, the same principles have been utilised in this thesis to analyse moving sediment in a tank or pipe. Acoustics has a very wide range of techniques available for characterisation, in this specific thesis an acoustic backscatter system (ABS) is used, therefore the range of acoustic backscatter equipment available is investigated to make it clear to the reader why a specific ABS was selected. The author also identifies gaps in current literature that are covered in this thesis which shows both the novelty and the drive for the research.

Throughout this thesis several experimental set-up variations are used. The main set-up includes a calibration rig which is used for all initial experiments and all calibration data. Once all experiments were complete in the calibration rig and data had been validated using previous literature, the author moved on to experiments in an engineered pipe loop. The experimental set-up changes with each results Chapter and the reader can follow the development of the pipe loop and how the design reflects the data that can be extracted. In the literature review, previous literature shows the extensive experimental set-ups used and a precedence for the use of calibration rigs and pipe loops.

2.1 Drive for this PhD

The drive for this PhD originates from the desire for *in situ* and online analysis of particulate suspensions which are seen across industries. Larger particle suspensions, colloidal suspensions and flocculated suspensions are present in the pharmaceutical industry, brewing industry, water treatment and nuclear waste treatment, amongst many more (Stille and Giere, 2004; Mewis and Wagner, 2012). Characterising the physical properties of particulate suspensions will provide information on concentration, rheology, particle size distribution and more (Moore *et al*., 2013; Rice *et al*., 2019; Tonge *et al*., 2021). The techniques which provide information on physical properties include microscopy, PVM, FBRM, XRD, XRF etc (Jia *et al*., 2008; Wang *et al*., 2020). Characterising the chemical properties of particulate suspensions provides information on chemical composition and elemental analysis. Raman Spectroscopy provide chemical analysis of materials (Yang *et al*., 2019). Physical properties provide information required from an operational perspective, where the physical properties can be used to underpin the method of transport and storage for the nuclear waste (Amgarou *et al*., 2021). SEPA, (2010) has said that physical properties of the waste should be understood so any risks posed by the waste can be assessed and comply with safety case standards. Oftentimes for the radioactivity of the suspension, dose modelling can be used which provides sufficient assurance on the activity of the suspension (Johansen *et al*., 2012). Therefore, chemical analysis is not imperative from a decommissioning perspective. Information on physical properties can be difficult to obtain where methods often require sampling for *ex situ* techniques. There are a variety of *in situ* techniques currently used in industry (see section 2.5) however, these methods are often expensive and require specialist training for operation (Maczulak, 2009).

2.2 Background to the nuclear industry and industrial context

The nuclear industry began in the UK in the 1940's when the UK decided to commission the wind scale pile nuclear reactors for military purposes. The Calder

Hall facility was later commissioned in the 1950's with a civil energy focus (Newtan, 2007). From the initial reactors in operation from the 1940's, there are a variety of temporary waste storages, particularly wet storage facilities at Sellafield (IAEA, 2021). The legacy storage facilities currently at Sellafield include the first generation magnox storage pond (FGMSP), pile fuel storage pond (PFSP), pile fuel cladding silo (PFCS) and the magnox swarf storage silos (MSSS) (see Fig. 2.1) (Ayoola, 2018).

Figure 2.1 Magnox swarf storage silo, cross section (RadioRoSo, 2022)

This PhD has been sponsored by Sellafield Ltd for *in situ* or online measurement of nuclear waste with a specific focus on the Magnox Pond which was used to store fuel cladding from the Magnox fleet of reactors (Ayoola, 2018). A legacy pond is shown for reference below in Fig. 2.2. The storage facilities have housed the nuclear waste over the last 80 years and the fuel cladding which was placed within the Magnox ponds has now hydrolysed into a sludge with unknown physical properties (Ayoola, 2018). However, with the current infrastructure available for analysis, there is equipment that can be used *in situ* to provide physical characterisation of the sludge before transport or disposal (NDA, 2022). Current stakeholders of the nuclear industry have expressed worries with regards to funding insecurity, therefore, there is apprehension with regards to new and

expensive equipment being deployed. Stakeholders have also expressed concerns with new experimental methods, this was specifically sprung due to the fuel element debris dissolution experiments at Bradwell which were unsuccessful and led to radioactivity and heavy metals being pumped in Blackwater estuary (Hirose and McCauley, 2022). Therefore, an *in situ* process which can be shown to be non-intrusive and provide accurate physical characterisation would be ideal and provide assurances for stakeholders to minimise concern.

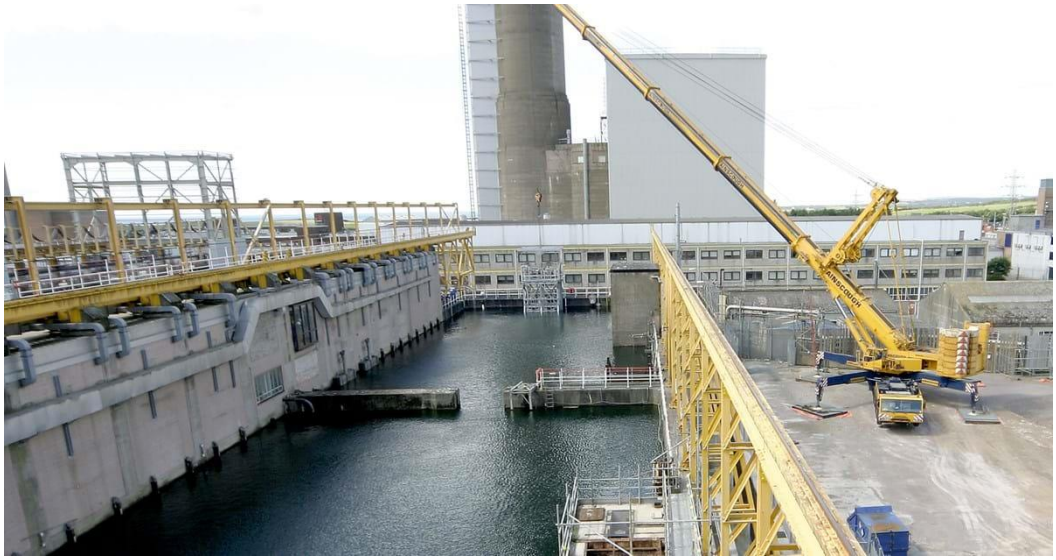

Figure 2.2 Pile fuel storage pond (RPS Group, 2022)

A range of nuclear waste analogues will be explored to understand whether the *in situ* non-contact method used here will be viable for deployment in the nuclear industry. The method employed in this thesis will be confirmed after exploration in various *in situ* techniques currently available and the requirements for a physical sensor. To be desirable by nuclear licensed sites, the physical sensor will need to be non-contact, *in situ*, provide information in real-time and be non-invasive (Degueldre, 2017). These specific properties are ideal for the use of a physical sensor in the characterisation of nuclear waste to maintain the integrity of the waste and equipment itself without the risk of contamination. To provide assurances that the technique chosen is ready for deployment the TRL systematic method is followed, this is shown below in Fig. 2.3 (Abaco, 2022).

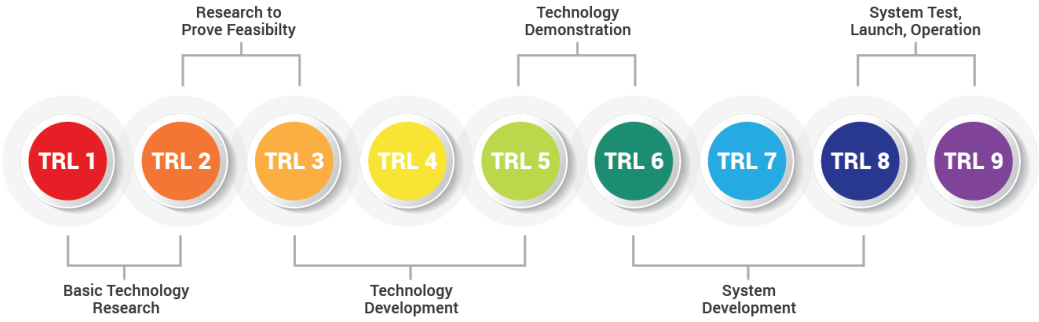

Figure 2.3 TRL (technology readiness levels) schematic (Abaco, 2022)

The '*basic technology research'* in TRL 1-2 is covered in section 2.7 in the literature review where examples of the non-contact method are explored. The '*research to prove feasibility*' will be shown by the literature covered. '*Technology development'* will be explored through the experimental procedures and results in Chapters 4-5. Simple homogeneous suspensions will be analysed for proof of concept and whether the physical characteristics required can be extracted, these properties include concentration, particle size and velocity. This will provide enough information to assist with the case for transport into an interim or permanent storage facility. '*Technology demonstration'* will be covered by results in Chapters 6-8. This is where complex mineral suspensions will be characterised, and flocculated suspensions will be monitored. In the nuclear industry, flocculation of polymers has been proven to improve the uptake of radioactive metal ions, therefore, it is imperative that the non-contact method is able to monitor flocculation and characterise the physical properties through that flocculation process (Rout *et al.*, 2006).

The nuclear waste analogues used are homogeneous silica glass bead suspensions, complex mineral suspensions of calcium carbonate and magnesium hydroxide (otherwise known as Versamag) and flocculated mineral suspensions of calcium carbonate and Versamag, (commercially magnesium hydroxide powder) is shown below in Fig. 2.4 (Hunter *et al.*, 2016; Lockwood *et al.*, 2021a; Tonge *et al.*, 2021). The homogeneous silica glass beads provide a simple homogeneous suspension which has been used in previous literature as a preliminary calibration

medium (Rice, 2013; Tonge *et al*., 2021). Colloids can be generated during the corrosion of nuclear waste glasses in groundwater, but, typically nuclear waste are concentrated suspensions of colloidal aggregates (Feng *et al*., 1994; Smith *et al*., 2010). Therefore, being able to prove that colloidal suspensions can be characterised using an *in situ* and non-contact method will prove that deployment is achievable in the nuclear industry. When specifically observing the Magnox ponds, the original fuel cladding was composed of Magnox (a magnesium-based alloy) which has now hydrolysed into a magnesium hydroxide-based sludge (Barlow *et al*., 2021). Therefore, the analysis of a magnesium hydroxide colloidal suspension will prove that a sludge with similar chemical composition can be characterised with accuracy.

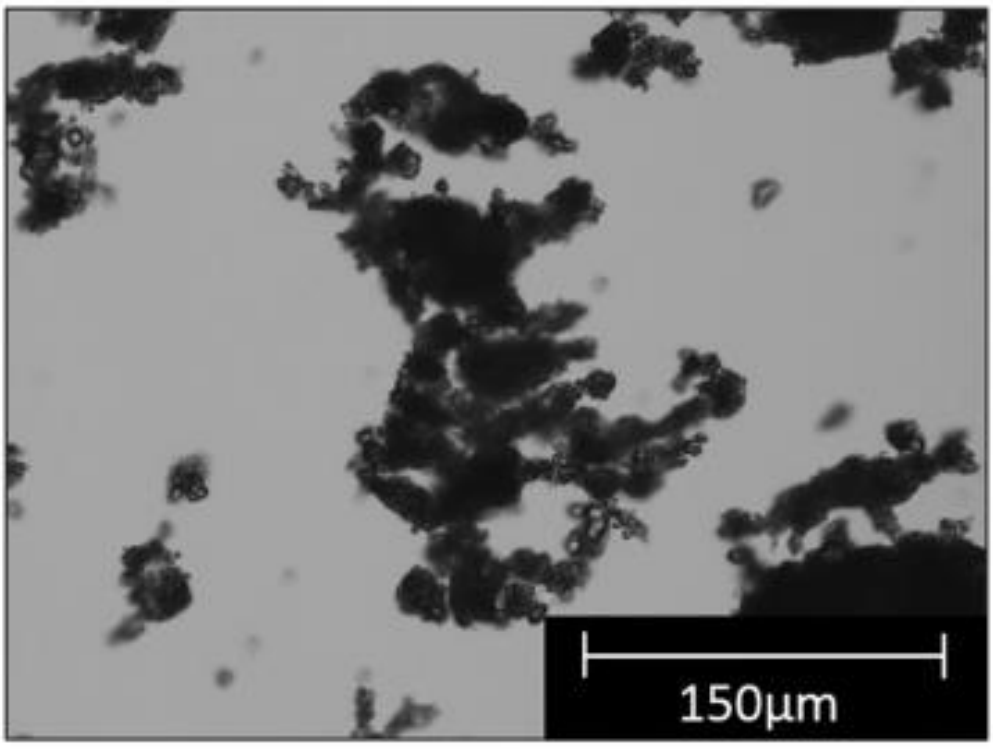

Figure 2.4 Optical microscope image of magnesium hydroxide suspensions mixed with 20 ppm 30% polymer (Lockwood, 2021a)

2.3 Why Characterisation

Quite often, sludges in the nuclear waste industry have been left over a certain period of time with no monitoring, sampling or characterisation to understand the physical properties of the waste. Properties like the particle size distribution, concentration and velocity are all physical properties which can be identified through characterisation methods. These three properties amongst others are required preliminarily for the safe and secure transport and storage of nuclear waste. If any properties are unknown, then the means for storage could be over-engineered or under-engineered which leads to excessive expense or potential integrity issues with the waste storage. Ideally for nuclear waste a non-contact *in situ* method which can provide the same accuracy as an invasive *in situ* technique would be identified (NDA, 2020). Through the characterisation methods described below, an ideal non-contact, non-invasive and *in situ* method will be specified.

2.4 Characterisation Methods

The accurate characterisation of the nuclear waste analogues identified will depend on the characterisation method chosen and developed throughout this PhD, therefore, the next section of this Chapter explores the characterisation techniques available. This next section will demonstrate the current infrastructure available in the nuclear industry for assay of nuclear waste. Only *in situ* methods are explored in the next section as i*n situ* characterisation allows the target medium, which in this case is suspensions or slurries, to be analysed on site. On the other hand, *ex situ* characterisation requires characterisation to be conducted off site. A number of methods are shown below which show *ex situ* characterisation, and why these techniques are not used for monitoring and control purposes in the nuclear industry.

When discussing *ex situ* characterisation, the author implies characterisation where analysis is conducted after material has been moved from its original position (NDA, 2022). For *ex situ* characterisation the author has looked at several

methods including microscopy. Specifically for microscopy, quite often the units are large and not easily moved which limits the flexibility for the technique in the nuclear industry (Hitachi, 2022a).

The function of all microscopes is to enlarge small features or objects which are otherwise invisible to human sight. This applies to both Scanning Electron Microscopy (SEM). Electron microscopes use an electron beam which can be utilised to form images. In an SEM images are obtained by scanning an electron beam of high energy onto a sample surface. The electrons are able to resolve finer features of material. The SEM consists of an electron column, specimen chamber and the computer. The electron column contains an electron gun which generates the electron beam. An electromagnetic lens will focus the beam into a few nano metre diameter probe. the electrons penetrate into the surface of a bulk sample, any secondary and backscattered electrons are collected and processed to obtain images (Ul-Hamid, 2018). Transmission Electron Microscopy (TEM) works in a similar way to SEMs except that transmitted electrons are detected with a movable detector at the bottom of the microscope column (Fultz and Howe, 2012).

In terms of sampling, the maximum specimen depth is approximately 100-200 nm for TEM (Sadamatsu *et al*., 2016). For SEM, the maximum sample size depends on the size of the specimen chamber. The maximum sample height is 145 mm for the Carl Zeiss EVO SEM (MA15) (Zeiss, 2022). A desktop TM3030 Plus, Hitachi SEM is also used which has a maximum sample height of 70 mm, an example is shown in Fig. 2.5 (Hitachi, 2014). Both microscopy techniques require extensively sample prep, Kenslea *et al.*, (2018) produces ultra-thin samples for analysis in the TEM which requires specialised preparation equipment. Guofu *et al*., (2022) studied the sample preparation of elastic silica aerogel which required little or no sample preparation, but samples are required which is not suitable for the nuclear industry where *in situ* analysis is preferrable. Amgarou *et al*., (2021) details recommendations for *in situ* measurements for characterisation in nuclear installations where *in situ* techniques are the only methods considered.

Figure 2.5. Hitachi desktop SEM (Hitachi, 2013)

When considering specimen prep, all specimens have to be dried before analysis in the Carl Zeiss EVO SEM (Hapca *et al*., 2015; Ul-Hamid, 2018). The extensive prepping and drying of the samples can often change the structure of the solid particles within the slurry leading to aggregation or shearing (Echlin, 2011). Therefore, the analysis of samples in microscopes is often not representative of the conditions *in situ.* However, for preliminary data and validation of characterisation results from other *in situ* techniques, microscopy is a very powerful tool.

Quite often throughout these papers, SEM images are used as a preliminary step for the reader to visualise the material being analysed which allows the reader to easily understand the scope of the work. Throughout this thesis, SEM and microscopy techniques have been utilised to help the reader visualise differences between various species of minerals and simulant material. Microscopy images allow the reader to differentiate between the materials and provides further insight into the particle size and shape of sediments which are suspended in aqueous suspensions for *in situ* analysis.

2.5 NON-ACOUSTIC PHYSICAL IN SITU CHARACTERISATION TECHNIQUES:

This section covers non-acoustic physical *in situ* methods. Optical techniques are one of the most diverse and universal techniques available across industries and includes a range of equipment including microscopes, Raman spectrometers, and a series of probes (Bishof *et al*., 2013; Simone *et al*., 2014; Sahin *et al.*, 2017; Kutluay, *et al.,* 2020; Lin *et al*., 2020). In this Chapter, only techniques which study the physical properties of particulate sludges and slurries are explored and therefore techniques which explore chemical properties such as Raman and NIR are out of scope (Kafle, 2019). Although these are robust methods which have been used extensively across industries and have been known to produce accurate results, all of these methods come with some drawbacks, all methods covered in this Chapter are summarised and shown in Table 2.1.

Table 2.1 Summary of techniques discussed in Chapter 2

Technique	Type	Advantages	Disadvantages	Particle Size Range	Particle Shape Limitations	Concentration Range	Portable/ Fixed	Literature			
Transmission electron microscopy (TEM)	*Ex situ*	Offer a very high magnification in comparison to SEM	Very expensive, large and immobile, extensive sample preparation	1-100 nm	None, this provides images of particles.	None, this provides images of particles.	TEM's are large and likely fixed equipment.	Sadamatsu *et al.*, (2016)	Kenslea *et al.*, (2018)	Amgarou *et al.*, (2021)	Guofu *et al.*, (2022)
Scanning electron microscopes (SEM)	*Ex situ*	Can examine larger samples than TEM	Very expensive, large and immobile, extensive sample preparation	200 nm – 200 μm	None, this provides images of particles.	None, this provides images of particles.	SEM's are large and likely fixed equipment.	Sadamatsu *et al.*, (2016)	Kenslea *et al.*, (2018)	Amgarou *et al.*, (2021)	Guofu *et al.*, (2022)
Ultrasonic attenuation spectroscopy (UAS)	*In situ*	Online characterisation of PSD	Requires the use of diluted samples	10 nm–3 mm	Most models are for spherical particles	Able to measure opaque systems without dilution.	Portable System	Takeda and Goetz, (1998)	Li *et al.*, (2005)	Falola *et al.*, (2021)	Belicard *et al.*, (2022)

Focused beam reflectance measurement (FBRM)	*In situ*	Probes are portable and can be mounted easily meaning experimental set-up is easy and less time consuming	The idealised chord length distribution (CLD) model assumes all particles are in the focal plane of the FBRM probe	0.1 – 1000 µm	Derivations are very complex for non-spherical particles.	Depends on individual particle visualisation. Suspensions need to have a clear distinction from dispersant.	Portable System	Ahmed *et al*., (2018)	Kyoda *et al*., (2019)	Kutluay *et al*., (2020)	Li *et al*., (2021)
Particle view and measurement (PVM)	*In situ*	Probes are portable and can be mounted easily meaning experimental set-up is easy and less time consuming	Limitations of the PVM is the post processing that is conducted once images have been produced images can sometimes be blurry	Greater than 2 µm	None, this is a visual instrument which provides images.	Depends on individual particle visualisation. Suspensions need to have a clear distinction from dispersant.	Portable System	Cardona *et al*., (2018)	Kutluay *et al*., (2020)	Li *et al*., (2021)	Wang *et al*., (2021)
Laser in situ scattering and transmissometery (LISST)	*In situ*	Self-contained battery-powered instrument	LISST is limited by particle size (2.5-500µm)	1.25 – 250 µm	Provides a particle size distribution which depends of the	1 – 800 mg/l	Portable System	Cartwright *et al*., (2011)	Felix *et al*., (2018)	Sandven *et al*., (2020)	

					orientation of particles, less accurate for non-spherical particles.						
Electrical Impedance Tomography (EIT)/ Electrical Resistance Tomography (ERT)	*In situ*	Low cost, portable	Properties are mainly for bulk flow	Do not measure particle size	Individual particle properties are not inferred, no limitations on shape.		Portable System.	Faia *et al*., (2020)	Ventura *et al*., (2008)	Wang *et al*., (2017)	
Ultrasonic velocity profiler (UVP)	*In situ*	Multiple transducers of varying frequency and active radii, easy to use	Transducers are expensive to replace	10-500 μm	All models for attenuation are for spherical particles.	For concentration inversions; up to 40 g/L	Portable System.	Hunter *et al*., (2011)	Kotze *et al*., (2011)	Rice, (2013)	Stener et al., (2014)
Acoustic Doppler current profiler (ADCP)	*In situ*	Samples rapidly	ADCPs cannot measure the water velocity near the streambed due to side-lobe interference	0-800 μm	All models for attenuation are for spherical particles.		Portable System.	Morlock *et al*., (2002)	Moore *et al*., (2013)	Fuller *et al*., (2013)	Son *et al*., (2020)

Acoustic Doppler velocimetry (ADV)	*In situ*	Does not require routine calibration	Large sample volume limits the resolution of turbulence eddy scales	0-800 µm	All models for attenuation are for spherical particles.		Portable System.	Harris *et al*., (2003)	VanderWerf *et al*., (2007)	Massey *et al*., (2011)	Jourdain de Thieulloy *et al*., (2020)
AQUAscat 1000	*In situ*	Flexible system, can monitor sediment in fresh and marine water environments	Lack of experimental data and theoretical expressions made it difficult to interpret the backscattered signal from the AQUAscat 1000	10-500 µm	All models for attenuation are for spherical particles.	For concentration inversions; up to 40 g/L	Portable System.	Hunter *et al*., (2012)	Bux *et al*., (2015)	Bux *et al*., (2017)	Bux *et al*., (2019)
Ultrasound array research platform (UARP)	*In situ*	Multiple transducers with varying frequency	Bulky transducers, bespoke system, complex coding needed to run the system	10-500 µm	All models for attenuation are for spherical particles.	For concentration inversions; up to 40 g/L	Portable System.	Hunter *et al*., (2011)	Cowell *et al*., (2015)	Hunter *et al*., (2020)	Tonge *et al*., (2021)

Electromagnetic radiation is a form of energy which is released and absorbed by charged particles. The wavelength range for electromagnetic radiation is termed the Electromagnetic Spectrum (EM). Electromagnetic radiation is used in various spectroscopic methods via different forms of interactions, these are: Absorption (radiation is absorbed), transmission (radiation passes through), reflectance (radiation reflected) and emission (radiation is emitted).

The range of techniques which are classified as electromagnetic methods are; MRI, thermal imaging, infared and near-infared imaging, ultraviolet imaging, X-ray methods, gamma ray imaging, optics (including microscopy). Some optical methods are covered in more detail below.

There are a wide variety of optical techniques which utilise lasers to provide information on particle size, chord length, and chemical composition through the production of images, chord length distributions and spectra (Simone *et al*., 2015; Asamoah *et al*., 2021). When taking a deeper dive into the analysis of particle size and concentration, *in situ* measurements can be taken using Doppler profilers (Vanrolleghem *et al.*, 2006; Tarud *et al*., 2010; Mohanarangam *et al*., 2013) image analysers (Concha *et al*., 2017; Derlon *et al*., 2017), focused beam reflectance measurement, etc (Simone *et al*., 2015; Kutluay *et al*., 2020; Kim and Ulrich, 2022; Liu *et al*., 2022). All techniques described above are explored in more detail below where specific results from each technique are shown using literature.

Huang and Zhang, (2021) utilised optical fibres to measure the backscatter intensity and determine the sediment concentration. The optical fibres were utilised to measure the natural sediment concentration after using natural sediment samples from coastal beaches for calibration, an example of the measuring instrument is shown in Fig. 2.6. This technique is purely used *in situ* and has limited potential for remote use as the optical fibre send out light signals which would not be able to penetrate through pipe walls.

Figure 2.6 Five-channel miniature optical fibre sediment concentration measuring instrument (Huang and Zhang, 2021)

Techniques which use radiation often produce spectra which can be analysed to understand the chemical composition of a suspension (Khodaei and Petaccia, 2017). X-ray techniques can also be utilised *in situ*, specifically X-ray diffraction (XRD) and X-ray fluorescence (XRF) (Ingale *et al*., 2020). XRD uses X-rays to irradiate the material and analyses the scattering angles to determine the chemical composition. XRF analyses the X-ray emitted from a sample when excited by an X-ray source (Wiescher and Manukyan, 2022). Both have been utilised for *in situ* analysis of slurries (Li *et al*., 2020; Bao *et al*., 2021). XRD has size limitations and is more accurate for measuring large structures which limits the ability of the technique for analysis whilst XRF has limitations on volume and elements it can detect (Natter *et al*., 2000; Muniz *et al*., 2016; Haschke *et al*., 2021). As the chemical composition of the slurries are unknown the author has chosen not to use XRF and XRD as primary techniques. Both of these techniques are used for solid particle crystal structure and therefore fall under physical and chemical characterisation, however, these methods will not provide information on particle size of aggregates (only on individual crystal size) and therefore, these techniques are not relevant to the nuclear sludge waste.

FBRM (focused beam reflectance measurement) and the PVM (particle vision and measurement) are both probe-based apparatus which can be inserted *in situ* for

analysis. The FBRM is a laser-based probe whilst the PVM is an optical probe, they have been grouped together as they are often used in tandem in literature (Kutluay *et al*., 2020; Hu *et al*., 2021; Li *et al*., 2021; Wang *et al*., 2021). Both probes are portable and can be mounted easily meaning experimental set-up is easy and less time consuming. In terms of results, the FBRM results in a chord length distribution which can be converted to the particle size distribution through a series of conversions (Lockwood *et al*., 2021a). On the other hand, the PVM produces images of the slurry *in situ* which can be used to determine particle size and concentration (Agimelen *et al*., 2018; Cardona *et al*., 2018; Shi *et al*., 2022). Limitations of the PVM is the post processing that is conducted once images have been produced (Cardona *et al*., 2018; Li *et al*., 2021). Agglomeration is difficult to detect as the images can sometimes be blurry, as the probe is inserted *in situ*, material can settle on the probe window causing obstruction or the particles may move past the window too fast for clear images (Jia *et al*., 2008). Therefore, the PVM is a valuable technique but collecting images of the slurry *in situ* produces unreliable results. The FBRM was also used by Kim *et al*., (2012) to understand whether the FBRM could be used to monitor precipitation. *In situ* probes were used to determine the chord length distribution measurements. An example of the results obtained from the FBRM are shown in Fig. 2.7 where the chord length distribution can be seen. This chord length can be attributed to the particle size with assumptions on the suspension medium. Example images from the PVM are also shown in Fig. 2.8 where the suspended particles can be seen. The images are slightly blurry which makes analysing the PVM images difficult as post processing is required.

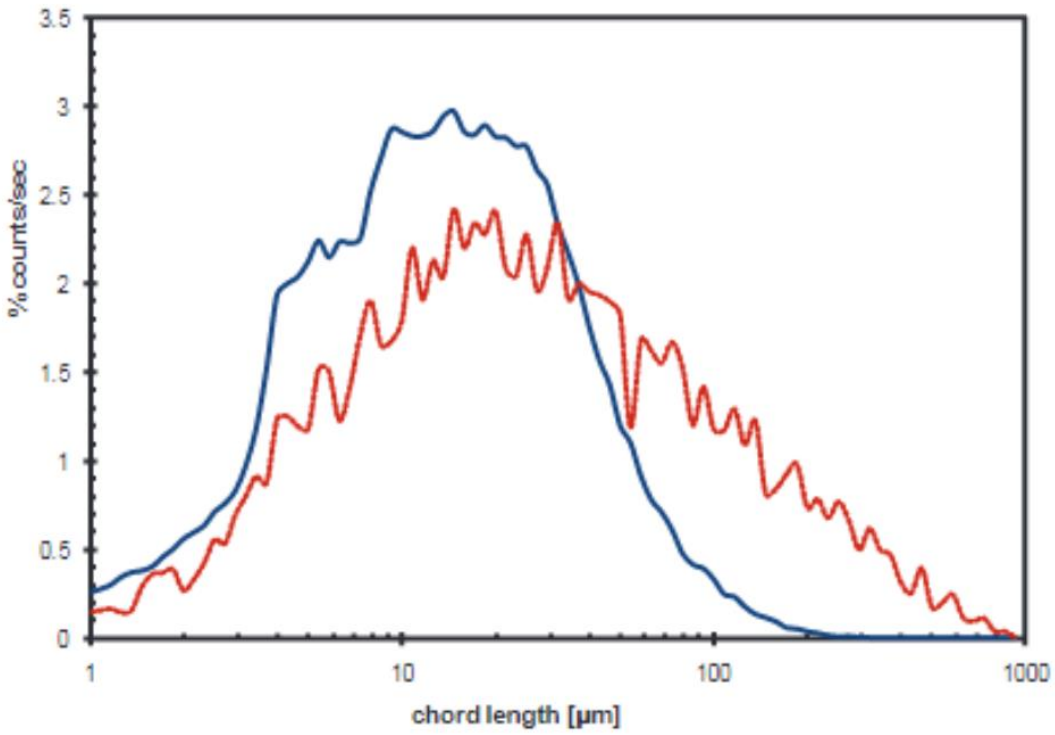

Figure 2.7 FBRM spectra of solids precipitated in Pz-H_2O solutions: in 34.5 and 61.5wt% Pz-H_2O solutions. Lines: (solid) 34.5 wt, (dashed) 61.5 wt % (Kim et al., 2012)

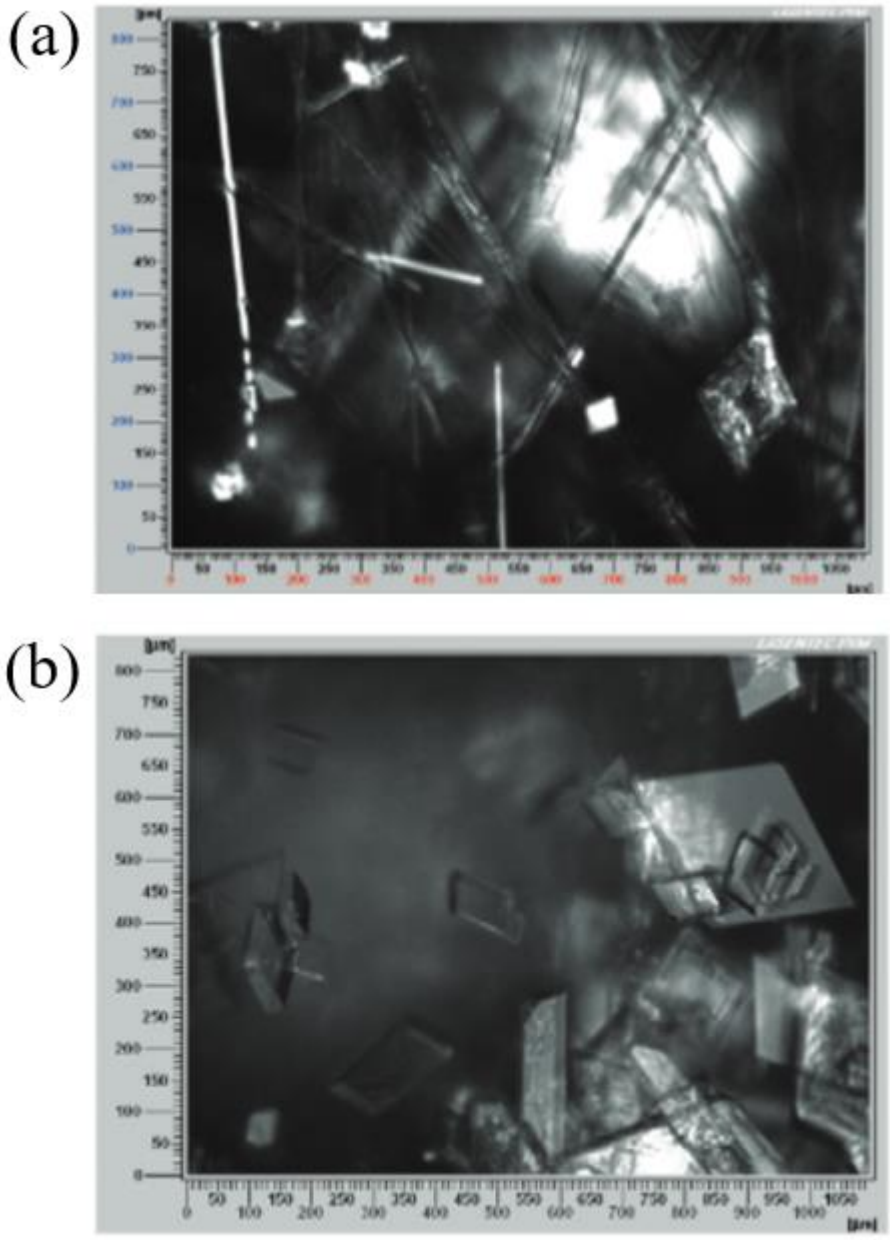

Figure 2.8 PVM pictures of crystals in the 61.5wt% piperazine solution: within 1 min (a) and in 4 min (b) after crystallization starts (Kim et al., 2012)

The FBRM has its own limitations, the idealised CLD model assumes all particles are in the focal plane of the FBRM probe (Ahmed *et al.*, 2018; Kyoda *et al.*, 2019). The FBRM also analyses the particles only in the focal plane, so unless the particles are perfectly spherical, the diameter of the particles will be different depending on the focal plane the FBRM is situated at (Grabsch *et al.*, 2020;

Acevedo *et al*., 2021). Despite the fact that the CLD may not be representative of the particle size distribution (PSD), the FBRM is still a powerful tool which can be used to monitor the PSD of particles *in situ* (Kutluay *et al*., 2020; Hu *et al*., 2021; Li *et al*., 2021; Wang *et al*., 2021). The FBRM can be used in this PhD as an in-line monitoring tool for changes in particle size (Shi *et al*., 2022). Owen *et al*., (2008) also used the FBRM as an in-line measurement technique on pipelines where the FBRM probe was inserted *in situ*. Owen *et al*., (2008) also used the FBRM to monitor aggregation and polymer-bridging flocculation in mineral systems which shows that it is a versatile and useful technique for both *in situ* and in line monitoring.

Following on from the FBRM, another laser-based technique is LISST (laser *in situ* scattering transmissometer) which measures the near-forward angular scattering distribution to determine a particle size distribution of slurries or suspensions in their environment (Sandven *et al*., 2020). The LISST can also be used to determine the mean density, mean settling velocity and volume concentration, LISST is limited by particle size (2.5-500 µm) which restricts the samples for analysis (Cartwright *et al*., 2011). Felix *et al.*, (2018) investigated suspension of fine sediment where the measurement range of the LISST was limited to 1.5 g/L which is highly restrictive to testing. Felix *et al*., (2018) produced volume concentration histograms and suspended sediment concentration plots but the degree of limitations prevented the LISST from being a valuable technique in the scope of this PhD. For the scope of this thesis a wide range of concentration environments are required as the specific concentration of nuclear sludge suspensions is unknown. Example results are shown below for the LISST from Felix *et al*., (2018).

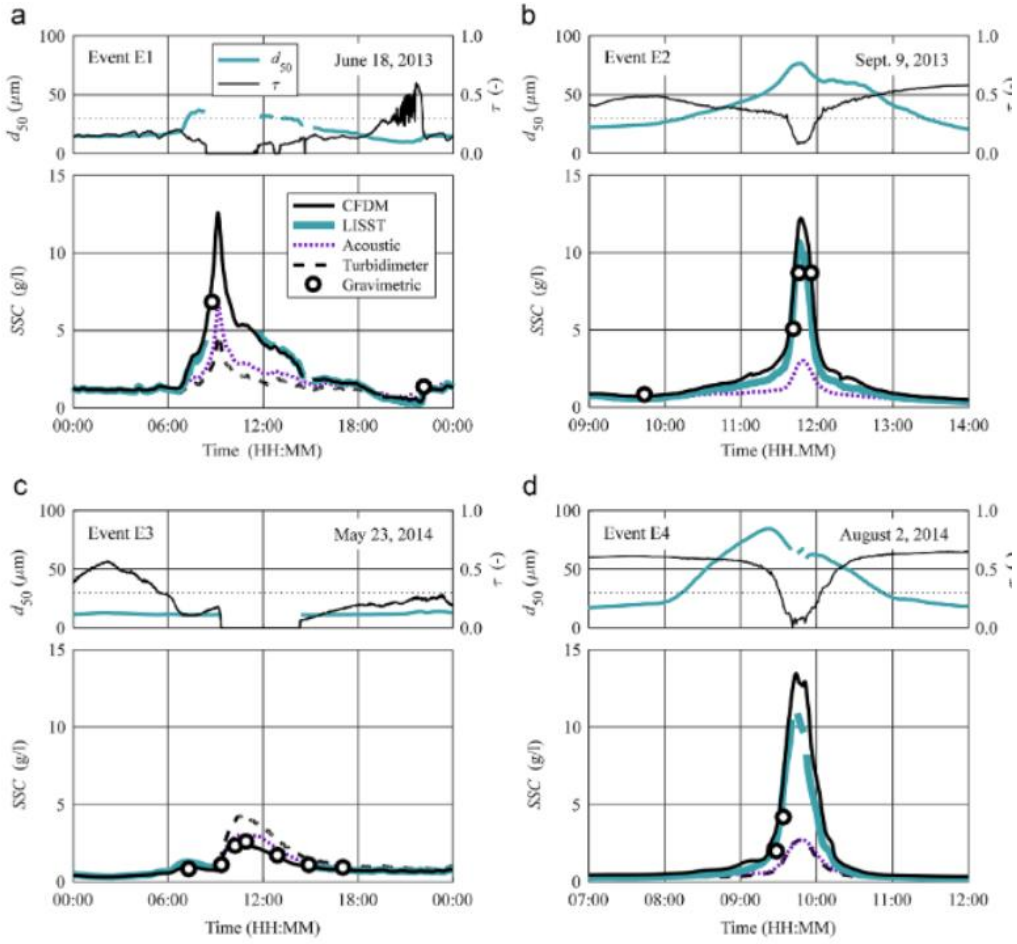

Figure 2.9 Time series of the median particle diameters, d_{50}, and of the optical transmission, τ, obtained from the LISST as well as of the suspended sediment concentration,(SSC), obtained from various techniques, measured at the HPP Fieschertal during the four sediment transport events defined in Fig. 11 (Felixe et al., 2017) (Fig. 12a modified from Felix et al., (2016a); Fig. 12b modified from Felix, (2017); Fig. 12c modified from Felix et al., (2016b)) (Felix et al., 2018)

Tomography techniques can be used to analyse industrial environments. The spatial distribution of phases, relative velocity between phases can be used for flow characterisation using Electrical Impedance Tomography (EIT). Non-invasive data collected by EIT can enable the reconstruction of cross-section images which provides material distribution profiles of a suspensions flowing through a pipe. EIT is simple and has a low cost, however, EIT is preferred for slug flows. When considering that the properties of individual particles is a

preferred outcome, EIT is not relevant for this specific thesis (Faia *et al*., 2020). EIT has been used by Ventura *et al*., (2008) to characterise pule fibre suspensions using EIT rings which were attached to a pilot rig. Ventura *et al*., (2008) were able to measure changes in pressure and velocity, however, in this thesis, the research goal is to provide specific properties of individual particles such as; particle size, particle concentration, attenuation coefficients for homogeneous suspensions.

Electrical Resistance Tomography (ERT) is also a technique which should be noted. ERT has been used in a novel approach with a dual modality ERT-Electrical Capacitance Tomography (ECT) by Wang *et al*., (2017) to visualise gas-oil-water flow in horizontal pipelines. This method incorporates information from spatial, temporal and frequency dimensions where an ERT-ECT sensor is mounted onto a pipeline and fused ECT and ERT images are taken. The results can be used to clearly identify individual phases when all phases are separated. However, artificial errors are introduced as a result of linear interpolation used in data alignment due to differences in speed and definition of the ERT and ECT. The results only show the bulk flow and are less relevant to this project, but perhaps can be considered for other work where bulk flow is to be characterised. Tomography data from Wang *et al*., (2017) is shown below in Fig. 2.10. As shown in Fig. 2.10, ERT and ECT are particularly valuable for the visualisation of slug flow however not so much for a graduated change in suspensions.

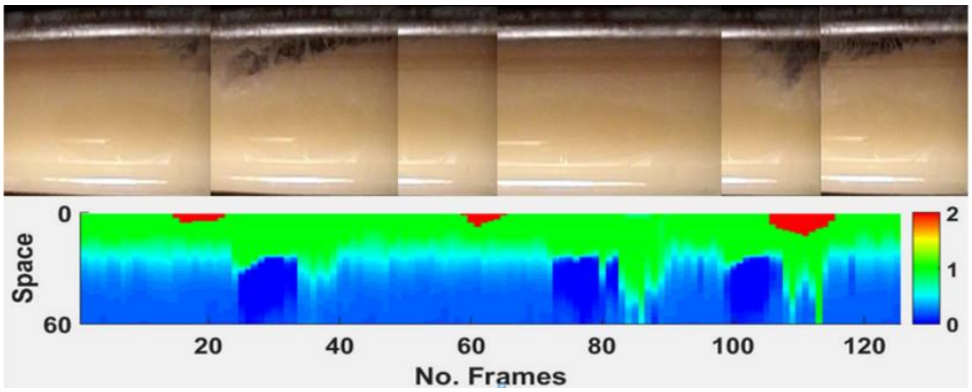

Figure 2.10 Visualisation Result of Plug Flow over 125 frames of measurement time 2 seconds using an ECT and ERT fused approach (Wang et al., 2017)

2.6 Acoustics Background

Acoustics is one of the branches of classic physics that has the oldest origins and also has the most modern applications. Experimentation into this branch of physics started with vibrations of strings and sound in music and led to computation of speed of sound, to now where acoustics can be used to analyse sediments, restaurant acoustics and architecture (Namorato, 2000; Randall, 2012; Butler and Sherman, 2016). Acoustics can also be used for defence purposes where sound waves can be utilised for the detection of nuclear weapons in surrounding waters (Butler and Sherman, 2016). Acoustics is specifically a branch focused on the properties of sound, where sound can be defined as vibrations transmitted through a medium (e.g., air, water, and metals) (Morris, 1992).

Ultrasonics is an area of acoustics which is concerned with sound vibrations using frequency ranges above audible levels, in other words, sound which exceeds 20 kHz (Butler and Sherman, 2016). Ultrasonics works on the principle of the transmission and reflection of acoustic energy (Bains *et al*., 2008). An ultrasonic transducer is a device which can convert electrical energy intro ultrasound energy (Denault *et al*., 2016). Transducers are probes (typical dimensions, length: 8 cm, diameter: 3 cm, (Met-flow, 2022) that can be suspended or attached to any flat surface. A pulse is propagated from the probe and the reflection is received by a probe, this can be a transducer which acts as transmitter and reciever or separate probes (Butler and Sherman, 2016). An ultrasonic transducer refers to a capacitive or a piezoelectrical probe, in this thesis, the focus is on piezoelectrical (Bakshi and Bakshi, 2020). These are electroacoustic probes that convert electrical energy into acoustic energy and vice versa. This functions on the principle of pressure. When a voltage is applied to the piezoelectric crystal it expands or contracts depending on the voltage polarity, this energy is then converted to ultrasound where the frequency depends on the crystal radius and thickness (El-Badawy, 2008). The development of underwater transducers expanded rapidly during the twentieth century (Randall, 2012; Butler and Sherman, 2016). An example of a piezoelectric transducer is shown below:

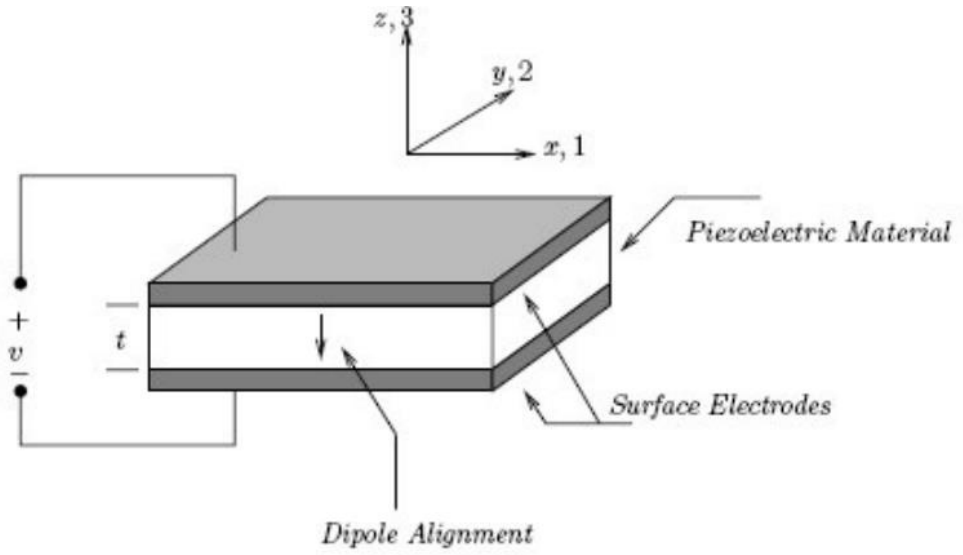

Figure 2.11 Schematic diagram of a piezoelectric transducer (El-Badawy, 2008)

The sound that propagates from the ultrasonic transducers can either reflect or attenuate (loss of sound), backscatter is the reflection of that sound signal back in the direction of origin, back to the transducer (Nakamura, 2012). An acoustic backscatter system analyses the strength of the backscattered signal and uses this to calculate sediment concentration (Rice, 2013; Tonge *et al*., 2021). The specific acoustic backscatter theory is covered in Chapter 3 and this section only covers the principles behind the theory. Acoustic backscatter systems have been used extensively in literature to characterise sediment suspensions (Rice *et al*., 2015; Hunter *et al*., 2016; Tonge *et al*., 2021). Acoustic backscatter systems function on the principle of a single transmitter reciever sending a pulse through a suspension. The system itself is relatively mobile where a transducer can be connected to the ABS and suspended in a suspension or mounted onto a flat surface (Rice, 2013; Hunter *et al*., 2016; Tonge *et al*., 2021). Data can be collected in real-time from ABS. The signal which is not scattered directly back to the transducer is lost, this loss of sound is called attenuation (Butler and Sherman, 2016). An example of an ABS set-up is shown below in Fig. 2.12.

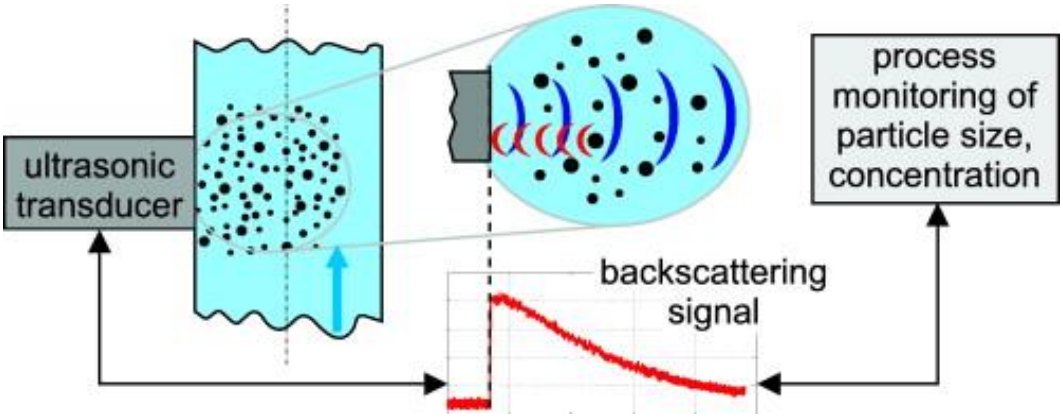

Figure 2.12 ABS set-up schematic (Weser et al., 2014)

Attenuation of a signal can be dissected into two mechanisms: scattering and viscous absorption (Urick, 1948; Betteridge *et al*., 2008). Scattering leads to the energy of the ultrasonic pulse being redirected, this contributes to attenuation as less energy reaches the detector. Viscous absorption is a hydrodynamic effect which is caused by shear friction in the boundary layer around the solid particles. This effect is sensitive to inter-particle interactions and leads to the loss of sound, both contribute to attenuation. From the received backscatter signal, the voltage of the pulse can be calculated over the measurement distance (Dong *et al*., 2020). This is then used to establish a range correct logarithmic voltage value which is utilised to extract the attenuation coefficient (Rice, 2013). This process is described in more detail in Chapter 3.

Ultrasonic attenuation spectroscopy uses ultrasound waves to probe a sample, attenuation is then measured and an attenuation spectrum is produced. The ultrasonic attenuation spectra is sensitive to both size and concentration (Mougin *et al.*, 2003) The technique is similar to acoustic backscatter systems where the techniques are non-destructive, give information on the particle size and can be used in-line. However, UAS gives information on the compressibility as well (Dukhin and Goetz, 2009). The main disadvantage of UAS is that several thermophysical properties are required and need to be known such as adiabatic compressibility and thermal conductivity (Nollet, 2004). In cases like the nuclear

waste, thermophysical properties are unknown and can be difficult to obtain as these are complex wastes.

Both UAS and ABS can be used to examine opaque and concentrated systems, for UAS there is a complex theory to convert the crystal size distribution whereas for the ABS, the theory is simple and does not require extensive knowledge of other thermophysical properties (Mougin *et al*., 2000). An example of an attenuation spectrum is shown below in Fig. 2.13. There is limited mention of UAS as a technique in the literature review because it requires extensive knowledge of properties that are difficult to determine from nuclear wastes and because the analysis to determine particle size is very complex (Mougin *et al*., 2000). Backscatter systems also use a single transmitter-reciever probe whereas spectroscopic systems use a separate transmitter and reciever which makes the equipment set-up more complicated (Richter *et al*., 2005).

The general particle size range for both techniques is shown in Table 2.1 where the general range for UAS (10 nm to 3 mm (ISO, 2006)) and ABS (10-500 μm). The size range for ABS is more limited but can provide more detailed information (e.g., particle concentration via dual frequency inversions) on particle suspensions. The general particle size of slurries ranges from submicron to 100 μm, therefore, although the ABS has a lower limit of 10 μm, the majority of the suspensions can be analysed by ABS (Chun *et al*., 2011).

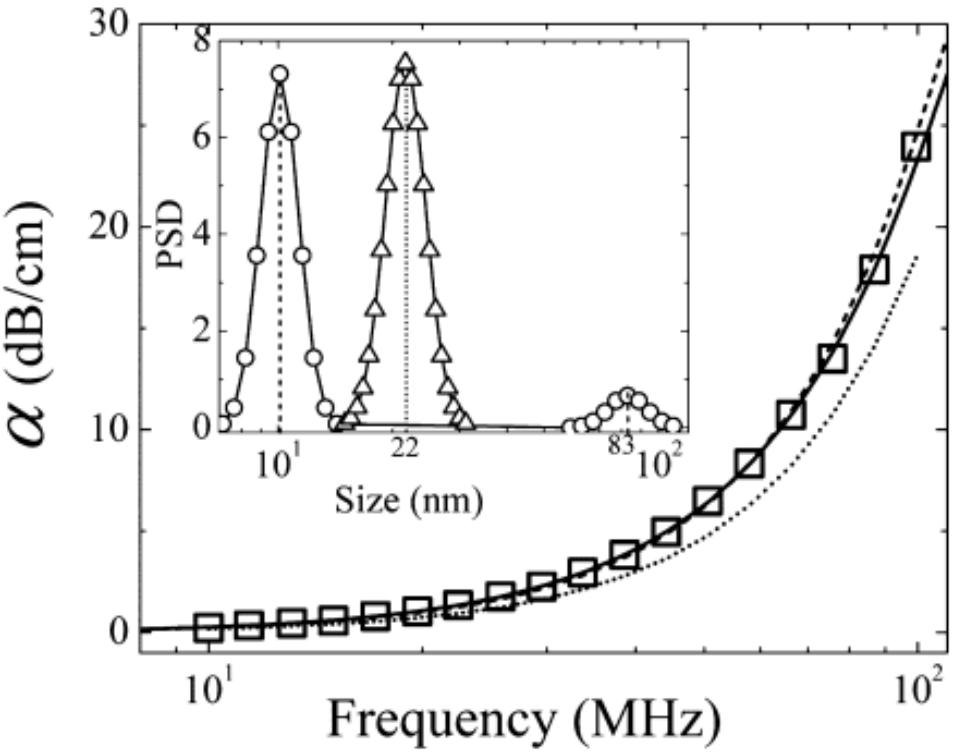

Figure 2.13 Attenuation spectrum (squares) for a 3% w/v Laponite suspension, dashed and solid lines are theoretical fits. The dotted line corresponds to the intrinsic attenuation in pure water. Unimodal and bimodal particle size distributions from the theoretical fits are plotted in the inset with triangles and circles, respectively (Ali and Bandyopadhay, 2013)

The general applied attenuation theory does not work for data extracted from attenuation spectroscopic systems and there is limited frequency data which can limit the applicability of the instrument on various suspensions mediums. The separate transmitter-reciever also needs to be positioned 180° from the pulsing transducer, this places limitations on the experimental set-up whereas the ABS transducers can be mounted anywhere at any angle, as long as the transducer face is mounted on a flat edge, this provides more flexibility in the set-up (Falola *et al.*, 2021).

2.7 ACOUSTIC PHYSICAL CHARACTERISATION TECHNIQUES

Acoustic systems are able to determine a range of particle properties *in situ* whilst the methods are flexible and can be applied in industry (Hunter *et al*., 2012; Thorne and Hurther, 2014; Stener *et al*., 2016). Acoustic techniques are applied environmentally and for monitoring purposes (Thorne and Hanes, 2002; Wilson and Hay, 2015; Guerrero *et al*., 2016). Settling in sediments can be tracked (Simmons *et al*., 2010; Hunter *et al*., 2012; Bux *et al*., 2015; Simmons *et al*., 2020), sediment flow velocity can be measured, and concentration profiles can be developed (Hunter *et al*., 2020; Wang *et al*., 2021).

The application of acoustics as an analysis method has been predominantly used in the marine and defence sector to analyse marine life on the seafloor, see Fig. 2.14 (Mondal *et al*., 2019; Ali and Miraz, 2020; Goossens *et al*., 2020; Zhang *et al*., 2020; Li *et al*., 2021; Rideout, 2022; Thomson and Binder, 2021; Wang *et al*., 2021). The same principle can be utilised to analyse moving sediment in a tank or pipe. Acoustics offer non-destructive *in situ* analysis of suspensions with fast data collection in real-time (Duchene *et al*., 2018; Shevchik *et al*., 2019; Wasmer *et al*., 2019; Hossain *et al*., 2020). Acoustics require ultrasonic transducers which act as pulsers and receivers, signals are pulsed and then detected using the reciever (Butler and Sherman, 2016). Ultrasonic transducers have been used in tandem with a variety of suspensions and sedimentologists have utilised acoustics to analyse sediment suspensions (Szupiany *et al*., 2019; Vyse *et al*., 2020; Sahin, 2021). Acoustic methods pulse a signal which can either be scattered or reflected, the level of signal scattered and detected provides a route for acoustic profiling which can lead to characterisation of particle size, concentration, and velocity (Moore *et al*., 2013; Butler and Sherman, 2016).

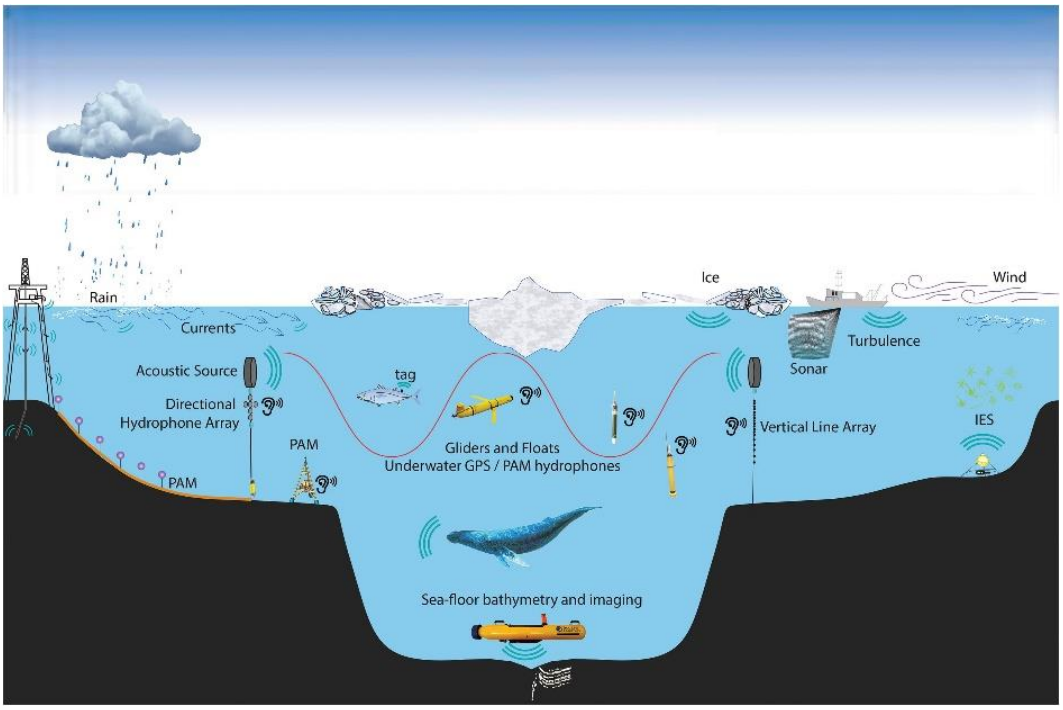

Figure 2.14 Schematic of acoustics used to analyse seafloor (Howe et al., 2019)

Typically, the echo amplitude is used to analyse suspensions, this requires the use of acoustic backscatter systems (Lee *et al*., 2018; Fernandez *et al*., 2021). There are a variety of systems used, namely the following: UVP - ultrasonic velocity profiler (Met flow Ltd) (Conevski *et al*., 2018; Gaeta *et al*., 2020; Montes-Quiroz *et al*., 2020), ADV - acoustic doppler velocimeter (Son Tek) (Chmiel *et al*., 2018; Canilho *et al*., 2022), ADCP - acoustic doppler current profiler (Priego-Hernandez *et al*., 2019; Klema *et al*., 2020), AQUAscat 1000 (Aquatec Group Ltd) (Bux *et al*., 2019; Smerdon, 2020; Brouwers *et al*., 2022) amongst others which have been used for characterisation over the years. This Chapter will go through the advantages of each system and characterise the methods by the probe placement. Ideally, this PhD is hoping to be able to move on towards remote analysis of suspensions, therefore, it is imperative that a system is chosen which can be utilised remotely to limit risk of contamination in the nuclear industry.

Acoustics are operational in a range of concentration suspensions, are not limited to dilute suspensions and have simple, flexible set-up (Williams *et al*., 1990; Challis *et al*., 2005; Gray and Gartner, 2009; Bontha *et al*., 2011). This cannot be

said for other *in situ* instrumentation which exists on active plants, examples of which are turbidity meters and electrical impedance techniques (Shukla *et al*., 2007). Acoustics also penetrate further than light waves (Temkin, 2005) and allow for characterisation of opaque and more concentrated suspensions (Hauptmann *et al*., 2002). Acoustics can be used *in situ* and in other placement types, therefore, the literature reflects the use of acoustics in an *in situ* placement first. There are limitations to using ultrasonic methods for particle or slurry sizing. These include the limited particle size range, see Table 2.1. Although most nuclear waste slurries will fall in the particle size limits of (10 – 500 μm), analysing particles smaller than 10 μm is complex. There are also limitations on the particle concentration, whereby concentration could not be predicted accurately using the dual frequency inversion method above 40 g/L (Tonge *et al*., 2021).

Takeda and Goetz, (1998) used ultrasonic attenuation spectroscopy (UAS) to determine the particle size distribution of suspensions where the system was utilised to monitor flocculated particles in a concentration slurry. In this paper, Takeda and Goetz, (1998) used UAS an *ex situ* technique which requires the sample to be pumped into a measuring chamber. If used, there is a high likelihood that the measuring chamber would become contaminated over time which decreases the lifetime of the equipment. However, there are online versions of ultrasonic spectroscopy devices (where the pitch-catch cell is inserted into the dispersions), these are explored below in section 2.7.1.

2.7.1 Acoustic physical in situ characterisation techniques:

There are many different types of acoustic techniques for *in situ* characterisation. The most common techniques are ultrasonic attenuation spectroscopy (UAS) and acoustic backscatter systems (ABS), both use different principles, this is shown above where the theory of UAS and ABS are covered. UAS can also be used *in situ* using online versions (where the pitch-catch cell is inserted into the dispersions). Mougin *et al*., (2000) used a commercial ultrasonic spectrometer (Ultrasizer by Malvern Instruments Ltd) *in situ* to examine solution phase crystallisation processes.

Falola *et al*., (2021) presented a method to determine unknown physical properties required to apply UAS for particle size distribution measurements where the properties are unknown or too difficult to measure. This was achieved using a model identification approach which iteratively determined the unknown properties from the attenuation spectra. This shows the complexities of establishing physical properties and using UAS where extensive modelling or physical properties need to be known for accurate use of the method. An example of the attenuation spectra is shown below. UAS has also been discussed in section 2.6 where the technique was shown to have complex theory, larger set-up and more preliminary information required in comparison to ABS. Therefore, UAS is not considered as a viable technique and is not discussed in detail within this literature review.

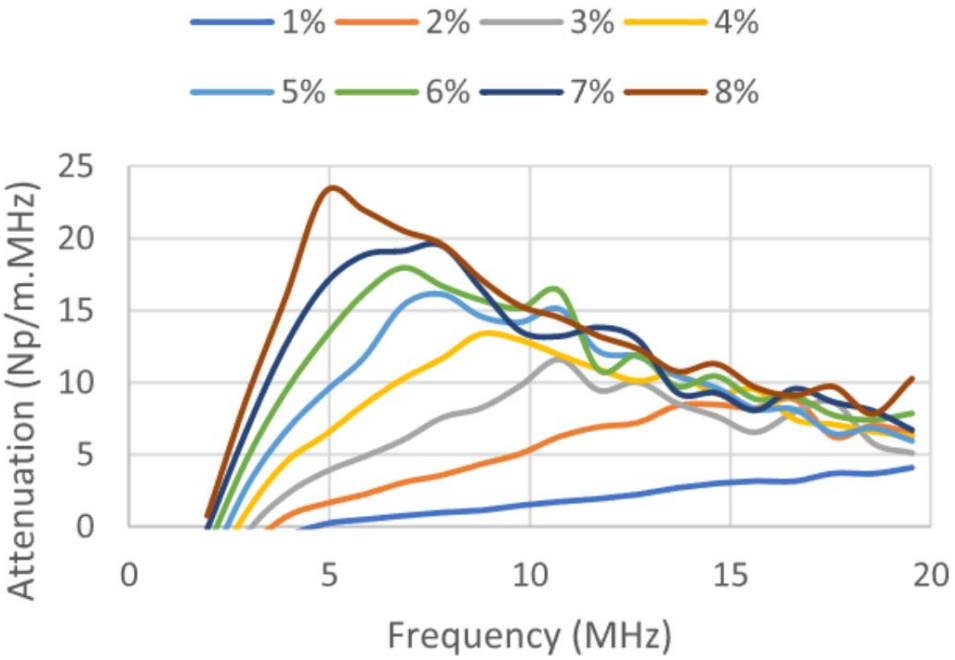

Figure 2.15 Attenuation spectra for $SrCL_2.6H_20$ at different concentrations (Falola et al., 2021)

Acoustics have been used to study particle flow with minimal intrusion and low running costs (Shevchik *et al*., 2018; Nsugbe *et al*., 2019; Poddar and Tandon,

2019; Prince *et al*., 2019; Wilson, 2022). There are several acoustic systems which use doppler shift measurements, this includes an ultrasonic velocity profiler (UVP) which uses a single frequency transducer (Hunter *et al*., 2011; Stener *et al*., 2014). Large dilute depths can be analysed using acoustic Doppler current profiling (ADCP) (Son *et* al., 2020). Son *et al*., (2020) analysed algal blooms using ADCPs over large dilute depths, whilst acoustic doppler velocimetry can be used for point profiling (ADV) (Liu *et al*., 2022). These acoustic Doppler profilers quantify the doppler shift of the baseline frequency and are used to track particle velocities in multiple applications such as environmental and engineering (Kostaschuk *et al.*, 2005; Hosseini *et al.*, 2006; Harbottle *et al*., 2011; Kotze *et al.*, 2011). Acoustics backscatter systems on the other hand measured the returned echo voltage from an ultrasonic pulse (Shi *et al*., 1999; McLelland, 2010). The ultrasonic velocity profiler above can be used as an ABS by measuring the echo amplitude as well as the velocity (Metflow, 2021). Acoustic backscatter systems (ABS) can use multiple frequency transducers and allow for *in situ* profiling of suspensions with minimally intrusive analysis (Metflow, 2021). The theoretical analysis for backscatter profiles from ABS data has been fully resolved by Thorne and Hanes, (2002) and Betteridge *et al*., (2008) for spherical glass dispersions. This allows the author to fully characterise ABS data by quantifying concentration values from the measured echo amplitude data (Hunter *et al*., 2012). Both acoustic doppler profilers and ABS were explored below when investigating the use of acoustics for *in situ* characterisation.

Panetta *et al.*, (2012) conducted on-line measurements of particle size and concentration using acoustic scattering properties. Panetta *et al.*, (2012) learned that existing methods become inaccurate at highly concentrated suspensions due to the dominant multiple scattering which requires complex mathematics and extensive expressions. Therefore, Panetta *et al*., (2012) measured the backscatter and diffuse field to characterise particle slurries of mixed glass particles. Multiple transducers of varying frequencies were mounted in a Teflon chamber to produce frequency dependant attenuation plots for two species of glass where the larger species were found to attenuate more. This provides evidence that the author is

able to use multiple frequency transducers to analyse suspensions in a range of environments.

Benoit-Bird and Waluk, (2021) found that understanding the behaviour of fish *in situ* was not achievable using aerial observations (Freon *et al*., 1992) as this would only show aggregations near the surface whilst visual observation is difficult due to decreased visibility underwater (Jaffe and Dunn, 1988). This led Benoit-Bird and Waluk, (2021) to investigate the use of ultrasonics and acoustic scattering properties for analysis as most techniques for subsurface imaging are invasive which would change the behaviours of the fish (Oppedal *et al*., 2001). Echosounders have been relatively successful in identifying shape and edge structure to identify groups of fish (Hewitt, 1975; Misund *et al*., 1995; Petitgas and Levenez, 1996; Brierley and Cox, 2010). Benoit-Bird and Waluk, (2021) found that using single frequency data provided echoes for schools of fish however, the single frequency was unable to segregate other fish or zooplankton. Acoustic scattering followed a distinctive pattern for schools of fish which require validation and modelling before they can be identified. This shows that acoustics can be used for a multitude of sectors which shows the flexibility of acoustics as a characterisation method. Acoustics has also been used to monitor the cleaning of food fouling in pipes, this was conducted using ultrasonic measurements (Escrig *et al*., 2019; Escrig *et al*., 2020). The use of ultrasonic measurements was an effective method for detecting fouling in circular pipes, the pipes were constructed of stainless steel and PMMA. Ultrasonics have been used to monitor mixing using in-line, non-invasive sensors where the sensors showed accuracy of up to 96.3% for honey-water blending (Bowler *et al*., 2020). This shows the efficiency of using ultrasonics to monitor mixing processes. The film thickness can also be monitored using ultrasonic pulse echo techniques as shown by Al-Aufi *et al*., (2019).

2.7.1.1 Acoustic Doppler Profilers

Three main profilers were investigated here, an ADCP (acoustic Doppler current profiler), ADV (acoustic Doppler velocimeter) and an ACVP (acoustic

concentration and velocity profiler) which were found to be dominant in literature (Kostaschuk *et al.*, 2005; Hosseini *et al.*, 2006; Kotze *et al.*, 2011; Jourdain de Thieulloy *et al.*, 2020; Son *et* al., 2020). The ADCP was found to give accurate concentration measurements where Moore *et al.*, (2013) was able to show the effect of grain size on attenuation regime (see Fig. 2.16) whilst Thorne *et al.*, (2021) was able to show the limitations of the ADCP to analyse mixed sediments.

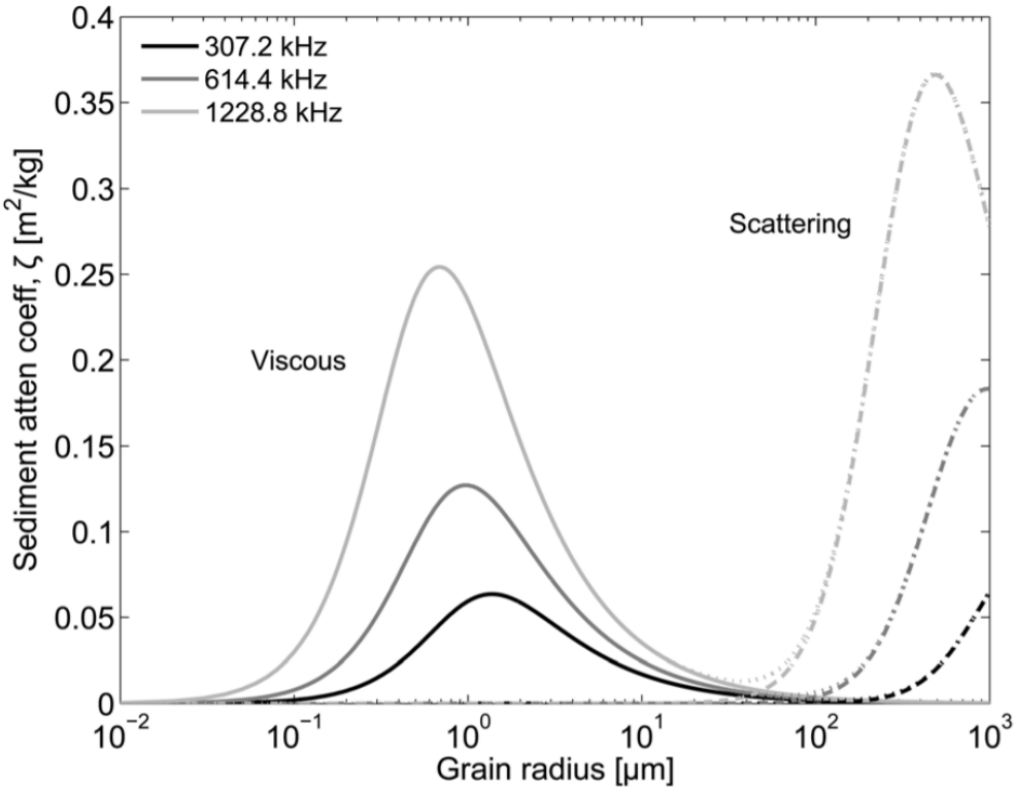

Figure 2.16 Sedimentation attenuation coefficients for a suspension on mono-sized particles (Moore et al., 2013)

ADCP

Moore *et al.*, (2013) used the ADCP to monitor the concentration and size of sediment particles suspended in fluid where multi-frequency profilers were used at 300, 600 and 1200 kHz. ADCPs are predominantly used to measure both flow speeds and sediment transport in rivers where an ADCP could be attached to a

traversing motorboat. Moore *et al*., (2013) specifically used side looking ADCPs which can be used to monitor flow speed (Morlock *et al*., 2002). Moore *et al*., (2013) was able to plot the viscous and scattering attenuation coefficients using Richards *et al*., (2003) and Thorne and Meral, (2008) where the viscous attenuation peaked at a grain radius of ~0.8 μm. It was found that an increase in operating frequency led to an increase in the magnitude of the peak at a lower grain radii. This correlated to a peak viscous attenuation of 0.8 μm when using a 1.2 MHz frequency in comparison to the peak viscous attenuation at 2 μm when using a 0.3 MHz frequency, see Fig. 2.17. The scattering attenuation coefficient followed the same relationship, but the peaks were at a higher grain radius where the attenuation peaked at an 800 μm grain radius using a 1.2 MHz transducer. The two regimes show that the grain radii have an effect on the attenuation where a particle size distribution of around 0.8 μm leads to a high viscous attenuation coefficient and limited or no scattering attenuation. Whilst at 800 μm, the attenuation is predominantly from scattering attenuation. This was the main result from Moore *et al*., (2013) which can be used as a reference for any acoustic system, see Fig. 2.16. The ADCP was used to monitor the concentration of a suspension, this confirms that acoustics can be used to monitor concentration in this thesis for other dispersions in varying environments.

Fuller *et al*., (2013) also used the ADCP to measure the suspended solids concentration in aqueous suspensions. Fuller *et al*., (2013) used colloidal suspensions which is useful for use in the nuclear industry where the size of the particles is unknown. Fuller *et al*., (2013) found that environments with elevated background noise could overshadow the signals due to the scattered particles where increased background noise was due to higher bubble concentrations. This is important as the author will need to limit the production of bubbles to enhance the signal detection of colloidal aqueous suspensions.

Thorne *et al*., (2021) was able to use the ADCP to monitor particle size in mixtures of muddy and sandy suspended sediments where most previous literature used suspensions which were considered to be in the sand regime (Vincent *et al*.,

1982; Young *et al*., 1982; Hanes *et al*., 1988; Lynch *et al*., 1991, 1994; Hay and Sheng, 1992; Thorne and Hardcastle, 1997; Villard *et al*., 2000; Thorne *et al*., 2002; Cacchione *et al*., 2008; O'Hara Murray *et al*., 2011; Moate *et al*., 2016). However, it was found that the suspended sediment size was over estimated, and concentration underestimated which shows the limitations of the ADCP in tandem with the acoustic theory where the backscatter characteristics could be expressed non-dimensionally using the form function (Sheng and Hay, 1988; Hay, 1991; He and Hay, 1993; Thorne *et al*., 1993; Thorne and Buckingham, 2004; Moate and Thorne, 2012).

Sahin *et al*., (2017) was able to investigate the effect of flocculating systems on the scattering from the acoustic Doppler current profilers where it was assumed that the flocs control the scattering characteristics instead of the primary particles. Gartner, (2004) and Ha *et al*., (2011) were able to use scattering from 1.2 – 2.4 MHz transducers to produce concentration profiles by using the flocs as scatterers. Inversion calculations were conducted by Sahin *et al*., (2013) by using flocs and primary particles as scatterers where a correction was required to consider the primary-particle viscous effect. This shows that flocculating simulants can be analysed using the ADCP where a correction is required to consider the viscous losses. An example of the physical set-up by Gartner, (2004) is shown in Fig. 2.17 where the mobile set-up is deployed in an estuarine bay.

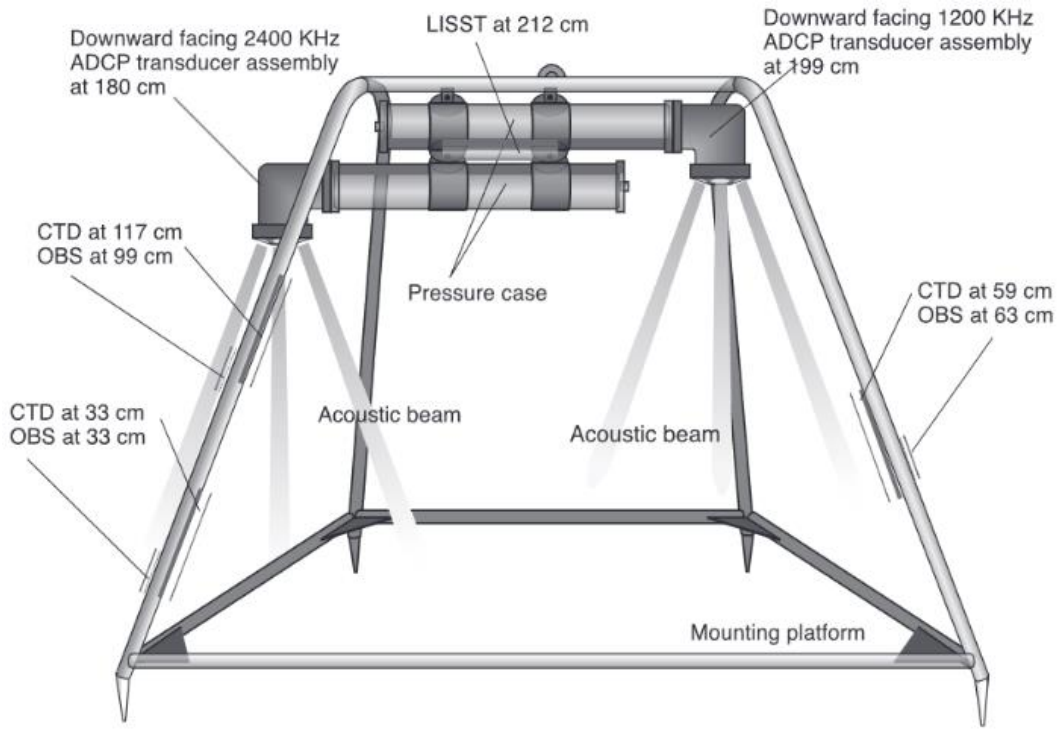

Figure 2.17 Experimental arrangement of 1200-kHz ADCP (transducer at 199 cm above bed) and 2400 kHz ADCP (transducer at 180 cm above bed). OBS sensors were located at 33, 63, and 99 cm above bed and CTD sensors were located at 33, 59, and 117 cm above bed. The LISST-100 was located at 212 cm above bed.(Gartner, 2004)

Massey *et al*., (2011) was able to demonstrate the use of an ADV (acoustic Doppler velocimeter) to track the settling velocity using assumptions of a local balance between downward settling and upward turbulent transport (Fugate and Friedrichs, 2002). The ADV was shown to produce a time series for mass concentration where it was found that measurements were relatively noisy due to the low frequency time limited bursts. However, it was found that the settling velocities estimated were positively correlated at a 95% confidence with current speed and Reynolds stress. This shows that acoustics can be used to determine accurate settling velocities.

The ACVP (acoustic concentration and velocity profiler) is capable of high-resolution profiling of flow velocity and suspended sediment concentration where

general velocity and concentration measurements were collected separately from two different apparatus (Harris *et al*., 2003; VanderWerf *et al*., 2007; Simmons *et al*., 2009; Thorne *et al*., 2009; O'Hara Murray *et al*., 2011). The ACVP provides non-intrusive high temporal-spatial resolution measurements of flow and sediment processes (Hurther *et al*., 2011). There have been limited ACVP instruments developed previously where Shen and Lemmin, (1999) produced a system which used back and forward scattering simultaneously for measured concentration and velocity. The main limitation for this system was the configuration required where both transducers needed to be mounted face-to-face. However, Hurther *et al*., (2011) was able to show a new ACVP system which was able to produce improved performance in terms of concentration and sediment flux measurements due to the multi-frequency capabilities where transducers were used between 1 and 2 MHz. Here Hurther *et al*., (2011) was able to demonstrate a novel dual-frequency inversion method for instabilities from the standard inversion methods by Thorne and Hanes, (2002) where two frequency transducers were used to determine backscatter intensities. The concentration profiles from the novel inversion method were found to give comparable results with OBS data (optical backscattering system). Thorne *et al*., (2018) was able to use the ACVP system to analyse boundary layer processes where direct measurements of sand flux and settling measurements allowed for estimation of sand diffusivity.

2.7.1.2 Acoustic Backscatter Systems (ABS)

Here, acoustic backscatter systems have been investigated which have been typically used in estuarine sediment transport studies (Thorne *et al*., 2021). The first being the AQUAscat 1000 which uses transducers of 0.5-5 MHz transducers and active radii of 1-1.8 cm (Thorne *et al*., 2001; Bux *et al*., 2015). The UVP (ultrasonic velocity profiler) was used which is a multi-frequency ABS that has the capability to mount transducers of frequency 0.5-8 MHz with active radii of 2.5 and 5 mm (Rice, 2013; Metflow, 2021). There is also the UARP, see Fig. 2.18 (ultrasonic array research platform), a non-commercial system produced by the University of Leeds. This UARP has been used in literature to analyse sediment suspensions (Cowell, 2016; Tonge *et al*., 2021). All systems covered

here are discussed in further detail below to provide scope of the techniques available for use.

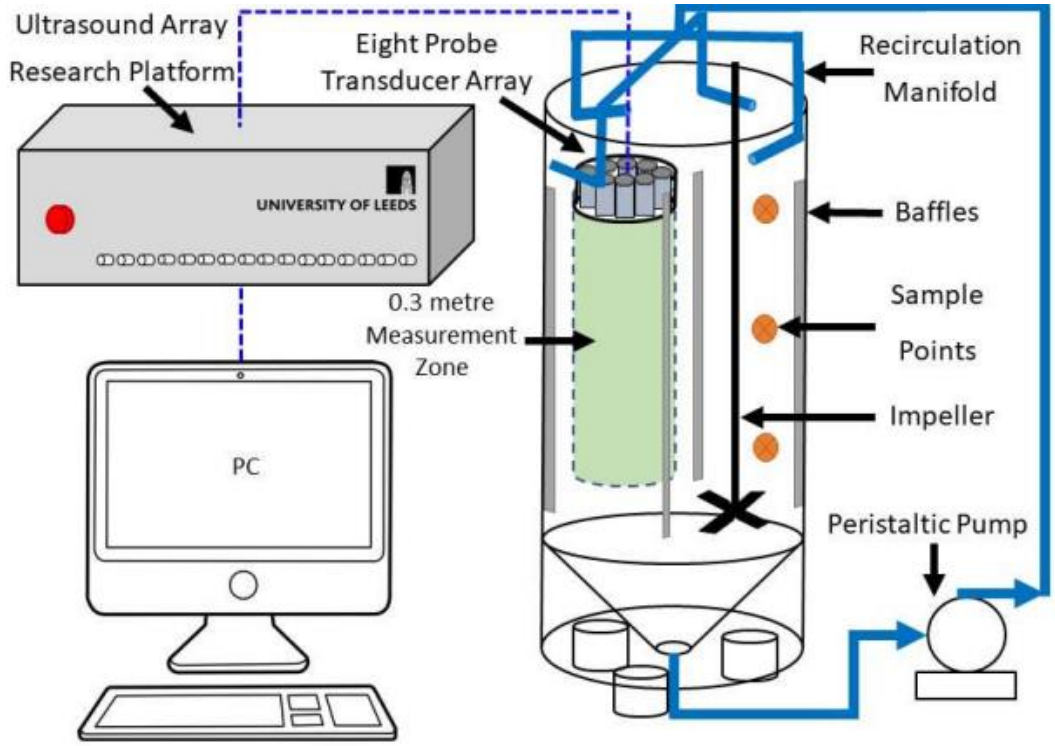

Figure 2.18 Experimental set-up using the UARP (Tonge et al., 2021)

AQUAscat 1000

The AQUAscat 1000 acoustic backscatter system (Aquatec Group Ltd, Hampshire, UK) is composed of transceiver probes with frequencies; 0.5-5 MHz (Bux *et al.*, 2015). The active diameters of the transducers range from 1-1.8 cm depending on frequency. Bux *et al.*, (2015) used the AQUAscat 1000 for application of the acoustic backscatter theory to determine concentration from measured backscatter data, this is applicable when particle backscatter and attenuation properties are known (Thorne *et al.*, 2001). Generally, concentrated suspensions which enhance inter-particle scattering (Hunter *et al.*, 2012) and small particle dispersions which are influenced by viscous attenuation (Moore *et al.*, 2013) deviate from the general acoustic backscatter theory. However, Bux *et*

al., (2015) was able to use a phenomenological approach to characterise high concentration suspensions. The phenomenological approach has been extended for fine colloidal mineral suspensions where the modelling was not established due to complex inter-particle interactions (Burger *et al*., 2010; Deboeuf *et al*., 2011; Dorrell *et al*., 2013). Bux *et al*., (2015) utilised the AQUAscat 1000 to characterise concentrated colloidal mineral suspensions using an empirical analysis approach where the concentration changes were characterised. The visualisation of the settling interface and sediment bed were both monitored successfully and compared well to data from optical methods. Conclusively, the ABS was able to characterise complicated sediment behaviour in polydisperse colloidal suspensions. The AQUAscat 1000 probes are shown below, these probes are mobile and can be mounted onto any flat surface.

Figure 2.19 AQUAscat 1000 transducers (Aquatec, 2022)

Directly following on from this research, Bux *et al.,* (2017) used the AQUAscat 1000 on a non-active, scaled, highly active storage tank (HAST) at Sellafield where the tank was profiled to produce concentration profiles. A bidisperse barytes suspension was utilised in tests for calibration experiments to characterise concentration changes. Attenuation was quantified using a method by Rice *et al*., (2014) where it was found that the attenuation of the barytes suspension was higher in comparison to previously investigated species due to the effect of viscous absorption on the smaller barytes species. The ABS was used to predict behaviour in industrial HASTs and provide more information on the settling behaviour to assist with future construction of the tanks.

Bux *et al*., (2019) was able to use AQUAscat 1000 acoustic backscatter measurements to determine the acoustic backscattering and attenuation constant where a streamlined approach for transducer calibration was validated with spherical particles. Expressions for spherical particles were used to measure the transducer constant which enables the calculation of the backscattering constant. A wide range of organic and fine material were used where the scattering and attenuation properties were compared to heuristic data. Bux *et al*., (2019) was able to determine that scattering properties of particles close to the colloidal regime could be measured accurately with the ABS showing how versatile the technique is. Tonge *et al*., (2019) also used the AQUAscat 1000 to monitor suspended solids concentration and aggregated sludges where the ABS was utilised to track the bed height in a suspension. The ABS was also used to determine changes in the bed density from measurement of the attenuation with distance. The specific calibration method is explored further in Chapter 3.

Bux *et al*., (2019) also developed a detailed calibration method for the calculation of backscattering and transducer constants from the attenuation coefficients established experimentally or heuristically, see Fig. 2.20. This calibration method skips the initial conversion of the raw echo amplitude into the sedimentation attenuation coefficient, which is covered in Rice, (2013). There is also limited error analysis conducted throughout this technique which is required for any

method where a case is being made for deployment. In this thesis, a novel error analysis will be conducted on the attenuation coefficient values determined experimentally.

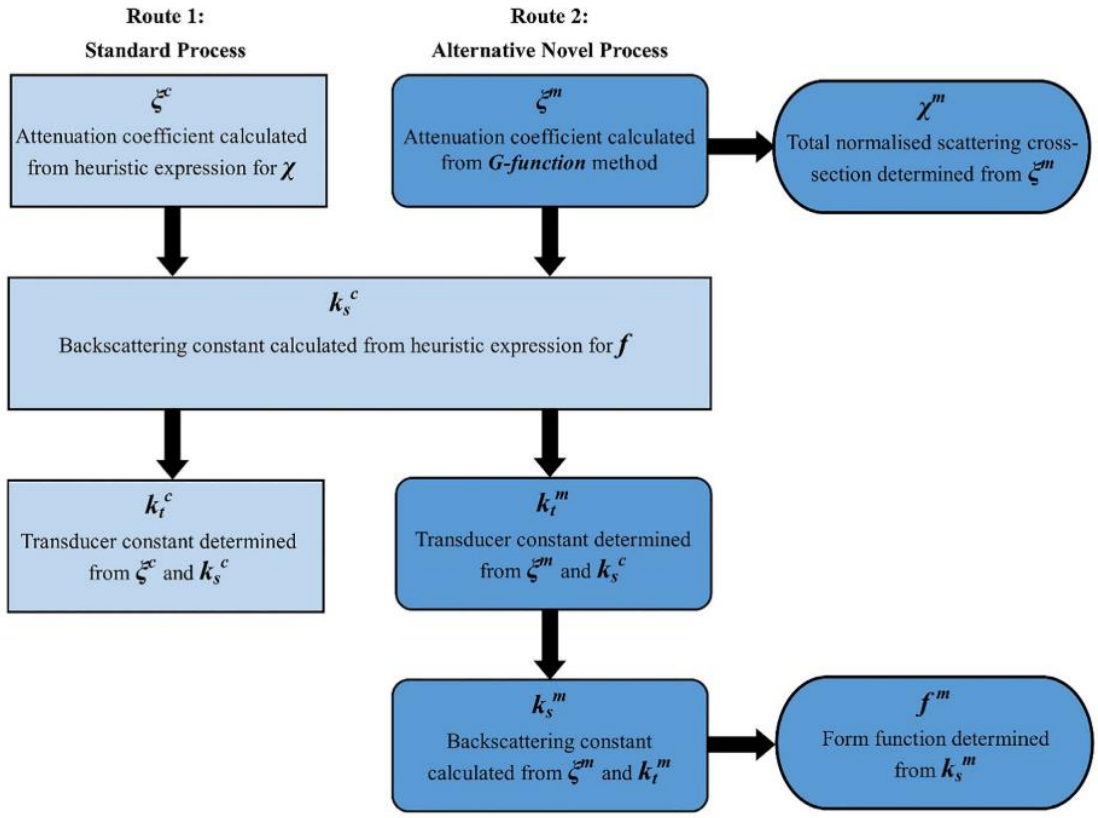

Figure 2.20 Calibration method for the calculation of a transducer and backscattering constant Bux et al., (2019)

Bux *et al*., (2019) also used this calibration method to determine the total normalised scattering cross section and form function from experimental data. This was achieved using *in situ* transducers which were suspended into a homogeneous suspension. This thesis will aim to provide similar data using combined attenuation predictions from Betteridge *et al*., (2008) and Urick, (1948) where Bux *et al*., (2019) had only used Betteridge *et al*., (2008) predictions. The combined attenuation should account for viscous losses which are dominant in smaller particle sizes and align predicted data with the measured data at the lower

ka values. Tonge *et al*., (2021) has done this for glass dispersions using the UARP but this is novel for the UVP. As shown in Fig. 2.21 (b), measured values at lower *ka* branch off from the prediction, this may be due to the increased viscous losses which should be considered. The author will also strive to provide measured values from non-contact probes to show that data can be collected to align with the nuclear industries requirements.

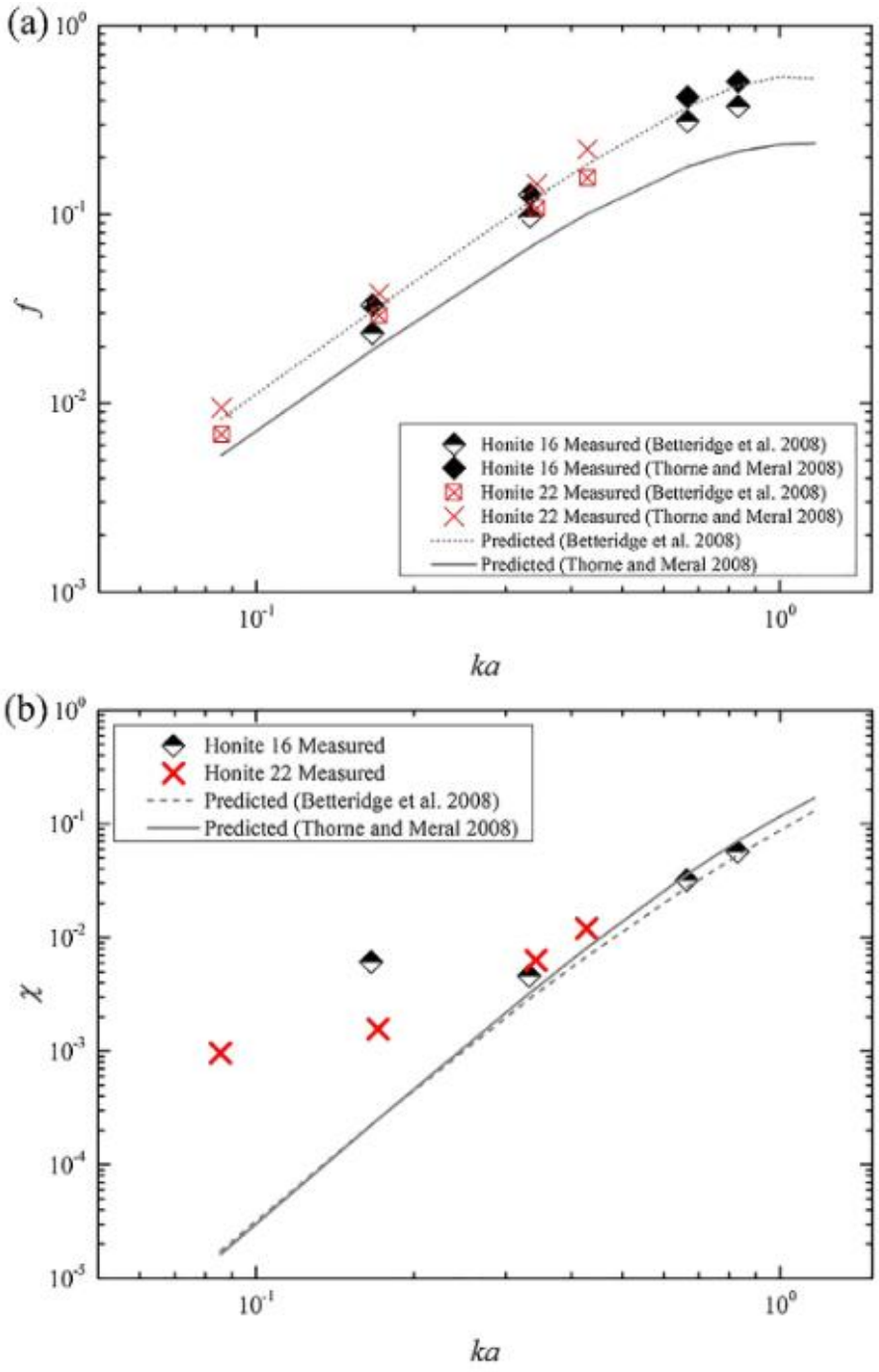

Figure 2.21 (a) form function vs ka and (b) normalised scattering cross section vs ka for homogeneous suspensions of silica glass beads with predictions from Betteridge et al., (2008) shown in the dashed line and predictions from Thorne and Meral, (2008) in the solid line (Bux et al., 2019)

Thorne *et* al., (2014) found that the lack of experimental data and theoretical expressions made it difficult to interpret the backscattered signal from the AQUAscat 1000. Therefore, Thorne *et al*., (2014) developed a hybrid model which considers a heuristic approach to study complex shaped scattering bodies (Stanton and Chi, 2000; Thorne and Meral, 2008). Meral *et al*., (2017) was able to use an artificial neural network (ANN) in conjunction with the AQUAscat 1000 to develop an acoustic method for determining sound scattering properties. This eliminates the requirement for complex expressions and inversions. However, this requires more ANN model studies with alternative sizes, shapes, and densities.

MacDonald *et al*., (2013) used the AQUAscat 1000 to determine the backscatter response from fine sediment suspensions. Transducer frequencies of 3-5 MHz were used, and the suspensions were flocculated at various levels to determine the change in backscatter response. MacDonald *et al*., (2013) found that the flocculated particle structure influences the scattering of sound where the backscatter form function increased with the degree of flocculation.

Ultrasonic Velocity Profiler (UVP)

The UVP is used predominantly for measuring flows in pipes and channels (Kotze *et* al., 2011) and assessing tank mixing systems (Ein-Mozaffari *et al*., 2007). The UVP has also been used in pipe flow for full rheological profiling (Birkhofer *et al*., 2008; Wiklund and Stading, 2008). Although this system has been mainly used to extract the Doppler frequency shift to measure flow velocity, a methodology for extracting concentration profiles has been used by extracting backscatter voltage (Rice *et al*., 2014; Rice *et al*., 2015). This UVP has also been used to determine the critical deposition velocity (Rice *et al.*, 2015) and characterise the settling and erosion of beds (Hunter *et al*., 2011; Hunter *et al*., 2013).

Rice, (2013) determined sedimentation attenuation coefficients using transducers mounted *in situ* on a pipe loop, this meant that data could be collected in-line. The face of the transducers was in contact with the suspension which is not viable for

deployment in the nuclear industry, therefore, in this thesis, the author will aim to mount transducers in-line but remotely to maintain a non-contact environment. The set-up by Rice, (2013) is shown below. Transducers were mounted at 90 and 135° to extract the echo amplitude and velocity, respectively, this was beneficial as the same minimal set-up was able to provide simultaneous echo and velocity measurements. Rice, (2013) was also able to determine the sedimentation attenuation coefficients and compare these to heuristic expressions. There are other expressions which consider scattering losses, which are given by Betteridge *et al*., (2008) and expressions for viscous losses by Urick, (1948). Both of these expressions combined can provide a predicted attenuation value which can be compared to measured attenuation coefficients. Therefore, in this thesis, the author aims to provide combined attenuation predictions which can be compared to measured experimental values, this has not been achieved using the UVP.

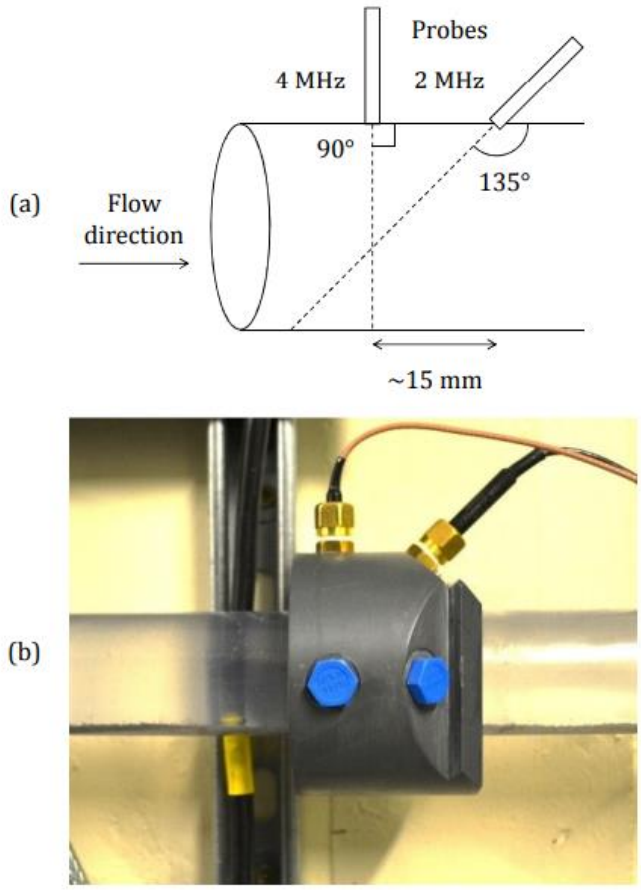

Figure 2.22 Probes mounted in-line on an engineered pipeline (Rice, 2013)

Hunter *et al*., (2011) utilised the ultrasonic velocity profiler to characterise settling dispersions where the UVP measured the transmitted Doppler shift of moving particulates. The settling rates of particles was examined and the reduction in settling rates was able to provide information on the level of segregation and hindered settling. In Hunter *et al*., (2011), the UVP was not used to measure the actual particle concentration. However, in Hunter *et al*., (2012), the UVP was used to determine concentration profiles for settling suspensions. Suspensions of low concentrations were used to determine the returned backscatter and convert this into concentration (Betteridge *et al*., 2008; Meral, 2008) as concentrations higher than 1 wt % could not be characterised from the effect of inter-particle sound absorption.

Hunter *et al.,* (2012) investigated the use of a multi-frequency acoustic backscatter system which uses 2, 4, and 5 MHz probes to understand the settling behaviour of flocculated glass dispersions. Both well-mixed suspensions and settling systems were measured where the echo strength of the settling systems was compared to the well-mixed systems to monitor the concentration changes in the suspension sludge zone. Hunter *et al*., (2012) found that well-mixed systems produced a linear function for the backscatter attenuation, therefore, the backscatter strength through the settling dispersions was tracked and compared. The levels of segregation could be determined by taking the attenuation decay and comparing the linear function. Hunter *et al*., (2012) found that this technique was limited due to the small depth penetration from higher frequency transducers due to the greater inter-particle attenuation. An example of the concentration profiles from Hunter *et al*., (2012) is shown in Fig. 2.23.

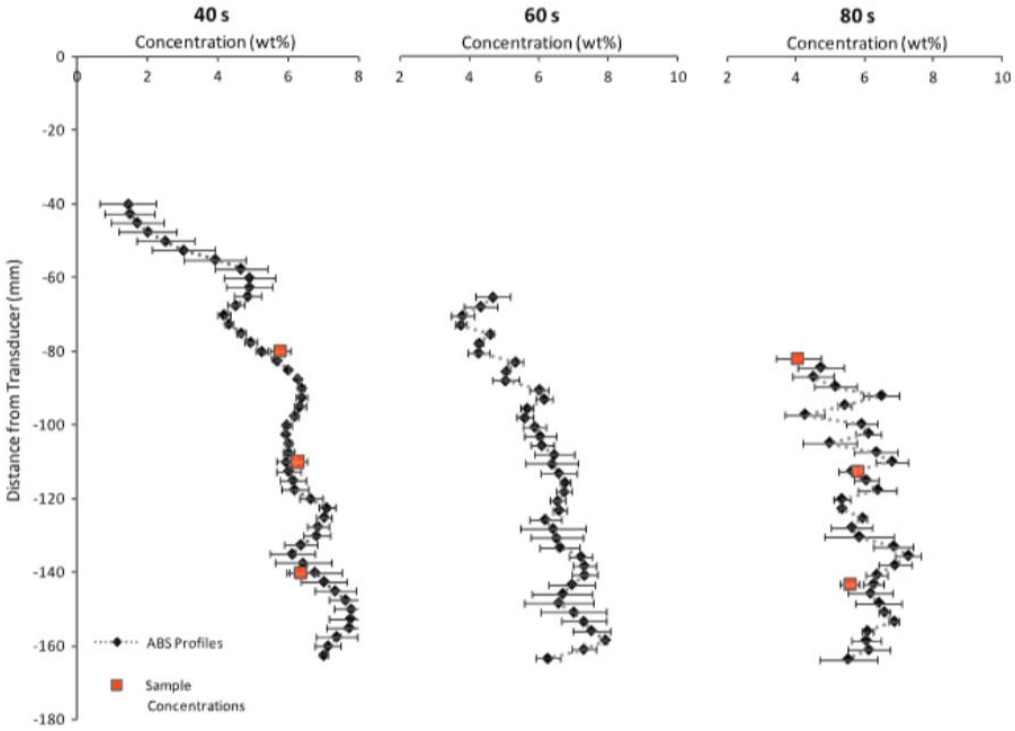

Figure 2.23 Concentration profile measurements through settling flocculated spheriglass dispersions (Hunter et al., 2012)

Stener *et al.*, (2016) used the UVP to produce good estimates of local flow velocity for flow through a pipe. The UVP was also used to monitor a transition between low and high solids concentration using the pulse-echo method. Stener *et al.*, (2016) conducted experiments in a pilot concentrator where the UVP was used to estimate particle velocity and concentration. This shows that the UVP is able to simultaneously monitor sediment flux and velocity much like the ACVP. However, the UVP is able to use multiple transducers for more advanced characterisation where three transducers can be mounted to determine a 3 D flow profile (Metflow, 2021).

Rice *et al*., (2012) analysed suspensions flowing through a horizontal pipe length using the UVP where transducers were mounted at 90 and 135° to flow. Echo amplitude profiles were taken across the cross section of the pipe. The sheet-flow thickness and bed thickness were determined and novel characterisation of

bedforms was conducted depending on the Reynolds number. Rice *et al*., (2012) was able to exploit acoustic methods in a novel manner where only one other author had utilised the same method to determine bed depth (McLelland, 2010).

Rice *et al*., (2014) was then able to adapt a model described by Thorne and Hanes, (2002) and Thorne *et al*., (2011) so attenuation and backscatter coefficients could be measured experimentally. These coefficients could then be used in a dual frequency inversion method for concentration profiling (Hurther *et al*., 2011). The novel approach was successful however, there were limitations from species which exhibit strong attenuation, therefore any large particle sizes and high concentrations were limited in analysis.

Faia *et al*., (2016) mounted a 4 MHz transducer with a 2.5 mm active radius onto a flow loop where the transducer was mounted at 70° to the flow and was in direct contact with the suspension. The transducer was mounted 3.5 m downstream from a bend in the pipe which ensures the flow is fully developed at the time of analysis. Faia *et al*., (2016) had used MRI data for validation where the two sets of data showed excellent agreement. At lower concentrations, UVP profiles were unaffected by velocity changes whereas MRI profiles become broader. At higher concentrations, the UVP and MRI (magnetic resonance imaging) profiles were affected equally where the profiles become flatter. Faia *et al*., (2016) found that the methods had a high level of agreement which has shown that the use of multiple techniques allows a better knowledge of suspension flow behaviour.

UARP

A new bespoke ultrasonic array research platform (UARP) was produced by the school of electronic and electrical engineering at the university of Leeds. This equipment was developed to further advance hardware and provide flexibility needed for on-site deployment of acoustic devices in the nuclear industry (Carpenter, 2020). The system uses a mobile measurement array with relatively cheap transducers which can be disposable if used in radioactive or toxic environments. The UARP was also designed for the user to access the raw

received signal which is not a feature available in most commercial systems (Cowell *et al*., 2015; Hunter *et al*., 2020). A schematic of the UARP is shown below, the system is quite large, although mobile, will take some effort to move around should the system need to be relocated.

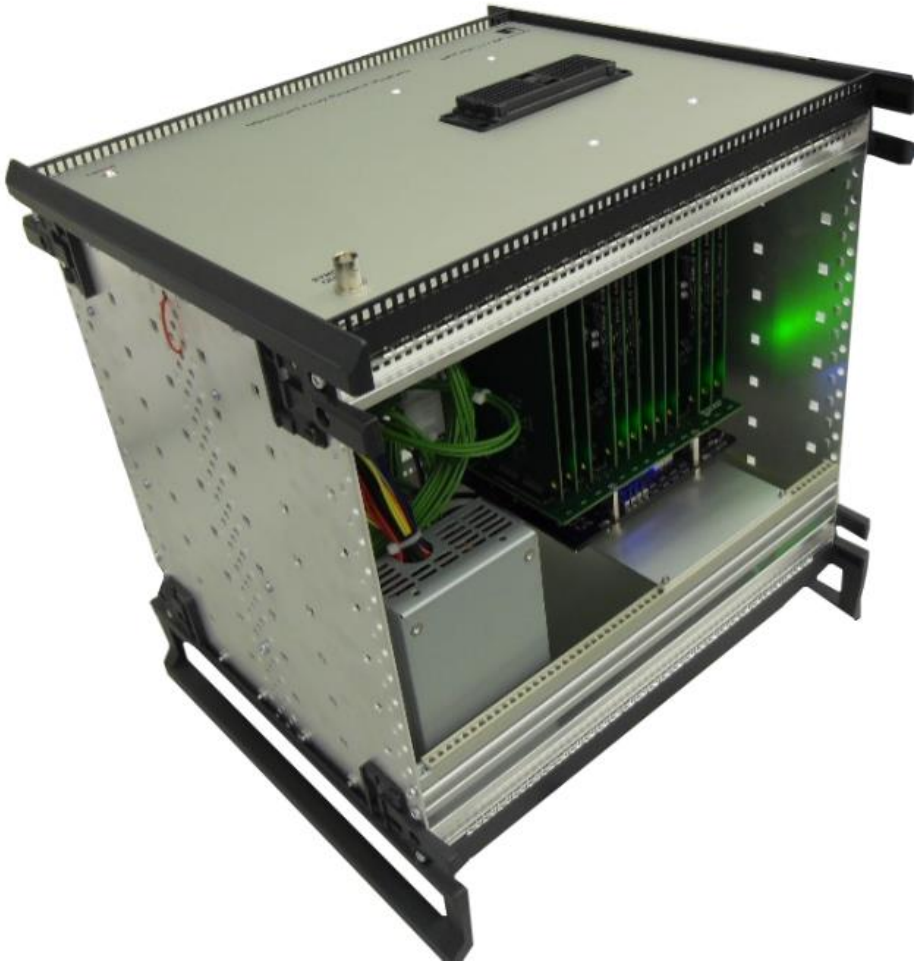

Figure 2.24 Picture of the UARP (University of Leeds, 2022)

Most of the acoustic systems have been tested in lab scale environments or small-scale tests, however Hunter *et al*., (2016) conducted large scale trials of the UARP ABS for concentration profiling. The UARP can be used to visualise particulate levels in real-time from the backscatter echo signal (Cowell *et al*., 2015). A large continual flow clarifier was used as it represented a nearly full scale on site nuclear waste separator. The backscatter signal was found to be more accurate for lower concentrations which was expected as other acoustic systems have had a

limit on sediment concentrations they are able to accurately analyse (Hunter *et al*., 2011). The UARP was able to prove effective for characterisation of complex flocculated suspensions in a large-scale test, this shows that this technique is applicable in industrial systems.

Hunter *et al*., (2020) has used the newly developed UARP due to the limitations of existing ABS to conduct high fidelity multipoint profiling. The UARP has specifically been used here for concentration profiling in a large-scale sedimentation tank. Real-time monitoring when using the UARP would be highly valuable in the nuclear industry (Hunter *et al*., 2016). To understand the settling process in the tank for the flocculated material, the UARP has been used in tandem with a CFD (computational fluid dynamics) model of the same system (Heath *et al*., 2006). The CFD model is validated against the measured data from the UARP. Simulations of concentration were found to be accurate to sample data using glass dispersions, however, the CFD model over-predicted the particle settling for the flocculating calcite. This could be attributed to additional shear break-up of aggregates.

Tonge *et al*., (2021) was able to present a log-linear relationship for glass dispersions using concentrations of up to 125 g/L for *ka* values between 0.2 and 0.4. For a larger glass species - where the *ka* was approximately 1 - the multiple scattering effect led to a higher limit in the noise floor where the measured attenuation was overpredicted. This overprediction meant the higher *ka* suspension was only accurate up to concentrations of 40 g/L (Tonge *et al*., 2017). This indicated a limit for analysis with the UARP when analysing glass dispersions. Single frequency inversions were accurate for the same concentration limits for each glass dispersion where the high concentrations for the larger particle size led to multiple scattering and a higher limit in the noise floor. A dual frequency inversion method was used (Hurther *et al.*, 2011) with the transducers where the frequency ranged from 2-2.5 MHz and were accurate until 20 g/L. The dual frequency inversions offer enhanced concentration characterisation for the UARP. The UARP is a useful method which has been shown to produce accurate

data, however, for applicability and reproducibility, the method itself is restricted. With the UARP being a novel instrument, the ability to reproduce results is limited. The scale-up to work on site will mean that the unit cannot be purchased off-shelf should the system become irradiated or need replacing for any other reason.

Tonge *et al.,* (2021) also determined the total normalised cross section and compared measured values to combined attenuation predictions from Betteridge *et al*., (2008) and Urick, (1948), this has not yet been achieved using the UVP.

2.7.2 Acoustic physical remote characterisation techniques:

The UVP was found to be the most applicable method for ongoing analysis and reproducibility in the nuclear industry. Therefore, the application of acoustic systems for remote placement and characterisation is explored below to understand whether the UVP can be deployed as an on-site, non-invasive characterisation method. Tezuka *et al*., (2008) measured velocity profiles within pipes using non-intrusive flow meters where the influence of surface roughness and Reynolds number was investigated on the velocity. Abbagoni *et al*., (2022) also mounted non-invasive transducers to measure oil-water two-phase flow in vertical pipes. This was conducted by using a Doppler ultrasonic (CWDU) flow sensor and a gamma densitometer. It was found that there were restrictions on the effective range where the water volume fraction needed to be between 25 – 75%. The UVP has been used in previous literature to monitor non-invasively, this is explored below.

Prateepasen *et al*., (2011) used a non-invasive microcontroller to detect internal air leakages of a valve by analysing the acoustic emission signals. This instrument was portable and a computational model was used in tandem with the instrument. Prateepasen *et al*., (2011) confirmed that the leakage rate of air could be measured. This data is useful in the knowledge that acoustics can be used in a non-invasive setting, however the results would not be applicable for this specific

thesis as Prateepasen *et al*., (2011) did not measuring aqueous suspensions. Haldenwang *et al*., (2008) mounted a 4 MHz probe remotely on a 40 mm pipe where the transducer was fitted at an angle of 20° to the vertical pipe. Signals were sent through the Perspex pipe wall with a small adaptor and acoustic couplant to enhance the signal penetration through the pipe wall. Two mineral suspensions of Kaolin and Bentonite with a concentration vol % of 8.25 and 5.66 % were used respectively in the pipe. The UVP was used to produce velocity profiles which compared very well to predicted velocity profiles. This research opened the door for analysis of complex non-Newtonian mineral suspensions using a non-invasive technique. A photograph of the experimental set-up from Prateepasen *et al*., (2011) is shown in Fig. 2.25.

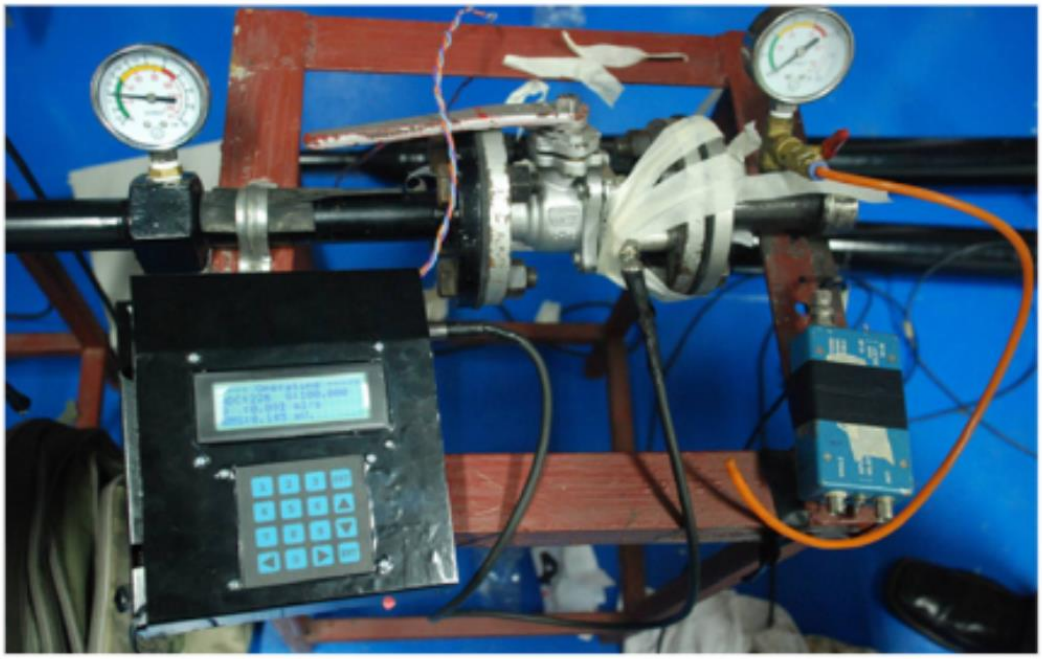

Figure 2.25 Experimental set-up employed by Prateepasen et al., (2011)

Flow loops have been used by Shi *et al*., (2022) for characterisation of suspensions using other means such as FBRM and PVM where the FBRM was used to produce a chord length distribution which can be correlated to the particle size distribution (provided the solids are spherical). The FBRM produced accurate chord length distributions which were used for monitoring whilst the PVM

produced microscopic images of the aggregates in flow (Shi *et al*., 2022). Acoustic sensors have also been used as a leakage detection method where transducers are mounted remotely and acoustic signals are extracted for real-time monitoring (Wang *et al*., 2021). Acoustic emission techniques can be used for corrosion testing in concrete cylinder pipes where damage can be detected at any stage of the life cycle of the pipes (Goldaran and Turer, 2020).

Kotze *et al*., 2016 was able to use the UVP in tandem with pressure difference (PD) measurements to obtain a full flow profile. A 2 MHz transducer was mounted remotely on the outside of a 47 mm pipe where shear rate and shear stress curve were determined. The transducer was mounted in-line but in contact with the suspension.

Montes *et al*., 2020 was able to mount a transducer remotely at an angle to the flow to determine the velocity of particles in flow. The specific material to be analysed were tailings which were slightly opaque and therefore laser Doppler anemometry was not suitable. The technique had to be non-invasive, therefore, X-ray radiography and MRI amongst other techniques could not be used (Powel, 2008; Martin Rodrigues and Martin Rodriguez, 2014; Kotze *et al*., 2016). As the velocity profile processing was conducted post-processing, the technique is not in-line however, the equipment is mounted remotely. A full ultrasonic signal flow was extracted from the transducers and a region of interest was selected between two peaks at the start and end of the suspension environment within the pipe.

Tashi *et al*., (2002) used the UVP to measure instantaneous velocity profiles where transducers were mounted non-intrusively. Tashi *et al*., (2002) investigated the effect of measurement volumes on the velocity profiles and shows that the velocity profile becomes higher than the true value near the wall. However, the profile was found to be satisfactory as the error of the flow rate was only ~ 0.8. Obayashi *et al*., (2008) mounted UVP transducers remotely onto a pipe surface to determine a velocity vector profile. This required multiple transducers to be mounted at varying angles non-invasively. This system was tested on a rigid body

motion of a fluid in a rotating cylinder and on unsteady flow where velocity vector profiles were measured. This information was used to provide a base understanding of what was required for velocity profiling of a pipe in a non-invasive set-up. In this thesis, the UVP has been used to determine simultaneous velocity and echo amplitude data which has not been achieved before for complex mineral suspensions.

All literature presented above show that acoustics can be used to analyse waste suspensions remotely, specifically the UVP has been used to provide concentration and sediment flux profiles on homogeneous suspensions. Therefore, moving forward, the author will be using the UVP to characterise nuclear waste simulant suspensions initially and then move on to in line remote characterisation of complex mineral suspensions. This will provide information and form a precedent for the deployment of the UVP for analysis of magnox sludge suspensions during transit to an interim storage facility.

To further understand why the UVP is chosen, physical limitations of the UVP can be found in Table 2.1. Almost all methods shown in the literature review are specifically tailored to characterise spherical particles. This is because historically, modelling and theoretical expressions are simpler for spherical particles. Although the particles in magnox sludge will not be spherical, the purpose of this characterisation method is to analyse and monitor. If the characterisation method can be used to analyse changes in particle size, concentration or rheology then it can be caveated that the theoretical models are for spherical particles but the system is still able to monitor successfully. Nuclear waste slurries often have low concentration of < 2.5 vol % which is less than the upper limit of 40 g/L for the UVP. Therefore, the UVP should still be able to accurately predict concentration via dual frequency inversion. The UVP is portable, which means it is easier to move around on site and allows flexibility for positioning.

The particle size limitations for all techniques including the UVP are shown in Table 2.1, these also inform the maximum flocculation of the suspension. As the

UVP has not been tested extensively within pipe flow, there is insufficient data to understand the flow rate limitations of the equipment. For the information in this thesis, the UVP was able to perform and extract attenuation coefficients from the flow rate used in this thesis.

2.8 SUMMARY

This literature review goes through past literature used for the analysis of sediment suspensions. This covered previous non-acoustic and acoustic techniques which were used *in situ* and in line. The novelty in this research is presented in the five results Chapters shown. The UVP has been used to determine sedimentation attenuation coefficients of various materials including silica glass bead suspensions. A calibration method has been detailed from Bux *et al*., (2019) which shows how attenuation coefficients can be used to determine the total normalised scattering cross section and the form function. The UVP was used to determine sedimentation attenuation coefficients from suspensions of similar silica glass bead suspensions where a novel error analysis was conducted on experimental data. Updated predictions have been used by Tonge *et al*., (2021) to compare experimental form function and normalised scattering cross section values to combined predicted attenuation using expressions from Betteridge *et al*., (2008) and Urick, (1948). This has not been achieved with the UVP. Previous literature shows that UVP probes were used to determine sedimentation attenuation coefficients from glass dispersions but not using remote transducers (Rice *et al*., 2015; Bux *et al*., 2019). Therefore, the placement of the non-contact UVP probes is novel. The form function and normalised scattering cross section values for measured data was compared using remotely placed and *in situ* transducers which has not been achieved before.

Several acoustic systems have been used to monitor flocculated dispersions (Hunter *et al*., 2012) but this has not been achieved using remotely placed transducers. The non-flocculated and flocculated dispersions have not been

compared in previous literature to show the change in acoustic behaviour through the flocculation process.

Rice *et al*., (2014) has used transducers mounted in line on a horizontal pipe length where the transducers were mounted into the pipe and in contact with the suspension. Velocity values were also extracted from the transducer but using *in situ* probes. Transducers have not been mounted remotely on varying pipe orientations for simultaneous extraction of echo amplitude and velocity. Flocculated suspensions have not been monitored remotely in line to simultaneously extract echo amplitude and velocity to monitor the flocculation process.

3. ANALYTICAL THEORY

This section covers all the theory and most if not all the equations used as reference throughout this thesis. Section 3.1.1 will cover all the UVP derivations required to collect and convert the raw echo amplitude into results which can be directly compared to literature, these include: voltages, *G* function profiles and sedimentation attenuation coefficients. Various literature is referenced here. Derivations from Rice, (2013) were utilised to convert the raw UVP data to voltage. General acoustic theory from Downing *et al*., (1995), Betteridge *et al*., (2008) and Thorne and Hanes, (2002) were used to determine the sedimentation attenuation coefficient, form function and normalised scattering cross section. This was achieved from heuristic expressions and experimentally. Equations from Urick, (1948) were then utilised to determine the viscous attenuation loss. This was combined with scattering losses from Betteridge *et al*., (2008) to form a combined attenuation prediction. The viscous boundary layer was calculated for the two transducer frequencies utilised and the numerous sediments used throughout this thesis. The shear and viscosity of individual particles was determined to investigate the effect on the acoustic theory. Pipe flow theory was investigated in section 3.1.2 where the speed of sound in sediment suspensions was determined for various concentrations, this theory was referenced from Urick, (1979) and Povey, (1997). The Reynolds number within the pipe was calculated in section 3.3 and the entry length was determined using two methods of analysis from Shames, (2003) and Zagarola and Smits, (1998) where the calculated entry length was compared to the actual. An error analysis was conducted for the two methods and compared to establish the most accurate calculation method.

3.1 ACOUSTIC THEORY

Acoustics have been used to analyse moving material in the defence sector and marine biology (Young *et al*., 1982; Jones and Clarke, 2004; Carrera *et al*., 2019; Guan *et al*., 2021). Analysis of material has been achieved by utilising the principle of sound propagation and attenuation (Guan *et al*, 2021). Acoustics have also been a dominant method for the analysis of moving sediment (Thorne, 1985;

Thorne and Hardcastle, 1993; Guerrero *et al*., 2013; Latosinski *et al*., 2014). The general acoustic theory has been extracted from Thorne and Hanes, (2002) with derivations taken from Rice, (2013), Bux, (2016) and other work which has been detailed below. The theory has progressed to analyse sediment suspensions in the Rayleigh regime (Bux, 2016), and suspensions in pipe flow (Rice, 2013). The acoustic theory has become more refined where simpler derivations have been adopted. This makes the process of analysing acoustic data easier to understand. This Chapter will detail the acoustic theory, derivations and heuristic expressions used to analyse moving homogeneous suspensions of silica glass beads and complex mineral suspensions, in later Chapters. The methodology used here will be referenced across all results Chapters where the same equations have been used for analysis.

3.1.1 UVP Derivations

The UVP was chosen through investigation of the literature. The first take away from the literature review was that acoustic backscatter systems were the most viable technique for analysis (Kotze *et al*., 2011; Rice *et al*., 2014; Bux, 2016). Several acoustic backscatter systems were investigated and from those systems the ultrasonic velocity profiler (UVP) was chosen (Kotze *et al*., 2011; Bux, 2016; Quiroz *et al*., 2020; Ohie *et al*., 2022). The ultrasonic velocity profiler (UVP) was selected due to its simple interface and because it is a commercial unit which meant that all data could be re-produced (Rice *et al*., 2015; Met-flow, 2021). The UVP is designed by Met-flow (SA) – a company based in Switzerland - and is generally used for velocity profiling. A logarithmic function of the voltage is produced by using the UVP to extract echo amplitude data (Met-flow, 2021). The use of the UVP to remotely extract simultaneous velocity and acoustic profiles has not been achieved using remote probes before which shows that this technique is novel. The set-up consists of a pulser/ receiver, a set of transducers and a digitiser with signal processing which is carried out on a connected laptop. The UVP is simple to operate, makes low computational demands and has several ports on the back for transducer connection. For analysis, a combination of same frequency or

multi frequency transducers can be connected. The ability to mount multiple transducers shows how versatile the UVP is (Met-flow, 2021).

The UVP sends out pulsed signals through the measurement domain and then detects any sound signal reflected, which shows that the UVP acts as a transmitter and reciever (Met-flow, 2021). Analysis is achieved through the signal detected (Butler and Sherman, 2016). Raw echo amplitude data can be extracted from the UVP where the amplitude shows the attenuation of sound as it travels through a suspension (Hamine *et al*., 2013; Vergne *et al*., 2019). The UVP detects the sound which has been scattered back to the detector and uses the ratio of sound scattered to determine the attenuation (loss) of sound (Butler and Sherman, 2016). A combination of the backscatter and attenuation can be analysed for comparison of suspensions with varying particle size and concentration (Rice, 2013). The raw echo amplitude *E(r)* extracted from the UVP can be converted to voltage using the gain function *g(r)* as shown in Eq. (3.01). Gain is a measure of the amplification of the sound signal and ranges in value between 1-9 on the UVP system (Rice, 2013). Lower gain values may produce too low a signal (where the signal is below the noise-floor and analysis cannot be achieved) (Mydlarz *et al*., 2017) whilst higher values may cause saturation of the signal (where the signal is higher than the maximum amplitude and therefore produces results which are not of value) (Rice, 2013; Auerback *et al.,* 2019). Therefore, a gain value of 6 was selected which was an intermediate gain value that produced accurate acoustic profiles (Rice, 2013). Eq. (3.01) is derived using the voltage variation of the transducer (+/- 2.5 V) and dividing this data into 14-bit (2^{14}) data, this corresponds to a multiplication value of 3.052 x 10^{-4}. This echo amplitude data is then converted to the voltage using the gain value provided by Met-flow (Rice, 2013)

$$V(r) = \frac{3.052\ x\ 10^{-4} E(r)}{g(r)} \tag{3.01}$$

The following derivation in Eq. (3.02) is used to calculate the root-mean-square (RMS) of the received voltage (Thorne and Hanes, 2002). The received voltage from the UVP varies with distance from the transducer. From Eq. (3.02) it is

shown that the RMS voltage is a function of the following: transducer constant, k_t ($V.m^{1.5}$), backscatter coefficient, k_s ($m.kg^{0.5}$), concentration, M ($kg.m^{-3}$), distance from transducer, r (m), attenuation due to solid and water, α_s (m^{-1}), α_w (m^{-1}) and the nearfield correction factor, ψ. The nearfield correction factor, ψ in Eq. (3.02) is calculated in Eq. (3.03) and shown as a function of r, transducer active radius, a_t (m) and wavelength, λ (m) (Downing *et al*, 1995). The nearfield correction factor accounts for the change from spherical spreading within the nearfield of the transducer face (Downing *et al*., 1995). The wavelength is calculated using the speed of sound in water (1480 $m.s^{-1}$) and the transducer frequency. Where 2 or 4 MHz transducers were used throughout this thesis. Transducers of 2 MHz frequency have been used for analysis of sediments in water columns previously by Thorne and Hanes, (2002), Betteridge *et al*., (2003), Williams *et al*., (2003), Hurther *et al*., (2011). Transducers of 4 MHz frequency have been used in literature to analyse sediment in pipes by Best *et al.*, (2009), Guney *et al*., (2013) and Rice *et al*., (2014). The attenuation due to water can be calculated using a derivation from Rice, (2013) where a general expression was adapted from Ainslie and McColm, (1998). This derivation in Eq. (3.04) shows that attenuation due to water is dependent on the ultrasonic frequency, f (MHz) and temperature, T (°C). As this derivation varies with the temperature, the temperature of the water was checked initially for experiments and was found to be around 20 °C. When considering a 5 °C variation in temperature, the attenuation of water shows a 17 % variation, however, when taking multiple tests, the water temperature varied by 1/2 °C which led to a 3.7 % variation. Variation in temperature was assumed to be negligible from the limited variability in temperature samples. The attenuation due to solid, α_s can be determined using the sedimentation attenuation coefficient, ξ and concentration, M ($\alpha_s = \xi M$), assuming the suspension is homogeneous (Rice, 2013).

$$V = \frac{k_s k_t}{\psi r} M^{1/2} e^{-2r(\alpha_w + \alpha_s)},\ V\psi r = k_s k_t M^{1/2} e^{-2r(\alpha_w + \alpha_s)} \qquad (3.02)$$

$$\psi = \frac{1+1.35\left(\frac{r}{\pi a_t{}^2/\lambda}\right)+\left(2.5\left(\frac{r}{\frac{\pi a_t{}^2}{\lambda}}\right)\right)^{3.2}}{1.35\left(\frac{r}{\pi a_t{}^2/\lambda}\right)+\left(2.5\left(\frac{r}{\frac{\pi a_t{}^2}{\lambda}}\right)\right)^{3.2}} \quad (3.03)$$

$$\alpha_w = 0.05641 f^2 e^{\left(-\frac{T}{27}\right)} \quad (3.04)$$

To produce an acoustic profile, the voltage values calculated in Eq. (3.01) were converted to the logarithmic function of the voltage, otherwise known as the *G*-function. *G* is calculated using k_s, k_t, *M*, α_w and α_s but can be determined experimentally using the near field constant (Downing *et al*, 1995), distance from transducer and the measured *V* from experimental data. This function is used to compare the attenuation of profiles using different suspension environments. Eq. (3.05) shows the calculation of the *G*-function using the experimental functions and the calculated (Rice, 2013).

$$G = \ln(\psi r V) = \ln(k_s k_t) + 0.5\ln(M) - 2r(\alpha_w + \alpha_s) \quad (3.05)$$

The attenuation constant (ξ, $m^2.kg^{-1}$) is determined by plotting the *G*-function vs the distance from the transducer, *r* and establishing the gradient from the resulting plot (Rice, 2013). The superscript *m* indicates values from experimental/ measured data.

$$\xi^m = -0.5\left(\frac{\partial^2 G}{\partial M \partial r}\right) = -0.5\frac{\partial}{\partial M}\left[\frac{\partial}{\partial r} ln(\psi r V)\right] \quad (3.06)$$

The normalised scattering cross section (χ) and the form function (*f*) can be calculated using heuristic expressions from Betteridge *et al*., (2008). Both are functions of the particle radius *a* (m) and angular wavenumber, *k* (m^{-1}). The wavenumber, *k* is calculated using the speed of sound in water, *c* ($m.s^{-1}$) and the transducer frequency, *f* (MHz) ($2\pi f/c$) (Betteridge *et al*., 2008). The superscript *c* indicates values determined through calculations or heuristic expressions.

$$\chi^c = \frac{\left[0.24\left(1-0.4e\left(-\frac{ka-5.5}{2.5}\right)^2\right)(ka)^4\right]}{[0.7+0.3(ka)+2.1(ka)^2-0.7(ka)^3+0.3(ka)^4]} \quad (3.07)$$

$$f^c = \frac{\left(1-0.5e\left(-\frac{ka-1.5}{0.5}\right)^2\right)\left(1+0.4e\left(-\frac{ka-1.5}{3}\right)^2\right)\left(1-0.5e\left(-\frac{ka-5.9}{0.7}\right)^2\right)(ka)^2}{1.17+0.95(ka)^2} \quad (3.08)$$

The scattering cross section and form function can be calculated experimentally using expressions from Thorne and Hanes, (2002), these expressions are shown in Eq. (3.09) and (3.10). The sedimentation attenuation coefficient can be used along with particle radius and density of solid, ρ_s (kg.m^{-3}) to calculate the experimentally determined χ (Bux, 2016). The form function can be calculated using the backscatter coefficient, k_s (m.kg$^{0.5}$) from experimental data, the particle radius, *a* and density of solid (Rice, 2013; Bux, 2016).

$$\chi^m = \xi^m \frac{4a\rho_s}{3} \quad (3.09)$$

$$f^m = {k_s}^m\sqrt{a\rho_s} \quad (3.10)$$

The sedimentation attenuation coefficient calculated in Eq. (3.06) only considers scattering losses (Urick, 1948). Therefore, the author has investigated the losses due to viscous attenuation. To understand whether viscous losses occur, the *ka* values need to be known for all systems used in this thesis. Table 3.1 shows all the *ka* values for each system using a 2 and 4 MHz transducer. The 2 and 4 MHz transducers were considered as they are the base transducer frequencies for the UVP where both frequencies have been used in previous literature to provide accurate acoustic profiles (Rice, 2013).

Table 3.1 ka values for all systems (sizes for the silica glass can be found in Chapter 5, Section 5.3.1 whilst sizes for the calcium carbonate and magnesium hydroxide are found in Chapter 6, Section 6.3.2)

Material	*a (m)*	*ka*	
		2 MHz	4 MHz
Silica glass d_{50} 170 µm	8.5E-05	0.71	1.43
Silica glass d_{50} 82 µm	4.1E-05	0.34	0.69
Silica glass d_{50} 48 µm	2.4E-05	0.20	0.40
Silica glass d_{50} 36 µm	1.8E-05	0.15	0.30
Calcium Carbonate	2.4E-06	0.02	0.04
Magnesium Hydroxide	2.5E-06	0.02	0.04

All particle sizes for the silica glass can be found in Chapter 5, section 5.3.1 where particle sizes were determined using a Mastersizer. Particle sizes for the calcium carbonate and magnesium hydroxide were determined using a Camsizer XT, this is shown in Chapter 6, section 6.3.2. For all systems apart from the 4 MHz probe analysing the largest glass species, $ka<1$ where the system is within the Rayleigh regime and viscous losses occur. These losses have to be taken account of (Bux *et al*., 2019; Tonge, 2021). Tonge, (2021) found that when $ka<0.6$, viscous losses are large, nearly all values are <0.6 when comparing this to Table 3.1. Viscous losses need to be considered to accurately calculate the normalised scattering cross section (Thorne *et al*., 2014). The theoretical models from Urick, (1948) are used to determine attenuation due to viscous losses from mono-sized spheres, where the intermediate non-dimensional variables, β, t and θ in Eq. (3.11) are used to calculate attenuation due to viscous losses, ξ_{sv} ($m^2.kg^{-1}$), the subscript *sv* indicated viscous losses. To calculate the intermediate variable β, the kinematic viscosity of water at room temperature is used, υ (10^{-6} $m^2.s^{-1}$) and the angular frequency, ω ($2\pi f$, where f is the transducer frequency) (Kestin *et al*., 1978). Where the kinematic viscosity is determined by dividing the dynamic viscosity at room temperature, (1 mPa.s at 20°C) by the density of water, 1000 $kg.m^{-3}$ (Rice, 2013). The dynamic viscosity is determined from data by Kestin *et*

al., (1978). Intermediate variables, β, t and θ and the density of the solid and water, ρ_w (kg.m^{-3}) are used to calculate attenuation due to viscous losses in Eq. (3.12).

$$\beta = \sqrt{\frac{\omega}{2v}}, \qquad t = \frac{9}{4a\beta}.\left(1 + \frac{1}{a\beta}\right), \qquad \theta = 0.5 + \frac{9}{4a\beta} \tag{3.11}$$

$$\xi_{sv} = \frac{k}{2\rho_s}\left(\frac{\rho_s}{\rho_w} - 1\right)^2 . \frac{t}{t^2 + \left(\frac{\rho_s}{\rho_w} + \theta\right)^2} \tag{3.12}$$

Eq. (3.09) can then be re-written in Eq. (3.13) to calculate the scattering cross section using the sedimentation attenuation coefficient due to viscous losses (Urick, 1948). The predicted sedimentation attenuation coefficient due to scattering losses is determined by using the scattering cross section predicted in Eq. (3.07). The predicted attenuation coefficient from combined attenuation due to scattering and viscous losses is shown in Eq. (3.14). This can then be compared to the attenuation coefficient from experimental data.

$$\chi_{sv} = \xi_{sv} \frac{4a\rho_s}{3} \tag{3.13}$$

$$\xi = \xi_{sv} + \frac{3\chi^c}{4a\rho_s} \tag{3.14}$$

3.1.2 Speed of Sound

The speed of sound of suspensions, c (m.s^{-1}) was calculated using expressions from Urick, (1979) and Povey, (1997) where density, ρ (kg.m^{-3}) and compressibility, k (m^2.N^{-1}) of the suspensions are both additive properties. Eq. (3.15) shows the density and compressibility calculated using volume fractions, ϕ of the suspension's components. Subscripts *s* and *w* indicate values for sediment and water, respectively whilst subscript *b* indicates bulk density. Eq. (3.16) shows the speed of sound equation (Urick, 1979; Povey, 1997).

$$\rho = \rho_{b,w}\phi + \rho_{b,s}(1-\phi) \qquad k = k_w\phi + k_s(1-\phi) \tag{3.15}$$

$$c = \frac{1}{\sqrt{\rho_b k}} \tag{3.16}$$

The speed of sound was calculated for the glass test materials (Honite, Guyson Ltd) (mainly composed of silica dioxide) from Guyson, (2021) as well as the mineral suspensions. The mineral suspensions used in this thesis are homogeneous suspensions of calcium carbonate (Omyacarb 2, Omya AG) and magnesium hydroxide (Versamag Martin Marietta Magnesia Specialties). Even though the glass test materials have varying particle size distributions, the speed of sound stays the same as Urick, (1979) does not consider changes in particle size. The bulk density of silica dioxide (2600 $kg.m^{-3}$) was used in calculations as the silica glass beads are ~75% silica dioxide (Guyson, 2021). The bulk densities for the mineral suspensions of calcium carbonate (Ito, 2017) and magnesium hydroxide (Patnaik, 2002) are 2711 ($kg.m^{-3}$) and 2340 ($kg.m^{-3}$), respectively. Compressibility was calculated by taking the inverse of the bulk modulus, where values for the compressibility of the three materials is; $k_{Calcium\ carbonate}$ = 77 GPa (Carmichael, 2017), $k_{Magnesium\ hydroxide}$ = 43.3 GPa (Hermann and Mookherjee, 2016) and k_{SiO_2} = 36.9 GPa (Kaye and Laby, 1995). The speed of sound values for all three materials are shown in Table 3.2, 3.3 and 3.4 for silica glass beads, calcium carbonate and magnesium hydroxide, respectively. It is shown that the speed of sound changes by a maximum of 1.18 %. This is assumed to be a negligible change, but no sensitivity analysis was conducted on the effect of speed of sound on attenuation. The change in attenuation is assumed to be solely due to the change in concentration. This is highlighted as an area for further research. There could be additional effects that the change in speed of sound has on the attenuation of a signal which have not been considered for results in this thesis.

The largest change in speed of sound occurs for the silica glass beads where the speed of sound decreases with increasing concentration. At the largest concentration the speed of sound decreases by ~1 %. Whilst for the smaller mineral species, the speed of sound decreases by 0.48 % and 0.28 % respectively for calcium carbonate and magnesium hydroxide. The smaller density of the

magnesium hydroxide suspensions shows a limited change in speed of sound whereas the higher density calcium carbonate has a higher change in speed. The larger particle glass species exhibits a larger change in speed of sound. Tables 3.2 – 3.4 show that an increase in density leads to a decrease in the speed of sound (this is only shown specifically in results shown below and cannot be said generally).

Table 3.2 Speed of sound calculations for silica glass beads (Compressibility and bulk density values for silica glass were taken from Kaye and Laby, (1995))

Concentration, M (kg.m^{-3})	Volume (%)	Density, ρ_b (kg.m^{-3})	Compressibility, k (m^2.N^{-1})	Speed of sound, c (m.s^{-1})	Δ c/ c0
11.9	0.46	1004	4.6E-10	1478	-0.15
35.7	1.35	1019	4.5E-10	1474	-0.44
47.6	1.80	1026	4.5E-10	1472	-0.57
59.5	2.24	1033	4.5E-10	1470	-0.70
83.3	3.11	1047	4.4E-10	1466	-0.95
107.5	3.97	1061	4.4E-10	1463	-1.18

Table 3.3 Speed of sound calculations for calcium carbonate suspensions (Compressibility values for calcium carbonate were found in Carmichael, (2017) and the bulk density value was taken from Ito, (2017))

Concentration, M (kg.m^{-3})	Volume (%)	Density, ρ_b (kg.m^{-3})	Compressibility, k (m^2.N^{-1})	Speed of sound, c (m.s^{-1})	Δ c/ c0
3.8	0.15	1000	4.6E-10	1479	-0.04
11.9	0.46	1005	4.6E-10	1478	-0.15
15.7	0.60	1007	4.6E-10	1477	-0.21
20.9	0.80	1011	4.5E-10	1476	-0.28
26.2	1.00	1014	4.5E-10	1475	-0.35
35.7	1.36	1020	4.5E-10	1473	-0.48

Table 3.4 Speed of sound calculations for magnesium hydroxide suspensions (Compressibility values for magnesium hydroxide were found in Hermann and Mookherjee, (2016) and the bulk density was found in Patnaik, (2002))

Concentration, M (kg.m^{-3})	Volume (%)	Density, ρ_b (kg.m^{-3})	Compressibility, k (m^2.N^{-1})	Speed of sound, c (m.s^{-1})	Δ c/ c0
3.8	0.17	999	4.6E-10	1480	-0.02
11.9	0.53	1004	4.6E-10	1479	-0.09
15.7	0.70	1006	4.6E-10	1478	-0.12
20.9	0.93	1009	4.5E-10	1478	-0.16
26.2	1.16	1013	4.5E-10	1477	-0.21
35.7	1.58	1018	4.5E-10	1476	-0.28

3.1.3 Viscous Boundary Layer Thickness

The particle viscous boundary layer is important for acoustic absorption and can be determined using the particle Reynolds number where the viscous boundary layer thickness can be calculated. The *ka* value is used to establish the importance of the boundary layer thickness and the effect of the boundary layer thickness on acoustic absorption (Kytomaa, 1995; Khamis and Brambley, 2017; Forrester *et al*., 2019).

When $ka < 1$, the system is in the long wavelength regime where the boundary layer thickness becomes important whilst when $ka >> 1$ the regime is in the multiple-scattering regime where it has been shown that sound will scatter randomly and penetrate poorly as the particles are randomly arranged in an assembly (Javanaud and Thomas, 1988; Kytomaa, 1995). Table 3.1 shows that all systems have a *ka* value < 1 apart from the largest glass species analysed using a 4 MHz transducer where the *ka* value is slightly larger than 1. Therefore, the multiple-scattering effect is assumed to be negligible (Javanaud and Thomas, 1988).

The viscous boundary layer is a thin layer of viscous fluid at the wall which is in

contact with the bulk moving fluid. This is often called Stokes layer thickness (Kytomaa, 1995). The Reynolds number can be calculated using the Stokes layer thickness to establish which regime the system is in (Kytomaa, 1995). The stokes layer thickness is a function of the dynamic viscosity, μ (10^{-3} kg.m^{-1}.s^{-1}), density of water, $\rho_{w,}$(1000 kg.m^{-3}), particle radius, a (m) and the angular frequency, ω (rad.s^{-1}). The dynamic viscosity (1 mPa.s at 20 °C) is taken from data by Kestin *et al.*, (1978). Angular frequency is calculated using the frequency of the transducer used ($\omega = 2\pi f$). By assuming a 2 MHz or 4 MHz transducer is used, Eq. (3.18) and (3.19) can be derived from Eq. (3.17) (Allegra and Hawley, 1972; Atkinson and Kytomaa, 1992; Kytomaa, 1995; Panetta *et al*., 2012).

$$Re_{particle} = \frac{a}{\delta} = \frac{a}{\sqrt{\frac{2\mu}{\rho_w \omega}}} = a\sqrt{\frac{\rho_w \omega}{2\mu}} \tag{3.17}$$

$$Re_{particle,2\ MHz} = \frac{a}{4.0E{-}07} \tag{3.18}$$

$$Re_{particle,4\ MHz} = \frac{a}{2.8E{-}07} \tag{3.19}$$

The particle Reynolds number using the viscous boundary layer has been calculated for all six suspension environments using a 2 and 4 MHz transducer where the viscous boundary layer, δ (m) is 4 E-07 when using a 2 MHz probe and 2.8 E-07 when using a 4 MHz probe.

Table 3.5 Reynolds number as a function of the viscous boundary layer thickness

Material	Particle Radius, *a* (m)	Re	
		2 MHz, δ (m) = 4.0E-07	4 MHz, δ (m) = 2.8E-07
Silica Glass d_{50} 170 µm	8.5E-05	212.5	303.6
Silica Glass d_{50} 82 µm	4.1E-05	102.5	146.4
Silica Glass d_{50} 48 µm	2.4E-05	60.0	85.7
Silica Glass d_{50} 36 µm	1.8E-05	45.0	64.3
Calcium Carbonate	2.4E-06	6.0	8.6
Magnesium Hydroxide	2.5E-06	6.3	8.9

All values in Table 3.5 are much greater than 1. Kytomaa, (1995) found that when Re >> 1, δ is very small and the fluid outside the boundary layer is dominated by inviscid inertial effects. This is where viscous forces are smaller than inertial forces (Gerhart *et al*., 2016). The viscous boundary layer is smaller when using a 4 MHz probe, therefore, it is expected that the 4 MHz probe will exhibit decreased viscous losses. When comparing the particle Reynolds number in Table 3.5, the particle Re is higher for the 4 MHz probe. This will be explored further in Chapters 5 where the silica glass is characterised using both 2 and 4 MHz transducers, this will also be investigated in Chapters 6 and 8 where the fine mineral suspensions are explored. The increased particle Re has been assumed to lead to an increase in viscous losses when comparing the 2 and 4 MHz probes. Therefore, by taking this a step further, the decrease in particle Re between the sediment types may lead to an increased viscous absorption. However, this theory has not been proven yet and is explored further in Chapters 5, 6 and 8. It is noted that an increase in viscous absorption may not necessarily lead to an increased sedimentation attenuation coefficient as the particles also attenuate through scattering losses.

3.1.4 Particle Shear and Viscosity

Following on from the discussion above, the shear interaction with the fluid and the viscosity of the suspensions is explored. The shear interaction with the fluid is expected to be minimal as the concentration of the particles is so small (0.46-3.97 vol % for silica glass, 0.11-1 vol % for calcium carbonate and 0.12-1.16 vol % for magnesium hydroxide) (Kytomaa, 1995; Stevenson *et al*., 2002). As the remaining dispersant was 96 vol% (or more), the viscosity is dominated by the aqueous dispersant. This is shown below using Fig. 3. 1.

To understand this further, both properties need to be investigated, these include the change in viscosity with the addition of the solid suspension and the effect of shear from the solid suspension. First, the viscosity change with the addition of the solid particles is explored. Only the kinematic viscosity of water was used to determine the Re as the contribution from particles on the viscosity was negated due to the small concentration of solid (0.46-3.97 vol % for silica glass, 0.11-1 vol % for calcium carbonate and 0.12-1.16 vol % for magnesium hydroxide). This was confirmed by investigating the dependence of relative viscosity predictions on solid fractions in Fig. 3.1 below, where Konjin *et al*., (2014) compared several theoretical and semi-empirical relations for the dependence of the relative viscosity on solid fraction. Annotations were made in Fig. 3.1 which correspond to a slight overprediction of the maximum solid fraction (4 vol%) used across all sediment suspensions. The relative viscosity was found to change by a maximum 1.14-1.24 when comparing four theoretical expressions including Eilers, (1941), Vand, (1948), Mooney, (1951) and Krieger and Dougherty, (1959). The change in relative viscosity from the viscosity of the dispersant was found to be negligible.

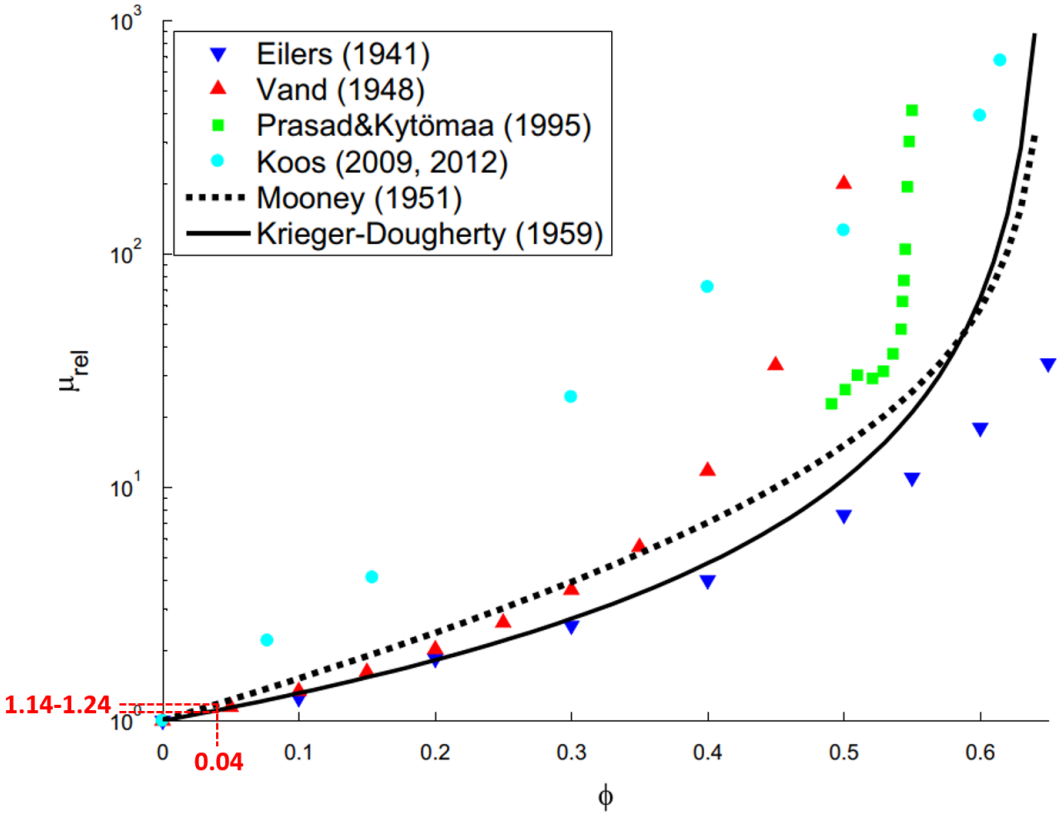

Figure 3.1 Dependence of relative viscosity with change in solid fraction with annotations correlating to the maximum solid fraction used for suspensions across this thesis, Fig extracted from Konjin et al., (2014)

The dependence of the viscosity on shear rate was investigated using results from Rice *et al*., (2020) to understand how the change in viscosity also effects the shear rate. The relationship between viscosity and shear rate is investigated in Fig. 3.2 (Papadopoulou *et al*., 2020). When using the maximum change in relative viscosity found in Fig. 3.1 for a 4% solid fraction, the viscosity was found to change by a maximum of 0.24, this figure is used to determine the maximum viscosity depending on the viscosity of the dispersant at room temperature (20°C), 10^{-3} kg.m^{-1}.s^{-1}. The maximum viscosity according to Fig. 3.2 is 1.24 x 10^{-3} (m^2.s^{-1}) whilst the viscosity of water is 10^{-3}. Rice *et al*., (2020) did not account for solid fractions lower than 10% so the change in shear rate was investigated for a solid fraction of 10% with the assumption that the change in shear rate would stay consistent. Fig. 3.2 shows the change in shear rate with relative viscosity where

the relative viscosity range in Fig. 3.1 was used to determine the change in shear rate. As shown above, the change in relative viscosity is so minimal that the change in shear rate can almost be assumed to be negligible (Papadopoulou *et al.*, 2020). The same is shown for dispersions of calcium carbonate and magnesium hydroxide suspensions in Fig. 3.3.

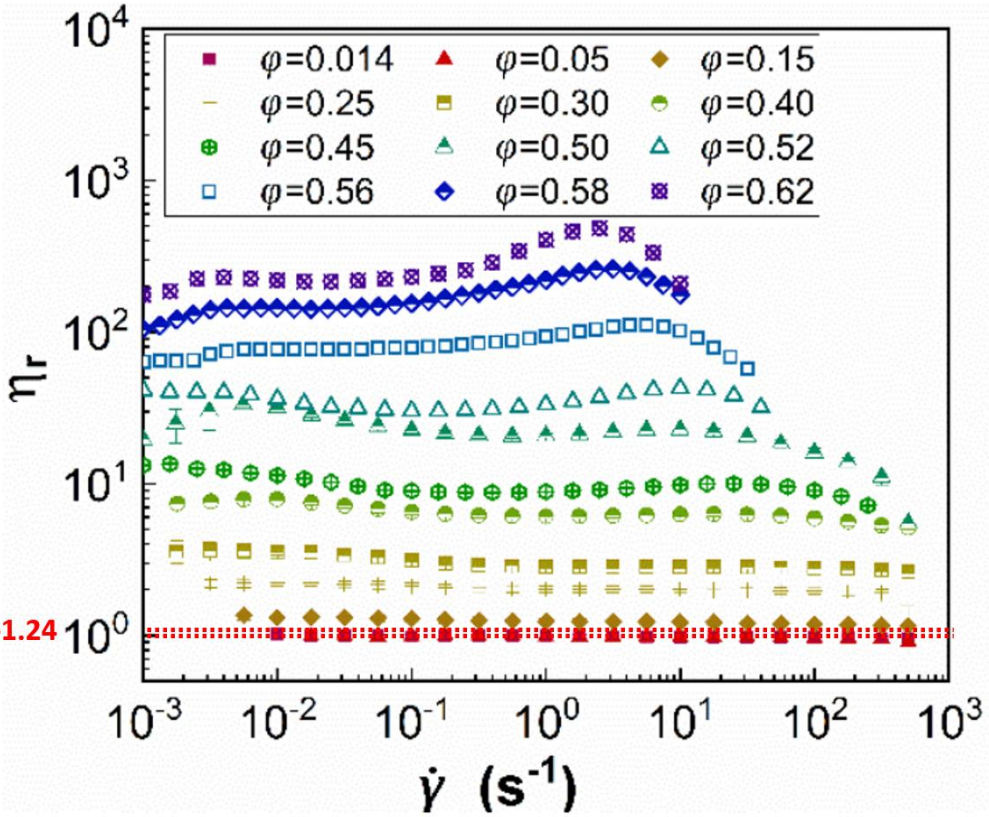

Figure 3.2 Dependence on shear rate with relative viscosity for glass silica dispersions where the relative viscosity of water and the relative viscosity of the suspensions has been shown by the two red dotted lines from Papadopoulou et al., 2020

Fig. 3.3 (a) and (b) shows the change in shear rate with viscosity of varying solid fractions from 10% - black, 20% - red and 30% - green with the circles shown for calcite suspensions and squares for magnesium hydroxide suspension. As the solid fraction decreases, the correlation crosses the y axis at a lower value. Under

this assumption, the correlation for a solid fraction of 4% would lead to a lower correlation which intercepts at a viscosity of 0.001. As shown in Fig. 3.3, the shear rate does not change significantly with a relative 1.24 change in viscosity, however for the magnesium hydroxide suspensions in 3.3 (b), the viscosity predictions do not go lower than 0.001. This is because of the overprediction of the solid fraction. However, the shear rate is expected to show a negligible change with the change in viscosity, therefore, the shear interaction with the fluid is expected to be minimal.

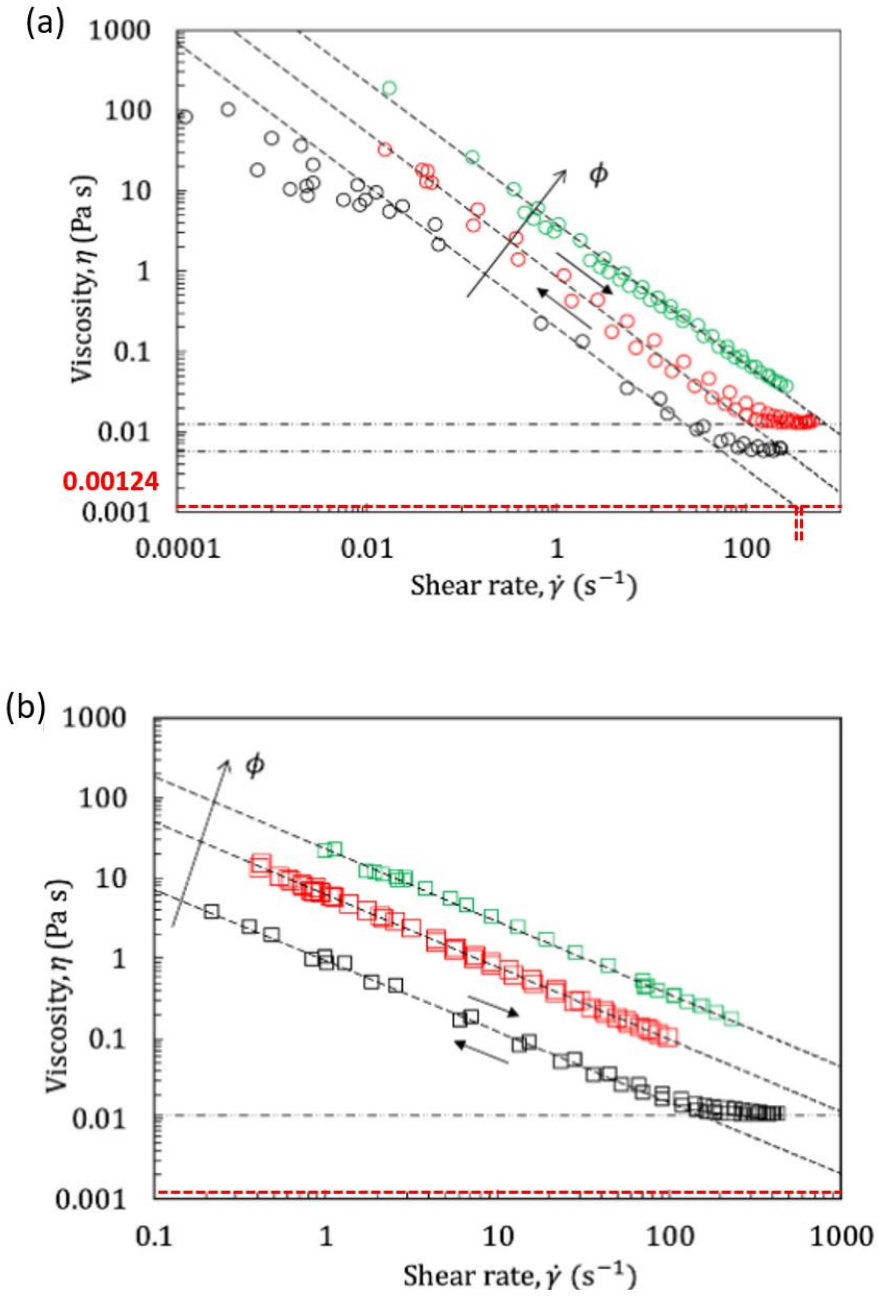

Figure 3. 3 Dependence of viscosity on shear rate for suspensions of (a) calcium carbonate and (b) magnesium hydroxide with solid fractions of: 10% - black, 20% - red and 30% - green

3.2 Engineered Pipe loop methodology

In terms of the pipe loop, the theory is used to determine the minimum entry length required. This allows the user to be sure that flow is fully developed at the

point of analysis (Laufer, 1954; Zagarola and Smits, 1998; Shames, 2003; Rice, 2013). Before this, the author has explored the several factors which effect the time required for flow to become fully developed. These include the pipe Reynolds number, Re (note that this is different from the particle Re which was determined above) which allows characterisation of the flow and the entry length which governs the development of the flow through the pipe (Young *et al*., 2010; Schlichting and Gersten, 2016; Beltran-Prieto and Kolomaznik, 2019).

3.2.1 Pipe Reynolds Number

The pipe Reynolds number is determined using the flow rate, pipe diameter and kinematic viscosity. The experimental flow rate for the pipeline was measured from the flow meters placed on the top of the pipeline, see Chapter 8. The flow rate and flow velocity were monitored over 5 minutes from the flow meters and averaged to give a representative value. The mean velocity, U_{Ave} (m.s^{-1}) recorded from the flow meters was used along with the internal pipe diameter, $D = 0.025$ m and the kinematic viscosity of water at room temperature (20 °C), $v = 10^{-6}$ (m^2.s^{-1}). These values were used in Eq. (3.20) to calculate the pipe Reynolds number for the flow rates measured subsequently (Hinze, 1959; Deen, 2016; Schlichting and Gersten, 2016). As shown in Fig. 3.1, the relative change in viscosity for the addition of the solid particles is negligible and therefore the kinematic viscosity of water (Kestin *et al*., 1978) is used for calculation of the pipe Re. Table 3.6 shows all the values required to calculated pipe Reynolds number in Eq. (3.20). The pipe Re is established with properties from the pipe and bulk fluid with no added assumptions from the addition of the solid in the suspensions. This is due to the negated shear and viscosity change which is explored in Fig. 3.1 – 3.3.

$$Re = U_{Ave}.\frac{D}{v} \tag{3.20}$$

Table 3.6 Properties required for Reynolds number calculations

Kinematic Viscosity, v, $m^2.s^{-1}$	0.000001
Inner (Outer) Pipe Diameter, m	0.025 (0.03)
Area of Pipe, m^2	0.00049

The pipe Reynolds number is calculated for varying pipe flow rates to identify whether the flow was turbulent. Turbulent flow occurs above a Re of 4000 (Dunne *et al*., 2019). The speed and rate of the pump is utilised for pipe Reynolds number calculations. Table 3.7 shows the range of experimental flow rates that can be used. The experimental flow rate is highlighted at the bottom of the table. The flow meter has an error of +/- 1% accuracy which is reflected in the +/- 1% error for the pipe Re, where the Re is determined using the linear function in Eq. (3.20). The flow velocities here were selected as the minimum and maximum speeds the experimental set-up could manage. The flow velocity of 0.39 m/s prevented settling in the mixing tank and ensured all solids were dispersed in the suspension, and the flow velocity of 0.88 m/s was the upper limit at which the pump ran. Flow velocities above 0.88 m/s risked the integrity of the piping.

Table 3.7 Calculation of Re using a variation of flow rates

Speed (RPM)	Flow Rate, (L/s) (+/- 1%)	Flow Velocity, U_{Ave} (m/s) (+/- 1%)	Reynolds Number, *Re* (+/- 1%)
600	2.36	0.39	9,770
750	3.16	0.53	13,188
900	3.98	0.66	16,543
1050	4.74	0.79	19,750
1131	5.22	0.88	21,913

3.3 Entry Length

When fluid enters the pipe, a boundary layer along the wall starts to develop. The boundary layer is thin near the pipe entrance and the viscous effects are restricted to the near wall region. However, as the flow develops, the boundary layer thickness grows and reaches the pipe-line. When the boundary layer thickness reaches the pipe centreline, the flow then becomes fully developed. The length taken for the flow to evolve into a fully developed flow is also known as the entrance length (Zagarola and Smits, 1998; Shames, 2003; Schlichting and Gersten, 2016; Moon, 2022).

Entry length can be calculated using several expressions (Zagarola and Smits, 1998; Shames, 2003) which provide varying minimum entry length values. The calculated entry lengths can then be compared to the actual distance to the UVP transducers to ensure fully developed flow at the point of analysis. The actual distance from the probes needs to be longer than the required minimum length, *L* (Rice, 2013). Two methods were used to determine the entry length to pipe diameter ratio. The first method utilised the Reynolds number and is shown in Eq. (3.21) where derivations from Shames, (2003) were used. The second method uses the Darcy friction factor (*f*) and is derived from Zagarola and Smits, (1998) as shown in Eq. (3.23) where D = 0.025 m as given earlier. To understand whether the flow was fully developed, the actual distance from the UVP probes in the pipe loop need to be known. The entry length for the horizontally mounted probe is 1.3 m whilst the entry length for the vertically mounted probe is 2.1 m, see Chapter 7.

3.3.1 Method 1: Shames, (2003)

Shames, (2003) derivation in Eq. (3.21) is used for turbulent flow, where all Re values in Table 3.7 confirm that flow is turbulent.

$$\frac{L}{D}(method\ 1) = 4.4Re^{1/6} \tag{3.21}$$

All *L/D* values are calculated using the array of Re in Table 3.7 and shown in Fig. 3.4 where the increase in flow velocity leads to an increase in Re and entry length. The entry length values range from 0.51 and 0.58 m which is significantly lower than the actual distances of 1.3 and 2.1 m. These entry length values show that the flow was fully developed at the point of analysis. Error bars shown in Fig. 3.4 show the 1% error from the flow rate measurements where the error for the entry length calculations is explored further at a later point in the Chapter.

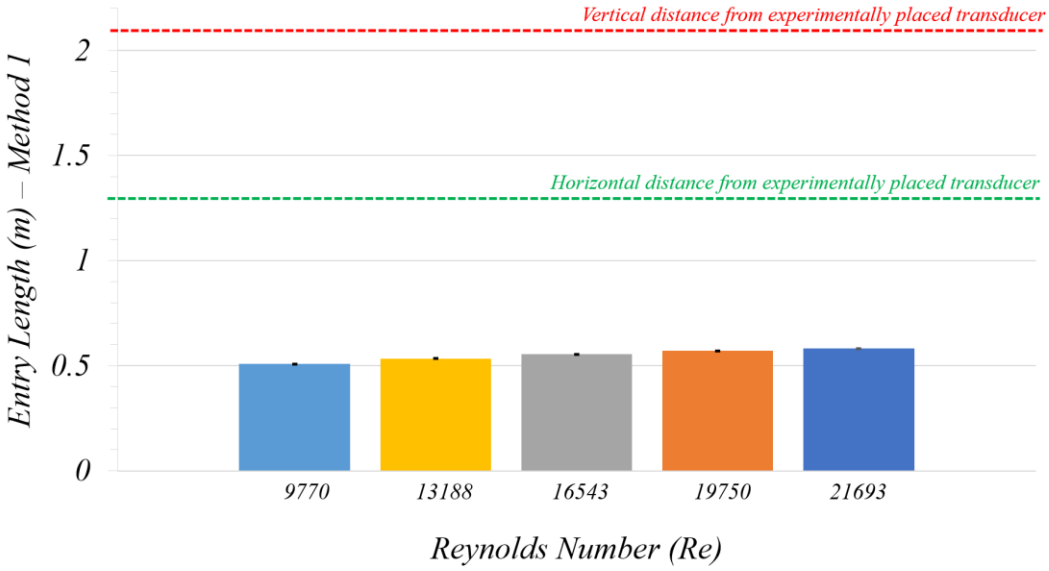

Figure 3.4 Error for entry length calculations using Shames, (2003) where the red and green dotted lines indicate the vertical and horizontal distance from experimentally placed transducers and the closest bend in the pipe, respectively

3.3.2 Method 2: Zagarola and Smits, (1998)

Another method was used to validate the calculation of the minimum entry length and to prove that the entry lengths determined were accurate. The entry length to diameter ratio in Eq. (3.23) uses the Darcy friction factor (f) which is calculated using the roughness coefficient, ε (m) (Haaland, 1983; Rice, 2013). This is dependent on the pipe material used, where ε for PVC pipes was used

(approximately 1.5 x 10^{-6} m) (Moody, 1944; Roberson and Crowe, 1996; Pahwa and Pahwa, 2014).

The method in Eq. (3.22) for determining the friction factor was validated by Rice, (2013) using data from previous literature which included Toonder and Nieuwstadt, (1997), McKeon *et* al., (2004), Wu and Moin, (2008) where the agreement was found to be very good. The friction factor is calculated in Eq. (3.22) from Haaland, (1983) using the Reynolds numbers shown in Table 3.7 and the pipe diameter in Table 3.6. The array of friction factor values is then used in Eq. (3.23) from Zagarola and Smits, (1998) to determine the entry length to pipe diameter ratio.

$$f^{-\frac{1}{2}} = -1.8 \log\left[\frac{6.9}{Re} + \left(\frac{\varepsilon}{3.7D}\right)^{1.11}\right] \tag{3.22}$$

$$\frac{L}{D}\ (method\ 2) = \frac{0.5}{f} + \frac{5}{f^{\frac{1}{2}}} \tag{3.23}$$

The entry length to diameter values calculated using Eq. (3.22 – 3.23) are shown in Fig. 3.5 with their corresponding Re. Errors for Re are shown where the initial error for flow rates was used to determine the overall error. The entry lengths using Shames, (2003) were found to be much lower than the actual entry lengths of 1.3 and 2.1 m which shows that the flow is fully developed before analysis in the horizonal and vertically mounted probes. In comparison, the entry lengths determined using Zagarola and Smits, (1998) were found to be almost double (1.11-1.28 m) where the highest entry length value was just 0.02 m smaller than the horizontal entry length.

Error bars shown in Fig. 3.5 show the 1% error from the flow rate measurements as shown in Fig. 3.4. For both Fig. 3.4 and 3.5 the error is negligible as the error bars can barely be seen. However, this error was determined using the initial error for flow rate measurements and not specifically for the entry length values

determined. Therefore, the error for all variables used to determine the entry lengths was determined. This is shown in the following error analysis section.

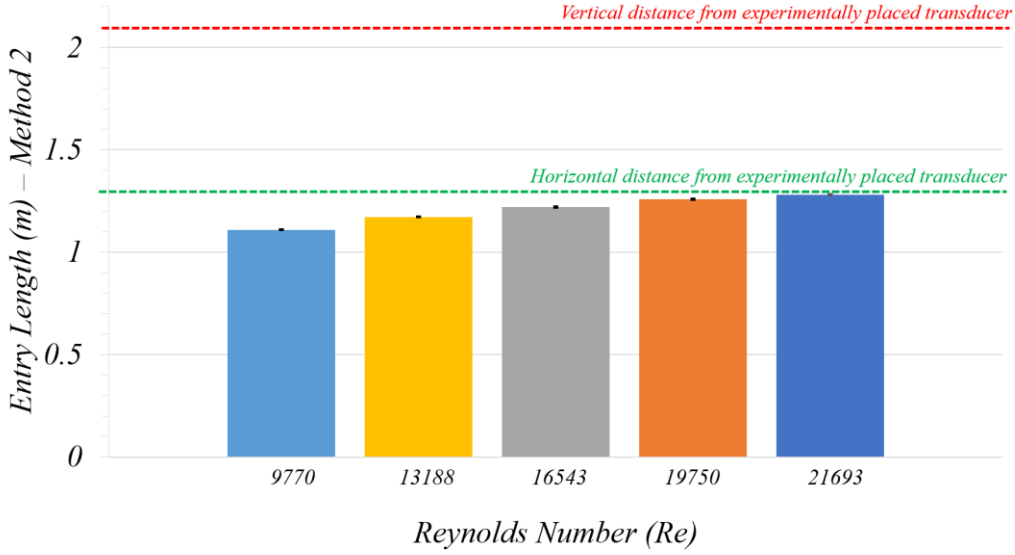

Figure 3.5 Error for entry length calculations using Zagarola and Smits, (1998) where the red and green dotted lines indicate the vertical and horizontal distance from experimentally placed transducers and the closest bend in the pipe, respectively

3.3.3 Error analysis

For a complete error analysis, the maximum and minimum flow velocities were used to determine the Re and consequently the minimum entry length. For example, the maximum flow velocity at the measured flow velocity of 0.88 m/s was 0.89 m/s whilst the minimum was 0.87 m/s. This led to a Re variation of +/- 1 % as Re is determined using a linear calculation as shown in Eq. (3.20). Table 3.8 shows the errors for all variables determined using both methods for entry length calculations.

Table 3.8 Entry length calculations using two methods with errors shown for each variable

Re (+/- 1%)	Method 1		Method 2			
	L/D (+/- 0.17%) (Shames, 2003)	*L* (m) (+/- 0.17%)	$f^{-0.5}$ (Haaland, 1983)	*f*	*L/D* (Zagarola and Smits, 1998)	*L* (m)
9770	20.3	0.51	5.67 (+/- 0.14%)	0.031 (+/- 0.28%)	44.3 (+/- 0.17%)	1.11 (+/- 0.17%)
13188	21.4	0.53	5.9 (+/- 0.13%)	0.029 (+/- 0.26%)	46.9 (+/- 0.17%)	1.17 (+/- 0.17%)
16543	22.2	0.56	6.07 (+/- 0.13%)	0.027 (+/- 0.26%)	48.8 (+/- 0.18%)	1.22 (+/- 0.18%)
19750	22.9	0.57	6.21 (+/- 0.12%)	0.026 (+/- 0.25%)	50.3 (+/- 0.18%)	1.26 (+/- 0.18%)
21913	23.3	**0.58**	6.29 (+/- 0.12%)	0.025 (+/- 0.25%)	51.2 (+/- 0.19%)	**1.28 (+/- 0.19%)**

3.3.3.1 Shames, (2003)

The ratio of entry length to diameter was determined using the minimum and maximum Re values which returned a variation of 0.17% for derivations using Shames, (2003). This error was consistent across all entry length to diameter values as the correlation in Eq. (3.21) is approximately linear in the region between a Re of 9000-22000, this is shown in Fig. 3.6 where the R^2 was 0.99 when applying a linear correlation for Re vs L/D. The minimum entry length is determined linearly by multiplying the entry length to diameter by the pipe inner diameter, this results in the error remaining consistent at +/- 0.17%. This error variation of +/- 0.17% leads to a maximum numerical error (for the largest Re = 21,913) of 0.000986 m which is considered negligible.

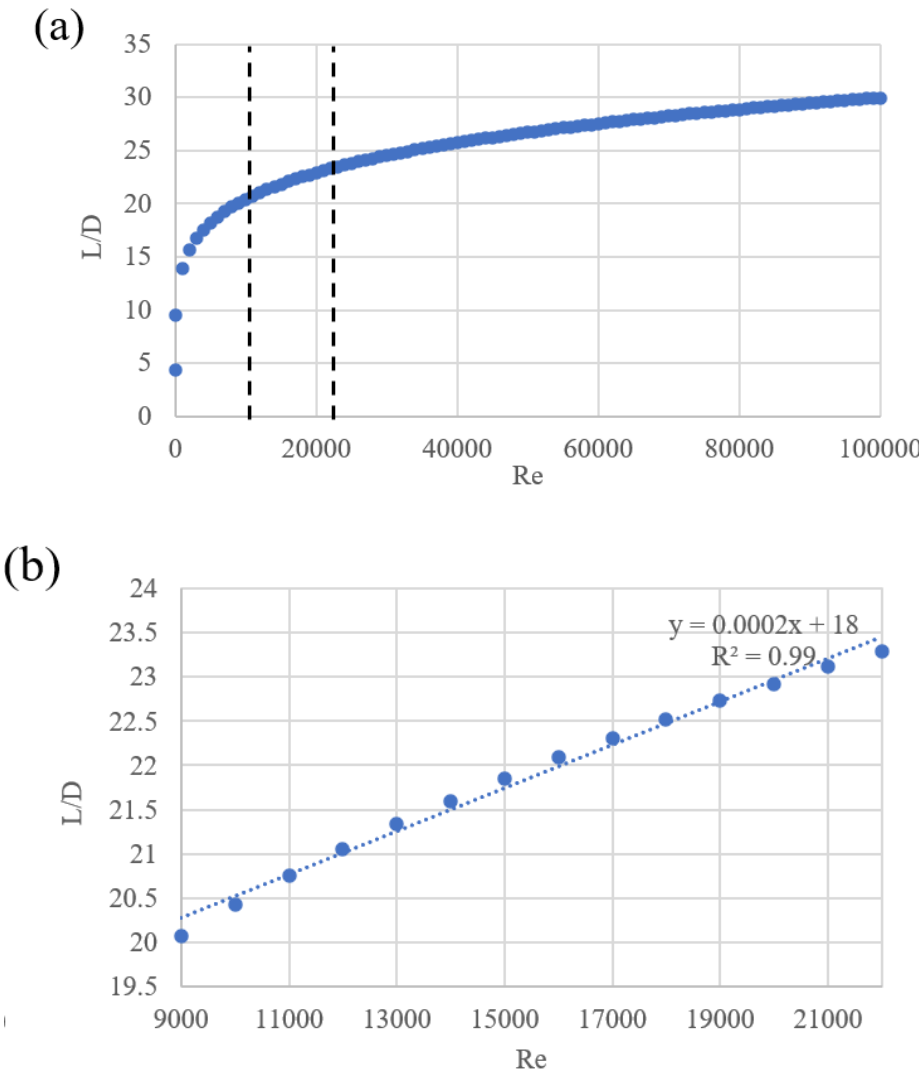

Figure 3.6 Variation of Entry length to diameter with Re and (b) isolation of experimental Re values where L/D was determined using Shames, (2003)

3.3.3.2 Zagarola and Smits, (1998)

The error for the friction factor values is determined by using the minimum and maximum Re in Eq. (3.22) and (3.23). The errors across the friction factor values are not consistent and decrease with an increasing Re. The error changes due to the logarithmic calculations shown in Eq. (3.22) where the log plot varies more at smaller Re and begins to level out at larger Re values. This is shown in Fig. 3.7 (a) and (b) which shows how $f^{-0.5}$ changes with an increase in Re from the experimental limits of 9000-22000 where the R^2 was found to be 0.98. The plot

varies more at lower Re and follows the linear prediction in Fig. 3.7 (b) at higher Re which is shown by the decrease in error for $f^{-0.5}$ with increasing Re.

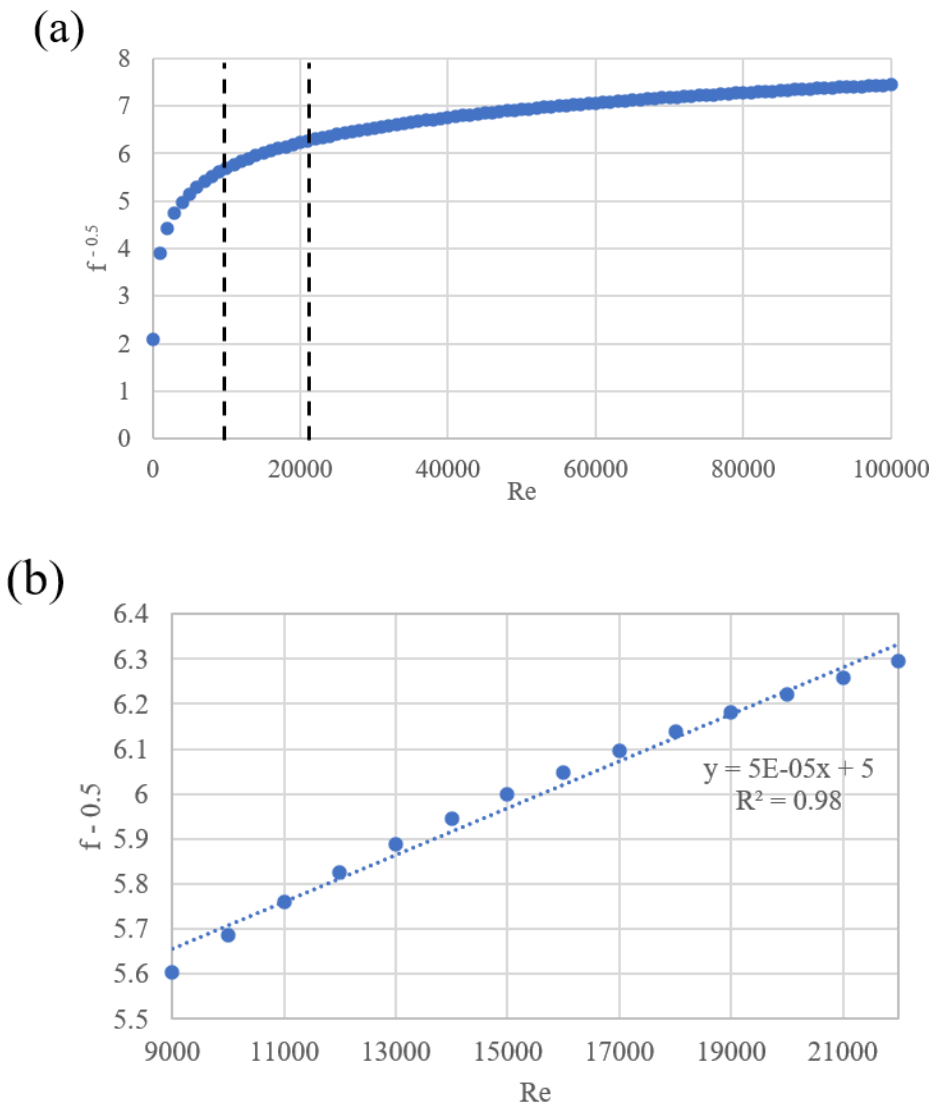

Figure 3.7 Variation of Darcy friction factor with Re and (b) isolation of experimental Re values

As shown in Table 3.8, the increase in Re led to a decrease in *f*. The error for the entry length to diameter increases with decreasing Re. This shown in Fig. 3.8 where the L/D values stray from the linear correlation at decreasing *f* values. Fig. 3.8 is isolated in the specific experimental Re in Fig. 3.8 (b). Error between both methods for the entry length values is comparable where the maximum error when

using Zagarola and Smits, (1998) correlation is 0.19% (specifically for a Re of 21,913) whilst the maximum error when using Shames, 2003 correlation is 0.17%. This shows that for this specific data (where the Re ranges from 9,770 – 21,913), the two methods had similar negligible errors. However, for another user who is using higher Re, the error when using Zagarola and Smits, (1998) increases with an increasing Re and therefore becomes less accurate at higher Re. Whilst the error when using Shames, (2003) stays relatively stable with variation of Re. Errors from the +/- 1% accuracy using the flow meter are shown in Fig. 3.4 and 3.5. In both figures, the error is almost negligible. However, when considering the error specifically for the entry length calculations, the error is significantly lower at 0.17-0.19% which shows that the error in flow rate measurements has no effect on the accuracy of the entry length values calculated.

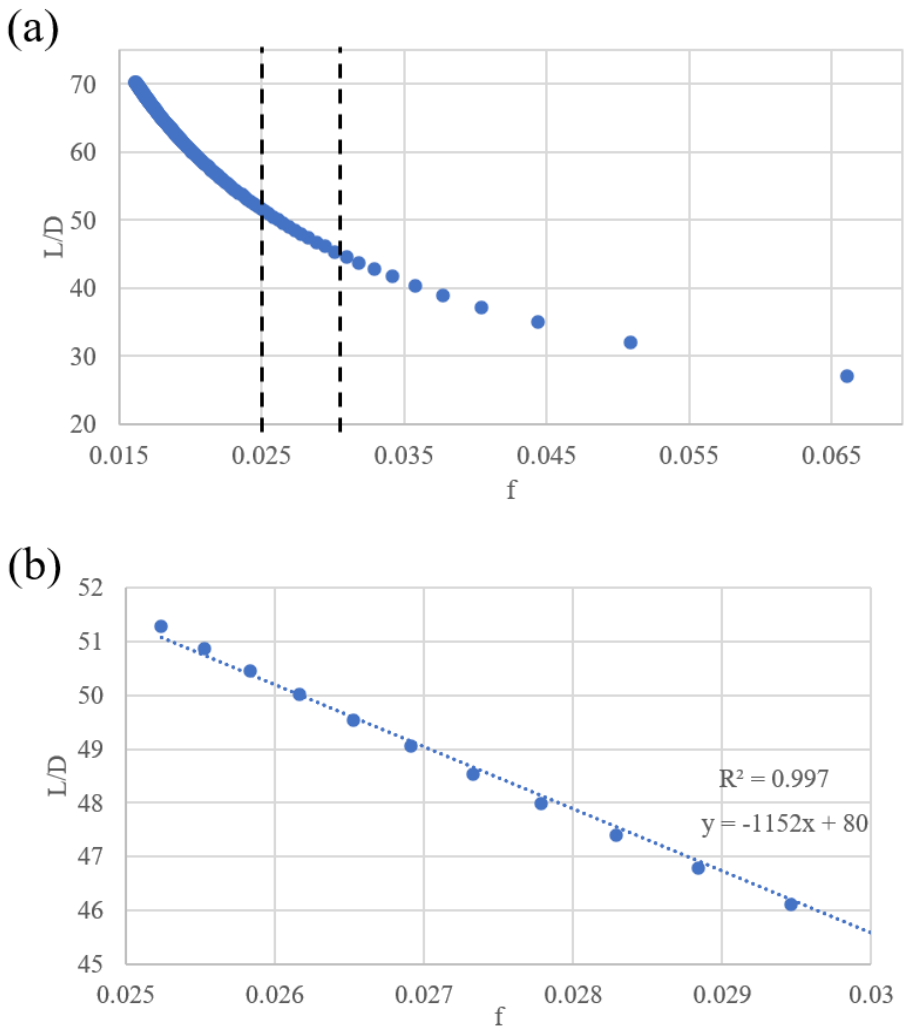

Figure 3.8 Variation of Entry length to diameter with Darcy friction factor and (b) isolation of experimental Re values

3.4 Conclusion

This Chapter covers all the theory required in this thesis where the first section covered the UVP derivations. These derivation are used to convert raw echo data to readable voltage data. Equations from Rice, (2013) and Ainslie and McColm, (1998) were required for the initial conversion. Equations from Thorne and Hanes, (2002) were then followed to convert this voltage data to a logarithmic voltage function. The attenuation coefficient was found from the logarithmic voltage values determined experimentally. Form function and the normalised

cross section values were calculated heuristically from Betteridge *et al*., (2008) and experimentally. Derivations for scattering (Betteridge *et al*., 2008) and viscous losses (Urick, 1948) were utilised to show the combined attenuation coefficient. These derivations from the UVP to the combined attenuation coefficient were required to convert the raw data obtained experimentally and establish whether the attenuation coefficients could be compared to heuristic expressions from literature in Chapters 4 and 5. The speed of sound was predicted using expressions from Urick, (1979) and used to illustrate the effect of concentration on the speed of sound for various sediment types. The change in speed of sound was found to be negligible from predicted values and this is used to compare to velocity profiles established in Chapter 7 and 8.

The viscous boundary layer thickness was calculated using the particle size data of various sediment types used in this thesis where the viscous boundary layer thickness was used to determine the particle Reynolds number. This boundary layer thickness was used to establish a trend between boundary layer thickness and viscous absorption in Chapters 5, 6 and 8 where the different sediment types were used. The relationship between boundary layer and viscous absorption was predicted for the two transducer frequencies used and results in later Chapters will be used to explain this theory further. The particle shear and viscosity were calculated and the effect of the sediment concentration on these properties was explored. It was found that the sediment had a negligible effect on particle shear and viscosity and therefore, this led to viscosity values of the dominant liquid to be used for further calculations.

The pipe loop methodology covers the calculated pipe Reynolds number when using various pump speeds. These pumps speeds were chosen as the minimum speed required for dispersion and the maximum speed before the pump integrity was at risk. The entry length was determined from these Reynolds numbers and the actual entry lengths (distance from the transducer placement and closest pipe bend) were compared. Where the calculated entry length needed to be shorter than the actual entry length to ensure flow was fully developed at the point of analysis.

The entry length was calculated using two separate methods which both found the actual entry lengths to be sufficient for the flow to be fully developed before analysis of the suspensions. The error analysis was determined from the experimental error from the pump and this was used to determine the error from the entry length values.

4. CALIBRATION OF THE UVP TRANSDUCERS

CHAPTER SUMMARY

The aim of this Chapter is to analyse a single grade of silica glass beads with transducers of varying frequency and active radius to determine whether the radius and frequency effect the sedimentation attenuation coefficient established. A detailed calibration method from Bux *et al*., (2019) was used here with an additional error analysis on the sedimentation attenuation coefficient using the array of echo amplitude values extracted from the UVP. This has not been achieved before. Tonge *et al*., (2021) used the UARP (a bespoke ABS) to determine the attenuation profiles for similar glass particles, however, an error analysis was never conducted on the sedimentation attenuation coefficients produced. Rice *et al*., (2014) determined sedimentation attenuation coefficients for two sizes of similar glass beads using a 2 and 4 MHz transducer. However, no error analysis was conducted, and attenuation coefficients were compared to predictions from Thorne and Hanes, (2002) and Thorne and Meral, (2008). Updated predictions from Betteridge *et al*., (2008) which are specifically for glass spheres were not used. Therefore, in this Chapter the Betteridge *et al*., (2008) prediction is utilised, this expression only considers scattering losses and therefore, expressions from Urick, (1948) are incorporated for viscous losses. The combined attenuation prediction from both was used to compare to measured attenuation values. This has not been achieved before using the UVP. Here, novel error analysis was conducted on the measured attenuation coefficients and these measured values were compared to attenuation predictions from scattering and viscous losses.

4.1 INTRODUCTION

In this Chapter, UVP (ultrasonic velocity profiler) transducers of varying active radii and frequency were used for analysis of nuclear waste simulant suspensions. The use of varying radii and frequency allowed the author to investigate whether differing probes would affect the acoustic profiles. Novel acoustic profiles were

extracted using transducer of varying transducer radii and frequency. Research has been done for the use of transducers with varying frequency for analysis of varying suspensions, but not for transducers of varying radii (Rice, 2013; Tonge, 2021). In this thesis, the aim was to mount transducers onto pipes which requires probes with a smaller diameter, therefore, the transducers were validated to ensure a change in active radii would not compromise the accuracy of the data produced. The frequency of the transducer also has an effect on the acoustic profiles as well as the attenuation coefficients extracted. The higher the frequency of a transducer, the higher the energy and the shorter the wavelengths (Jackson, 2019). This means the transmitted signal strength are higher but the effective penetration depth decreases.

This Chapter details the calibration method used to extract the attenuation coefficients for glass dispersions which were used for validation of coefficients extracted in ongoing experiments. The results from this Chapter were also compared to previous literature to ensure the attenuation coefficients were accurate for this type of nuclear simulant (Rice, 2013; Bux, 2016). Bux *et al*., (2019) applied a calibration method for the extraction of attenuation properties where a calibration mixing tank was used with dimensions of 0.8 m height and 0.3 m diameter. The calibration method used by Bux *et al*., (2019) is shown in Fig. 2.19. A mixer impeller system with a mini-impeller around halfway through the tank was used to disperse the suspensions whilst four transducers were submerged into the suspension. In this literature, similar glass beads were used where Bux *et al*., (2019) utilised a concentration of 0.5 - 10 $kg.m^{-3}$. The methodology for determining the attenuation coefficient provided by Bux *et al*., (2019) used logarithmic voltage profiles. From this attenuation coefficient, the normalised scattering cross section and the form function can be calculated using heuristic expressions from Betteridge *et al*., (2008). The backscattering constant can be predetermined using the form function. The measured transducer constant can then be calculated using the measured attenuation coefficient and the heuristic backscattering constant. The measured backscattering constant can be determined using the measured transducer constant which allows for the calculation of the

measured form function. The process is relatively simple and only requires analysis of homogeneous suspensions within a calibration rig. Attenuation coefficients from Bux *et al*., (2019) can be used as a measure of how accurate the calibration system is in this Chapter. Tonge *et al*., (2021) followed the same calibration method highlighted from Bux *et al*., (2019) where a similar calibration tank was used with the same dimensions as shown in Bux *et al*., (2019) and a mixer impeller system with a single impeller. Similar glass particle suspensions were used with a d_{50} of 40 μm with a concentration range between 2.5 – 78.6 g/L. Tonge *et al*., (2021) focused on the determination of a dual frequency inversion profile where the concentration of the suspension can be measured with distance from the transducer.

Transducers have been used to determine solids concentrations from backscatter intensity extensively (Spelt *et al*., 2001; Gartner, 2004; Moore *et al*., 2013; Huang *et al*., 2019). Huang *et al*., (2019) used optical fibres to determine concentration measurements from backscatter intensity. These experiments were on a smaller scale and required *in situ* analysis, however the focus of this thesis is to transition into remote analysis. Moore *et al*., (2013) used multi-frequency transducers to monitor grain size and concentration where the sedimentation attenuation coefficient was plotted for corresponding grain radius. This demonstrated the various regimes of attenuation; viscous and scattering where lower grain radii attenuated predominantly due to viscous losses and larger due to scattering. This will allow the author to predict the attenuation from silica glass beads depending on the grain radius. This will also allow the characterisation of suspensions of varying particle sizes to be differentiated depending on attenuation regimes. Moore *et al*., (2013) was also able to show attenuation as a function of transducer frequency where higher frequency probes led to an increase in sedimentation attenuation coefficient. This increase in coefficient value was more predominant in regions of high viscous and scattering losses where the author will be able to differentiate between transducers using the experimental sedimentation attenuation coefficients. Thorne *et al*., (2021) have focused on the scattering characteristics of mixed sands where stratification effects above the bed were not

accurately accounted for which led to divergence from modelled concentration in the suspension. In this Chapter, only monodisperse systems were explored and polydispersity in the suspensions was considered to be negligible, this was to allow for a simple calibration procedure where attenuation properties can be extracted and compared to previous monodisperse calibration procedures described by Rice *et al*., (2014), Bux *et al*., (2019) and Tonge *et al*., (2021).

The actual frequency of the transducers was not determined in this thesis. However, the frequency of the transducers was determined previously by Rice, (2013) using Fast Fourier Transform (FFT). The maximum frequency shift was determined to be double the sample rate by using the Nyquist sampling theorem. From conclusions, it was found that the 2 and 4 MHz frequency probes have minimal frequency shift and the measurement window was limited to limit the frequency bandwidth. This limitation led to slight truncation of the velocity profiles at the highest flow rates. However, this had a limited effect on the attenuation profiles.

Novelty is in the practical validation. Transducers of varying frequencies and active radii have not been used to test silica glass beads. The distance required for accurate profiling is unknown and can be validated through experiments. For the UVP, the transducers need to be tested to understand whether transducers of varying active radii and frequency produce accurate profiles and what the accurate profiling distance is for the silica glass bead suspensions used in this thesis.

4.2 Materials and Methods

4.2.1 Materials

Silica glass bead dispersions (Honite, Guyson Ltd) with a d_{50} of 36 µm were used for acoustic profiling; more information on the measurement data is shown in Fig. 4.6 (Guyson Ltd, 2021). This specific material has been utilised in tandem with acoustics in previous literature (Rice *et al*., 2014; Hunter *et al*., 2016; Bux *et al*., 2019; Tonge *et al*., 2021) for extraction of the attenuation profiles and sedimentation attenuation coefficient. The silica glass beads should acoustically

have a distinct scattering attenuation profile based on Moore *et al.*, (2013) where the particle size determines whether the majority of the attenuation is in the viscous or scattering regime.

This specific silica glass bead blend is composed of spherical particles that are assumed to behave ideally with acoustics however this will be investigated in this Chapter by observing the acoustic behaviour. The glass bead dispersion is shown in Fig. 4.1 where the sphericity of the particles is easily visible. There is a single non-spherical piece of contamination, however this is assumed to be a contaminant and is therefore statistically insignificant. A Carl Zeiss EVO SEM (MA15) was used to image the blend silica glass beads.

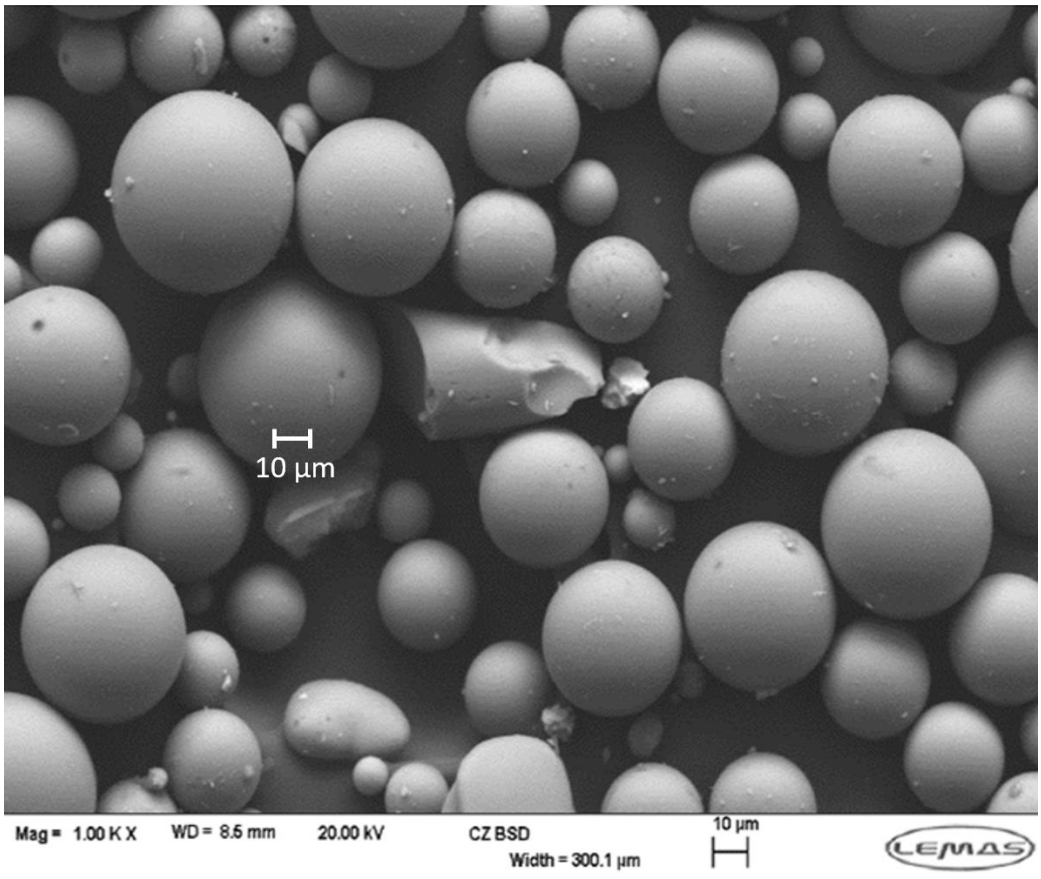

Figure 4.1 SEM EVO images of silica glass beads with a d_{50} of 36 µm (1000 X magnification)

4.2.2 Particle size analysis

Samples (5 ml vials) were taken at each concentration for the silica glass bead dispersion using a pump which extracts samples from the middle of the tank, this is just above the impeller system and below the *in situ* transducer placement as shown in Fig. 4.2. These samples were analysed in a Mastersizer 2000E (Malvern Panalytical Ltd) to determine the particle size distribution of the silica glass and to establish if it was a monodisperse suspension. The Mastersizer uses laser diffraction to measure the intensity of light scatter as the laser passes through a dispersed particulate sample. The scattering pattern is analysed to calculate the size of the particles (Blott *et al*., 2004; Kippax, 2005; Bux *et al*., 2015; Rice *et al*., 2015). The Mastersizer outputs data as a relative distribution on the volume of particles in their range of size classes. These samples were added to the Mastersizer Hydro 2000SM aqueous dispersion cell with external dimensions of 140 x 175 x 390 mm (Lockwood *et al*., 2021b). The dispersion cell was filled with ~120 ml of deionised water and analysed to produce a background measurement. A small agitator provided shear in the vessel at a rate of ~900 rpm. Small amounts of the sample vials were added to the dispersion cell using a pipette until the Mastersizer detected a sufficient amount of attenuation needed for diffraction. Data were taken over a time period of 2 minutes with data outputted to a CSV-type file every 10 seconds. Once the experiment was complete, the dispersion cell was emptied and cleaned with deionised water several times until the background measurement showed that no particles were left in the cell.

4.2.3 UVP testing parameters

All experiments were conducted with a commercial ultrasonic velocity profiler (UVP) used in backscatter mode from Met-flow S.A. The UVP-DUO (Met-flow S.A.) outputs a raw echo amplitude where the backscatter amplitude signal was extracted as outlined in Eq. (3.01). The same UVP parameters were used throughout this calibration experiment to ensure the same experimental set-up for the three transducers. A summary of the experimental UVP testing parameters is

given in Table 4.1 for the 2 and 4 MHz probes. It is noted importantly, that the backscatter was profiled to a maximum distance of ~40 cm for each measurement.

Table 4.1 UVP Instrument Parameters using 2 MHz and 4 MHz probes

Parameter	2 MHz Probe	4 MHz Probe	Units
Number of channels	272	272	
Number of profiles	1023	1023	
Sampling period	60	60	ms
Speed of sound	1480	1480	m/s
Maximum depth	399	399	mm
Pulse repetition frequency	1.86	1.86	kHz
Minimum-maximum measurement distance (mm)	0.37 - 302	0.37 - 302	mm
Channel distance	1.11	1.11	mm
Channel width	0.74	0.37	mm
Angle	90	90	°
Frequency of transducer	2	4	MHz
US voltage	150	150	V
Gain start and end	6-6	6-6	

The travel time between the instrument emitting the pulse and receiving the echo corresponds to the sampling period of 60 ms at a pulse repetition frequency of 1.86 kHz. This sampling period was chosen so a sufficient period of time was given for sampling of the suspension. The minimum and maximum measurement distances show the window of measurement in the tank. The depth measurements were segregated into 1.11 mm bins which shows the resolution limits of the UVP. Over the maximum measurement distance of 302 mm, there were 272 channels split into the 1.11 bins. The maximum depth shows the maximum distance available for analysis, however, for this experiment a shorter distance was selected

to ensure the suspension was homogeneous for analysis. The distance beyond 302 mm would go beyond the impeller where the turbulence would affect the acoustic profiles. An average backscatter voltage vs depth profile was recorded using an average of 1023 profiles where the 60 ms sampling period was repeated 1023 times. The angle and frequency correspond to transducer properties where the angle shows how the transducer has been mounted and the frequency of the transducer itself. The gain is a function of the amplification of the sound (Auerback *et al.,* 2019) which is used to convert the raw echo amplitude to a voltage value (Rice, 2013). The gain value is constant through the start and end of the measurement window which shows that the gain is consistent through the tank. The values available for the gain range from 1-9 where a compromise value of 6 was chosen where the signal was amplified enough but not too much to produce an artificial signal (Rice, 2013). The US voltage shows the strength of the transmitted signal (Coll, 2022). The speed of sound corresponds to the speed of sound in water which is a user defined property as the addition of particles was assumed to have a negligible effect on the speed of sound; this was proven in Chapter 3. The only property that changes with the frequency of the transducer is the channel width which shows that the 2 MHz probe has a wider channel in comparison to the 4 MHz probe. This shows that the lower frequency probe is able to analyse a larger span of the tank.

The transducers focal distance, r_f is defined in Eq. (4.01) and is a function of the radius of the active face of the transducer, a_t and the wavelength, λ (Rice, 2013; Sorrell and Jayasuriya, 2019) where the wavelength is determined using the speed of sound in water, c_{water} and the frequency, f ($\lambda = c_{water}/f$) (Behrman, 2021). This can be used to calculate the near-field distance of the transducer, r_n as shown in Eq. (4.02) (Rice, 2013). The beam divergence angle can also be determined in Eq. (4.03) which shows how much the beam has spread out over the increasing distance from the transducer (Anan'ev, 2020). The beam divergence has been found to produce errors of small magnitude of ~ a few percent for the measured flow rate and therefore, the calculated velocity (Rice, 2013). As a result, the beam divergence has been calculated but is not assumed to have an effect on the

acoustic profiles. All properties are shown in Table 4.2 for the three transducers used in this Chapter.

$$r_f = \frac{{a_t}^2}{\lambda} \tag{4.01}$$

$$r_n = \pi\, r_f \tag{4.02}$$

$$\gamma_0 = \sin^{-1}\left(0.255\frac{\lambda}{a_t}\right) \tag{4.03}$$

Table 4.2 Transducer Properties for the 2.5 mm 2 and 4 MHz transducers

Frequency, f, (MHz)	Radius of active face of transducer, a_t (mm)	Focal distance, r_f (mm)	Near-field distance, r_n (mm)	Beam divergence angle, γ_0 (degrees)
2	2.5	8.5	26.5	4.38
2	5	33.4	104.9	2.19
4	2.5	16.9	53.1	2.19

The beam divergence of the 2.5 mm radius 4 MHz transducer and the 5 mm 2 MHz transducer was the same due to the compromise between wavelength and active radii.

4.2.4 Methods

The calibration rig shown in Fig. 4.2 (a) was used to submerge the three transducers of varying active radii and frequency. This tank was used for all experiments from Chapter 4-6 to ensure that tests were completed in the same environment.

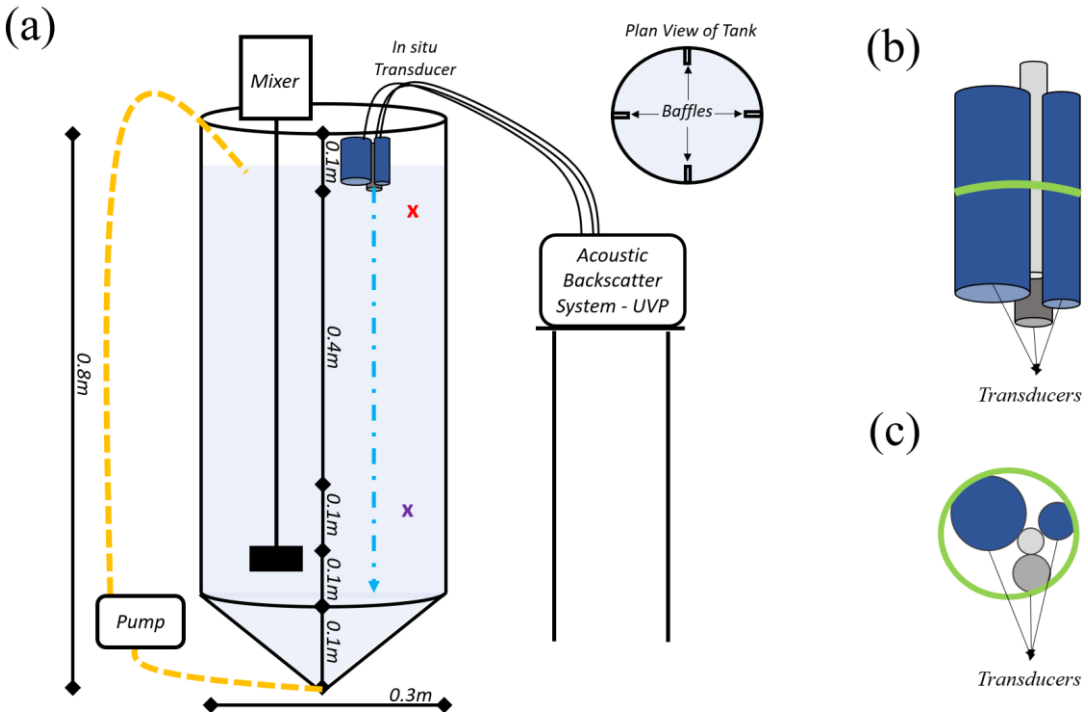

Figure 4.2 (a) Schematic of calibration rig for the calibration of the UVP transducers where the red and purple crosses indicate the height at which samples were taken, (b) schematic of the three transducers from the side and (c) in plan view

A cylindrical tank was engineered with four baffles distributed equally on the inner diameter of the tank. This is shown in the plan view of the tank in Fig. 4.2 (a). The baffles were secured into the tank to enhance dispersion and ensure a top to bottom flow which limits the possibility of sediment settling at the bottom (Kokossis *et al.*, 2021). A pump was also connected to the bottom of the tank and recirculated suspension to the top which is shown in Fig. 4.2 (a). Recirculation of the suspension enhanced mixing and collected any material which had settled, this ensured the concentration of the sediment was consistent across the tank (Schoeddert *et al*., 2019). The tank was constructed with a conical bottom in Fig. 4.2 (a) where a cylindrical PVC base had been installed to prevent the tank from falling over and ensure a stable testing environment. The tank's conical bottom prevented a layer of material settling on the bottom of the rig and funnelled material into the pump pipe for recirculation (Meesters and Merkus, 2015). The

mixer-impeller system (500 rpm impeller speed, 100 mm impeller diameter) promoted dispersion across the tank and maintained a homogeneous suspension environment (Satjaritanun *et al*., 2021).

Three different transducers were placed *in situ* in the tank with varying active face radii and frequency. The transducers were connected to a rod and secured using a cable tie which is shown in Fig. 4.2 (b) and (c). This rod was connected to a clamp and placed into the tank, so all transducers were submerged into the suspension. The mixer and rod were connected to the same clamp which ensured limited movement of the transducers and a steady experimental run. Inside the tank were a: 2 MHz 2.5 mm probe, a 2 MHz 5 mm probe and a 4 MHz 2.5 mm probe. Probes with frequencies of 2 and 4 MHz have previously been found to give accurate acoustic profiles for similar silica glass beads to those used in this Chapter (Rice, 2013; Bux *et al*., 2019; Tonge *et al*., 2021). In Fig. 4.2 (b) and (c), the blue probes indicate 2 MHz frequency transducers whilst the grey indicate a 4 MHz transducer. The light blue line in Fig. 4.2 (a) shows the projection of the sound signal through the tank from all three probes.

In this thesis, the question is whether the transducers can accurately analyse in both the rig and in a pipe (which is used in later Chapters). Jackson, (2019) found from theoretical learnings that 2 MHz probes were able to penetrate further due to the longer wavelength, however the lower frequency meant that profiles close to the probe were inaccurate. This distance is unknown for the transducers used in this thesis where the near field distance is known but the distance required for accurate profiling is unknown. This needed further investigation through experimental validation. The pipe width used in later Chapters has a diameter of 0.03 m. Therefore, the transducers used in this thesis need to be tested on suspensions to understand whether the pipe width is enough distance for accurate profiling. Data produced in this Chapter will be used to determine which frequency probe is most appropriate for use in the tank and pipe.

Probes with active radii of 2.5 mm can be mounted onto pipe loops without significant shaving down of the pipe wall (Prateepasen *et al*., 2011; Rice, 2013). Therefore, both 5 and 2.5 mm probes were compared to ensure the smaller probes were able to accurately analyse suspensions. Jackson, (2019) found that larger probes with a larger active radius of 5 mm were able to analyse a larger breadth of the tank. However, this was primarily a theoretical approach which required practical validation. In this thesis, the larger radius makes it difficult to mount onto a cylindrical surface where the wall will need to be shaved down for flat mounting. From the onset, higher frequency probes with a smaller diameter appear to be best suited for analysis in pipes, whilst lower frequency probes with a smaller diameter are better suited for large tanks. However, this still needs to be shown in the resulting data. Calibration data from this Chapter for all three transducers can be used to validate data in further Chapters using various experimental set-ups.

There was a concern of interfering signals as all three transducers were connected to the UVP (ultrasonic velocity profiler) in frequency dependent ports. The UVP is limited where multiple transducers can only be activated if they are the same frequency. Therefore, the two 2 MHz probes were activated using a 60 ms pulse with a 100 ms echo disturbance delay between each transducer; this is shown in Table 4.1. After this, the 4 MHz transducer was activated. All UVP parameters for the 4 MHz probe are also shown in Table 4.1 where the transducer pulse and delay were maintained for both transducer frequencies. Data was collected from all three probes at a single concentration and repeated for each change in concentration. When using the three transducers in this calibration set-up there was a 280 ms per profile total time. For the full experiment there were 1023 profiles, and the total experiment time was 286 seconds.

Dry powdered suspension was added to the tank slowly at a rate of 100 g/min (to produce a concentration of 11.9 g/L) to prevent air entrainment and coagulation of material in one area of the tank. The suspension was then left to disperse for 5 minutes to ensure a homogeneous suspension. The mixer-impeller system was

maintained at 500 rpm throughout the addition of the powder and left on for the experiments. The pump was only turned on at a rate of 125 rpm after 5 minutes of mixing to ensure the powder had sufficiently dispersed. Data were collected from the three transducers for that specific solid suspension concentration; after this, powder was added to increase the concentration. This methodology was repeated until data were collected for a concentration range of 11.9 to 107.5 g/L.

Samples were taken at each concentration in the tank at the heights indicated in the red and purple crosses in Fig 4.2 (a) where the red and purple crosses are noted as measurement points 1 and 2, respectively. A multi-headed pump was used to fill 5 ml sample vials at the two heights once the suspension had been dispersed for 5 minutes to ensure a homogeneous concentration. These 5 ml sample vials were weighed and then dehydrated to ensure only the solid particles were left in the vials. The weight of the vials with the solid particles was compared to the empty weight (which was taken before the experiment). This weight was converted to the concentration by determining the volume of water in each 5 ml sample vial (using the vial weight with the suspension and the vial weight with the solid particles) and using the concentration = mass / volume equation (Kolev, 2007).

4.2.5 Raw echo amplitude to G-function

The raw echo amplitude, *E(r)* is extracted from the UVP and converted to the voltage, *V(r)* using Eq. (3.01) where the gain from Table 4.1 is used. The gain value of 6 translates to an arbitrary *g(r)* value of 6.67 which is used in Eq. (3.01) (Rice, 2013). An example of the conversion from the raw echo to the voltage is shown below in Fig 4.3 where the data are shown as a function of the distance from the transducer. In Fig. 4.3 (a), the raw echo amplitude is shown as a time averaged value where the echo across 1023 profiles at each distance point has been consolidated into a root mean square value. This echo amplitude value, *E(r)*, is then converted into the root mean squared voltage using Eq. (3.01), see Fig. 4.3 (b). The backscatter response is calculated by converting the voltage to decibels

(dB), see Fig. 4.3 (c) (Backscatter (dB) = $20\log_{10}$ (Voltage in Volts)) (Paul, 2006). The data in Fig. 4.3 was taken from a 5 mm 2 MHz transducer.

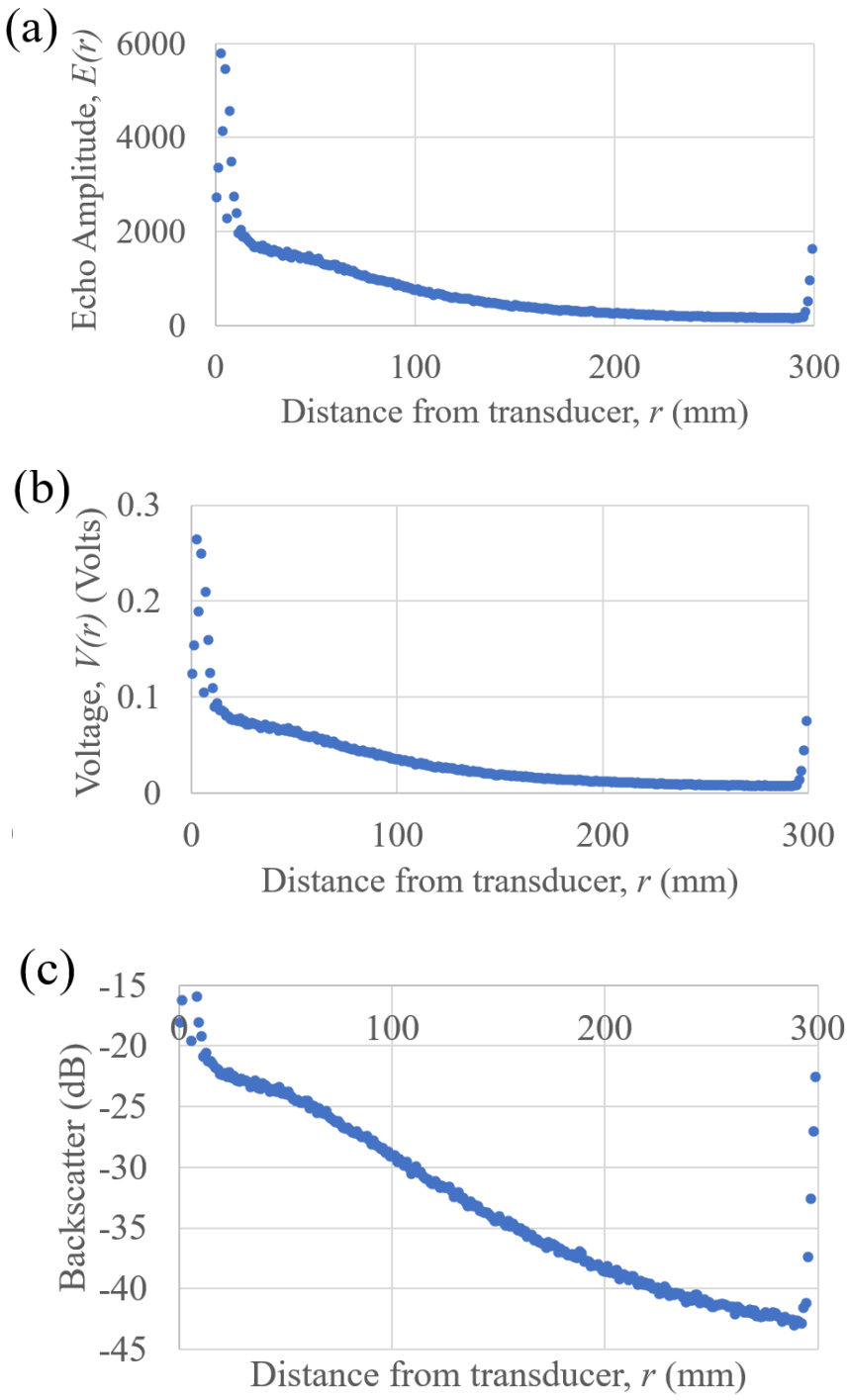

Figure 4.3 (a) Echo amplitude profile as a function of the distance from the transducer and the converted (b) voltage profile and (c) backscatter profile

The calibration method is detailed below in Fig. 4.4 where the experimental data have been used to determine the sedimentation attenuation coefficient. Fig. 4.4 also details the process for converting the raw echo amplitude data to the logarithmic voltage, *G*. This procedure has been developed from the calibration method detailed by Bux *et al*., (2019) and Rice *et al*., (2014).

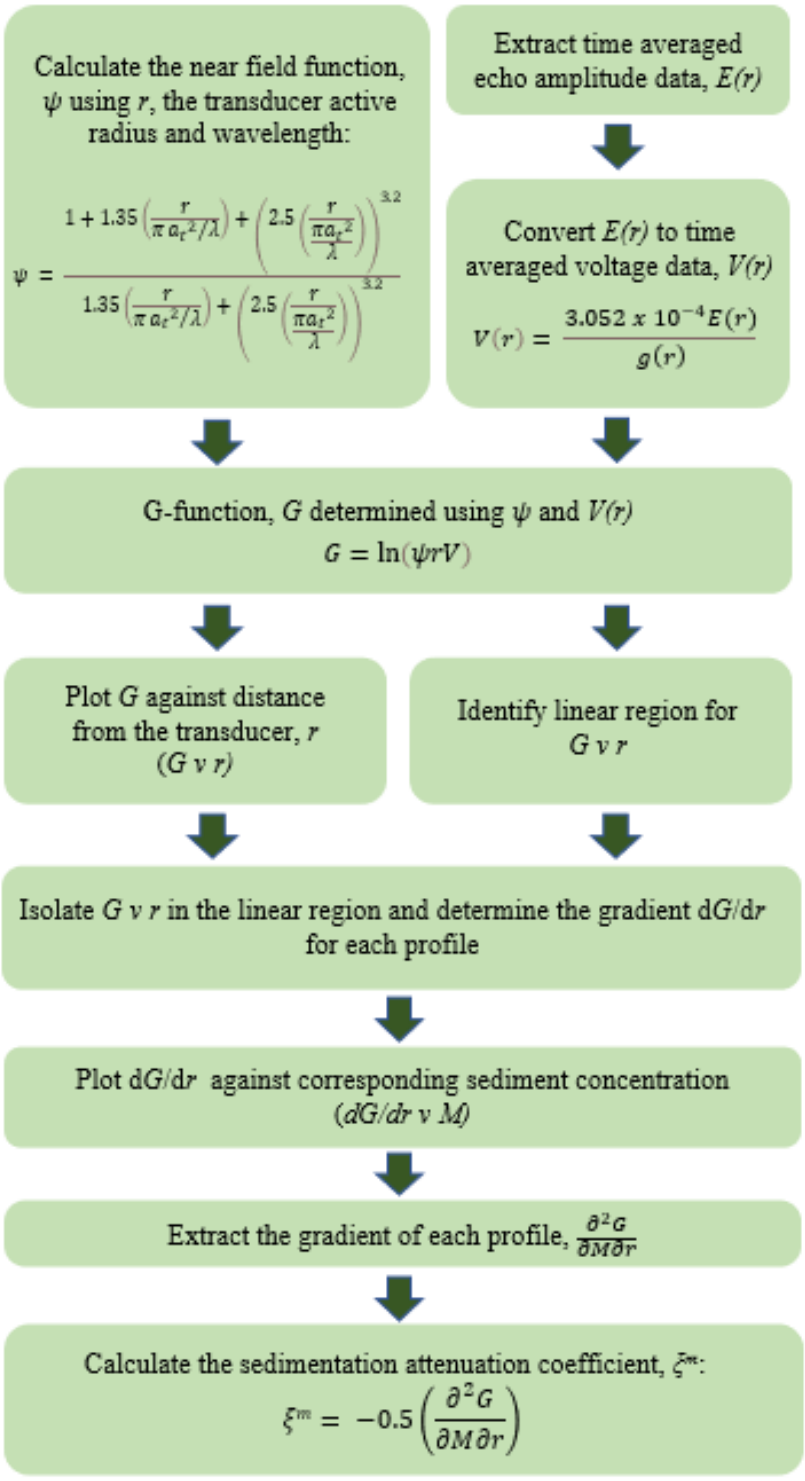

Figure 4.4 Detailed calibration method using the UVP

4.2.6 Error Analysis of Sedimentation Attenuation Coefficients

The *G*-function in Eq. (3.05) is determined experimentally and requires a root mean square of the voltage values, as shown in Fig. 4.3 (b). As the sedimentation attenuation coefficients are extracted from linear gradients which are user dependant there is a need to ensure that the resulting coefficients are accurate. Therefore, an error analysis is conducted on all experimental values extracted from the UVP. This is used to determine the error in sedimentation attenuation coefficient extracted. Across the raw echo amplitude data, there are 1023 profiles for each distance point. The error is established from the variation in these 1023 profiles. The distance points are limited to only include the error where the profiles are linear.

The raw echo amplitude is converted to the voltage using Eq. (3.01) where the gain (*g(r)*) required for the calculation is 6.67. Table 4.1 shows the UVP parameters where the gain at the start and end of the experiment is 6, this translates to an absolute gain value of 6.67 (Rice, 2013).

Once all raw echo amplitude data have been converted to voltage values using Eq. (3.01), the root mean square of the voltage can be calculated and shown as a function against distance. The error is calculated in Eq. (4.04) where N is the number of profiles (1023), V is each individual voltage value and V_{rms} is the rms voltage value at that distance point. Only the minimum and maximum concentrations are required to determine the error as these concentrations dictate the minimum and maximum *G*-function gradients used to determine the attenuation coefficient as shown in Eq. (3.06).

$$V_{err} = \frac{\sum_{i=1}^{N}(V_i - V_{rms,i})^2}{N} \tag{4.04}$$

The voltage values determined using Eq. (3.01) were converted to the *G*-function using Eq. (3.05) where the voltage array across the 1023 profiles was used as *V*. The distance values range from a limited linear region which is user identified. The distance values cannot range within the nearfield region as this region is

highly unpredictable. The active radius and wavelength are also used to determine the near field correction factor as shown in Eq. (3.03). The same methodology required to determine V_{err} in Eq. (4.04) was utilised to determine the error across the *G*-function values. The corresponding equation for G_{err} is shown in Eq. (4.05).

$$G_{err} = \frac{\sum_{i=1}^{N}(G_i - G_{rms,i})^2}{N} \tag{4.05}$$

The d*G*/d*r* values from the *G*-function profiles can be extracted using the linear predictions for each profile, this is shown below in Eq. (4.06).

$$\frac{dG}{dr}(M, g/L) = \frac{Change\ in\ G}{Change\ in\ r} \tag{4.06}$$

To calculate the minimum and maximum sedimentation attenuation coefficient, the minimum and maximum $d^2G/drdM$ need to be calculated. These are determined in Eq. (4.07) and (4.08) using minimum and maximum gradients for lowest and highest concentration values. The corresponding minimum and maximum sedimentation attenuation coefficients are determined using Eq. (3.06). The final values show the error of the coefficients determined. This process was repeated for every species.

$$\frac{d^2G}{dMdr}_{minimum} = \frac{\frac{dG}{dr}_{minimum,highest\ concentration} - \frac{dG}{dr}_{minimum,lowest\ concentration}}{Highest\ Concentration\ Value - Lowest\ Concentration\ Value} \tag{4.07}$$

$$\frac{d^2G}{dMdr}_{maximum} = \frac{\frac{dG}{dr}_{maximum,highest\ concentration} - \frac{dG}{dr}_{maximum,lowest\ concentration}}{Highest\ Concentration\ Value - Lowest\ Concentration\ Value} \tag{4.08}$$

4.3 Results and Discussion

All results are discussed below where the samples from the experimental rig were analysed to determine if dispersions were homogeneous. Mastersizer 3000 data were analysed for an evaluation of the particle size distribution. The acoustic profiles were analysed, and a calibration procedure highlighted for the extraction of sedimentation attenuation coefficients. This Chapter lays the ground for following Chapters where data from the transducers were used for calibration. Transducers for ongoing work were chosen depending on results from this Chapter.

4.3.1 Concentration Sampling

Samples were taken from the rig at multiple heights at each concentration to ensure the system was fully homogeneous. This is shown in Fig. 4.5 (a) and (b) where it was found that the expected concentration was comparable to the measured concentration. Measured values were found to be slightly lower than the expected. This could be attributed to particles depositing in the pump recirculation system which reduces the bulk concentration slightly.

Fig. 4.5 (b) shows the variation in measured concentration at varying points across the tank. Measured points 1 and 2 correspond to sampling at; the height of the transducer, and above the mixer respectively. The data collected from below the mixer did not vary much with increase in concentration whilst the data collected above the mixer and at the transducer level were found to compare well to the actual concentration. Satjaritanun *et al*., (2021) found that a large impeller diameter or too much clearance from the bottom of the tank can lead to most if not all material dispersing above the impeller. This leads to a clear water region on the bottom of the tank which is why samples were not taken below the impeller.

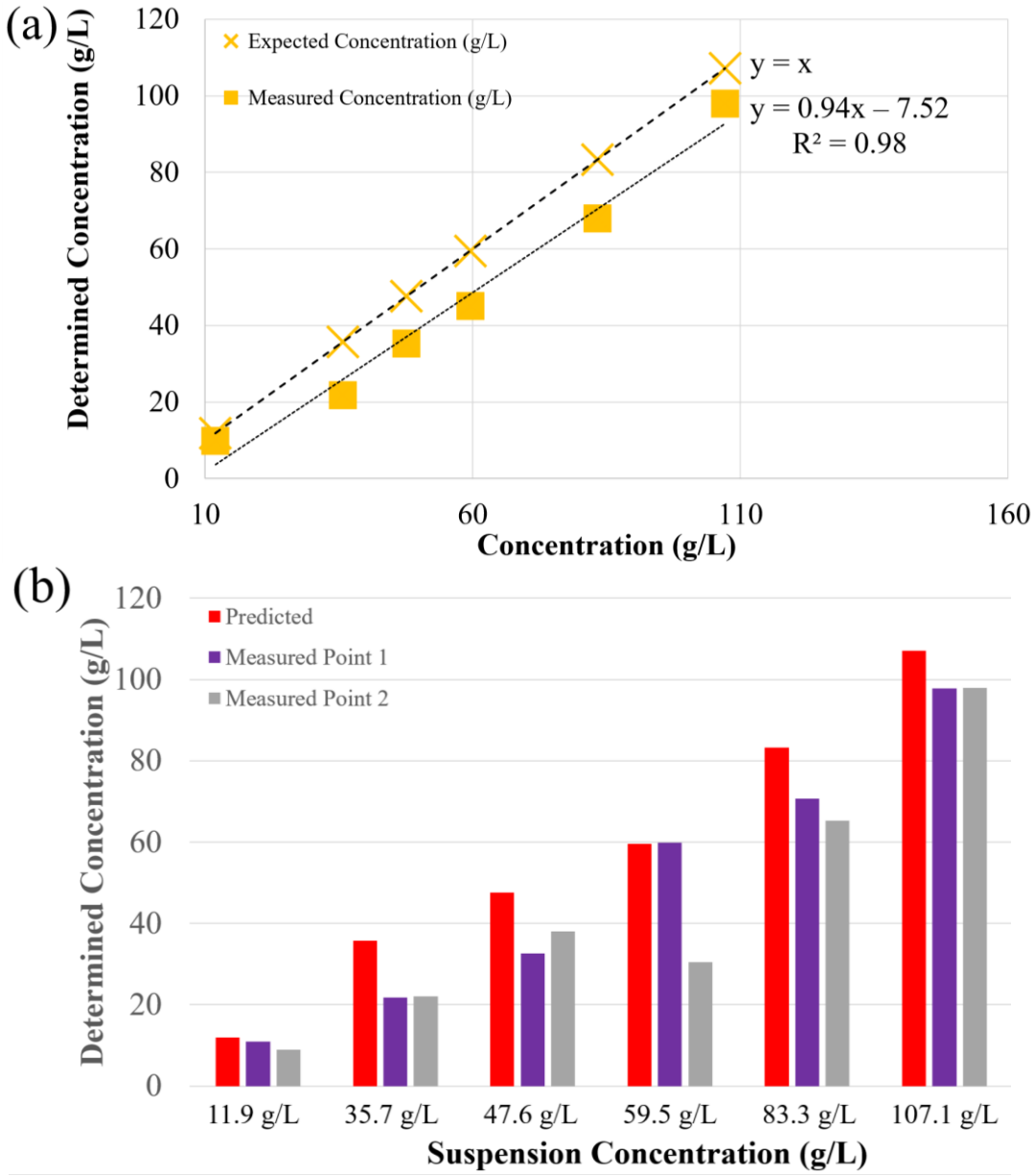

Figure 4.5 Concentration measurements from multiheaded pump with comparisons between the (a) predicted concentration (g/L) and the average measured concentration across 2 measuring points in the rig where measuring point 1 and 2 correspond to the height of the transducer and above the impeller and (b) the comparison between the predicted concentration and individual measuring points.

4.3.2 Mastersizer

The silica glass bead suspension was analysed to understand what the average particle size was and whether there was a single mode distribution. The average particle size distribution (PSD) is shown in Fig. 4.6 and measured by laser diffraction using a Mastersizer 3000 (Malvern Panalytical Ltd). The intensity of the light scattered is measured as the laser beam passes through the dispersed glass bead suspensions. The dispersant used in this thesis is water.

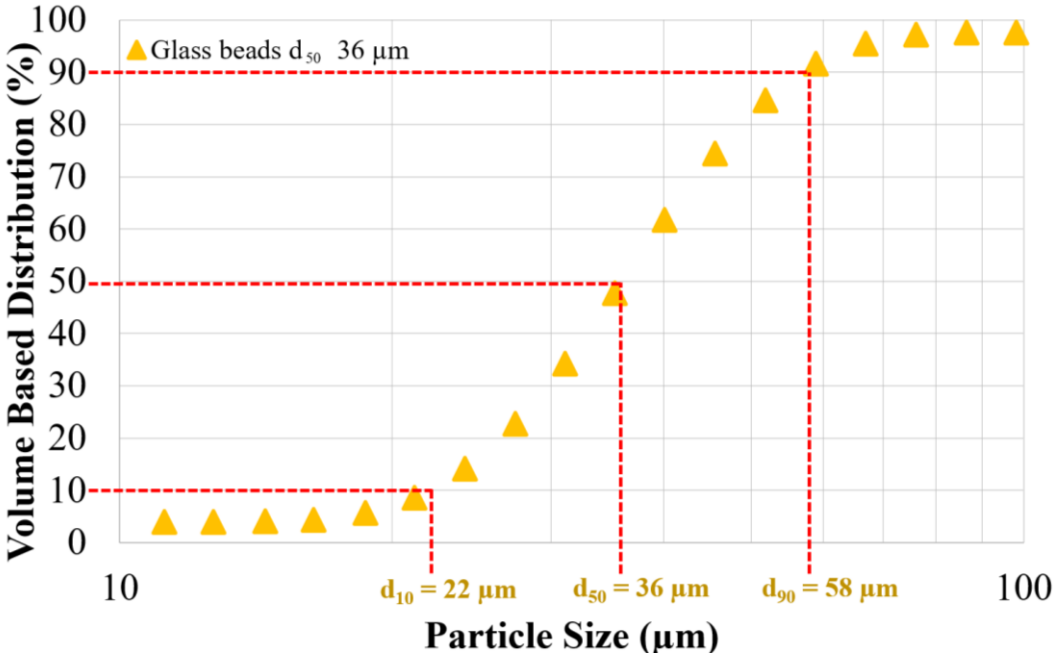

Figure 4.6 Particle size data of silica glass bead species measured using a Malvern Mastersizer 3000

The median particle size is shown to be 36 µm where d_{10} is shown to be at 22 µm and d_{90} is 58 µm which shows that there are a small proportion of fines and larger particles in the suspension. From here, the suspension is assumed to be monodisperse.

4.3.3 Acoustics

4.3.3.1 G-function Profiles

Figures 4.7 and 4.8 present corresponding acoustic profiles for the glass dispersions, using the 2 MHz 2.5 mm and 5 mm active radii respectively. The *G*-function is shown in (a) and the backscatter strength in (b). As considered by Moore *et al*., (2013), the glass would be expected to attenuate a significant proportion of the sound waves due to viscous losses and a minimal proportion of sound to scattering losses.

When comparing the backscatter strength data between the various transducer frequencies and active radii, the distance dependent average signal strength decreases to approximately -45 dB at intermediate distances (correlating to the probe noise-floor). Therefore, the signal strength was similar for all three transducers used. The backscatter decreases with distance from the transducer as the sound signal dissipates. The differences in backscatter with concentration increases are observed in Fig. 4.7 (a) where the G-function is plotted against the concentration. As the concentration increases, the backscatter profile shows a steeper gradient where the signal is scattered more due to the increased density of particles.

The gradients in the *G*-function (d*G*/d*r*) for each corresponding particle concentration are slightly reduced with a decrease in concentration (when taken from the given linear regions). Sahin *et al*., (2020) found that attenuation followed two particle regimes as Moore *et al*., (2013) had found. Sahin *et al*., (2020) built on this and determine that attenuation increased with an increase in concentration, this is shown below in Fig. 4.7 (a) and 4.8 (a) where the attenuation profile is steeper for higher concentrations. The gradient appears to be limited (as expected) for lower attenuating species in Fig. 4.7 (a) and Fig 4.8 (a) (Moore *et al.*, 2013; Bux *et al.*, 2019). However, some further complications arise. Firstly, it is evident with the smaller transducer (Fig. 4.7 (a)) that the low average backscatter level with the glass leads to the signal becoming very weak and approaching the noise-floor at intermediate distances (leading to a second inflection of the *G*-function

versus distance. The decreased backscatter can be seen in Atalar, (2008) where the formula for determining the voltage uses the transducer radius. This voltage can then be converted to backscatter, therefore, the backscatter is dependant on the transducer radius. Haught *et al*., (2017) found that profiles became nonlinear (concave or convex) when the profiles reach the noise floor. This is less obvious for lower transducer frequencies of 600 kHz and 1200 kHz in comparison to the transducer frequencies used in this thesis of 2 and 4 MHz. Concavity was less severe at lower concentrations. The concavity in the profiles was found not to appear due to changes in concentration or grain size. Therefore, the inflection is purely due to the signal reaching the noise floor. Haught *et al*., (2017) found that there were two methods to avoid profile concavity, the first would be to conservatively truncate the profile above the noise floor at low concentrations or correct the profile concavity which requires an objective method for estimating the noise floor that reflects the variation where the profiles reach the noise floor at different flows. In this thesis, the author has used the second method and assumed a linear profile across the distance of the tank.

Therefore, a smaller region was taken to quantify the linear gradients (0.1 to 0.15, as indicated). Additionally, it would be expected that particles of a mean size of ~40 μm may also attenuate sound via viscous absorption mechanisms, in addition to scattering (Betteridge *et al*., 2008; Rice *et al*., 2014; Bux *et al.*, 2019; Tonge *et al*., 2021), which would elevate the level of overall attenuation. This is shown by regimes of attenuation identified for smaller particles as shown by Moore *et al*., (2013) and Sahin *et al*., (2020). Sahin *et al*., (2020) also shows typical backscatter profiles and determined that for particles smaller than 200 μm, the overall trend of backscatter with the increase of Suspended Sediment Concentration (SSC) can be divided into two stages; increasing and decaying. This is not shown in Fig. 4.7 (b) and 4.8 (b) however, it can be seen in Fig. 4.7 (a) and 4.8 (a) which is explained by the linear correlation from voltage to the G-function.

The differences in signal attenuation as concentration increases are observed in changes to the *G*-function with concentration. The gradients in the *G*-function

(dG/dr) for each corresponding particle concentration are extracted and plotted against the corresponding concentration, see Fig. 4.12.

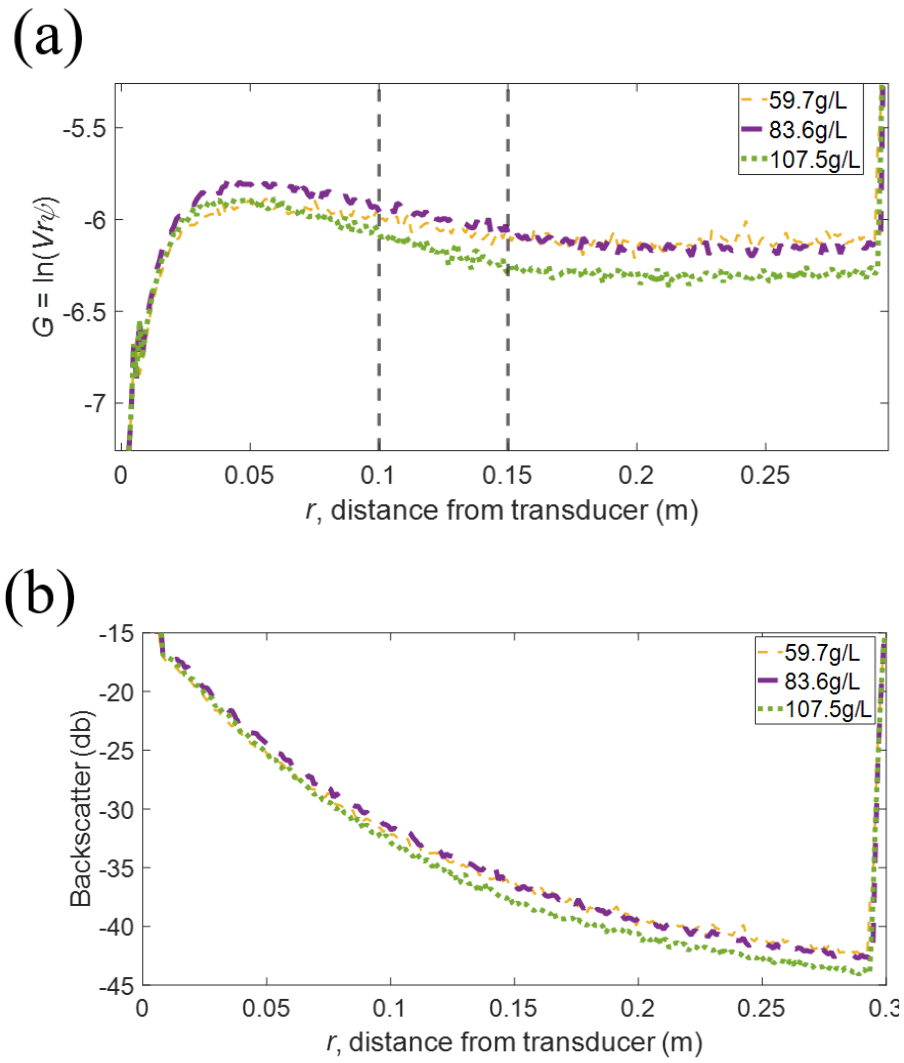

Figure 4.7 Silica glass particles of d_{50} 36 µm analysed using a 2 MHz 2.5 mm active radius transducer to produce (a) G-function and (b) backscatter profiles

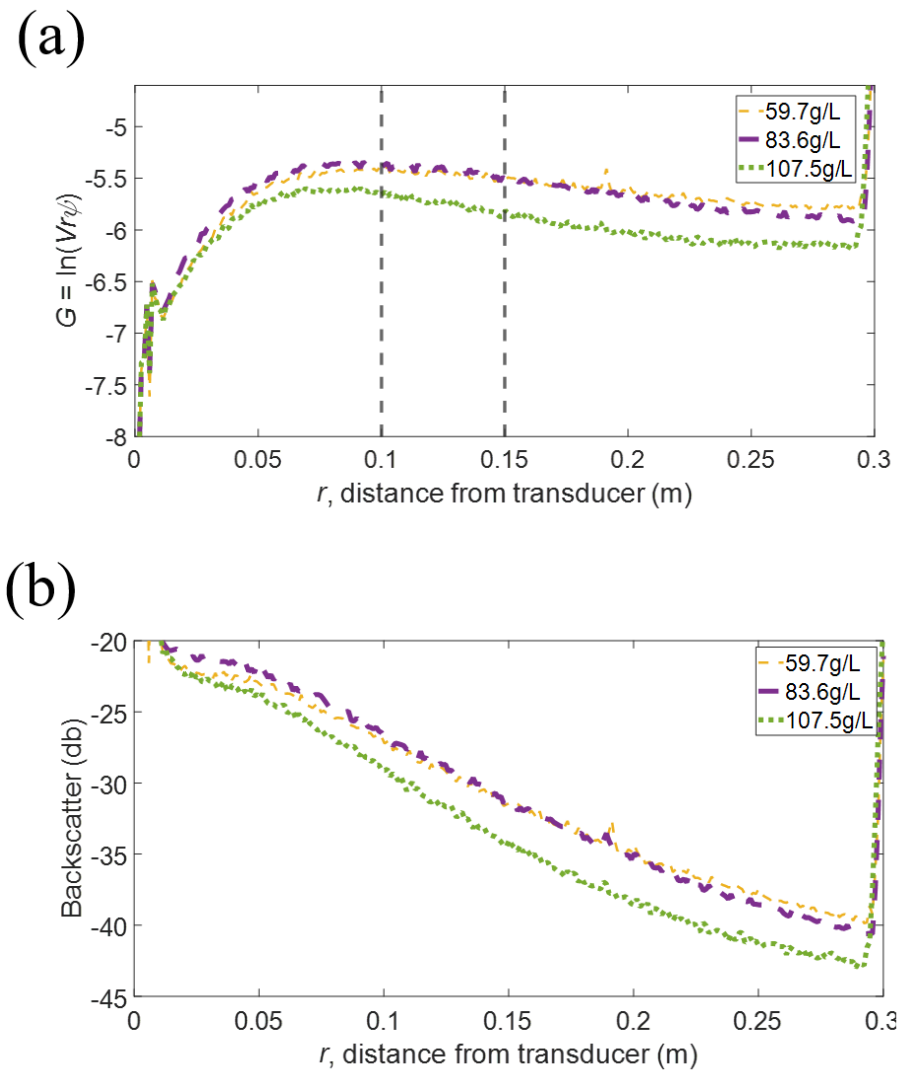

Figure 4.8 Silica glass particles of d_{50} 36 µm analysed using a 2 MHz 5 mm active radius transducer to produce (a) G-function and (b) backscatter profiles

Figure 4.9 (a) and (b) show the *G*-function profiles and backscatter profiles respectively for the glass using a 4 MHz probe. An apparent second inflection in the *G*-function versus distance profile is observed, at ~0.15 m for all concentrations, which is an artefact of a weak signal approaching the transducer noise-floor. This was observed for the 2 MHz small transducer data in Fig. 4.7 (a), Haught *et al*., (2017) also found these concave profiles which were corrected by assuming a linear profile and ignoring the noise floor. Thus, a closer linear region was taken from 0.05–0.1 m to estimate d*G*/d*r* values. Nonetheless, it is evident that the glass leads to significantly higher levels of attenuation for the 4 MHz

frequency probe (observed from the higher average d*G*/d*r* gradient values for particular concentrations) in comparison to the 2 MHz data. This result is consistent with theories of scattering and viscous losses, where higher frequencies lead to scattering dominant interactions, this is also shown in Guerrero *et al.*, (2015).

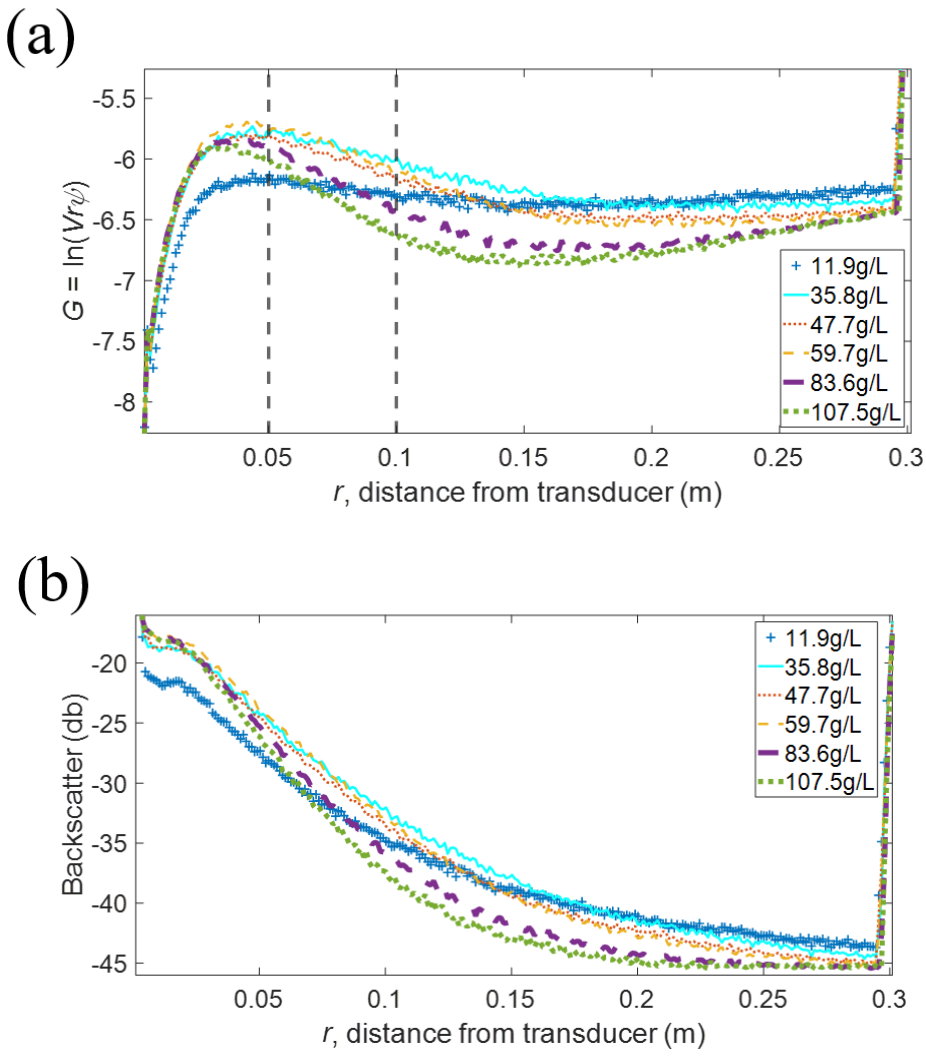

Figure 4.9 Silica glass particles of d_{50} 36 µm analysed using a 4 MHz 2.5 mm active radius transducer to produce (a) G-function and (b) backscatter profiles

4.3.3.2 Sedimentation Attenuation Coefficient

The calibration procedure for the calculation of the attenuation coefficient is shown below for the 2 MHz 2.5 mm transducer and repeated for all other transducers used. The *G*-function profiles are isolated in the linear regions shown by the dashed lines in Fig. 4.7 - 4.9 to extract the sedimentation attenuation coefficients. Linear predictions for each concentration are used to determine the d*G*/d*r* values. Fig. 4.10 (b) shows how the gradient is extracted for the 107.5 g/L concentration plot. This is repeated for all three concentration profiles.

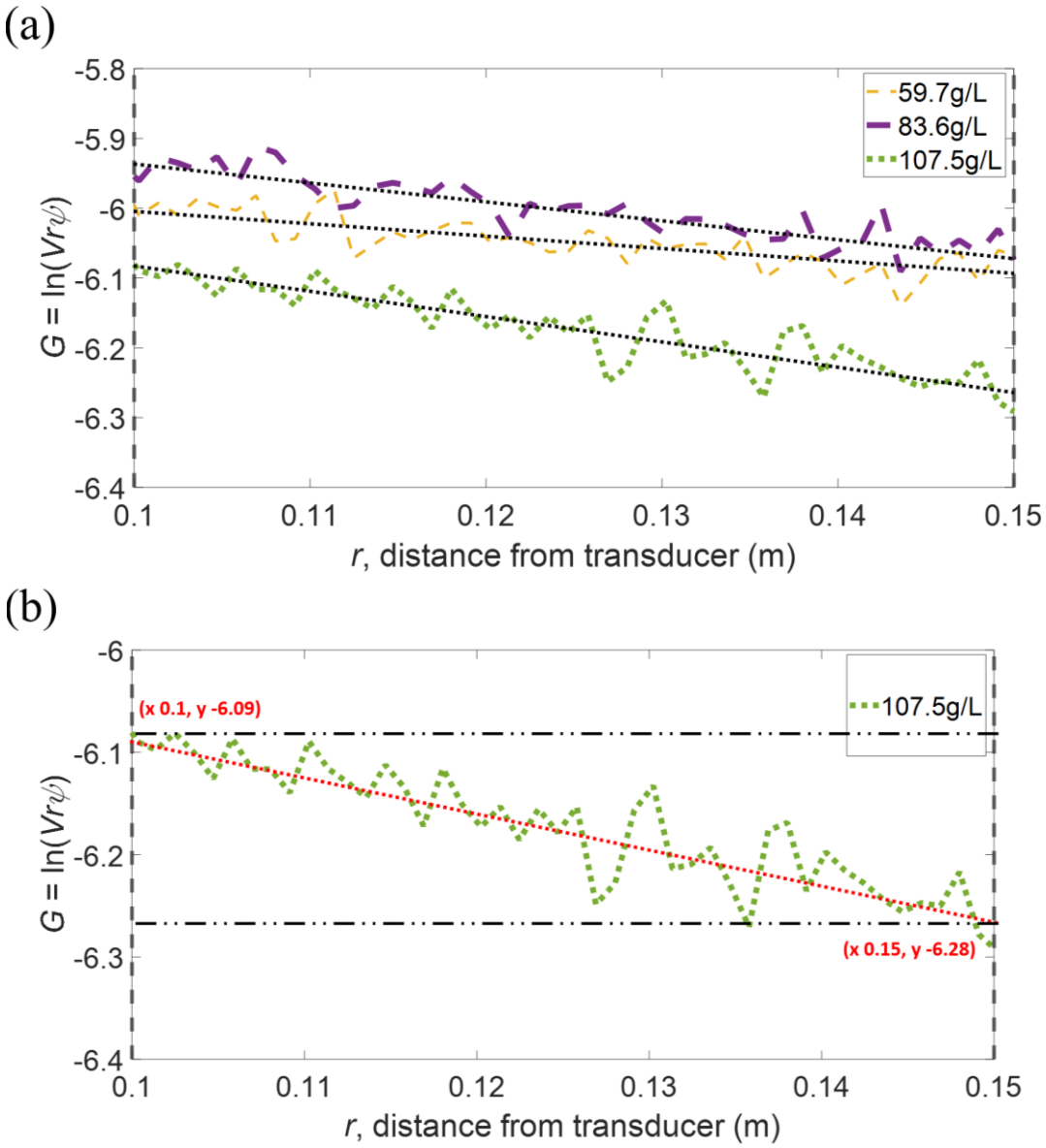

Figure 4.10 (a) Isolation of the linear region in Fig. 4.7 with linear predictions shown in the dotted black lines and (b) the extraction of the dG/dr value for the 107.5 g/L profile

Each d*G*/d*r* value for the three concentration plots in Fig. 4.7 (a) is plotted against their corresponding concentration and shown in Fig. 4.11.

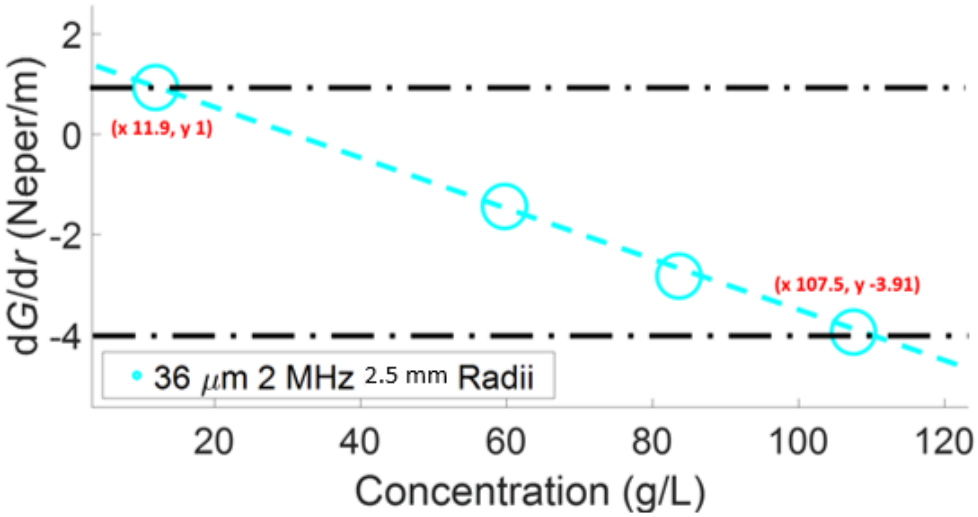

Figure 4.11 Extraction of the gradient for dG/dr v M

The sedimentation attenuation coefficient can be extracted from Fig. 4.11 using Eq. (3.06) where the gradient is multiplied by -0.5. This is also shown in Eq. (4.09) for the 2 MHz 2.5 mm transducer. This is repeated for all transducers and all d*G*/d*r* v M profiles are shown in Fig. 4.12. Table 4.3 shows the calculated sedimentation attenuation coefficients when using all three transducers.

$$\xi_s = -0.5\left(\frac{\partial^2 G}{\partial M \partial r}\right) = -0.5\,\frac{\partial}{\partial M}\left[\frac{\partial}{\partial r} ln(\psi r V)\right] = -0.5\frac{Change\ in \frac{\partial G}{\partial r}}{Change\ in\ M} = 0.0257 \tag{4.09}$$

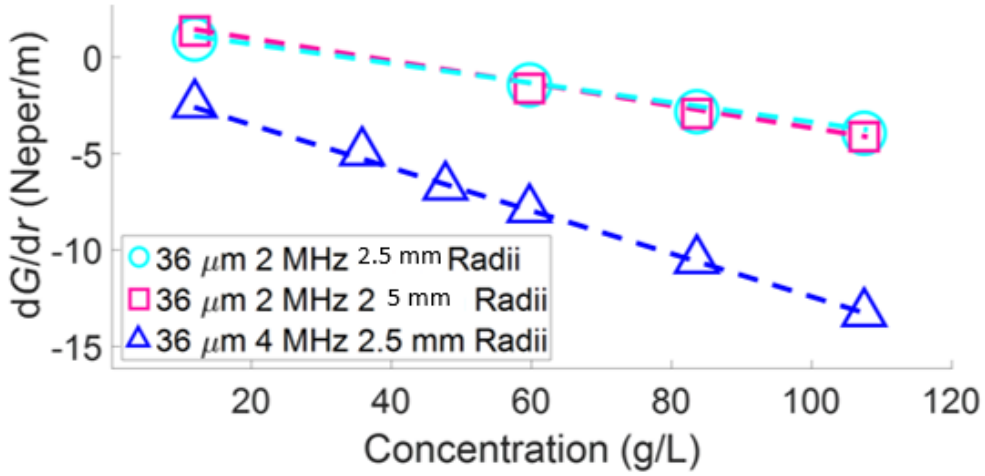

Figure 4.12 Change in logarithmic function G with distance for silica glass bead suspension of d_{50} (a) 36 μm using 2 and 4 MHz transducers with varying active radii

Fig. 4.12 and Table 4.3 show that the two 2 MHz transducers were found to produce comparable attenuation coefficients with minimal variation between the two values in Table 4.3 (1.9%). The 4 MHz transducer attenuated more than the 2 MHz transducers where the higher frequencies led to higher scattering losses (Rice, 2013; Guerrero *et al*., 2015; Bux *et al*., 2019; Tonge *et al*., 2021).

Table 4.3 Measured sedimentation attenuation coefficients from experiments for two silica glass bead suspensions of silica glass beads of d_{50} 36 μm using 2 and 4 MHz transducers with varying active radii (mm)

Transducer Frequency (MHz)	Transducer Active Radii (mm)	Sedimentation Attenuation Coefficient ξ ($m^2.kg^{-1}$)
2	5	0.0262
	2.5	0.0257
4	2.5	0.0412

4.3.3.3 Error Analysis of Attenuation Coefficients

As shown in the methodology, the error for the profiles is calculated across the 1023 profiles. The error calculation is shown here only for the 2 MHz 2.5 mm transducer for simplicity. When observing Fig 4.7 (a) it can be seen that the profiles are linear from 0.1 – 0.15 m, all properties at the start and end of that measurement window are shown in Table 4.4 where all properties are required to determine the *G*-function.

Table 4.4 Properties required for conversion of echo amplitude to G-function

Properties	Start of Measurement Window	End of Measurement Window
Active Radius, a^t (m)	0.0025	0.0025
Speed of Sound, c (m.s^{-1})	1480	1480
Frequency, f (Hz)	2000000	2000000
Wavelength, λ (m) (c/F)	0.0007	0.0007
Distance, r (m)	0.10	0.15
Near Field Correction Factor, ψ	1.0007	1.0002

The voltage values are determined for each profile and plotted as error bars on the root mean squared voltage to visualise the variation of the profiles across 1023 profiles. This is shown in Fig 4.13 for the 2.5 MHz 2.5 mm transducer where only a single transducer's data were used for visualisation of the error determination. The distance points are limited to only include the error where the profiles are linear. There are 46 distance points between 0.1 and 0.15 m in Fig. 4.7 which shows the overall breadth of data to be 1023x46. The error from the *G*-function is determined in Eq. (4.05) and plotted in Fig. 4.14.

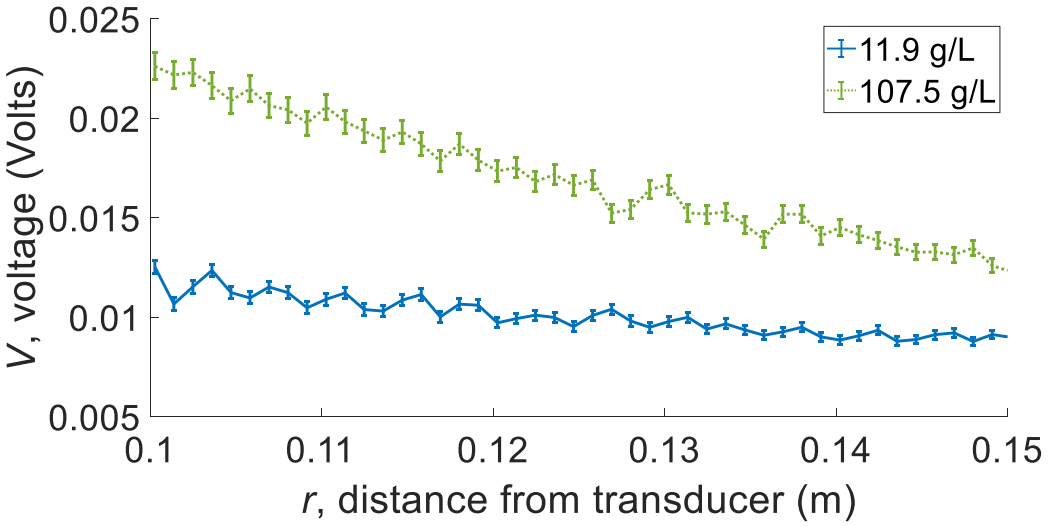

Figure 4.13 Voltage plotted against r with the error bars determined using the standard deviation of voltage values across the 1023 profiles output from the UVP

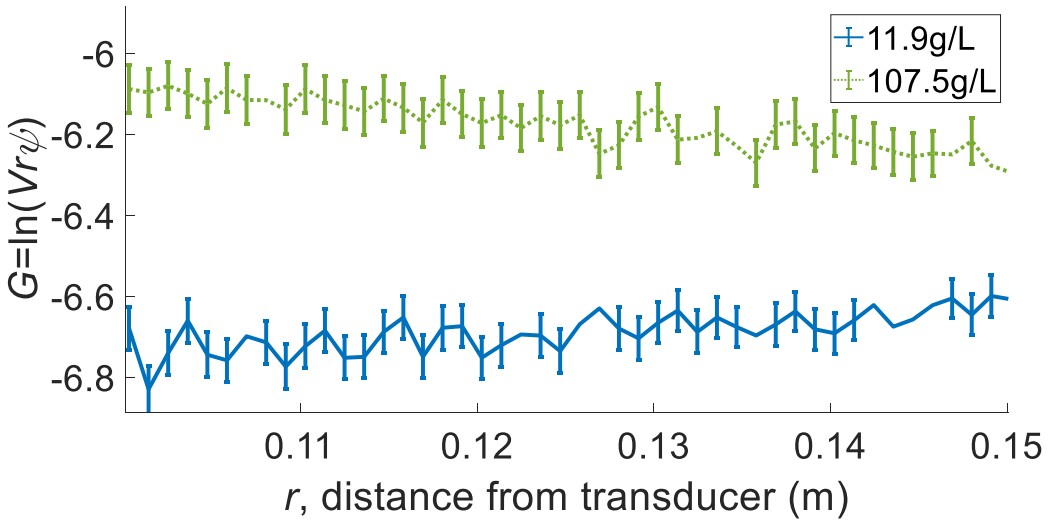

Figure 4.14 G-function plotted against r with the error bars determine using the standard deviation of G values calculated from the voltage values across 1023 profiles.

The minimum and maximum dG/dr values can be determined by selecting the minimum and maximum G values at the start and end of the measurement window. This can be extracted from Fig. 4.14 where the maximum G value at the start of the measurement window is shown by the top of the error bar for both 11.9 and 107.5 g/L. Or this can be calculated using the G_{rms} at the start and end of

the measurement window; G_{rms} is calculated in Eq. (3.05) by using V_{rms} as $V(r)$. The minimum and maximum gradients are shown in Fig. 4.15 (a) and (b), respectively. Table 4.5 shows the quantitative values for the minimum and maximum G at the start and end of the measurement window.

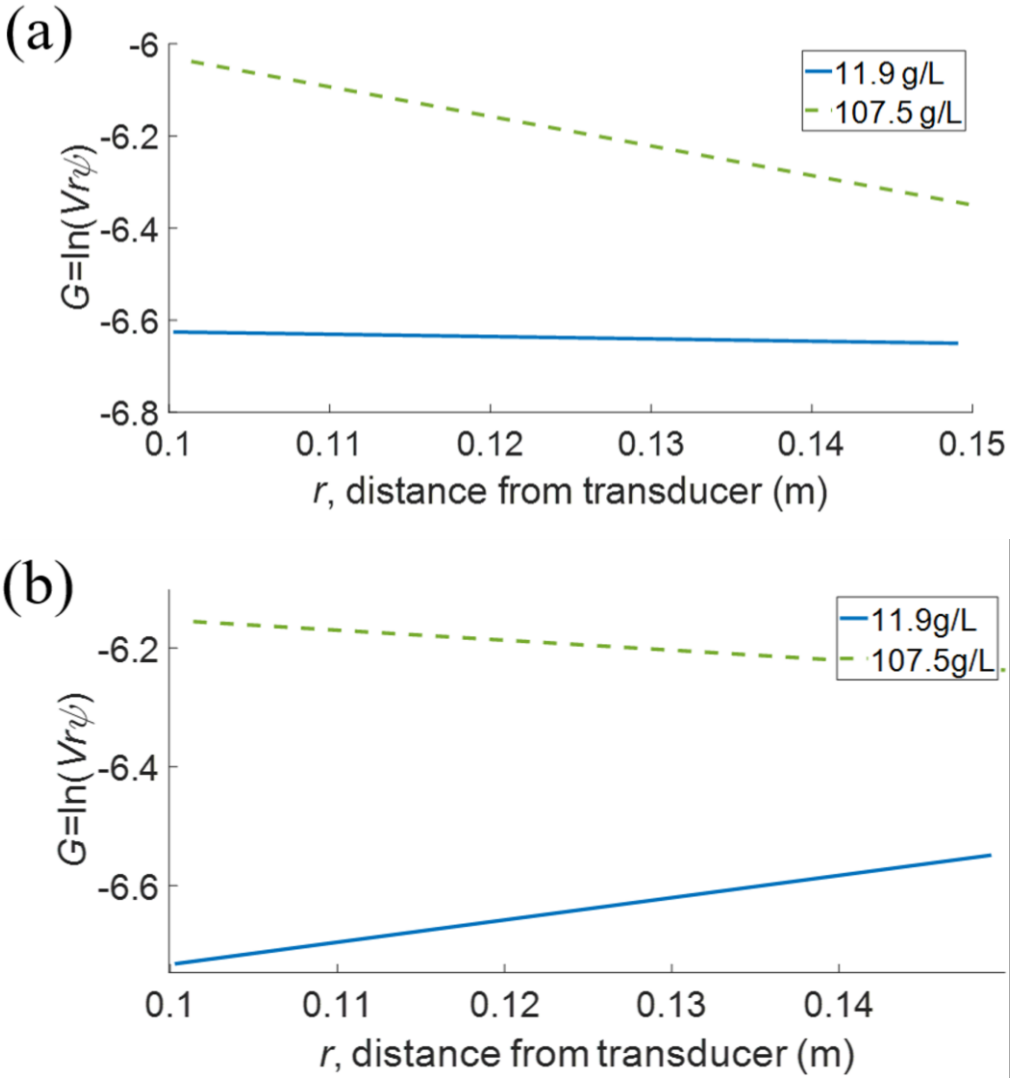

Figure 4.15 Minimum and maximum gradients for G using a suspension concentration of 11.9 and 107.5 g/L

Table 4.5 Minimum and maximum G at the start and end of the measurement window

Concentration (g/L)	Start of Measurement Window (G_{rms} +/– G_{err} at r = 0.10)		End of Measurement Window (G_{rms} +/– G_{err} at r = 0.15)	
	$G_{min,\ start}$	$G_{max,\ start}$	$G_{min,\ end}$	$G_{max,\ end}$
11.9	-6.73	--6.63	-6.65	-6.55
107.5	-6.16	--6.04	-6.33	-6.22

Minimum and maximum dG/dr in Table 4.6 for both concentration environments are extracted from Table 4.5 (the methodology is in the headings of Table 4.6).

Table 4.6 Minimum and maximum dG/dr values

Concentration (g/L)	Minimum dG/dr value ($G_{max,\ start}$ - $G_{min,\ end}$) Gradient	Maximum dG/dr value ($G_{min,\ start}$ - $G_{max,\ end}$) Gradient
11.9	-0.49	3.66
107.5	-5.91	-1.33

The minimum and maximum sedimentation attenuation coefficients can be extracted from Eq. (4.07) and (4.08) respectively as shown in Chapter 4.2.5, the quantitative values are shown in Table 4.7.

Table 4.7 Minimum and maximum sedimentation attenuation coefficients

Min $d^2G/drdM$	Min ξ	Max $d^2G/drdM$	Max ξ
-0.052	0.026	-0.057	0.028

The overall sedimentation attenuation coefficients for all three probes as well as the error can now be shown in Fig. 4.16. Coefficients estimated from the Betteridge *et al.,* (2008) model are displayed for validation. These Betteridge *et al*., (2008) heuristic expressions are shown in Eqs. (3.07-3.08) and have also been highlighted in Fig. 4.4. It was found that the measured values from the 4 MHz transducer are closer to Betteridge *et al.,* (2008) predictions which shows that the measured attenuation from 4 MHz probes is less affected by viscous losses. This has been explored by Guerrero *et al*., (2015) whereby viscous attenuation was found to be less sensitive to frequency and PSD heterogeneity than scattering attenuation. Guerrero *et al*., (2015) determined this was because scatter attenuation is due to acoustic cross-section of particles whilst viscous attenuation is produced by an oscillation friction process in relation with particle mass. The measured attenuation is 0.06 in comparison to the predicted 0.03 attenuation coefficient, where the predicted value is only half the measured data. While the 4 MHz probe has a wavelength that is one half of the 2 MHz probe, these systems have almost identical *ka* terms. It is also emphasised that as estimations of the large and small transducers overlay precisely, it indicates both transducers are performing as predicted for calibration (as there should be no dependence of transducer properties on measured attenuation coefficients for a given frequency). However, there are clearly certain systems that compare less well to the estimated values. These measured attenuation values are an order of magnitude out from the Betteridge *et al*., (2008) estimations where the measured values are ten times more than the predictions. Therefore, viscous losses need to be incorporated for an accurate estimation of the attenuation coefficient.

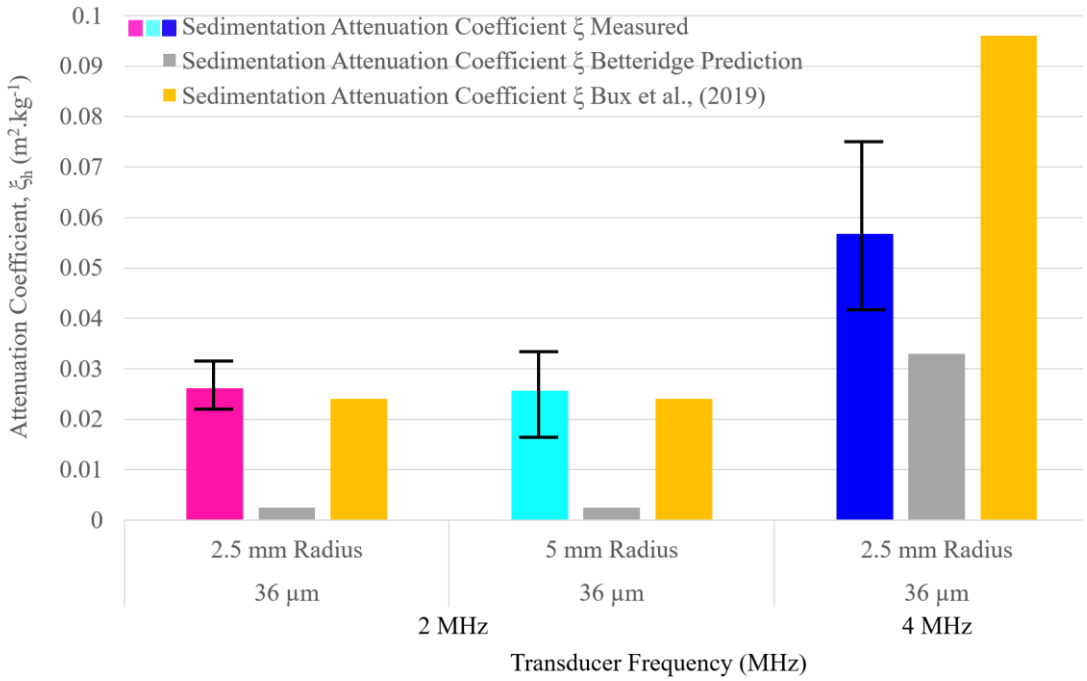

Figure 4.16 Measured sedimentation attenuation coefficient values for two species of silica glass beads using 2 and 4 MHz transducers of varying active radii compared to predicted values where expressions from Betteridge et al., (2008) were used for scattering predictions and Urick, (1948) predictions were used for incorporation of viscous losses, measured values from Bux et al., (2019) were also shown for comparison

In particular, the attenuation determined using 2 MHz probes for the glass species is approximately 0.026 in comparison to the prediction value of 0.0025. It is assumed this is because of enhanced viscous absorption attenuation with small particles and the lower 2 MHz frequency transducers, where the given prediction is only based on scattering attenuation. This can be shown by Moore *et al.*, (2013) and Sahin *et al.*, (2020) who determined that viscous attenuation is dominant at smaller particle sizes. Similar measured enhancements have been observed for particles in the same size range by Bux *et al.*, (2019). The error bars shown in Fig. (4.16) were calculated from the variation of echo amplitude across the measured distance (*r*), as has been discussed in detail above. The coefficients for the 36 µm species using a 2 MHz probe are underpredicted by Betteridge *et al.*, (2008); the error bars do not overlap but this is due to enhanced viscous absorption

attenuation. The error bars for the 4 MHz data are significantly larger where the accuracy of attenuation coefficients extracted from 2 MHz probes is higher.

Results from Bux *et al*., (2019) compare very well to measured data using the 2 MHz transducers. The measured coefficient for the 4 MHz probe is slightly lower than the measured Bux *et al*., (2019) values but they are similar enough to show the accuracy of the UVP's ability to analyse homogeneous suspensions using varying transducer frequencies and radii.

4.3.3.4 Considering Viscous Losses

Eqs. (3.11) and (3.12) were utilised to predict attenuation due to viscous losses whilst Eq. (3.14) was used to predict total losses due to scattering and absorption, this is shown by the red bars in Fig. 4.17. The predicted scattering attenuation coefficients were combined with predicted viscous losses to determine overall attenuation. The viscous losses were incorporated from Urick, (1948) and are shown in Eqs. (3.11-3.14) in Chapter 3. When considering viscous losses, the attenuation predictions are much closer to the measured attenuation coefficients for the two systems which had underestimated predictions, namely the two 2 MHz systems for the 36 µm glass species. The coefficients from the 2 MHz measured data also compare very well to previous data from Bux *et al*., (2019). The 4 MHz probe compare much better than in Fig 4.16 where the coefficients were found to compare very well to previous experimental data from Bux *et al*., (2019). As outlined previously, the higher frequency led to the signal decaying rapidly towards the noise-floor of the instrument at intermediate distances, significantly limiting the linear attenuation range, however, this had limited effect on the quality of data. This concavity of the profile is shown by Haught *et al*., (2017) where one of the two methods for treating the concave profile was to use a lower particle concentration array. If required, this problem could be overcome in future work by utilising a lower particle concentration range for 4 MHz calibration and incorporating a nearfield correction factor, improving the accuracy of the measurements closer to the region of the transducer (Butler and Sherman, 2016).

However, to emphasise the quality of the data in this Chapter, the author has proven that it is possible to extract high quality backscatter data from the UVP and determine attenuation coefficients for dispersions which compare very closely to both combined theory and also previous experimental studies with the specialist UVP acoustic backscatter system.

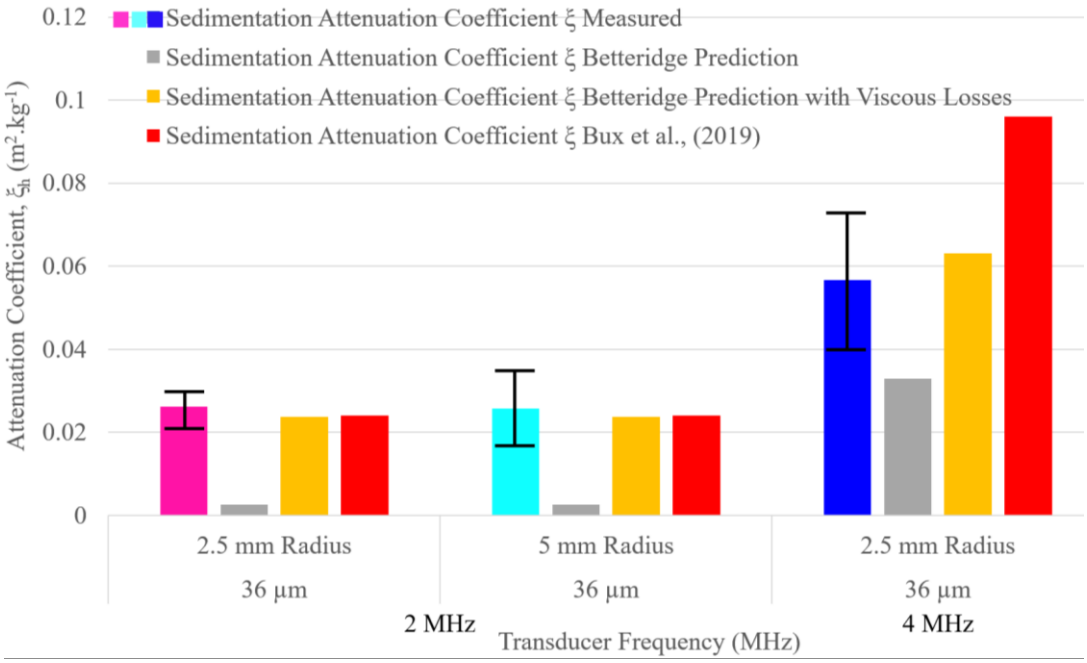

Figure 4.17 Measured sedimentation attenuation coefficient values due to scattering for two species of silica glass beads using 2 and 4 MHz transducers of varying active radii compared to attenuation coefficient values determined using heuristic expressions where predictions from Betteridge et al., (2008) were used for scattering predictions and Urick, (1948) predictions were used for incorporation of viscous losses. Measured values from Bux et al., (2019) were also shown for comparison.

4.4 CONCLUSIONS

In this Chapter, spherical glass dispersions (of ~36 μm) were characterised by acoustic backscatter, utilising a commercial ultrasonic velocity profiler (UVP). In particular, a well-mixed recirculating tank was used to determine the sediment attenuation coefficients, with two 2 MHz probes (of 2.5 mm and 5 mm active radii) and a 4 MHz probe (also of 2.5 mm active radius) following a calibration procedure outlined by Rice *et al*., (2015) and Bux *et al*., (2019). Measured attenuation coefficients were compared to estimates produced by the Betteridge *et al*., (2008) heuristic model for spherical particle scattering, as well as combined viscous attenuation predictions from Urick, (1948). Both sizes of 2 MHz probes produced consistent values of the attenuation coefficients. This highlights the smaller probe's applicability for online monitoring of pipeline slurries. The smaller probe was also found to provide a higher accuracy of data from a minimal echo variation. Measured data from Bux *et al*., (2019) were found to compare very well to measured coefficients in this Chapter. This shows the accuracy of the UVP and the ability to deliver reproducible results.

The 4 MHz probe varied slightly from previous measured coefficients from Bux *et al*., (2019) but the data were still found to be comparable. When comparing to Betteridge *et al*., (2008) predictions the measured data were severely underpredicted as the glass species used in this Chapter were found to attenuate predominantly due to viscous losses. This was proven when comparing the measured attenuation coefficients to heuristic values where the scattering losses from Betteridge *et al*., (2008) predictions and viscous losses from Urick, (1948) predictions were combined. The measured values compared very well to attenuation predictions from the combined heuristic expressions. The 4 MHz measured data were overestimated slightly but were still found to compare well. The attenuation coefficients from this Chapter were used as a calibration measure for the following Chapter where the silica glass beads were investigated in further detail.

For the first time, UVP transducers with varying frequency and active radii have been used on these silica glass beads to produce concentration profiles and sedimentation attenuation coefficients. When using the 4 MHz probes, a measurements distance of at least 0.05 m was required, however, the data here did not have a near field correction factor applied and therefore measurement was limited in the distance closest to the transducer. Here, in this Chapter, the three transducers were calibrated for use in a tank to reflect the sound behaviour of silica glass bead suspensions. Jackson, (2019) had looked at transducer active radii and frequency in theory, in this Chapter, the author has been able to calibrate the transducers experimentally and produce attenuation profiles of silica glass bead suspensions.

5. THE USE OF REMOTE ACOUSTIC PROBES FOR MEASURING CONCENTRATION OF GLASS PARTICLE DISPERSIONS: COMPARISON TO IN SITU ACOUSTIC PROBE PERFORMANCE

CHAPTER SUMMARY

The aim of this Chapter is to produce measured attenuation coefficients from both *in situ* and remotely placed transducers. Tonge *et al*., (2021) has analysed homogeneous suspensions of similar glass beads using a bespoke ABS, here, the author has found similar results when using a commercial system. Rice *et al*., (2015) and Bux *et al*., (2019) have both used similar glass beads to produce sedimentation attenuation coefficients from *in situ* probes but not remotely placed probes. Coefficients from Rice *et al*., (2015) and Bux *et al*., (2019) have been used to confirm the accuracy of coefficients from remotely placed and *in situ* transducers. The author produces form function and normalised scattering cross section values experimentally and through heuristic expressions where values from remotely placed transducers align very well to predictions which shows the applicability of acoustic probes in non-contact environments. This has not been achieved before for remotely placed transducers in a non-contact environment.

5.1 INTRODUCTION

Chapter 4 detailed the analysis of monodisperse suspensions of silica glass beads with transducers of varying active radius and frequency. This Chapter details a full in-depth analysis of four species of silica glass beads with varying particle size distributions (PSDs) using 2.5 mm active radii transducers of varying frequency. A Mastersizer was used to determine the PSDs of four grades of silica glass beads where the particle size information allowed the author to highlight the sensitivities of the UVP to particle size. Acoustic profiles and attenuation coefficients are extracted from all grades of silica glass where the largest glass size is critically analysed to account for high scattering losses. Suspensions of all

four species with varying concentrations are analysed using four transducers of a 2 and 4 MHz frequency where the probes were placed *in situ* and remotely (i.e., external to the tank wall). Remote placement indicates a probe which has been fixed externally to the tank wall. Attenuation profiles are developed, and sedimentation attenuation coefficients are calculated and used to compare the accuracy of the UVP for varying particle size species depending on the frequency and placement of the transducer. These are compared to sedimentation attenuation coefficients from previous literature (Rice *et al*., 2014; Guerrero *et al*., 2015; Bux *et al.,* 2016). The scattering cross section and form function are determined to provide information on the changes in attenuation regime with changes in particle size where the larger species predominantly attenuates through scattering losses whilst the small species attenuates through viscous losses (Moore *et al*., 2013; Sahin *et al*., 2020). Backscatter and sediment constants are calculated to ensure the constants were consistent throughout the tank.

For context, ultrasonic transducers have been used to analyse silica glass beads before in other commercial or bespoke acoustic backscatter systems. Tonge *et al*., (2021) used three grades of similar silica glass beads in a calibration rig to determine concentration profiles using a single submerged *in situ* transducer at multiple frequencies. In previous research, Tonge *et al.*, (2017) was able to produce scattering cross section plots which showed the various regimes of attenuation for varying particle sizes of silica glass beads. The aim of this Chapter is to be able to produce similar data for remotely placed transducers with the UVP in backscatter mode for similar silica glass bead suspensions. By placing the transducers remotely, the transducers can be used in a nuclear environment where direct contact would likely have an effect on the integrity of the transducers. UVP transducers of varying frequency have not been mounted remotely for characterisation of silica glass beads. However, from Chapter 4 it was shown that transducers can be used to produce accurate attenuation coefficients which could be compared to predictions from heuristic expressions from Betteridge *et al*., (2008) with incorporation of viscous losses from Urick, (1948). Ultrasonic transducers have been mounted remotely for velocity profiling, for instance

Obayashi *et al*., (2008) mounted UVP transducers non-invasively for velocity profiling using multiple transducers. Kotze *et al*., (2016) also mounted a non-invasive sensor unit through a stainless steel pipe, so remote profiling is possible.

Rice *et al*., (2014) placed UVP transducers remotely onto a Perspex pipe to extract sedimentation attenuation coefficients from similar silica glass beads and plastic bead suspensions. Rice *et al*., (2015) used the UVP to determine velocity profiles of similar silica glass bead suspensions using the same set-up and transducers in Rice *et al*., (2014). Rice *et al*., (2014) determined the sedimentation attenuation coefficients experimentally and compared this to predicted values using the wavenumber and particle radius. Guerrero *et al*., (2015) determined sedimentation attenuation coefficients for sand and silt suspensions. These attenuation coefficients were compared to functions for mono-size suspensions at varying transducer frequencies. Vergne *et al*., (2021) analysed fine river sediments and determined acoustic profiles but no comparison was made to combined predictions. In this Chapter, the author has determined the measured attenuation coefficients and compared this to a combined predicted attenuation coefficient using heuristic expressions from Betteridge *et al*., (2008) and Urick, (1948). The form function and normalised scattering cross section have also been determined experimentally which was not done in Rice *et al*., (2014). This can be used to fully characterise the experimental process and establish whether the values determined experimentally compared to predicted values.

The original purpose of the UVP is for velocity profiling, however, Rice *et al*., (2014) has proven that the UVP can be used for accurate acoustic backscatter profiling and extraction of attenuation coefficients. Rice *et al*., (2014) used transducers mounted in-line placed *in situ*. Therefore, with precedent from Obayashi *et al*., (2008) and Rice *et al*., (2014), the UVP transducers can in theory be mounted remotely and used for extraction of echo amplitude data. However, it is important to emphasise that the full limits of the UVP instrument, in terms of ability to gain backscatter data for size and concentration has never been quantified previously. Tonge *et al*., (2021) used a bespoke ABS to extract

attenuation coefficients and Rice *et al*., (2014) used the UVP to extract attenuation coefficients from in-line transducers. Here for the first time, the utility of externally mounted UVP acoustic probes for the collection of concentration data within pipes, is assessed. Data are compared against identical probes mounted in situ within the pipe.

The instrument is not commercially sold to extract particle data, and the limits of using these probes remotely (from increased attenuation through the pipe wall) are unknown. While this instrument is industrially appealing, there may be significant restrictions on its ability to gain particle characterisation data from acoustic backscatter. This will be investigated in this Chapter. The remote probes generate data which is consistent with combined predictions of attenuation from Betteridge *et al*., (2008) which details scattering losses and Urick, (1948) which considers viscous losses. Measured remote data align well with measured *in situ* data where the maximum difference between values is 0.015. Despite losses in signal strength from remotely placed transducers, attenuation is almost identical which provides confidence that the remote probes can be used in an online environment. These are the prominent results in the Chapter and make the case for the novelty.

5.2 Materials and Methods

5.2.1 Materials

Silica glass bead particles were used for characterisation of homogeneous suspensions in Chapter 4, these silica glass bead species were manufactured by Guyson Ltd, (2021), and similar species have been used in previous literature for analysis using acoustics (Rice *et al*., 2014; Hunter *et al*., 2016; Bux *et al*., 2019; Tonge *et al.*, 2021). In this Chapter, four silica glass bead species were used, all of the same chemical composition but with different particle size distributions; these are shown in Fig. 5.1 and 5.2 where the nominal size (d_{50}) for the grades shown in Fig. 5.1 (a) and (b) are 200 μm and 79.5 μm, respectively. The nominal sizes in Fig. 5.2 (a) and (b) are 67.5 μm and 24.5 μm, respectively. The nominal particle sizes from Guyson will be confirmed with the Mastersizer. In Chapter 4, the

smallest glass bead size was used, this is shown in Fig. 5.2 (b). The silica glass beads (Honite, Guyson Ltd) are composed of approximately 75% silica dioxide with the other 25% consisting of sodium oxide, calcium oxide, magnesium oxide and free iron (Guyson Ltd, 2021).

This silica glass bead was chosen because it is chemically inert and can be purchased commercially (Croft *et al*., 2019; Guyson, 2021). The three larger species were analysed using a desktop SEM (TM3030 Plus, Hitachi) as shown in Fig. 5.1 (a) – (b) and Fig. 5.2 (a). Fig. 5.2 (b) shows the smallest glass species which was used in Chapter 4 where the desktop SEM did not have a high enough resolution and therefore, a Carl Zeiss EVO SEM (MA15) (Zeiss, 2022) was used to extract images. In Fig. 5.1 and Fig. 5.2, the SEMs broadly show spherical particles in a small size range for each glass bead size with a small portion of irregular particles with the smaller particles in Fig. 5.2 (b).

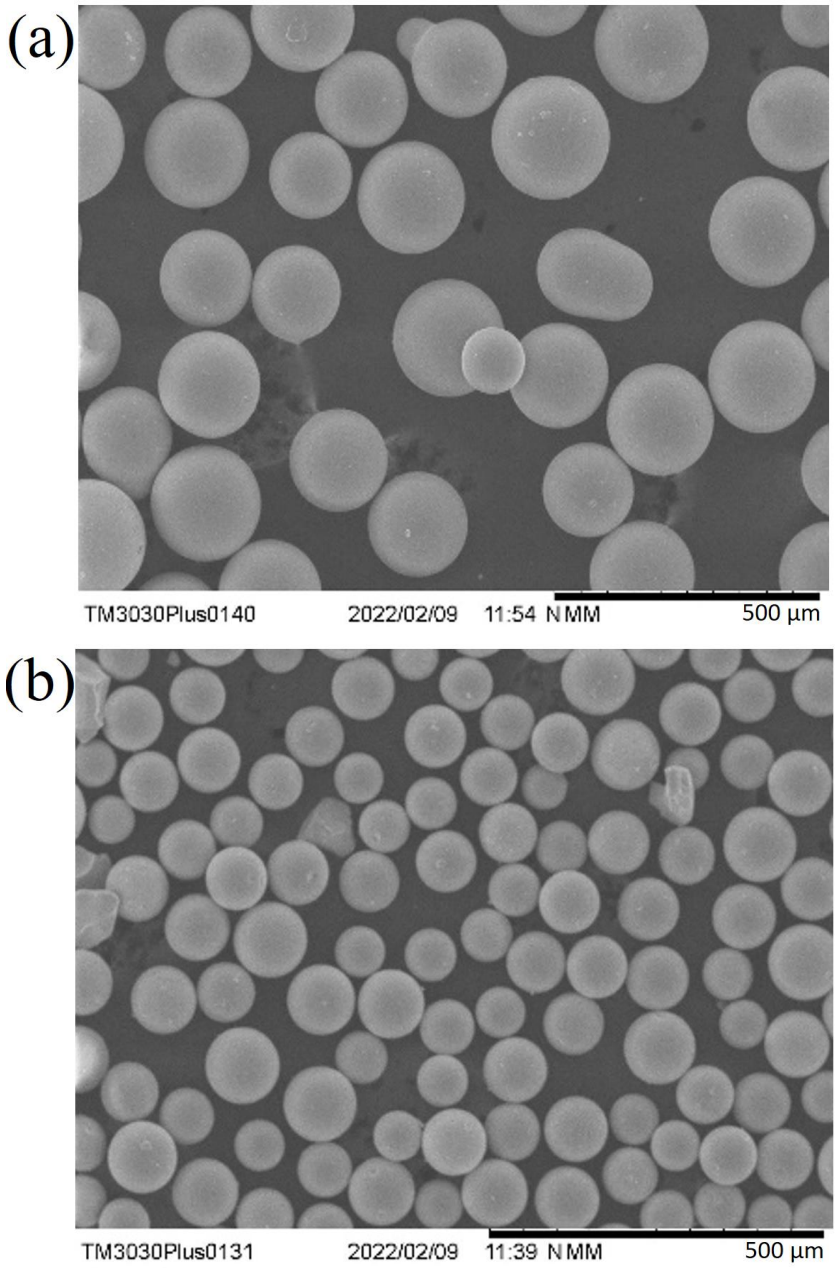

Figure 5.1 SEM (TM3030Plus, Hitachi) images of silica glass beads with a d_{50} of (a) 170 µm and (b) 82 µm (1000 X magnification)

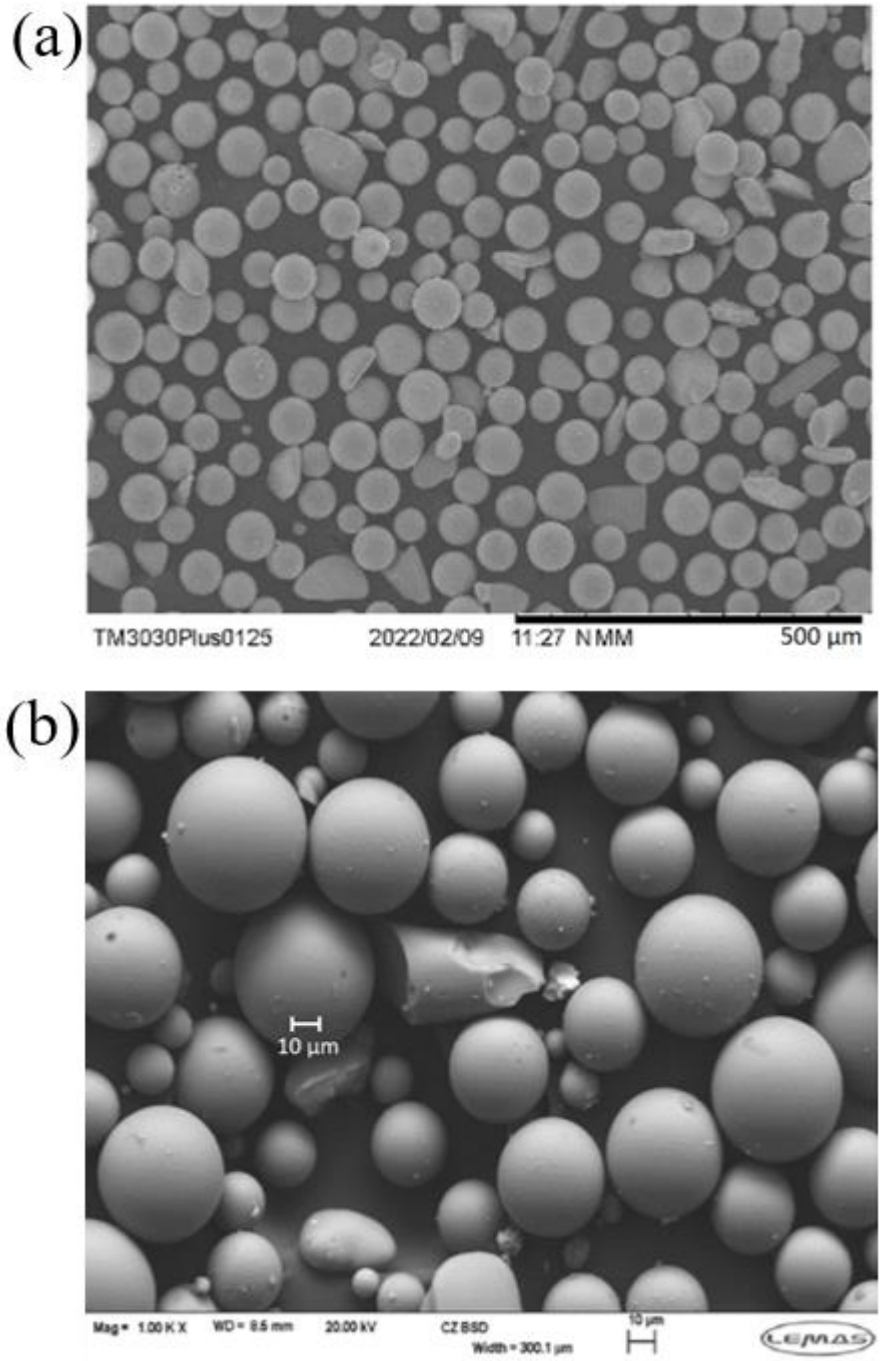

Figure 5.2 SEM (TM3030Plus, Hitachi) images of silica glass beads with a d_{50} of (a) 48 µm and SEM EVO images of silica glass beads with a d_{50} of (b) 36 µm (1000 X magnification)

In this Chapter, four species of silica glass beads were used to determine the attenuation coefficients of remotely placed and *in situ* transducers to establish

whether the signal loss from remotely placed probes led to inaccuracies in measured attenuation values. Attenuation values were then compared to predicted attenuation from Betteridge *et al*., (2008) and Urick, (1948) to provide a predicted combined attenuation value. In Chapter 4, a single glass bead species was used to understand whether the UVP was able to analyse the glass using transducers with a varying active radii and frequency. The size of the active radii had a negligible effect on the attenuation coefficients extracted and therefore, the transducer with a smaller 2.5 mm active radii was used. This smaller transducer can be mounted onto the surface of the tank or pipe easily without the need for the surface to be shaved flat.

The larger particle species was expected to undergo high scattering and minimal viscous attenuation in comparison to the other species (Moore *et al*., 2013; Sahin *et al*., 2020). This difference in scattering regime will help the author differentiate between attenuation profiles for each species (Moore *et al*., 2013; Tonge *et al*., 2021).

5.2.2 Methods

The experimental set-up is shown in Fig. 5.3 and was used to analyse homogeneous suspensions of the silica glass beads and produce acoustic profiles. When selecting transducers, the results from Chapter 4 were used where it was found that the 2 and 4 MHz transducers were able to produce accurate results when comparing to sedimentation attenuation coefficients found in literature (Betteridge *et al*., 2008; Bux *et al*., 2016). Therefore, both 2 and 4 MHz transducers were used. Both 2 and 4 MHz transducers were placed *in situ* as done in Chapter 4 (see Fig. 4.2) as well as remotely on the outer diameter of the calibration rig.

The same calibration tank and set-up in Fig. 4.2 were used to ensure all results were repeatable and could be compared to the initial calibration results in Chapter 4. Both 2 and 4 MHz transducers were placed *in situ* and remotely to understand whether the transducer placement would affect the sedimentation attenuation

coefficient extracted. In Fig. 5.3 the probes are colour-coded much like Fig. 4.2 where blue probes indicate a 2 MHz probe and grey indicates a 4 MHz probe. The set-up for the *in situ* transducers is detailed in Chapter 4 (see 4.2.2). Placement of the remote transducers considered the dynamics of the tank and particularly the impeller. Satjaritanun *et al*., (2021) found that the impeller diameter, impeller-bottom clearance and rotation speed had a high impact on the dispersion of sediment in a tank where the turbulence from the impeller torque led to unequal dispersion of material around the impeller. Therefore, remote transducers were slotted into a PVC mounting unit which was secured on the side of the tank above the impeller position. This was primarily to avoid the region around the impeller which is affected by the impeller torque. From previous investigation on the dispersion of the suspension in Chapter 4, the environment above the impeller was found to produce accurate measured concentration in comparison to predicted concentration. This was shown in Fig 4.5 where the suspension concentration was sampled across the concentration range used experimentally (11.9 – 107.1 g/L in Chapters 4 and 5) at varying heights in the tank to ensure the sediment had dispersed equally across the tank.

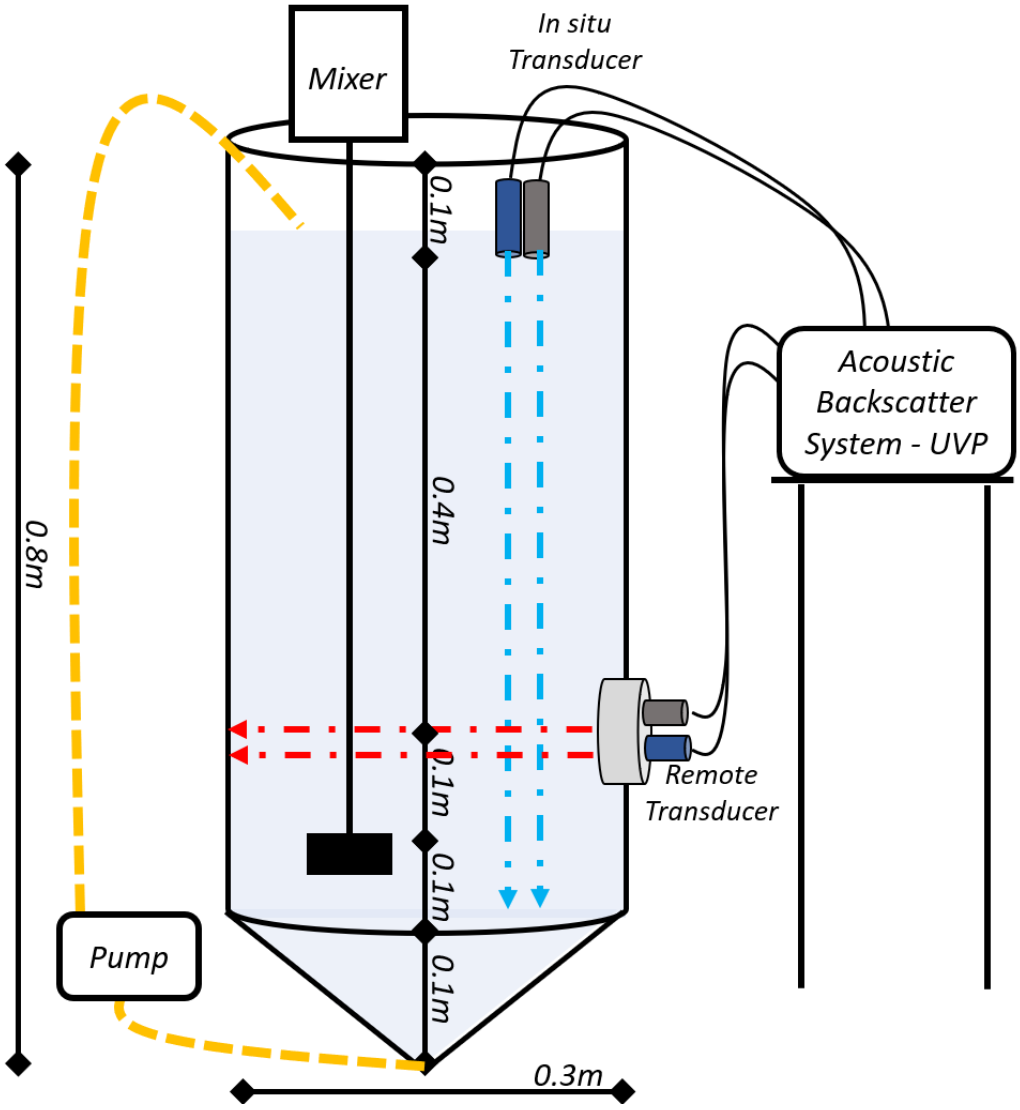

Figure 5.3 Schematic of calibration rig for analysis of silica glass bead dispersions using in situ and remotely placed ultrasonic transducers of 2 and 4 MHz frequency

There were several ports in the PVC mounting unit for remote placement of transducers to ensure multiple transducers could be mounted externally. There were approximately 3 mounting ports but only 2 were used in this Chapter, the actual unit was cylindrical with a 10 cm diameter and 5 cm thickness. The side which was attached to the rig was shaved down to allow the unit to be glued flush against the rig. The blue and red lines in the tank show the projection of the sound

signal for the *in situ* and remote transducers, respectively. The *in situ* probe does not require additional support to allow for analysis of the suspension environment. However, the remote transducer is placed on the outer diameter, therefore, a medium is required to assist with the penetration of the sound signal through the rig wall. For this experiment, an acoustic couplant is placed between the probe face and rig wall which is similar to the acoustic couplant used in ultrasounds, the specific gel used is Anagel ultrasound transmission gel. The Anagel works as an acoustic couplant to enable the transmission of the sound from the probe through the tank and back (e.g., Syked *et al*., 2006).

The four transducers were all connected to the UVP at the same time. As mentioned in Chapter 4, the UVP is unable to run multiple frequency transducers simultaneously therefore, the two 2 MHz transducers were activated with the 100 ms time delay and a 60 ms pulse (as noted in Table 4.1) each. After data were collected from the 2 MHz transducers, the 4 MHz transducers were then activated with the same delay and pulse. The experiment time is different from Chapter 4 as this experiment uses four transducers instead of three which leads to a time of 440 ms per profile. With the 1023 profiles this produces a total experiment time of 450 seconds. The same experimental methodology for dispersion was utilised here where a small amount of solid (to produce a 11.9 g/L suspension concentration) was added to the tank in Fig. 5.3 and suspended for 5 minutes before analysis. The impeller speed was maintained throughout the Chapters where the speed and diameter of the impeller were 500 rpm and 100 mm, respectively. More suspension was added after data were collected from the four transducers. At each concentration point approximately 5 mins clearance was required before analysis of the suspension. This was to ensure the suspension was fully homogeneous at the time of analysis. The experiment concluded when all four transducers had collected data from a final concentration of 107.5 g/L.

5.2.3 Mastersizer

The methodology for taking samples of silica glass beads from the rig for analysis in the Mastersizer is detailed in Chapter 4, section 4.2.2. The only difference in Chapter 5 is that there are four silica glass bead species to analyse.

5.2.4 Transducer and backscattering constants

The acoustic theory is covered in Chapter 3 extensively. However, only in this Chapter, the silica glass beads are to be fully characterised which required the determination of two constants. The measured transducer constant (k_t) and measured backscattering constant (k_s) were calculated using an alternative route to the novel process from Bux *et al*., (2019) which uses heuristic expressions from Betteridge *et al*., (2008). The process to determine the sedimentation attenuation coefficient is detailed in Chapter 4, Fig. 4.4 where Fig. 5.4 builds on the methodology further. The superscript *c* indicates calculations from heuristic expressions whilst *m* indicated measured experimental values.

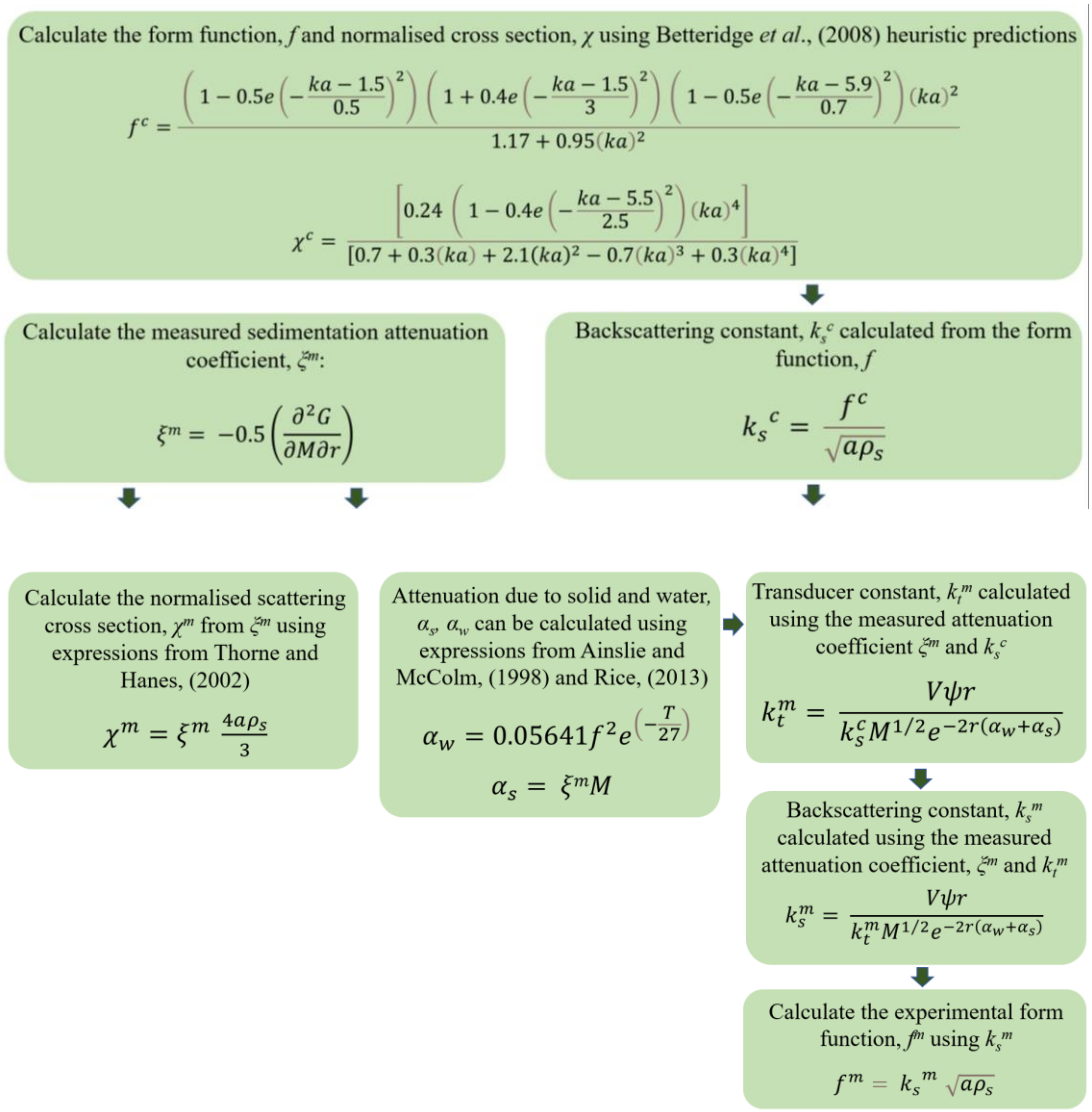

Figure 5.4 Alternative Route for calculation of k_t and k_s using derivations from Rice et al., (2015) and Bux et al., (2019) and heuristic predictions from Betteridge et al., (2008) (Rice et al., (2015); Bux et al., (2019))

The normalised scattering cross section, χ^m can be determined from the experimentally measured sedimentation attenuation coefficient, ξ^m. The attenuation due to solid, α_s and water α_w can also be derived with the known ξ^m using expressions from Ainslie and McColm, (1998) and Rice, (2013). From here, the heuristic expressions are used to determine the calculated form function, f^c and normalised scattering cross section, χ^c where *ka* was required for calculations. For the silica glass bead species, *ka* increases with increased particle

size, *a* and an increase in the wavenumber, *k*. The wavenumber is dependent on the speed of sound and transducer frequency. Therefore, *ka* was calculated for the four transducers and for each silica glass bead size where *ka* was the same for the *in situ* and remote transducers of each frequency. Each *ka* value was used in Eq. (3.08) to determine the heuristic form function value, this is also shown in the top box in Fig. 5.4. The backscattering constant, k_s^c was first calculated by using the calculated form function using an expression from Thorne and Hanes, (2002). The transducer constant k_t^m can be determined by rearranging Eq. (3.10) and using the experimental data as well as k_s^c, this is shown in Eq. (5.01). The expressions for the attenuation due to solid and water were also used in Eq. (5.01).

$$k_t^m = \frac{\psi r V}{k_s^c} M^{-1/2} e^{-2r(\alpha_w + \xi^m M)} \tag{5.01}$$

The measured backscattering constant, k_s^m can be determined by using Eq. (5.01) and rearranging to make k_s^m the subject and using k_t^m determined in Eq. (5.01). The final step is to determine the measured form function using the measured backscattering constant. Similar equations are shown in the methodology section (see Chapter 3) where the equations are also detailed in Fig. 5.4.

5.3 Results and Discussion

The UVP was utilised to determine the acoustic profiles of each species using 2 and 4 MHz transducers both *in situ* and remotely. Attenuation profiles were extracted from this acoustic data and attenuation coefficients were calculated for each species. Additionally, the further calibration procedure outlined in Fig. 5.4 allowed estimation of the specific transducer coefficients, meaning that both sediment attenuations coefficients and backscatter coefficients could be measured. Critical analysis was conducted on the largest particle size to account for high scattering where a lower concentration array was found to produce more accurate sedimentation attenuation coefficients. The scattering cross section and form

function were determined to establish the effect of the particle size on the scattering losses.

5.3.1 Mastersizer

Fig. 5.5 shows the particle size distribution for the four silica glass bead species as a cumulative distribution. The d_{50} corresponds to the median particle size. Each species has a distinct d_{50} with at least a 10 µm difference between the four glass particle species. This will provide more information on the sensitivity of the UVP to small changes in particle size. The smallest glass bead size has already been used in Chapter 4 (with the data being shown again here for easy comparison) and the other three bead sizes are first introduced in this Chapter.

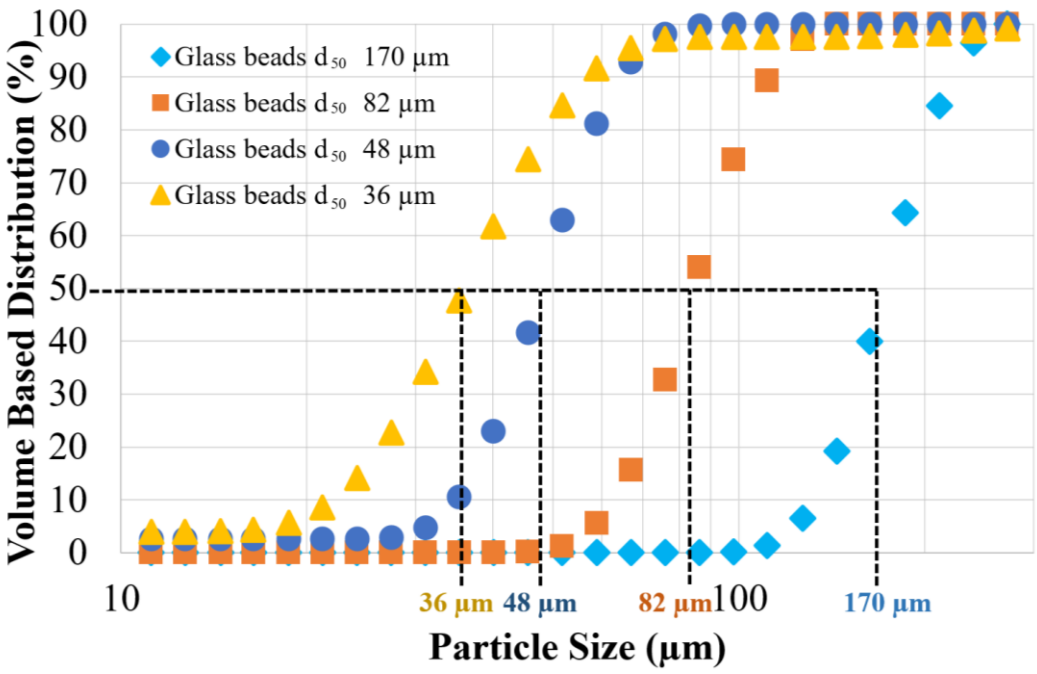

Figure 5.5 Particle size data for four species of silica glass species where the dashed lines indicate the d_{50} for each species

5.3.2 Acoustics

5.3.2.1 G function profiles

Fig. 5.6 (a), (b) and Fig. 5.7 (a), (b) show *G*-function profiles for the 170 μm silica glass beads using four transducers where Fig. 5.6 (a) shows results from a 2 MHz probe placed *in situ* and (b) indicates a 2 MHz probe placed remotely. Fig. 5.7 (a) shows results from a 4 MHz probe placed *in situ* and (b) indicates a 4 MHz probe placed remotely.

These four probes (see Fig. 5.3) were used to analyse well-mixed suspensions of silica glass particles. Fig. 5.8 (a), (b) and Fig. 5.9 (a) and (b) show the *G*-function profiles for the 82 μm glass using the same four transducer frequency and placement, respectively. Only the largest two silica glass bead suspension sizes are shown here, the profiles for the two smaller glass beads are shown in the Appendix in Fig. A1-A4. The backscatter profiles for all four species of silica glass are shown in the Appendix in Fig. A5–A8.

As shown in Chapter 4, the first observation noted in all of the figures in Fig. 5.6 to Fig. 5.9 are that the greater particle concentration leads to steeper gradients in *G*, at least within the far field. This far field distance varies for the transducer frequency and active face used. The near field distance for 2 MHz frequency transducers is 0.0253 m in comparison to the near field for 4 MHz transducers which is 0.0507 m (Rice, 2013; Met-flow, 2021). For all profiles shown, the near field correction factor has been incorporated so the profiles should remain linear throughout the near field distance (Downing *et al*., 1995). However, the profiles only become linear at 0.05 m when utilising the 2 MHz transducers as shown in Fig. 5.6 (a), (b) and Fig. 5.8 (a), (b). When using the 4 MHz transducers as shown in Fig. 5.7 (a), (b) and Fig. 5.9 (a), (b), the profiles are linear in the near field region. Therefore, it can be said that the near field correction factor is more accurate for profiles using the 4 MHz transducer in comparison to the 2 MHz where the profiles are only linear outside the near field distance. This could be attributed to the larger wavelength of the lower 2 MHz transducer which is able to penetrate the tank at a further depth but has a weaker transmission and therefore

does not perform efficiently in distances close to the probe (Butler and Sherman, 2016; Jackson, 2019).

In some profiles, the lowest concentration of 11.9 g/L produces a positive profile, this is specifically shown in Fig. 5.8 (a) and (b). This suggests a larger reflection of sound at greater distances with the lower density of particles. Such behaviour would be considered un-physical but positive gradients in the *G*-function have been shown in other work (Rice, 2013). For the remote probes in Fig. 5.8 (b) this is likely from near field interference from penetration through the Perspex. This will be investigated in future Chapters to establish whether this is a consistent feature for profiles from external transducers. The near field correction factor is not going to be accurate for remote configurations specifically due to the complex near field interference.

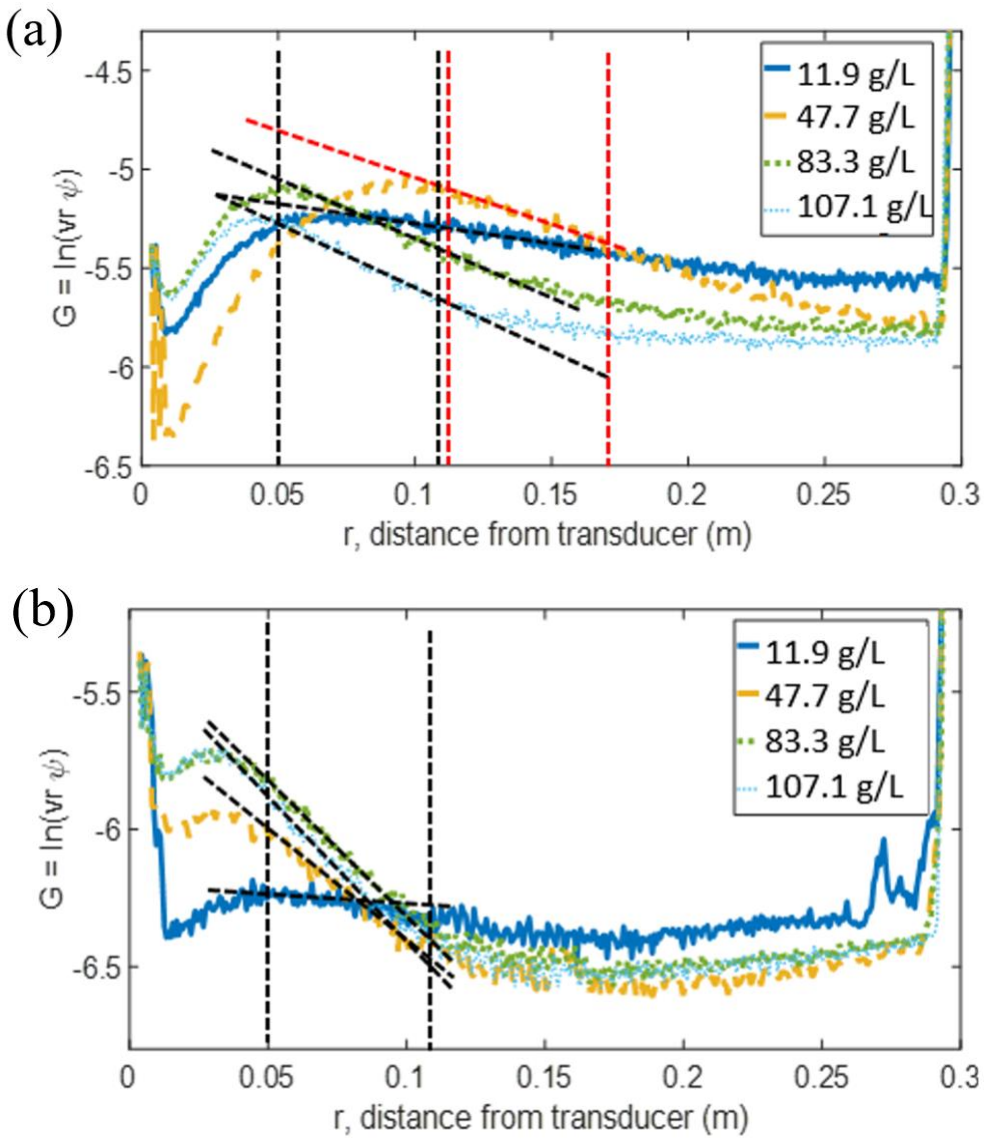

Figure 5.6 G function profiles of silica glass beads with a d_{50} of 170 µm utilising a 2 MHz transducer in an (a) in situ and (b) remote placement

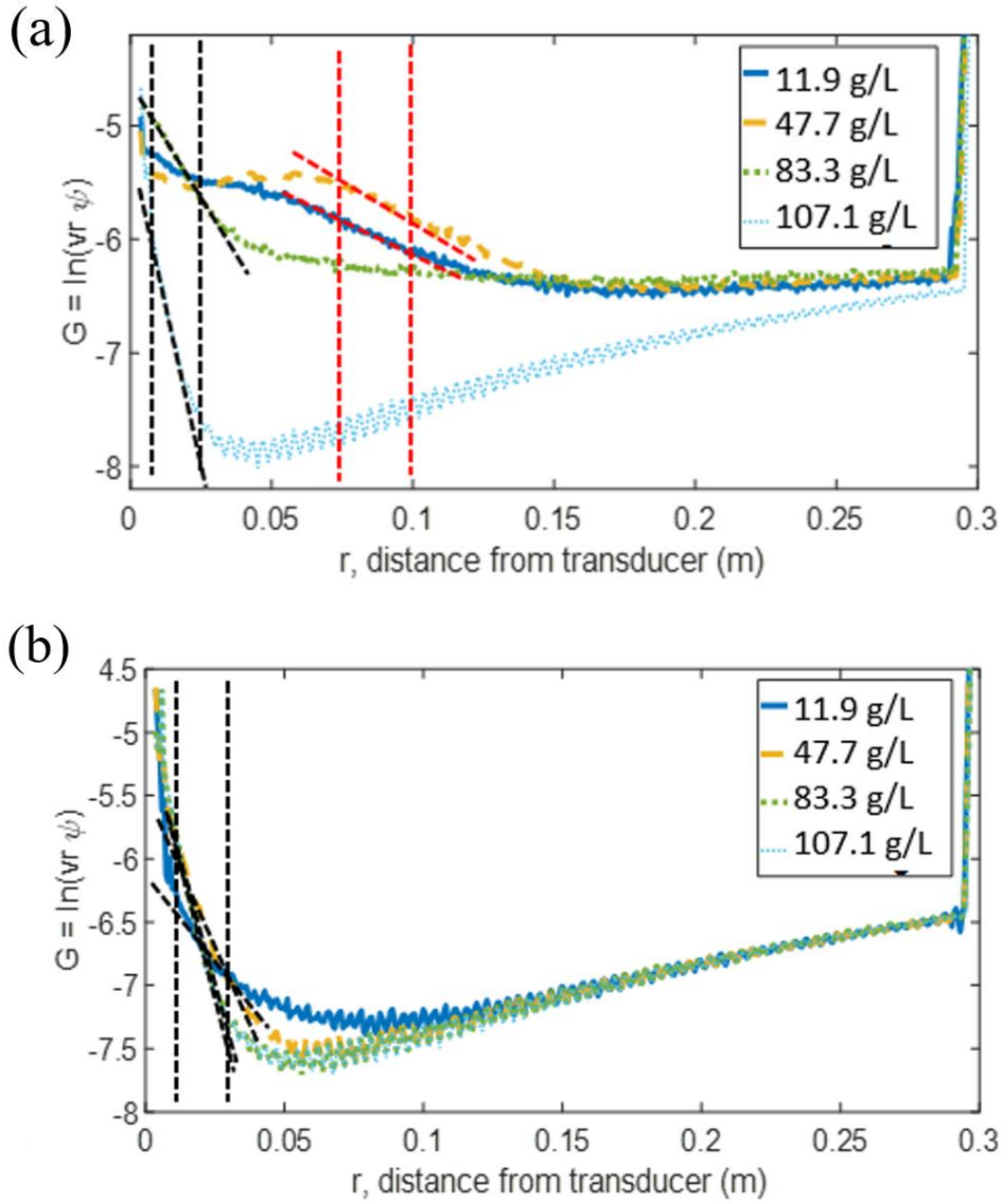

Figure 5.7 G function profiles of silica glass beads with a d_{50} of 170 µm utilising a utilising a 4 MHz transducer in an (a) in situ and (b) remote placement

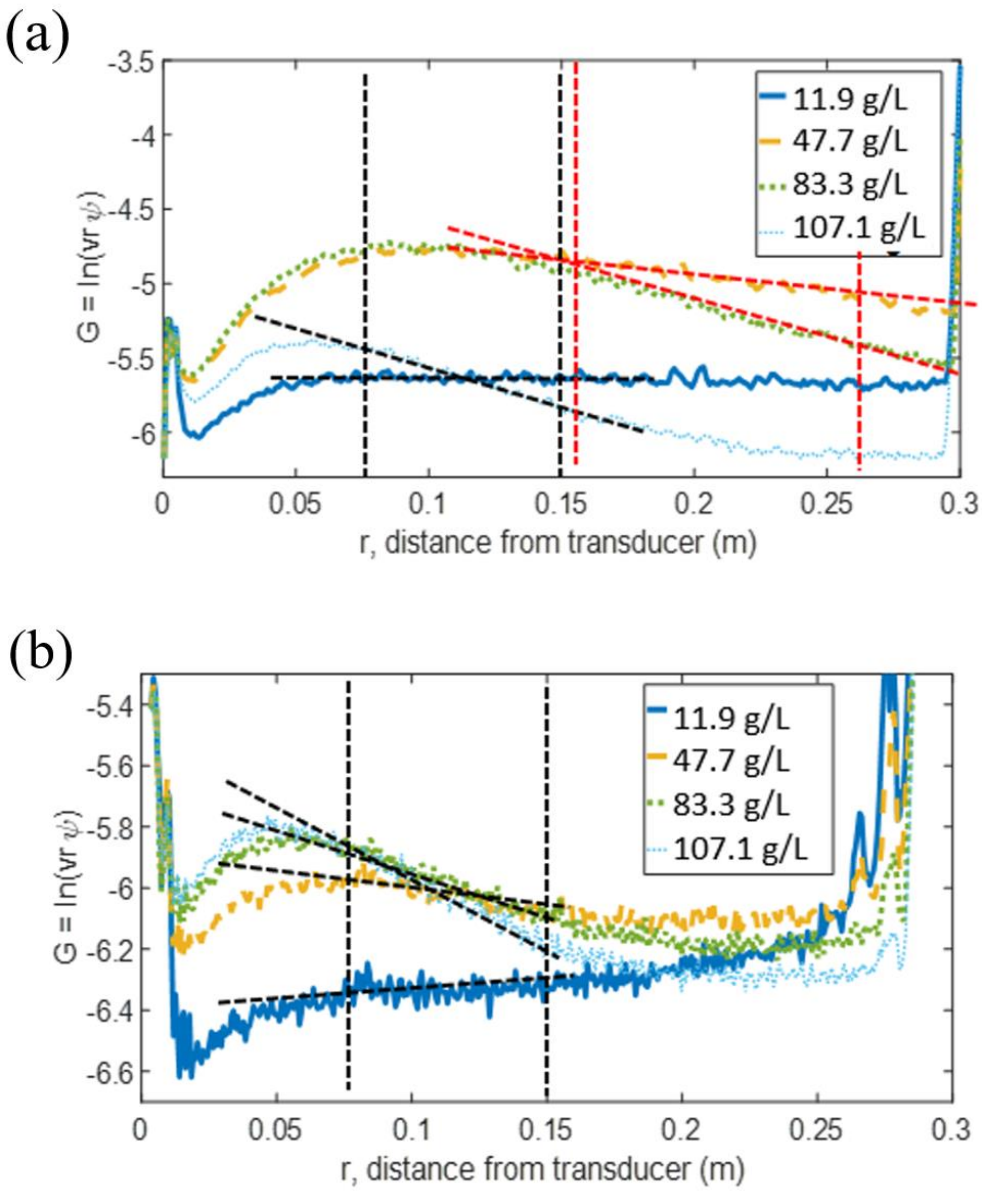

Figure 5.8 G function profiles of silica glass beads with a d_{50} of 82 µm utilising a 2 MHz transducer in an (a) in situ and (b) remote placement

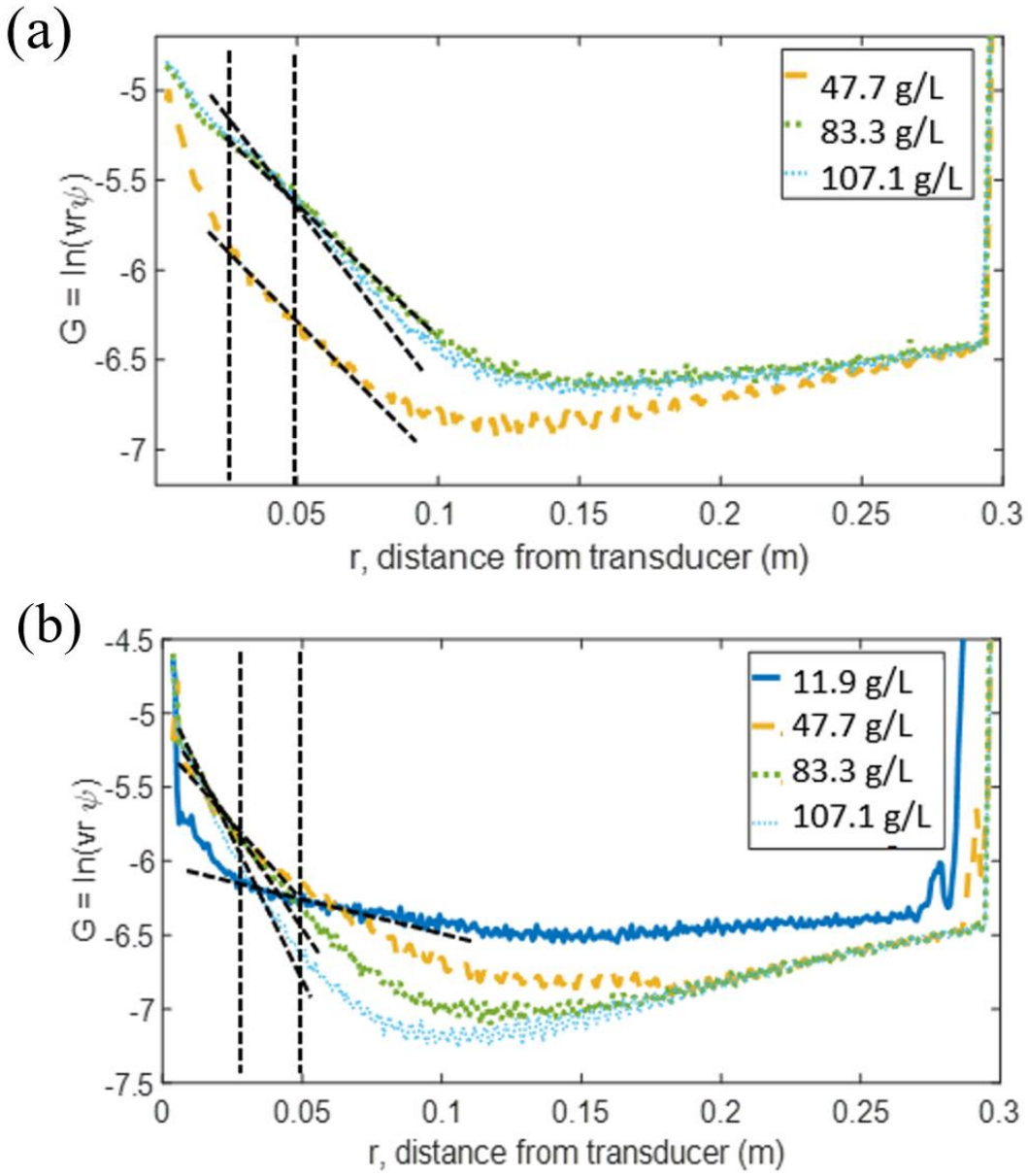

Figure 5.9 G function profiles of silica glass beads with a d_{50} of 82 µm utilising a 4 MHz transducer in an (a) in situ and (b) remote placement

The dashed vertical lines in Fig. 5.6 to Fig. 5.9 show the regions where most profiles are linear and where the attenuation coefficients are extracted from. The angled dashed lines show the linear fits for each concentration profile. In Fig. 5.6 (a) and (b) where the 2 MHz probe was used, the isolated linear region is from 0.05 – 0.11 m which is a total measurement zone of 0.06 m. The only profile where the linear fit was taken outside these limits was the 47.7 g/L profile in (a)

where the measurement distance of 0.06 m was taken between 0.11 – 0.17 m. This disturbance in the region 0.05 - 0.11 in Fig. 5.6 (a) for 47.7 g/L could be attributed to a disturbance near the transducer face. The measurement distance for the smaller glass species in Fig. 5.8 (a) and (b) for the 2 MHz probe was from 0.08 – 0.15 m which was a longer measurement distance. The intermediate concentration profiles in (a) required a longer measurement distance on 0.155 – 0.26 m. This was because there is a clear peak in the attenuation values for those intermediate concentrations in the original measurement distance. The measurement distances in Fig. 5.8 are longer as the smaller glass particle species undergoes less particle scattering, the signal decays less with distance and the profiles remain linear for a longer distance.

The 4 MHz profiles for the larger glass species in Fig. 5.7 (c) and (d) show a smaller measurement distance of 0.01- 0.03, this is a mere 0.02 m which is sufficient for analysis in the rig and for further experiments in the pipe (as the inner pipe diameter is 25 mm). For the two lower concentrations, the gradient is taken in a zone in the far field, from ~ 0.07 – 0.1 m. This is because there is a clear peak in the G-values, between the near and far field regions at the lower concentrations. For the higher concentrations, the attenuation is too much to see a delineation between the near and far field, and the original measurement distance close to the probe face is fine. Again, when investigating the 4 MHz profiles for the smaller glass species in Fig. 5.9 (c) and (d), the measurement distance was found to be longer (0.025 – 0.05 = 0.025 m) due to the decreased attenuation. These linear fits shown in Fig. 5.6 to Fig. 5.9 were used to extract the gradient and produce dG/dr plots as shown in Fig. 5.10.

As shown in Fig. 5.6 to 5.9, the measurement distances for the *in situ* profiles occasionally had to be taken in the far field region, this makes analysis difficult if analysing over a smaller distance, which is expected in a pipe loop. However, the remote profiles in Fig. 5.6 (b), 5.7 (b), 5.8 (b) and 5.9 (b) appear to show more consistent profiles with less disturbance in the near field.

A maximum of four concentration profiles were shown in Fig. 5.6 to 5.9 in each subplot to show the effect of concentration on the attenuation of the signal. The profiles which exceed -6.8 tend to show reverberations where the signal increases, this is a sign of the UVP's limit for analysis and is attributed to the noise floor. This is shown more readily in Fig. 5.7 and Fig. 5.9 where 4 MHz transducers have been utilised. As the frequency of the signal is higher, the wavelength is shorter which results in the signal hitting the instrument noise-floor at intermediate distances, this is also shown in Chapter 4. This results in the second inflection point in the *G* profile. The 4 MHz probes also attenuate more where the profiles are steeper in comparison to the 2 MHz profiles, this again is attributed to the smaller wavelength of the pulse. The profiles are noisier for the remote probes in all (b) subplots which is due to the signal weakening as it travels through the rig wall. All profiles show a reflection at around 0.029-0.03 m in the tank. This is attributed to an impeller reflection in the tank for the *in situ* probes whereas for the remote probes this is produced by the signal hitting the back end of the rig diameter. In Fig. 5.3 it is shown that the *in situ* transducers measured the length of the tank whilst the remote probes analyse the width. The larger particle species in Fig. 5.6 and Fig. 5.7 attenuate much more than the smaller glass species in Fig. 5.8 and Fig. 5.9 which is shown by the steeper linear fits. This increased attenuation is due to the increased particle size which enhances signal scattering.

The acoustic profiles in Fig. 5.6 and Fig. 5.8 show that the 2 MHz probes are not suitable for the smaller 3 cm pipes as the measurement distance requires longer distances in comparison to the 4 MHz probes. When comparing the remote and *in situ* probes, the remote profiles did not require gradients to be taken in the far field and therefore accurate data can be extracted solely in the near field region. This is preferential for analysis over small distances, such as the smaller 3 cm pipes used in the engineered pipeline.

Fig. 5.10 and Fig. 5.11 show attenuation profiles for the four silica glass bead species using the four transducers. Fig. 5.10 (a) and (b) shows attenuation profiles for the silica glass with a size of 170 and 82 μm whilst Fig. 5.11 (a) and (b) shows

attenuation profiles for silica glass with a size of 48 and 36 μm. The isolated linear regions shown by the dashed vertical lines in Fig. 5.6 to Fig. 5.9 were utilised to extract the gradients from each concentration. These gradients were plotted against their corresponding concentration values and are shown in Fig. 5.10 (a) and (b), respectively. The linear fits in Fig. A.1-4 were also extracted and shown in Fig. 5.11 (a) and (b). The two highest concentration plots were negated for Fig. 5.10 where the two largest particle species were utilised. This was because attenuation from the two largest particle species were not estimated accurately by the four transducers as the attenuation was underestimated and limited the attenuation coefficient value. In comparison, the dG/dr profiles for the smaller glass species were accurate when using the 2 MHz transducers, however the 4 MHz profiles were not accurate when taking into consideration the two largest concentration values; this is attributed to the higher level of scattering for the higher frequency transducers. Therefore, the 4 MHz profile linear fits negated the two highest concentrations to accurately predict the sedimentation attenuation coefficient. Generally, the attenuation profiles become less steep with decreasing particle size where the largest particle species attenuate the most in comparison to the smallest species which attenuate the least. The sedimentation attenuation coefficients are extracted from Fig. 5.10 and Fig. 5.11 by taking the negative half of the gradients for each transducer at each silica glass bead size.

The attenuation shown in Fig. 5.10 and Fig. 5.11 considers all forms of attenuation. For the smaller glass species, viscous losses have a predominant effect on the attenuation (Moore *et al*., 2013) whereas for the larger species, attenuation is predominantly due to scattering losses. This will have a larger effect on the smaller glass species which undergo predominantly viscous losses (Moore *et al*., 2013). Due to the higher scattering for the larger glass species, it was shown in Fig. 5.6 and Fig. 5.7 that the profiles tend to reach the instrument noise floor prematurely which is attributed to the high concentration and large particle size. This is also shown in Fig. 5.10 where the highest concentration values for the largest particle size led to underestimation of the attenuation coefficient. Therefore, a further critical analysis was conducted for the 170 μm glass beads,

where a lower concentration array is used to produce acoustic profiles (see section 5.3.2.3).

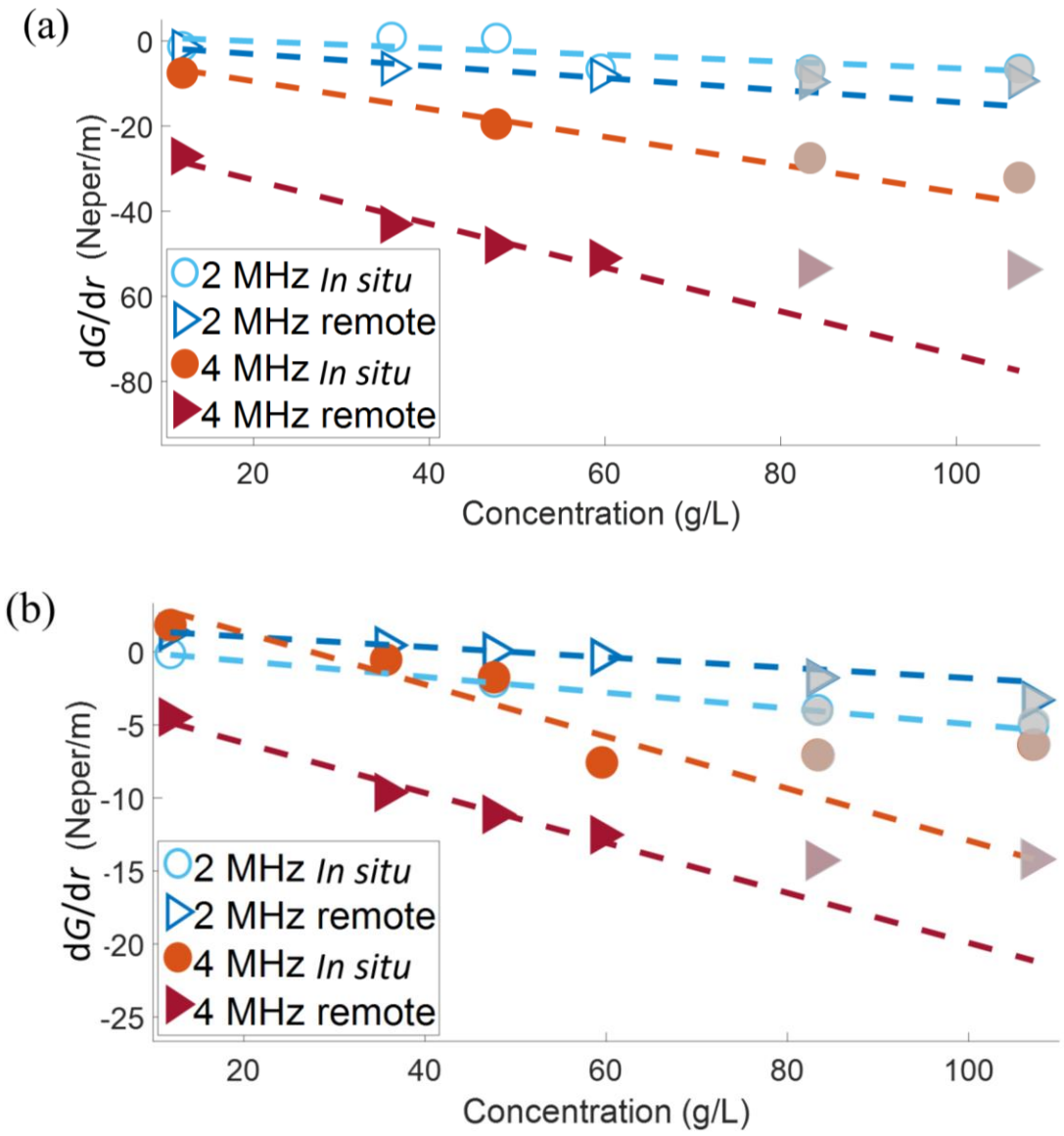

Figure 5.10 Change in the logarithmic function G with distance depending on the concentration range from 0-120 g/L using 2 MHz and 4 MHz transducers in situ and remotely for suspensions of silica glass beads with a d_{50} of (a)170µm and (b)82 µm

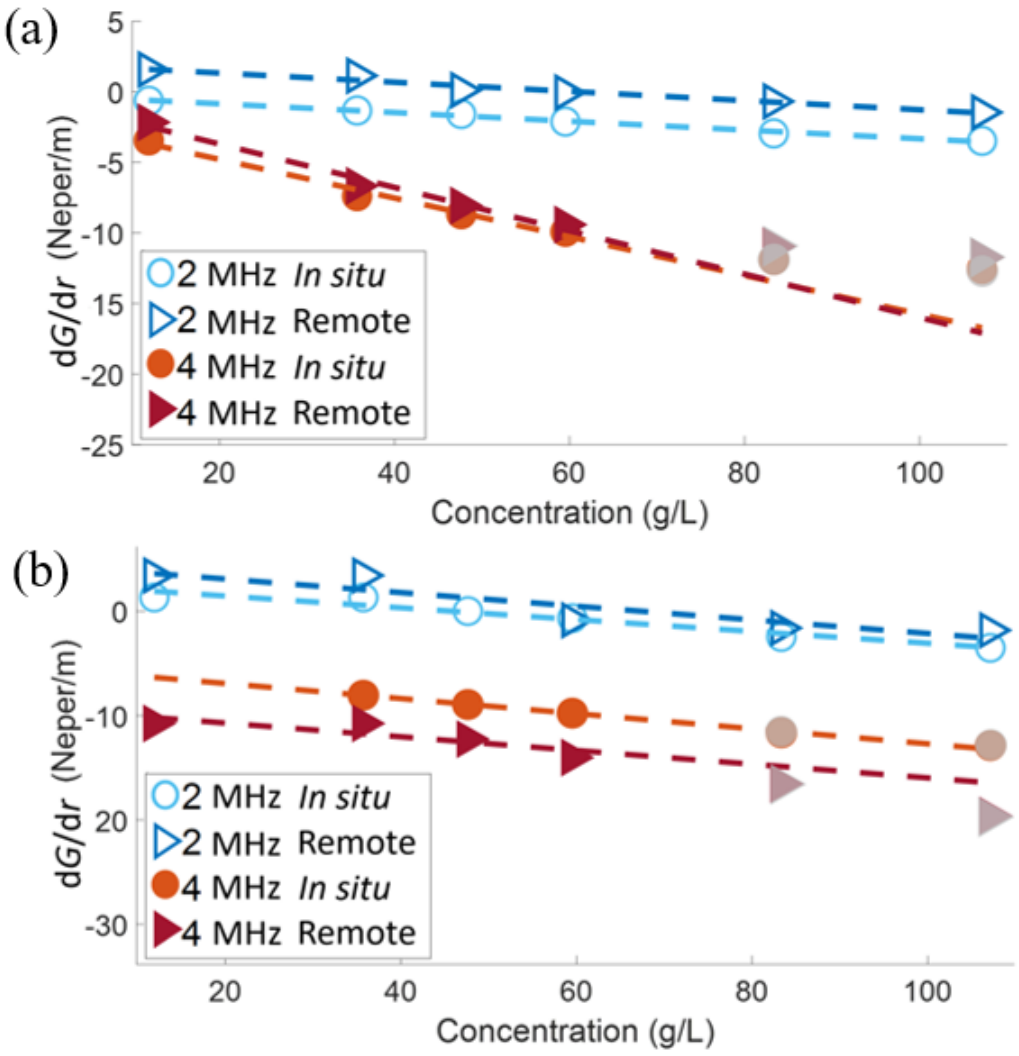

Figure 5.11 Change in the logarithmic function G with distance depending on the concentration range from 0-120 g/L using 2 MHz and 4 MHz transducers in situ and remotely for suspensions of silica glass beads with a d_{50} of (a)48 µm, and (b)36 µm

5.3.2.2 Attenuation Coefficient

The attenuation coefficient values from Fig. 5.10 and Fig. 5.11 were extracted and shown below in Fig. 5.12 and Table 5.1. The attenuation coefficients from the *in situ* and remote transducers were comparable for all four silica glass species with the largest difference being a 56% difference for the largest glass bead species using a 4 MHz transducer. The remote attenuation coefficient is larger for all

species apart from the 82 μm glass when using a 2 MHz probe. The *in situ* probe measures the length of the rig whilst the remote measures the width, this difference could have led to a slight difference in attenuation. However, 75 % of the measured coefficients are within 28 % of each other and the difference is almost negligible.

Predicted attenuation coefficients from the Betteridge *et al*., (2008) expression are shown alongside the attenuation coefficient values in Fig. 5.12 where the prediction compares well to most species except for the largest glass species where the measured data are overpredicted. As the largest glass species undergoes more scattering attenuation, experimental concentration range used here (11.9 – 107.1 g/L) may have been too high for the largest silica glass bead species. This is also shown in Haught *et al*., (2017) where it was identified that concavity can be prevented by using a lower concentration range for a larger particle size. The smaller species are highly underestimated by the Betteridge *et al*., (2008) prediction but this is likely due to the fact that the smaller species mainly attenuate due to viscous losses. When considering viscous losses (see yellow bar) in Fig. 5.12, the measured data for the two smaller glass species compare very well to the predicted combined attenuation. Apart from the largest glass species, the results are very close for most systems with the predicted combined modelled attenuation. This is important as it proves that the UVP is excellent at measuring the attenuation properties of the glass, provided that the user stays within a concentration region. The remote probes generate data which has a maximum difference of 0.0153 where values were close to the *in situ* measured values, so, despite losses in signal strength, attenuation is almost identical which provides confidence that the remote probes can be used in an online environment.

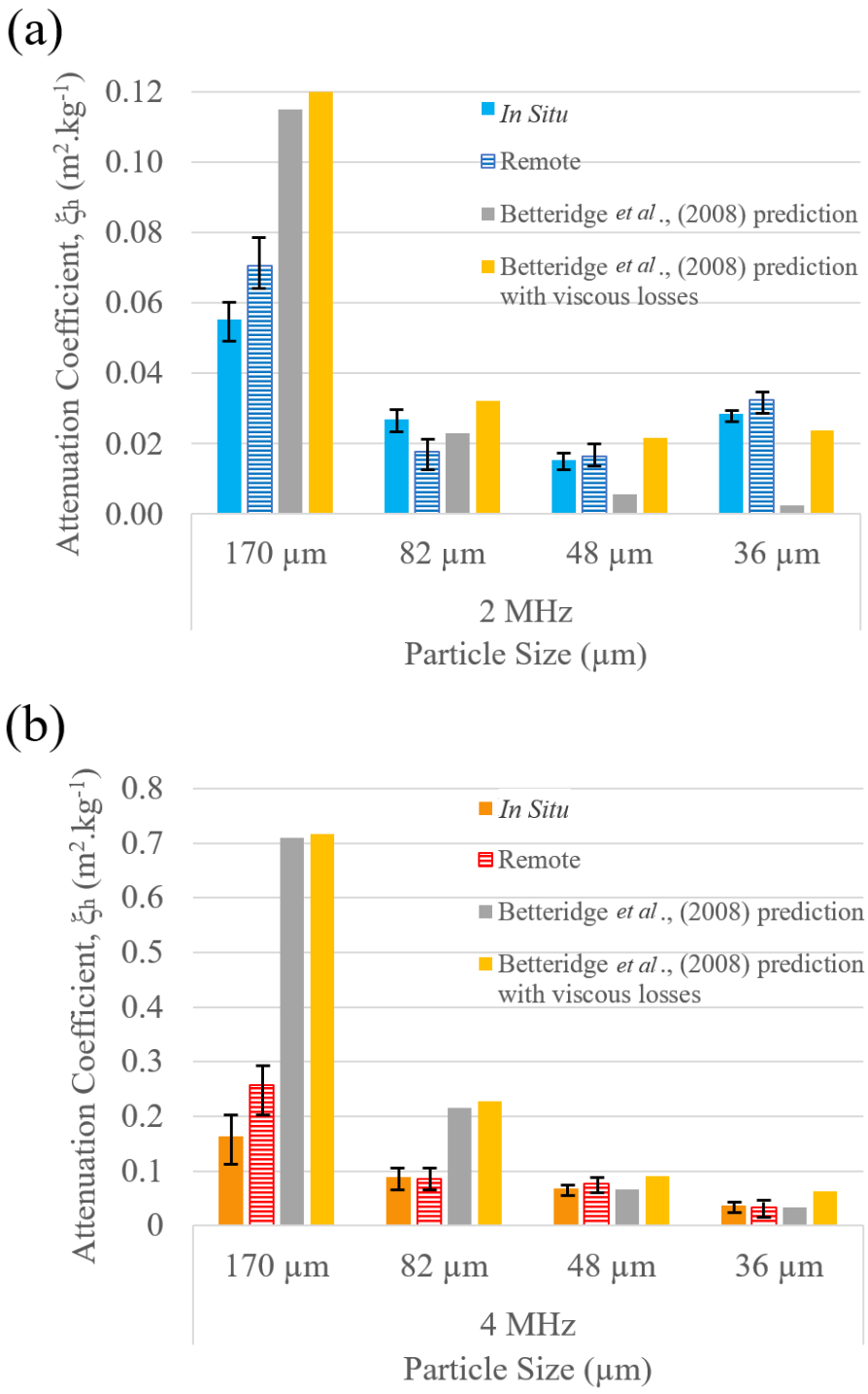

Figure 5.12 Measured, concentration independent, sediment attenuation coefficients in comparison to predicted measurements from the Betteridge et al., (2008) heuristic expressions in Eqs. (3.07) and (3.09) and comparison to the Betteridge et al., (2008) heuristic expressions with viscous losses in Eqs. (3.11) – (3.14) for glass beads species of d_{50} 170 µm – 36 µm using a (a) 2 MHz and (b) 4 MHz ultrasonic probes

Table 5.1 shows the measured sedimentation attenuation coefficients in comparison to measured values from Rice *et al*., (2014) and Bux *et al*., (2019). The average measured values for the 82 μm particle sizes (0.0225) when using the 2 MHz probe compare very well to measured values from Rice *et al*., (2014). The measured coefficient from Bux *et al*., (2019) is slightly overestimated which compares better to the predicted values in Fig. 5.12. However, the similarity between the measured values and values from Rice *et al*., (2014) show that the experimental set-up was accurate and the fact that these coefficients compare well to predictions in Fig. 5.12 shows that the predictions are accurate. The coefficients for the same sized glass when using a 4 MHz probe are underestimated in comparison to values from Rice *et al*., (2014), this could be due to the concentration range being too limiting for the attenuation. When looking at the smaller 36 μm particle size data, the measured values when using a 2 MHz probe compare well to measured coefficients from Bux *et al*., (2019) whilst the values from a 4 MHz probe are underestimated in comparison to previous literature. However, as these values compare well to predicted combined attenuation values in Fig. 5.12, the values determined experimentally here are found to be accurate.

Rice *et al*., (2014) and Bux *et al*., (2019) compared measured values to predictions from Betteridge *et al*., (2008) without considering viscous losses. Therefore, comparison to a prediction was not as accurate as shown here. Measured values from the 4 MHz probes were particularly underestimated in comparison to values from Rice *et al*., (2014) this is because the highest concentration tested was 250 g/L in Rice *et al*., (2014) whereas in this Chapter, the most concentrated solution was at 107.1 g/L. Bux *et al*., (2019) used a concentration range of 0.1 – 75.9 g/L and showed a higher attenuation coefficient. This difference in attenuation coefficient shows that the experimental concentration range effects the attenuation measured.

Guerrero *et al*., (2015) also analysed sediments of silt and clay with a particle size of ~ 92 μm and ~ 83 μm. The attenuation coefficients from this data can be compared specifically to the 82 μm silica glass bead data below in Table. 5.1 The

average measured attenuation coefficients for the 82 µm silica glass is 0.023 whilst the attenuation coefficient from Guerrero *et al*., (2015) is 0.013 which is smaller. This may be due to the decreased transducer frequency (1.2 MHz) used by Guerrero *et al*., (2015). Which aligns with the theory from Sahin *et al*., (2020) that higher frequency transducers led to increased attenuation coefficients. This is because the scattering losses increase with increase in frequency and the 82 µm silica glass beads will undergo attenuation predominantly due to scattering losses (Guerrero *et al*., 2015).

Table 5.1 Measured sedimentation attenuation coefficient from experiments for four silica glass bead suspensions of varying d_{50} values using 2 and 4 MHz transducer placed in situ and remotely

Transducer Frequency	Silica Glass Bead d_{50}	Sedimentation Attenuation Coefficient ζ^m, ($m^2.kg^{-1}$)			
		In Situ Transducer	Remote Transducer	Measured Coefficients from Rice *et al*., (2014)	Measured Coefficients from Bux *et al*., (2019)
2 MHz	170 µm	0.055	0.071		
	82 µm	0.027	0.018	0.021	0.036
	48 µm	0.016	0.017		
	36 µm	0.029	0.033	0.018	0.024
4 MHz	170 µm	0.164	0.257		
	82 µm	0.089	0.086	0.135	0.247
	48 µm	0.069	0.077		
	36 µm	0.036	0.033	0.069	0.096

5.3.2.3 Further G function critical analysis for 170 µm beads

A concentration range of 1-30 g/L was investigated to obtain the attenuation coefficients for the large 170 µm particles, due to the higher concentrations in the original calibration leading to high attenuation that was beyond the instrument

noise floor. This was established after determining that the concavity of the profile could be prevented by using a lower concentration array for larger particle sizes (Haught *et al*., 2017). The *G*-function profiles in Fig. 5.13 and Fig. 5.14 between the *in situ* and remote profiles now show similar peaks in the *G*-function, flow patterns and peak signal. This is not shown in Fig. 5.6 and Fig. 5.7 where the *in situ* and remote profiles are visibly different. This shows that the UVP was able to provide consistent profiles regardless of transducer placement when using a lower concentration array. The signal strength for Fig. 5.13, Fig. 5.14 and Fig. 5.6, Fig. 5.7 are comparable where the profiles exist from -4.5 to -7. The dashed lines which follow the profiles are all linear fits and the vertical dashed lines are the distance points between which the linear fits are predicted.

In Fig. 5.13 (a) and (b), the linear region varies from 0.09-0.17 whilst the linear region in Fig. 5.14 (a) and (b) was 0.02–0.05 m which shows measurement distances of 0.08 m and 0.03 m for the *in situ* and remote probes, respectively. Whereas Fig. 5.6 and Fig. 5.7 (a) and (b) shows a shorter measurement distance (0.06 and 0.02 m) where the distances were limited by the reflections in the profiles. Reverberations in Fig. 5.6 (a) and (b) occur at 0.15 m whilst reverberations in Fig. 5.7 (a) and b) occur at 0.03 m respectively. In comparison, the reflections in Fig. 5.13 (a) and (b) occur at 0.2 whilst reflections in Fig. 5.14 (a) and (b) occur at 0.1 m which provides a larger distance from which gradients can be extracted from. This indicates that the UVP gives a more consistently decaying profile when using the lower concentration array for the larger particle species.

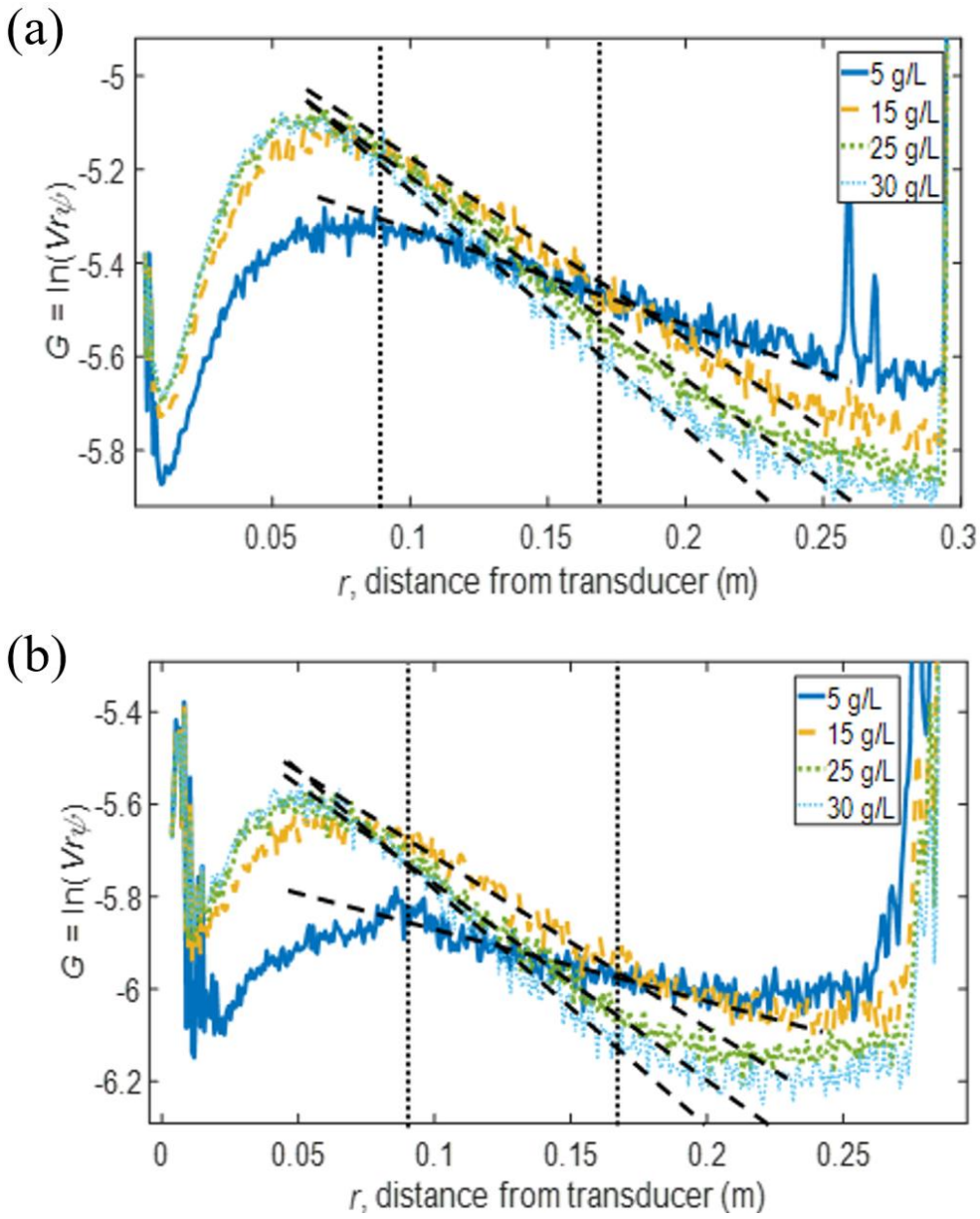

Figure 5.13 G function profiles of silica glass beads of d_{50} 170 µm utilising a 2 MHz transducer in an (a) in situ and (b) remote placement with dashed lines showing the linear predictions

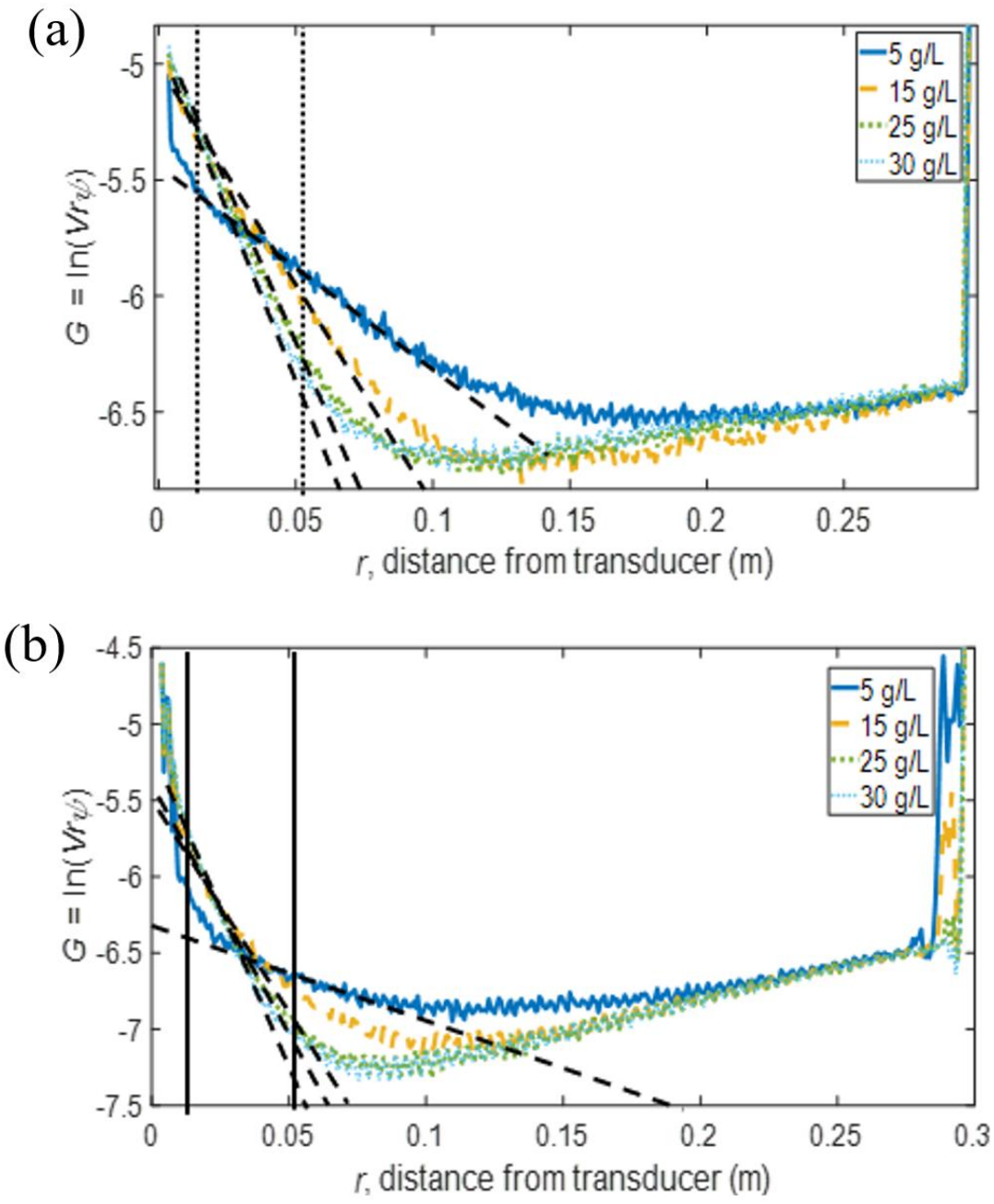

Figure 5.14 G function profiles of silica glass beads of d_{50} 170 µm utilising a 4 MHz transducer in an (a) in situ and (b) remote placement with dashed lines showing the linear predictions

The *G*-function profiles produced using a lower concentration array in Fig. 5.13 and Fig. 5.14 were used to determine an improved attenuation profile when considering lower concentration values at the highly scattering larger glass bead

size. The linear fits were plotted as gradients with respect to their corresponding concentration values and are shown in Fig. 5.15. When comparing to Fig. 5.10 (a), the linear fits for the four transducers align better where all data points lie on the linear prediction. In Fig. 5.10 (a) only data below 47 g/L aligned with the linear fit whilst the higher concentration plots led to an underestimation of the gradient. In comparison to Fig. 5.15, the linear fits are steeper which leads to a higher sedimentation attenuation coefficient. The *in situ* and remote profiles for the two frequency transducers compare very well to each other. Whereas in Fig. 5.10 (a) the profile gradients were similar, but the signal strength varied by ~5 for the 2 MHz profiles and ~20 for the 4 MHz profiles.

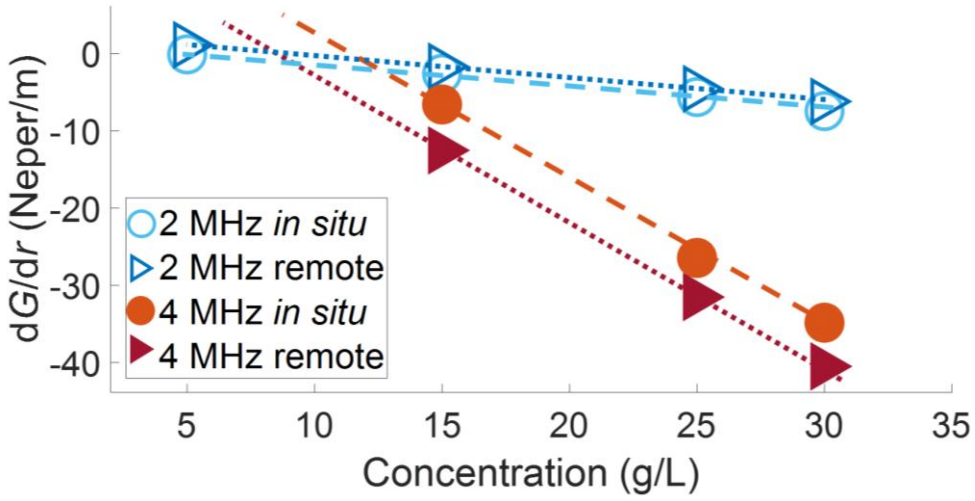

Figure 5.15 Change in the logarithmic function G with distance depending on the concentration range from 0-30 g/L using 2 MHz and 4 MHz transducers in situ and remotely for suspensions of silica glass beads with a d_{50} of (a)170 μm

In Fig. 5.15, the 2 MHz profiles align very well with a signal strength difference of approximately ~1 whilst the 4 MHz profiles vary by ~5 which is significantly smaller. This shows that the UVP was able to analyse the suspensions more accurately with less variation between the *in situ* and remote data. Therefore, the UVP has limitations on analysing larger particle size data at higher concentrations. In the nuclear industry, the general solids concentration in the SPP1 which is a series of settling tanks designed to remove the sludge and

produce a supernatant is approximately < 2.5 vol% (Grant *et al*., 2016). In these data the concentration array of 11.9-107.5 g/L produces a solids content of 0.5 – 4 vol %, whereas the 1-30 g/L concentration array corresponds to a solids content of 0.03 – 1.1 vol% which is significantly lower than the approximate concentration in SPP1 (Grant, *et al*., 2016). Therefore, to ensure that the profiles produced from the sludge are accurate, the sludge must be significantly diluted for analysis.

5.3.2.4 Attenuation Coefficients with Improved Analysis of 170 μm beads

The sedimentation attenuation coefficients are extracted from Fig. 5.15 by taking the negative half of the gradient as shown in Eq. (3.06). The sedimentation attenuation coefficients for all four glass species are shown below for the two transducer placements and the two frequency transducers. This figure is the same as Fig. 5.10 (a), but the new sedimentation attenuation coefficients have been input for the 170 μm glass species. The coefficients compare much better to the combined attenuation shown below, this shows that the UVP is unable to accurately predict the attenuation of the larger glass species at higher concentration values, therefore, a limit is placed on the highest concentration value used in the experimental concentration range (11.9 – 107.1 g/L). As the dG/dr plot in Fig. 5.10 (a) was accurate up to ~50 g/L, the attenuation of the larger glass species can be predicted accurately provided the highest concentration is below 50 g/L.

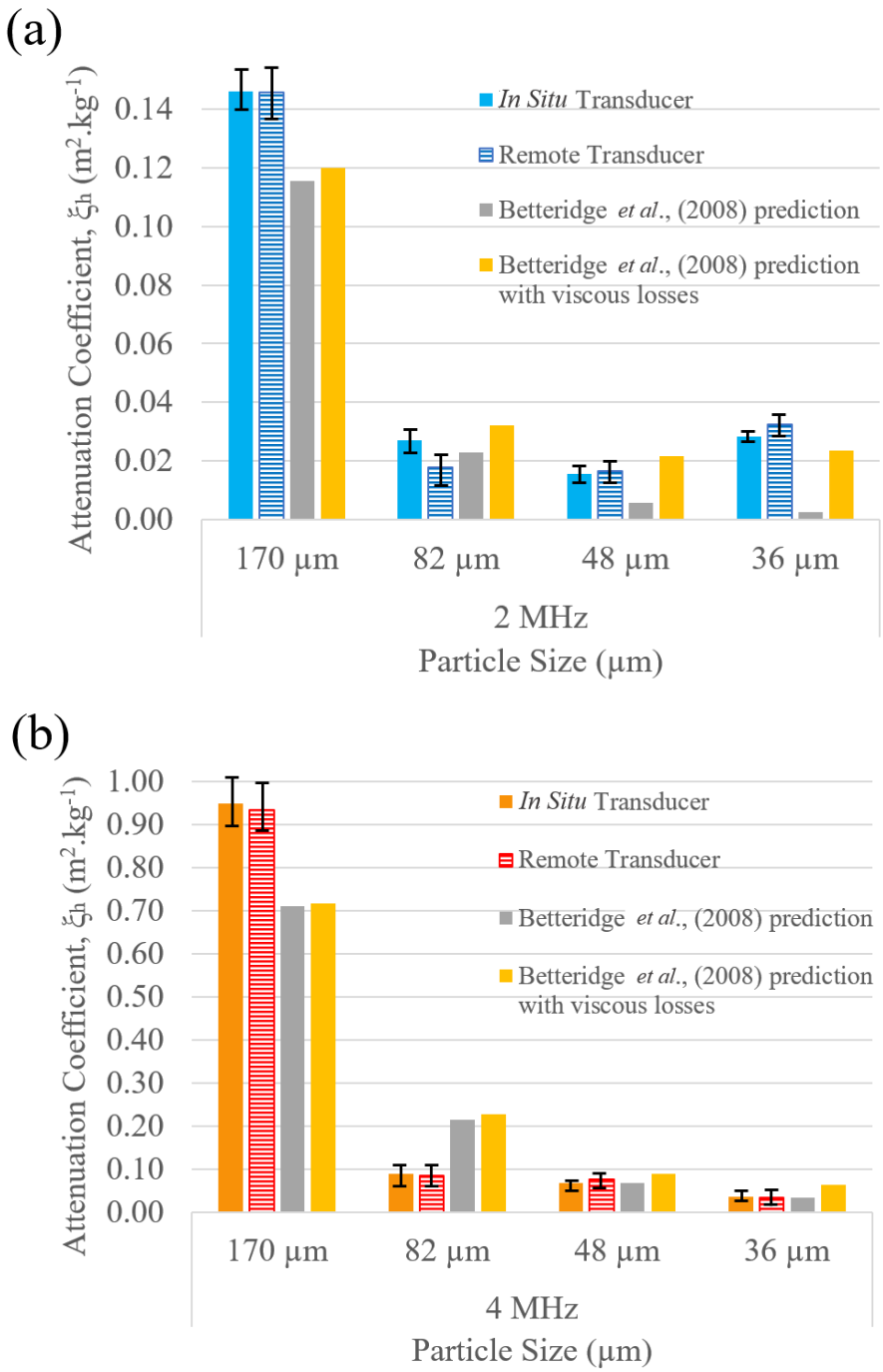

Figure 5.16 Measured, concentration independent, sediment attenuation coefficients in comparison to predicted measurements from the Betteridge et al., (2008) heuristic expressions in Eqs. (3.07) and (3.09) and comparison to the Betteridge et al., (2008) heuristic expressions with viscous losses in Eqs. (3.11) – (3.14) for glass beads species of d_{50} 170 µm – 36 µm using a (a) 2 MHz and (b) 4 MHz ultrasonic probes where the lower concentration array was used for the largest particle size

The attenuation coefficients now only show a 1.48% difference between the *in situ* and remote measured coefficients for the 170 μm silica glass when using the 4 MHz probe using and a 0% difference for the 2 MHz. This is significantly smaller than the difference between the two transducer placements for 170 μm in Fig. 5.12 which is 29% and 56.7% for the 2 and 4 MHz transducer respectively. The largest error in Table 5.1 is between the *in situ* and remote transducer coefficients for the second largest particle species using the 2 MHz transducer, this can be attributed to the highest concentration in the concentration range being too concentrated for this size of glass.

For the four silica glass beads from largest to smallest, the contribution of viscous losses in Fig. 5.16 (a) is 4.5E-03, 9.4E-03, 1.6E-02, 2.1E-02. This corresponds to a proportion of 14, 29, 74 and 89 % for the four silica glass beads from largest to smallest. In comparison to the contribution for the same respective silica glass beads when using the 4 MHz transducer which is 6.4E-03, 1.3E-02, 2.3E-02, 3E-02. This corresponds to a viscous loss proportion of 3, 6, 25 and 48 % which is lower than the contribution for the 2 MHz transducer. This shows that the 4 MHz transducer has an added viscous loss which is incorporated into the attenuation coefficient, this is due to the increase attenuation losses. However, when breaking down the proportional viscous losses, this decreases for the higher frequency probe. This is comparative to the decreased viscous boundary layer for the 4 MHz probe which is determined in Chapter 3. The viscous losses increase with decrease in particle size, this relationship can be directly compared to the decrease in particle Reynolds number in Table 3.5, Chapter 3. For the increased particle Reynolds number for the 4 MHz probe, the viscous losses decrease in proportion. Therefore, it can be inferred that the increase in particle Re may lead to a decrease in proportional viscous losses. This relationship will have to be explored further however, this is out of the scope for this thesis.

5.3.2.5 Transducer and backscattering constants

The transducer constant determined using Fig. 5.4 was plotted in Fig. 5.17 and Fig. 5.18 against the varying distance from the transducer. Only the silica glass beads with a d_{50} of 82 μm were used to determine the transducer constant as k_t is sediment dependent and only changes with the following transducer properties; frequency, active radii etc. Therefore, changes in sediment should not affect the transducer constant. This intermediate silica glass bead was chosen because it does not undergo high scattering or viscous attenuation. The profiles were negated in the near field distance (~ 0 - 0.05 m) and were shown to be approximately constant through the distance from the transducer. The profiles were more consistent across the concentrations when using the 4 MHz transducer. The most important feature from Fig. 5.17 and Fig. 5.18 was that the transducer constant remained approximately constant for all concentration values across the rig. Any peak at 0.029 m was due to the impeller reflection or wall reflection in the tank. These k_t^m values can be used to determine k_s^m by following Fig. 5.3.

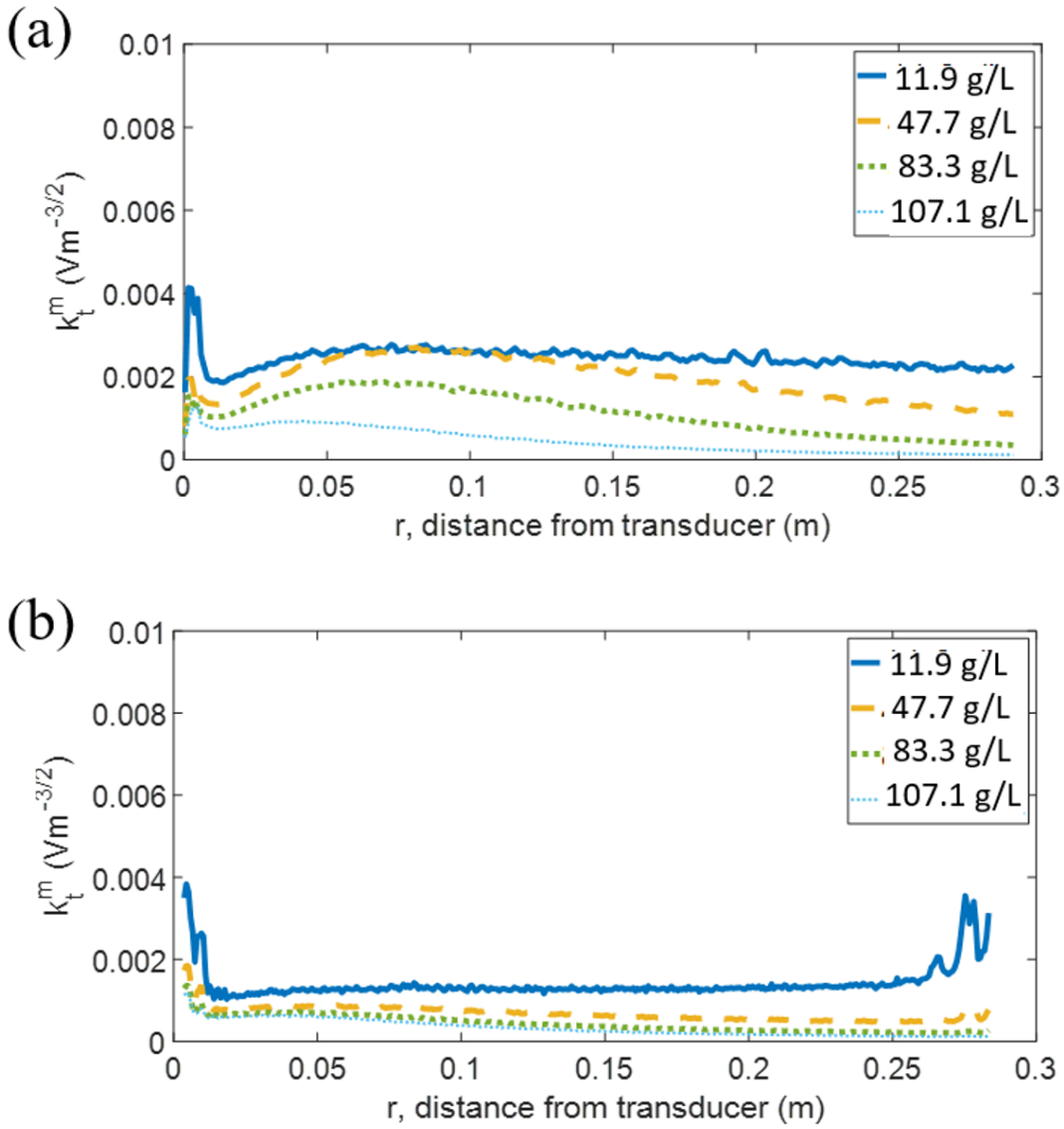

Figure 5.17 Transducer constant (k_t^m, V.m$^{1.5}$) profiles of silica glass beads of d_{50} 82 µm utilising ultrasonic transducers with a 2 MHz frequency placed (a) in situ and (b) remotely in the tank

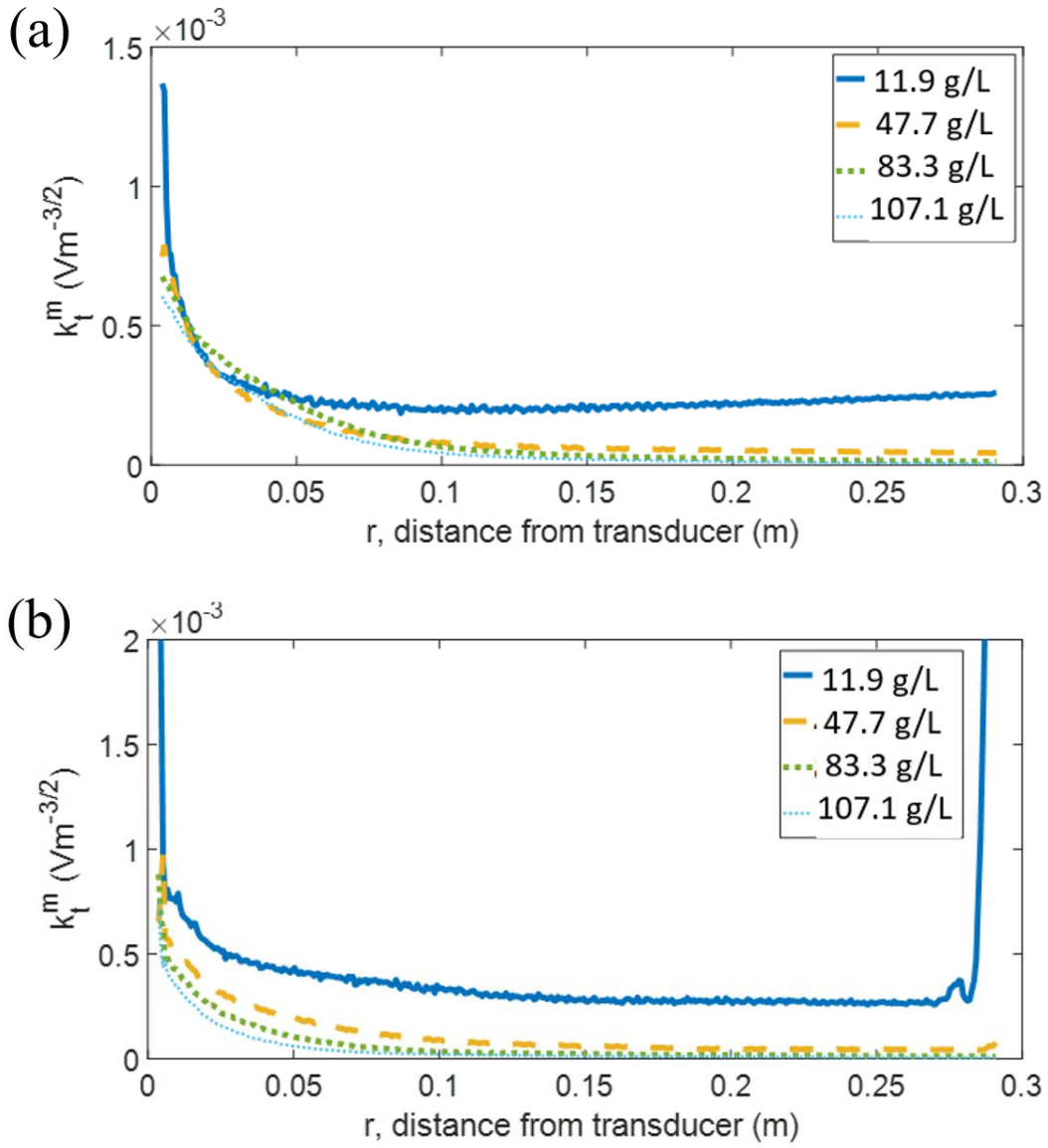

Figure 5.18 Transducer constant (k_t^m, $V.m^{1.5}$) profiles of silica glass beads of d_{50} 82 µm utilising ultrasonic transducers with a 4 MHz transducer placed (c) in situ and (d) remotely in the tank

The backscattering constant, k_s^m for the four silica glass species for the four transducers is shown below in Fig. 5.19 - Fig. 5.22. Fig. 5.19 and 5.20 shows the backscattering constant for the four silica glass bead grades when using the remote 2 MHz transducer, whilst Fig. 5.21 and Fig. 5.22 show the backscattering constant when using the remote 4 MHz transducer. Profiles are shown for all four silica glass beads as the backscattering constant is dependent on the sediment

used. Fig. 5.19 - Fig. 5.22 show that k_s^m was also relatively constant across the length of the transducer, when negating the near field region. As this region was ignored the concentration range has limited effect on the backscattering constant. However, the small differences at high concentrations are indicative of dominant interparticle scattering where the transducer coefficient stops being a constant value. Therefore, the backscattering constant is an average value of the 11.9 g/L systems (outside the near field region and before the peak at the end of the profile), these values are recorded and shown in Table 5.2.

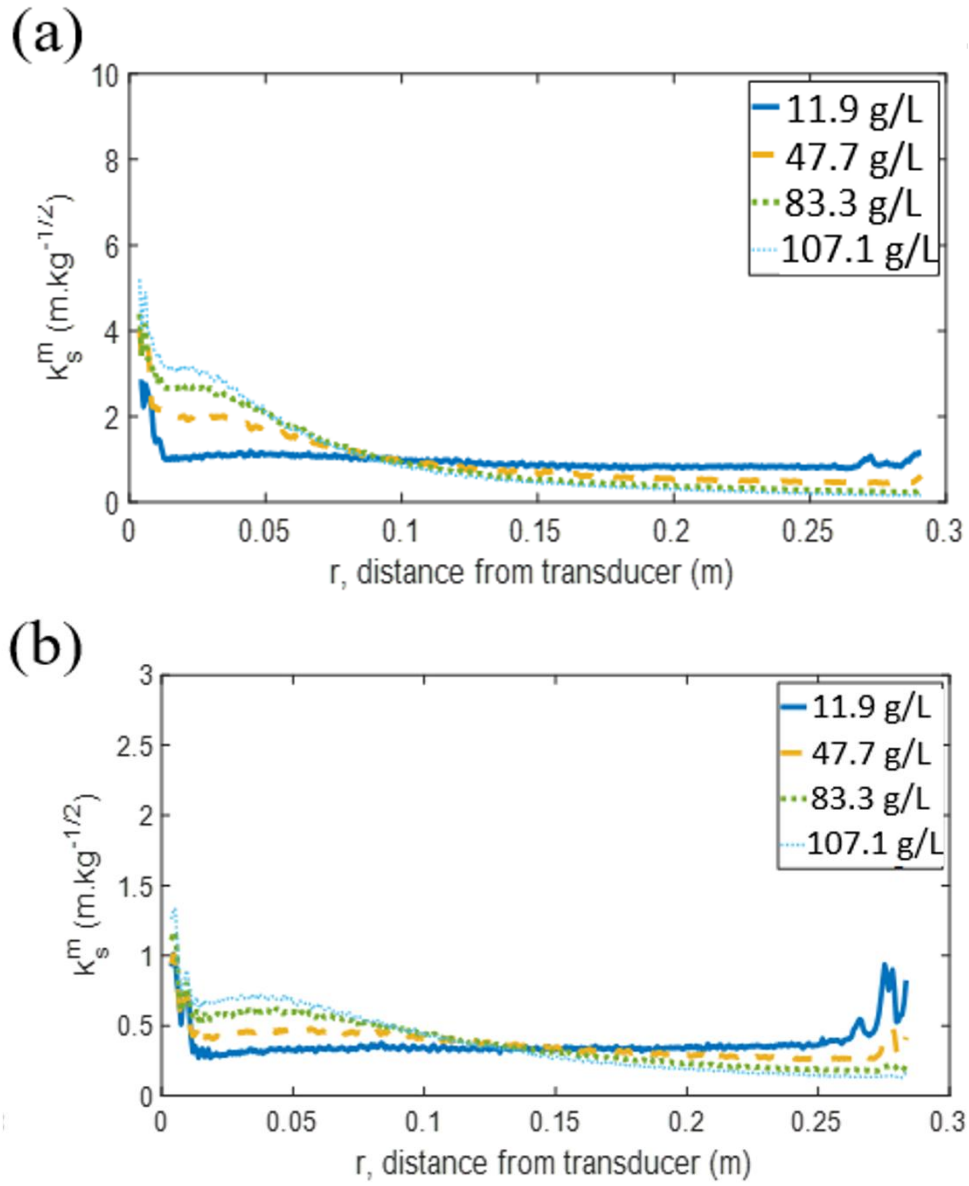

Figure 5.19 Backscattering constant (k_s^m, m.kg$^{-0.5}$) profiles of silica glass beads of d_{50} (a) 170 µm and (b) 82 µm utilising ultrasonic transducers with a 2 MHz frequency placed remotely in the calibration tank

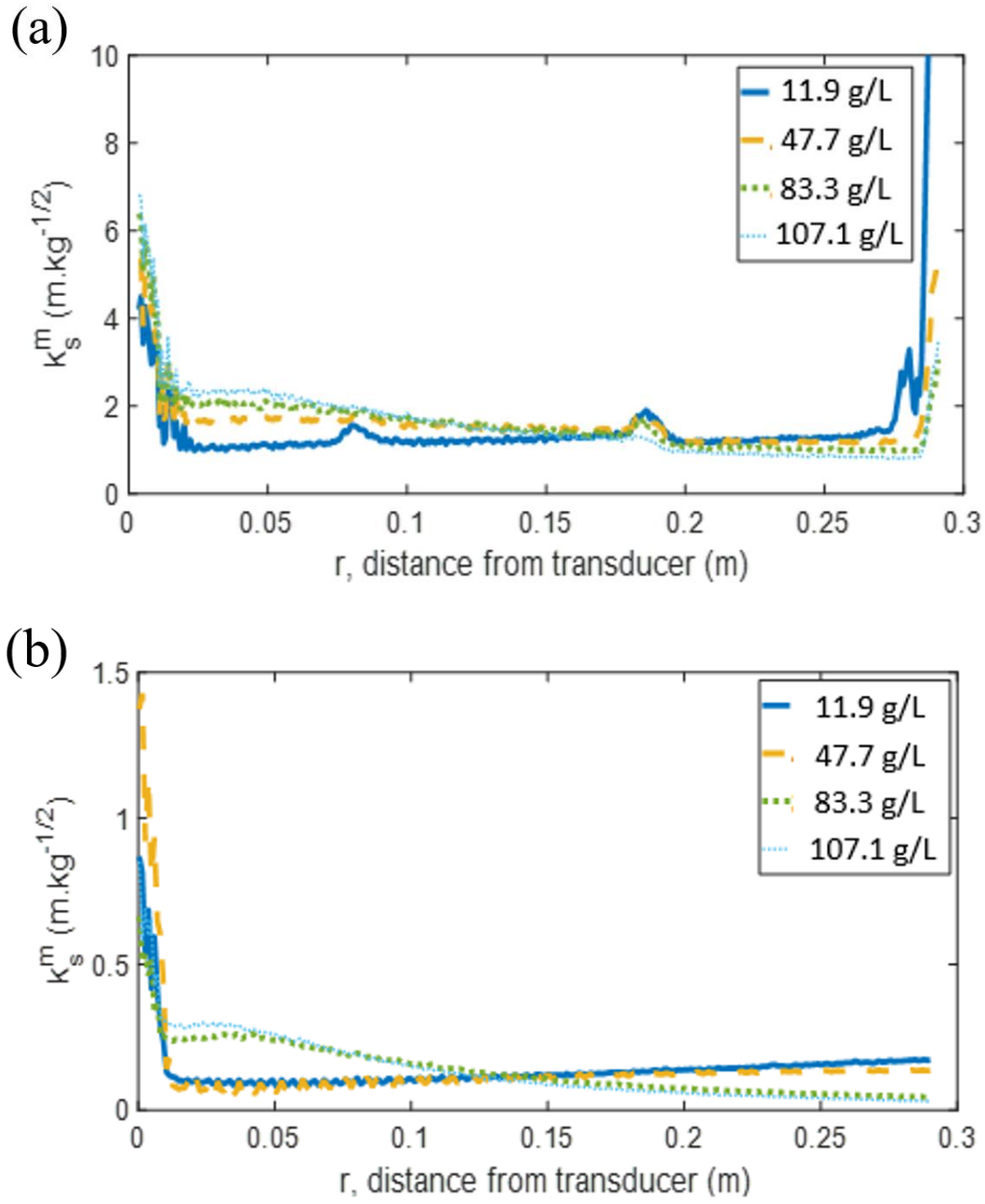

Figure 5.20 Backscattering constant (k_s^m, m.kg$^{-0.5}$) profiles of silica glass beads of d_{50} (a) 48 µm and (b) 36 µm utilising ultrasonic transducers with a 2 MHz frequency placed remotely in the calibration tank

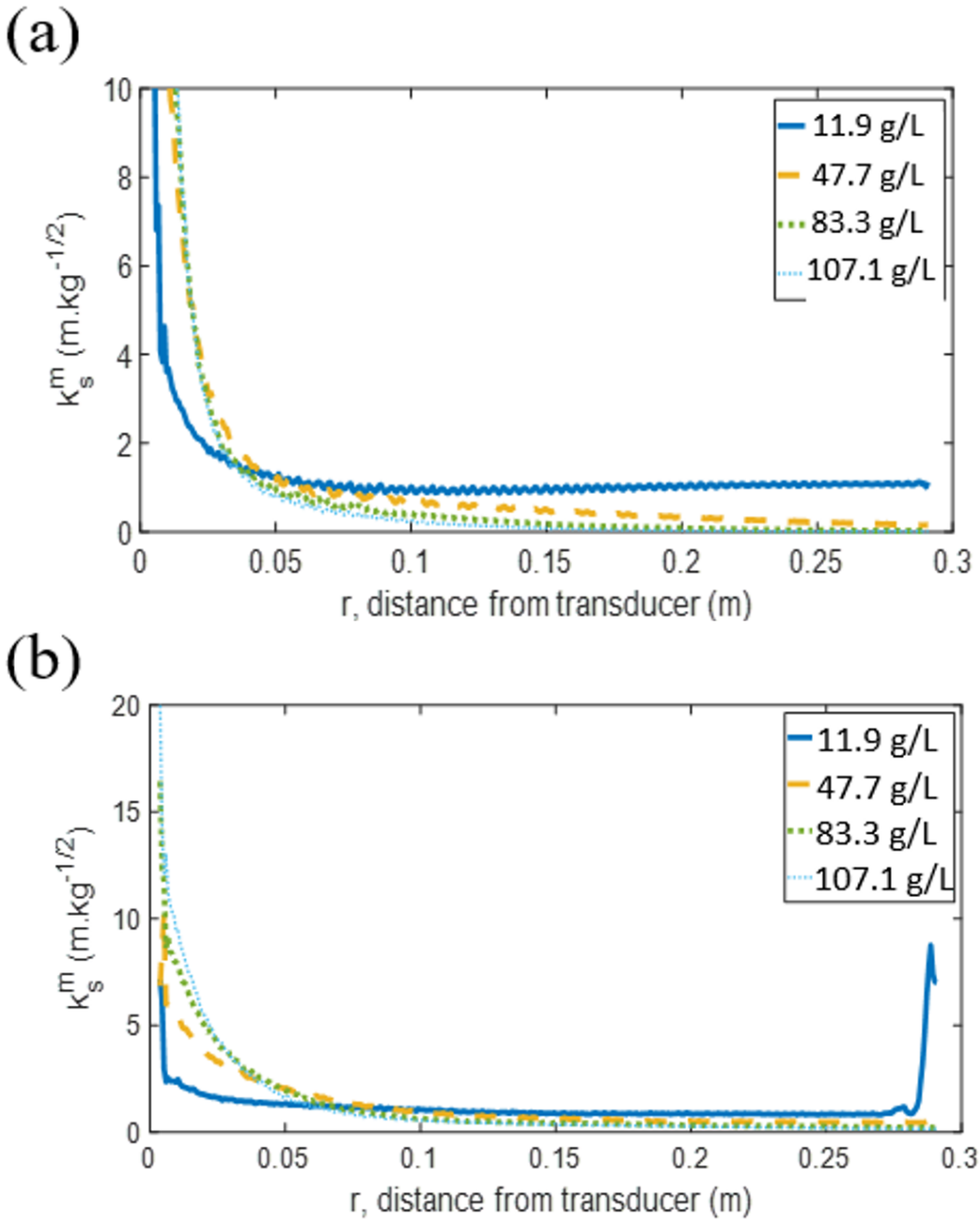

Figure 5.21 Backscattering constant (k_s^m, m.kg$^{-0.5}$) profiles of silica glass beads of d_{50} (a) 170 µm and (b) 82 µm utilising ultrasonic transducers with a 4 MHz frequency placed remotely in the calibration tank

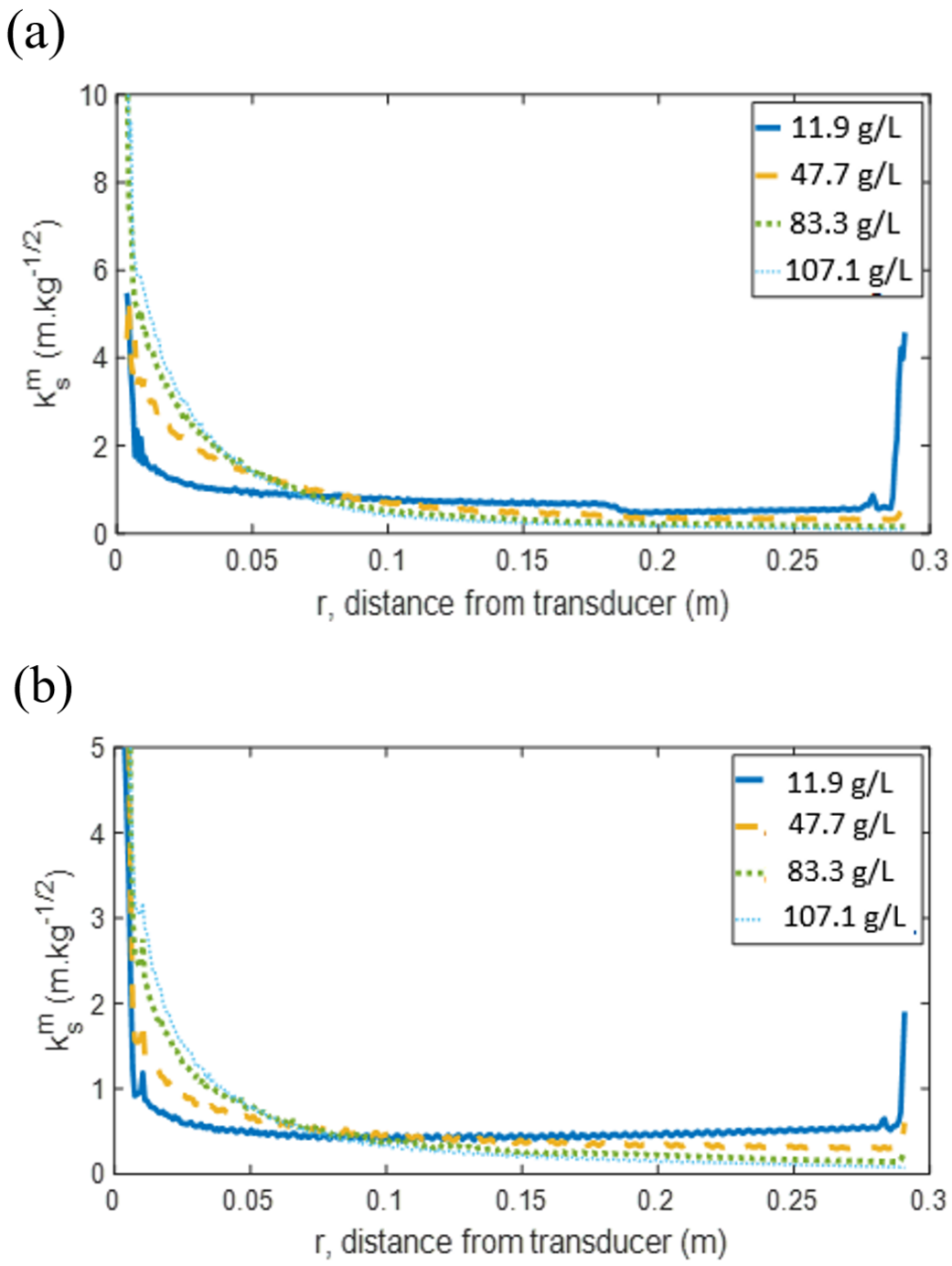

Figure 5.22 Backscattering constant (k_s^m, m.kg$^{-0.5}$) profiles of silica glass beads of d_{50} (c) 48 µm and (d) 36 µm utilising ultrasonic transducers with a 4 MHz frequency placed remotely in the calibration tank

Table 5.2 k_s^m values for all species of silica glass beads using 2 and 4 MHz frequency ultrasonic transducers

Transducer Frequency (MHz)	Silica Glass Bead d_{50}	Sediment backscatter constant, k_s^m ($m.kg^{-0.5}$)
2 MHz	170 µm	0.97
	82 µm	0.37
	48 µm	1.61
	36 µm	0.14
4 MHz	170 µm	1.30
	82 µm	1.12
	48 µm	0.82
	36 µm	0.53

5.3.2.6 Scattering cross section and form function

The scattering cross section and form function were determined using Eq. (3.09) and (3.10) respectively and plotted in Fig. 5.23 (a) and (b) for each silica glass species using the 2 and 4 MHz transducers. Instead of using both the *in situ* and remote coefficients, the remote attenuation coefficient value was used in Eq. (3.09). When using both *in situ* and remote coefficients, the plots directly overlapped which made it hard to compare the measured values to predicted. The Betteridge *et al.*, (2008) prediction is shown in the black dashed line and increased with an increase in *ka* where the larger particle species scatter more. The red crosses show the combined attenuation which incorporates viscous losses from Urick, (1948) where smaller particle species attenuate predominantly due to viscous losses. In Fig. 5.23, the larger particle species align very well with the Betteridge *et al.*, (2008) model whilst the smaller particle species show an increased attenuation which aligns very well with the combined attenuation. The measured values compare very well to the predicted combined attenuation which shows how accurate the UVP is when determining the attenuation of silica glass beads. When considering that the larger glass species had underestimated

sedimentation attenuation coefficients, the normalised scattering cross section was lower than shown below in Fig. 5.23 (a). Therefore, the critical analysis of the larger glass species led to increased normalised scattering cross section values which align very well to the Betteridge *et al*., (2008) prediction.

In Fig. 5.23 (b), the form function values were determined by following Fig. 5.4. The measured form function values compare very well to the Betteridge *et al*., (2008) prediction where values were almost directly aligned with the prediction. When considering that the form function was calculated using the backscattering constant, the constants determined experimentally are highly accurate. This shows that the UVP was able to produce accurate backscattering and transducer constants.

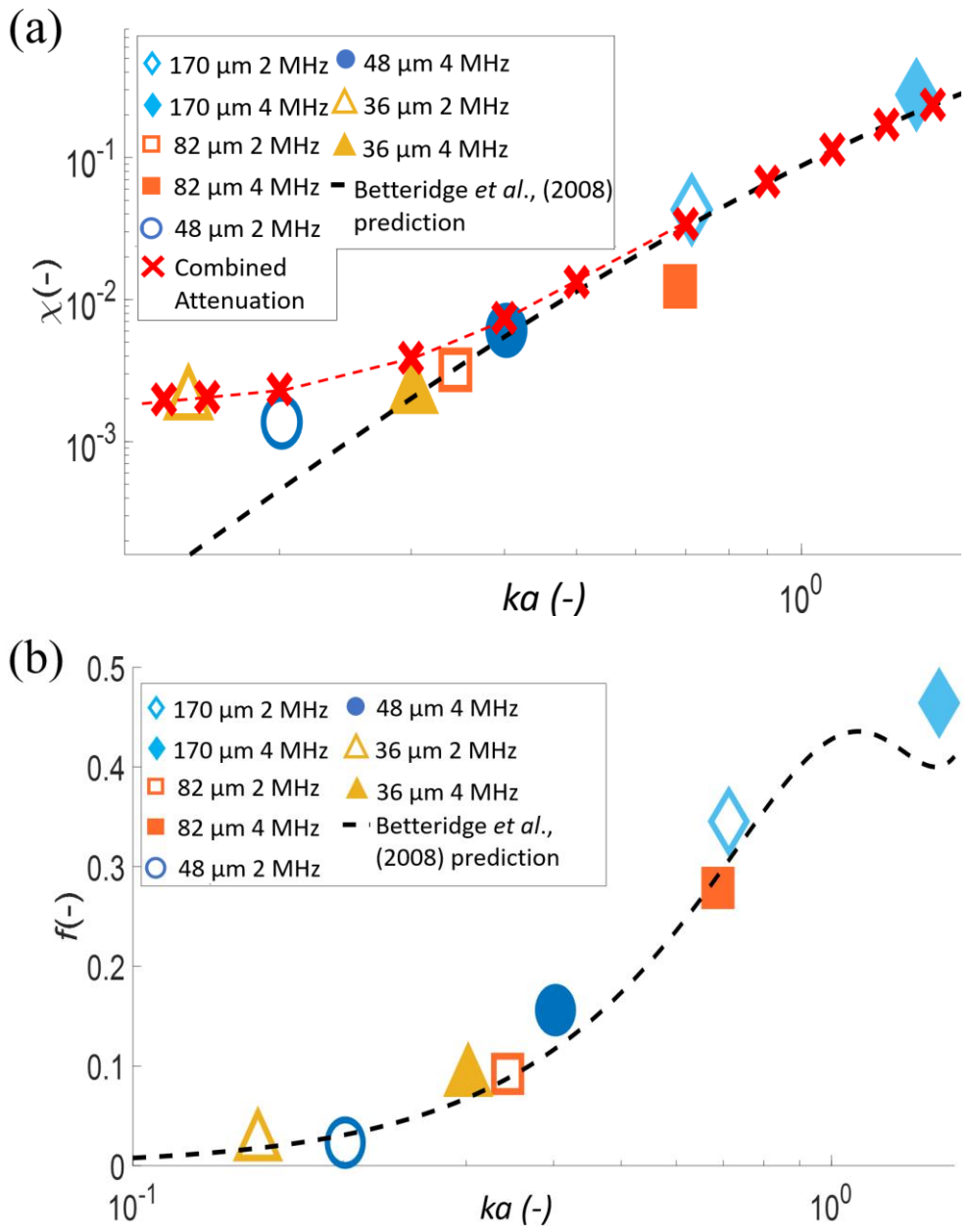

Figure 5.23 (a) Dimensionless scattering cross section (χ) and (b) Dimensionless form function (f) vs product of the wavenumber and particle radius (ka) for all silica glass bead experimental systems in comparison to the scattering model of Betteridge et al., (2008) where red crosses indicate the combined attenuation when using heuristic expressions from Betteridge et al., (2008) and Urick, (1948)

5.4 CONCLUSIONS

This Chapter entails an in-depth analysis of the silica glass beads where four silica glass bead species were used with varying particle size distributions. The glass beads were found to attenuate more with an increase in frequency, particle size or concentration, where all three variables effect the attenuation of the signal. It was found that the largest particle species required a lower concentration array to prevent acoustic profiles which reflected at intermediate distances. This shows the limits of the UVP to analyse material where a particle species larger than 82 μm can only be analysed at concentrations below 47 g/L. This was also shown by Tonge *et al.*, (2021) however, this has only been confirmed for the UVP commercial instrument. The 4 MHz transducer was found to reverberate at intermediate distance for all species where the linear profile ends at approximately 0.1 m. This limits the analysis of a larger tank, however for smaller depths, for example in a pipe width of approximately 3 cm, the 4 MHz transducer is able to analyse the depth with higher strength than the 2 MHz transducer. The four transducers used in this Chapter were characterised where the average transducer and backscattering constant was determined for each of the four silica glass bead species. This shows that the UVP was able to analyse a full breadth of data where the difference between the d_{50} of the particle species was a minimum of 12 μm.

The remote probe configurations gave consistent attenuation values to the *in situ* and therefore, this gives confidence that the remote arrangement may be suitable for pipe flow. This is the main novelty of this Chapter where measured values from remotely placed probes compared very well to combined attenuation predictions from Betteridge *et al.*, (2008) and Urick, (1948) which consider scattering and viscous losses, respectively. In this Chapter, the author has proven that the UVP can be utilised in backscatter mode to produce highly accurate sedimentation attenuation coefficients and constants dependent on the sediment and transducers. These measured coefficients compare well to values from Rice *et al.*, (2014) when using 2 MHz probes, however measured values from 4 MHz probes were underestimated in comparison to values from Rice *et al.*, (2014). This is attributed to the larger experimental concentration range used by Rice *et al.*,

(2014). Going forward, the author will be investigating systems which are more relevant to the nuclear industry where the UVP will be used to characterise more complex flocculated or aggregated dispersions. However, it has been shown that the experimental method established in Chapters 4 and 5 have led to accurate measured attenuation coefficients when using both *in situ* and remotely placed probes.

6. THE USE OF IN SITU PROBES TO MONITOR THE FLOCCULATION OF MINERAL SUSPENSIONS IN A CALIBRATION RIG

CHAPTER SUMMARY

In this Chapter, mineral suspensions of calcium carbonate and magnesium hydroxide were analysed using UVP transducers in the calibration rig used in Chapters 4 and 5. The mineral suspensions were flocculated, and sedimentation attenuation coefficients were extracted from both non-flocculated and flocculated suspensions which is novel. Hunter *et al*., (2012) used 2, 4 and 5 MHz transducers for an Aquascat1000 ABS to analyse mixed flocculated dispersions of spheriglass, so there is precedence that an acoustic system can be used to monitor flocculating dispersions, but this has not been achieved with the UVP. Homogeneous suspensions and settling suspensions were investigated by Hunter *et al*., (2012) to determine the backscatter profile, however, sedimentation attenuation coefficients were not established and there was no comparison to non-flocculated suspensions. Hunter *et al*., (2016) utilised a bespoke ABS (UARP) to determine the attenuation for flocculated calcium carbonate in a large-scale trial, this is another acoustic system, but this was only conducted on flocculated calcium carbonate and there was no direct comparison between non-flocculated calcium carbonate suspensions. Lockwood *et al*., (2021a) calculated the fractal dimension of flocculated magnesium hydroxide suspensions, here the fractal dimension was determined for non-flocculated and flocculated calcium carbonate and magnesium hydroxide. Both calcium carbonate and magnesium hydroxide were analysed here as flocculated and non-flocculated dispersions to determine the change in sedimentation attenuation coefficient, this has not been done before. Error analysis was conducted on all data using the methodology established in Chapter 4. Measured attenuation values were compared to combined predicted attenuation from scattering and viscous losses. The normalised scattering cross section was determined for each suspension environment and compared to predictions, this has been done previously by Tonge *et al*., (2021) for glass beads but not for flocculated and non-flocculated mineral suspensions.

6.1 INTRODUCTION

Chapter 6 details the use of flocculated mineral suspensions in a calibration rig where calcium carbonate and magnesium hydroxide were suspended and analysed using 2 MHz ultrasonic transducers. The work in this Chapter is novel as the UVP has not been used in backscatter mode to monitor flocculating mineral suspensions. In Chapters 4 and 5, the UVP has been used to observe the attenuation of homogeneous silica glass suspensions using transducers with a range of frequencies and sizes. This Chapter sets up the use of the UVP to monitor the flocculation process for minerals which exhibit complex viscous absorption. As the transducers used in this Chapter have a small active radius, there should be no issues in mounting these transducers onto a pipeline and monitoring the flocculation of mineral suspensions in pipe flow.

For context, the following techniques have been used to monitor flocculation; complex electrical conductivity, laser diffraction spectroscopy (LDS), fibre optic monitoring. Unfortunately, these methods often require extensive modelling and *ex situ* sampling which is not suitable for the nuclear industry (Huang and Chen 1996; Rasteiro *et al*., 2007; Mortadi *et al*., 2020). Acoustics provide a non-invasive technique where Thorne *et al*., (2014) was able to monitor acoustic scattering for suspended flocculating sediments whilst MacDonald *et al*., (2013) was able to measure acoustic scattering from a suspension of flocculated sediments using an Aquatec Aquascat-1000. Takeda and Goetz, (1998) monitored flocculation of alumina particles using ultrasonic attenuation spectroscopy where the ultrasonic method was able to distinguish the primary size from the flocculated size. This has also been achieved by Hunter *et al*., (2012) where an *in situ* concentration profiler was used to determine acoustic backscatter responses for settling flocculated suspensions. Recently Hunter *et al*., (2020) was able to use experimental data and CFD to investigate the flocculation of calcite in a horizontal sedimentation tank. In this Chapter, the author aims to provide extensive monitoring of the flocculation process using acoustics in tandem with a particle size monitoring technique.

In terms of particle size monitoring, Grabsch *et al*., (2020) used the FBRM to monitor flocculation of fine and coarse particles where chord length distributions were square weighted when displayed. Kyoda *et al*., (2019) also found the FBRM could monitor flocculation of fragile aggregates readily, the resulting data was displayed as volume weighted chord length distributions. Both Grabsch *et al*., (2020) and Kyoda *et al*., (2019) found that the FBRM has potential for monitoring feed properties to control the flocculation process. Benn *et al*., (2018) used the FBRM to monitor flocculation in-line where data was collected in real-time using a probe placed *in situ* in a perspex pipe. Lockwood *et al*., (2021a) used the Mastersizer to determine floc sizes and used output data to determine the fractal dimension and floc density. In this Chapter, Mastersizer data of the flocculated suspensions is collected to establish the relationship between floc density and attenuation. This is completely novel as the author has been able to conduct detailed studies cross-checking the size of complex mineral flocs using several methods including the UVP, FBRM and Mastersizer.

6.2 Materials and Methods

6.2.1 Materials

Calcite (Omyacarb 2, Omya AG) is a crystal form of calcium carbonate which is manufactured as a fine white powder and is easily dispersed into aqueous suspensions (Omya, 2021). Similar material has been used in previous literature as a nuclear simulant (Njobuenwu and Fairweather, 2016; Mann *et al*., 2017; Mortimer and Fairweather, 2019; Narayanasamy *et al*., 2019). Secondarily, a commercial magnesium hydroxide powder (Versamag Martin Marietta Magnesia Specialties) was also used, which was predicted to have similar fine particle sizes (Hunter *et al*., 2011; Martin Marietta, 2021). Both nuclear waste simulants are a fine white powder which fully disperse within aqueous suspensions (Ippolito *et al*., 2021; Lockwood *et al*., 2021a; Lockwood *et al*., 2021b; Cayirli, 2022). Calcite and magnesium hydroxide are mineral powders with a d_{50} of around 4-5 µm which is much smaller than the silica glass species shown in Chapter 5 (Martin Marietta, 2021; Omya, 2021). The d_{50} of both mineral powders is so small that the particles exhibit viscous attenuation as shown by Moore *et al*., (2013). A water-

soluble anionic polyacrylamide-poly (acrylic acid) copolymer, AN934SH (SNF Ltd) with a molecular weight of roughly 1.4 x 10^6 $g.mol^{-1}$ was used to flocculate both mineral suspensions (Lockwood *et al*., 2021b). The UVP was utilised to understand whether the system could monitor the change in particle size through the change in regime from viscous attenuation to scattering.

Both materials are fine particulates which require complex analysis. Therefore, an EVO SEM (Zeiss Group) was used to produce micrographs of calcite and the magnesium hydroxide powders. Fig. 6.1 (a) shows the micrograph for calcite. The calcite shows a varied particle size distribution with a complicated structure where fines of less than 2 µm can be seen across the micrograph (Omya, 2021; Cayirli, 2022). Fig. 6.1 (b) show the SEM images taken when analysing the magnesium hydroxide. From Fig. 6.1 (b), the magnesium hydroxide shows a varied particle size distribution, much like the calcite. Larger aggregates can be seen in Fig. 6.1 (b). Finer particles are shown as well, and the EVO SEM is able to clearly distinguish between the individual particles (Galeev *et al*., 2009). The range of aggregate sizes in Fig. 6.1 (b) is what leads to an increased d_{50} for magnesium hydroxide in Fig. 6.6. The EVO SEM was used to image both calcite and magnesium hydroxide as the particle size was so small that the desktop SEM used in Chapters 4 and 5 had too low a resolution. Fig. 6.2 (a) and (b) show the flocculated calcite and magnesium hydroxide, respectively. The coagulation of particles can be seen in Fig. 6.2 (a) for the calcite particles; however, this is harder to see for the magnesium hydroxide where all the smaller particles have coagulated together but large aggregates are not shown. The existence of fines in Fig. 6.2 (a) explains the smaller particle size for the flocculated calcite in comparison to the flocculated magnesium hydroxide in Fig. 6.6.

(a)

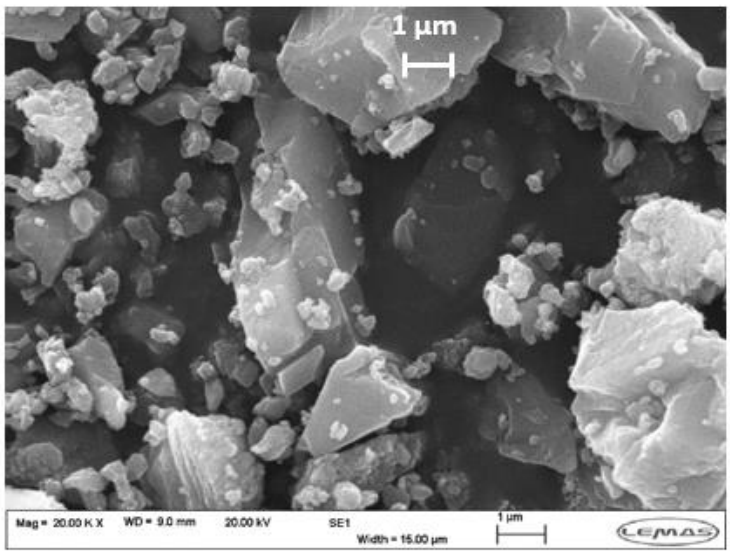

(b)

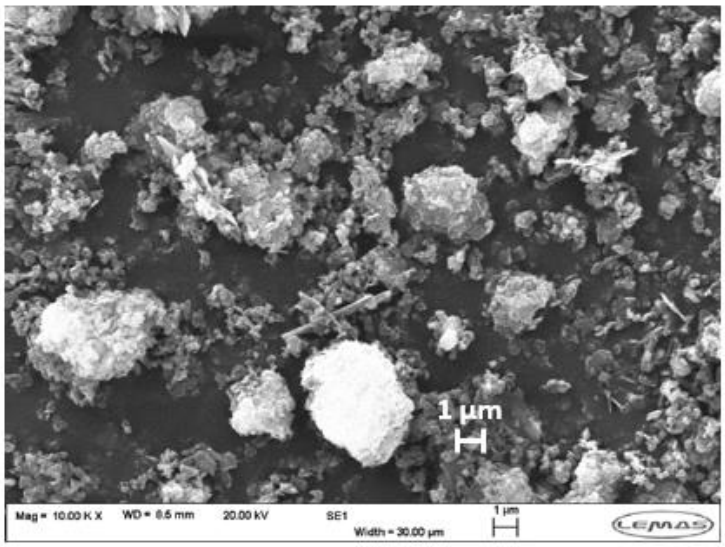

Figure 6.1 SEM images of (a) calcite (20 KX magnification) and (b) magnesium hydroxide (10 KX magnification) using an EVO SEM.

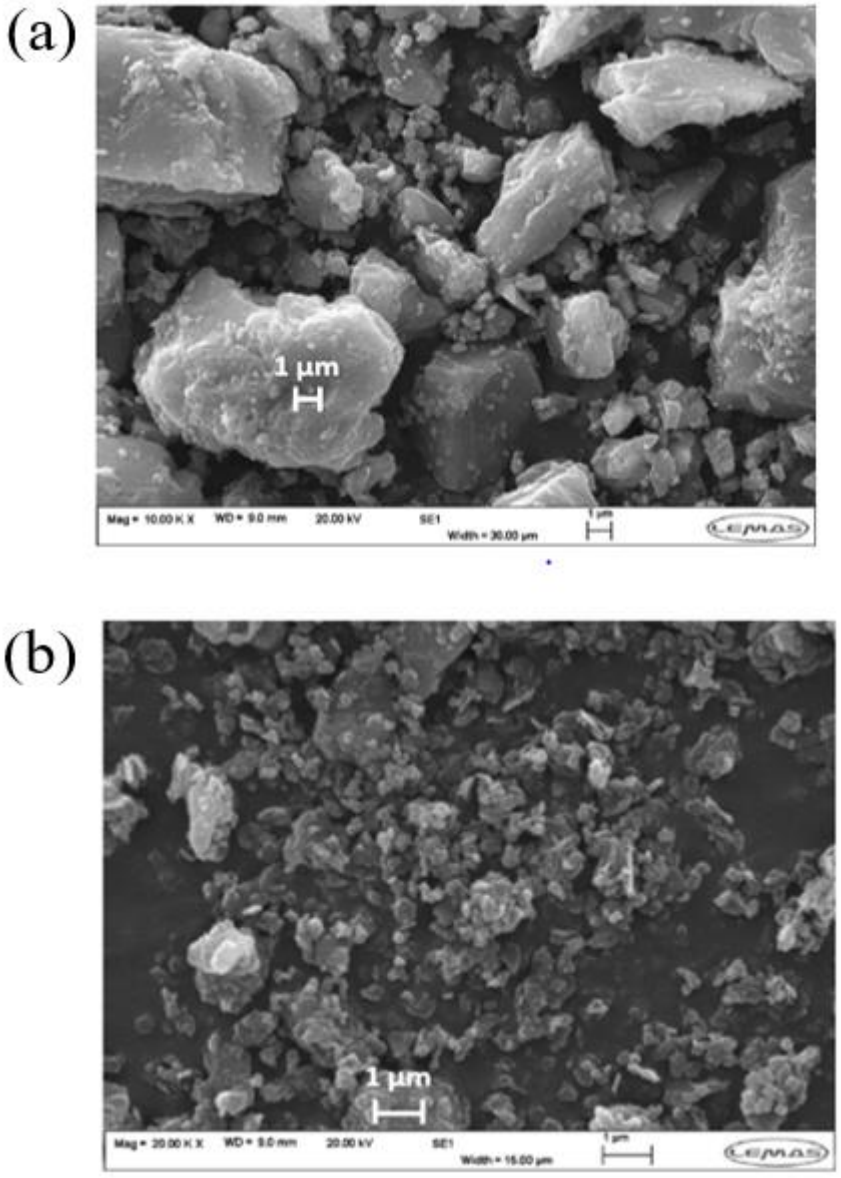

Figure 6.2 SEM images of (a) flocculated calcium carbonate (10 KX magnification) and (b) flocculated magnesium hydroxide (20 KX magnification) using an EVO SEM.

6.2.2 Methods

In Chapter 5, the experimental set-up was used to analyse homogeneous suspensions and results show that accurate acoustic profiles were produced which directly compared to literature. In this Chapter the next step was to move towards analysis of a changing system. The author looked at flocculating systems which

increased in particle size. The change was expected to be a homogeneous change where the d_{50} of the suspension was tracked and assumed to be representative of the suspension.

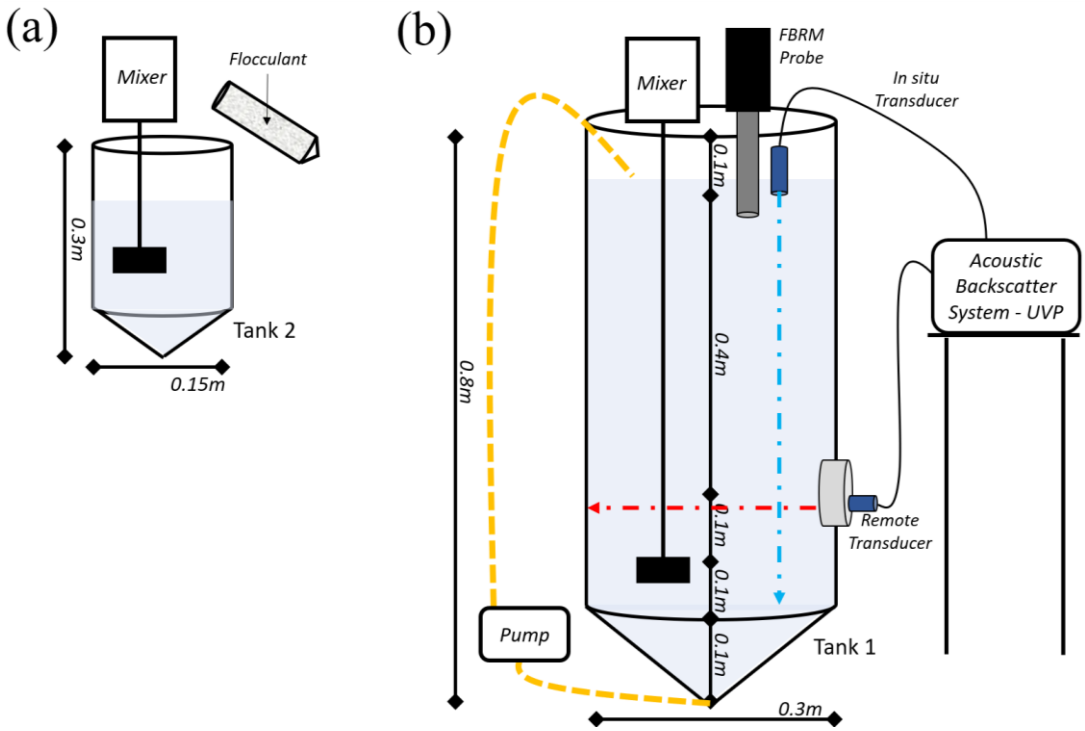

Figure 6.3 Schematic of (a) the tank used to produce the flocculation stock solution and (b) the calibration rig for analysis of flocculating suspensions using an in situ and remotely placed 2 MHz transducer where an FBRM probe was submerged into the tank

As shown in Chapter 4, the lower frequency 2 MHz probes were able to penetrate the full length of the tank with a weaker signal whilst higher frequency 4 MHz probes had a stronger signal which could not penetrate to the same depth (Butler and Sherman, 2016). The 2 MHz probes were also found to produce accurate acoustic profiles in the calibration tank; therefore, ultrasonic transducers of a 2 MHz frequency were utilised to monitor a change in particle size. Two transducers were used in this experiment; one fully submerged *in situ* transducer and a flat mounted remote transducer. In Chapters 4 and 5, the *in situ* transducers were fully submerged which provided accurate attenuation profiles of the silica

glass species (Fearns *et al*., 2018; Oggier *et al*., 2021). Remote transducers required acoustic couplant and flat mounting for good penetration through the rig (Gaeta *et al*., 2020; Joshi, 2021). Each transducer has a 60 ms pulse with a 100 ms delay between each transducer which is required to prevent crosstalk and signal disruption (Goncalves *et al*., 2013). This leads to a 220 ms per profile time with a total experiment time of 225 seconds for the 1023 profiles.

A Lasentec® Focused Beam Reflectance Measurement (FBRM) model PI-14/206 (Mettler-Toledo) probe was inserted into the tank to ensure the sizes of the flocs were consistent. The FBRM (Mettler-Toledo) continuously collected data throughout the experiment from the point the tank was filled with water until the drainage of the suspension. Initially, chord length data was collected for the non-flocculated species. The FBRM probe was used to monitor the gradual change in particle size once flocculant had been added to the tank. The probe emits a laser which interacts with any particle that passes by the probe window. The software on the Lasentec® system then converts the interaction into intensities corresponding to the time the particles were detected. The time taken to analyse particles can be used to determine the chord length, this is achieved by utilising scan speed and recognising each interaction is caused by individual particles (Kumar *et al*., 2013). Unless perfectly spherical, the chord length may not be representative of the particle diameter but as a monitoring technique, the change in chord length will be useful in determining the change in particle size with the addition of a flocculant. The chord length is then converted to a number and square weighted distribution, this is shown at a later point in this Chapter (Kim *et al*., 2012; Simone *et al*., 2014).

Fig. 6.3 (a) shows the flocculation tank where a 1000 ppm stock solution was produced by adding 1 g of the AN934SH (SNF Ltd) copolymer into a 1 L water filled vessel at a rate of 0.1 $g.min^{-1}$ to form a homogeneous stock solution. The mixer rate was maintained at 400 rpm throughout the addition of the flocculant and was left on overnight to ensure the polymer was fully distributed in the vessel and the flocculant powder had fully dissolved.

For this experiment, non-flocculated dry powder was added to the tank in Fig. 6.3 (b) to produce a suspension concentration of 27.5 g/L. The mixer and pump rate were lowered to 350 rpm and 75 rpm, respectively. The lower rate was to prevent shear of any aggregates/ flocs that were produced. A concentration array of non-flocculated aqueous suspensions was analysed first for comparison to flocculated data. This entailed diluting the 27.5 g/L suspension by emptying the tank by 50% and then diluting the tank with 50% water. The transducers were used to analyse the suspension at each concentration until the suspension concentration was 3.4 g/L in the tank. The tank was fully emptied, cleaned, refilled with water, and then concentrated to a 27.5 g/L suspension concentration within the tank. This ensured the system was as similar as could be for the flocculated experiments. Stock solution was then added to the calibration tank dropwise over 4 minutes for a bulk polymer concentration of 20 ppm in the tank. This was consistent with previous polymer levels for efficient flocculation (Lockwood *et al*., 2021b).

The suspension was dispersed for 5 minutes to allow time for the flocculation process. After 5 minutes the transducers were used to analyse the suspension. The suspension was diluted with the same method used for the non-flocculating suspensions. The results were then compared to the non-flocculated suspensions as the concentrations for both runs were consistent. The only difference between both experimental runs was the particle size distribution. This allowed the author to understand whether the UVP was able to distinguish between different particle size distributions of the same simulant. The whole process was completed for the following mineral species: calcium carbonate and magnesium hydroxide. Samples were taken at each concentration for both experimental runs and these samples were then sent to the Mastersizer 2000E and the Camsizer XT (Retsch Technology) for analysis of the particle size.

This specific dilution method was chosen to ensure that the flocs remained consistent throughout the experiment. In Chapters 4 and 5, the suspension concentration was increased gradually and UVP measurements taken at each concentration. However, for the flocculated systems, the entire suspension would

need to be flocculated at the lowest concentration. Adding more dry powder to increase the concentration would lead to a decrease in the particle size distribution and therefore, produce results which were not consistent. To analyse in the same incremental concentration method used in Chapters 4 and 5, the tank would need to be emptied and refilled for each concentration. This would require four times the flocculant, water and sediment as well as result in a longer experiment time. When using this specific dilution method, the integrity of the flocs can be maintained in the same system and a single experiment is required whilst multiple experiments can lead to small errors in change of experimental conditions. Small changes in flocculant can lead to changes in floc sizes which can result in changes to the acoustic profiles. Dilution was shown not to affect the size of the flocs in previous literature from Burger *et al.*, (2017) where floc suspensions were diluted for visibility of flocs for phase contrast microscopy. Seo *et al.*, (2012) found that floc sizes tended to stay constant when diluting a flocculated suspension, where a ground calcium carbonate suspension was flocculated with a cationic polyacrylamide (C-PAM).

6.2.3 Mastersizer

Samples were taken at 27.5 g/L for the non-flocculated and flocculated suspensions using a 5 ml sample vial, this was done for both calcium carbonate and magnesium hydroxide. All four 5 ml sample vials were taken to the Mastersizer 2000E (Malvern Panalytical Ltd) to investigate the effect of flocculation on the particle size. The Mastersizer uses laser diffraction to measure the intensity of light scatter as the laser passes through a dispersed particulate sample. The scattering pattern is analysed to calculate the size of the particles (Bux *et al.*, 2015; Rice *et al.*, 2015). The Mastersizer outputs data as a relative distribution on the volume of particles in their range of size classes. These samples were added to the Mastersizer Hydro 2000SM aqueous dispersion cell with external dimensions of 140 x 175 x 390 mm (Lockwood *et al.*, 2021b). The dispersion cell was filled with ~120 ml of deionised water and analysed to produce a background measurement. A small agitator provided shear in the vessel at a rate of ~900 rpm. Small amounts of the sample vials were added to the

dispersion cell using a pipette until the Mastersizer detected a sufficient amount of attenuation needed for diffraction. Data was taken over a time period of 2 minutes with data outputted to a CSV-type file every 10 seconds. The dispersion cell was emptied and cleaned with deionised water several times until the background measurement showed that no particles were left in the cell.

The agitator rate was lowered to 500 rpm when analysing the flocculated suspensions to prevent break-up of flocs. The agitator was increased again to 900 rpm once analysis was complete to ensure that no flocs settled in the cell. All data from the CSV files were plotted to produce a particle size distribution, this was then converted to a normalised size distribution by adding the particle sizes cumulatively and weighting them depending on a 100 % volume. Burger *et al*., (2017) analysed flocculated suspensions in a Mastersizer 2000 and found that the stirring speed used for the dispersion unit had a negligible effect on the floc size distribution.

6.2.3.1 Flocculation Theory

These flocculated systems are complex to characterise and analyse. Through using several particle sizing techniques, (including the Mastersizer 2000E and Camsizer XT) the author was able to establish an accurate particle sizing method. However, the flocculated particles themselves have complex particle shapes which can be characterised using further analysis. Aggregates have complex fractured surfaces due to the coagulation of several particles. A variable known as the fractal dimension was calculated using data from the Mastersizer 2000E to describe the fractured surfaces quantitatively.

The fractal dimension is established by plotting the scattering wave intensity, *I(Q)* and scattering wave vector, *Q* (μm^{-1}). Where *Q* (μm^{-1}), the scattering wave vector is a function of the refractive index, *n* (*n-Calcium carbonate = 1.50, n-Magnesium hydroxide = 1.57)* (Jonasz and Fournier, 2011; Wypych, 2016), the wavelength of incident light in vacuo, λ (0.665 µm) (Malvern Instruments, 2007) and the scatter angle, θ. All components required to calculate *Q* in Eq. (6.01) are

known apart from the scatter angle which is given in the measured Mastersizer data (Lockwood *et al*., 2021a).

$$Q = \frac{4\pi n}{\lambda} \sin\left(\frac{\theta}{2}\right) \tag{6.01}$$

The scattering intensity, *I(Q)* is directly proportional to the scattering wave vector with a negative power of the fractal dimension as shown in Eq. (6.02). The scattering intensity is also given in the Mastersizer data. The fractal dimension, *df* can be calculated by plotting ln*(I(Q))* vs ln(*Q*) and establishing the gradient (Lockwood *et al*., 2021a). The correlation in Eq. (6.03) was achieved by taking log of both sides in Eq. (6.02).

$$I(Q) \propto Q^{-df} \tag{6.02}$$

$$\ln\big(I(Q)\big) = -df ln(Q) \tag{6.03}$$

The log*(I(Q))* vs log*(Q)* plots are shown in Fig. 6.4 (a) and 6.5 (a) for calcium carbonate and magnesium hydroxide, respectively. There were three runs of the same experiment using the Mastersizer 2000E and all three sets of data were plotted in Fig. 6.4 (a) and 6.5 (a) to provide an average fractal dimension. The linear regions in both Fig. 6.4 (a) and 6.5 (a) shown by the dashed lines were isolated and expanded in Fig. 6.4 (b) and 6.5 (b). The fractal dimensions can be extracted from Fig. 6.4 (b) and 6.5 (b) for calcium carbonate and magnesium hydroxide, respectively. The fractal dimension, d_f can be taken as the negative gradient value from the isolated linear regions shown in Fig. 6.4 (b) and 6.5 (b). The fractal dimensions for both mineral suspensions are recorded and shown in Table 6.1 and 6.2.

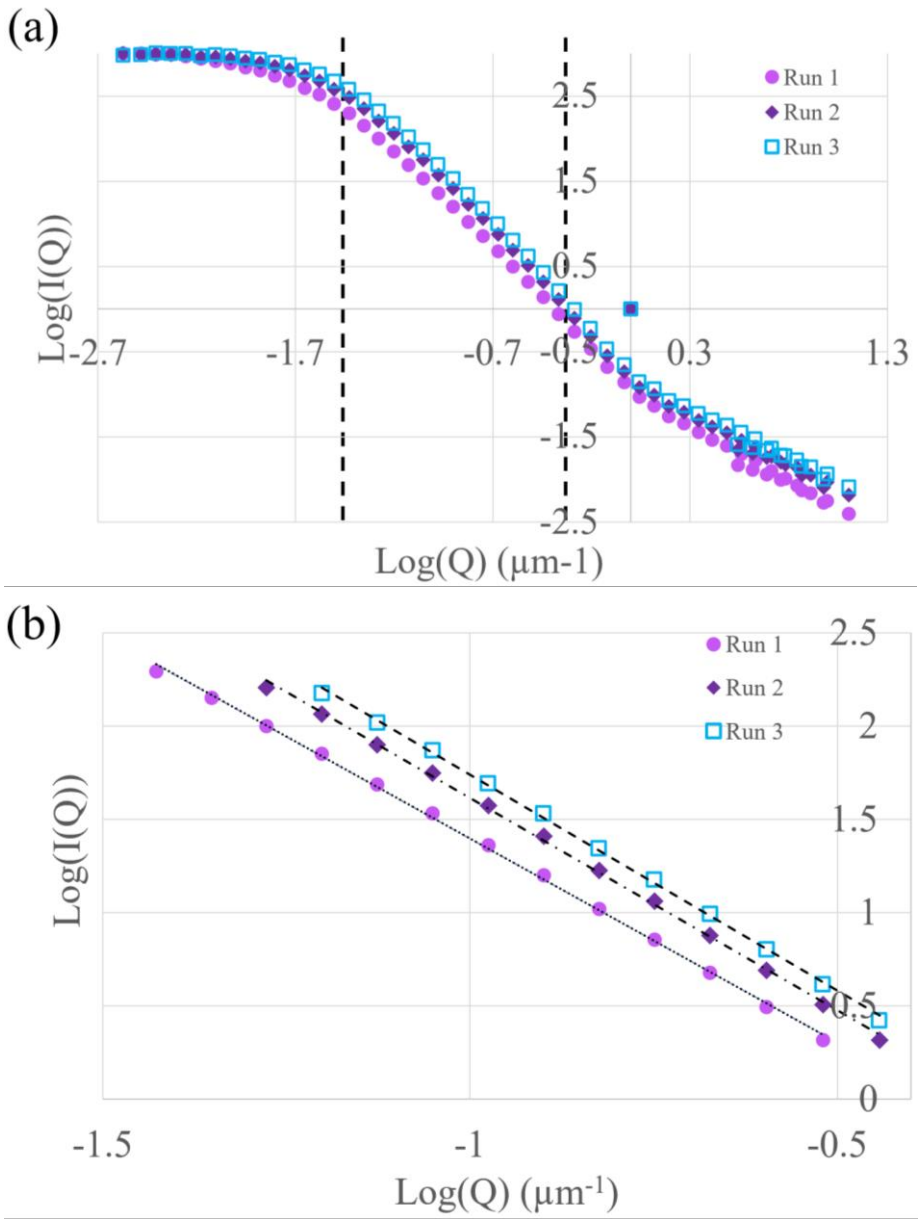

Figure 6.4 (a) Log(I(Q)) vs log(Q) for calcium carbonate and (b) with a limited linear region

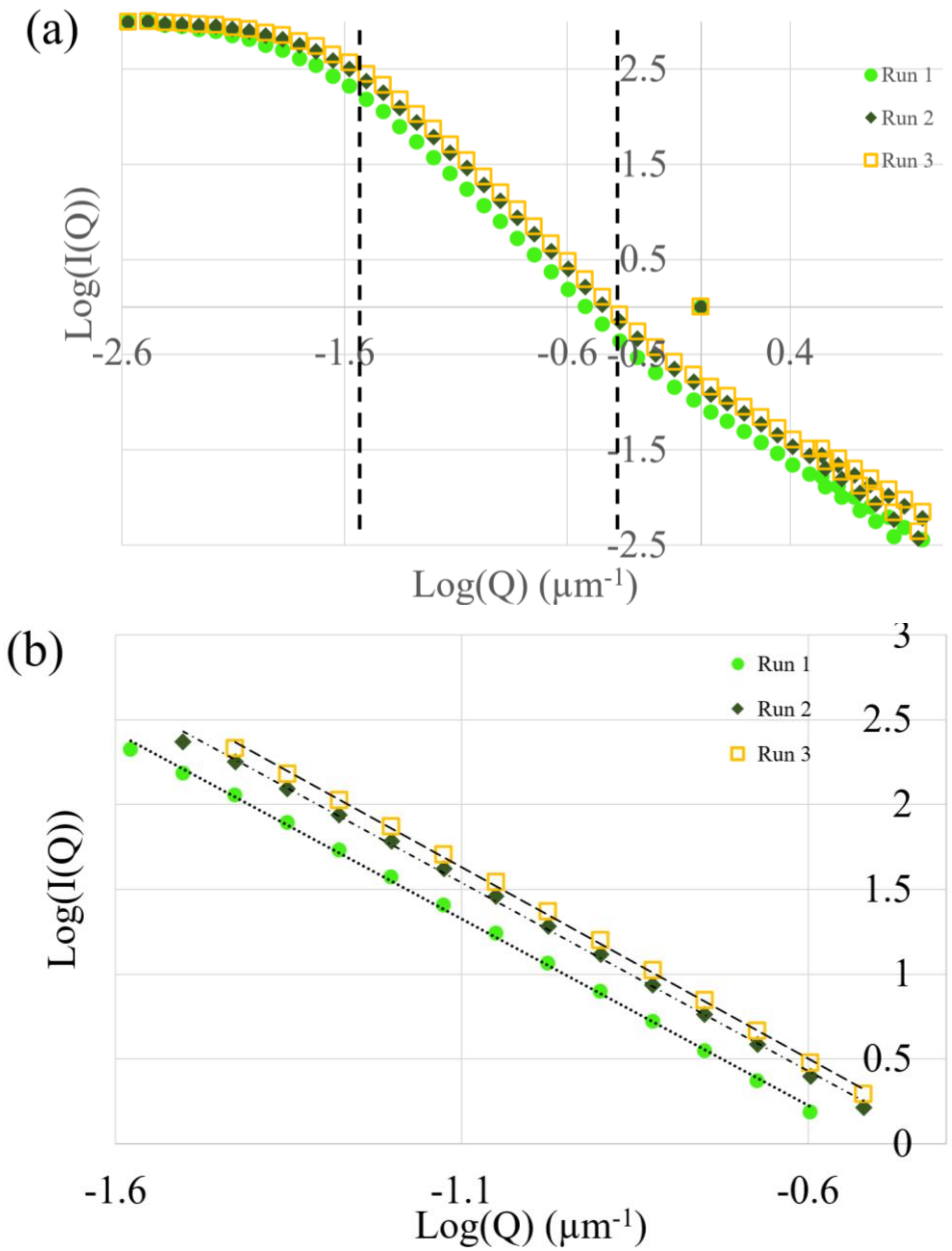

Figure 6.5 (a) Log(I(Q)) vs log(Q) for magnesium hydroxide and (b) with a limited linear region

For further analysis, the floc density can be determined. This requires several derivations. First, the structure prefactor was calculated in Eq. (6.04) using the fractal dimension (Lockwood *et al.*, 2021a).

$$\psi = 0.414 d_f - 0.211 \tag{6.04}$$

The number of particles in an aggregate, N can then be established in Eq. (6.05) by using the structure pre-factor and fractal dimension. Fig. 6.4 (b) and 6.5 (b) can be used to determine the diameter of the floc, D_f, and the diameter of the primary particles, D_p. The minimum floc diameter D_f and primary particle diameter, D_p, can be established by extracting the wave scatter vector (Q) reciprocals from the upper and lower scattering intensity values in the limited linear regimes (Lockwood *et al*., 2021a).

$$N = \psi \left(\frac{D_f}{D_p}\right)^{d_f} \tag{6.05}$$

The volume of the floc (V_f (kg.m^{-3})) and primary particles (V_p (kg.m^{-3})) was calculated in Eq. (6.06) using the diameters extracted from Fig. 6.4 (b) and 6.5 (b). The particles were assumed to be spherical for ease of calculation (Lockwood *et al*., 20201a). Determining floc characteristics is difficult due to the highly irregular three-dimensional structure of flocs (Jarvis *et al*., 2005). Each floc structure will also be different which makes it almost impossible to quantify the volume. The fractal dimension for both calcium carbonate and magnesium hydroxide ranges from 2.22 to 2.26 which is approaching a spherical shape. The acoustic models also assume a spherical particle shape.

$$V_{f,p} = \frac{4}{3}\pi \left(\frac{D_{f,p}}{2}\right)^3 \tag{6.06}$$

The density of water, ρ_w, density of the particles, ρ_p and the remaining properties calculated were used to determine the density of the floc in Eq. (6.07) (Lockwood *et al*., 2021a).

$$\rho_f = \frac{(\boldsymbol{NV_p\rho_p}) + (V_f - \boldsymbol{NV_p})\boldsymbol{\rho_w}}{V_f} \tag{6.07}$$

Table 6.1 and 6.2 show the properties calculated for both calcium carbonate and magnesium hydroxide, respectively.

Table 6.1 Calcium carbonate flocculant calculations

Properties	Repeat			Average
	1	2	3	
Gradient	-2.19	-2.28	-2.32	-2.2609
R^2	0.999	0.999	0.999	0.999
Fractal Dimension, *df*	2.19	2.28	2.32	2.26
Structural Pre-factor, ψ	0.695	0.732	0.749	0.725
Diameter of floc, D_f (m)	2.67E-05	1.89E-05	1.59E-05	2.05E-05
Diameter of primary particles, D_p (m)	3.31E-06	2.77E-06	2.77E-06	2.95E-06
Number of particles in an aggregate, *N*	67	58	43	56
Volume of floc, V_f (m^3)	1.00E-14	3.54E-15	2.11E-15	5.22E-15
Volume of primary particles, V_p, (m^3)	1.90E-17	1.11E-17	1.11E-17	1.37E-17
Density of primary particles, ρ_p ($kg.m^-$	2711	2711	2711	2711
Density of water, ρ_w ($kg.m^{-3}$)	1000	1000	1000	1000
Density of floc ρ_f ($kg.m^{-3}$)	1218	1312	1389	1306

Table 6.2 Magnesium hydroxide flocculant calculations

Properties	Repeat			Average
	1	2	3	
Gradient	-2.19	-2.22	-2.25	-2.22
R^2	0.999	0.999	0.999	0.999
Fractal Dimension, *df*	2.19	2.22	2.25	2.22
Structural Pre-factor, ψ	0.697	0.707	0.721	0.708
Diameter of floc, D_f (m)	3.78E-05	3.18E-05	2.67E-05	3.21E-05
Diameter of primary particles, D_p (m)	3.95E-06	3.31E-06	3.31E-06	3.52E-06
Number of particles in an aggregate, *N*	100	107	80	95
Volume of floc, V_f (m^3)	2.84E-14	1.68E-14	1.00E-14	1.84E-14
Volume of primary particles, V_p, (m^3)	3.22E-17	1.90E-17	1.90E-17	2.34E-17
Density of primary particles, ρ_p ($kg.m^-$	2340	2340	2340	2340
Density of water, ρ_w ($kg.m^{-3}$)	1000	1000	1000	1000
Density of floc ρ_f ($kg.m^{-3}$)	1151	1161	1202	1171

6.2.4 Camsizer

A small 1 L stirred tank reactor was used to suspend calcium carbonate and magnesium hydroxide at a concentration of 27.5 g/L. The mixer rate was maintained at 500 rpm much like the acoustics column used in Chapters 4 and 5. Flocculant was generated in a separate tank where polymer was added to water to produce a 1000 ppm stock solution, the same process detailed in Chapter 6.2.2 was used here. The stock polymer solution was added to the dispersed mineral suspension in the stirred tank reactor down the impeller shaft to produce a polymer concentration of 20 ppm. The mixer rate was lowered to 350 rpm to prevent the break-up of flocs from high shear. A five-minute period was given to allow the flocculant to fully incorporate with the mineral suspension to produce flocs. The Camsizer X2 was set-up to measure the particle size using a CCD-Basic camera where the images are deleted after the experiment has been concluded and the output data is given as a particle size distribution (Retsch Technology, 2012). A pipette was used to add the flocs to the Camsizer X2 cell where the suspension was imaged, and the minimum diameter (C_{min}) was used to determine the volume of the particles where the particle shape was assumed to be spherical (Microtrac, 2021). The same dilution procedure was used here as conducted in Chapter 6.2.2 to mimic the acoustic cell in Chapters 4 and 5. The data is output from the Camsizer XT as a cumulative size distribution (*Q3*) based on the volume of the particles detected where the particle radius is determined using C_{min}.

6.2.5 FBRM

The FBRM was inserted into the calibration rig and data was collected in real-time where raw chord length values were output into a CSV-type file. The chord length values (CL) are converted to cumulative size distribution % (*Fv*), this is shown in Eq. (6.08). This is used to determine the particle size distribution in Fig. 6.8.

$$Fv^i\ (\%) = 100\,.\ \frac{CL^i + Fv^{i-1}}{\sum_{i=1}^{n} CL^i} \tag{6.08}$$

The raw chord length values can be translated to the number weighted frequency (CL_{num}) using Eq. (6.09) - (6.10) where D corresponds to the particle size. The number weighted chord length can then be converted to a cumulative size distribution, (Fv_{num}) where the subscript num indicates number weighted values.

$$CL_{num}{}^{i} = CL^{i} x D^{i} \tag{6.09}$$

$$Fv^{i}{}_{num}(\%) = 100 \, . \, \frac{CL_{num}{}^{i} + Fv^{i-1}}{\sum_{i=1}^{n} CL_{num}{}^{i}} \tag{6.10}$$

The square weighted distribution can be determined using Eq. (6.11) - (6.12) where the subscript sq indicates square weighted values.

$$CL_{sq}{}^{i} = CL^{i} x (D^{i})^{2} \tag{6.11}$$

$$Fv^{i}{}_{sq}(\%) = 100 \, . \, \frac{CL_{sq}{}^{i} + Fv^{i-1}}{\sum_{i=1}^{n} CL_{sq}{}^{i}} \tag{6.12}$$

The number and square weighted distributions are shown for calcium carbonate in Fig. 6.9 (a) and (b).

6.3 Results and Discussion

All results are discussed in this Chapter where particle size data is analysed using the Mastersizer 2000E, the Camsizer XT (Retsch Technology) and the FBRM. The concentration and attenuation were analysed using acoustic data from the UVP. Together the data produces a cohesive and novel understanding of the behaviour of complex mineral suspensions as they flocculate.

6.3.1 Mastersizer

When looking at previous literature, Seo *et al.*, (2012) flocculated calcium carbonate suspensions with a 0.15 ppm polymer dose where floc sizes were found to be around 30 μm, the dose rate was significantly lower than used in this

experiment (20 ppm). Lu *et al*., (2016) found that dosing extraction tailings with Magnafloc polymer with a 20 ppm polymer dose led to floc sizes of ~ 100 μm when using a square weighted chord length. The cumulative particle size distributions for the calcium carbonate and magnesium hydroxide are shown in Fig. 6.6. The particle size distributions for both calcite and magnesium hydroxide exhibit approximately bimodal distributions, which shows that there are a two particle size groups.

The fines in the calcium carbonate are shown by the early peak in particle size where 30% of the suspension has a particle size smaller than 2.5 μm. The fines within the suspension were likely generated from production milling (Anivi, 2020). However, all calcite particles possess a fairly small particle size range with 50% of the suspension at 4 μm and 85% below 10 μm. The magnesium hydroxide also shows a broader bimodal distribution, which in this case is attributed to aggregate build-up within the suspension. Henrist *et al*., (2003) found that magnesium hydroxide powder aggregated in aqueous suspensions to form large agglomerates. The large difference between the d_{50} of calcite and magnesium hydroxide is attributed to aggregate build-up for the magnesium hydroxide as the particle size of both are comparable in their dry powder forms. The calcium carbonate and magnesium hydroxide floc sizes are ~67 and 86 μm which was slightly lower than the floc sizes shown by Lu *et al*., (2016), this could be attributed to shear break-up in the Mastersizer 2000E cell. The floc sizes from Seo *et* al., (2012) are significantly smaller due to the lower polymer dose.

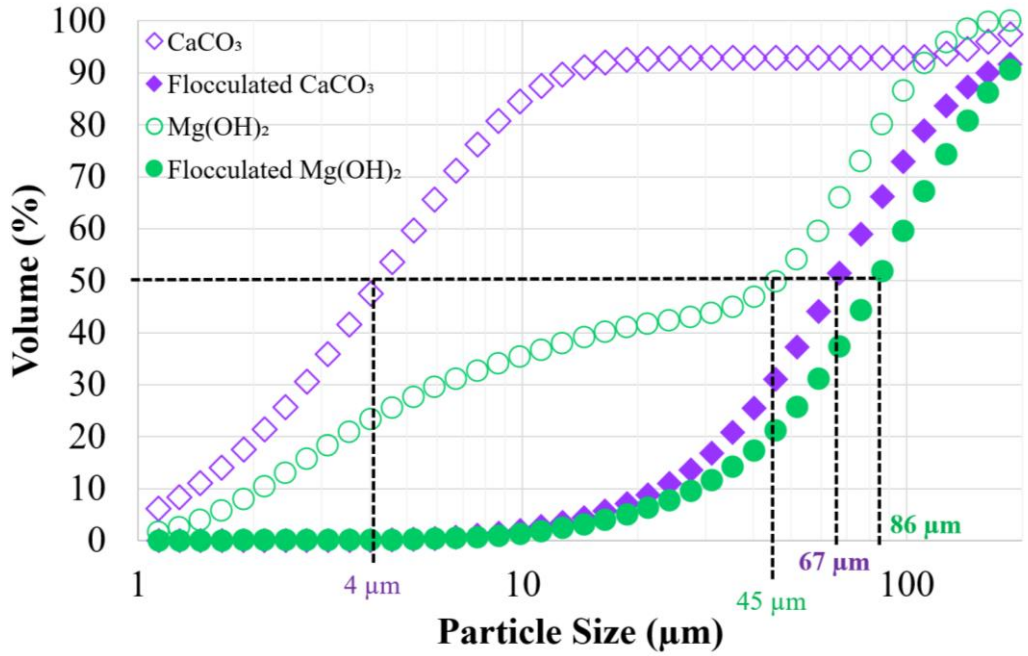

Figure 6.6 Particle size data of non-flocculated and flocculated species of calcite and magnesium hydroxide using a Malvern Mastersizer 2000E,

The floc density and fractal dimension are calculated using the Mastersizer data as shown in Chapter 6.2.3.1. Several runs were conducted for the suspensions when using the Mastersizer 2000E where average values were calculated and shown in Fig. 6.6. The multiple runs were also used to determine an average floc density and fractal dimension with the variation shown across all three runs. This is shown in Table 6.3 for both calcium carbonate and magnesium hydroxide, respectively.

The fractal dimension for calcium carbonate was higher and showed a larger error between the three runs. The number of particles in an aggregate were found to be lower for calcium carbonate which resulted in floc with a smaller diameter. The density of the floc was found to be higher for calcium carbonate which could be attributed to the higher density of the primary calcium carbonate particles. Larger floc sizes for magnesium hydroxide could be attributed to the lower floc density where it was found that the lower floc density led to an increased N which resulted in an increased diameter of floc. The effect of the floc density on the

attenuation of the suspensions was investigated further at a later point in this Chapter. The author would like to point out the novelty of this analysis where the effect of floc density and floc size has been linked to the attenuation of complex mineral suspensions.

The shape of flocs depends on the fractal dimension (*df*) of the floc, when the *df* of the floc is around 1-2, the floc appears as a branched structure of bridged polymer structures. When *df* is closer to 1 the floc appears as a linear polymer with small branches off the main body. Whilst when *df* approaches 3, the structure becomes more tightly packed and more spherical in shape. Reference images can be fonud in Klassen *et al*., (2013).

Table 6.3 Error calculations from calcium carbonate flocculant calculations

		Fractal Dimension, *df*	Number of particles in an aggregate, *N*	Diameter of floc, D_f (m)	Diameter of primary particles, D_p (m)	Density of floc ρ_f (kg.m^{-3})
Calcium carbonate	Average	2.26	56	2.05E-05	2.95E-06	1306
	Error	0.04	7	3.23E-06	1.80E-07	50
Magnesium hydroxide	Average	2.22	95	3.21E-05	3.52E-06	1171
	Error	0.02	8	3.21E-06	2.12E-07	16

6.3.2 Camsizer XT (Retsch Technology)

A Camsizer XT (Retsch Technology) was used to determine the cumulative size distributions of calcite and magnesium hydroxide and validate the particle size distributions. The cumulative distributions are shown in Fig. 6.7 (a) and (b), respectively. In Fig. 6.7 (a) and (b) it is shown that both have a single modal distribution with a smooth cumulative distribution curve which shows that shear in the Camsizer cell led to smaller floc sizes. The sizes of the primary particles of calcium carbonate and magnesium hydroxide are in-line with the particle sizes shown in the micrographs in Fig. 6.1. These measurements were also taken using samples from a small tank where the data was analysed immediately. When using the Mastersizer 2000E, the samples had to be stored and then transferred to the

Mastersizer 2000E when a booking slot was available, this could have led to natural aggregation in the sample vials. Therefore, the size data shown in Fig. 6.7 was used in the following acoustic modelling. Fines are shown in Fig. 6.7 (b) where 30% of the suspension has a particle size of 3 μm or below. The d_{50} for both calcite and the magnesium hydroxide were calculated using Fig. 6.7 (a) and (b). The particle size corresponding to a 50% volume is correlated to the d_{50} of the suspension. The d_{50} extracted for calcite and magnesium hydroxide are 4.8 and 5 μm, respectively. The difference in particle size is due to the increased existence of larger aggregates in the magnesium hydroxide and the existence of fines in calcite. However, the difference between both is so small that the presence of fines and the larger aggregates are almost negligible, as the Camsizer XT (Retsch Technology) produces similar d_{50} values for both.

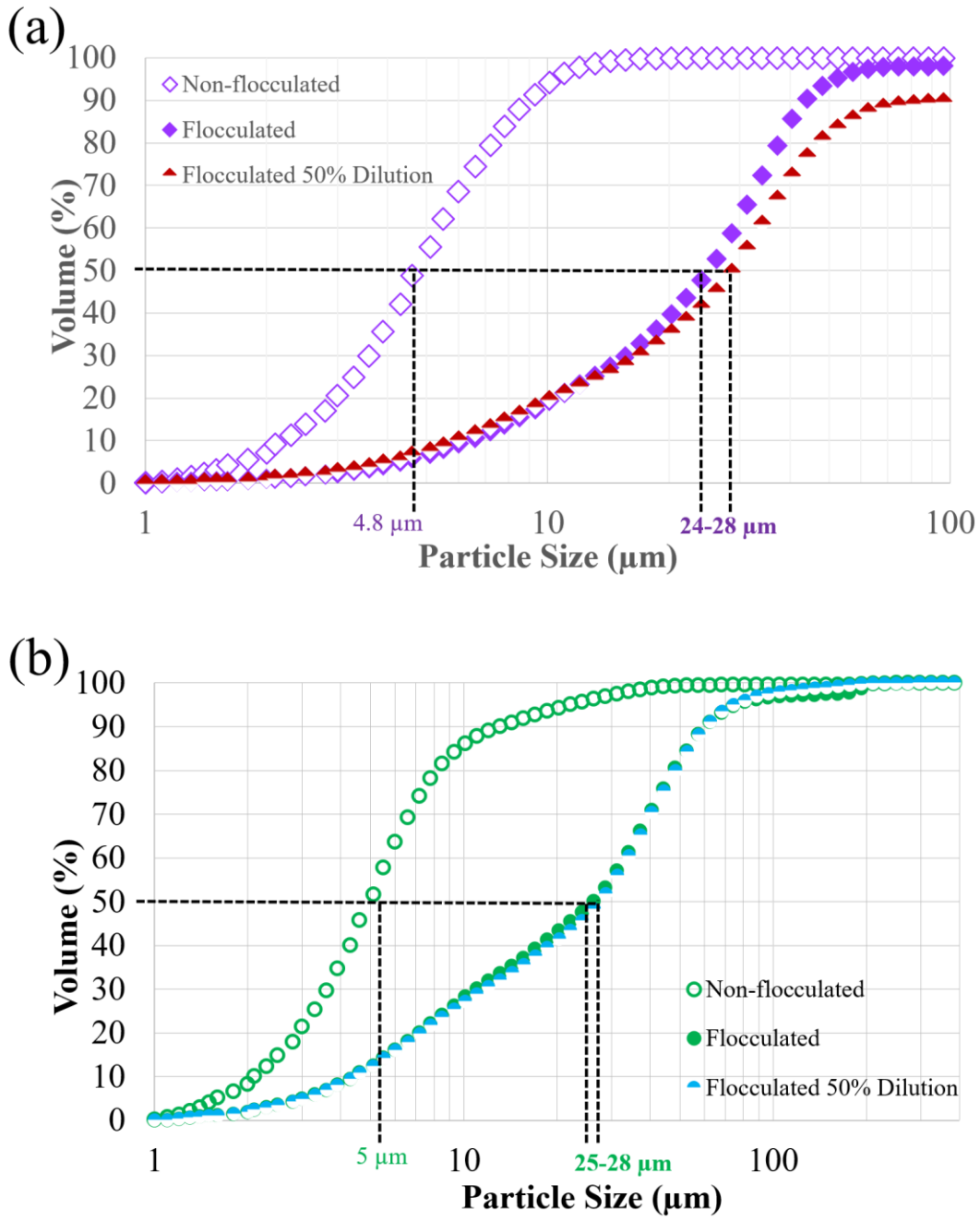

Figure 6.7 Particle size distributions of flocculating (a) calcite and (b) magnesium hydroxide using a Camsizer XT (Retsch Technology) where the suspension was diluted by 50% to see if the flocculates would retain size

The diameter of the flocs in Table 6.3 for calcium carbonate and magnesium hydroxide are 25 and 31.2 µm, respectively which are comparable to the floc diameters in Fig. 6.7 (a) and (b). This shows that both the Mastersizer 2000E data

and the derivations to produce the floc diameters are comparable to the experimental floc diameters from the Camsizer XT. The Mastersizer data was taken *ex situ* where samples were taken to the Mastersizer cell, whilst the Camsizer data was taken *in situ*. This extra time may attribute to the increased aggregation for magnesium hydroxide in the Mastersizer data.

6.3.3 FBRM

The FBRM was installed as shown in Fig. 6.3 to analyse the size of the flocs *in situ*. The FBRM used a large probe which was submerged into the tank. The chord length extracted from the FBRM was plotted as a raw chord length distribution in Fig. 6.8 which could be directly compared to the Mastersizer data. The particle size of the non-flocculated calcium carbonate starts at 4.3 μm and slowly increases as the flocculant is added where the particle size increases to 7.5 μm after 10 minutes and 19 μm after 30 minutes. This is similar to the data found using the Camsizer XT (Retsch Technology). The non-flocculated particle size is slightly lower than shown in Fig. 6.6, however, the difference is almost negligible (0.5 μm). The floc size is underestimated by around 5-9 μm, however, as the FBRM analyses particles which appear in front of the probe, this could just be due to a high presence of fines in the probe window at the time of measurement.

When diluting the suspension by 50%, the d_{50} is stable, however, when diluting the suspension by 75% the particle size decreases by approximately 4 μm. This could be attributed to break-up of flocs in the dilution process. Only the 50% dilution is shown when analysing with the Camsizer XT. The sizes of the flocs and primary particles appear to be consistent with the Camsizer XT data in Fig. 6.7. However, there are some differences in actual particle size derived due to the interference of fines in the probe window of the FBRM. The results from Fig. 6.7 and 6.8 show that generally, the flocs are stable with dilution. The Camsizer XT was found to determine the volume of particles using a minimum diameter which explains the smaller floc size than expected from literature (Lu *et al.*, 2016).

However, the FBRM uses the maximum diameter shown in the probe window which depends on the orientation of the particles as they pass the window.

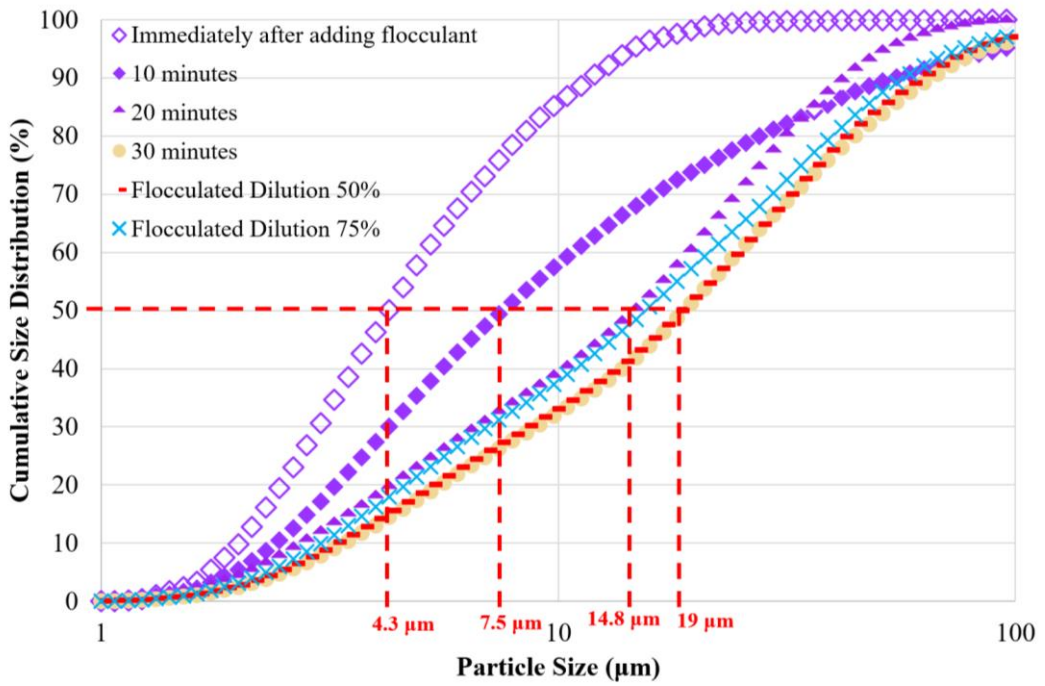

Figure 6.8 Size data of flocculating calcium carbonate using a FBRM (focused beam reflectance measurement)

The raw chord length distributions values were converted to number and surface weighted distributions in Eq. (6.09-6.10) and Eq. (6.11-6.12), respectively. These distributions are shown below in Fig. 6.9 (a) and (b) where it was found that when plotting the number and surface weighted distributions, the size of the primary particles and flocs is overestimated, producing data which is not representative of the sizes seen when using the Camsizer XT and Mastersizer 2000E. Therefore, only the raw chord length distributions from the unweighted data are used to determine the particle size.

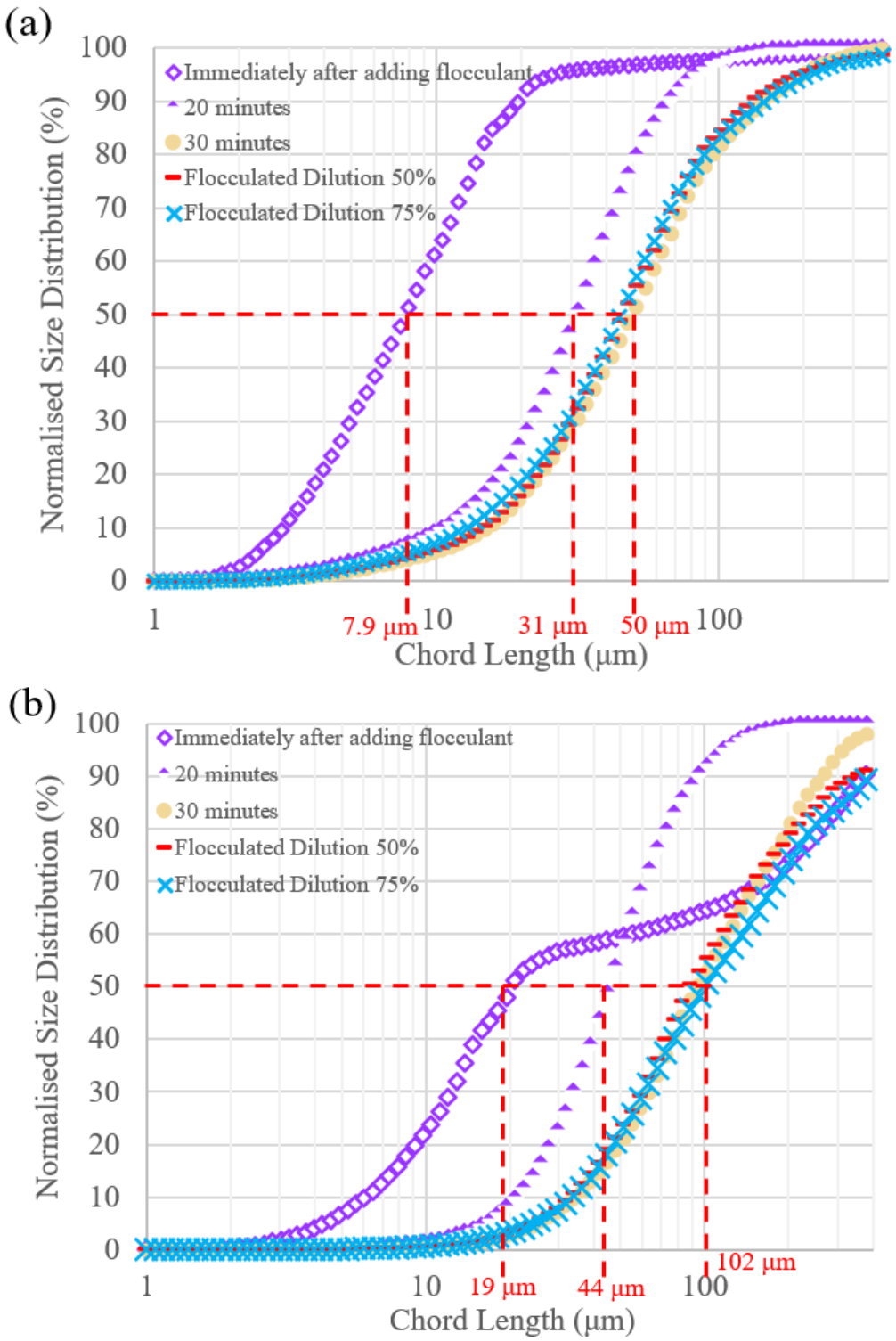

Figure 6.9 Size data of flocculating calcium carbonate using (a) number weighted and (b) square weighted distributions of FBRM chord length data

Fig. 6.10 shows the tracking of the d_{50} throughout the experiment where it was found that upon adding flocculant, the floc sizes increased steadily until around 30 minutes had lapsed. Pink crosses in Fig. 6.10 indicate a UVP measurement was taken, green crosses indicate the FBRM data was plotted and the yellow indicate that both UVP and FBRM data was extracted. The tank was diluted by 50% and the particle size was monitored using the FBRM output data. The particle size appeared to stay consistent, and an FBRM measurement was extracted within 10 minutes of starting the dilution process. The tank was then diluted a second time where the particle size was found to decrease steadily which is likely due to the shear of the flocs during dilution. An FBRM measurement was extracted after 10 minutes had lapsed from the start of the dilution step. UVP measurements were taken of the non-flocculated suspension and 30 minutes after adding the flocculant where the sizes of the particles and flocs were consistent for a period of time.

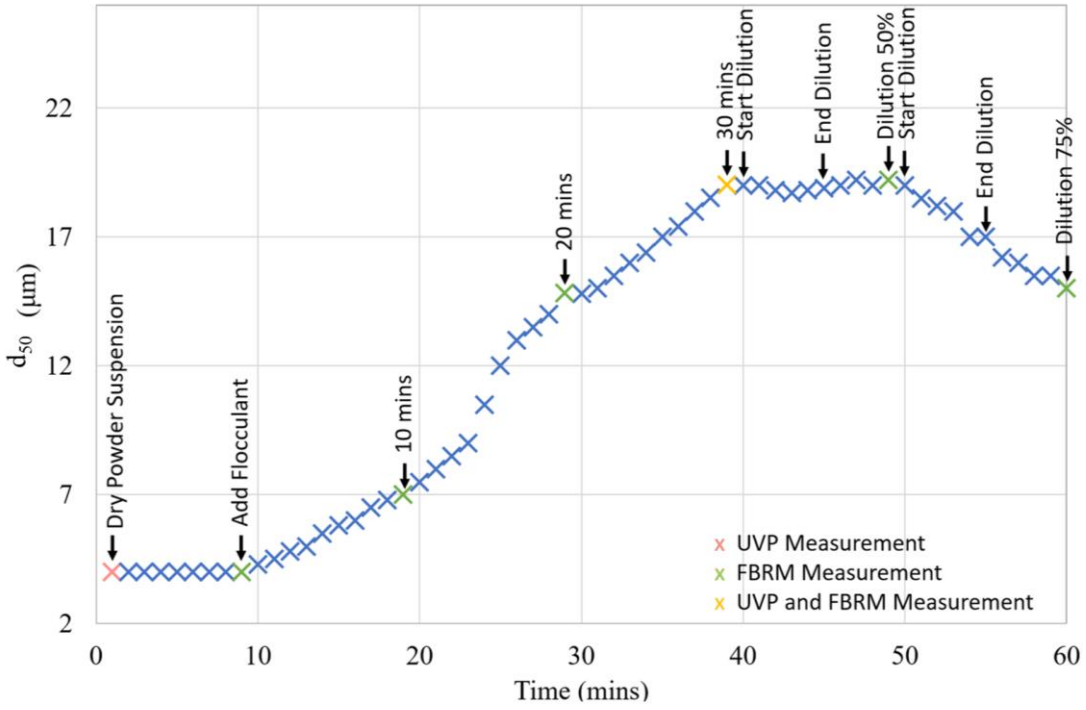

Figure 6.10 Tracking of average particle size during flocculation of calcium carbonate

Chord length distributions for the flocculating magnesium hydroxide are shown in Fig. 6.11 where the particle sizes shown are slightly higher than found in Fig. 6.9. The primary particle sizes are approximately 1.3 µm higher than the calcium carbonate which is consistent with data from the Camsizer and Mastersizer.

The flocs were found to increase to 29.7 µm, this is ~10.7 µm larger than the calcium carbonate flocs which is attributed to the lower density of magnesium flocs in Table 6.1 and 6.2. The number of particles in magnesium hydroxide flocs were found to be higher which results in a larger floc size. The primary magnesium hydroxide particles were found to have a bimodal distribution much like the Mastersizer data in Fig. 6.6 which is attributed to large aggregates present in the suspension.

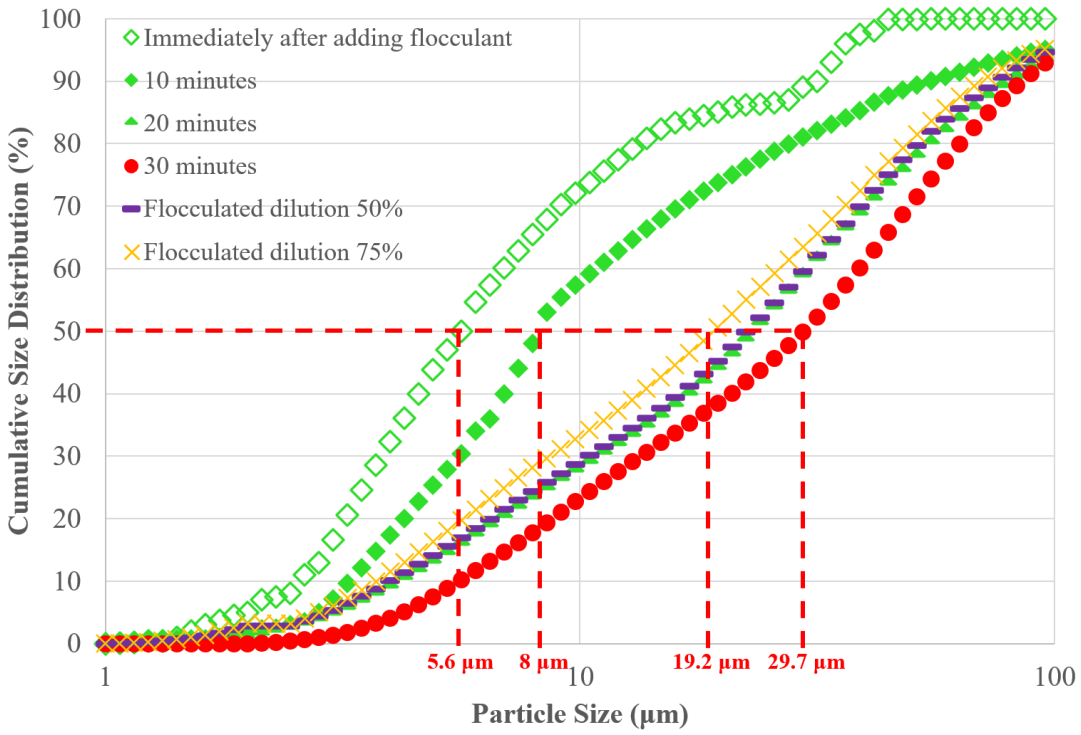

Figure 6.11 Particle size data of flocculating magnesium hydroxide using a FBRM (focused beam reflectance measurement)

The average particle size is shown in Fig. 6.12 as a function of the time lapsed. Before the addition of flocculant, the particle size of the dry powder suspension increases with time, this is due to aggregation in the suspension. Once the flocculant is added, the size steadily increases for 10 minutes and then the flocs dramatically increase in size until 30 minutes had lapsed. The dilution steps are identical to the calcium carbonate experiment; however, the floc size dramatically decreases in the first dilution step which shows how sensitive the magnesium hydroxide flocs are to dilution.

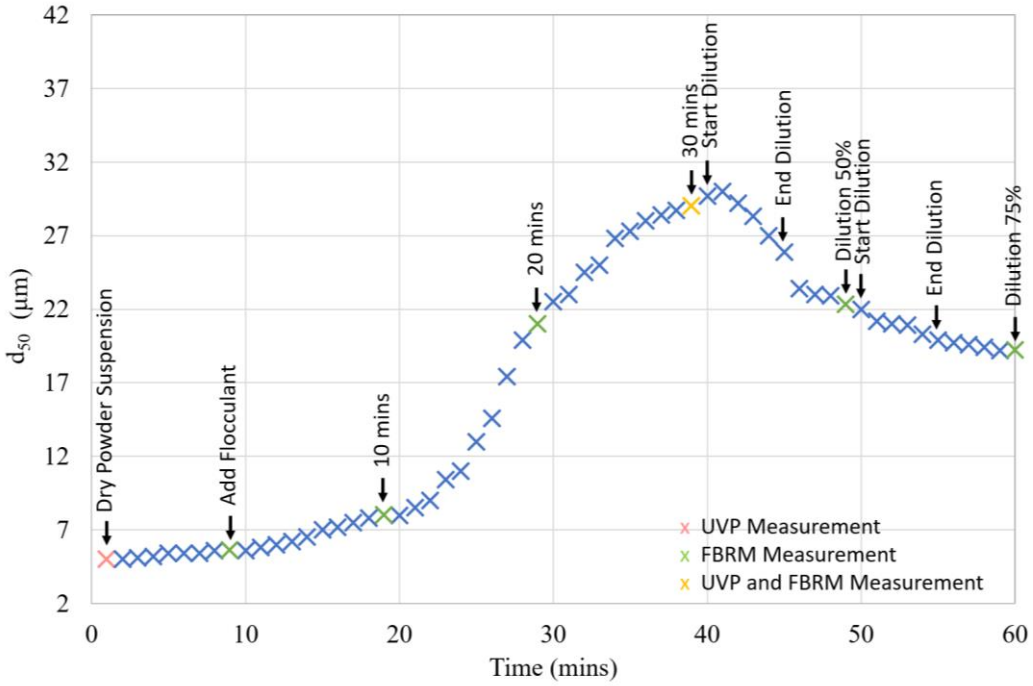

Figure 6.12 Tracking of average particle size during flocculation of magnesium hydroxide

6.3.4 Acoustics

6.3.4.1 G function profiles

Acoustic *G*-function profiles collected from the *in situ* probe analysing calcium carbonate are shown in Fig. 6.13 (a) and (b), for two concentrations. Brown profiles indicate flocculated calcium carbonate data and dark purple profiles

shows data from non-flocculated calcium carbonate. Peak decay in all profiles within the first 0.04 m infer a complex nearfield environment (Rice *et al*., 2013). Therefore, this region is ignored, and all data was extracted from 0.04 to 0.12 m. Average gradient (d*G*/d*r*) values for each system in this region are shown by dashed black lines, and as described in Chapter 3, were used to calculate attenuation coefficients. The secondary increase in *G* at larger distances after 0.12 m are indicative of mathematical artifacts, from hitting the system noise floor (Bishof *et al*., 2013; Kutluay *et al*., 2020). This trend is shown for 27.5 g/L profiles, where it suggests the noise floor is reached at a *G*-function value of approximately -6.8, highlighting the UVP limit for sound profiling, this is also shown in Chapters 4 and 5 which shows that the noise floor is not affected by sediment type.

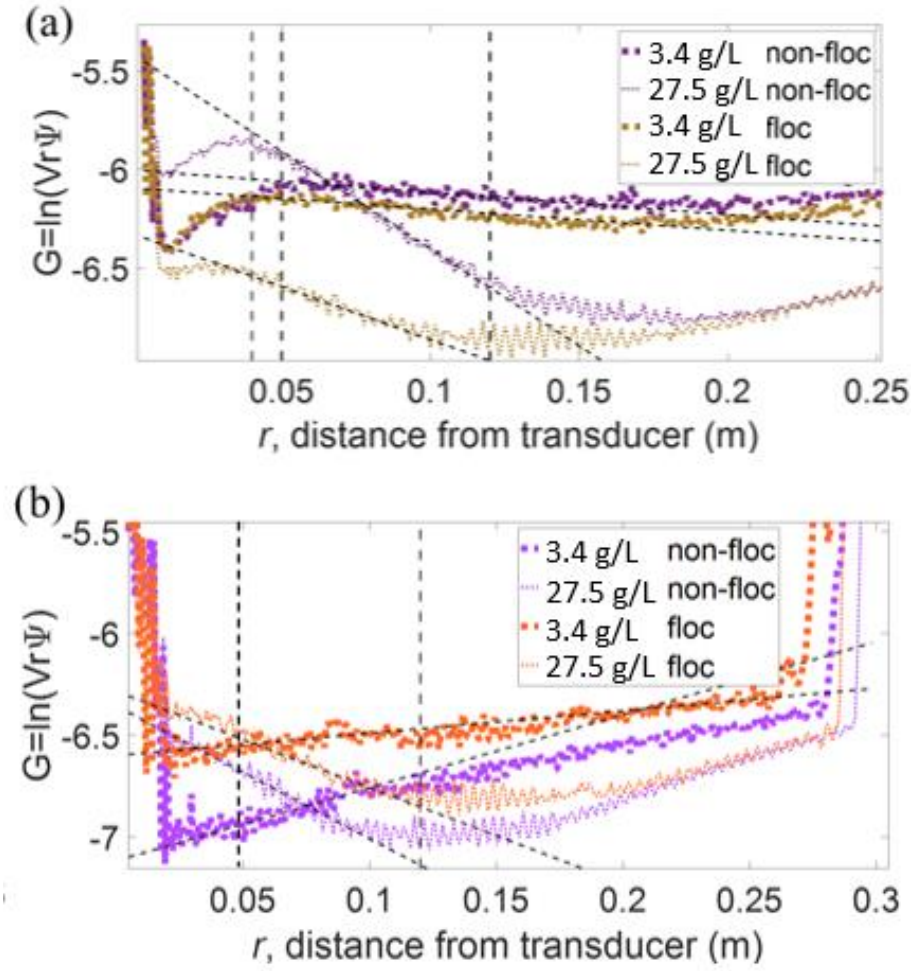

Figure 6.13 G-function profiles for the flocculated calcium carbonate system using an (a) in situ transducer and a (b) remote transducer

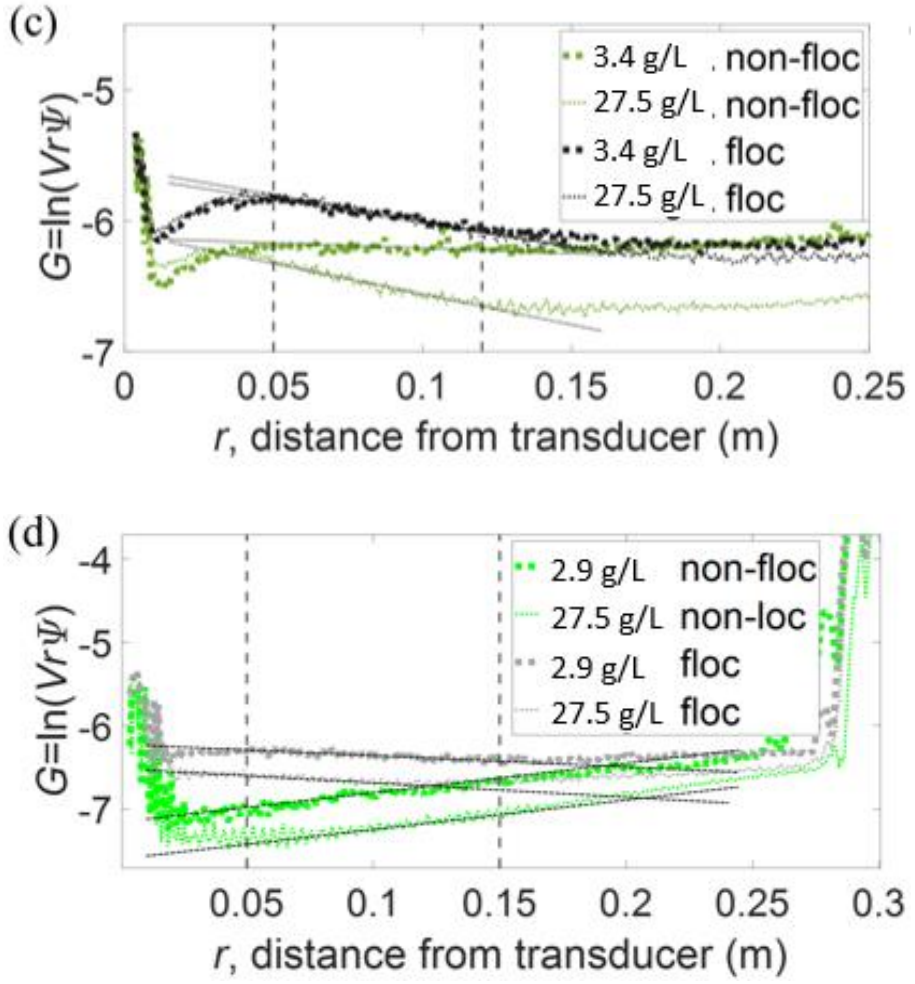

Figure 6.14 G-function profiles for the flocculated magnesium hydroxide system using an (c) in situ transducer and a (d) remote transducer

At 3.38 g/L in Fig. 6.13 (a) and (b), acoustic profiles of flocculated calcium carbonate and non-flocculated calcium carbonate show slight differences in attenuation (as measured from the gradient). The higher concentration of 27.5 g/L allows the user to observe clearer deviations between flocculated and non-flocculated environments. The non-flocculated profile in Fig. 6.13 (a) shows a much steeper gradient in G versus r, inferring a higher level of overall attenuation for non-flocculated suspensions. Such differences were considered counter intuitive, as it is expected that the greater particulate size of flocculated systems would enhance attenuation through greater non-directional particle scattering (Moore *et al.*, 2013). In this case though, the non-flocculated systems are small

enough in size to cause a considerable increase in viscous absorption effects that increases overall attenuation. Similar enhanced viscous attenuation has previously been evidenced in other fine nuclear waste analogues (Tonge *et al*., 2021).

Fig. 6.14 (a) shows the *G*-function profiles from the *in situ* probes analysing magnesium hydroxide for the same two concentrations used for calcium carbonate. The black profiles indicate flocculated magnesium hydroxide whilst the dark green indicate non-flocculated profiles. The peak decay for magnesium hydroxide occurs at 0.04 m as well for which everything before this distance point is attributed to the complex nearfield environment and is hereby ignored. The peak decay is the same for both mineral species as the nearfield distance is dependent on the transducer frequency and active radii. The same transducers were used throughout this experiment; therefore, the nearfield region was the same. The x axis scale has been kept the same for both Fig. 6.13 (a) Fig. 6.14 (a) for the reader to easily visualise the differences between both. The magnesium hydroxide does not attenuate as much as the calcium carbonate. Whether that be the non-flocculating species or the flocculating. The effects of viscous absorption on calcium carbonate are greater due to the presence of fines (Urick, 1948; Anivi, 2020) which leads to increased attenuation due to the incorporation of viscous losses as well as scattering losses. This is shown in the *G*-function profiles where the magnesium hydroxide does not attenuate as much with a smaller difference between the peak decay at 0.04 and the end of the measurement environment at 0.12 m. The secondary increase in Fig. 6.14 (a) is shown at 0.12m for the non-flocculated profile for 27.5 g/L where the UVP has reached the noise floor. This corroborates the notion that the noise floor is at -6.8 which is the limit of sound profiling for the UVP.

Fig. 6.13 (b) presents the acoustic *G*-function profiles extracted from the calcite suspensions using remote transducers. The respective relationship between flocculated and non-flocculated systems are similar, as for the *in situ* probes in Fig. 6.13 (a), with flocculated systems showing lower levels of attenuation (lower gradient of *G*). Interestingly, for lower concentrations, *G*-function gradients were

positive across the distance range, suggesting a larger reflection of sound at greater distances with lower concentration of particles. Such behaviour would be considered un-physical, but similar positive gradients in *G*-function have been found in various systems at low concentrations, when incorrect nearfield correction factors have been used (Hunter *et al*., 2020). The profiles are at the limit of the ability of the UVP to sound profile where the positive profiles are below -6.8.

This is also shown in Chapter 5 where positive gradients were found for the lowest concentrations when using glass particles. It appears impedance and signal disruption through the tank wall cause additional nearfield interference than evidenced with *in situ* probes. It was evident that average signal strength for remote probes was weaker (lower average *G*-values) due to signal loss with propagation through tank walls (Muggleton and Brennan, 2004; Thirumalaiselvi and Sasmal, 2019).

Fig. 6.14 (b) shows the acoustic *G*-function profiles extracted using remote transducers for suspensions of magnesium hydroxide. The relationship between the non-flocculated and flocculated systems are the same as the *in situ* probes in Fig. 6.14 (a). For both non-flocculating systems, the *G*-function gradients were positive which suggests a larger reflection of sound at the smaller particle size. This is consistent with previously highlighted conclusions for sound signals travelling through the pipe wall.

The gradients for all calcium carbonate profiles over the operational distance sections in Figs. 6.13 (a) and (b) (d*G*/d*r*) – shown by the dashed black lines – are plotted against the corresponding concentration to produce an attenuation profile, as presented in Fig. 6.15 (a). The same has been repeated for the magnesium hydroxide profiles in Fig. 6.14 (a) and (b) and is shown in Fig. 6.15 (b). This is given for the two environments (non-flocculating and flocculating) using both *in situ* and remote ultrasonic transducers. The concentration independent attenuation coefficients (ξ) are extracted by taking half of the negative gradient value for each system as detailed in Eqs. (3.05) – (3.06) in Chapter 3. The non-flocculated

suspensions both exhibit a steeper attenuation gradient, indicative of the greater loss of sound across the suspension, due to the viscous attenuation as described. Interestingly, while the values of G are smaller for the remote probes for all concentrations (due to signal loss through the tank wall, as discussed) the actual overall gradient values of dG/dr for all systems are within 10% of the *in situ* profiles. This result provides evidence that the remote transducers can accurately analyse the acoustic properties, highlighting the applicability of non-contacting probe arrangements for onsite applications. The magnesium hydroxide does not attenuate as much as the calcium carbonate, which is likely due to the density of the floc or the larger particle size of primary particles which attenuate less due to decreased viscous attenuation.

This results in a limited difference between attenuation of non-flocculating and flocculating material. The presence of fines in the calcite increases the viscous losses which leads to a greater attenuation of the signal (Richards and Heathershaw, 1996; MacDonald *et al*., 2013; Arenas and Crocker, 2021).

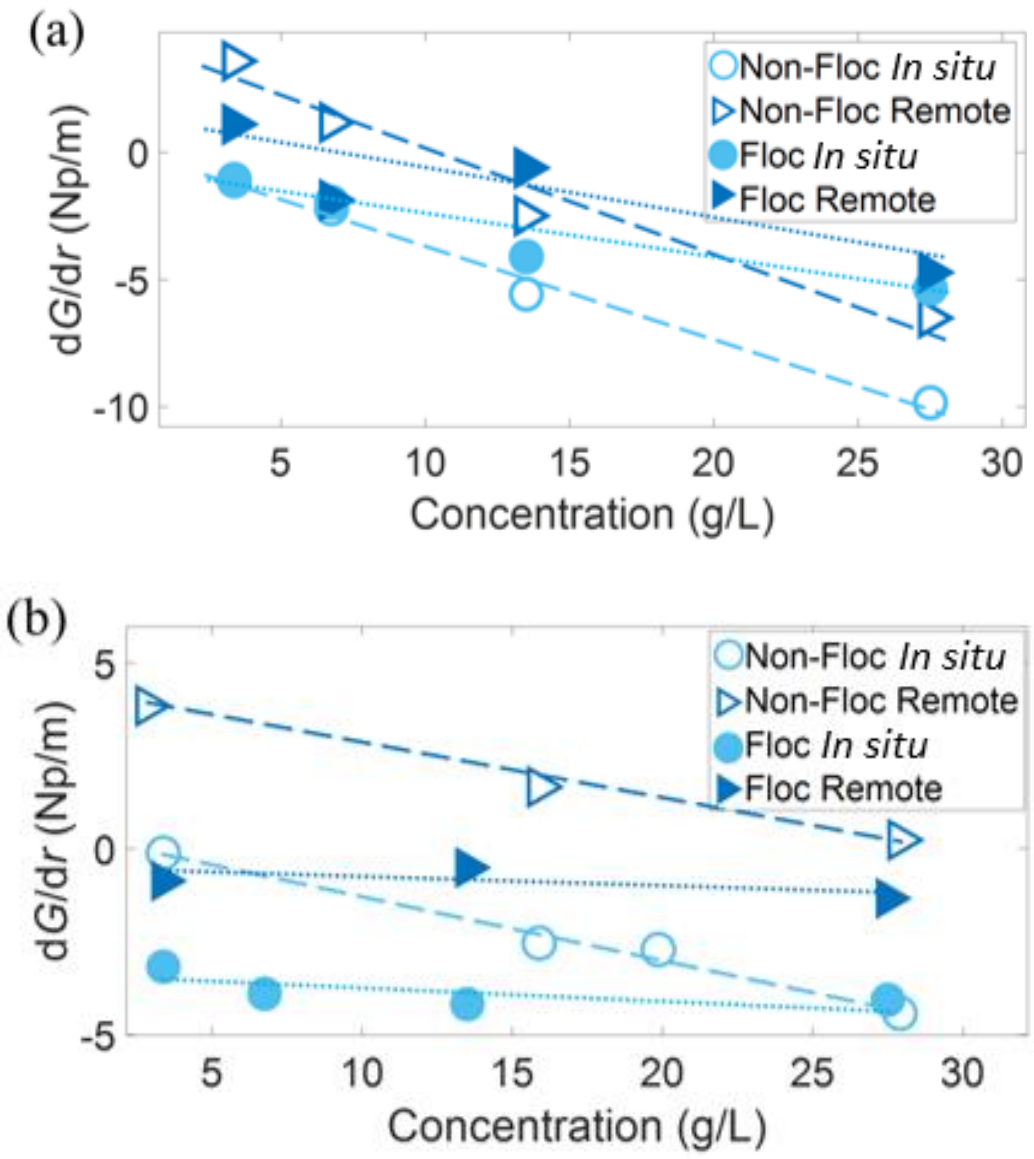

Figure 6.15 (a) Change in G-function with distance with a concentration array ranging from 0-30 g/L using (a) a flocculated calcium carbonate system and (b) a flocculated magnesium hydroxide system

6.3.4.2 Sedimentation attenuation coefficient

The sedimentation attenuation coefficients were extracted from Fig. 6.15 (a) and (b) by taking the negative half of the gradient, this is also shown in Eq. (3.06). The sedimentation attenuation coefficient for the non-flocculated systems is higher than the flocculated systems. This is shown for both mineral suspension

types. The attenuation coefficient for the non-flocculated magnesium hydroxide was more than six times the value of the coefficient for the flocculated magnesium hydroxide. Whereas the coefficient for the non-flocculated calcium carbonate is more than two times the value of the coefficient for the flocculated calcium carbonate. This could be attributed to the lower density of the flocs as shown in Tables 6.1 and 6.2 or that the flocs are larger than expected where the viscous attenuation and scattering is limited. Throughout this thesis there is an assumption that the flocs are spherical, however, the non-spherical floc shape will lead to a different degree of scattering. Gronarz *et al*., (2017) found that there was a negligible influence on scattering and absorption due to changes in the particle shape however, this was for larger particles which predominantly attenuate due to scattering. It was found by Richards *et al*., (2003) that changes in particle shape led to varying particle size distributions which effected predictions for absorption of sound. All models and predictions assume monodisperse systems, however, in reality, the flocculating systems are polydisperse which leads to complications in predicted sound attenuation.

Fig. 6.16 shows how the sedimentation attenuation coefficients compare to values from the Betteridge *et al*., (2008) heuristic expression with consideration of the viscous losses from Urick *et al*., (1948). The magnesium hydroxide coefficients are lower than the heuristic data determined using scattering (see Eqs. (3.07) and (3.09)) and viscous (see Eq. (3.11) – (3.14)) predictions in Chapter 3. This could be due to the non-flocculated and flocculated particles being larger than predicted by the FBRM which would lead to increased scattering attenuation. The calcium carbonate coefficients are higher than predictions. This can be attributed to excess scattering from the fine particles (Richards and Heathershaw, 1996; MacDonald *et al*., 2013; Arenas and Crocker, 2021).

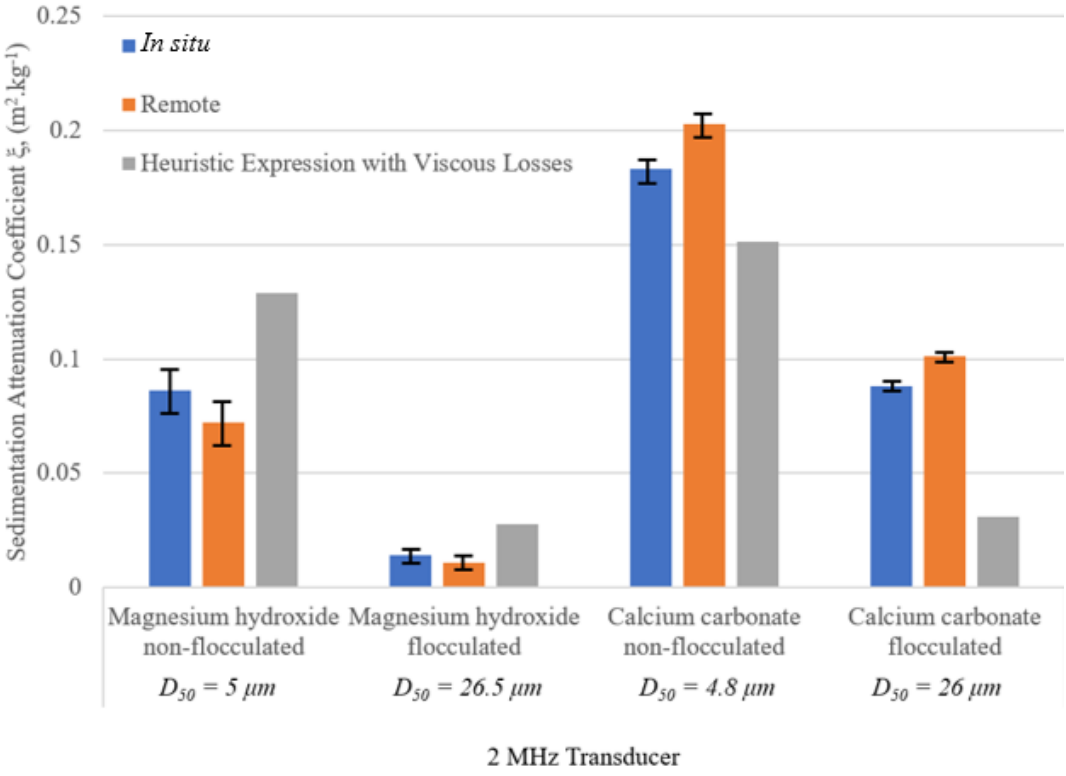

Figure 6.16 Sedimentation attenuation coefficients for non-flocculated and flocculated mineral suspensions of calcium carbonate and magnesium hydroxide

The sedimentation attenuation coefficients for calcium carbonate are higher due to the increased density and the presence of fines which enhance attenuation. The discrepancy between the heuristic expression and measured values is thought to be due to the natural aggregation both undergo due to the low surface charges. It may also be due to the lower shear conditions in the tank in comparison to the Camsizer XT (Retsch Technology) test cell and therefore, the actual representative size of the particles is larger than measured.

Sedimentation attenuation coefficients can also be compared to data for sand and silt suspensions from Guerrero *et al.*, (2015). Samples were taken from the environment which meant that particle shape was not spherical, therefore, data can be compared to the non-spherical mineral suspensions. The lowest particle size in Guerrero *et al.*, (2015) of ~1 μm had the highest viscous attenuation amongst other sediments, which is the case here where calcium carbonate had the highest

attenuation coefficient value. This is also due to fine fractions which Guerrero *et al*., (2015) showed result in appreciable viscous attenuation. The mean size of 1 μm is much smaller than the mineral suspensions used in this Chapter and the attenuation coefficient was ~ 0.1 which was comparable to data from magnesium hydroxide. However, this attenuation could be due to several factors including a difference in transducer frequency used by Guerrero *et al*., (2015), 1.2 MHz and the difference of particle size.

Guerrero *et al*., (2015) also looked at sediments with a mean size of ~ 4μm which led to a combined attenuation coefficient of ~ 0.032 which is comparable to the calcium carbonate attenuation coefficient. The smaller measured coefficient of calcium carbonate could be due to decreased viscous losses of the larger calcium carbonate in comparison to the 4 μm sediment.

Error bars in Figure 6.16 have been determined using the error calculations in Chapter 4 and applied here. The error bars for the magnesium hydroxide suspension were larger than for the calcium carbonate suspensions. This is attributed to the lower density of the magnesium hydroxide particles and flocs which likely led to a weaker backscatter response. However, all error bars are relatively small which shows that the data is consistent. The flocculated suspensions have a smaller error bar which shows that the flocculated suspensions provided more accurate characterisation of the attenuation. The error bars are determined by the variation of the echo amplitude data, as the actual floc attenuation values are lower, the raw echo voltages are lower and therefore, the error bars are lower in absolute terms but similar in percentage terms. The following particle radii were used to calculate the sedimentation attenuation coefficient from the Betteridge *et al*., (2008) model; $a_{calcite}$: 2.4, $a_{magnesium\ hydroxide}$: 2.5, $a_{flocculated\ calcite}$: 13, $a_{flocculated\ magnesium\ hydroxide}$: 13.25. These particle sizes were taken from the Camsizer data shown in Fig. 6.7.

The attenuation of the two mineral systems can be compared to the floc density values determined in Tables 6.1 and 6.2. The floc density values for calcium

carbonate and magnesium hydroxide are 1306 and 1171 kg.m^{-3}, respectively, whereas the density of the primary particles is 2711 and 2340 kg.m^{-3}. This shows that the density decrease through the flocculation process directly correlates to the decrease in the attenuation as the particle sizes in Fig. 6.7 are similar for both floc systems. The larger flocculated aggregates are less dense which can be assumed to scatter more and absorb less which leads to decreased loss of sound and greater backscatter to the reciever. This research is novel in that the density of flocculated particles has been linked to attenuation which has not been achieved before.

The predicted viscous losses in Fig. 6.16 account for 0.15, 0.13, 0.03 and 0.027 for the calcium carbonate and magnesium hydroxide non-flocculated then the flocculated versions of these species, respectively. This shows that the viscous losses are larger for the calcium carbonate species, which may be a result of the increased combined attenuation losses. When comparing these in terms of percentage values of the combined attenuation, the viscous losses make up more than 99 % of the attenuation for both non-flocculated species. However for the flocculated calcium carbonate and magnesium hydroxide, the viscous contribution is 96.9 % and 95.8 % which shows that for larger sizes of these mineral species, the viscous contribution is slightly higher. This may be due to the decreased particle size of calcium carbonate which is more effected by viscous losses. This has been investigated in Chapter 5 where an increase in particles Reynolds number (for the higher 4 MHz frequency probe and increased particle size species) led to a decrease in the proportion of attenuation that was viscous losses. This can be investigated further but not in the scope of this thesis.

6.3.4.3 Normalised scattering cross section

In Fig. 6.17 and 6.18, the normalised scattering cross section (χ) was calculated for all datasets, using measured attenuation coefficients. The heuristic expression from Betteridge *et al.*, (2008) for spherical glass particles is plotted for comparison. It is noted that to calculate χ, the mean particle radius for non-flocculated and flocculated species determined from the Camsizer is used, as

shown in Fig. 6.6 ($a_{Calcite}$ = 2.4 μm, $a_{Magnesium\ hydroxide}$ = 2.5 μm, $a_{Calcite\text{-}Flocculated}$ = 13 μm, $a_{Magnesium\ hydroxide\text{-}Flocculated}$ = 13.25 μm). Initially, the particle density of calcium carbonate ($\rho_{Calcite}$ = 2711 kg/m^3 (Ito, 2017)) and magnesium hydroxide ($\rho_{Magnesium\ hydroxide}$ = 2340 kg/m^3 (Patnaik, 2002)) was used in the calculation shown in Eq. (3.09) in Chapter 3. Consistent with similar attenuation values evidenced in Fig. 6.16, χ values calculated from remote probes are almost identical to the *in situ* data, for flocculated and non-flocculated systems of both mineral systems.

In Fig. 6.17 it is evident that non-flocculated values are considerably greater than predicted by the theoretical Betteridge *et al*., (2008) expression for calcium carbonate. Betteridge *et al*., (2008) underpredicts the χ values as the prediction only considers scattering attenuation where it has been shown that for fine particles, attenuation is predominantly due to viscous losses (MacDonald *et al*., 2013; Arenas and Crocker, 2021).

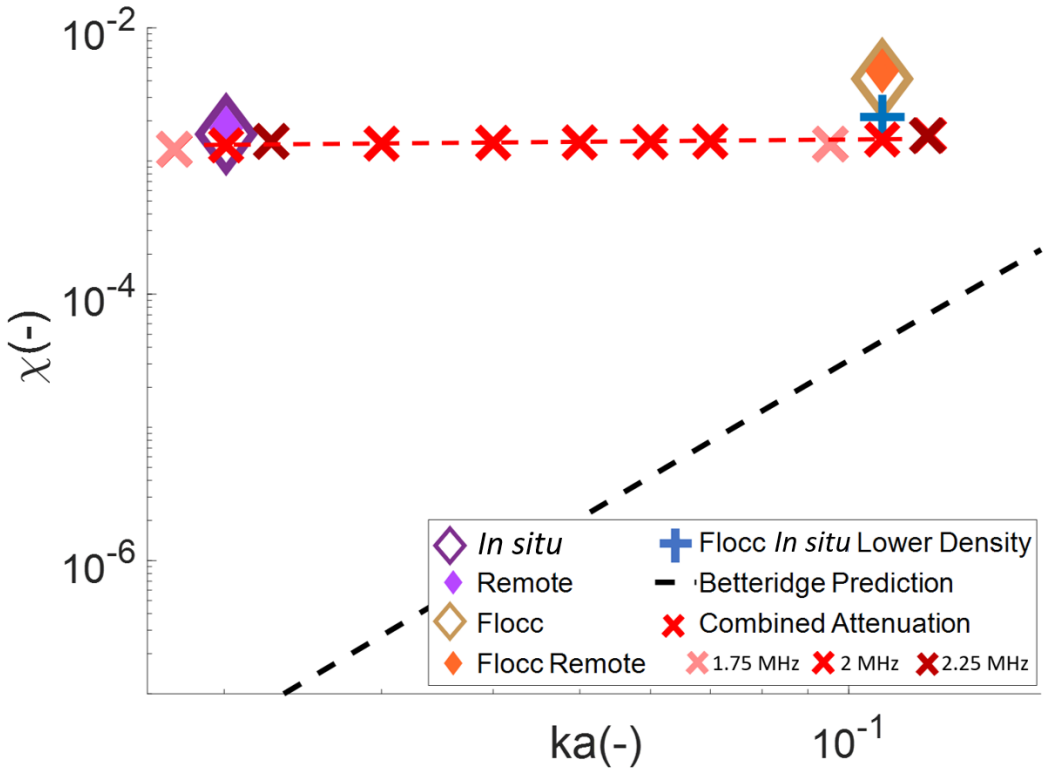

Figure 6.17 The dimensionless scattering cross function vs product of the wavenumber and particle radius (ka) using a (a) flocculated calcium carbonate system where the red line shows the prediction for combined losses when using a 2 MHz transducer, light and dark red crosses show predictions using a 1.75 MHz and 2.25 MHz frequency, respectively

Flocculated calcium carbonate data (in orange/brown) compares more closely to the Betteridge estimation, although χ values are still underpredicted. One potential reason is that as flocculated aggregates contain significant bound water between particles, therefore the use of particle density is likely not correct. And so, a further calculation was made to estimate flocculated χ value, using a lower density value from Table 6.1 ($\rho_{Calcite\text{- }flocculated\ density}$ = 1306 kg.m^{-3}) denoted by the blue cross. This lower density was validated based on values for similar flocculated magnesium hydroxide systems and provides a low limit for χ, highlighting the difficulty in accurately deriving values (Lockwood *et al.*, 2021a). As most of the suspension is water, bulk density is expected to be closer to the lower flocculant

density limit. Despite uncertainties, it is clear that using lower floc density results in closer correlation to Betteridge spherical scattering theory, suggesting additional scattering attenuation contributions of aggregates are low, as long as the overall density is taken account of.

Viscous losses were accounted for by using expressions from Urick, (1948) and shown as a combined attenuation prediction in the red dashed line in Fig. 6.17. The prediction compares much closer to the measured χ values plotted where the lower density flocculated plots compare very well to the combined prediction. The non-flocculated plots also align very well with the combined prediction as the fine particles attenuate predominately from viscous losses. The underprediction of the flocculated values is likely due to the fact that the original particle density was used in Eq. (3.09) where it is clearly shown in Tables 6.1 and 6.2 that the density of the floc decreases significantly.

The Betteridge *et al*., (2008) prediction only accounts for the single frequency used in experiments where the combined attenuation predictions is shown in the red crosses. The dashed red line only considers the 2 MHz transducer frequency used. The combined attenuation was found to be approximately linear in the region between the non-flocculated and flocculated plots. Incorporating viscous losses leads to a dramatic increase in χ at lower *ka* values whereas at higher *ka* values, viscous attenuation has a limited effect on χ. A +/- 0.25 MHz change in frequency is also considered where the pink crosses correspond to a 1.75 MHz frequency and the red a 2.25 MHz frequency. When increasing the frequency, the χ value increases and the *ka* value increases, the opposite is shown when decreasing the frequency. This is attributed to the fact that *ka* is calculated using the angular wavenumber which is a function of the transducer frequency which also results in a higher χ in Eq. (3.07).

The magnesium hydroxide suspensions shown in Fig. 6.18 shows χ values which are lower than the Betteridge prediction, this could be due to the lower particle density of magnesium hydroxide and decreased attenuation ($\rho_{Magnesium\ hydroxide-}$

$_{flocculated\ density}$ = 1171 kg.m^{-3} from Table 6.2). Magnesium hydroxide also attenuates less than calcium carbonate due to the slightly larger particle size which leads to lower χ values. It is lastly noted also that the Camsizer XT natively measures the minimum diameter rather than particle size directly. Particle radius values (a) can be varied from the Camsizer XT depending on whether the minimum diameter is used or another property. The FBRM results vary significantly as well depending on whether unweighted or weighted distributions are extracted. Values reported in this Chapter are based on raw chord lengths, as they provide reliable values when comparing to manufacturer listed particle radius for non-flocculated dispersions. However, it was found that the χ values determined from Camsizer XT particle sizes provided results which were comparable to the predictions. Again, this uncertainty shows how complicated it is to analyse flocculated suspensions.

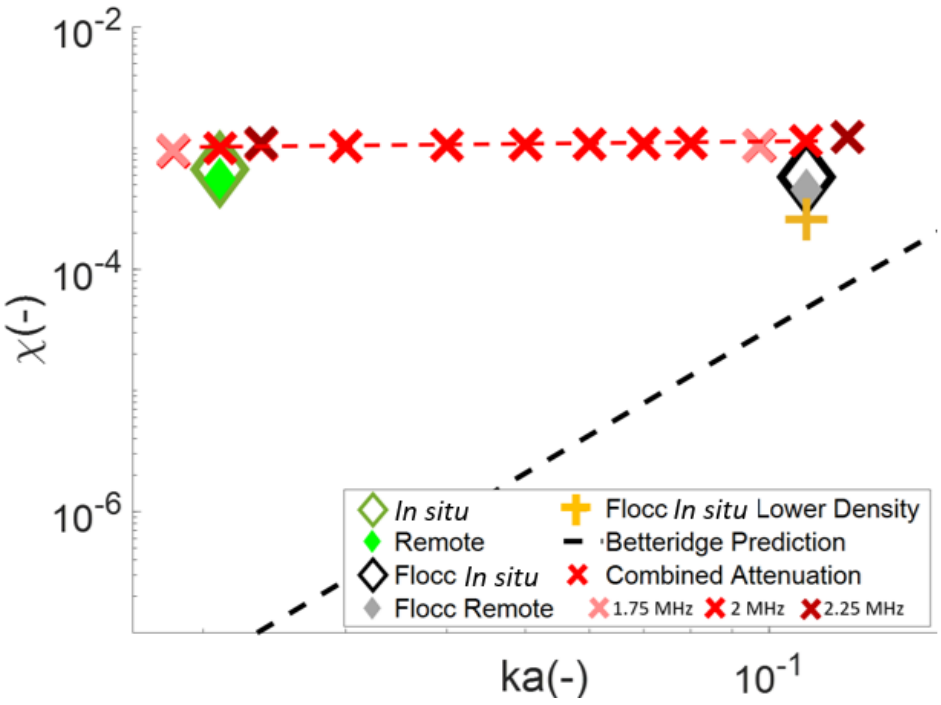

Figure 6.18 The dimensionless scattering cross function vs product of the wavenumber and particle radius (ka) using a flocculated magnesium hydroxide system where the red line shows the prediction for combined losses when using a 2 MHz transducer, light and dark red crosses show predictions using a 1.75 MHz and 2.25 MHz frequency, respectively

It is shown that the frequency change is the same as shown above where the *ka* and χ increase with frequency. The lower density pushes the χ value further from the combined attenuation prediction. This could be attributed to the polydispersity of the systems where the Betteridge *et al*., (2008) prediction only accounts for monodisperse systems. However, here, the effect of polydispersity has differing effects on the magnesium hydroxide and calcium carbonate which shows the complexity of predicted normalised scattering values for flocculating systems. However, the combined attenuation predictions are close to χ values determined from experimental sedimentation attenuation coefficients.

Pedocchi and Mosquera, (2022) found that the total scattering cross section dominates sound attenuation with no deviations that can be directly associated to flocculation. Therefore, any changes with the scattering cross section may be due to the effect of attenuation on the increased particle size.

6.4 Conclusions

In this Chapter, a UVP in backscatter mode was used to characterise flocculated and non-flocculated nuclear waste simulant suspensions. Where probes in a calibration tank were positioned *in situ* and in a non-contacting 'remote' arrangement, for future monitoring applications. *In situ* and remote probes gave comparable suspension attenuation coefficients for all systems using both mineral systems. Remote probes had a lower signal-to-noise ratio, due to loss through tank walls. The noise floor for the UVP, using the *G*-function, was found to be approximately -6.8 for all profiles. Flocculated suspensions (larger particle size) attenuated less and exhibited a predictable scattering cross section specifically for calcium carbonate suspensions, if the reduced overall aggregate density is taken account of. Flocculated magnesium hydroxide suspensions showed predictable scattering cross section values when considering the higher particle density. Non-flocculated particulate suspensions had greater attenuation and overall scattering cross section, where the increased attenuation was due to viscous losses. Magnesium hydroxide systems were found to attenuate less than calcium

carbonate due to their lower floc density and increased absorption. Analysing flocculated suspensions is difficult, due to variation of density and particle radius, but the quality of data in this Chapter has been found to be accurate.

In this Chapter the author was able to successfully monitor the flocculation of two complex fine particulates and provide attenuation values which were very close to predictions. This was all achieved using non-invasive remotely placed transducers where data could be extracted in real-time. The attenuation regime was identified for the differing particle sizes where viscous losses were dominant for non-flocculating materials. Attenuation could be predicted by comparing the normalised scattering cross function where measured data compared very well to predicted, especially when taking into consideration the change in density from flocculation. The success of this Chapter will lead onto the use of the pipe loop for analysis of homogeneous suspensions and then flocculated mineral suspensions.

7. ANALYSIS OF SILICA GLASS SUSPENSIONS IN VERTICAL AND HORIZONTAL PIPE LOOP ARRANGEMENTS USING TRANSDUCERS MOUNTED IN SITU AND REMOTELY IN A NON-CONTACT PLACEMENT

CHAPTER SUMMARY

Homogeneous silica glass dispersions of two sizes were analysed in an engineered pipeline using transducers mounted on horizontal and vertical pipe lengths. Transducers were mounted at 90 and 135° to the direction of flow. Rice *et al*., (2014) extracted echo amplitude data from transducers on a horizontal pipe using 2 and 4 MHz transducers. However, here, 4 MHz transducers were mounted on horizontal and vertical pipe length to determine the effect of transducer placement on attenuation profiles, this has not been done before. Velocity and echo amplitude data were extracted simultaneously from the transducers to produce velocity and attenuation profiles. Rice *et al*., (2014) determined the velocity of suspensions simultaneously using *in situ* probes. Attenuation coefficients were extracted and compared to combined attenuation predictions from scattering and viscous losses. Normalised scattering cross function was determined for both silica glass bead sizes and compared to predictions from combined attenuation by Tonge *et al*., (2021). However, the novelty in this Chapter is that this has been achieved using in-line non-contact probes.

7.1 INTRODUCTION

This Chapter explores the use of horizontally and vertically mounted transducers in a pipe loop to characterise previously used silica glass particles. In Chapters 4-6 the author has proven that ultrasonic transducers can be mounted *in situ* and remotely on a calibration rig to produce accurate acoustic profiles for homogeneous silica glass suspensions and flocculating complex mineral suspensions. In this Chapter, the author aims to upgrade from the calibration rig to analysis in an engineered pipe loop where the same silica glass dispersions used in Chapter 5 were used as these were known to produce accurate sedimentation

attenuation coefficients. Remote transducers were mounted onto the pipe loop using the same PVC mounting units used in Chapter 5. Remote analysis in a pipe loop will provide in-line measurements of attenuation. Existing literature has been explored to understand whether in-line non-invasive measurements of homogeneous suspensions has been conducted before and what measures are required for this. Steiner and Podd, (2006) were able to mount ultrasonic transducers onto pipes in a non-invasive and non-intrusive manner where the received waveform was displayed, this shows that the mounting of the transducer should provide accurate data from ultrasonic transducers. In this Chapter, the mounting of the transducer onto a pipe is non-invasive and non-intrusive where the echo amplitude is extracted using the ultrasonic pulse doppler method, this has also been done by Tezuka *et al*., (2008). Munasinghe and Paul, (2020) and Comes *et al*., (2006) stated that pipes need to be full for measuring properties inside the pipe using mounted ultrasonic devices. This is to ensure the transducers can calculate the flow rate of the pipe cross section. Munasinghe and Paul, (2020) were able to use readings of the water level of the pipe and reflective patterns to determine the flow rate even with a partially filled pipe. However, for ease of understanding, the aim is to have a full pipe for analysis.

In previous Chapters, the transducers were mainly used to extract acoustic data. However, in this Chapter, the in-line transducers can be used to fully characterise the flow where acoustic and velocity data can be extracted. This can be conducted on the pipe loop as the fluid is continuously flowing through the pipe.

Tezuka *et al*., (2008) mounted transducers remotely onto a pipe and used the ultrasonic pulse doppler method to determine velocity profiles. The surface roughness on the pipe effects the shape of the velocity profile where a higher surface roughness leads to a more rounded velocity profile shape. When comparing the PVC pipes used in this Chapter, the surface roughness of PVC was significantly lower than the roughness used by Tezuka *et al*., (2008) so it is expected that the velocity profile will have a more linear profile with a flat peak across the middle of the pipe. The tests were done at 12D and 30D away from the

closest pipe bend where the profiles were symmetrical at a distance of 30D. The actual entry lengths on the horizontal and vertical pipe length correspond to 52D and 84D so the profiles are expected to be symmetrical across the pipe length. Tezuka *et al*., (2008) displayed velocity profiles as a normalised velocity where the peak value was 1 across the pipe. The velocity profiles displayed in this Chapter will be formatted like this for direct comparison between heuristic velocity profiles.

Kotze, (2016) used non- invasive sensors to extract doppler measurements through a stainless-steel pipe section placed horizontally. Voltage and echo profiles were extracted much like the profiles shown in Chapter 4. Kotze, (2016) was also able to extract velocity profiles from the in-line data as the fluid is flowing through the pipe. Kotze, (2016) only tested velocities between 0.1 and 0.6 m/s therefore, this work needs progress for industrial applications. However, Kotze, (2016) has shown that it is possible to obtain echo and velocity data from transducers mounted onto a pipe. Taishi *et al*., (2002) used the UVP to determine velocity profiles with data from a non-invasive transducer mounted onto a pipe radius of 25 mm. Taishi *et al*., (2002) found that using the UVP could be used to accurately measure mean velocity profiles, therefore, it is expected that the UVP should be able to reproduce accurate velocity profiles for homogeneous suspensions of silica glass dispersions. Abbagoni *et al*., (2022) used non-invasive vertically mounted transducers to determine the measured velocity in the pipe therefore, different pipe orientations should provide accurate velocity and acoustic profiles.

Shoham, (2006) has shown that in vertical and near-vertical pipes the flow patterns are more symmetric around the pipe axis and less dominated by gravity. Therefore, both a horizontal and vertical pipe arrangement were compared to understand which orientation was best suited for extraction of acoustic and velocity profiles. The author has proven in Chapters 4-5 that the UVP can be used to extract concentration profiles and attenuation coefficients from silica glass beads suspended in a tank whilst Chapter 6 shows that the UVP can be used to

monitor flocculation of mineral suspensions in a rig. This Chapter will investigate the use of the UVP to determine concentration profiles, velocity profiles and attenuation coefficients of silica glass beads in flow using in line, non-invasive transducers.

7.2 Materials and Methods

7.2.1 Materials

The same silica glass particle sizes in Chapter 5 were used here as their acoustic scattering profiles are well understood and attenuation values are available for well mixed systems. SEM images of the silica glass beads are shown in Fig. 5.2 where the four silica glass bead sizes are shown. In this Chapter only the 36 μm and 82 μm glass sizes are used to understand the effects of viscous and scattering attenuation on a range of particle sizes. The 170 μm particle size were not used as they undergo high scattering attenuation and are limited to a concentration range as shown in Chapter 5.

7.2.2 Methods

For an industrial application in radioactive effluent, it is imperative that the transducers don't physically interact with the effluent, so a non-contacting 'remote' arrangement is critical. Therefore, only remote transducer arrangements were used hereafter. From preliminary pipe flow data that is not presented in this thesis, the author found that the horizontal pipe was showing signs of deteriorating data. This was attributed to settling of material in the horizontal pipe which caused blockages in the flow of the suspension. Therefore, in this Chapter, transducers were mounted on a horizontal and vertical pipe orientation to see if comparable attenuation and velocity profiles could be extracted from both. The original purpose of the UVP was to extract velocity profiles, however for this thesis, the UVP was utilised to additionally extract echo amplitude data for acoustic profiles. Both velocity and echo amplitude data were extracted in this Chapter to maximise the scientific insights gained from using the UVP. This was achieved by mounting probes at 90° and 135° to the flow for extraction of echo

amplitude and velocity data, respectively. Only two 4 MHz transducers were used throughout this Chapter.

The transducers mounted at 90° to the flow were used to extract echo amplitude data as has been done previously. The transducers mounted at 135° were used to extract velocity data. The 135° angle was chosen for analysis so the transducer pointed upstream which causes less flow disturbance. This specific angle was chosen by Rice, (2013) as a compromise where a shallower angle to the flow would project the probe further into the flow. The mounting also becomes more difficult as the signal has a larger distance to travel before entering the suspension environment. Whereas Rice, (2013) has shown that a less shallow angle reduces the accuracy of axial velocity measurements. This also allows for minimal gap between the transducer face and the pipe wall. The acoustic couplant is able to assist the sound signal in penetrating the pipe wall, however the more angled the transducer is, the greater the gap between the transducer face and the pipe wall. At the angle of 135°, the transducer signal was strong enough to penetrate the pipe wall (with the added acoustic couplant). The UVP-DUO was used for data collection.

The experimental set-up in Fig. 7.1 (a) is slightly more complicated for this experiment than it is for analysis in the calibration rig in Chapters 4-6. The pipe is composed of uPVC (unplasticised polyvinyl chloride) with a pipe diameter of D = 0.025 m whilst the probe holder was made from PVC (polyvinyl chloride). The small diameter of the pipe is the main reason why 4 MHz transducers are used. When observing the results in Chapter 5, it is shown that the 4 MHz probes analyse the distance closest to the transducer (between 0 – 0.1 m). Whilst the 2 MHz transducers analyse the signal after 0.05 m which would not be suitable for the smaller pipe diameter of 0.025 m. In these pipe loop experiments a single flowrate of 5.22 L/s was used throughout the experiments, more details of this are shown in Table 3.7, see Chapter 3. The corresponding speed and Re for this flow rate are 1131 rpm and 21, 913.

Smaller diameter pipes can be used through Nuclear Power Plants (NPP), typically in areas like primary cooling waterpipes, steam generator tubes and other equipment (Nippon, 2019). These pipes have a typical pipe diameter of 0.24 to 37.5 inches in outer diameter. The pipes used in this thesis have an outer diameter of 30 mm which is approximately 1.18 inch, this lies in between the typical pipe diameter of pipes used in NPPs (Nippon, 2019). In Schaller and Huber, (2023), 2-inch pipes were taken as samples from nuclear reactors which had been contaminated through primary steam. These 2-inch pipes are equivalent to a 50.8 mm pipe which is comparable to the 30 mm Outer Diameter (OD) pipes used throughout this thesis in Chapters 7 and 8.

The horizontal and vertical probe placements need to be at least 1.28 m away from a turn in the pipe, this ensures the flow is fully developed at the point of measurement. This is shown in Chapter 3 where the entry length was determined using two correlations where the minimum entry length for fully developed flow at a Re = 21, 913 was ~ 1.28 m. The actual entry lengths for the horizontal and vertical mounting is 1.3 and 2.1 m which is above the minimum entry length calculated. For this experiment, only the horizontal pipe loop or the vertical pipe loop can run with the bulk suspension. Therefore, the suspension had to be analysed in the horizontal and vertical pipe sections separately.

Fig. 7.1 (b) and (c) show the mounting of the two 4 MHz transducers at each pipe orientation at 90° and 135° to the flow, these were selected as they produced accurate profiles at distances close to the transducer which is necessary for the small pipe diameter. The mixing tank in Fig. 7.1 (a) was utilised the same as the rig in Chapters 4-6 where the mixing tank was isolated for ~ 5 minutes for powder dispersion before running the homogeneous suspension through the loop. The bulk suspension ran through the horizontal pipe length first where the valve on the far left prevents the suspension from going down through the vertical probe holder. The transducers ran consecutively with a time delay of 100 ms, this specific time delay has been used in Chapters 4-6 and has produced accurate profiles when using multiple transducers. This has also been shown in literature to

be a sufficient time delay between multiple transducers (Camnasio *et al*., 2010). As only two transducers of the same 4 MHz frequency were used with a 60 ms pulse at a given time, the total measurement time was 220 seconds. For analysis in both the horizontal and vertical, the total measurement time was 440 seconds. For each concentration, the bulk suspension was first analysed in the horizontal pipe section. All other settings for the UVP-DUO are shown in Chapter 4, see Table 4.1 for more details.

Once all data had been collected, the valve on the far left was opened and the bulk suspension ran through the vertical measurement section. The suspension was emptied using the drainage point shown at the bottom right of Fig. 7.1 (a). The pump and mixer were turned off and the experiment was repeated where the valve to the horizontal pipe section was closed, and the vertical pipe section was opened. The tank was filled, and the powder dispersed after which the suspension was circulated around the pipe and given 5 mins to ensure the bulk suspension was running through the vertical probe holder. The transducers on the vertical pipe length were then activated and the suspension was analysed using both transducers consecutively with the 100 ms time delay. The suspension concentrations used in this experiment ranged from 11.9 to 107.5 g/L.

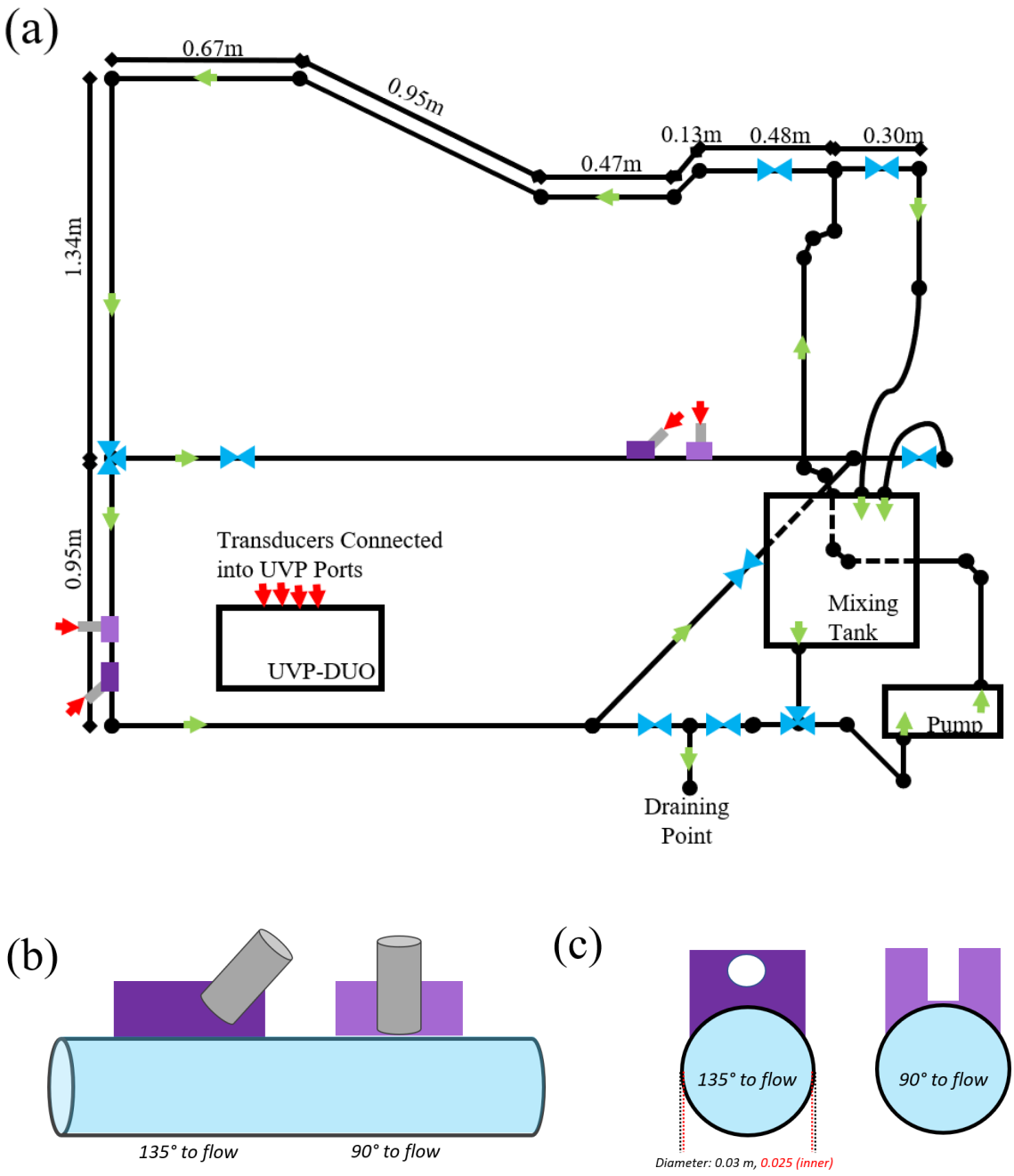

Figure 7.1 Schematic of pipe loop for remote analysis of suspensions in a horizontally and vertically mounted probe at 90° and 135° to the flow (red arrows indicate UVP connection) and (b) visual representation of the probe holders from the front and (c) side

7.2.3 Pipe Materials

The acoustic impedance of the uPVC is investigated to determine whether the pipe material will have an effect on the penetration of sound through the wall. The acoustic impedance of PVC = 3.27 MPa was used from Selfridge, (1985) and Manwar *et al*., (2022). The impedance of water (Bushberg *et al*., 2002; Manwar *et al*., 2022) is also needed (1.48 MPa) to understand the impedance at the pipe wall – water interface. The acoustic impedance can be used to determine the reflection coefficient where the coefficient determines the sound signal which is reflected at the interface. Figueiredo *et al*., (2020) mounted ultrasonic transducers onto a steel pipe using a thermoplastic resin transducer support. The reflection coefficient of steel is ~88% which would mean only 12% of the pulse would reach the flow and therefore a thermoplastic resin with a reflection coefficient of 17% was used. Gibbs *et al*., (2011) used Eq. (7.01) to determine the reflection coefficient, R at the PVC-water interface. Where R is a function of I_r (reflected intensity) and I_i (transmitted intensity). Both I_r and I_i can be broken down into Z_1 and Z_2 which are the acoustic impedances for the two substances, here the subscripts 1 and 2 correspond to PVC and water. For this experiment, the calculated R values for the PVC-water interface is 14.2% where 85.8% of the pulse should reach the flow and so the signal should provide accurate profiles.

$$R = \frac{I_r}{I_i} = \frac{(Z_1 - Z_2)^2}{(Z_1 + Z_2)^2} \tag{7.01}$$

7.2.4 Velocity Calculations

The velocity values are given as a raw output of the velocity in ($mm.s^{-1}$), where the velocity output needs to be converted to SI units of $m.s^{-1}$ before analysis. Once the velocity array is in SI units, the velocity needs to be re-calculated to show the velocity in the direction of flow. As the transducers for velocity profiling are mounted at 135°, the velocity values extracted are shown as the velocity in that specific direction. To convert to velocity in direction of flow, Pythagoras theorem is used to convert the maximum measured velocity values (Bolton, 2016), this is shown as a schematic in Fig. 7.2. The velocity in the direction of flow is expected

to be greater in the direction of flow, this can be seen in Fig. 7.2 where the velocity in the direction of flow is representative of the hypotenuse (longest length) of the triangle.

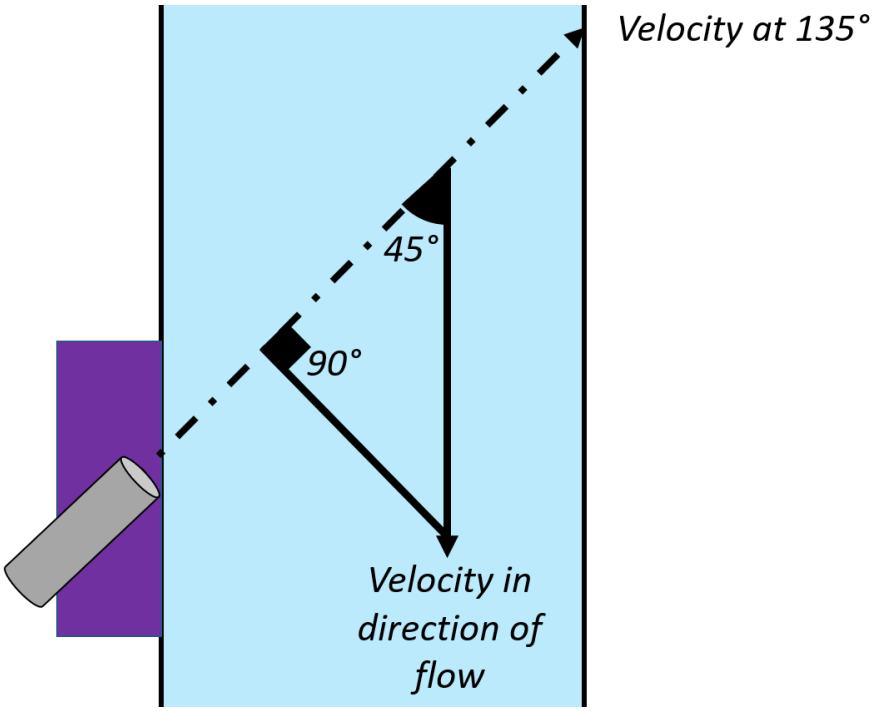

Figure 7.2 Calculation of velocity in the direction of flow

The velocity profiles are displayed in this thesis as a normalised velocity profile much like Tezuka *et al.*, (2008) this ratio is shown in Eq. (7.02). The peak velocity in the direction of flow can be converted to a normalised velocity value v/v^m as shown in Eq. (7.02). The Reynolds number for the suspensions is 21,913 at the experimental pump speed which is high enough for a turbulent flow velocity profile.

$$\frac{v}{v^m} = \frac{measured\ velocity\ \left(\frac{mm}{s}\right)}{maximum\ velocity\ \left(\frac{mm}{s}\right)} \tag{7.02}$$

7.2.5 Calculated velocity profiles

To compare measured velocity profiles to predicted, the power law velocity profile can be determined using Eq. (7.03) from Stigler, (2014). Eq. (7.03) is a function of the pipe radius, *R*, a coefficient, *n* and the distance from the middle of the pipe, *r*. The velocity profile is shown until the velocity peaks in the middle of the pipe.

$$\frac{v}{v_{max}} = \left(1 - \frac{r}{R}\right)^{\frac{1}{n}} \tag{7.03}$$

The coefficient *n* is calculated using Eq. (7.04) which is a function of the *Re*.

$$n = 1.03 \ln(Re) - 3.6 \tag{7.04}$$

When inputting the *Re* = 21,913, the *n* coefficient is calculated to be ~ 6.7. Munson *et al*., (2006) and Stigler, (2014) found that *n* = 7 is a good approximation for many practical flow approximations which shows that the coefficient value calculated is accurate.

7.3 Results and Discussion

7.3.1 Velocity Profiling

As the UVP simultaneously captured velocity data from the Doppler shift, the pipe velocity profiles were measured to confirm the instrument's capability to measure the flowrate. It is noted that only velocity components in the direction of the transducer are measured, and thus, the probes at 135° were used to ensure the transducers could detect the streamwise flow. As the transducer is mounted at a 135° angle, the relative inner pipe distance is 0.035 m. Transducers mounted at 90° to the flow were not used as flow velocity across the pipe is negligible, and any velocity detected using a probe mounted at 90° would be attributed to turbulence fluctuations in the pipe. Although there was segregation of flow in the horizontal arrangement, velocity profiles were extracted from both pipe

orientations to further investigate the degree and effect of segregation on the flow field.

Measurements were made with both particle sizes at two intermediate concentrations to investigate whether the suspension concentration affected the accuracy of the velocity determination. Profiles are shown in dimensionless form in Fig. 7.3 (a) and (b) for 36 μm glass using a horizontal and vertical pipe arrangement. Fig. 7.4 (a) and (b) show the same profiles for the 82 μm glass. The velocity profiles were taken from where the velocity peaks until the middle of the pipe (which, for the probe at 135° is a span of ~ 0.018 m). The diameter of the pipe is 0.025 m whereas, the sound signal travels through 0.035 m for the transducer mounted at 135° because the signal travels a further distance. This should be translated in the velocity profiles where the radius of the pipe is approximately 0.018 m. The velocity profiles start at 0 near the pipe walls and peak to a normalised velocity of 1 in the middle.

For both particle systems in the horizontal pipe arrangement there was a marked increase in velocity at 0.018 m. This increase occurred at 0.011 m when using the vertical arrangement which shows that the horizontal pipe arrangement sees the solid moving suspension at a later point in the pipe. For the vertical probe the peak velocity occurs after 0.018 m (collective 0.029 m) which is the actual radius of the probe path. On the other hand, the peak velocity for the horizontal probes occurs after 0.012 m which shows that the horizontally placed probe has a smaller distance to analyse across due to the decreased pipe area from the layer of settling material. The increase in velocity at ~0.011 m when using the vertical pipe arrangement is where the probe enters the suspension from the pipe wall, and peaks in the middle of the pipe at ~0.029 m. The flattened profile shape is indicative of turbulent pipe flow (*Re* = 21,913 for all experiments) as the strength and proximity of the peaks to the wall increases with increasing *Re* (Laufer, 1954; Rennels and Hudson, 2012).

The measured profiles in Fig. 7.3 (a) and 7.4 (a) show inconsistencies for varying concentration where the concentration affects the velocity in the pipe. This shows

that the attenuation of the increased concentrations has an effect on the velocity in the pipe. The measured profiles in Fig. 7.3 (b) and 7.4 (b) show consistency with at least two concentrations where the velocity profiles are less effected by particle concentration. This indicates the Doppler signal is accurately measured despite the greater attenuation in the more concentrated systems.

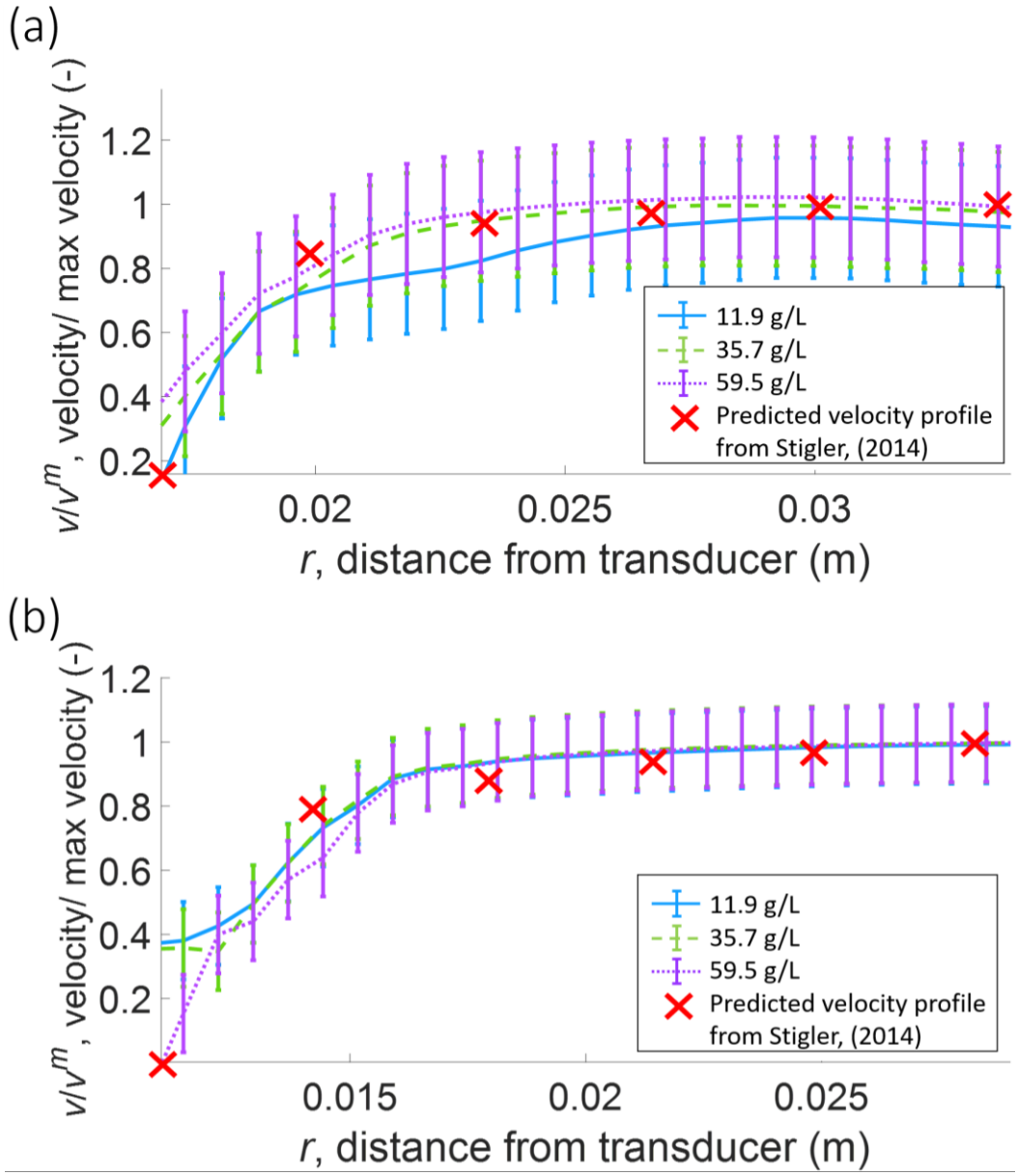

Figure 7.3 Velocity profiles for silica glass bead of d_{50} 36 µm extracted from the (a) horizontally and (b) vertically mounted probe for 3 concentrations of silica glass beads where the red crosses indicate a predicted velocity profile using expressions in section 7.2.5 from Stigler, (2014)

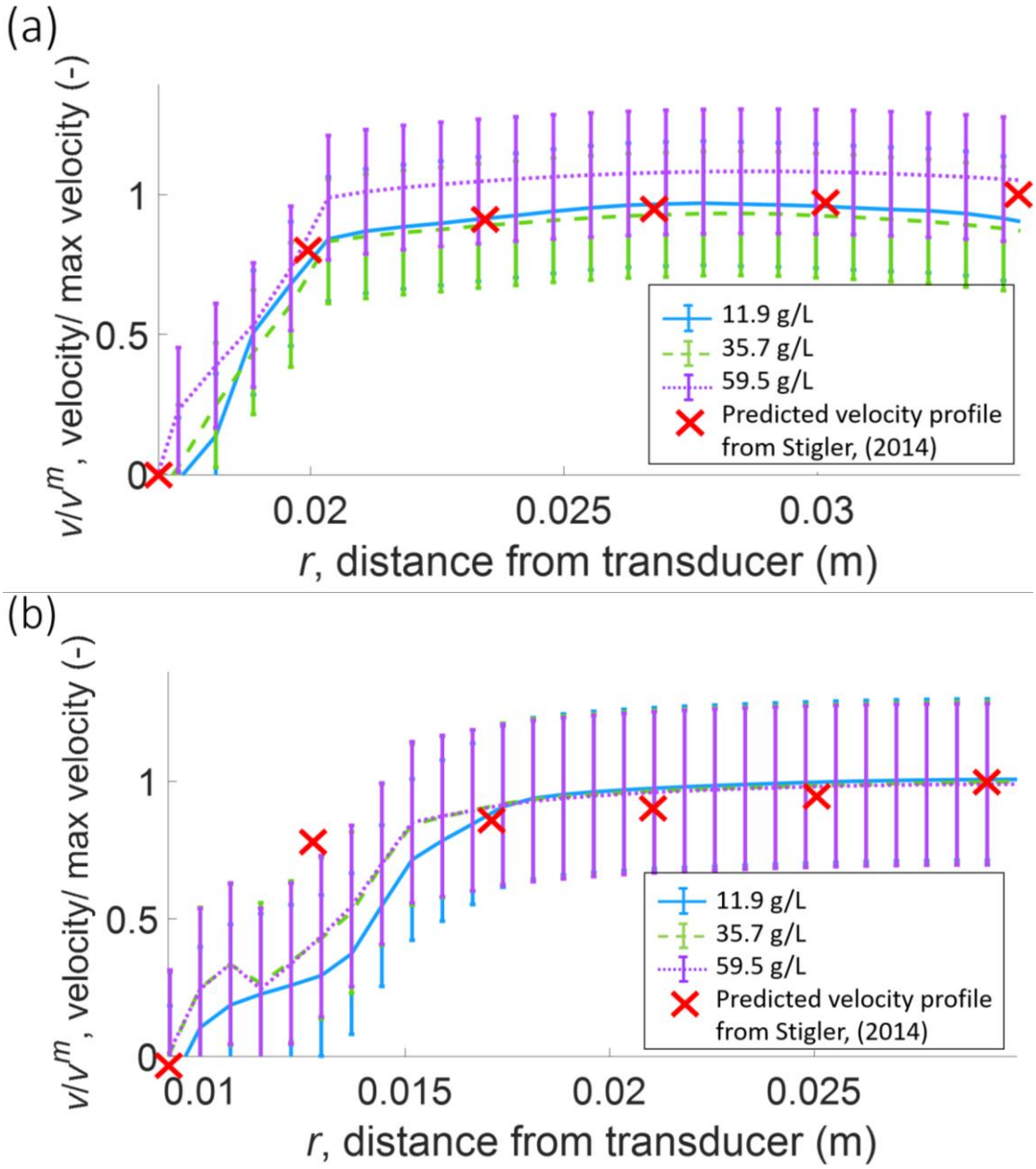

Figure 7.4 Velocity profiles for silica glass bead of d_{50} 82 µm extracted from the (a) horizontally and (b) vertically mounted probe for 3 concentrations of silica glass beads where the red crosses indicate a predicted velocity profile using expressions in section 7.2.5 from Stigler, (2014)

When comparing both species in Fig. 7.3 (b) and 7.4 (b), the profiles were generally smoother towards the middle of the pipe with less variation for the smaller glass species. When only considering the two higher concentration

profiles, the profiles were smoother for the larger glass species which is likely due to their enhanced scattering intensity.

Table 7.1 shows the actual velocity values where the max measured velocity was converted to the velocity in direction of flow using Fig. 7.2. The velocity for the individual glass species is similar for different pipe orientations where the smaller glass beads show a higher peak velocity. This could be attributed to the decreased particle size as larger particle species likely limit the pipe velocity (Khalitov and Longmire, 2003; Prochaska *et al*., 2008).

Hitomi *et al*., (2021) also determined velocity profiles of quartz suspensions and mounted two 4 MHz transducers to determine the velocity. The velocity profiles determined show a peak in the centre of the pipe much like the velocity profiles shown above. This shows that UVP transducers with a 4 MHz frequency can extract velocity profiles in line.

Table 7.1 Velocity measurements in comparison to predicted velocity in the direction of flow

Silica Glass Bead d_{50}	Transducer Arrangement	Max Measured Velocity at 135° (m/s)	Velocity in direction of flow (m/s)
36 µm	Vertical	0.999	1.412
	Horizontal	0.991	1.402
82 µm	Vertical	0.990	1.399
	Horizontal	0.990	1.399

7.3.2 Acoustics

7.3.2.1 G function profiles

Fig. 7.5 (a) shows the *G*-function profiles for the silica glass bead suspensions with a d_{50} of 36 µm travelling through the horizontal pipe arrangement. The sound

signal travels initially through a thin layer of the probe holder before penetrating through the pipe wall, where a layer of acoustic couplant is placed between the transducer face and pipe wall to promote acoustic transmission. The noisy profile in the first ~ 0.005–0.009 m is attributed to internal reflections in the probe holder and pipe wall. The speed of sound through solid uPVC pipe is ~ 2300 m/s which is given by Podesta, (2020) however, the input for the UVP uses the speed of sound in water (1480 m/s) which leads to some ambiguity in where the pipe interface is. Inside from the pipe wall, the profile is still noticeably noisy within the first 0.012 m, this is due to the complex near field interference from the ultrasonic transducers, and potential suspension segregation in the pipeline. Segregation in the suspension may lead to settling in the pipe and a clear-water region from 0.009 to 0.012 m. The estimated inner and outer pipe walls are indicated by the vertical lines in (a). The increase in signal at 0.034 m is attributed to reflections at the bottom of the pipe wall, by extrapolating, the inner pipe wall is assumed to be at 0.009 m by using the actual measured inner pipe diameter of 0.025 m. It is also noted that the estimated speed of sound calculated for silica glass beads using Eqs. (3.11-3.14) from Urick, (1979) (Table 3.2) indicate that the highest concentration produces a speed of sound of 1463 m/s, which is only 1.2% lower than water, and therefore would make a negligible difference on the echo distance estimations within the pipe.

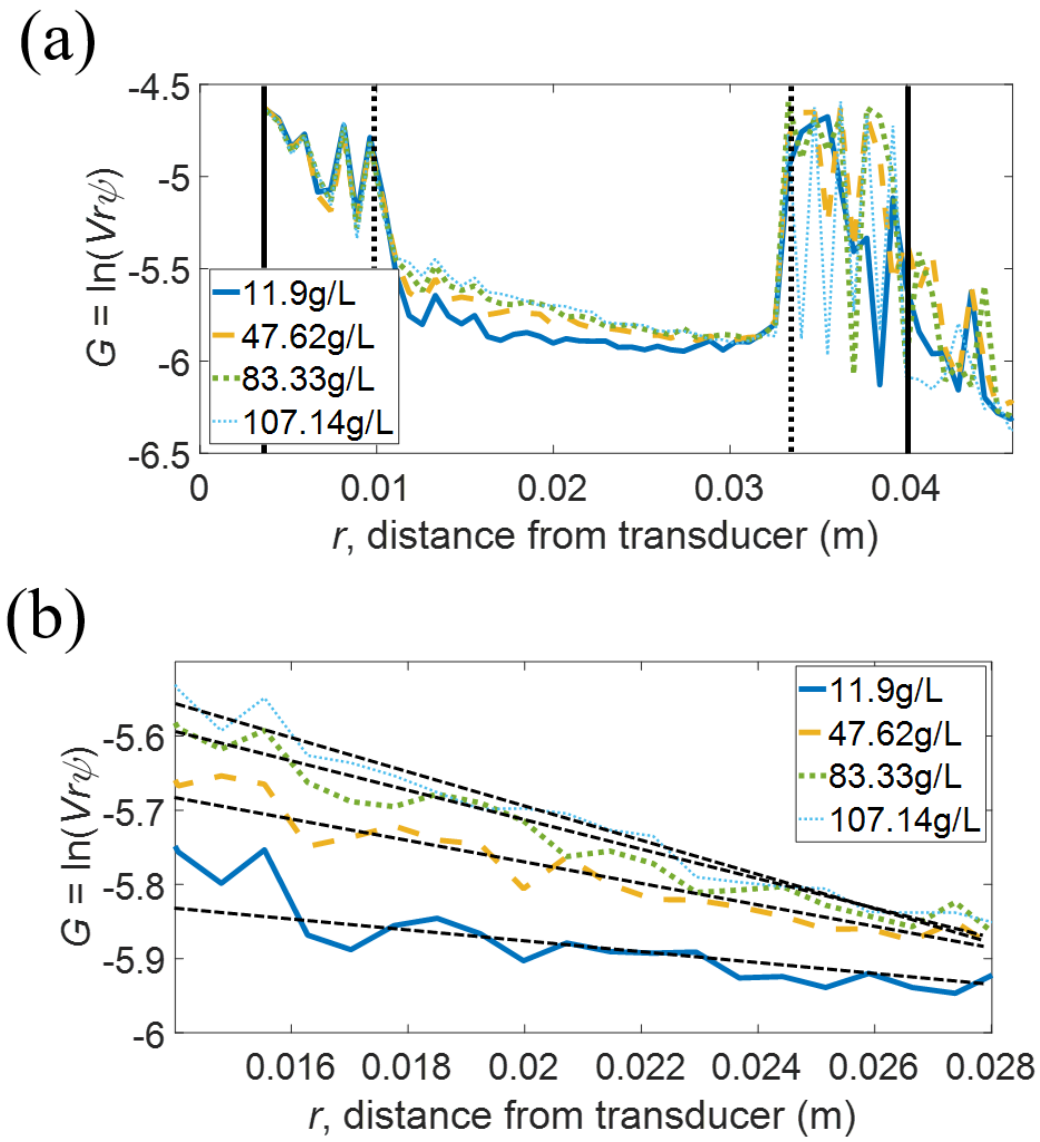

Figure 7.5 (a) G-function versus distance for 36 µm glass at varying concentrations in a horizontal arrangement and (b) Isolation of linear region in (a). Vertical lines in (a) indicate pipe boundaries and dashed lines in (b) are linear fits of profiles

To use the profile data more accurately for calibration purposes, a section between 0.014-0.028 m was selected to take the linear gradient (d*G*/d*r*) values, as this zone gave consistent profiles outside of the nearfield region but was before scattering interference from the far inner pipe wall. The profiles in this region are expanded in Fig. 7.5 (b), where the decay trendlines are shown. The profiles are approximately linear in this region (as would be expected for a largely constant

concentration, from Eqs. (3.05-3.06)), although there is some degree of elevated noise in the averaged signal. The signals show a slight curvature till 0.016 m in 7.5 (b) which is attributed to gravitational segregation in the pipe. The signal will skew in the clear water region and the high solid region. The relatively low signal to noise ratio may indicate that the horizontal pipe orientation enhances suspension segregation in the pipe (Rice *et al*., 2015). The smaller glass beads also have a limited backscatter response due to the decreased particle size, therefore, the noise in the profiles can also be attributed to the limitations of the UVP when analysing a limited backscatter response. The Reynolds number in the pipe is approximately 21,913 as shown in Table 3.7 where it is expected that the flow is turbulent. It has been shown by Dutta *et al.*, (2016) that when the flow travels through a pipe bend, the radial pressure gradient from the centrifugal force on the fluid may lead to flow separation. It was found by Dutta *et al*., (2016) that at higher Reynolds number, the separation points for the fluid moved towards the upstream which could account for the segregation of flow. From the high Reynolds number, it is expected that the fluid should be fully suspended, however, the short entry length from the 90° pipe bend could have affected the fluid segregation. Nevertheless, sedimentation attenuation gradients extracted by the dashed lines indicated the higher particle concentrations lead to increased attenuation, from increased dG/dr values which is evidenced in Chapters 4-6.

Fig. 7.6 (a) similarly shows the acoustic profiles for small glass bead suspensions travelling through a vertical pipe arrangement, while again Fig. 7.6 (b) presents a highlighted region used to extract the linear attenuation profiles for calibration. As with the horizontal arrangement, signals from the initial 0.005-0.008 m region are ignored, as they are within the pipe wall, where there is additional signal noise within the first 0.012 m from nearfield interference.

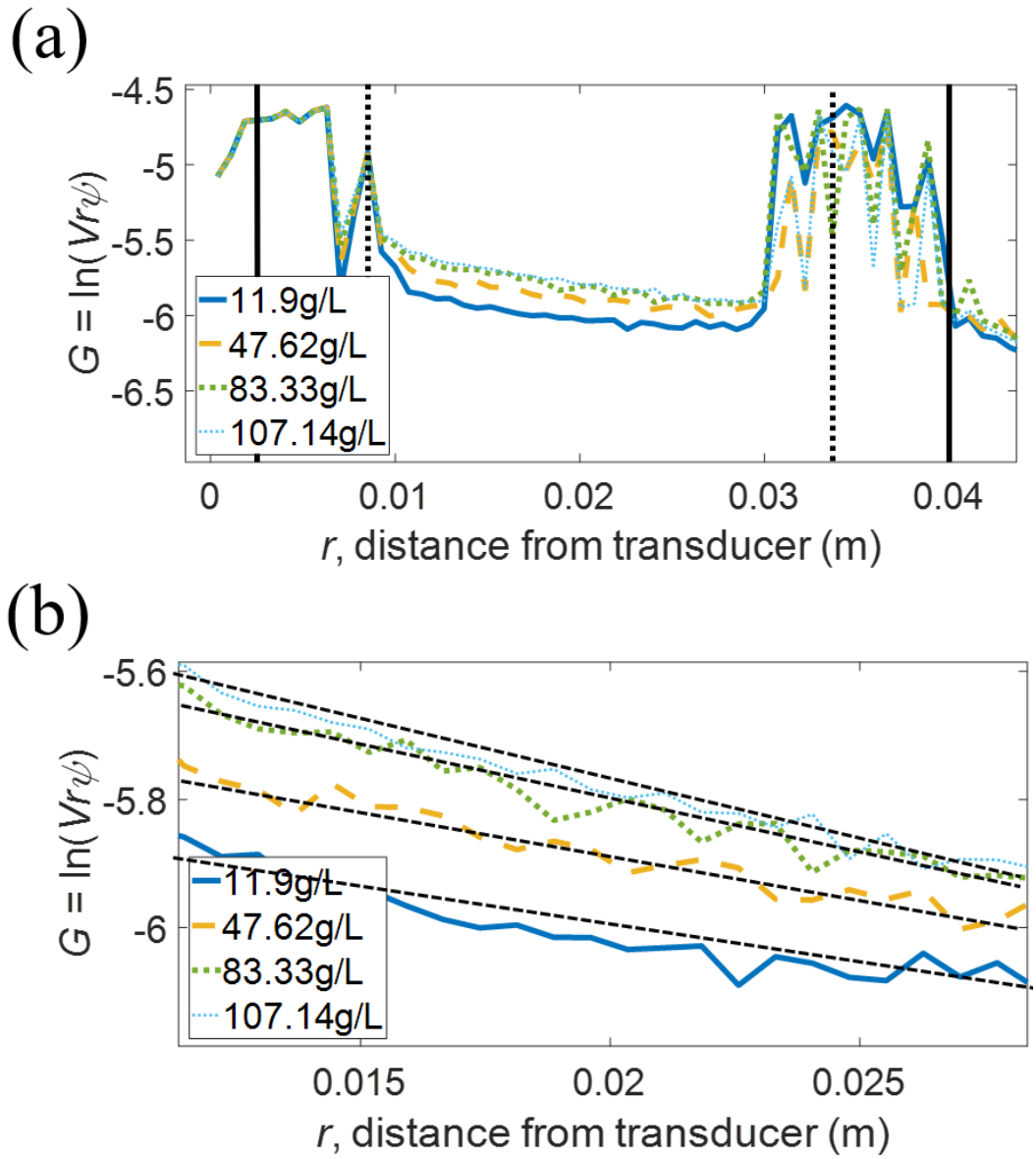

Figure 7.6 (a) G-function versus distance for 36 µm glass at varying concentrations in a vertical arrangement and (b) Isolation of the linear region in (a). Vertical lines in (a) indicate estimated pipe boundaries and dashed lines in (b) are linear fits of profiles

The profiles show a more linear profile across the isolated region in Fig. 7.6 (b) which is attributed to the gravitational segregation in the horizontal pipe. The profiles in Fig. 7.5 (b) show curvature in the first half of the profile. As there would not be any gravitational segregation across the pipe in the vertical

arrangement, the improved linearity in the profiles further indicates that suspension segregation within the horizontal pipe led to a limited linear region for analysis. The signal to noise ratio for both pipe orientations are similar which shows that the transducer signal was not affected by the pipe orientation. Interestingly, both pipe orientation profiles have a similar range of *G*-function values (approximately -5.5 to -6 in the suspension region) which shows that the signal strength of the transducers was consistent for both pipe orientations, as it is dominated by the relatively low backscatter from the smaller glass particles.

The acoustic profiles extracted from glass bead suspensions with a d_{50} of 82 μm travelling through the horizontal and vertical pipe arrangements are shown in Fig. 7.7 and 7.8 respectively. The same general features are present, as with the 36 μm glass, with the profiles from the first 0.012 m being ignored, due to the internal reflections from the pipe wall and nearfield interference from the initial suspension zone. Again, the level of signal noise from the averaged profiles was higher for the horizontal arrangement where there is curvature in the clear water and high solid region. Here, it was especially evident with the lowest 11.9 g/L concentration, where the delay within the suspension deviated from a linear trend expected from a homogeneous concentration, inferring even higher levels of segregation due to the larger particle size. Indeed, the deviation in the expected linear signal decay meant that a smaller region in the far side of the pipe was taken to obtain average d*G*/d*r* values for the horizontal arrangement (from 0.018–0.029 m) as shown in Fig. 7.7 (b). For the vertical arrangement, a larger section from 0.01–0.029 m (Fig. 7.8 (b)) was taken to gain average linear gradient values for the calculation of attenuation coefficients.

The isolated linear regions shown in Fig. 7.5 (b), 7.6 (b), 7.7 (b) and 7.8 (b) were utilised to extract the gradients (d*G*/d*r*) at each concentration. These gradients were then plotted against their corresponding concentration values to produce an attenuation profile, where Fig. 7.9 (a) and (b) present the profiles for the 36 μm and 82 μm glass suspensions, respectively (with horizontal and vertical arrangements being directly compared). The dashed linear trendlines in these

figures are used to directly calculate the concentration independent attenuation coefficients (using Eq. (3.06)) where for both particle sizes, the vertical pipe arrangement attenuates less (gradient versus concentration is less steep). It is assumed that the higher attenuation in the horizontal arrangement may be again from suspension segregation which invalidates the use of the horizontal arrangement for acoustic profiling.

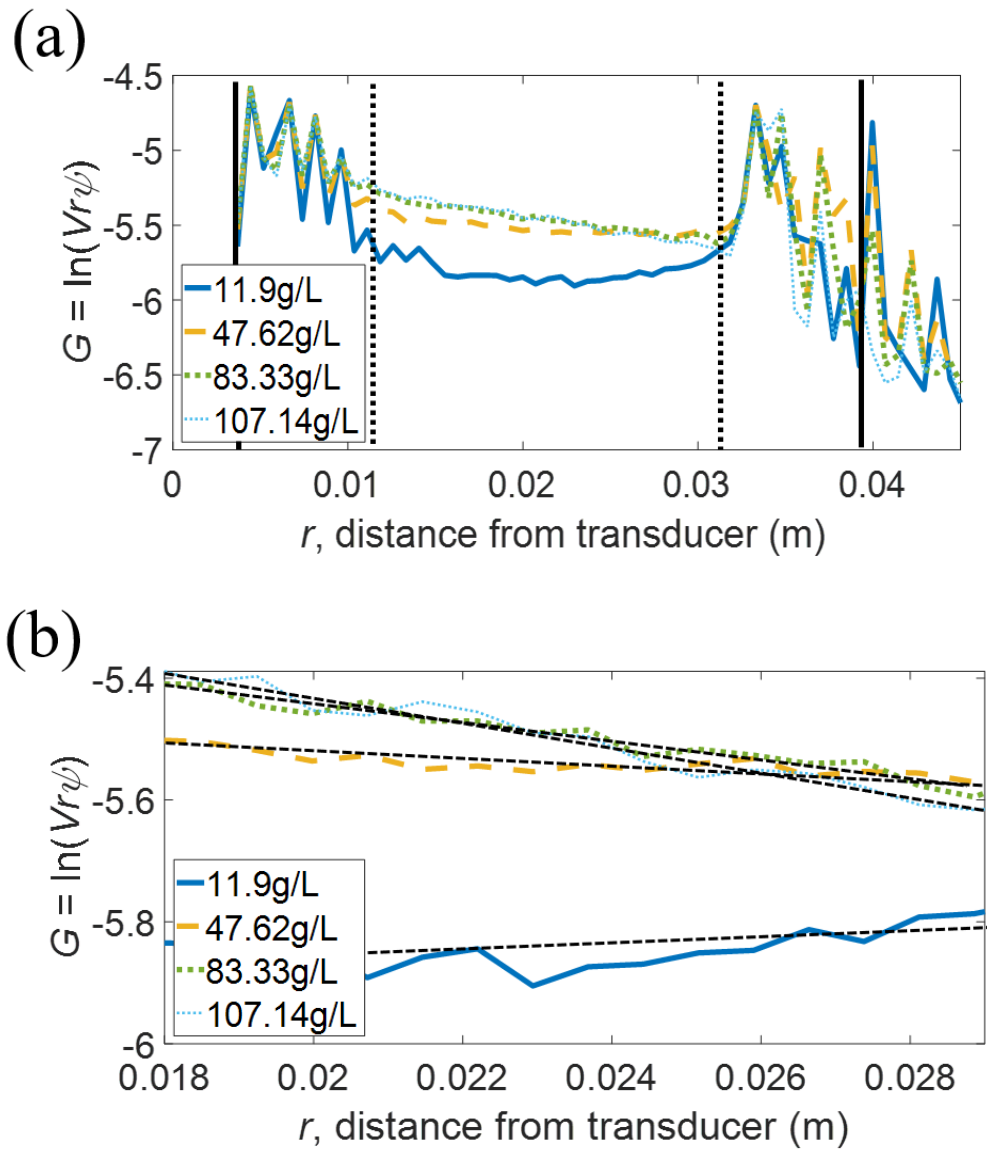

Figure 7.7 G-function versus distance for glass beads with an 82 μm d_{50} at varying concentrations in a horizontal arrangement and (b) Isolation of the linear region in (a). Vertical lines in (a) indicate estimated pipe boundaries and dashed lines in (b) are linear fits of profiles

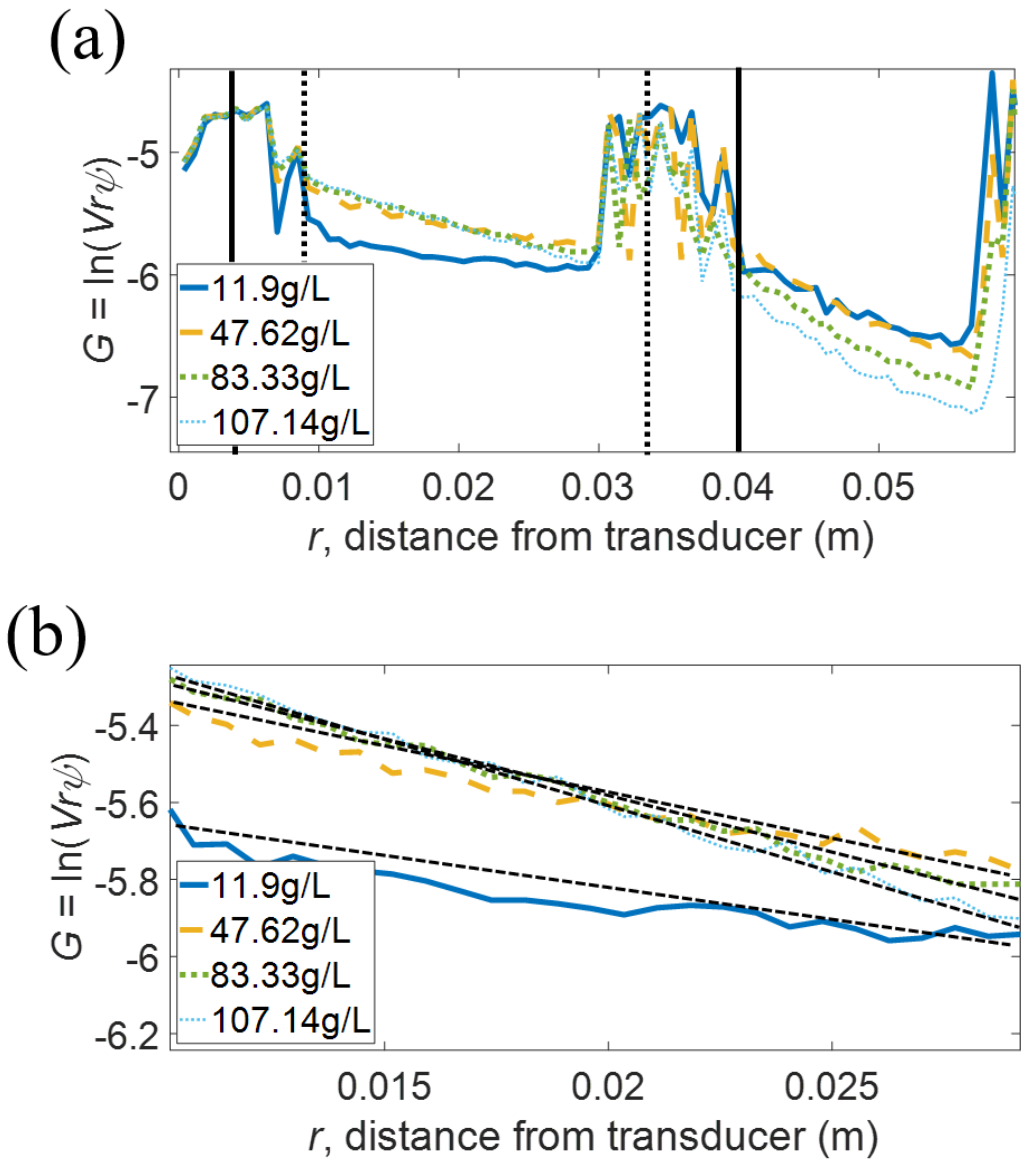

Figure 7.8 G-function versus distance for glass beads with an 82 μm d_{50} at varying concentrations in a vertical arrangement and (b) Isolation of the linear region in (a). Vertical lines in (a) indicate estimated pipe boundaries and dashed lines in (b) are linear fits of profiles

As the isolated linear suspension region was towards the bottom of the horizontal pipe, any segregation may increase the relative concentrations as they become depleted from the top of the pipe. Such an increase in relative concentration would lead to higher relative attenuation, as the actual concentrations in the measurement

zone may be greater than assumed from the added particle levels.

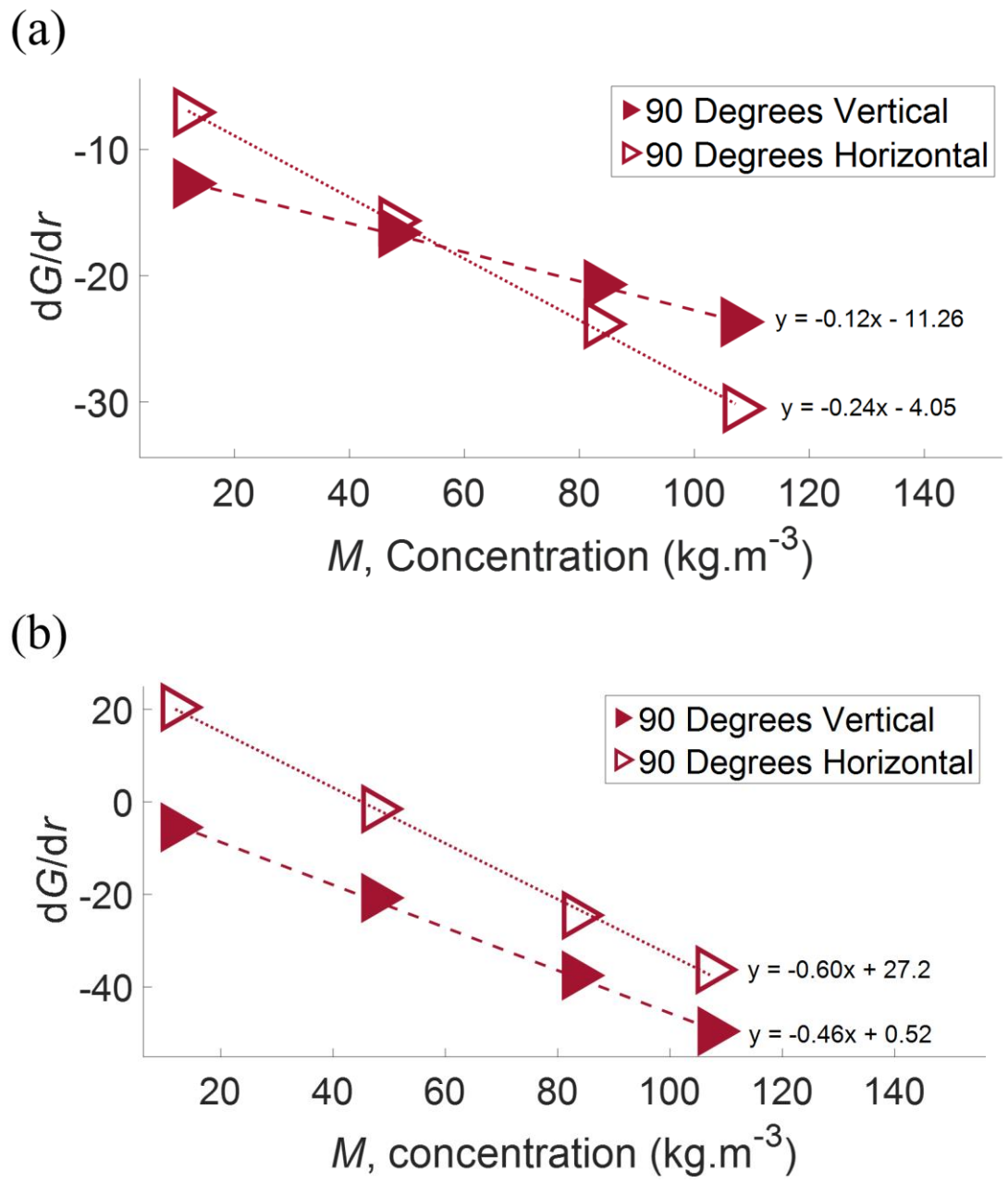

Figure 7.9 Change in G-function with distance with a concentration array ranging from 0-107 g/L using a silica glass bead medium of d_{50} (a) 36 and (b) 82 µm

Interestingly also, for the 36 µm glass, actual d*G*/d*r* values for both arrangements are relatively similar at lower concentrations, implying a similar backscatter

profile, where differences are extenuated as concentration is increased. For the 82 μm glass, however, dG/dr values are very different for both arrangements across the entire concentration range. Specifically at low concentrations, it is hypothesised that the level of segregation with the large glass is great enough that the backscatter is considerably affected by the depletion of the suspension. The larger glass is slightly underestimated at the higher concentrations which is shown in Chapter 4 for the largest glass size of 170 μm. Given that these correlations require a region of homogenous concentration to accurately estimate suspension attenuation, it is likely therefore that measured attenuation values for the horizontal pipe arrangement may be inaccurate.

7.3.2.2 Sedimentation attenuation coefficient

To directly compare concentration independent attenuation coefficients, values were calculated from the gradients in Fig. 7.9 (a) and (b) using Eq. (3.06), as shown in Fig. 7.10 and Table 7.2. Calibration values extracted from Chapter 5 using the same particle species in a homogenous mixing tank are also shown for direct comparison, where error bars for all systems are calculated from the array of echo data across the 1023 profiles, see Chapter 4, section 4.2.6. Combined theoretical attenuation was determined using heuristic expressions from Betteridge *et al*., (2008) which predicts scattering losses and Urick, (1948) which predicts viscous losses. Both of these predictions were combined to provide a theoretical attenuation that can be compared to the measured attenuation coefficients.

Table 7.2 Sedimentation attenuation coefficients for silica glass beads of varying sizes using a horizontally and vertically placed transducer

Transducer Frequency (MHz)	Silica Glass Bead d_{50}	Sedimentation Attenuation Coefficient ξ^m ($m^2.kg^{-1}$)			Theoretical attenuation using heuristic expressions ξ ($m^2.kg^{-1}$)
		Horizontal Transducer	Vertical Transducer	Calibration Data from Chapter 5, see Table 5.1	
4 MHz	82 µm	0.30	0.23	0.09	0.228
	36 µm	0.12	0.06	0.04	0.063

The coefficient values for the horizontal arrangement in both particle suspensions are much higher than those of the vertical arrangement (which again is assumed to be due to segregation in the pipe leading to an increase in attenuation) where values from the vertical arrangement are closer to the calibration data. This correlation is particularly true for the 36 µm beads, where the overestimation of the horizontal arrangement is considerable. It is also noted that, in line with theoretical expectations, attenuation values for the larger particles are higher, due to the enhanced scattering from the larger particle cross sections as evidenced in Chapters 4 and 5 (Moore *et al*., 2013), (Rice, 2013), (Bux *et al*., 2013). Hence, it is evident that transducers mounted on a vertical pipe arrangement are able to produce accurate acoustic profiles and attenuation coefficients, and thus it is recommended that any future industrial monitoring applications should use vertical mounting configurations. When comparing to the theoretical attenuation, the measured attenuation coefficients from the vertically placed transducer compare very well with minimal difference. This shows that the theoretical expressions were found to produce very accurate predictions of measured attenuation for these two silica glass bead sizes. Coefficients from Chapter 5 were underestimated in comparison to the attenuation coefficients from the vertical transducer, this is because the pipe has a limited area for analysis.

The differences between the data from Chapter 5 (when using the calibration rig) and when using the pipe loop are significant. This could be due to increased attenuation from increased dissipation due to particle drag at higher speeds (Leskovec *et al*., 2020). Attenuation coefficients for varying rig arrangements has not been explored in literature. However, the change in attenuation coefficient should not effect the industrial capability of the system. Provided that the flow rate and pipe diameter can be tested before industrial deployment, calibration coefficients can be used for comparison. The UVP has been shown to produce accurate coefficients in comparison to previous literature. There is a lack of data for suspensions in pipe flow and this leads to a lack of data for comparison.

Sedimentation attenuation coefficients from Guerrero *et al*., (2015) could not be compared as the transducer frequency used was too low (1.2 MHz) in comparison to the 4 MHz transducer used above.

The error bars in Fig. 7.10 are calculated using the error analysis process in Chapter 4 where the error bars for the horizontal attenuation coefficients are larger due to the increased variation of echo amplitude. The lower attenuation coefficients from the calibration rig could be due to increased scattering in the smaller pipe loop width which leads to increased attenuation in the pipe. As shown below in Table 7.10, the theoretical expression compared very well to the vertical measured data. This shows that the vertical pipe loop orientation was able to provide accurate attenuation coefficients which compared very well to theoretical predictions.

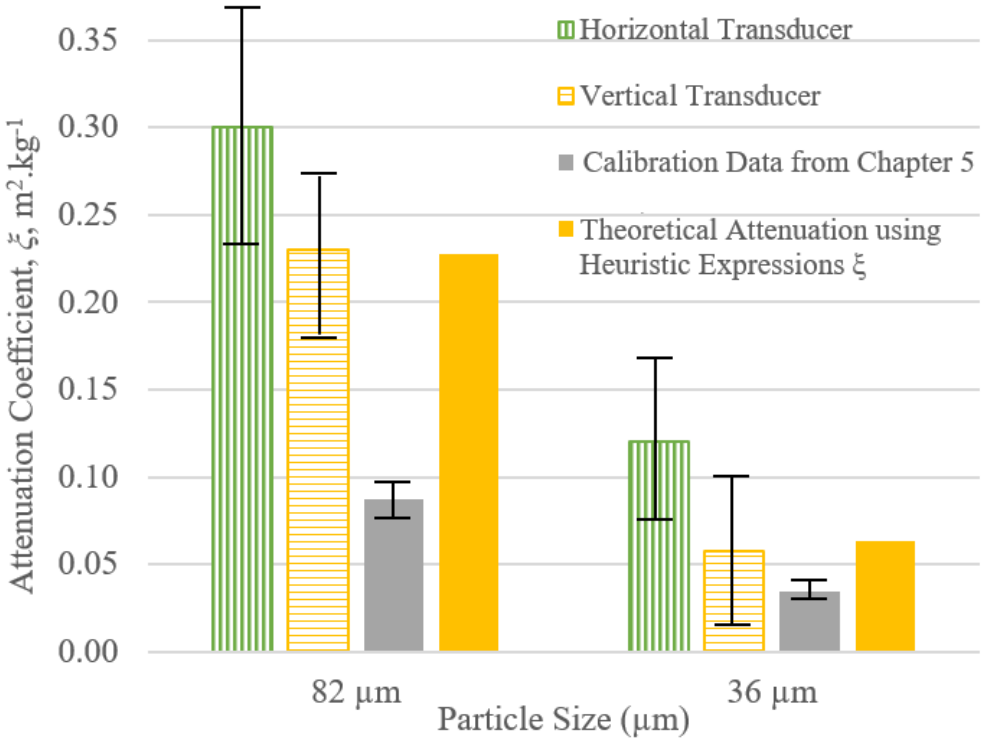

Figure 7.10 Sedimentation attenuation coefficients for silica glass beads using a vertical and horizontally placed transducer

The measured *in situ* values for the calibrated data in Chapter 5 for the 82 µm glass was underestimated, this is likely due to taking concentration measurements over too large a concentration range. This may also be that in the restricted pipe loop environment, these effects are mitigated somewhat as the attenuation is taken over a very small distance with respect to the distance in Chapters 4-6. The pipeline data here fits much better to the combined theoretical estimate which incorporates scattering losses from Betteridge *et al.*, (2008) and viscous losses from Urick, (1948).

7.3.2.3 Normalised Scattering Cross Section

The normalised scattering cross section (χ) shown in Fig. 7.11 was calculated using the sedimentation attenuation coefficients from Fig. 7.10 and Eq. (3.09). The Betteridge *et al.*, (2008) prediction was calculated using the heuristic

expression in Eq. (3.07). The 36 and 82 μm measured cross section values are underpredicted by the Betteridge *et al*., (2008) function with the larger of the glass species aligning better. In both glass species, the vertical cross section values are lower than the horizontal due to the lower attenuation coefficient. When taking into consideration the viscous losses in Eq. (3.11-3.14), a new prediction is shown by the red dashed lines which shows the vertical measured cross section values align much better to the heuristic expression.

A 3.75 and 4.25 MHz frequency were input into Eq. (3.07) to understand how the frequency of the transducer effects the normalised cross section values. A lower frequency leads to lower ka and χ values, and vice versa for a higher frequency. When comparing to combined viscous and attenuation models, the inline UVP data achieves a remarkable level of consistency with these two particle sizes. This is despite the very restricted acoustic volume in the pipeline as the inner pipe diameter is only 2.5 cm wide. This clear result demonstrates very good audio connection using the novel mounting arrangement (with the addition of acoustic couplant) where, there is now a high level of confidence of potential direct application of these mount systems to industrial pipeline movements. This concentration and size data was taken simultaneously with the velocity profiling which shows that the UVP could be used as a 'complete' slurry monitoring system. This work can be adapted to other pipeline materials where the limitations of this technique on other pipes can be explored.

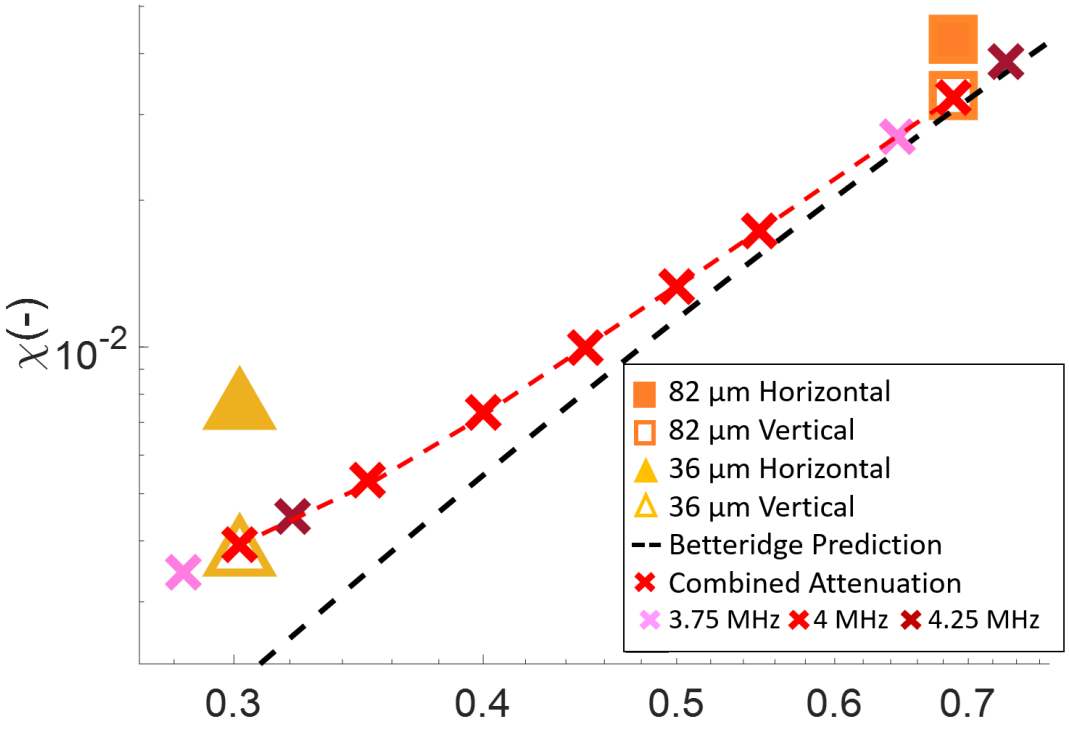

Figure 7.11 Normalised scattering cross function for silica glass beads from vertical and horizontal probes in comparison to the Betteridge et al., (2008) prediction in the black dashed line and the Betteridge prediction with consideration of viscous losses in the red dashed line

7.4 Conclusion

Presented in Chapter 7 is an investigation into the characterisation of slurry pipe flows with acoustic backscatter, using a commercial ultrasonic velocity profiler. A bespoke pipe loop system was utilised to understand the attenuation of 36 and 82 µm glass bead suspensions in horizontally and vertically mounted transducer holders, where the vertical pipe orientation was found to provide the most accurate attenuation and velocity profiles. The larger 82 µm glass bead suspensions were found to attenuate more due to an increased rate of scattering from the larger cross-sectional area with both pipe configurations. When comparing pipe orientations, the horizontal arrangement was found to enhance attenuation producing higher coefficient values, which was likely caused by suspension segregation. This effect was especially evident with the larger glass. In

comparison, attenuation coefficients from the vertical pipes correlated very closely to previous calibration values for both particle species. Simultaneous velocity profile measurement using the Doppler effect was also achieved, where, in general, profiles were as expected for highly turbulent flow.

This Chapter proves that the UVP ultrasonic transducers can be mounted in-line and non-invasively to provide real time data analysis of echo and velocity data. Velocity profiles were found to compare very well to measured profiles for varying concentrations and particle sizes on homogeneous silica glass bead suspensions. Whilst echo amplitude data was able to provide accurate sedimentation attenuation coefficients which provided normalised scattering cross section values that compare very well to predicted viscous attenuation values using expressions from Betteridge *et al*., (2008) and Urick, (1948). The predicted combined attenuation compares very well to measured attenuation values which shows the accuracy of this technique to acoustic models.

8. FLOCCULATION OF MINERAL SUSPENSIONS IN VERTICAL PIPELOOP ARRANGEMENTS

CHAPTER SUMMARY

In this Chapter, flocculated and non-flocculated mineral suspensions were analysed using transducers mounted on vertical pipe lengths to simultaneously extract the echo amplitude and velocity data. The echo amplitude and velocity were used to determine the sedimentation attenuation coefficient and velocity profiles. Rice *et al*., (2020) determined velocity profiles from non-flocculated suspensions of calcium carbonate and magnesium hydroxide using a mixing tank, here, both non-flocculated and flocculated suspension of both species was analysed, and sedimentation attenuation coefficients were extracted simultaneously with velocity data, this is an entirely novel approach.

8.1 INTRODUCTION

In Chapter 6 polymer flocculants were used to monitor flocculation of complex mineral suspensions in a calibration rig. In this Chapter, the same process has been conducted in a pipe loop to understand whether the UVP is able to monitor flocculation in-line. Thorne *et al*., (2014) and MacDonald *et al*., (2013) were able to measure acoustic scattering from suspensions of flocculating sediments. The author has found that acoustics have not yet been used to monitor flocculation in-line, however, acoustics have been used to monitor monodisperse suspensions in-line. This is discussed in detail in Chapter 7 where the pipe loop was first used for analysis of homogeneous suspensions of silica glass beads. Other particle sizing instruments have been used for monitoring flocculation. For example, Heath *et al*., (2006) used a Lasentec® FBRM to monitor the particle size of calcite particles flocculated with a high molecular weight polymer flocculant. A feed suspension storage tank was fed into a pump and flocculant was dosed into the tank at several dosing points. Transparent acrylic pipe was used with a 0.024 m internal diameter. This is directly comparable to the internal pipe diameter of the rig used in Chapters 7 and 8 (0.025 m). Various floc doses were used and the size

of flocs was estimated using the FBRM where it was found that the aggregate size increased as a function of the flocculant dose. The aggregate diameter increases from ~ 5 to 120 μm with a flocculant dose of 20 ppm which is the same dosage used in Chapter 6 (Heath *et al*., 2006). The pipe was suspended in a horizontal arrangement where the FBRM probe was inserted into the tank through a port facing the flow. In Chapter 7 it was found that horizontal probes promoted segregation in the pipe and therefore, a vertical pipe arrangement was used in this Chapter. Owen *et al*., (2008) also used a linear Perspex pipe reactor with an FBRM inserted *in situ* which was used to monitor the particle size in-line and in real time. Owen *et al*., (2008) also used an FDA (Floc density analyser) where samples were taken from the pipe for *ex situ* measurements of particle size, shape, density and settling velocity. Calcite was also used by Owen *et al*., (2008) and Benn *et al*., (2018) where a larger primary particle size was found (11.7 μm). Benn *et al*., (2018) built on this research by conducting column profiling and taking particle size measurements using a Mastersizer 2000.

Other methods have been used to monitor flocculation, Huang and Chen, (1995) used fibre-optics to monitor the fluctuating light intensity from a flowing suspension. Huang and Chen, (1995) used a photometric dispersion analyser (PDA) to monitor flocculation where particle aggregation can be indicated by a ratio value from the PDA. A PDA analyses flowing suspensions and emulsions whereby the flowing suspension is illuminated by a narrow beam of light perpendicular to the direction of flow. Optical fibres carry the incident and transmitted light. Transmitted light is continuously monitored by a photodiode which outputs a voltage (McFarlane *et al*., 2017). The output of the PDA accurately reflected the formation of the floc however, the results are complex to analyse and limited quantitative information can be extracted (Huang and Chen, 1995).

Chapter 7 shows that acoustics can be used to monitor suspension flow in pipes whilst Chapter 6 shows the UVP can be utilised to monitor flocculation, therefore, the UVP can theoretically be utilised to monitor flocculation in-line.

8.2 Materials and Methods

8.2.1 Materials

The complex mineral suspensions used in this Chapter were calcium carbonate and magnesium hydroxide, which were the same materials used in Chapter 6. SEM images of the species are shown in Fig. 6.1 where both species were differentiated based on the presence of fines in calcite and larger aggregates in magnesium hydroxide.

8.2.2 Methods

The final development stage in the pipe loop is the addition of a port for a Lasentec® Focused Beam Reflectance Measurement (FBRM) model PI-14/206 (Mettler-Toledo) on the vertical section of the pipe. From the previous rig set-up, it was shown that the horizontal orientation produced results which increased in attenuation over time. This is likely attributed to the fact that the horizontal pipe arrangement promotes settling in the pipe, causing blockages, and limits the movement of the suspension through the pipe. Much like Chapter 7, the transducer mounted at 90° was used to extract echo amplitude data. The transducer mounted at 135° was used to extract velocity data. The probe mounting units are shown in Chapter 7.

The entry lengths of the horizontal and vertical pipe arrangements are 1.3 and 2.1 m, this was due to the limitations of the pipe loop lengths where these were the maximum entry lengths available. Chapter 3 shows how the minimum entry length required for fully developed flow was calculated, both methods for calculating the minimum entry length had varying lengths for a range of pump speeds used in experiments. Method 1 (see Chapter 3.3.1 and Table 3.8) which used the Reynolds number produced a minimum entry length of 0.58 m whilst the second method which used the Darcy friction factor led to a minimum entry length of 1.28 m (see Chapter 3.3.2 and Table 3.8). The actual entry length for the horizontal pipe arrangement is 1.3 m which is just slightly above the minimum entry length of 1.28 m. Therefore, the vertical pipe section will be used for

analysis to ensure that the flow is fully developed. Two 4 MHz transducers will be utilised, mounted at 90° and 135° to the flow. The probe mounted at 90° will be used to extract echo amplitude data and the probe at 135° was used for extraction of velocity data, this was shown in Chapter 7. A single flowrate was used for experiments, where the speed of the pump was 1131 rpm and the Reynolds number (Re) was 21, 913.

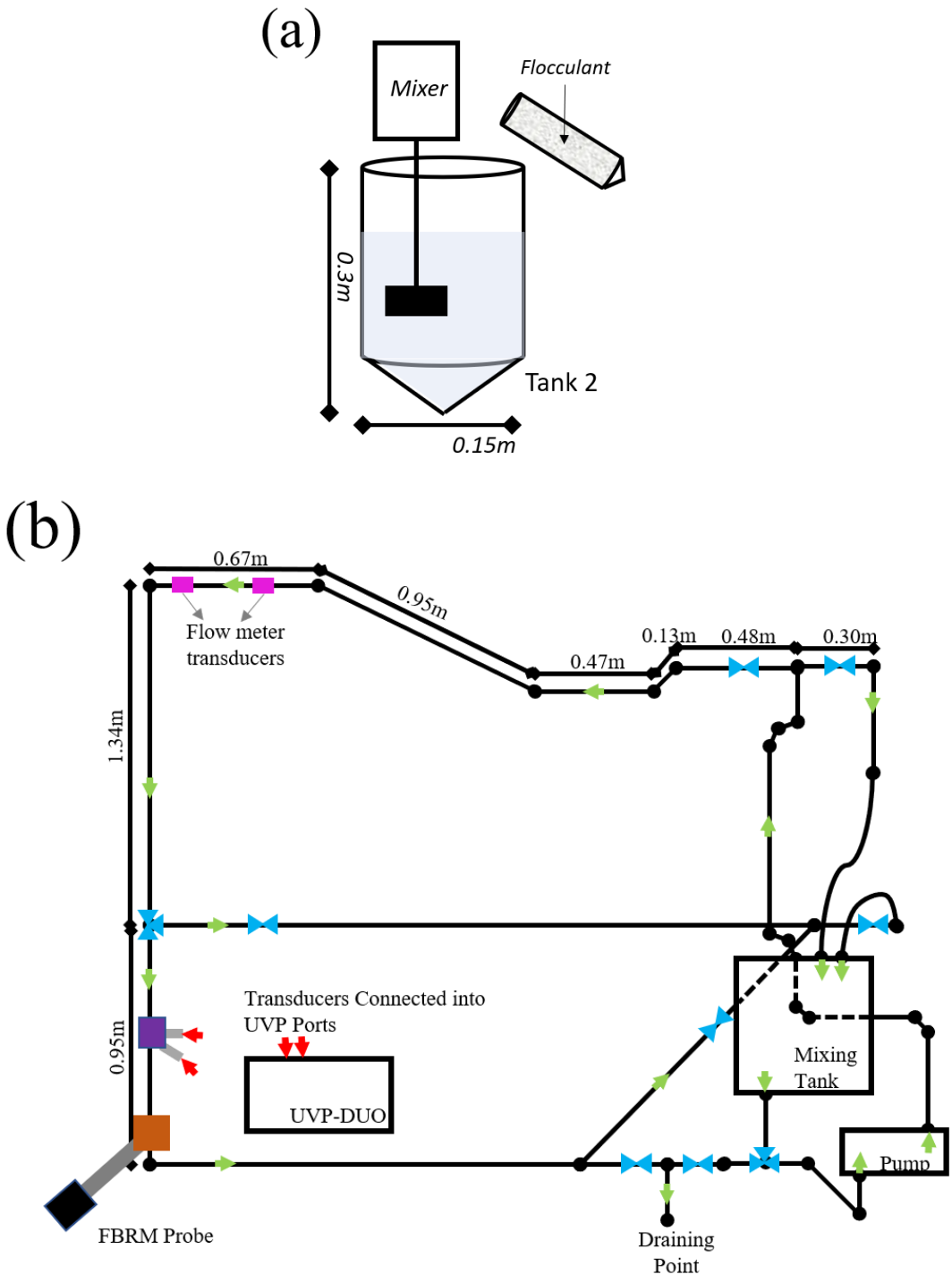

Figure 8.1 Schematic of engineered pipe loop for remote analysis of suspensions in a vertically mounted probe at 90 and 135° to the flow with an FBRM port and flow meter for monitoring

Much like Chapter 6.1, mineral suspensions were utilised with this complex pipe loop set-up. This is to demonstrate the versatility of this process and the ability of the UVP to analyse mineral suspensions in flow. On the right in Fig 8.1 (b) is the mixing tank which was used to disperse the complex mineral suspensions. The tank was filled with ~42 L water and the pump and mixer were maintained at a speed of 1131 and 750 RPM, respectively. The valves required for the vertical loop were then opened, and the suspension ran from the pump, up to the T junction, left through the flow meter and down the vertical testing section. The first mineral suspension was added to the tank to produce a concentration of 3.38 g/L within the loop. A time period of 5 mins was given to allow the suspension to disperse homogeneously through the loop. Two transducers were used with a measurement time of 60 ms and a time delay of 100 ms. The measurement time per profile is 220 ms which leads to a total measurement time of 225 seconds across the 1023 profiles.

The UVP was used to analyse the non-flocculated suspension first where echo amplitude and velocity data were extracted from the 90 and 135° probes, respectively. The impeller rate was then lowered from 750 RPM to 300 RPM and the pump was also turned down from 1131 RPM to 750 RPM to prevent shearing of the flocs. The flocculation methodology in Chapter 6.2.2 is utilised here where the flocculant is added to a 1 L aqueous suspension over a rate of 0.1 $g.min^{-1}$ to produce a 1000 ppm stock solution. The same water-soluble anionic polyacrylamide-poly(acrylic acid) copolymer, AN934SH (SNF Ltd) in Chapter 6 was used here to ensure the stock solution was the same. As the pipe loop has a smaller diameter (D = 0.025 m) than the calibration rig (D = 0.3 m) used in Chapters 4-6, the effects of the smaller pipe diameter will have an effect on the expected floc size. The stock solution in Fig 8.1 (a) was added to the mixing tank on the left in Fig. 8.1 (b) and added dropwise down the impeller shaft, this was to ensure the flocculant dispersed across the mixing tank. The flocculant was added until a polymer concentration of 40 ppm existed in the tank. A higher polymer concentration than in the calibration rig in Chapter 6 was needed for flocculation in the pipe loop as the shear of the mixer and pump immediately broke down flocs

at a polymer dose of 20 ppm. After adding the flocculant, the two UVP probes were activated 5 mins after to extract both echo amplitude and velocity data.

The tank was then emptied from the draining point and repeated with a higher concentration of 27.5 g/L. The same process was repeated so the UVP was used to collect data from the non-flocculated mineral suspension and flocculated mineral suspension at 27.5 g/L. The whole process was repeated with another mineral suspension so two species were analysed at two different suspension concentrations. Only two concentrations were specified in this experimental section. A lower concentration of 3.38 g/L and a higher concentration of 27.5 g/L were used for analysis, these concentrations were found to produce an accurate sedimentation attenuation coefficient in Chapter 6. Two experiments were conducted, one experiments was run with the 3.38 g/L concentration and a separate experimental run with 27.5 g/L concentration. In both experiments the same polymer dose was used. In Chapter 6, a dilution method was used where the tank was emptied by 50% and diluted with 50% water, however, in the pipe loop, the suspension would need to be drained at the drainage point and then refilled in the mixing tank. The floc sizes were stable with dilution in the calibration rig, however, for the pipe loop, the shear of the pump and mixer meant that flocs were less stable and would likely break down through the dilution procedure. The mixing tank cannot be emptied by 50% as the bulk of the suspension is in the pipe, where emptying the tank by 50% could lead to the pump running dry and causing air entrainment.

The FBRM port on the bottom left of the pipe rig in Fig. 8.1 (b) is inserted much like the *in situ* probes in Chapters 4 and 5 where the FBRM probe is in direct contact with the suspension. The port is blocked when the FBRM is not in use. The FBRM is utilised to monitor changes in particle size throughout the experiment where the FBRM is inserted facing the flow of the suspension to ensure the probe is able to visualise most particles in flow. The flow of the suspension could prevent fines from settling on the probe window in comparison to the probe placement in Chapter 6 where it was found that fines in the probe

window led to underestimation of the calcium carbonate floc size (Saraka *et al.*, 2019). The FBRM was run at both experiments for the concentrations of 3.38 and 27.5 g/L where an average FBRM profile was shown below.

8.2.3 Flowmeter

A wall mounted ultrasonic flowmeter (Omega Engineering, Model FDT-25W) was installed into the pipe loop on the top left in Fig. 8.1 (b). This flowmeter was only installed after tests in Chapter 7 to give a better correlation for estimated bulk flowrates. The transducers have a water-proof function with a measurement limit of 15-6000 mm pipe diameter (Omega Engineering, 2022). The flow meter measures the fluid velocity of the suspension within a pipe and has two transducers which are non-contacting, and clamp-on which makes the analysis in Fig. 8.1 (b) entirely remote. The transducers function as transmitters and receivers, where the difference between the transit time is directly related to the velocity of the suspension. The W-method was used for installation and is shown below in Fig. 8.2, this method is generally used on pipes with a diameter from 15-50 mm (Omega Engineering, 2022).

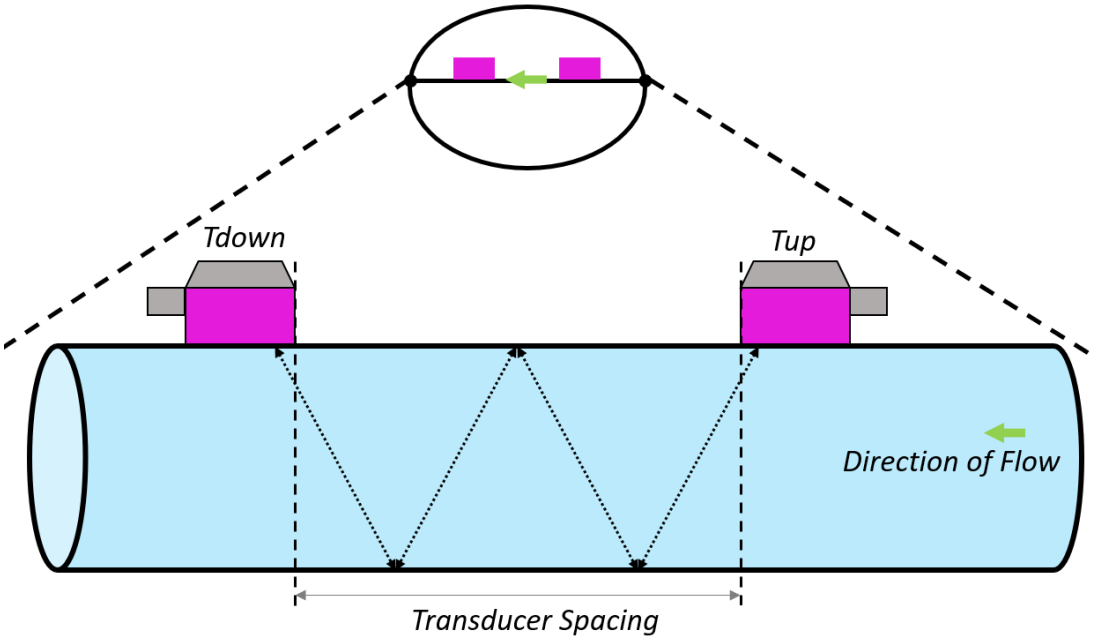

Figure 8.2 FDT-25W wall mounted transducer in W configuration

The velocity, v (m.s^{-1}) was calculated in Eq. (8.01) using the angle to flow direction, θ, the travel time of the ultrasonic beam, M (s), the pipe diameter, D (m). As well as the time for the beam to travel from the upstream to downstream transducer, T_{up} (s) and the time for the beam to travel from the downstream to the upstream, T_{down}, $\Delta T = T_{up} - T_{down}$. The flow meter has a +/- 1 % accuracy error which is shown in Table 3.8 to have a negligible effect on the entry length calculated using derivations from Shames, (2003) and Zagarola and Smits, (1998).

$$v = \frac{MD}{\sin(2\theta)} x \frac{\Delta T}{T_{up}.T_{down}} \tag{8.01}$$

8.2.4 FBRM

Data was collected in real time from the FBRM probe and converted to a cumulative size distribution using the methodology shown in Chapter 6.2.5. Number and square weighted distributions are also shown for comparison, these were calculated in Eqs. (6.10) and (6.12), respectively.

The original raw chord length values were used to determine the particle size of both the non-flocculated and flocculated species. This is because raw chord length values produced accurate particle sizes for the non-flocculated species in Chapter 6. In this Chapter the suspensions were not diluted, instead agitation was used to determine whether the FBRM could monitor the breakup of flocs. The in-line floc size in Chapter 6 was found to be 19 and 29.7 μm for calcium carbonate and magnesium hydroxide, respectively where the polymer dose was 20 ppm. The floc size is expected to be larger due to the increased polymer dose (40 ppm).

8.3 Results and Discussion

8.3.1 FBRM

The FBRM was installed at the bottom left of the loop in Fig. 8.1 (b) below the vertical probe holder for analysis of flocs in-line. The FBRM is mounted *in situ* where the probe window is in direct contact with the suspension. The suspension flows downwards onto the FBRM face so there is a high likelihood that material will flow past the window and limit the settling of fines which will prevent the limitation of the floc size readings. Saraka *et al*., (2019) found that if untreated, the FBRM probe window can become coated which leads to deterioration of data. In this thesis, the probe window was left untreated as the author did not want to risk the integrity of the probe window. The data collected from the non-flocculated and the flocculated mineral suspensions is shown below in Fig. 8.3 as a cumulative distribution of the data. The flocculated data was taken approximately 10 minutes after adding the flocculant where the particle size peaked. The non-flocculated data was taken after the suspension had fully dispersed in the tank.

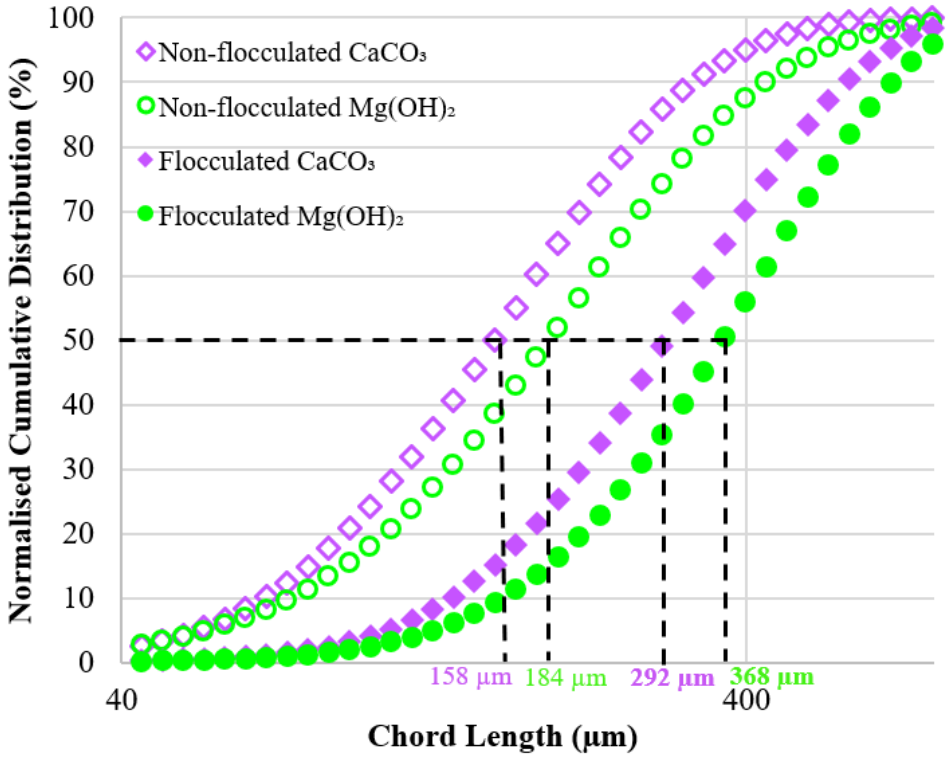

Figure 8.3 Non-weighted chord length distributions for non-flocculated and flocculated suspensions of calcium carbonate and magnesium hydroxide using an FBRM

The non-flocculated calcite and magnesium hydroxide is shown to be 158 and 184 µm whilst in-line values in Chapter 6 were found to be 4.3 and 5.6 µm in Figs. 6.7 and 6.10. The sizes in the rig are significantly larger which can be attributed to a number of things including; the angle the device is inserted, particles may be attached onto the end of the probe leading to false measurements. The FBRM being used in this experiment is an old device which has been used in other experiments, this could have an effect on the reliability of the probe itself (Saraka *et al.*, 2019). The non-flocculated magnesium hydroxide was still shown to be larger due to the presence of fines found in the calcite. However, the particle sizes shown in Fig. 8.3 were more than 36 times the values shown in Fig. 6.8 for the calcite and more than 32 times for the magnesium hydroxide in Fig. 6.11. This is attributed to the lower shear rate within the pipe loop which promotes agglomeration within the suspension. The lower shear rate was maintained to

prevent break-up of the flocs but has also meant the particle sizes are much greater than expected from data in the well-mixed tank in Chapter 6.

When using the well-mixed rig, sizes from the *ex situ* data was found to be comparable in Fig. 6.7 (a) and (b) where the magnesium hydroxide floc sizes were slightly larger. For the suspensions within the pipe loop, the flocculated calcite and magnesium hydroxide were found to have a 76 μm difference where the magnesium hydroxide was larger. This is likely attributed to the presence of aggregates in magnesium hydroxide. Both the flocculating suspensions increase in particle size which was the aim of the flocculation process. The goal of the FBRM was to successfully monitor changes in particle size which has shown to be a success, however, the particle sizes found were not representative of original data in Chapter 6.

The chord length distributions in Fig. 8.3 were converted to number and square weighted distributions in Fig. 8.4 (a) and (b) using Eqs. (6.10) and (6.12), respectively. The average sizes are much larger than in Fig. 8.3 where the weighted distributions led to changes of 100 μm or more. This shows how complex it is to extract data from the FBRM chord length and correlate this to a reliable PSD. The raw chord length distributions were found to be most accurate in Chapter 6, however, the particle sizes for non-flocculated species are significantly larger from in-line particle sizes. Therefore, for ongoing acoustic models, the *ex situ* particle sizes in Fig. 6.7 are used.

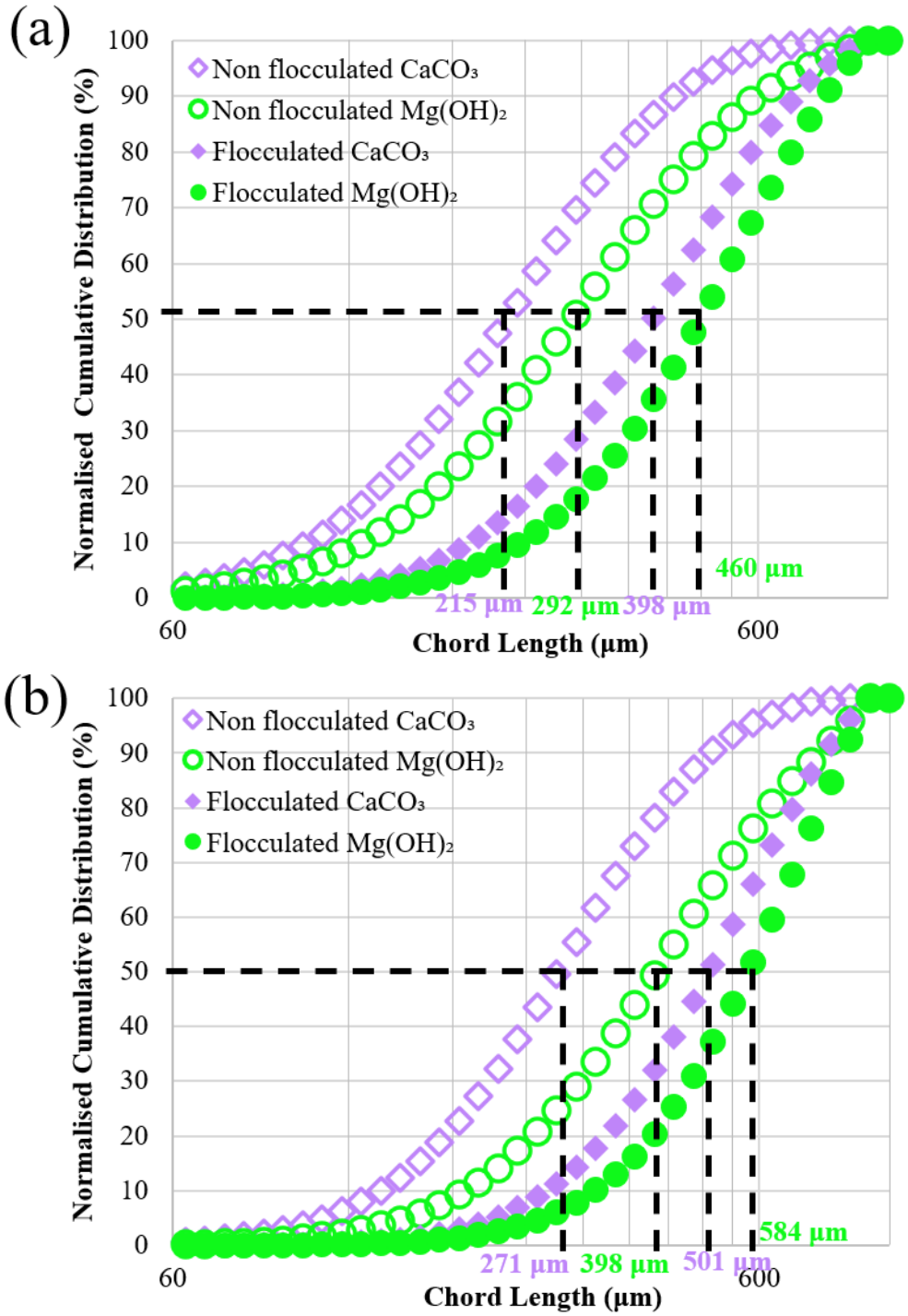

Figure 8.4 (a) Number weighted and (b) square weighted PSDs of non-flocculated and flocculated calcium carbonate and magnesium hydroxide using a FBRM

Fig. 8.5 (a) and (b) show the change in particle size with time for the flocculation of calcite and magnesium hydroxide, respectively. The calcite shows a particle

size of 158 μm before adding the flocculant. Once added, the suspensions take approximately 10 mins to peak in particle size before the flocs begin to break up. Which shows that the pipe loop is not able to provide a stable floc size. The suspension particle size in Figs. 6.9 and 6.11 peaked after 30 mins but were found to be relatively stable. This could be due to the higher polymer dose in the pipe where a higher polymer dose was used because the mixing tank did not show a significant size increase with the lower polymer dose. The calcite particle size in Fig. 8.5 (a) increases from 158 to 292 μm which is a 134 μm increase. In comparison, the magnesium hydroxide flocculation process in Fig. 8.5 (b) shows that the magnesium hydroxide starts at 184 μm and increased by 184 μm to 368 μm. The magnesium hydroxide has a larger increase in particle size in comparison which shows that the magnesium hydroxide is more effected by the flocculation process. This is likely due to the increased non-flocculated particle size which agglomerate to produce larger floc sizes. Table 6.3 also shows that the number of particles in an aggregate was higher for the magnesium hydroxide.

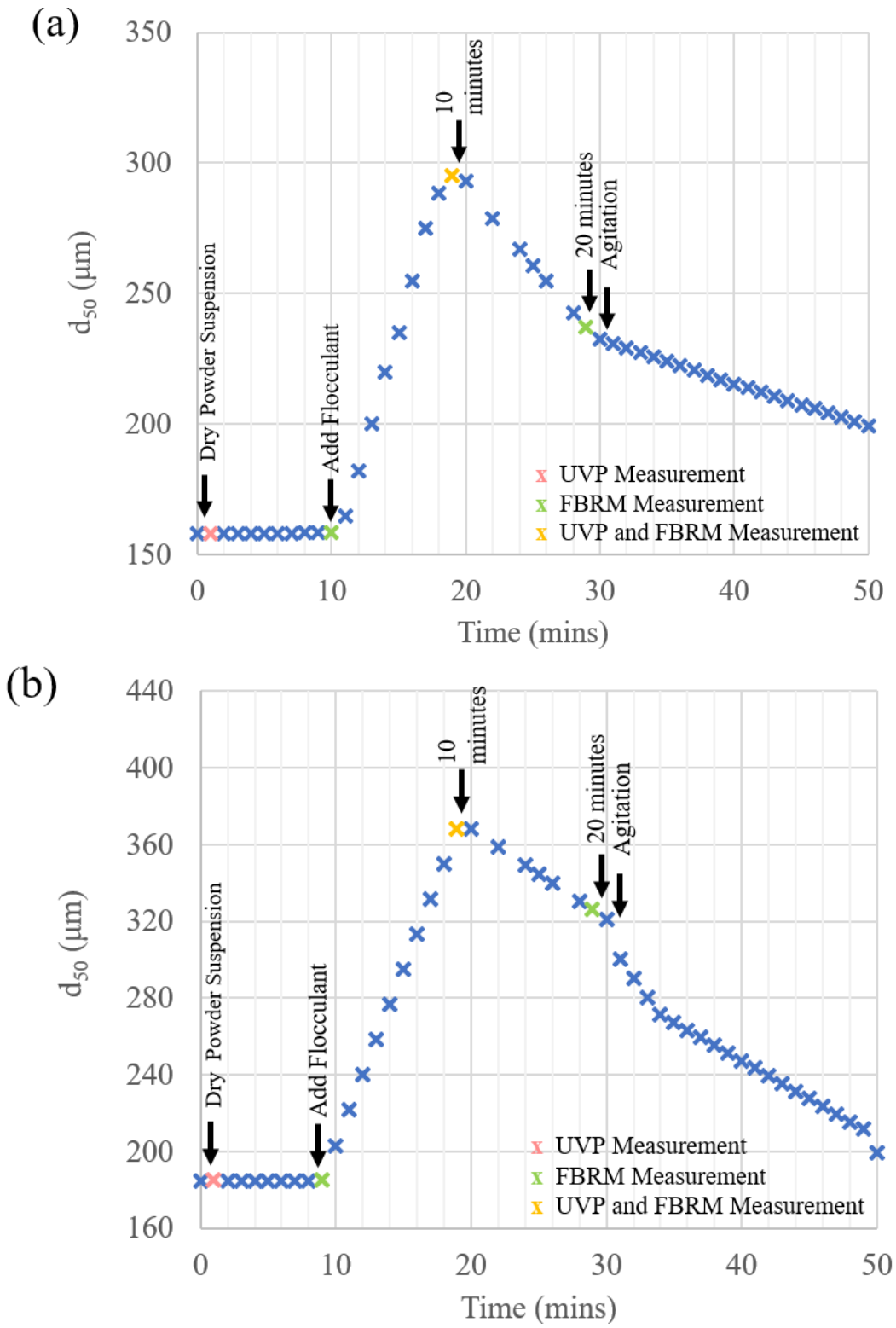

Figure 8.5 d_{50} tracking for flocculation of (a) calcium carbonate and (b) magnesium hydroxide

Fig. 8.6 shows the change in particle size with time where it was found that the flocs peaked in size 10 minutes after adding flocculant. The flocs then started to breakup and the floc size decreased for both species after another 10 minutes. The pipe loop breaks down the aggregates more slowly, in Chapter 6 the flocs became stable over a certain time whilst for the pipe loop, there is no stable size region in pipe flow. This shows that the flocs are less stable in the pipe loop which is likely due to the turbulent flow.

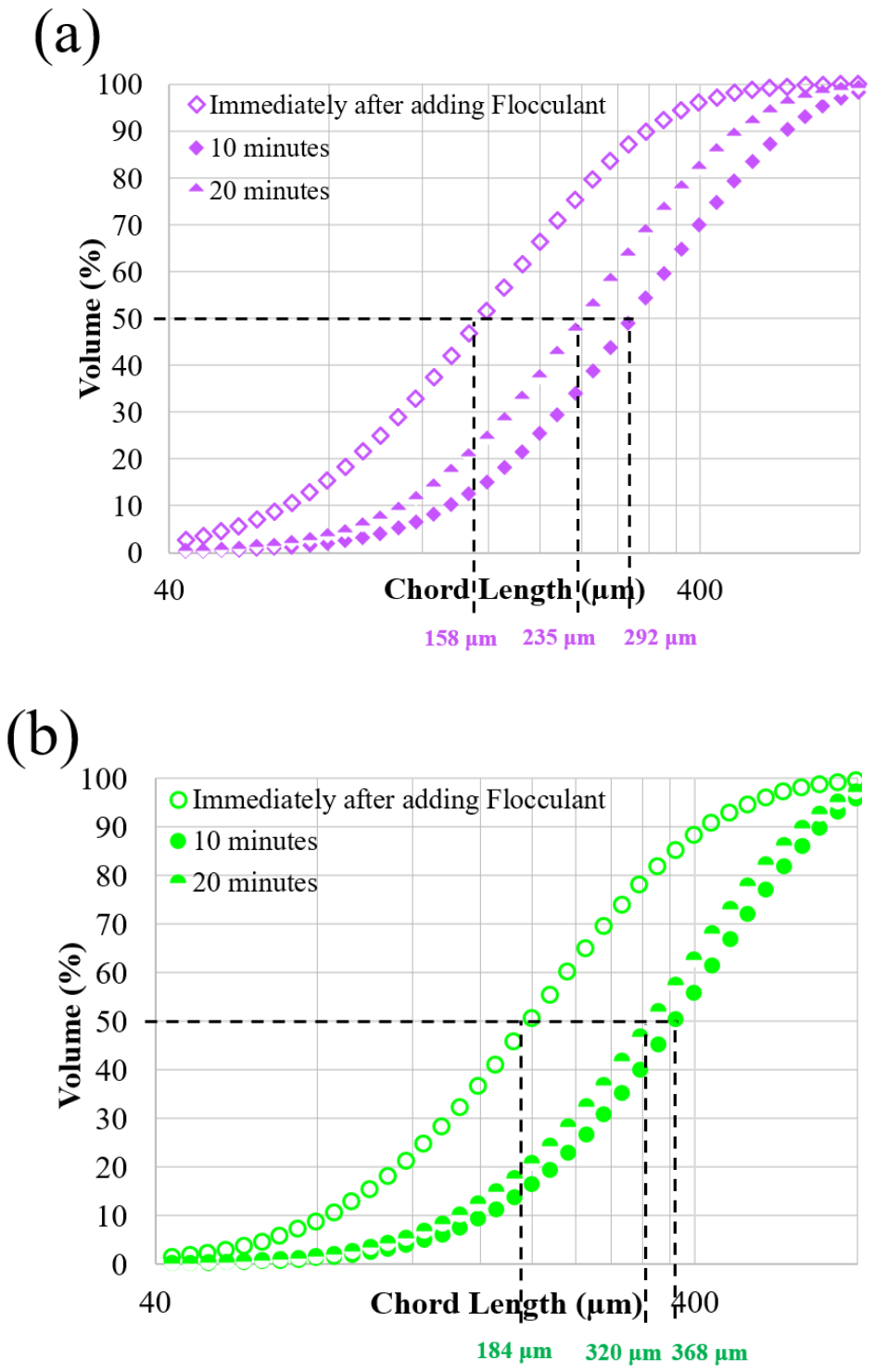

Figure 8.6 Change in particle size with time for flocculating suspensions of a) calcium carbonate and (b) magnesium hydroxide when using volume-based chord length distributions in Fig. 8.3

8.3.2 Velocity Profiling

The velocity profiles are determined using raw velocity values extracted from the transducer mounted at 135°, this is shown in Chapter 7. The transducer analyses the velocity across the pipe with the transducer facing the flow of the suspension. Fig. 8.7 shows profiles for calcite and magnesium hydroxide, respectively. The Reynolds number at this pump speed is shown in Table 3.8 to be 21,913 where the flow is turbulent. This can be used to calculate the expected velocity profile from turbulent flow in a pipe using the power law velocity profile equation. This is shown in Chapter 7 where the Reynolds number is used to determine the velocity ratio. The blue crosses in Fig. 8.7 (a) and (b) show the calculated velocity profile using derivations from Stigler, (2014). The predicted velocity profile aligns very well with the measured velocity profiles in Fig. 8.7(a) and (b). The lower concentration flocculated profile in Fig. 8.7 (a) is overpredicted by the predicted velocity whilst the higher concentration and non-flocculated profiles align very well. The velocity profiles are predicted using the Re whereas in Fig. 8.7 (a), the measured profiles vary with changes in concentrations and particle size. The measured velocity profiles in Fig. 8.7 (b) vary between particle size where the predicted velocity profile does not align with either and instead transgresses across all profiles. It is assumed that the effect of attenuation is as of yet unknown, and this could be the reason for the slight difference in measured and predicted velocity values.

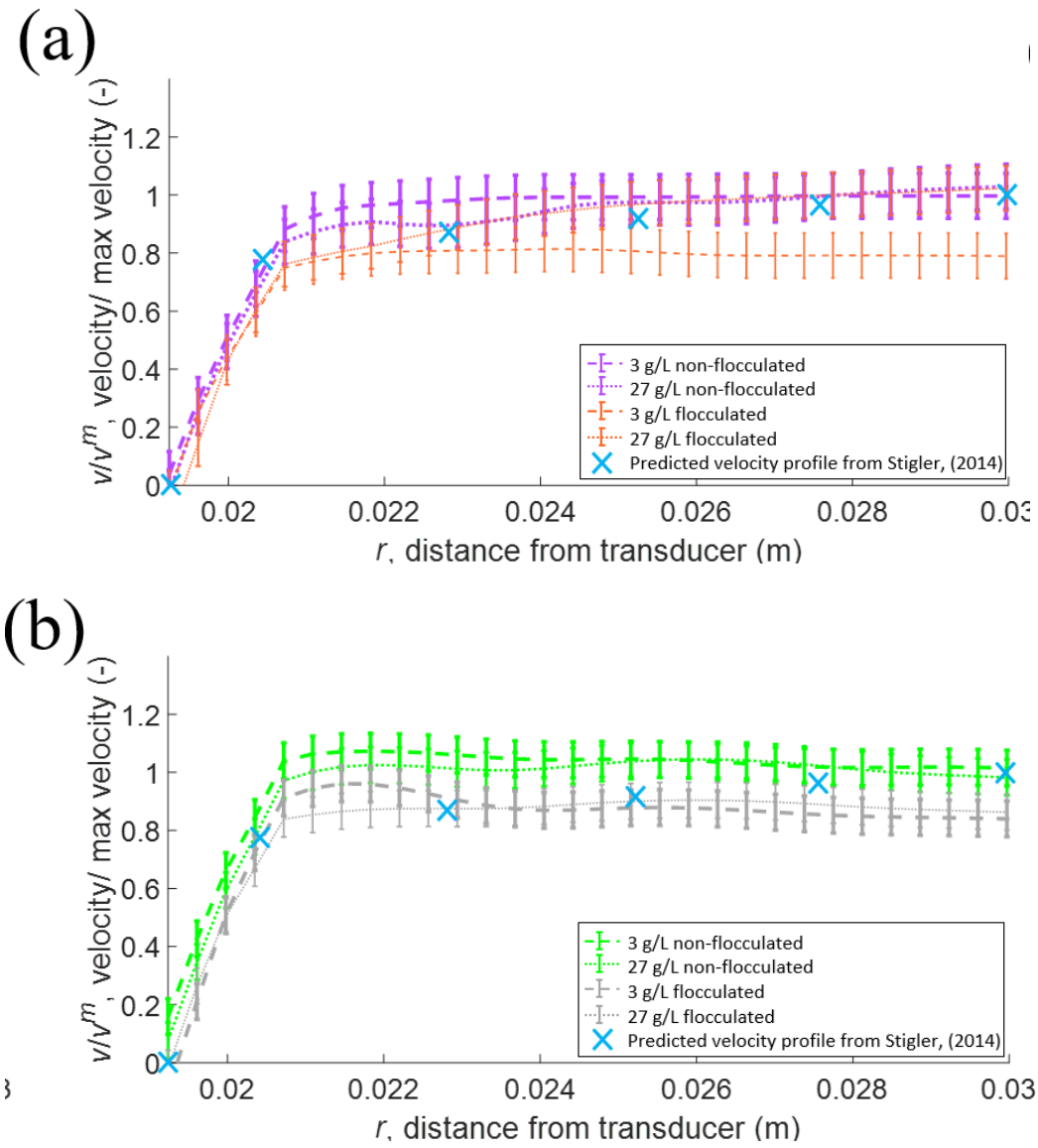

Figure 8.7 Velocity profiles for varying concentrations of non-flocculated and flocculated (a) calcium carbonate and (b) magnesium hydroxide with predicted velocity profiles from Stigler, (2014)

Apart from the 3 g/L flocculated data most profiles are within the expected single-phase profile in experimental variation. In previous literature the influence of particles on turbulence modification have been explored. Harbottle *et al.*, (2011) found that colloidal silica suspensions were sensitive to particle-particle interaction energy. Aggregation of the silica suspensions led to enhanced turbulence at lower *Re*, however at the experimental *Re* (21, 913) the fluid shear is

sufficient to cause breakup of the aggregated which leads to reduced micro-hydrodynamic disturbances and a reduction in turbulence. This effect of turbulence modification from particles is not accounted for in the predicted velocity profiles and this could have caused in the differences between the theoretical estimates.

The profiles in Fig. 8.7 (a) show that the higher concentrations have the highest peak velocity in the pipe. The density of the suspension increases with an increase in concentration as shown in Tables 3.3 and 3.4 which in unexpected as Eq. (3.16) shows that an increase in density leads to a decrease in speed of sound. This could be explained by the effect of attenuation on velocity. The lower concentration attenuates less than the higher concentration suspensions and has a lower peak velocity whilst the flocculated 3 g/L suspensions attenuate the least. This is shown in Fig. 8.7 (b) where the non-flocculated suspensions show a greater peak velocity than the flocculated, however, the individual concentration values do not show a significant difference. The measured velocity values are shown below in Table 8.1 with the conversion to the velocity in direction of flow. This is detailed in Chapter 7. The velocity in the direction of flow is higher than at 135°. The non-flocculated suspensions show a higher velocity which could be attributed to the smaller particle size or attenuation effects. The calcite shows higher velocity values, this could be attributed to the fines within the suspension.

Table 8.1 Velocity measurements in comparison to predicted velocity in the direction of flow for non-flocculated and flocculated suspensions of calcite and magnesium hydroxide

Mineral Suspension	Suspension Environment	Concentration (g/L)	Max Measured Velocity at 135° (m/s)	Average Velocity at 135° (m/s)	Velocity in Direction of Flow (m/s)
Calcite	Non-flocculated	3.4	4.13	4.33	6.12
		27.5	4.52		
	Flocculated	3.4	3.38	3.96	5.60
		27.5	4.54		
Magnesium hydroxide	Non-flocculated	3.4	4.02	3.96	5.60
		27.5	3.91		
	Flocculated	3.4	3.64	3.51	4.97
		27.5	3.38		

8.3.3 Acoustics

8.3.3.1 G function profiles

The acoustic profiles for calcite and magnesium hydroxide were displayed as distance dependent *G*-function values, as done in Chapter 6.3.4.1. Much like Chapter 6, the *G*-function profiles were used to extract the sediment attenuation coefficient values for the two different sediment types, which were compared to coefficients from Betteridge *et al*., (2008). Fig. 8.8 (a) and (b) show the non-flocculated and flocculated acoustic profiles for calcium carbonate and magnesium hydroxide travelling through a vertical pipe arrangement. In Fig. 8.8 (a) and (b), the end of the pipe was indicated by a dramatic increase in sound signal at approximately 0.0285 m, this was also noted in Chapters 4 and 5. The increase in signal was due to reflections from the back end of the pipe. The inner pipe wall was assumed to be at 0.0035 m using the actual inner pipe diameter of 0.025 m and the back end of the pipe. The peak decay in the profiles in the first 0.0035 m infer a complex nearfield environment, as shown in Fig. 6.13 and Fig.

6.14 for profiles from the calibration rig. This can also be attributed to internal reflections in the probe holder and pipe wall. The averaging of the signals across the 61 second measurement time period (for each transducer) produces noisy signals, which was shown in all acoustic profiles. However, the likely main reason was that the expected backscatter strength from both sediments is minimal, as they were comprised of fine particulate material that does not scatter significantly. The small proportion of backscatter available for analysis makes it difficult for the UVP to produce a smooth profile. This is shown in Chapter 6 where profiles fluctuated across the distance of the calibration rig.

The speed of sound in calcite and magnesium hydroxide suspensions were calculated using Eqs. (3.15) – (3.16). The calculated speed of sound for calcite suspensions at the highest concentration was 1473 m/s, which is slightly slower than the speed of sound in water. This should have translated to an increased measured inner diameter; however, the difference in speed of sound was smaller than 1%, as shown in Tables 3.3 and 3.4. Due to the potential complexities from nearfield interference, in-pipe calibration was performed on the vertical pipe in the lower pipe section from 0.013-0.024 m. This same method to isolate linear sections of the profile is seen in Chapters 4-7.

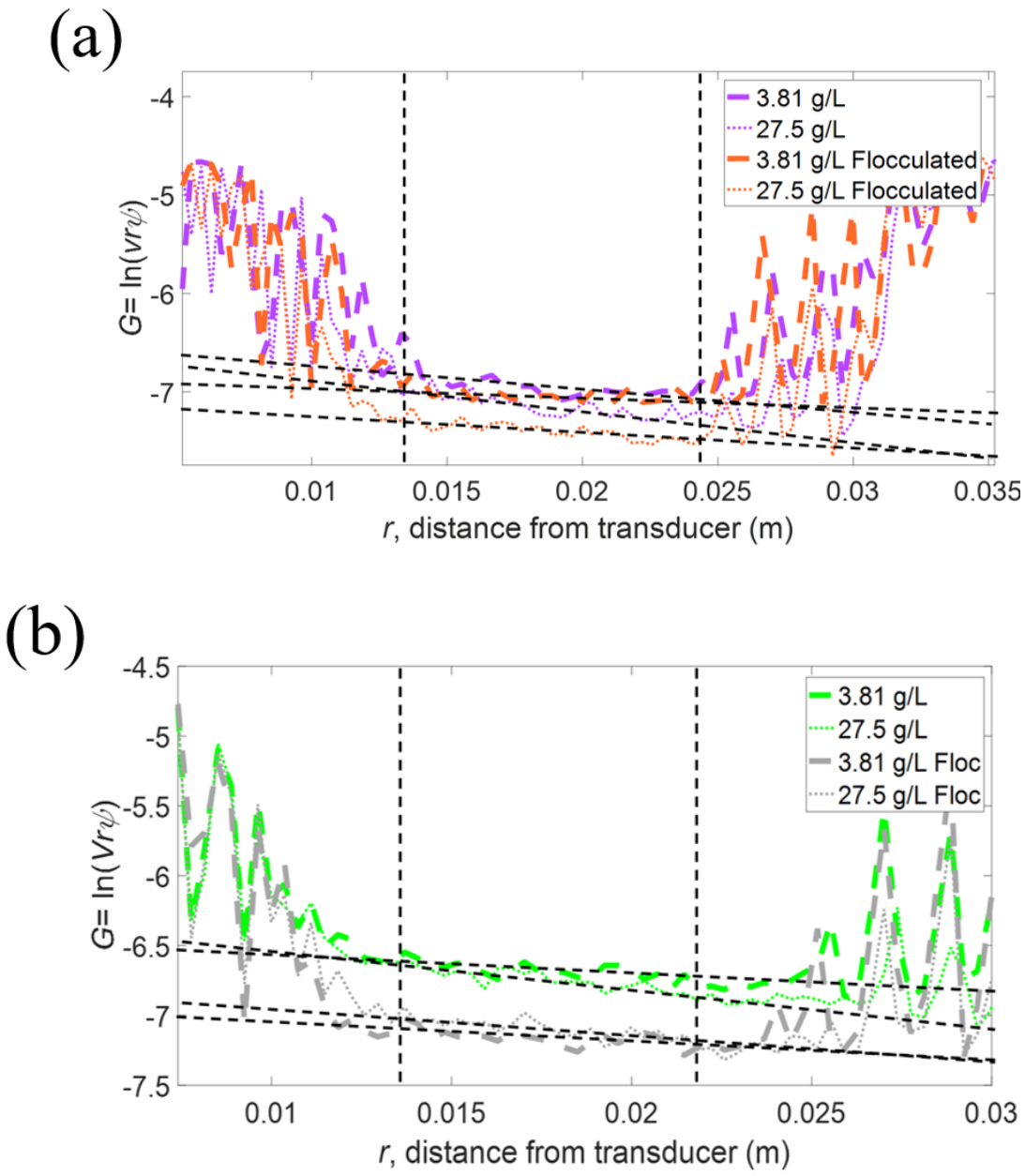

Figure 8.8 G-function profiles for non-flocculated and flocculated suspensions of (a) Calcium carbonate and (b) magnesium hydroxide using a remote 4 MHz transducer mounted on a vertical pipe length

In the non-contacting arrangement in Fig. 8.1 (b), the sound signal travelled through a thin layer of the probe holder before penetrating the pipe wall, with a thin layer of acoustic couplant between them. The UVP expects the signal to travel at the speed of sound in water (1480 m/s), however, the speed of sound

through the uPVC solid pipe wall was much faster (2300 m/s) (Podesta, 2020). This increased speed of sound through solid was due to the increase in vibrations (Denny, 1993; Johnson *et al*., 2013; Lingireddy and Wood, 2021). The faster speed of sound resulted in the signal travelling through the pipe wall quicker than the UVP expected. Therefore, it is assumed that the suspension environment starts at 0.0035 m as the UVP determines the time taken for the signal to enter the suspension environment and uses the speed of sound in water to calculate the distance. However, when using the increased speed of sound and assuming the same time taken, the distance at which the suspension environment should start is 0.0054 m. The calculation required for this analysis is shown in Table 8.2. As this only occurs in the region outside the pipe environment, this does not affect the profiles in the suspension environment and is therefore ignored for analysis purposes. The profile between 0 and 0.0035 m corresponds to the sound travelling through the pipe wall and probe holder where the wall thickness is approximately 0.0025 m and the probe holder thickness is calculated (0.001 m). The distance between 0.0035 m and 0.012 m where the profiles are noisy is due to the complex nearfield region. Finally, the distance between 0.0035 to 0.0285 (0.025 m) corresponds to the inner diameter of the pipe and the suspension environment. This has also been covered in Chapter 7 when using the pipe loop to analyse silica glass bead suspensions. The data here and the noisy nearfield region align well with previous data and the general G v r profile relationship is similar to G profiles in Chapter 7.

Table 8.2 Distance prediction for varying speed of sound in water and uPVC

Material	Speed of Sound (m/s)	Distance (m)	Seconds Taken (s)
Water	1480	0.0035	2.36E-06
uPVC	2300	0.0054	2.36E-06

Within this section, the change in G with distance (dG/dr) was approximately linear for each specific concentration, as would be expected for well-mixed

suspensions although there was still a large degree of noise associated. However, the overall averaged attenuation gradients (shown by the dashed lines) do indicate the expected change between concentrations, where higher particle levels lead to greater attenuation and associated d*G*/d*r* values, as shown in Chapters 4-7 (Rice *et al*., 2015). The flocculated suspensions appear to attenuate less. This was discussed in Chapter 6 where the flocculated systems were expected to enhance attenuation through greater non-directional particle scattering. It was found for both the mineral suspensions; the non-flocculated particles are small enough to cause a considerable increase in viscous absorption which increases overall attenuation. The profiles are noisier in Fig. 8.8 (a) which is likely due to the increased density of calcite (Omya North America, 2021). Magnesium hydroxide acoustic profiles in Fig. 8.8 (b) appeared to attenuate less with little difference between varying concentration profiles. This is evidenced in Chapter 6.

The acoustic profiles in Fig. 8.8 (a) intercept the y-axis at -7 whereas profiles in Chapter 6 from the calibration rig intercept the y-axis at approximately -6. This shows that the UVP signal strength is higher when analysing in the calibration rig but not statistically different in the pipe loop. In this Chapter 4 MHz probes were used whilst 2 MHz probes were used in Chapter 6, this may account for small differences in the *G* intercept. This decreased signal strength is likely attributed to the limited analysis width and the fact that the complex nearfield region (0.0035 – 0.012 m) limits the distance for analysis (0.025 m) by 33%. The signal strength in Fig. 8.8 (b) is between -6.5 and -7 which aligns very well with the signal strength in Chapter 6. This shows that the larger magnesium hydroxide particles were analysed with similar strength in both the calibration rig and the pipe loop. This could be attributed to the decreased density of magnesium hydroxide suspensions.

The gradients are extracted from Fig. 8.8 and plotted against their respective concentrations in Fig. 8.9 as shown in Chapters 4-7. Only two concentration plots have been shown in Fig. 8.9. However, when considering the previous gradient plots (see Fig. 5.10, 6.13, 7.9) all plots follow the linear gradient. Therefore, it is expected that although the gradient plots in Fig. 8.8 have two concentration plots,

the attenuation gradient extracted from these is accurate.

The difference in attenuation is as expected from Fig. 6.16, however, the d_{50} of all four species is dramatically different from in-line FBRM measurements. This is unexpected as the size of the particles determines whether the suspension attenuates predominantly by scattering or viscous losses. The concentration of the suspensions is consistent with Chapter 6, the transducer frequency is 4 MHz instead of 2 MHz which can lead to an increased sedimentation attenuation coefficient as evidenced in Chapter 4. The size of the primary particles from Fig 8.4 is 184 µm for calcite and 158 µm for magnesium hydroxide which is taken from in-line FBRM measurements. At this large size, the particles are within the size range of the largest particle species in Chapter 5 which is known to have enhanced scattering losses. According to the principle that the particles will undergo mainly scattering losses and the calcite should attenuate less due to its decreased particle size (Moore *et al*., 2013). As the calcite attenuates more than the magnesium hydroxide as evidenced in Chapter 6, it is much more likely that the size of the primary particles is similar to the *ex situ* measurements from the Camsizer XT in Chapter 6. Therefore, for ongoing models, the same *ex situ* particle sizes used in Chapter 6 were used here where $a_{calcite}$: 2.4, $a_{magnesium\ hydroxide}$: 2.5, $a_{flocculated\ calcite}$: 13, $a_{flocculated\ magnesium\ hydroxide}$: 13.25. Attenuation behaviour here is consistent with the primary particles having considerable viscous attenuation which is expected from particle sizes which are much smaller than the in-line raw chord length distributions.

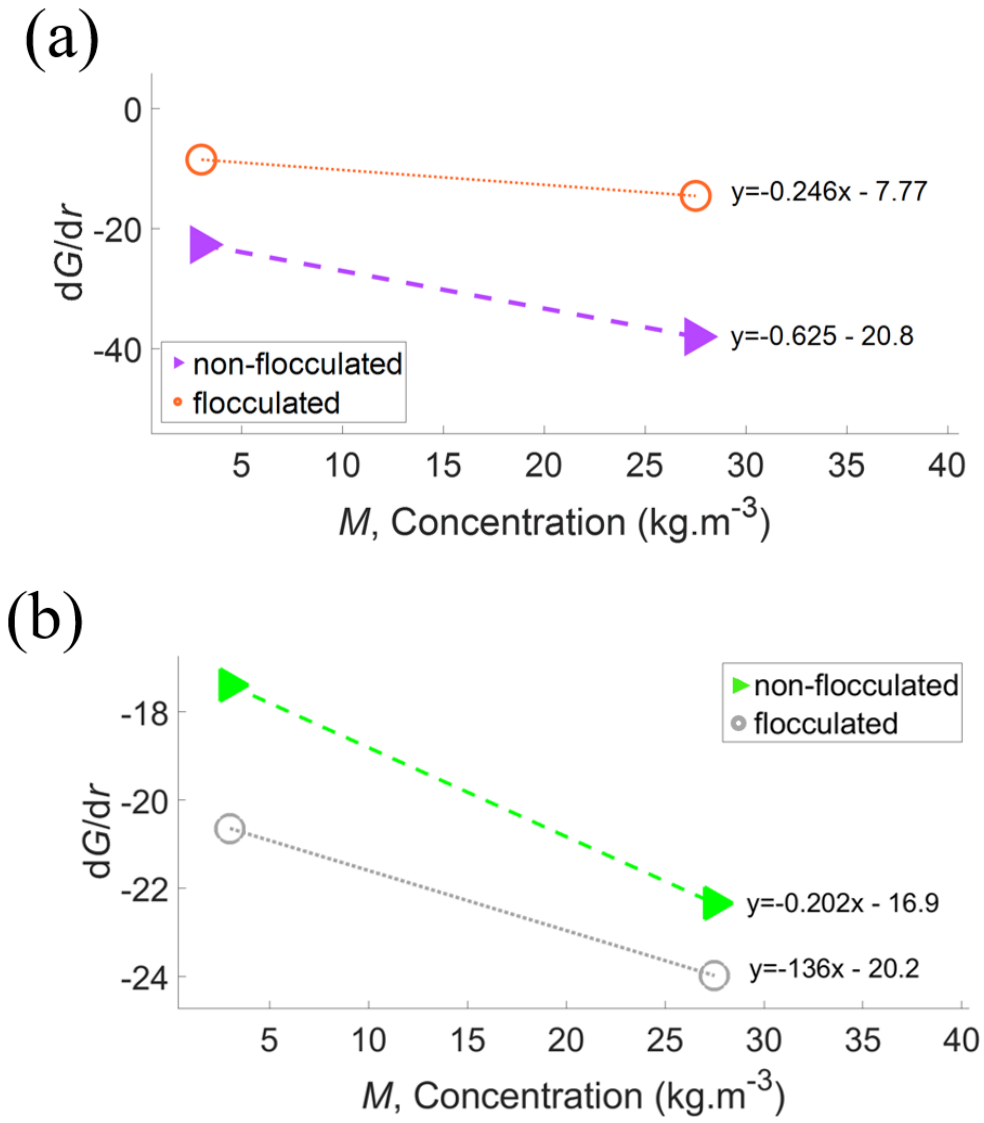

Figure 8.9 Change in G with distance for varying concentrations in vertical pipe arrangement of non-flocculated and flocculated (a) calcium carbonate and (b) Magnesium hydroxide

8.3.1.2 Sedimentation attenuation coefficient

The gradient of all acoustic profiles shown in Fig. 8.9 (a) and (b) were extracted and converted to the sedimentation attenuation coefficient using Eq. (3.06) in Chapter 3, this is shown throughout Chapters 4-7. Fig. 8.10 shows all attenuation coefficients where the coefficients from Fig. 8.9 (a) and (b) are shown by the blue vertically striped bars. The yellow bars show previous data from a probe mounted on a vertical pipe whilst the red horizontally striped bars show data collected

previously from a probe mounted on a horizontal pipe. The data from the vertical pipe lengths are very similar which shows that the data was reproducible in this arrangement. The horizontal transducer showed increased attenuation as evidenced in Chapter 7 where the horizontal pipe likely promoted settling in the pipe. The attenuation coefficients from calcite suspensions are higher due to increased viscous absorption from the smaller particle size, this is evidenced in Chapter 6.

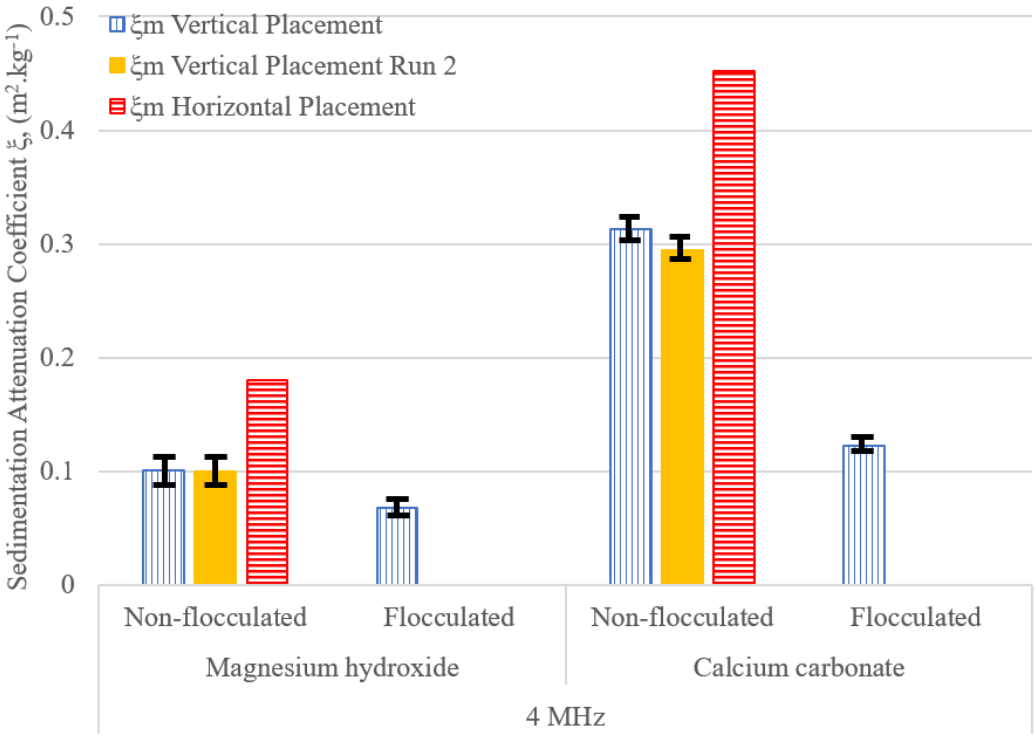

Figure 8.10 Sedimentation attenuation coefficient for non-flocculated and flocculated mineral systems in a vertical and horizontal pipe length

Below in Fig. 8.11 was where the effect of viscous absorption was probed further by comparing the measured attenuation coefficients to estimations from Betteridge *et al.*, (2008) (see Eq. 3.07) and Urick, (1948) (see Eq. 3.11-3.12) for combined scattering and viscous attenuation. The predictions are highly dependent on the particle size which is why both the Camsizer XT *ex situ* data from Chapter 6 and the FBRM in-line data were both used to determine the

predicted attenuation coefficient. It was found that the attenuation coefficients predicted when using the larger FBRM in-line particle sizes highly overestimated the measured attenuation coefficient. This is because the scattering losses were expected to be dominant at that larger particle size.

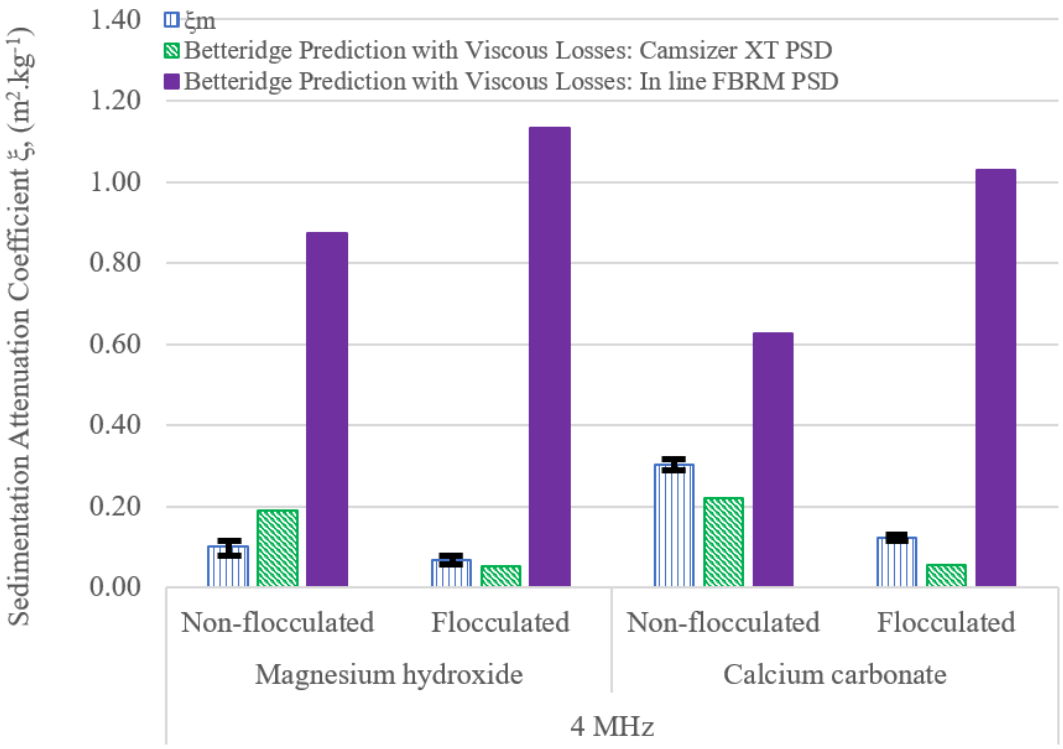

Figure 8.11 Sedimentation attenuation coefficient for non-flocculated and flocculated mineral systems in a vertical transducer placement in comparison to coefficients calculated using various PSD in Betteridge heuristic expressions with viscous attenuation accounted for

The error bars in Fig. 8.11 were calculated by determining the variation in echo amplitude, this is shown in Chapter 4. When using the *ex situ* particle size data, the predictions are much more comparable to measured values. This is unexpected as the *ex situ* data was not representative of in-line particle size data from the pipe loop. It is clear that the in-line FBRM data is not providing a realistic PSD where the models actually compare very well to data when using the *ex situ* particle sizes. There is a slight underprediction for most systems where the estimated coefficients are higher and this is likely from the fact that the models do not taken

into account polydispersity. The measured and predicted values from Camsizer XT PSD are isolated in Fig. 8.12 where it is shown that the predictions are slightly underestimated for all systems apart from the non-flocculated magnesium hydroxide. The values could be underpredicted due to the particle size being larger in actuality and therefore viscous losses are limited. The opposite could be said for the non-flocculated magnesium hydroxide. This shows how complicated it is to analyse flocculating systems in a pipeline however, the data here correlated very well to predicted data and the differences in predictions may also be due to changes in density of the floc, this is explored later in the Chapter.

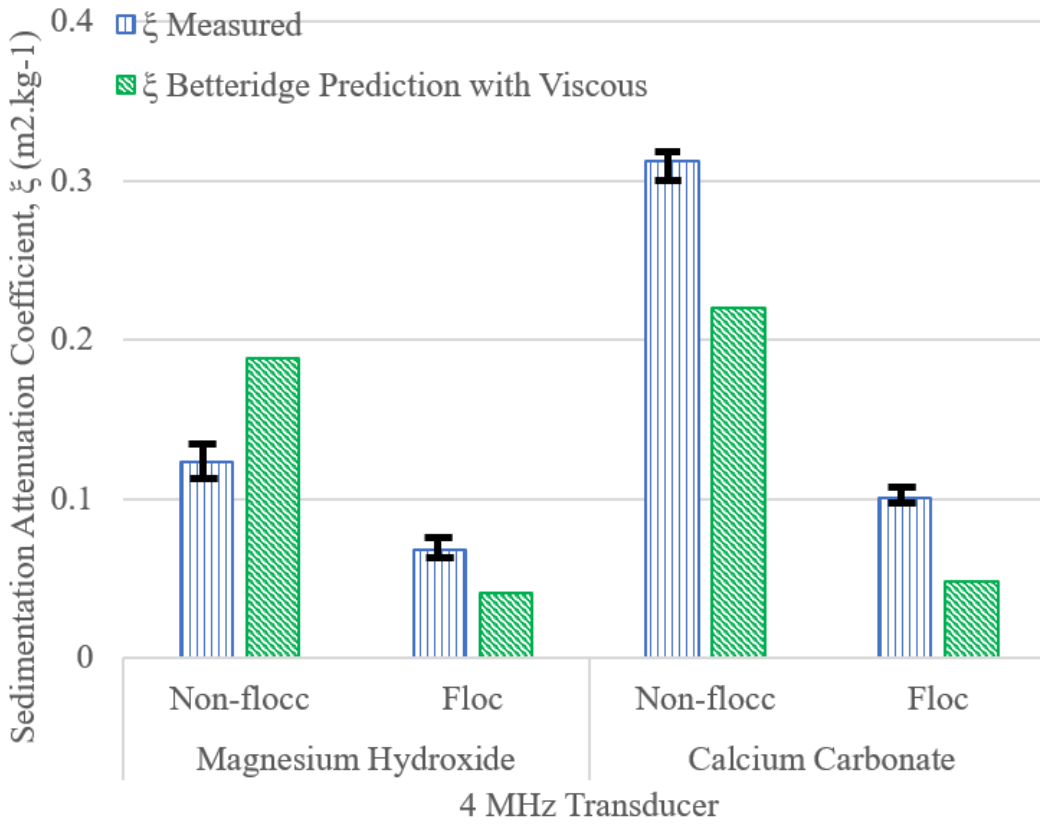

Figure 8.12 Sedimentation attenuation coefficient for non-flocculated and flocculated mineral systems in a vertical transducer placement in comparison to coefficients calculated using ex situ particle sizes from Chapter 6 in Betteridge heuristic expressions with viscous losses accounted for

The attenuation coefficients in Guerrero *et al*., (2015) for sediment with a mean size of ~ 4 μm was ~ 0.032 whilst the measured data in Fig. 8.12 shows attenuation coefficients of approximately 0.1 and 0.3 for magnesium hydroxide and calcium carbonate, respectively. This is an order of magnitude different, but this can be explained by the changes in transducer frequency as well as the set-up. The data from Guerrero *et al*., (2015) was collected from free-flowing water where scattering is minimal as the only scattering is from presence of solid material in the water. Whilst in a pipeline, the sound signal scatters off the pipe wall.

In Fig. 8.12, viscous losses account for the majority of losses in the combined attenuation shown, this is because the particle size is so small that scattering losses are minimal as shown by Moore *et al*., (2013). This is also shown in Fig. 6.16 where the same mineral species were used. Viscous losses for the non-flocculated calcium carbonate and magnesium hydroxide were 0.15 and 0.13, respectively. However, in Fig. 8.12 when using a 4 MHz transducer, the viscous losses were 0.22 and 0.19, respectively. The increased viscous losses may be due to the increased attenuation from the higher frequency transducer. When looking at the proportion of attenuation is from viscous losses, this translates to 99.95 and 99.93 % which is lower than the proportion in Fig. 6.16. Therefore the increased viscous losses is due to the increased attenuation. When observing the flocculated species, the viscous losses for calcium carbonate and magnesium hydroxide are 0.043 and 0.038 which correspond to 76 and 69.8 %. Whereas when using the 2 MHz transducer in Fig. 6.16, the viscous losses were 96.9 and 95.8 % for the same respective species with a numerical value of 0.03 and 0.027. The proportional viscous losses were lower when using a higher frequency transducer for both the 2 and 4 MHz transducer. This can be compared to Table 3.5 where the particle Reynolds number was higher when using a 4 MHz transducer and for magnesium hydroxide, in both cases, the viscous loss contribution was lower. This is something that will have to be explored further however, this is out of scope for this thesis. This is also seen in Chapter 5 where the increase in

transducer frequency led to a decrease in proportional viscous losses in comparison to combined attenuation.

8.3.1.3 Scattering cross function

Scattering cross function (χ) values from the non-flocculated and flocculated suspensions are calculated using the sedimentation attenuation coefficients, particle size and density as shown in Eq. (3.09), these calculated values are shown below in Fig. 8.13 and 8.14. The floc densities calculated in Tables 6.1 and 6.2 were also used to calculate the scattering cross function as an alternative to the particle density (also as completed in Chapter 6). Fig. 8.13 and 8.14 correspond to scattering cross function values for calcium carbonate and magnesium hydroxide, respectively. The χ values in Fig 8.13 are all underpredicted by the Betteridge *et al*., (2008) prediction shown by the black dashed line. The red dotted line shows combined attenuation where viscous losses have been considered and the prediction is much closer to the measured χ values. However, the prediction still underestimates the measured values. For the flocculated values this could be due to the increased particle density used in calculations.

Whereas for the non-flocculated values this could be because the particle size in the pipe loop was actually smaller than predicted in *ex situ* data and therefore the attenuation coefficient was lower. The combined attenuation prediction is calculated using a 4 MHz frequency transducer, the crosses in pink and red correspond to values calculated using a 3.75 and 4.25 MH transducer where the increased frequency led to increased ka and χ. The measured flocculated χ value with the lower density aligns very well to the predicted χ value which shows that accounting for the lower density of the floc allows for better alignment with predicted χ values.

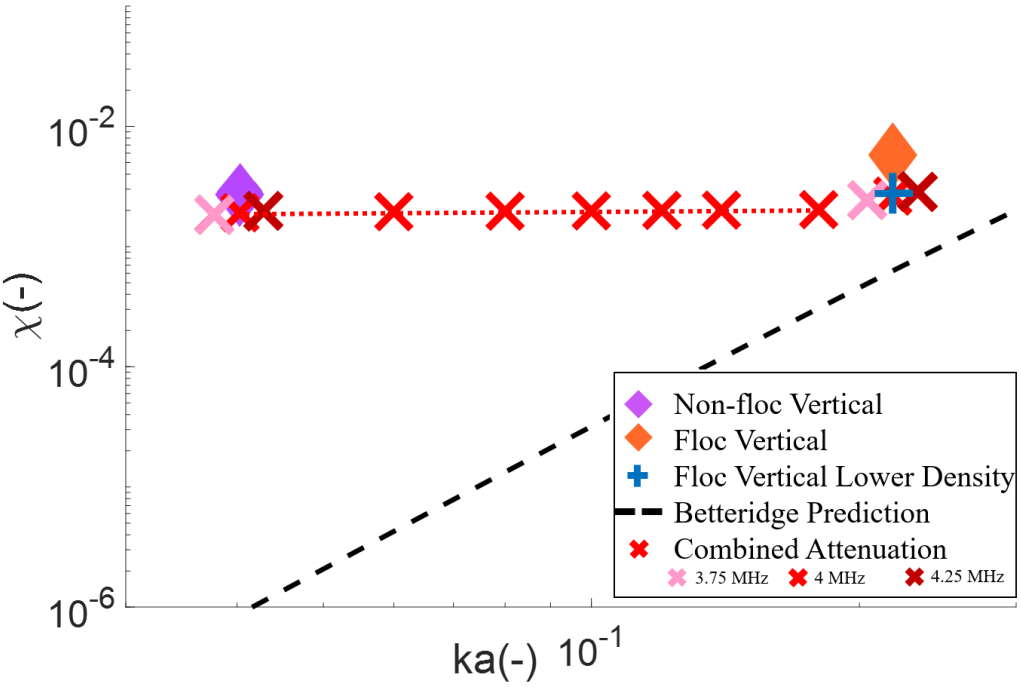

Figure 8.13 The dimensionless scattering cross function vs product of the wavenumber and particle radius (ka) using a (a) flocculated calcium carbonate system where the red line shows the prediction for combined losses when using a 4 MHz transducer, light and dark red crosses show predictions using a 3.75 MHz and 4.25 MHz frequency, respectively

Fig. 8.14 shows the normalised scattering cross function values for non-flocculating and flocculating magnesium hydroxide suspensions. The alignment for the magnesium hydroxide is slightly worse due to the complex aggregation with both the non-flocculated and flocculated species. It was found that the combined attenuation prediction aligned much better with the measured values as shown previously. When accounting for the lower floc density, the measured value decreases to below the prediction which is unexpected. A likely reason for this is that in the case of magnesium hydroxide, it is not sufficient to say they behave as spherical particles. the scattering losses are more complex and slightly less than would be expected for a low-density sphere, this could be due to the shape of the particle floc. The non-flocculated measured χ values are overpredicted by the combined attenuation prediction. Both are likely due to the

particle size being smaller than predicted which would lead to increased viscous losses. As evidenced above, the increase in transducer frequency leads to an increase in *ka* and χ. Predicting the scattering cross function is highly complicated and depends on the particle size of the suspensions. However, as we are dealing with polydisperse systems, the ability to predict scattering depending on a single particle size becomes very complex and is quite often not representative of the suspension. The influence of polydispersity on acoustic measurements has been explored by Guerrero and Federico, (2018) where multiple frequency transducers were used to determine sound attenuation. They predicted a likely attenuation coefficient to determine the mass concentration as a function of the sound attenuation. Guerrero and Federico were able to propose a method which enables indirect measurements of concentration which is weakly dependant on actual PSD. Future work will delve into using this newer method for determination of concentration profiles which have a limited dependency on PSD.

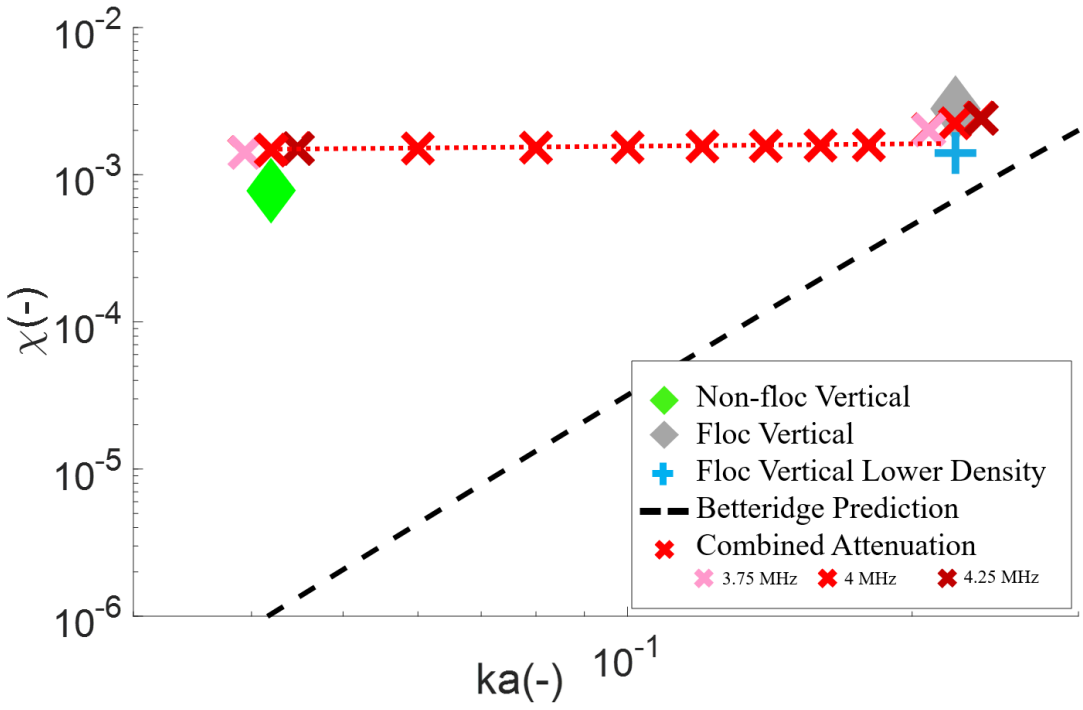

Figure 8.14 The dimensionless scattering cross function vs product of the wavenumber and particle radius (ka) using a flocculated magnesium hydroxide system where the red line shows the prediction for combined losses when using a 4 MHz transducer, light and dark red crosses show predictions using a 3.75 and 4.25 MHz frequency, respectively

Results in this Chapter show an inline UVP can be used to simultaneously gain velocity data and calibrated concentration data for both flocculated and non-flocculated fine mineral systems. Through χ figures and theoretical expressions the particle size during flocculation can be predicted. If more *in situ* size validation data had been taken the UVP can also be used to measure the state of flocculation directly. Future work will focus on understanding the limitations of the FBRM for validation purposes. The combined viscous + scattering model seems to compare very well broadly and gives good confidence that the flocculated systems can also largely be modelled spherically.

8.4 CONCLUSIONS

An increase in concentration within the pipe leads to increased attenuation across the pipe due to the increased density of particles. Calcite attenuates the signal more due to the presence of fines which increases the viscous attenuation. Particles which are non-spherical shape create an effective diameter larger than that for a sphere of equal volume which leads to underestimation of the attenuation when using predictions based on spherical particles (Baker and Lavelle, 1984). When observing Table 6.1 and 6.1, magnesium hydroxide has a lower fractal dimension value which infers a more elliptical shape. If the orientation of the particles in relation ot the transducer were not showing the transducer the effective larger diameter, this could have led to a decreased attenuation (Atlas *et al*., 1953).

The prediction of the normalised scattering cross function and sedimentation attenuation coefficient was found to be complex. Where the predictions did not account for the polydisperse systems and estimations in particle size led to significant changes in predicted χ and ξ values. The in-line particle size data was found to produce very high attenuation coefficient predictions in comparison to measured values where the particle size data from *ex situ* sampling compared much better. The attenuation of the suspensions was assumed to govern the peak velocities within the pipe. The particle size for both calcite and magnesium hydroxide are very small, this means that the level of backscatter is low. A lower backscatter level produces a noisy profile as the UVP is trying to analyse the small component of scatter. Predicted velocity profiles from Stigler, (2014) were found to follow the measured velocity profiles quite well.

The author has been able to characterise and monitor the flocculation process of complex fine particulates in line and non-invasively. Data in Chapter 8 really highlights the UVP could be a viable online monitor system to characterise realistic complex aggregated dispersions – giving, not only velocity information, but concentration information (from the *G*-function) and also particle size information/degree of flocculation (from the measured attenuation coefficients/χ

figures). Differences with flocculation are also evident online where the *in situ* work in Chapter 6 can be directly correlated. Data correlates well with combined spherical scattering models, especially when considering changes in density. The magnesium hydroxide looks to be slightly more complex where the need to account for non-spherical particle shapes may need to be considered in the future. Data has been found to be accurate and results were comparable to validation experiments in previous Chapters. Future work will detail the use of particle size validation data where the accuracy of the FBRM will be explored for a more robust non-invasive monitoring process. The full extent of the complexities of flocculated scattering losses need to be considered where the change in floc density has a significant effect on predicted scattering losses.

9. CONCLUSIONS & FUTURE WORK

9.1 CONCLUSIONS

This section will provide more clarity on the scientific contributions of the thesis. The novelty across the thesis will be described and any potential gaps still left in the research will be flagged as future work in the next Chapter.

Comparing Results to Physical Properties

Provided knowledge of two properties from particle size, concentration and transducer frequency are known, a property can be inferred from the sedimentation attenuation coefficient measured. This can be further developed by applying the dual frequency inversion method which can be utilised to develop a concentration profile. From this, the attenuation coefficient can be used solely to infer the particle size.

Combined Scattering and Viscous Loss Prediction for the UVP

The author has been able to provide a consolidated calibration method where the novel method developed by Bux *et al*., (2019) was compared to heuristic predictions from Betteridge *et al*., (2008). This provides a clearer understanding of which heuristic predictions to use. Although these predictions were specifically for spherical glass beads, they were used in tandem with viscous loss predictions using derivations from Urick, (1948) and provided accurate predictions for the sedimentation attenuation coefficients of aqueous suspensions of silica glass beads, magnesium hydroxide and calcium carbonate. The scientific contribution in this thesis is the combination of the Betteridge *et al*., (2008) expressions (for scattering losses) and Urick, (1948) expressions (for viscous losses) to determine a combined sedimentation attenuation coefficient when using the UVP. As this was proven to provide accurate attenuation coefficients, future researchers can use this combined approach for the prediction of attenuation for homogeneous suspensions of silica glass beads, magnesium hydroxide and calcium carbonate. This can also be used for flocculating suspensions of magnesium hydroxide and calcium carbonate. The author will caveat that this approach has only proven

accurate for specific particle sizes and concentrations of each sediment type. This approach has been used previously by Tonge *et al*., (2021) for use with the UARP but the scientific contribution in this thesis is the combined prediction approach for use with the commercial UVP system. As the UARP is a novel system, data is less easily reproduced. Whereas, the UVP can be purchased off-the-shelf which allows the data to be re-produced easily by other researchers.

Novel Error Analysis Method for UVP Raw Echo Data

In this thesis, the author identified that several researchers had determined sedimentation attenuation coefficients from experimental data when utilising ABS's, including Bux *et al*., (2019), Tonge *et al*., (2021) and Rice *et al*., (2014). However, none of the researchers identified had performed an error analysis on the raw echo amplitude data extracted from the ABS's. The author determined the spread of data across an individual distance point from the 1023 profiles extracted from the UVP. From this spread of echo amplitude values, the author established the maximum sedimentation attenuation coefficient from a specified linear section of an attenuation profile. Linearity in an attenuation profile denotes a homogeneous suspension, which is specifically why only the variation of echo amplitude across the linear section was analysed. The determination of attenuation coefficients is via a user identified cut off for the linear section. Providing an error analysis for the attenuation coefficient values shows that the attenuation coefficients are accurate and can be defined as representative for the suspension. In terms of scientific contribution, this error analysis provides other researchers with a process to determine whether experimentally determined sedimentation attenuation coefficients are accurate for the data gathered. This combined with the consolidated scattering and viscous loss prediction shows a systematic approach to extracting accurate sedimentation attenuation coefficients. This form of error analysis has not been identified across the researchers reviewed for various forms of ABS's and is displayed in this thesis as a novel approach.

Accurate Sedimentation Attenuation Coefficients

Using the combined attenuation prediction and the novel error analysis, the author has been able to determine accurate attenuation coefficients experimentally for the following suspensions:

- Utilising *in situ* and remote transducers in a calibration rig for:
    - Homogeneous suspensions of silica glass beads for a concentration range of 11.9 – 107.5 g/L and a particle size range of 36 – 170 μm.
    - Flocculating suspensions of calcium carbonate and magnesium hydroxide for a concentration range of ~3 - 27.5 g/L where the primary particle size was ~ 5 μm and the flocculated particle size was ~ 28 μm.
- Utilising remote and in-line transducers on a pipe loop for:
    - Homogeneous suspensions of silica glass beads for a concentration range of 11.9 – 107.5 g/L and a particle size range of 36 – 82 μm.
    - Flocculating suspensions of calcium carbonate and magnesium hydroxide for a concentration range of ~4 - 27.5 g/L where the primary particle size was ~ 5 μm and the flocculated particle size was ~ 28 μm.

There were several novel scientific contributions in this thesis which are for the determination of accurate attenuation coefficients. In this thesis accurate attenuation coefficients were determined for homogeneous silica glass bead suspensions utilising a remote, non-invasive transducer both in a calibration rig as well as a pipeline, which has not been achieved before. Attenuation coefficients were also established for non-flocculated and flocculated calcium carbonate and magnesium hydroxide when using both invasive and non-invasive transducers which is novel. Other researchers have used other ABS systems to analyse flocculated dispersions but not for comparison to non-flocculated suspensions (Hunter *et al*., 2012). This provides a non-invasive approach for monitoring aggregated suspensions, this is vital for the nuclear sector but is also applicable to other industries as well.

Combined Characterisation Approach

Throughout this thesis, several methods have been used for characterisation of various suspensions. To analyse the flocculating suspensions, the fractal dimension and floc size were determined theoretically alongside acoustic analysis of the suspensions. This combined theoretical and experimental analysis of the flocculated suspensions has not been conducted before to monitor flocculation of complex mineral suspensions. A combined approach was also utilised for the analysis of suspensions in the pipe loop. An *in situ* FBRM was used to determine particle size, a flow meter was mounted non-invasively to measure flow rate and the UVP was mounted non-invasively to extract velocity and acoustic data simultaneously. This set-up is completely novel for the extraction of data from homogeneous suspensions of silica glass beads and flocculating suspensions of complex minerals.

9.2. Future Scientific Research

The conclusion chapter describes a summary of the scientific contribution throughout the thesis. Research gaps have been highlighted below and this future work section will delve further into the next steps for future research depending on the scientific contribution of this thesis.

Future Scientific Areas to Explore

Going forward, the author would like to point out a series of other topics that were out of scope for this thesis. One of these include the relationship between the viscous boundary layer thickness and the effect on viscous absorption explicit. This relationship was touched on but not proved in this thesis as the topic itself required a multitude of research which was not explicitly relevant for this line of research.

Only a limited range of suspensions were used throughout this thesis and the scientific field may benefit from a more expanded index of materials which have been experimented on with the UVP. This would provide a better understanding of how the UVP is affected by materials of various properties including particle

shape, viscosity and particle size. Homogeneity is assumed for all suspensions and all acoustic models assume a single particle size to be representative of the suspension. However, this is not always the case and it would be useful to understand the effects of polydispersity on the acoustic models and experimental data. This would improve the systems capabilities for work in industry.

The author would like to investigate whether the acoustics could be pushed to analyse suspensions of unknown chemical composition to extract particle size and concentration, however, this is something that requires maturity of the acoustic theory and derivations as well.

Therefore, to understand this further, more investigation is required into the limitations of concentration range against particle size for accurate attenuation values. A more thorough attenuation value may be required for varying concentration ranges of a specific material.

The FBRM was also used which is an *in situ* instrument, however, The process for converting raw chord length data from the FBRM to particle size distribution becomes very complex. Additional scope would be ideal to understand the process of converting chord lengths to particle sizes for the glass suspensions.

In this thesis only one type of pipe was used which was a uPVC pipe with an inner diameter of 0.025 m. Therefore, these results are only applicable for this specific pipe. To build on this research, the effect of pipe material on the speed of sound through the pipe wall would need to be investigated. The pipe diameter would also need to be changed and several experiments conducted to see the applicability of this method with several types of pipe size and material.

<u>Next Steps for Technology</u>

The UVP has been proven to be able to analyse homogeneous suspensions of varying particle sizes and suspensions of changing particle size via flocculation in

a calibration rig as well as via pipelines. Therefore, for this method to be deployed in the industry, the author refers back to the TRL schematic, see Fig. 2.3.

To prove feasibility, the following steps are suggested:

- Use the UVP to analyse sediments with varying particle size, shape, viscosity and concentration to understand the effect of all four parameters on attenuation.
- Analyse heterogeneous suspensions to understand the effect of polydispersity on velocity profiles, attenuation profiles and attenuation coefficients.
- Use more relevant nuclear simulants, these would have to be provided by Sellafield, if possible, to prove the online, non-invasive system can be utilised to analyse sludge accurately.
- Data from the magnesium hydroxide commercial powder suspensions can be used to compare to the nuclear sludge analysed.

Applications for Technology Outside the Nuclear Sector

When describing this system in its simplest form. The data in this thesis has highlighted the applicability of the UVP as a viable online monitoring system to characterise realistic complex aggregated suspensions. Where velocity, concentration, flow and particle size data can be extracted simultaneously in a single experiment. The flexibility of this pipe rig shows the potential for this method to be deployed industrially. A few examples have been provided below for where this technique can be used outside the nuclear sector.

Flocculation and coagulation in the water treatment sector are used to remove suspended solids to clarify the water before discharge. However, these flocculants will need to be removed as some can contain potentially toxic residues (Boer *et al.*, 2015). The method of monitoring in this thesis can be utilised whereby non-invasive transducers can be mounted onto wastewater pipes to detect the presence of flocculants. Transducers can be mounted before and after filtration methods to determine the efficiency of the filtration for the removal of flocculated particles.

Viscosity is an important quality parameter which can serve as an indicator for food spoilage (Xu *et al*., 2020). The UVP can be used to measure changes in concentration via sedimentation attenuation coefficients or changes in the attenuation profiles. This can function as an early indicator for potential food spoilage and allow companies to prevent food from becoming spoiled. Or if food is spoiled, prevent it from being distributed which maintains public safety.

10. REFERENCES

Abaco. 2022. *Technology Readiness Level*. [Online]. [Accessed 16 November 2022]. Available from: https://www.abaco.com/technology-readiness-level

Abbagoni, B.M., Yeung, H. and Lao, L. 2022. Non-invasive measurement of oil-water two-phase flow in vertical pipe using ultrasonic Doppler sensor and gamma ray densitometer. *Chemical Engineering Science*. **248**(part B), pp.117-218.

Acevedo, D., Wu. W.L., Yang, X., Pavurala, N., Mohammad, A. and O'Connor, T.F. 2021. Evaluation of focused beam reflectance measurement (FBRM) for monitoring and predicting the crystal size of carbamazepine in crystallisation processes. *CrystEngComm.* **23**(4), pp.972-985.

Adams, J.F.W., Biggs, S.R., Fairweather, M., Yao, J. and Young, J. 2011. Transport of Nuclear Waste Flows: A Modelling and Simulation Approach. In: *ASME 14th Conference on Environmental Remediation and Radioactive Waste Management, January 2011, France.* France: ASME. Doi: 10.1115/ICEM2011-59136.

Agimelen, O.S., Svoboda, V., Ahmed, B., Cardona, J., Dziewierz, J., Brown, C.J., McGlone, T., Cleary, A., Tachtatzis, C., Michie, C., Florence, A.J., Andonovic, I., Mulholland. A.J. and Sefcik, J.2018. Multi-sensor inline measurements of crystal size and shape distributions during high shear wet milling of crystal slurries. *Advanced Powder Technology*. **29**(12), pp.2987-2995.

Ahmad, M.I., Rahim, M.H.A., Nordin, R., Mahamed, F., Abu-Samah, A. and Abdullah, N.F. 2021. Ionising Radiation Monitoring Technology at the Verge of Internet of Things. *Sensors*. **21**(22).

Ahmed, B., Svoboda, V., Agimelen, O., Cardona, J., Dziewierz, J., Brown, C., McGlone, T., Cleary, A., Tachtatzis, C., Michie, C., Florence, A.J., Andonovic, I., Mulholland, A. and Sefcik, J. 2018. Monitoring API crystal breakage in wet milling using inline imaging and chord length distribution measurements. In: *8th*

world congress on particle technology, 22-26 April 2018, Orlando. Orlando: AICHE.

Ainslie, M.A. and McColm J.G. 1998. A simplified formula for viscous and chemical absorption in sea water. *Journal of the Acoustical Society of America*. **103**(3), pp.1671-1672.

Al-Aufia, Y.A., Hewakandambya, B.N., Dimitrakisa, G., Holme, M., Hasan, A. and Watson, N.J. Thin film thickness measurements in two phase annular flows using ultrasonic pulse echo techniques. 2019. *Flow measurement and control.* **66**(1), pp. 67-78.

Alderman, N.J. and Heywood, N.I. 2011. The Importance of Rheological Assessment in the Mobilisation, Mixing and Transport of Nuclear Waste Sludges. In: *WM2011 Conference Proceedings. Waste Management Conference 2011, 27 February 3 March 2011, Phoenix.* Phoenix: Waste Management Symposia.

Ali, M. and Miraz, M.H. 2020. A review of underwater acoustic, electromagnetic and optical communications. *International conference for emerging technologies in computing.* **332**(1), pp.86-97.

Allegra, J.R. and S.A. Hawley. 1972. Attenuation of Sound in Suspensions and Emulsions: Theory and Experiments. *The Journal of the Acoustical Society of America.* **51**(5), pp.1545-1564.

Allen, R.M., Variano, E.A. and Lacy, J.R. 2019. Measuring settling velocity in a strongly tidal estuary. *Coastal Sediments*. **1**(1), pp.2423-2434.

Amgarou, K., Aspe, F., Idoeta, Q. and Herranz, M. 2021. Recommendations for the selection of *in situ* measurement techniques for radiological characterisation in nuclear/ radiological installations under decommissioning and dismantling processes. *Progress in Nuclear Energy*. **137**(1), pp. 1-14.

Anan'ev, Y.A. 2020. *Laser resonators and the beam divergence problem.* Boca Raton: CRC Press.

Anivi. 2022. *Uses of calcium carbonate*. [Online]. [Accessed 27 October 2022]. Available from: https://www.anivi.com/ball-mills-to-obtain-calcium-carbonate/?lang=en

Aquatec. 2022. *AQUAscat 1000R.* [Online]. [Accessed 15 November 2022]. Available from: https://www.aquatecgroup.com/aquascat/aquascat-1000r

Arenas, J.P. and Crocker, M. 2010. Recent trends in porous sound-absorbing materials. *Sound and* Vibration. **44**(7), pp.12-17.

Asamoah, B.O., Uurasjarvi, E., Raty, J., Koistinen, A., Roussey, M. and Peiponen, K.E. 2021. Towards the development of portable and *in situ* optical devices for detection of micro and nanoplastics in water: a review on the current status. *Polymers (Basel).* **13**(5), pp.730.

Atalar, A. 2008. A backscattering formula for acoustic transducers. *Journal of Applied Physics*. **51**(1), pp. 3093-3098. Doi:10.1063/1.328098.

Atkinson, C.M. and Kytomaa, H.K. 1992. Acoustic wave speed and attenuation in suspensions. *International Journal of Multiphase Flow.* **18**(4), pp.577-592.

Atlas, D., Kerker, M. and Hitschfeld, W. 1953. Scattering and attenuation by non-spherical atmospheric particles. *Journal of Atmospheric and Terrestrial Physics.* **3**(2), pp. 108-119. Doi: 10.1016/0021-9169(53)90093-2.

Auerbach, B.D., Radziwon, K. and Salvi, R. 2019. Testing the central gain model: loudness growth correlated with central auditory gain enhancement in a rodent model of hyperacusis. *Neuroscience.* **407**(1), pp.93-107.

Ayoola, O.S. 2018. *In situ* monitoring of the legacy ponds and silos at Sellafield. University of Manchester. School of electrical and electronic engineering. Thesis.

Bains, V.K., Mohan, R. and Bains, R. 2008. Application of ultrasound in periodontics: Part 1. *J Indian Soc Periodontol.* **12**(2), pp.29-33.

Baker, E.T. and Lavelle, J.W. 1984. The effect of particle size on the light attenuation coefficient of natural suspensions. *Journal of geophysical research: Oceans*. **89**(C5), pp.8197-8203.

Bakshi, U.A. and Bakshi, A.V. 2020. *Electrical Instrumentation and Process Control.* England: Unicorn Publishing Group.

Bao, J., Li, K., Ning, P., Wang, C., Song, X., Luo, Y. and Sun, X. 2021. Study on the role of copper converter slag in simultaneously removing SO_2 and NO_x using $KMnO_4$/ copper converter slag slurry. *Journal of Environmental Sciences*. **108**(1), pp.33-43.

Barlow, S.T., Fisher, A.J., Bailey, D.J., Blackburn, L.R., Stennett, M.C., Hand, R.J., Morgan, S.P., Hyatt, N.C. and Corkhill, C.L. 2021. Thermal treatment of nuclear fuel-containing magnox sludge radioactive waste. *Journal of Nuclear Materials.* **552**(1).

Belicard, N., Niemet-Mabiala, M.J., Tourvieille, J.N. and Lidon, P. 2022. Acoustic monitoring of the gelation of a colloidal suspension. *Soft condensed matter*. **1**(1), pp. 1-18.

Benn, F.A., Fawell, P.D., Halewood, J., Austin, P.J., Costine, A.D., Jones, W.G., Francis, N.S., Druett, D.C. and Lester, D. 2018. Sedimentation and consolidation of different density aggregates formed by polymer-bridging flocculation**.** *Chemical Engineering Science.* **184**(1), pp.111-125.

Benoit-Bird, K.J. and Waluk, C.M. 2021. Remote acoustic detection and characterisation of fish schooling behaviour. *The Journal of the Acoustical Society of America*. **150**(6).

Berhman, A. and Finan, D. 2021. *Speech and Voice Science.* 4th ed. San Diego: Plural Publishing.

Best, J.L., Kirkbride, A.D. and Peakall, J. 2009. Mean Flow and Turbulence Structure of Sediment-Laden Gravity Currents: New Insights using Ultrasonic

Doppler Velocity Profiling. *Particulate Gravity Currents*. Doi: 10.1002/9781444304275.ch12.

Betteridge, K.F., Thorne, P.D. and Cooke, R.D. 2008. Calibrating multifrequency acoustic backscatter systems for studying near-bed suspended sediment transport processes. *Continental Shelf Research*. **28**(2), pp.227-235.

Betteridge, K.F.R., Williams, J.J., Thorne, P.D. and Bell, P.S. 2003. Acoustic Instrumentation for Measuring Near-bed Sediment Processes and Hydrodynamics. *Journal of Experimental Marine Biology and Ecology*. **285-286**(1), pp.105-118. Doi: 10.1016/S0022-0981(02)00522-1.

Biggs, S., Fairweather, M., Hunter, T., Omokanye, Q., and Peakall, J. 2009. Engineering Properties of Nuclear Waste Slurries. In: *International Conference on Radioactive Waste Management and Environmental Remediation, 11-15 October 2009, Liverpool.* Liverpool: ASME. Doi: 10.1115/ICEM2009-16378.

Birkhofer, B.H., Jeelani, S.A.K., Windhab, E.J., Ouriev, B., Lisner, K., Braun, P. and Zeng, Y. 2008. Monitoring of fat crystallization process using UVP-PD technique. *Flow Measurement and Instrumentation*. **19**(3-4), pp.163-169.

Bishof, M., Zhang, X., Martin, M. and Ye, J. 2013. Optical Spectrum Analyser with Quantum-Limited Noise Floor. *Physical Review Letters*. **111**(9).

Boer, K., McHenry, M.P., Moheimani, N.R. and Bahri, P.A. 2015. *Biomass and Biofuels from Microalgae: Advances in Engineering and Biology*. Berlin: Springer International Publishing.

Bolton, W. 2016. 5th ed. *Engineering Science*. Abingdon: Routledge.

Bontha, J., Denslow, K., Adkins, H., Jenks, J., Burns, C., Schonewill, P., Morgen, G., Greenwood, M.S. and Wooley, T. 2011. Evaluation of Three Ultrasonic Instruments for Critical Velocity Determination during Hanford Tank Waste Transfer Operations. In: *WM2011 Conference, February 27 – March 3, Phoenix, AZ, USA.* USA: Waste management symposia.

Bowler, A.L., Bakalis, S. and Watson, N. 2020. Monitoring Mixing Processes Using Ultrasonic Sensors and Machine Learning. *Sensors.* **20**(7).

Bowler, A.L., Bakalis, S. and Watson, N.J. 2020. A review of in-line and on-line measurement techniques to monitor industrial mixing processes. *Chemical Engineering Research and Design*. **153**, pp.463-495.

Briggs, K.B., Williams, K.L., Jackson, D.R., Jones, C.D., Ivakin, A.N. and Orsi, T.H. 2002. Fine-scale sedimentary structure: implications for acoustic remote sensing. *Marine Geology*. **182**(1-2), pp.141-159.

Brouwers, B., Beeck, J. and Lataire, E. 2022. Acoustic attenuation of cohesive sediments (mud) at high ultrasound frequencies. *Proceedings of meetings on acoustics*. **47**(1). DOI:10.1121/2.0001594.

Burger, R., Donat, R., Mulet, P. and Vega, C.A. 2010. Hyperbolicity analysis of polydisperse sedimentation models via a secular equation for the flux Jacobian. *SIAM Journal on Applied Mathematics.* **70**(7/8), pp.2186-2213.

Burger, W., Krysiak-Baltyn, K., Scales, P.J., Martin, G.J.O., Stickland, A.D. and Gras, S.L. 2017. The influence of protruding filamentous bacteria on floc stability and solid-liquid separation in the activated sludge process. *Water Research.* **123**(12).

Burton, B. 2002. *Nuclear Power, Pollution and Politics*. London: Routledge.

Bushberg, J.T., Selbert, J.A., Boone, J.M. and Leidholdt, E.M. 2002. *The essential physics of medical imaging.* New York: Lippincott.

Butler, J.L. and Sherman, C.H. 2016. *Transducers and Arrays for Underwater Sound.* 2nd ed. Switzerland: Springer.

Bux, J. 2016. *Novel characterisation of concentrated dispersions by in situ acoustic backscatter systems.* Ph.D. thesis, University of Leeds.

Bux, J., Hunter, T.N., Paul, N., Dodds, J.M., Peakall, J. and Biggs, S.R. 2013. Characterising Nuclear Simulant Suspensions *In Situ* with an Acoustic Backscatter System. In: *Proceedings of the ASME International Conference on Environmental Remediation and Radioactive Waste Management, September 2013, Brussels*. Belgium: ASME, pp. 1-2.

Bux, J., Peakall, J., Biggs, S. and Hunter, T.N. 2015. *In Situ* characterisation of a concentrated colloidal titanium dioxide settling suspension and associated bed development: Application of an acoustic backscatter system. *Powder Technology***.** **284**(1), pp.530-540.

Bux, J., Peakall, J., Rice, H.P., Manga, M.S., Biggs, S. and Hunter, T.N. 2019. Measurement and density normalisation of acoustic attenuation and backscattering constants of arbitrary suspensions within the Rayleigh scattering regime. *Applied Acoustics*. **146**(1), pp.9-22.

Cacchione, D.A., Thorne, P.D., Agrawal, Y. and Nidzieko, N.J. 2008. Time averaged near bed suspended sediment concentrations under waves and currents; comparison of measured and model estimates. *Continental Shelf Research.* **28**(3), pp.470-484.

Camnasio, E., De Cesare, G. and Kantoush, S. A. 2010. Flow field and sediment deposition in a rectangular shallow reservoir with non-symmetric inlet and outlet configuration. *Proceedings of the Seventh International Symposium on Ultrasonic Doppler Methods for Fluid Mechanics and Fluid Engineering.* **1**(1), pp. 53-56.

Canilho, H., Santos, C., Taborda, C., Falorca, I. and Fael, C. 2022. Measurements of suspended ashes concentration in turbulent flow with acoustic doppler velocimeter. *Flow measurement and instrumentation*. **87**(1), pp.1-10.

Cardona, J., Ferreira, C., McGinty, J., Hamilton, A., Agimelen, O.S., Cleary, A., Atkinson, R., Michie, C., Marshall, S., Chen, Y., Sefcik, J., Andonovic, I. and Tachtatzis, C. 2018. Image analysis framework with focus evaluation for *in situ* characterisation of particle size and shape attributes. *Chemical Engineering Science*. **191**(1), pp.208-231.

Carmichael, R.S. 2017. *Practical Handbook of Physical Properties of Rocks and Minerals (1988)*. Boca Raton: CRC Press.

Carpenter, T.M. 2020. *Advanced Technologies for Next Generation Open Ultrasound Research Platforms.* Ph.D. thesis, University of Leeds.

Carrera, E.V. and Paredes, M. 2019. Analysis and Evaluation of the Positioning of Autonomous Underwater Vehicles Using Acoustic Signals. *Developments and Advances in Defence and Security*. **152**(1), pp.411-421.

Cartwright, G.M., Friedrichs, C.T. and Sanford, L.P. 2011. *In situ* characterisation of estuarine suspended sediment in the presence of muddy flocs and pellets. *The proceedings of the coastal sediments.* **1**(1), pp.642-655.

Cayirli, S. 2022. Analysis of grinding aid performance effects on dry fine milling of calcite. *Advanced Powder Technology*. **33**(3).

Challis, R.E., Povey, M.J.W., Mather, M.K. and Holmes, A.K. Ultrasound techniques for characterising colloidal dispersions. *Reports on Progress in Physics*. **68**(7).

Chmiel, O., Baselt, I. and Malcherek, A. 2019. Applicability of acoustic concentration measurements in suspensions of artificial and natural sediments using an acoustic doppler velocimeter. *Acoustics*. **1**(1), pp.59-77.

Chun, J., Oh, T., Luna, M. and Schweiger, M. 2011. Effect of particle size distribution on slurry rheology: Nuclear waste simulant slurries. *Colloids and Surfaces A: Physicochemical and Engineering Aspects.* **384**(1-3), pp. 304-310. Doi: 10/1016/j.colsurfa.2011.04.003.

Coll, E. *Telecom 101*. 6th ed. Canada: Teracom Training Institute Ltd.

Comes, M., Drumea, P., Blejan, M., Dutu, I. and Vasile, A. 2006. Ultrasonic flowmeter. In: *29th International spring seminar on electronics technology, 10-14 May 2006, Marienthal, Germany.* Germany: IEEE.

Conevski, S., Ruther, N., Guerrero, M. and Burckbuchler, M. 2018. Bedload measurements using ultrasound velocity profilers (UVP) in controlled laboratory conditions. In: *Particles in Europe, October 14-18 2018*. Lisbon, Portugal: Sequoia Scientific.

Cowell, D.M.J., Freear, S., Peakall, J., Smith, I., Rice, H.P., Njobuenwu, D., Fairweather, M., Barnes, M., Randall, G. and Hunter, T.N. 2016. Development of a real-time acoustic backscatter system for solids concentration measurement during nuclear waste cleanup. In: *IEEE International Ultrasonics Symposium IUS, 21-24 October 2015, Taiwan.* Taiwan: IEEE.

Cowell, D.M.J., Harput, S. and Freear, S. 2015. Arbitrary waveform generation based on phase and amplitude synthesis for switched mode excitation of ultrasound imaging arrays. In: *IEEE International Ultrasonics Symposium IUS, 21-24 October 2015, Taiwan.* Taiwan: IEEE.

Crawford, A.M. and Hay, A.E. 1993. Determining suspended sand size and concentration from multifrequency acoustic backscatter. *The Journal of the Acoustical Society of America*. **94**(1), pp.3312.

Crocker, M.J. and Arenas, J.P. 2021. *Engineering Acoustics: Noise and Vibration Control.* New Jersey: John Wiley and Sons.

Croft, J, Peakall, J, Rice, H. and Hunter, T.N. 2019. Erosion and Mobilisation of Highly Active Simulant Suspensions using Impinging Vertical Jets. In: *WM2019 Conference Proceedings. WM2019: 45th annual Waste Management Symposia, 03-07 Mar 2019, Phoenix, Arizona*. USA: WM Symposia. ISBN 978-0-9828171-9-3.

Deboeuf, A., Gauthier, G., Martin, J. and Salin, D. 2011. Segregation and periodic mixing in a fluidised bidisperse suspension. *New J. Phys*. **13**(7).

Deen, W.M. 2016. *Introduction to Chemical Engineering Fluid Mechanics.* Cambridge: Cambridge University Press.

Degueldre, C.A. 2017. *The analysis of nuclear materials and their environments.* NYC: Springer International Publishing.

Denault, A., Couture, P. and Vegas, A. 2016. *Transesophageal Echocardiography Multimedia Manual.* Boca Raton: CRC Press.

Denny, M. 1993. *Air and Water.* Princeton: Princeton University.

Den-Toonder, J.M.J. and Nieuwstadt, F.T.M. 1997. Reynolds number effects in a turbulent pipe flow for low to moderate Re. *Physics of Fluids*. **9**(1), pp.3398-3409.

Dong, T., Norisuye, T., Nakanishi, H. and Tran-Cong_Miyata, Q. 2020. Particle size distribution analysis of oil-in-water emulsions using static and dynamic ultrasound scattering techniques. *Ultrasonics*. **108**(1), pp.106-117.

Dorrell, R.M., Hogg, A.J. and Pritchard, D. 2013. Polydisperse suspensions: Erosion, deposition, and flow capacity. *Journal of Geophysical Research: Earth Surface.* **118**(3), pp.1939-1955.

Downing, A., Thorne, P.D. and Vincent, C.E. 1995. Backscattering from a suspension in the near field of a piston transducer. *Journal of the Acoustical Society of America*. **97**(3), pp.1614-1620.

Duchene, P., Chaki, S., Ayadi, A. and Krawczak, P. 2018. A review of non-destructive techniques used for mechanical damage assessment in polymer composites. *Journals of materials science*. **53**(1), pp.7915-7938.

Dukhin, A.S. and Goetz, P.J. 2009. Bulk viscosity and compressibility measurement using acoustic spectroscopy. *J.Chem.Phys.* **130**(1).

Dunne, R.C., Kawatra, S.K. and Young, C.A. ed. 2019. *SME Mineral Processing and Extractive Metallurgy Handbook.* Colorado: Society for Mining, Metallurgy and Exploration.

Dutta, P., Saha, S.K., Nandi, N. and Pal, N. 2016. Numerical study on flow separation in 90° pipe bend under high Reynolds number by k-ε modelling. *Engineering Science and Technology, an International Journal.* **19**(2), pp.904-910.

Echlin, P. 2011. *Handbook of sample preparation for scanning electron microscopy and X-ray microanalysis.* New York: Springer.

Eilers, H. 1941. The viscosity of emulsions of highly viscous substances as a function of concentration. *Colloid journal.* **97**(1), pp.313-321.

Ein-Mozaffari, F., C.P.J. Bennington, G.A. Dumont, and D. Buckingham. 2007. Measuring flow velocity in pulp suspension mixing using ultrasonic Doppler velocimetry. *Chemical Engineering Research and Design*. **85**(5), pp.591-597.

El-Badawy, A.A. 2008. Active vibration suppression of a cutting tool utilising the finite element method. *Journal of Al Azhar University Engineering Sector*. **3**(9), pp.1034-1046.

Escrig, J., Woolley, E., Rangappa, S., Simeone, A. and Watson, N.J. 2019. Clean-in-place monitoring of different food fouling materials using ultrasonic measurements. *Food Control.* **104**(1), pp.358-366.

Escrig, J., Woolley, E., Simeone, and Watson, N.J. 2020. Monitoring the cleaning of food fouling in pipes using ultrasonic measurements and machine learning. *Food Control.* **116**(1).

Faia, P., Krochak, P., Costa, H., Lundell, F., Silva, R.C., Garcia, F.A.P. and Rasteiro, M.G. 2016. A comparative study of magnetic resonance imaging, electrical impedance tomography and ultrasonic Doppler velocimetry for semi-dilute fibre flow suspension characterisation. *International Journal of Computational Methods and Experimental Measurements.* **4**(2), pp.165-175.

Faia, P., Silva, R., Rasteiro, M.G and Garcia, F. 2020. Electrical Tomography: A Review of Configurations, and Application to Fibre Flow Suspensions

Characterisation. *Applied Sciences*. **10**(2355), pp. 1-30. Doi: 10.3390/app10072355.

Falola, A.A., Huang, M.X., Zou, X.W. and Wang, X.Z. 2021. Characterisation of particle size distribution in slurries using ultrasonic attenuation spectroscopy: addressing challenges of unknown physical properties. *Powder Technology*. **392**(1), pp.394-401.

Fearns, P., Dorii, P., Broomhall, M., Branson, P. and Mortimer, N. 2018. *Plume characterisation – laboratory studies.* Australia: Western Australian marine science institution.

Felix, D., Albayrak, I. and Boes, R. 2018. In-situ investigation on real-time suspended sediment measurement techniques: Turbidimetry, acoustic attenuation, laser diffraction (LISST) and vibrating tube densimetry. *International Journal of Sediment Research.* **33**(1), pp.3-17.

Feng, X., Buck, E.C., Mertz, C., Bates, J.K., Cunnane, J.C. and Chaiko, D.J. 1994. Characteristics of colloids generated during the corrosion of nuclear waste glasses in groundwater. *Radiochimca Acta*. **1**(197).

Fernandez, A., Ibanez, A., Parilla, M., Elvira, L., Bassat, Q. and Jimenez, J. 2021. Estimation of the concentration of particles in suspension based on envelope statistics of ultrasound backscattering. *Ultrasonics*. **116**(1).

Figueiredo, M.D.M.F., Carvalho, F.D.C.T., Fileti, A.M.F.F. and Serpa, A.L. 2020. Flow pattern classification in water-air vertical flows using a single ultrasonic transducer. *Experimental Thermal and Fluid Science.* **119.**

Finzi, A., Oberti, R., Negri, A.S., Perazzolo, F., Cocolo, G., Tambone, F., Cabassi, G. and Provolo, G. 2015. Effects of measurement technique and sample preparation on NIR spectroscopy analysis of livestock slurry and digestates. *Biosystems Engineering.* **134**(1), pp.42-54.

Fugate, D.C. and Friedrichs, C.T. 2002. Determining concentration and fall velocity of estuarine particle populations using ADV, OBS and LISST. *Continental Shelf Research.* **22**(1), pp.1867-1886.

Fuller, C.B., Bonner, J.S., Islam, M.S., Oko, T., Page, A. and Kirkey, W.D. 2013. Estimating colloidal concentration using acoustic backscatter. *IEEE Sensors.* **13**(11), pp.4546-4555.

Fultz, B. and Howe, J.M. 2012. *Transmission Electron Microscopy and Diffractometry of Materials*. Berlin: Springer.

Gaeta, M.G., Guerrero, M., Formentin, S.M., Palma, G. and Zanuttigh, B. 2020. Non-intrusive measurements of wave-induced flow over dikes by means of a combined ultrasound doppler velocimetry and videography. *Water*. **12**(11), pp.30-53.

Galeev, A., Vinokurov, V.M., Mouraviev, F. and Osin, Y.N. 2009. EPR and SEM study of organo-mineral associations in Lower Permian evaporite dolomites. *Applied Magnetic Resonance.* **35(**3), pp.473-479.

Gartner, J.W. 2004. Estimating suspended solids concentration from backscatter intensity measured by acoustic Doppler current profiler in San Francisco Bay, California. *Mar. Geol.* **211**(1), pp.169-187.

Gerhart, P.M., Gerhart, A.L. and Hochstein, J.I. 2016. *Munson, Young and Okiishi's Fundamentals of Fluid Mechanics.* USA: Wiley.

Gibbs, V., Cole, D. and Sassano, A. 2011. *Ultrasound Physics and Technology: How, Why and When*. Berkeley: Elsevier Health Sciences.

Goldaran, R. and Turer, A. 2020. Application of acoustic emission for damage classification and assessment of corrosion in pre-stressed concrete pipes. *Measurement*. **160**(1).

Gomez, F., Althoefer, K. and Seneviratne, L.D. 2003. Modeling of ultrasound sensor for pipe inspection. In: *2003 IEEE international conference on robotics*

and automation, 14-19 September 2003, Taipei. Taipei: IEEE. ISBN: 0-7803-7736-2.

Goncalves, J., Varghese, K. and Pfleger, S. 2013. *Advances in Human-Computer Interaction. Human Comfort and Security*. Berlin: Springer Berlin Heidelberg.

Goossens, J., T'Jampens, M., Deneudt, K. and Reubens, J. 2020. Mooring scientific instruments on the seabed – design, deployment protocol and performance of a recoverable frame for acoustic receivers. *Methods in ecology and evolution*. **11**(8), pp.974-979.

Grabsch, A.F., Yahyaei, M. and Fawell, P.D. 2020. Number-sensitive particle size measurements for monitoring flocculation responses to different grinding conditions. *Minerals Engineering*. **145**(1).

Grant, I., Weintrager, U., Richardson, I.E., Gull, M. and Wilson, D. 2016. Sellafield FGMSP additional sludge retrievals a significant step in decommissioning part of the UK's nuclear legacy – 16180. In: *WM2016 Conference Proceedings. Waste Management Symposia, 6-10 March 2016, Phoenix*. Phoenix: Waste Management Symposia.

Gray, J.R. and Gartner, J.W. 2009. Technological advances in suspended-sediment surrogate monitoring. *Water Resources Research*. **45**(4).

Gregson, C.R., Goddard, D.T., Sarsfield, M.J. and Taylor, R.J. 2011. Combined electron microscopy and vibrational spectroscopy study of corroded Magnox sludge from a legacy spent nuclear fuel storage pond. *Journal of Nuclear Materials.* **412**(1), pp.145-156.

Gronarz, T., Schnell, M., Siewert, C., Schneiders, L., Schroder, W. and Kneer, R. 2017. Comparison of scattering behaviour for spherical and non-spherical particles in pulverised coal combustion. *International Journal of Thermal Sciences***. 111**(1), pp.116-128.

Guan, S., Brookens, T. and Vignola, J. 2021. Use of Underwater Acoustics in Marine Conservation and Policy: Previous Advances, Current Status, and Future Needs. J. *Mar. Sci. Eng*. **9**(173).

Guerrero, M. and Federico, V.D. 2018. Suspended sediment assessment by combining sound attenuation and backscatter measurements – analytical method and experimental validation. *Advances in Water Resources*. **113**(1), pp.167-179.

Guerrero, M., Ruther, N., Szupiany, R., Haun, S., Baranya, S. and Latosinski, F. 2015. The acoustic properties of suspended sediment in large rivers: consequences on ADCP methods applicability. *Water*. **8**(13), pp. 1-22. Doi:10.3390/w8010013.

Guerrero, M., Szupiany, R.N. and Latosinski, F. 2013. Multi-frequency acoustics for suspended sediment studies: an application in the Parana River. *Journal of Hydraulic Research*. **51**(6).

Guney, M.S., Bombar, G., Aksoy, A.O. and Dogan, M. 2013. Use of UVP to Investigate the Evolution of Bed Configuration. *KSCE Journal of Civil Engineering*. **17**(1), pp. 1188-1197. Doi: 10.1007/s12205-013-0131-5.

Guo, D. and Kundu, T. 2001. A new transducer holder mechanism for pipe inspection. *The Journal of the Acoustical Society of America*. **110**(1).

Guyson Ltd. 2020. *Glass Blast Media*. [Online]. [Accessed June 13, 2020]. Available from: https://www.guyson.co.uk/aftersales/guyson-blast-media/glass-blast-media

Ha, H.K., Maa, J.P.Y., Park, K. and Kim, Y.H. 2011. Estimation of high-resolution sediment concentration profiles in bottom boundary layer using pulse-coherent acoustic Doppler current profiles. *Mar. Geol*. **279**(1-4), pp.199-209.

Haaland, S.E. 1983. Simple and explicit formulas for the friction factor in turbulent pipe flow. *J. Fluids Eng*. **105**(1), pp.89-90.

Haldenwang, R., Kotze, R., Slatter, P. and Mariette, O. 2006. An investigation in using UVP for assisting in rheological characterisation of mineral suspensions. In:

5th International Symposium on Ultrasonic Doppler Methods for Fluid Mechanics and Fluid Engineering, Switzerland, 12-14 September 2006, Zurich Switzerland. Switzerland: ISUD.

Hamine, A., Faiz, B. and Moudden, A. 2013. Ultrasonic measurements of attenuation and velocity in clay suspensions: Application to characterise the dam water. *IJERT International Journal of Engineering Research and Technology.* **2**(8).

Hanes, D.M., Vincent, C.E., Huntley, D.A. and Clarke, T.L. 1988. Acoustic measurements of suspended sand concentration in the C2S2 experiment at stanhope land, Prince Edwards Island. Mar. Geol. **81**(1), pp.185-196.

Hapca, S.M., Baveye, P., Wilson, C.A., Lark, R.M. and Otten, W. 2015. Three-Dimensional Mapping of Soil Chemical Characteristics at Micrometric Scale by Combining 2D SEM-EDX Data and 3D X-Ray CT Images. *PLoS ONE.* **10**(9).

Harbottle, D., Fairweather, M. and Biggs, S. 2011. The minimum transport velocity of colloidal silica suspensions. *Chem Eng Sci.* **66**(11), pp.2309-2316**.**

Harris, K., Butman, B. and Traykovski, P. 2003. Winter-time circulation and sediment transport in the Hudson Shelf Valley. *Cont. Shelf Res*. **23**(8), pp.801–820.

Haschke, M., Flock, J. and Haller, M. 2021. *X-ray fluorescence spectroscopy for laboratory applications.* New Jersey: Wiley.

Haught, D., Venditti, J.G. and Wright, S.A. 2017. Calculation of in situ acoustic sediment attenuation using off-the-shelf horizontal ACDPs in low concentration settings. *Water Resources Research*. **53**(6). Doi:10.1002/2016WE019695.

Hauptmann, P., Hoppe, N., Puttmer, A. 2002 Application of ultrasonic sensors in the process industry. *Measurement Science & Technology*. **13**(8).

Hay, A.E. 1991. Sound scattering from a particle-laden, turbulent jet. *The Journal of the Acoustical Society of America.* **90**(4), pp.2055-2074.

Hay, A.E. and Sheng, J. 1992. Vertical profiles of suspended sand concentration and size from multifrequency acoustic backscatter. *Journal of Geophysical Research Atmospheres*. **97**(10), pp.15661-15667.

He, C. and Hay, A.E. 1993. Broadband measurements of the acoustic scattering cross section of sand particles in suspension. *J Acoust Soc Am*. **94**(4), pp.2247-2254.

Heath, A., Bahri, P., Fawell, P.D. and Farrow, J.B. 2006. Polymer flocculation of calcite: Experimental results from turbulent pipe flow. *AIChE*. **52**(4), pp.1284-1293.

Heath, A.R., Bahri, P.A., Fawell, P.D., Farrow, J.B. 2006. Polymer flocculation of calcite: population balance model. *AIChE J*. **52**(1), pp.1641-1653.

Henrista, C., Mathieua, J.P., Vogels, C., Rulmont, A. and Cloots, R. 2003. Morphological study of magnesium hydroxide nanoparticles precipitated in dilute aqueous solution. *Journal of Crystal Growth*. **249**(1-2), pp.321-330.

Hermann, A and Mookherjee, M. 2016. High-pressure phase of brucite stable at Earths mantle transition zone and lower mantle conditions. *PNAS*. **113**(49), pp.13971-13976.

Hill, C. 2013. *Atomic Empire. An: A Technical History of the Rise and Fall of the British Atomic Energy Programme*. London: Imperial College Press.

Hinze, J.O. 1959. *Turbulence: an introduction to its mechanism and theory*. New York: McGraw-Hill.

Hirose, R. and McCauley, D. 2022. The risks and impacts of nuclear decommissioning: stakeholder reflections on the UK nuclear industry. *Energy Policy*. **164**(1).

Hitachi. 2013. *Hitachi Tabletop Microscope TM3030: Gateway to Innovation*. [Online]. [Accessed 1 June 2023]. Available from: https://www.hitachi-hightech.com/file/us/pdf/library/literature/TM3030_brochure_letter.pdf

Hitachi. 2014. *Instruction manual for model TM3030Plus table top microscope (users operation/ maintenance edition).* Japan: Hitachi.

Hitachi. 2022a. *Electron microscopes (SEM/TEM/STEM).* [Online]. [Accessed 4 November 2022]. Available from: https://www.hitachi-hightech.com/eu/product_list/?ld=sms2&md=sms2-1&version=

Hodgkinson, P. 2018. *Modern methods in solid-state NMR: A practitioner's guide.* London: Royal Society of Chemistry.

Holmer, C.I., and Heymann, F.J. 1980. Transmission of sound through pipe walls in the presence of flow. *Journal of Sound and Vibration.* **70**(2), pp. 275-301.

Hossain, M.S. and Taheri, H. 2020. *In situ* process monitoring for additive manufacturing through acoustic techniques. *Journals of materials engineering and performance.* **29**(1), pp.6249-6262.

Hosseini, S.A., Shamsai, A. and Ataie-Ashtiani, B. 2006. Synchronous measurements of the velocity and concentration in low density turbidity currents using an acoustic Doppler velocimeter. *Flow Measurement and Instrumentation*. **17**(1), pp.59-68.

Howe, B.M., Miksis-Olds, J., Rehm, E., Sagen, H., Worcester, P.F. and Haralabus, G. 2019. Observing the Oceans Acoustically. *Mar. Sci*. **1**(1).

Hoyt, N.C., Agar, E., Nagelli, E.A., Savinell, R. and Wainright, J. 2018. Electrochemical Impedance Spectroscopy of Flowing Electrosorptive Slurry Electrodes. *Journal of the Electrochemical Society*. **165**(10), pp.439-444.

Hriljac, J, Boxall, C, Currell, F.J., Day, J., Fairweather, M., Harbottle, D., Holdich, R., Hunter, T.N., Hyatt, N.C., Kaltsoyannis, N., Kerridge, A., Lee, W.E., Lennox, B., Lunn, R.J., Pimblott, S.M., Read, D., Ryan, M., Scott, T.B., Tovey, L. and Vandeperre, L.J. 2018. The DISTINCTIVE University Consortium Theme 3: Legacy Ponds and Silo Wastes. In: *Proceedings of the 44th Annual Waste Management Conference. WM2018: 44th Annual Waste Management Conference,*

18-22 Mar 2018, Phoenix, AZ, USA. USA: Waste Management Symposia, pp. 6180-6194. ISBN 978-1-5108-6764-2.

Hu, P., Liang, L., Li, B. and Xia, W. 2021. Delving into the heterocoagulation between coal and quartz at different shear rates by the focused beam reflectance measurement (FBRM) and particle vision and measurement (PVM) techniques. *Fuel*. **286**(Part 2).

Huang, C. and Chen, G.S. 1996. Use of the fibre-optical monitor in evaluating the state of flocculation. *Water Research*. **30**(11), pp.2723-2727.

Huang, R. and Zhang, Q. 2021. Concentration measurement without calibration of natural sediment particles using backscatter sensing with optical fibres. *Measurement*. **167**(1).

Huang, R., Zhang, Q., Qi, P. and Liu, W. 2019. Concentration measurement of uniform particles based on backscatter sensing of optical fibres. *Water*. **11**(9).

Hunter, T., Biggs, S., Young, J., Fairweather, M. and Peakall, J. 2012. Ultrasonic Techniques for the *In Situ* Characterisation of 'Legacy' Waste Sludges and Dispersions. In: *ASME 2011 14th International Conference on Environmental Remediation and Radioactive Waste Management, Parts A and B. International Conference on Radioactive Waste Management and Environmental Remediation, 17 August 2012, Reims.* Reims: ASME Digital Collection, pp. 801-806

Hunter, T., Biggs, S., Young, J., Fairweather, M., and Peakall, J. 2011. Ultrasonic Techniques for the *In Situ* Characterisation of Nuclear Waste Sludges. In: *WM2011 Conference, February 27 – March 3, Phoenix, AZ, USA.* USA: Waste management symposia. Doi: 10.1115/ICEM2011-59111

Hunter, T., Peakall, J., Tonge, A., Fairweather, M., Rice, H. and Barnes, M. 2020. Development of acoustic backscatter for *in situ* monitoring of nuclear sludge wastes during transfer. In: *WM2020 Conference Proceedings. Waste Management Symposiua, 8-12 March 2020, Phoenix*. Phoenix: Waste Management Symposia.

Hunter, T.N., Cowell, D., Rice, H., Smith, I., Tonge, A., Freear, S., Randall, G., Barnes, M., Peakall, J., Malone, K., Burt, D., Horton, L., Egarr, D. and Biggs, S. 2016. Utilising a novel acoustic backscatter array to characterise waste consolidation and settling in a horizontal flow clarifier – 16051. In: *WM2016 Conference Proceedings. Waste Management Symposia, 6-10 March 2016, Phoenix*. Phoenix: Waste Management Symposia.

Hunter, T.N., Cowell, D.M.J., Carpenter, T., Freear. S, Peakall, J., Rice, H.P., Tonge, A., Fairweather, M. and Barnes, M. 2016. Large-scale trials of a real-time acoustic backscatter system for solids concentration measurement during nuclear waste cleanup. In: *IEEE International Ultrasonics Symposium IUS, 18-21 September 2016, France.* France: IEEE.

Hunter, T.N., Darlison, L., Peakall, J. and Biggs, S. 2012. Using a multi-frequency acoustic backscatter system as an *in situ* high concentration dispersion monitor. *Chemical Engineering Science*. **80**(1), pp.409-418.

Hunter, T.N., J. Peakall, and S.R. Biggs. 2011. Ultrasonic velocimetry for the *in situ* characterisation of particulate settling and sedimentation. *Minerals Engineering*. **24**(5), pp. 416-423.

Hunter, T.N., Peakall, J. and Biggs, S. 2012. An acoustic backscatter system for *in situ* concentration profiling of settling flocculated dispersions. *Minerals Engineering.* **27-28**(1), pp.20-27.

Hunter, T.N., Peakall, J., and Biggs, S.R. 2011. Ultrasonic velocimetry for the *in-situ* characterisation of particulate settling and sedimentation. *Minerals Engineering.* **24**(5).

Hunter, T.N., Peakall, J., Egarr, D., Cowell, D.M.J., Freear, S., Tonge, A.S., Horton, L., Rice, H.P., Smith, I., Malone, K., Burt, D., Barnes, M., Randall, G., Biggs, S. and Fairweather, M. 2020. Concentration profiling of a horizontal sedimentation tank utilising a bespoke acoustic backscatter array and CFD simulations. *Chemical Engineering Science*. **218**(1), pp.1-12.

Hunter, T.N., Peakall, J., Unsworth, T.J., Acun, M.H., Keevil, G., Rice, H. and Biggs, S. 2013. The influence of system scale on impinging jet sediment erosion: Observed using novel and standard measurement techniques. *Chemical Engineering Research and Design*. **91**(4), pp.722- 734.

Hurther, D., Thorne, P.D., Bricault, M., Lemmin, U. and Barnoud, J.M. 2011. A multi-frequency acoustic concentration and velocity profiler (ACVP) for boundary layer measurements of fine-scale flow and sediment transport processes. *Coastal Engineering*. **58**(7), pp.594-605.

Hussain, S.T., Hunter, T.N., Peakall, J. and Barnes, M. 2020. Utilisation of underwater acoustic backscatter systems to characterise nuclear waste suspensions remotely. *Proceedings of meeting on acoustics, Acoustical Society of America.* **40**(1), pp.1-12.

Hussain, S.T., Hunter, T.N., Peakall, J. and Barnes, M. 2021. Characterising flocculated suspensions with an ultrasonic velocity profiler in backscatter mode. In: *IEEE International Ultrasonics Symposium (IUS), September 2021.* China: IEEE.

Hussain, S.T., Hunter, T.N., Peakall, J. and Barnes, M. 2021. Simultaneous velocity and concentration profiling of nuclear waste suspensions in pipe-flow, using ultrasonic Doppler and backscatter analysis. *Proceedings of meeting on acoustics, Acoustical Society of America.* **150**(4), pp.1-13.

Hussain, S.T., Hunter, T.N., Peakall, J., Barnes, M. and Rice, H. 2022. Remote analysis of complex mineral suspensions in engineered pipelines: utilising underwater acoustic backscatter systems – 22142. In: *WM Symposia Conference Proceedings, March 2022, Phoenix.* Phoenix: WM Symposia.

IAEA. 2021. *Storage of spent nuclear fuel: specific safety guide.* Austria: IAEA.

Ingale, P., Knemeyer, K., Hermida, M.P., d'Alnoncourt, R.N., Thomas, A. and Rosowski, F. 2020. Atomic Layer Deposition of ZnO on Mesoporous Silica:

Insights into Growth Behavior of ZnO via In-Situ Thermogravimetric Analysis**.** **10**(5), pp.981.

Ippolito, F., Hubner, G., Claypole, T. and Gane, P. 2021. Calcium carbonate as functional filler in polyamide 12-manipulation of the thermal and mechanical properties. *Processes*. **9**(6).

ISO. 2006. *Measurement and characterisation of particles by acoustic methods – Part 1: Concepts and procedures in ultrasonic attenuation spectroscopy*. Geneva: ISO.

Ito, J., Matsushima, Y., Unuma, H., Horiuchi, N., Yamashita, K. and Tajika, M. 2017. Preparation and properties of pressure less-sintered dense calcite ceramics. *Materials Chemistry and Physics.* **192**(1), pp.304-310.

Jackson, R.G. 2019. *Novel sensors and sensing*. Oxfordshire: Taylor and Francis.

Jarvis, P., Jefferson, B. and Parsons, S.A. 2005. Measuring Floc Structural Characteristics. *Reviews in Environmental Science and Biotechnology*. **4**(1-2), pp. 1-18. Doi: 10.1007/s11157-005-7092-1.

Javanaud, C. and Thomas, A. 1988. Multiple scattering using the Foldy-Twersky integral equation. *Ultrasonics*. **26**(6), pp.341-343.

Jayasuriya, S. and Sorrell, V.L. 2019. *Questions, tricks, and tips for the echocardiography boards.* Tattenhall: Wolters Kluwer Health.

Jia, C.Y., Yin, Q.X., Zhang, M.J., Wang, J.K. and Shen, Z.H. 2008. Polymorphic transformation of pravastatin sodium monitored using combined online FBRM and PVM. *Org. Processes. Res. Dev.* **12**(6), pp.1223-1228.

Johnson, B.L., Holland, M.R., Miller, J.G., and Katz, J.I. 2013. Ultrasonic Attenuation and Speed of Sound of Cornstarch Suspensions. *The Journal of the Acoustical Society of America***.** **133**(1).

Johnson, M., Peakall, J., Fairweather, M., Barnes, M., Davison, S., Jia, X., Clare, M.A., Harbottle, D. and Hunter, T.N. 2019. Sediment Microstructure and the Establishment of Gas Migration Pathways during Bubble Growth. *Environmental Science and Technology*. **53**(21), pp.12882-12892.

Jonasz, M. and Fournier. G.R. 2011. *Light Scattering by Particles in Water: Theoretical and Experimental Foundations*. 2nd. USA: Elsevier Science.

Jones, A.D. and Clarke, P.A. 2004. Underwater sound received from some defence activities in shallow ocean regions. *Proceedings of Acoustics, 3-5 November 2004, Gold Coast Australia.* Australia: Australian Acoustical Society.

Joshi, S.G. 2021. Ultrasonic flow meter using mode coupling transducers. *Ultrasonics*. **116**(1).

Jourdain de Thieulloy, M., Dorward, M., Old, C., Gabl, R., Davey, T., Ingram, D.M. and Sellar, B. 2020. Single-beam acoustic doppler profiler and co-located acoustic doppler velocimeter flow velocity data. *Data*. **5**(1).

Jung, J., Maeda, M., Chang, A., Bhandari, M., Ashapure, A. and Landivar-Bowles, J. 2021. The potential of remote sensing and artificial intelligence as tools to improve the resilience of agriculture production systems. *Current opinion in biotechnology*. **71**(1), pp.15-22.

Kafle, B.P. 2019. *Chemical analysis and material characterisation by spectrophotometry.* Amsterdam: Elsevier Science.

Kaye, G.W.C. and Laby, T.H. 1995. *Tables of physical and chemical constants*. London: Longman.

Kenneth, G. 2014. Discriminating between the nearfield and the farfield of acoustic transducers. *The Journal of the Acoustical Society of America*. **136**(4).

Kenslea, A., Hakala, C., Zhong, Z., Lu, Y., Fretwell, J. and Hager, J. 2018. Characterising Impact of TEM Sample Preparation on CD Metrology. In: *29th*

Annual SEMI Advanced Semiconductor Manufacturing Conference (ASMC), 30 April 2018- 3 May 2018. Saratoga Springs: IEEE.

Kestin, J., Sokolov, M. and Wakeham, W.A. 1978. Viscosity of liquid water in the range -8C to 150C. *Journal of Physical and Chemical Reference Data.* **7**(3). DOI: 10/1063/1.555581.

Khalitov, D. and Longmire, E.K. 2003. Effect of particle size on velocity correlations in turbulent channel flow. In: *4th joint fluids summer engineering conference, Minneapolis.* Minnesota: ASME.

Khamis, D. and Brambley, E.J. 2017. Acoustics in a Two-Deck Viscothermal Boundary Layer over an Impedance Surface. *AIAAJ*. **55**(10).

Khodaei, M. and Petaccia, L. 2017. *X-ray characterisation of nanostructured energy materials by synchrotron radiation.* London: IntechOpen.

Kim, I., Ma, X. and Andreassen, J.P. 2012. Study of the solid-liquid solubility in the piperazine-H 2O-CO2 system using FBRM and PVM. *Energy Procedia.* **23**(1), pp.72-81.

Kim, J. and Ulrich, J. 2021. Thermodynamic study on the amorphous form and crystalline hydrates using *in situ* Raman and FBRM. *Chemical Engineering and Technology*. **45**(2), pp.291-301.

Klassen, I., Hillebrand, G., Olsen, N.R.B., Vollmer, S., Lehmann, B. and Nestmann, F. 2013. Flocculation processes and sedimentation of fine sediments in the open annular flume – experiment and numerical modelling. *Earth Surface Dynamics.* **1**(1), pp. 437-481. Doi: 10.5194/esurfd-1-437-2013.

Klema, M.R., Pirzado, A.G., Venayagamoorthy., S.K. and Gates, T.K. 2020. Analysis of acoustic Doppler current profiler mean velocity measurements in shallow flows. *Flow measurement and instrumentation*. **74**(1).

Kokossis, A., Thongchul, N, and Assabumrungrat, S. 2021. *A-Z of Biorefinery: A comprehensive view.* USA: Elsevier Science.

Konjin, B.J., Sanderink, O.B.J. and Kruyt, N.P. 2014. Experimental study of the viscosity of suspensions: effect of solid fraction on particle size and suspending liquid. *Powder Technology*. **266**(1), pp.61-69.

Kostaschuk, R., Best, J., Villard, P., Peakall, J. and Franklin, M. 2005. Measuring flow velocity and sediment transport with an acoustic Doppler current profiler. *Geomorphology*. **68**(1-2), pp.25-37.

Kotze, R., Ricci, S., Birkhofer, B. and Wiklund, J. 2016. Performance tests of a new non-invasive sensor unit and ultrasound electronics. *Flow measurement and instrumentation.* **48**(1), pp.104-111.

Kotze, R., Wiklund, J. and Haldenwang, R. 2016. Application of ultrasound Doppler technique for in-line rheological characterisation and flow visualisation of concentrated suspensions. *International conference on hydrotransport special issue.* **94**(6), pp.1066-1075.

Kotze, R., Wiklund, J., Haldenwang, R. and Fester, V. 2011. Measurement and analysis of flow behaviour in complex geometries using the Ultrasonic Velocity Profiling (UVP) technique. *Flow Measurement and Instrumentation*. **22**(2), pp.110-119.

Krieger, I.M. and Dougherty, T.J. 1959. A mechanism for non-newtonian flow in suspensions of rigid spheres. *Transactions of the society of rheology*. **3**(137).

Kumar, V., Taylor, M.K., Mehrotra, A. and Stagner, W.C. 2013. Real-Time Particle Size Analysis Using Focused Beam Reflectance Measurement as a Process Analytical Technology Tool for a Continuous Granulation–Drying–Milling Process. *AAPS PharmaSciTech*. **14**(2), pp.523-530.

Kutluary, S., Sahin, O., Ceyhan, A.A. and Izgi, M.S. 2017. Design and optimization of production parameters for boric acid crystals with the crystallization process in an MSMPR crystalliser using FBRM and PVM technologies. *Journal of Crystal Growth.* **467**(1), pp.172-180.

Kutluay, S., Ceyhand, A.A., Sahin, O. and Izgi, M.S. 2020. Utilisation of *In Situ* FBRM and PVM Probes to Analyse the Influences of Monopropylene Glycol and Oleic Acid as Novel Additives on the Properties of Boric Acid Crystals. *Ind. Eng. Chem. Res*. **59**(19), pp. 9198-9206.

Kyoda, T., Costine, A.D., Fawell, P.D., Bellwood, J. and Das, G.K. 2019. Using focused beam reflectance measurement (FBRM) to monitor aggregate structures formed in flocculated clay suspensions. *Minerals Engineering*. **138**(1), pp.148-160.

Kytomaa, H.K. 1995. Theory of sound propagation in suspensions: a guide to size and concentration characterisation. *Powder Technology*. **82**(1), pp.115-121.

Latosinski, F., Szupiany, R.N., Garcia, C.M., Guerrero, M. and Amsler, M.L. 2014. Estimation of concentration and load of suspended bed sediment in a large river by means of acoustic doppler technology. *Journal of Hydraulic Engineering*. **140**(7).

Laufer, J. 1954. *Report 1174: The structure of turbulence in fully developed pipe flow*. Washington, D.C.: National Bureau of Standards.

Lee, J.H., Boning, D.S. and Anthony, B.W. 2018. Measuring the absolute concentration of microparticles in suspension using high-frequency B-mode ultrasound imaging. *Ultrasound in medicine and biology*. **44**(5), pp.1086-1099.

Leskovec, M., Lundell, F. and Innings, F. 2020. Pipe flow with large particles and their impact on the transition to turbulence. *Physical Review Fluids*. **5**(112301), pp. 1-8. Doi: 10.1103/PhysRevFluids.5.112301.

Li, D., Liang, Y., Wang, H., Yang, L., Yan, X., Wang, L. and Zhang, H. 2020. Effects of slurry preconditioning on the occurrence of major minerals in the flotation products of coal. *International Journal of Coal Preparation and Utilisation*. **42**(9), pp.2597-2612.

Li, J., White, P.R., Roche, B., Bull, J.M., Leighton, T.G., Davis, J.W. and Fone, J.W. 2021. Acoustic and optical determination of bubble size distributions –

quantification of seabed gas emissions. *International journal of greenhouse gas control.* **108**(1).

Li, M., Wilkinson, D. and Patchigolla, K. 2005. Comparison of particle size distributions measured using different techniques. *Particulate Science and Technology*. **23**(3), pp.265-284.

Li, Q., Liang, L., Hu, P. and Xie, G. 2021. Contribution of friction to the heterocoagulation between coal surface and quartz particles studied by the particle vision and measurement (PVM). *Colloids and Surfaces A: Physicochemical and Engineering Aspects.* **626**(1).

Li, X., Xu, D., Yang, J., Yan, Z., Luo, T., Li, X., Zhang, Z. and Wang, X. 2021. Utilisation of FBRM and PVM to analyse the effects of different additives on the crystallisation of ammonium dihydrogen phosphate. *Journal of Crystal Growth*. **576**(1).

Lin, M., Wu, Y. and Rohani, S. 2020. Simultaneous Measurement of Solution Concentration and Slurry Density by Raman Spectroscopy with Artificial Neural Network using a probe. *Crystal. Growth Des*. **20**(3), pp.1752-1759.

Lingireddy, S. and Wood, D.J. 2021. *Surge analysis and the wave plan method: A powerful, accurate and stable method for water hammer studies*. Lexington: KYPipe LLC.

Liu, D., Alobaidi, K. and Valyrakis, M. 2022. The assessment of an acoustic Doppler velocimetry profiler from a user's perspective. *Acta Geophysica.* **70**(1), pp.2297-2310.

Liu, J., Kuang, W., Liu, J., Gao, Z., Rohani, S. and Gong, J. 2022. In-situ multi-phase flow imaging for particle dynamic tracking and characterisation: Advances and applications. *Chemical Engineering Journal*. **438**(1).

Liu, W., Aldahri, T., Liang, B and Lv, L. 2020. *Absorption of SO_2 with recyclable melamine slurry.* **251**(1), pp.117-285.

Liu, Y., Lu, H., Li, Y., Xu, H., Pan, Z., Dai, P., Wang, H. and Yang, Q. 2021. A review of treatment technologies for produced water in offshore oil and gas fields. *Science of the Total Environment*. **775**(7).

Lockwood, A.P.G., Peakall, J., Warren, N.J., Randall, G., Barnes, Martyn., Harbottle, D. and Hunter, T.N. 2021a. Structure, and sedimentation characterisation of sheared $Mg(OH)_2$ suspensions flocculated with anionic polymers. *Chemical Engineering Science*. **231**(1).

Lockwood, A.P.G., Warren, N.J., Peakall, J., Hussain, S., Randall, G., Barnes, M.G., Harbottle, D. and Hunter, T.N. 2021b. A Comparison of the Sedimentation Dynamics of Statistical and Diblock Copolymer Flocculation Aids in Radwaste Dewatering. In: *Waste Management Symposium, 7-11 March 2021, Phoenix, Arizona*. UDA: WM Symposia. ISBN: 0000-0003-3382-4578.

Lu, Q., Yan, B., Xie, L., Huang, J., Liu, Y. and Zeng, H. 2016. A two-step flocculation process on oil sands tailings treatment using oppositely charged polymer flocculants. *Sci Total Environment*. **565**(1), pp.369-375.

Lucklum, F. 2021. Phononic-fluidic cavity sensors for high-resolution measurement of concentration and speed of sound in liquid solutions and mixtures. *Measurement Science and Technology*. **32**(8).

Lynch, J.F., Gross, T.F., Brumley, B.H. and Filyo, R.A. 1991. Sediment concentration profiling in HEBBLE using a 1-MHz acoustic backscatter system. *Marine Geology*. **99**(3-4), pp.361-385.

Lynch, J.F., Irish, J.D., Sherwood, C.R. and Agrawal, Y.C. 1994. Determining suspended sediment particle size information from acoustical and optical backscatter measurements. *Continental Shelf Research*. **14**(10-11), pp.1139-1165.

Lynnworth, L.C., Jossinet, G. and Cherifi, E. 1996. 300/spl deg/C clamp-on ultrasonic transducers for measuring water flow and level. In: *1996 IEEE Ultrasonics Symposium, 3-6 November, 1996, San Antonio.* USA: IEEE. DOI: 10.1109/ULTSYM.1996.584002.

MacDonald, I. T., Vincent, C.E., Thorne, P.D. and Moate, B.D. 2013. Acoustic scattering from a suspension of flocculated sediments. *Journal of Geophysical Research: Oceans*. **118** (5), pp.2581-2594.

Maczulak, A.E. 2009. *Cleaning up the environment: Hazardous waste technology.* UK: Facts on file.

Malvern Instruments Ltd. 2007. *Mastersizer 2000 Essentials: MANO393 Issue 1.0*. [Online]. [Accessed 31 May 2022]. Available from: https://warwick.ac.uk/fac/cross_fac/sciencecity/programmes/internal/themes/am2/booking/particlesize/mastersizer_2000_essentials_manual.pdf

Mann, C., Thorpe, C.L., Milodowski, A.E., Field, L., Shaw, R.P., Boast, L., Hand, R., Hyatt, N.C., Provis, J. and Corkhill, C.L. 2017. Interactions between Simulant Vitrified Nuclear Wastes and high pH solutions: A Natural Analogue Approach. *MRS Advances*. **2**(12), pp.1-6.

Manwar, R., Saint-Martin, L. and Avanaki, K. 2022. Couplants in Acoustic Biosensing Systems. *Chemosensors*. **10**(5).

Martin Marietta. 2022. *A Global Leader of High Purity Magnesia Products.* [Online]. [Accessed 27 October 2022]. Available from: https://magnesiaspecialties.com/download-category/versamag-mh/

Massey, G.M., Friedrichs, C. and Sanford, L.P. 2011. *In situ* characterisation of estuarine suspended sediment in the presence of muddy flocs and pellets. In: *The Proceedings of the Coastal Sediments, May 2-6 2011, Miami.* Miami: World Scientific, pp.1-14.

McFarlane A.J., Klauber, C., Robinson, D.J. and Grafe, M. 2017. *Clays in the Minerals Processing Value Chain*. Cambridge: Cambridge University Press.

Mckeon, B.J., Swanson, C.J., Zagarola, M.V., Donnelly, R.J. and Smits, A. J. 2004. Friction factors for smooth pipe flow. *Journal of Fluid Mechanic*. **511**(1), pp.41-44.

McLelland, S.J., 2010. *Observing Bedload/Suspended Load Using Multi-Frequency Acoustic Backscatter*. USA: U.S Geological Survey Scientific Investigations Report.

Mechtcherine, V., Khayat, K. and Secrieru, E. 2019. *Rheology and Processing of Construction Materials: RheoCon2 & SCC9.* New York: Springer Nature.

Meesters, G.M. and Merkus, H.G. Ed. 2016. *Production, handling and characterisation of particulate materials* (Vol. 25). Switzerland: Springer International Publishing.

Meral, R. 2018. Analyses of turbidity and acoustic backscatter signal with artificial neural network for estimation of suspended sediment concentration. *Applied ecology and environmental research.* **16**(1), pp.697-708.

Met-flow. 2021. *Products/ Profilers*. [Online]. [Accessed 16 April 2021]. Available at: https://met-flow.com/technology/products/uvp-duo-profilers/

Mewis, J. and Wagner, N.J. 2012. *Colloidal Suspension Rheology*. Cambridge: Cambridge University Press.

Microtrac. 2022. *Particle size and shape analyser*. [Online]. [Accessed 27 October 2022], Available from: https://www.microtrac.com/products/particle-size-shape-analysis/dynamic-image-analysis/camsizer-x2/

Mirlean, N., Baraj, B., Niencheski, L.F., Baisch, P. and Robinson, D. 2001. The Effect of Accidental Sulphuric Acid Leaking on Metal Distributions in Estuarine Sediment of Patos Lagoon. *Marine Pollution Bulletin.* **42**(11), pp.1114-1117.

Moate, B.D. and Thorne, P.D. 2012. Interpreting acoustic backscatter from suspended seidments of different and mixed mineralogical composition. *Continental Shelf Research*. **46**(1), pp.67-82.

Moate, B.D., Thorne, P. and Cooke, R.D. 2015. Field deployment and evaluation of a prototype autonomous two-dimensional acoustic backscatter instrument: the

bedform and suspended sediment imager (BASSI). *Continental Shelf Research*. **112**(1).

Mondal, K., Banerjee, T. and Panja, A. 2019. Autonomous underwater vehicles: recent developments and future prospects. *International Journal for Research in Applied Science and Engineering Technology.* **7**(11), pp.215-222.

Moody, L.F. 1944. Friction factors for pipe flow. *Transactions of the American Society of Mechanical Engineers*. **66**(1), pp.671-684.

Mooney, M. 1951. The viscosity of a concentrated suspension of spherical particles. *Journal of colloid science.* **6**(2), pp.162-170.

Moore, S.A., Coz, J.L., Hurther, D. and Paquier, A. 2013. Using multi-frequency acoustic attenuation to monitor grain size and concentration of suspended sediment in rivers. *J Acous Soc Am.* **133**(4), pp.1959-1970.

Morlock, S. E., Nguyen, H. T., and Ross, J. H. 2002. *Feasibility of acoustic Doppler velocity meters for the production of Discharge Records from U.S. Geological Survey streamflow-gaging stations*. Indianapolis: U.S Geological Survey.

Morris, C.W. 1992. *Academic Press Dictionary of Science and Technology: Volume 10*. Oxford: Academic press.

Mortadi, A., Chahid, E.G., Elmelouky, A., Chahbi, M., Ghyati, N.E.L., Zaim, S., Cherkaoui, O. and Moznine, R.E.L. 2020. Complex electrical conductivity as a new technique to monitor the coagulation-flocculation processes in the wastewater treatment of the textile industry. *Water resources and industry*. **24**(1).

Mougin, P., Wilkinson, D., Roberts, K.J., Jack, R. and Kippax, P. 2003. Sensitivity of particle sizing by ultrasonic attenuation spectroscopy to material properties. *Powder Technology.* **134**(3), pp.243-248.

Muggleton, J.M. and Brennan, M.J. 2004. Leak noise propagation and attenuation in submerged plastic water pipes. *Journal of Sound and Vibration*. **278**(3), pp.527-537.

Munasingh, N. and Paul, G. 2006. Ultrasonic-based sensor fusion approach to measure flow rate in partially filled pipes. *IEEE Sensors Journal*. **20**(11).

Muniz, F.T.L., Miranda, M.A.R., Santos, C.M.D. and Sasaki, J.M. 2016. The Scherrer equation and the dynamical theory of X-ray diffraction. *Acta Cryst.* **A72**(1), pp.385-390.

Munson B.R., Young D.F. and Okiishi T.H. 2006. *Fundamentals of Fluid Mechanics*. 5th Ed. New York: John Wiley & Sons.

Murray, R.B.O., Thorne, P. and Hodgson, D.M. 2011. Intrawave observations of sediment entrainment processes above sand ripples under irregular waves. *Journal of Geophysical Research Atmospheres*. **116**(C1).

Mydlarz, C., Salamon, J. and Bello, J.P. 2017. The implementation of low-cost urban acoustic monitoring devices. *Applied Acoustics*. **117**(Part B), pp.207-218.

Nakamura, K. 2012. *Ultrasonic Transducers: materials and design for sensors, actuators, and medical applications.* Amsterdam: Elsevier Science.

Namorato, M.V. 2000. A concise history of acoustics in warfare. *Applied Acoustics*. **59**(2), pp.101-135. DOI: https://doi.org/10.1016/S0003-682X(99)00021-3

Narayanasamy, S., Jollivet, P., Godon, N., Angeli, F., Gin, S., Cabie, M., Cambedouzou, J., Guillou, C.L. and Abdelouas, A. 2019. Influence of composition of nuclear waste glasses on vapor phase hydration. *Journal of Nuclear Materials.* **525**(1), pp.53-71.

Natter, J., Schmelzer, M., Loffler, M.S., Krill, C.E., Fitch, A. and Hempelmann, R. 2000. Grain-growth kinetics of nanocrystalline iron studied *in situ* by

synchrotron real-time X-ray diffraction. *The Journal of Physical Chemistry B.* **104**(11), pp.2467-2476.

NDA. 2019. *Waste stream 2D11 pond sludge.* Cumbria: NDA.

NDA. 2020. *Nuclear industry aqueous waste management good practice guidance.* Cumbria: NDA.

NDA. 2022. *Solid radioactive waste characterisation good practice guide.* Cumbria: NDA.

Newtan, S.U. 2007. *Nuclear war I and other major nuclear disasters of the 20th century.* Bloomington: AuthorHouse.

Nippon Steel Corporation. 2019. *Pipes and Tubes for Nuclear Application.* Tokyo: Nippon Steel.

Nishiwaki, Y. and Sato, Y. 2022. Exothermic reaction of fine and coarse magnesium powders with water. *Science and Technology of Energetic Materials.* **83**(1), pp.20-27.

Njobuenwu, D.O. and Fairweather, M. 2016. Large eddy simulation of particle-particle interactions in turbulent flow: collision, agglomeration and break-up events. In: *11th international ERCOFTAC symposium on engineering turbulence modelling and measurements, 21-23 September 2016, Palermo.* Palermo: ETMM.

Nollet, L.M.L. ed. 2004. *Handbook of food analysis: methods and instruments in applied food analysis.* Mark Dekker: Belgium.

Nsugbe, E., Starr, A., Jennions, I. and Carcel-Ruiz, C. 2018. Estimation of online particle size distribution of a particle mixture in free fall with acoustic emission. *Particle Science and Technology*. **37**(8), pp.953-963.

Obayashi, H., Tasaka, Y., Kon, S. and Takeda, Y. 2008. Velocity vector profile measurement using multiple ultrasonic transducers. *Flow measurement and instrumentation.* **19**(3-4), pp.189-195.

Ogasawara, H., Mori, K. and Yagi, H. 2019. A Study of Acoustic Characteristics at Sea Bottom Sediment Including Organic Matter. In: *ICA. 23rd International Congress on Acoustics, 9-13 September 2019, Aechen.* Germany: ICA, pp1-5.

Oggier, M., Eicken, H., Wilkinson, J., Petrich, C. and O'Sadnick, M. 2020. Crude oil migration in sea-ice: laboratory studies of constraints on oil mobilisation and seasonal evolution. *Cold regions science and technology.* **174**(1).

Ohie, K., Yoshida, T., Tasaka, Y., Sugihara-Seki, M. and Murai, Y. 2022. Rheological characterisation and flow reconstruction of polyvinylpyrrolidone aqueous solutions by means of velocity profiling-based rheometry. *Experiments in Fluids.* **63**(135).

Omega Engineering. 2022. *Wall Mount Ultrasonic Flow Meter.* [Online], [Accessed 27 October 2022]. Available from: https://www.omega.co.uk/pptst/FDT-25W.html 2022

Omya North America. 2021. *AZ Calcium Carbonate. Omya.* [Online]. [Accessed 10 November 2021]. Available from: OMYACARB® Technical Data Sheets (matweb.com)

Osborne, P.D. and Vincent, C.E. 1996. Vertical and horizontal structure in suspended sand concentration and wave-induced fluxes over bedforms. *Marine Geology*. **131**(3-4), pp.195-208.

Osman, M.A., Atallah, A., Schweizer, T. and Ottinger, H.C. 2004. Particle-particle and particle-matrix interactions in calcite filled high-density polyethylene-steady shear. *Journal of Rheology*. **48**(1).

Owen, A.T., Fawell, P.D., Swift, J.D., Labbett, D.M., Benn, F.A. and Farrow, J.B. 2008. Using turbulent pipe flow to study the factors affecting polymer-bridging flocculation of mineral systems. *International Journal of Mineral Processing.* **87**(3-4), pp.90-99.

Pahwa, P.K. and Pahwa, G.K. 2014. *Hydrogen Economy*. New Delhi: Energy and Resources Institute.

Panetta, P.D., Bland, L.G., Cartwright, G. and Friedrichs, C.T. 2012. Acoustic scattering to measure dispersed oil droplet size and sediment particle size. In: *Oceans, 14-19 October. 2012*. Hampton Roads, VA: IEEE. DOI: 10.1109/OCEANS.2012.6405103.

Papadopoulou, A., Gillissen, J.J.J., Tiwari, M.K. and Balabani, S. 2020. Effect of Particle Specific Surface Area on the Rheology of Non-Brownian Silica Suspensions. *Materials (Basel).* **13**(20).

Patnaik, P. 2002. *Handbook of Inorganic Chemicals*. NYC: McGraw-Hill Education.

Paul, C.R. 2006. *Introduction to Electromagnetic Compatibility.* 2nd ed. New Jersey: Wiley.

Poddar, S. and Tandon, N. 2019. Detection of particle contamination in journal bearing using acoustic emission and vibration monitoring techniques. *Tribology International*. **134**(1), pp.154-164.

Podesta, M. *Understanding the Properties of Matter.* Oxford: CRC Press, 2020.

Povey, M.J.W. 1997. *Ultrasonic techniques for fluids characterisation*. Cambridge: Academic Press.

Powel R. 2008. Experimental techniques for multiphase flows. *Physics Of Fluids*. **20**(4).

Prateepasen, A., Kaewwaewnoi, W. and Kaewtrakulpong, P. 2011. Smart portable noninvasive instrument for detection of internal air leakage of a valve using acoustic emission signals. *Measurement*. **44**(2), pp.378-384.

Priego-Hernandez, G., Rubio-Arias, H. and Rivera-Trejo, F. 2019. ADCP, multi-frequency analysis for flow measurements in rivers. *Acta Sci.Pol. Formatio Circumiectus.* **18**(1), pp.101-112.

Prince, P., Hill A., Covarrubias, E.P., Doncaster, P., Snaddon, J.L. and Rogers, A. 2019. Deploying acoustic detection algorithms on low-cost, open-source acoustic sensors for environmental monitoring. *Sensors*. **19**(3).

Prochaska, A.B., Santi, P.M. and Higgins, J.D. 2008. Relationships between size and velocity for particles within debris flows. *Canadian geotechnical journal*. **1**(1), pp. 1778-1783.

Qu, G., Feng, X., Wang, Y., Du, Q., Ma, X., Li, Q., Wang, Y. and Liu, W. 2022. Study on Preparation of Elastic Silica Aerogel Based on SEM Analysis. *Wireless Communication and Mobile Computing.* **2022**(1), pp.1-6.

Quiroz, W.M., Ruiz, P and Moscoso, C. 2020. Inline characterisation of mining slurries by ultrasonic velocity profile technique. In: *23rd International Conference on Paste, Thickened and Filtered Tailings, 2-6 November, 2020, Chile.* Chile: PASTE. DOI: 10.36487/ACG_repo/2052_15.

RadioRoSo. 2022. *Motivation.* [Accessed 9 November 2022]. Available from: http://radioroso.ciirc.cvut.cz/task/motivation/

Raman, A. and Gonzalez-Prida, V. 2015. *Promoting Sustainable Practices Through Energy Engineering and Asset Management*. Pennsylvania: IGI Global.

Randall, R.H. 2012. *An introduction to Acoustics.* Dover: Dover Publications.

Rasteiro, M.G., Garcia, F.A.P. and Perez, M.D.M. 2007. Applying LDS to Monitor Flocculation in Papermaking. *Particulate Science and Technology*. **25**(3), pp.303-308.

Rennels, D.C., and Hudson, H.M. 2012. *Pipe Flow: A Practical and Comprehensive Guide.* Oxford: Wiley.

Retsch Technology. 2012. *Operating Instructions/ Manual.* Germany: Retsch Technology.

Rice, H. P. 2013. *Transport, and deposition behavior of model slurries in closed pipe flow.* Ph.D. thesis, University of Leeds.

Rice, H.P., Fairweather, M., Hunter, T.N., Mahmoud, B.A., Biggs, S.R. and Peakall, J. 2014. Measuring particle concentration in multiphase pipe flow using acoustic backscatter: Generalization of the dual-frequency inversion method. *J. Acoust. Soc. Am*. **136**(1), pp.156-169.

Rice, H.P., Fairweather, M., Peakall, J., Hunter, T.N., Mahmoud, B. and Biggs, S.R. 2015. Measurement of particle concentration in horizontal, multiphase pipe flow using acoustic methods: Limiting concentration and the effect of attenuation. *Chemical Engineering Science*. **126**(1), pp. 745-758.

Rice, H.P., Fairweather, M., Peakall, J., Hunter, T.N., Mahmoud, B. and Biggs, S.R. 2015. Constraints on the functional form of the critical deposition velocity in solid–liquid pipe flow at low solid volume fractions. *Chemical Engineering Science*. **126**(1), pp.759-770.

Rice, H.P., Peakall, J., Fairweather, M. and Hunter, T.N. 2020. Extending estimation of the critical deposition velocity in solid–liquid pipe flow to ideal and non-ideal particles at low and intermediate solid volume fractions. *Chemical Engineering Science*. **211**(1), pp. 115-308.

Rice, H.P., Pilgrim, J.L., Fairweather, M., Peakall, J., Harbottle, D. and Hunter, T.N. 2020. Extending acoustic in-line pipe rheometry and friction factor modelling to low Reynolds number, non-newtonian slurries. *Transport phenomena and fluid mechanics.* **66**(8).

Richards, S. D., Leighton, T. G. and Brown, N. R. 2003. Visco-inertial absorption in dilute suspensions of irregular particles. *Proceedings of the Royal Society of London A.* **459**(2037), pp. 2153 – 2167. DOI: 10.1098/rspa.2003.1126.

Richards, S.D. and Heathershaw, A.D. 1996. An investigation of viscous absorption of sound energy in turbid seawater at mine hunting frequencies. *The journal of the acoustical society of America.* **100**(3).

Richards, S.D., Leighton, T.G. and Brown, N.R. 2003. Sound absorption by suspensions of nonspherical particles: Measurements compared with predictions using various particle sizing techniques. *J Acoust Soc Am.* **114**(Part 1), pp.1841-1850.

Rideout, B. 2022. *A review of passive acoustic marine mammal call detection techniques.* Canada: Defence Research and Development Canada.

Roberson, J.A. and Crowe, C.T. 1996. *Engineering Fluid Mechanics*. New York: John Wiley & Sons.

Rodriguez, P.M. and Rodriguez, E.M. 2014. Use of a constant temperature hot wire anemometer for air velocity measurements in a wind tunnel. *EAC*. **35**(1).

Rose, C.P. and Thorne, P.D. 2001. Measurements of suspended sediment transport parameters in a tidal estuary. *Cont. Shelf Res*. **21**(15), pp.1551–1575.

Rout, T.K. and Sengupta, D.K. and Besra, L. 2006. Flocculation improves uptake of 90Sr and 137Cs from radioactive effluents. *International Journal of Mineral Processing.* **79**(4), pp. 225-234.

RPS Group. 2022. *Pile fuel storage pond (PFSP).* [Online]. [Accessed 9 November 2022]. Available from: https://www.rpsgroup.com/projects/pile-fuel-storage-pond-pfsp/

Sabbatini, L. and Giglio, E.D. 2022. *Polymer Surface Characterisation*. Bari: De Gruyter.

Sadamatsu, S., Tanaka, M., Higashida, K. and Matsumura, S. 2016. Transmission electron microscopy of bulk specimens over 10 μm in thickness. *Ultramicroscopy.* **162**(1), pp.10-16.

Sahin, C. 2021. Effect of particle size distribution on acoustic doppler velocimeter backscatter for suspended sediment measurements. *Flow measurement and instrumentation.* **79**(1).

Sahin, C., Ozturk, M. and Aydogan, B. 2020. Acoustic doppler velocimeter backscatter for suspended sediment measurements: effect of sediment size and attenuation. *Applied Ocean Research*. **94**(1), pp. 1-10. Doi: 10.1016/j.apor.2019.101975.

Sahin, C., Safak, I., Hsu, T. and Sheremet, A. 2013. Observations of suspended sediment stratification from acoustic backscatter in muddy environments. *Mar. Geol*. **336**(1), pp.24-32.

Sahin, C., Verney, R., Sheremet, A. and Voulgaris, G. 2017. Acoustic backscatter by suspended cohesive sediments: Field observations, Seine Estuary, France. *Continental Shelf Research.* **134**(1), pp.39-51.

Sandven, H., Kristoffersen, A.S., Chen, Y.C. and Hamre, B. 2020. *In situ* measurements of the volume scattering function with LISST-VSF and LISST-200X in extreme environments: evaluation of instrument calibration and validity. *Optics Express*. **28**(25), pp.37373-37396.

Saniie, J., Wang, B. and Huang, X. 2018. Information transmission through solids using ultrasound invited paper. In: *2018 IEEE International Ultrasonics Symposium (IUS), Japan, 22-25 October 2018.* Japan: IEEE.

Sankaran, S. and Ehsani, R. 2014. Imaging with the Electromagnetic Spectrum. In: Sankaran, S. and Ehsani, R. *Introduction to the Electromagnetic Spectrum.* Berlin: Springer, pp.1-15. Doi:10.1007/978-3-642-54888-8_1.

Saraka, C., Machada, M.B., Webster, S.E., Gomez, C. and Kresta, S.M. 2019. Effective sapphire repellency treatment to reduce fouling of a focused beam reflectance measurement (FBRM) probe in bituminous systems. *The Canadian Journal of Chemical Engineering.* **97**(6), pp.1949-1952.

Satjaritanun, P., Regalbuto, J.R., Regalbuto, J.A., Tippayawong, N. and Shimpalee, S. 2021. Mixing optimization with inward flow configuration contra-rotating impeller, baffle-free tank. Alexandria Engineering Journal. **60**(4), pp.3759-3779.

Savic, V., Knezevic, D.M., Lovrec, D., Mitar, J. and Karanovic, V. 2009. Determination of Pressure Losses in Hydraulic Pipeline Systems by Considering Temperature and Pressure. *Strojniski Vestnik.* **55**(4), pp.237-243.

Schaller, K.G. and Huber, B. 2023. Decommissioning of Nuclear Power Plants. *Proceedings of a European Conference Held in Luxembourg.*

Schlichting, H. and Gersten, K. 2016. *Boundary layer theory*. Berlin: Springer Berlin Heidelberg.

Schoeddert, A., Babooram, K. and Pelletier, S. 2018. Reduction of Water Waste in an Organic Chemistry Laboratory Using a Low-Cost Recirculation System for Condenser Apparatus. *Journal of Chemical Education*. **96**(1).

Selfridge, A.R. 1985. Approximate Material Properties in Isotropic Materials. *IEEE Transactions on Sonics and Ultrasonics*. **SU-32**(3), pp.381-394.

Seo, D., Wanhee, I.,Youn, H.J. and Lee, H/L/ 2012. The effects of process variables for GCC pre-flocculation on floc and handsheet properties. *Nordic Pulp and Paper Research Journal*. **27**(2), pp.382-387.

SEPA. 2010. *The management of higher activity radioactive waste on nuclear licensed sites.* [Online]. [Accessed on 9 November 2022]. Available from: https://www.sepa.org.uk/media/101623/part_3a_-waste_minimisation_characterisation_and_segregation.pdf

Shames, I.H. 2003. *Mechanics of fluids*. New York: McGraw-Hill.

Sheng, J. and Hay, A.E. 1988. An examination of the spherical scatterer approximation in aqueous suspensions of sand. *The Journal of the Acoustical Society of America*. **83**(2), pp.598-610.

Shevchik, S.A., Kenel, C., Leinenbach, C., Wasmer, K. 2018. Acoustic emissions *for in situ* quality monitoring in additive manufacturing using spectral convolutional neural networks. *Additive Manufacturing*. **21**(1), pp.598-604.

Shevchik, S.A., Masinelli, G., Kenel, C., Leinenbach, C. and Wasmer, K. 2019. Deep learning for *in situ* and real-time quality monitoring in additive manufacturing using acoustic emission. *IEEE transactions on industrial informatics.* **15**(9), pp.5194-5203.

Shi, B., Chen, Y., Wang, X., Song, S., Fu, S., Zhou, J., Liu, Y., Lv, X., Gong, J. and Liu, Y. 2022. Flowloop investigation into hydrate formation and slurry flow in the presence of micron-sized sand particles. *Journal of Petroleum Science and Engineering.* **212**(1).

Shi, Z., Ren, L.F. and Hamilton, L.J. 1999. Acoustic profiling of fine suspension concentration in the Changjiang Estuary**.** *Estuaries*. **22**(1), pp. 648-656.

Shoham, O. 2006. *Mechanistic modeling of gas-liquid two-phase flow in pipes*. USA: Society of Petroleum Engineers.

Shukla, A., Prakash., A. and Rohani, S. 2007. Particles settling studies using ultrasonic techniques. *Powder Technology*. **177**(2), pp.102-111.

Simmons, S.M., Azpiroz, M., Cartigny, M.J.B., Clare, M., Cooper, C., Parsons, D.R., Pope, E., Sumner, E.J. and Talling, P.J. 2020. Novel acoustic method provides first detailed measurements of sediment concentration structure within submarine turbidity currents. *Journal of Geophysical Research*. **125**(5).

Simmons, S.M., Best, J.L., Parsons, D.R., Keevil, G.M., Oberg, K.A., Malzone, C., Johnson, K.K. and Czuba, J.A. 2009. Measuring suspended sediment concentrations and flow velocities using multibeam sonar. *The Journal of the Acoustical Society of America.* **126**(4), pp.22-32.

Simmons, S.M., Parsons, D.R. and Best, J.L. 2012. Field methods for imaging suspended sediment dynamics and fluxes with a multi-beam echosounder. In: *11th European conference on underwater acoustics, 2-6 July 2012, Edinburgh.* Edinburgh: ECUA.

Simmons, S.M., Parsons, D.R., Best, J.L., Oberg, K.A., Czuba, J.A. and Keevil, G.M. 2017. An evaluation of the use of a multibeam echo-sounder for observations of suspended sediment. *Applied Acoustics.* **126**(3), pp.81-90.

Simmons, S.M., Parsons, D.R., Best, J.L., Orfeo, O., Czuba, J.A., Boldt, J.A. and Oberg, K.A. 2013. Analysis of coherent flow structures over alluvial dunes revealed by multi-beam echo-sounder acoustic backscatter. In: *Marine and river dune dynamics (MARID) IV, Bruges, April 2013.* Bruges: MARID.

Simmons, S.M., Parsons, D.R., Best, J.L., Orfeo, O., Lane, S., Kostaschuk, R., Hardy, R.J., West, G., Malzone, C., Marcus, J. and Pocwiardowski, P. 2010. Monitoring suspended sediment dynamics using MBES. *Journal of Hydraulic Engineering.* **136**(1).

Simone, E., Saleemi, A. and Nagy, Z., 2014. *In Situ* Monitoring of Polymorphic Transformations Using a Composite Sensor Array of Raman, NIR, and ATR-UV/vis Spectroscopy, FBRM, and PVM for an Intelligent Decision Support System. *Organic Process Research & Development*. **19**(1), pp.167-177.

Smerdon, A. 2020. Measurements of settling velocity with an acoustic backscatter instrument. In: *Ocean Sciences Meeting, 16-21 February 2020, San Diego*. San Diego: ESSOAR.

Smith, P., Rector, D.R. and Shekarriz, A. 2010. Microstructural and rheological characterisation of colloidal aggregates of nuclear waste slurries. *Mineral processing and extractive metallurgy review.* **20**(1), pp. 311-324.

Son, G., Kim, D., Kim, Y.D., Lyu, S. and Kim, Soojeong. 2020. A forecasting method for harmful algal bloom(HAB)-prone regions allowing preemptive countermeasures based only on acoustic doppler current profiler measurements in a large river. *Water*. **12**(20).

Sourdeval, O., Gryspeerdt, E., Kramer, M., Goren, T., Delanoe, J., Afchine, A., Hemmer, F. and Quaas, J. 2018. Ice crystal number concentration estimates from

lidar–radar satellite remote sensing – Part 1: Method and evaluation. *Atmos. Chem. Phys.* **18**(1), pp.14327-14350.

Steiner, G. and Podd, F. 2006. A Non-Invasive and Non-Intrusive Ultrasonic Transducer Array for Process Tomography. In: *XVIII IMEKO WORLD CONGRESS Metrology for a sustainable development, September 17-22 2006, Rio de Janeiro.* Brazil: IMEKO world congress.

Stener, J.F., Carlson, J.E., Palsson, B.I. and Sand, A. 2014. Evaluation of the applicability of ultrasonic velocity profiling in conditions related to wet low intensity magnetic separation. *Minerals Engineering*. **62**(1), pp.2-8.

Stener, J.F., Carlson, J.E., Sand, A. and Palsson, B.I. 2016. Monitoring mineral slurry flow using pulse echo ultrasound. *Flow measurement and instrumentation.* **50**(1), pp.135-146.

Stevenson, P., Thorpe, R.B. and Davidson, J.F. 2002. Incipient motion of a small particle in the viscous boundary layer at a pipe wall. *Chemical Engineering Science*. **57**(21), pp.4505-4520.

Stigler, J. 2014. Analytical Velocity Profile in Tube for Laminar and Turbulent Flow. *Engineering Mechanics*. **21**(6), pp.371–379.

Stille, P. and Giere, R. 2004. *Energy, waste, and the environment: a geochemical perspective.* London: Geological Society.

Striebig, B., Ogundipe, A.A., Papadakis, M. and Heine, L.G. 2022. *Environmental engineering and sustainable design.* Boston: Cengage Learning.

Sykes, A., Appleby, M., Perry, J. and Gould, K. 2016. An investigation of the microbiological contamination of ultrasound equipment. *Journal of Infection Prevention.* **7**(4).

Szupiany, R.N., Weibel, C.L., Guerrero, M., Latosinski, F., Wood, M., Ruben, L.D. and Oberg, K. 2018. Estimating sand concentrations using ADCP-based acoustic inversion in a large fluvial system characterised by bi-modal suspended-

sediment distributions. *Earth Surface Processes and Landforms*. **44**(6), pp.1295-1308.

Takeda, S. and Goetz, P.J. 1998. Dispersed/flocculated size characterisation of alumina particles in highly concentrated slurries by ultrasonic attenuation spectroscopy**.** *Colloids and Surfaces A: Physicochemical and Engineering Aspects*. **143**(1), pp.35-39.

Tashi, T., Kikura, H. and Aritomi, M. 2002. Effect of the measurement volume in turbulent pipe flow measurement by the ultrasonic velocity profile method (mean velocity profile and Reynolds stress measurement). *Experiments in Fluids*. **32**(1), pp.188-196.

Temkin, S. 2005. *Suspension Acoustics: An Introduction of the Physics of Suspensions*. Cambridge: Cambridge University Press.

Tezuka, K., Mori, M., Suziki, T., Aritomi, M., Kikura, H. and Takeda, Y. 2008. Assessment of effects of pipe surface roughness and pipe elbows on the accuracy of meter factors using the ultrasonic pulse Doppler method. *Journal of Nuclear Science and Technology*. **45**(4).

Thirumalaiselvi, A. and Sasmal, S. 2019. Acoustic emission monitoring and classification of signals in cement composites during early-age hydration. *Construction and Building Materials*. **196**(1), pp.411-427.

Thomson, M.D.J.M. and Binder, C.M. 2021. Recalibrating the department of national defence approach to active sonar impact management. *Marine pollution bulletin*. **173**(part B), pp.1-4.

Thorne, P. and Buckingham, M.J. 2004. Measurement of scattering by a suspension of irregularly shaped sand particles and comparison with a single parameter modified sphere model. *The journal of the acoustical society of America*. **116**(5).

Thorne, P. D. and Meral, R. 2008. Formulations for the scattering properties of suspended sandy sediments for use in the application of acoustics to sediment transport processes. *Cont. Shelf Res*. **28**(1), pp.309–317.

Thorne, P., Hardcastle, P.J. and Soulsby, R.L. 1993. Analysis of acoustic measurements of suspended sediments. *Journal of Geophysical Research Atmospheres*. **98**(C1), pp.899-910.

Thorne, P., Hurther, D. and Moate, B.D. 2011. Acoustic inversions for measuring boundary layer suspended sediment process. *The Journal of the Acoustical Society of America.* **130**(3), pp.188-200.

Thorne, P., Williams, J.J. and Davies, A.G. 2002. Suspended sediments under waves measured in a large scale flume facility. *Journal of Geophysical Research Atmospheres*. **107**(8).

Thorne, P.D. 1985. The measurement of acoustic noise generated by moving artificial sediments. *The Journal of the Acoustical Society of America*. **71**(1).

Thorne, P.D. and Hanes, D.M. 2002. A review of acoustic measurement of small scale sediment processes. *Continental Shelf Research.* **22**(1), pp.603-632.

Thorne, P.D. and Hardcastle, P.J. 1997. Acoustic measurements of suspended sediments in turbulent currents and comparison with in-situ samples. *The Journal of the Acoustical Society of America*. **101**(1), pp.2603.

Thorne, P.D. and Meral, R. 2008. Formulations for the scattering properties of suspended sandy sediments for use in the application of acoustics to sediment transport processes. *Continental Shelf Research.* **28**(2), pp.309-317.

Thorne, P.D., Davies, A.G. and Bell, P.S. 2009. Observations and analysis of sediment diffusivity profiles over sandy rippled beds under waves. *Journal of Geophysical Research Atmospheres*. **114**(C2).

Thorne, P.D., Hardcastle, P.J. and Soulsby, R.L. 1993. Analysis of acoustic measurements of suspended sediments. *Journal of Geophysical Research: Oceans*. **98**(C1), pp.899-910.

Thorne, P.D., Hurther, D., Cooke, R.D., Caceres, I., Barraud, P.A. and Sanchez-Arcilla, A. 2018. Developments in acoustics for studying wave-driven boundary layer flow and sediment dynamics over rippled sand-beds. *Continental Shelf Research*. **166**(1), pp.119-137.

Thorne, P.D., Lichtman, I.D. and Hurther, D. 2021. Acoustic scattering characteristics and inversions for suspended concentration and particle size above mixed sand and mud beds. *Continental Shelf Research.* **214**(1).

Thorne, P.D., MacDonald, I.T. and Vincent, C.E. 2014. Modelling acoustic scattering by suspended flocculating sediments. *Continental Shelf Research*. **88**(1), pp.81-91.

Thorne, P.D., Vincent, C.E., Hardcastle, P.J., Rehman, S. and Pearson, N. Measuring suspended sediment concentrations using acoustic backscatter devices. 1991. *Marine Geology*. **98**(1), pp.7-16.

Tonge, A., Usher, S. and Peakall, J. 2019. Use of *In Situ* Acoustic Backscatter Systems to Characterise Spent Nuclear Fuel and its Seperation in a Thickener. In: *WM2019 Conference Proceedings. Waste Management Conference 2019, 3-7 March 2019, Phoenix*. Phoenix: Waste Management Symposia.

Tonge, A.S., Bux, J., Hunter, T.N., Freear, S., Cowell, D.M.J. and Peakall, J. 2017. Concentration profiling using a novel acoustic backscatter system with single transducers pulsed at multiple frequencies. In: *2017 IEEE International Ultrasonics Symposium (IUS), 2 November 2017, Washington.* Washington: IEEE.

Tonge, A.S., Peakall, J., Cowell, D.M.J., Freear, S., Barnes, M. and Hunter, T.N. 2021. Experimental validation of acoustic inversions for high concentration

profiling of spherical particles, using broadband technology in the Rayleigh regime. *Applied Acoustics*. **180**(1).

Ul-Hamid, A. 2018. *A Beginners' Guide to Scanning Electron Microscopy.* New York: Springer International Publishing.

University of Leeds. 2022. *Ultrasonics and Instrumentation: Ultrasound Array Research Platform (UARP).* [Online]. [Accessed 15 November 2022]. Available from: https://institutes.engineering.leeds.ac.uk/ultrasound/facilities_instrumentation.html

Urick, R. J., 1948. The Absorption of Sound in Suspensions of Irregular Particles. *The Journal of the Acoustical Society of America.* **20**(3), pp.283-289.

Urick, R.J. 1979. *Sound propagation in the sea*. Washington: Defence advanced research projects agency.

Vand, V. 1948. Viscosity of solutions and suspensions. I. Theory. *J. Phys. Chem*. **52**(2), pp.277-299.

VanderWerf, J.J., Doucette, J.S., O'Donoghue, T., Ribberink, J.S., 2007. Detailed measurements of velocities and suspended sand concentrations over full-scale ripples in regular oscillatory flow. *J. Geophys. Res*. **112**(1).

Vendettuoli, D., Clare, M.A., Sumner, E.J., Cartigny, M.J.B., Talling, P., Wood, J., Bailey, L., Azpiroz-Zabala, M., Paull, C.K., Gwiazda, R., Stacey, C.D., Lintern, G., Simmons, S.M., Pope, E.L., Hage, S. and Xu, J. 2020. Global monitoring data shows grain size controls turbidity current structure. *ESSOAR.* **1**(1), pp.1-22.

Ventura, C., Garcia, F.A.P., Ferreira, P., Rasteiro, M.G. 2008. Flow Dynamics of Pulp Fibre Suspensions. *Tappi J.* **1**(7), pp.20–26.

Vergne, A., Le Coz, J., Berni, C. and Pierrefeu, G. 2019. Using a down-looking multifrequency ABS for measuring suspended sediments in rivers. *Water Resources Research.* **56**(2).

Villard, P.V., Osborne, P.D. and Vincent, C.E. 2000. Influence of wave groups on SSC patterns over vortex ripples. *Continental Shelf Research.* **20**(17), pp.2391-2410.

Vincent, C.E., Young, R.A. and Swift, D.J.P. 1982. On the relationship between bedload and suspended transport on the inner shelf, Long Island, New York. Jounral of Geophysical Research: Oceans. **87**(C6), pp.4163-4170.

Vyse, A.S., Herzschuh, U., Andreev, A.A., Pestryakova, L.A., Diekmann, B., Armitage, S.J. and Biskaborn, B.K. 2020. Geochemical and sedimentological responses of arctic glacial Lake Ilirney, Chukotka (far east Russia) to palaeoenvironmental change since ~51.8 ka BP. *Quaternary Science Reviews*. **247**.

Wada, S., Kikura, H., Aritomi, M., Mori, M. and Takeda, Y. 2004. Development of Pulse Ultrasonic Doppler Method for Flow Rate Measurement in Power Plant Multilines Flow Rate Measurement on Metal Pipe. *Journal of Nuclear Science and Technology.* **41**(3), pp.339-346.

Wang, B., Du, Z., Luan, Z., Zhang, X., Wang, M., Wang, X., Lian, C. and Yan, J. 2021. Seabed features associated with cold seep activity at the Formosa Ridge, South China sea: integrated application of high-resolution acoustic data and photomosaic images. *Deep sea research part I: oceanographic research papers.* **177**(1), pp.1-16.

Wang, K., Hu, Y., Qin, M., Liu, G., Li, Y. and Wang, G. 2021. A leakage particle-wall impingement based vibro-acoustic characterisation of the leaked sand-gas pipe flow. *Particuology***. 55**(1), pp.84-93.

Wang, Q., Li, F., Jiang, X., Wu, S. and Xu, M. 2020. On-stream mineral identification of tailing slurries of tungsten via NIR and XRF data fusion

measurement techniques. *Analytical Methods: advancing methods and applications*. **12**(25), pp.3296-3307.

Wang, Q., Wang, M., Wei, K. and Qiu, C. 2017. Visualisation of Gas-Oil-Water Flow in Horizontal Pipeline Using Dual-Modality Electrical Tomography Systems. *IEEE Sensors*. **17**(24), pp. 8146-8156. Doi: 10.1109/JSEN.2017.2714686.

Wang, W., Sun, H., Guo, J., Lao, L., Wu, S. and Zhang, J. 2021. Experimental study on water pipeline leak using in-pipe acoustic signal analysis and artificial neural network prediction. *Measurement*. **186**(1), pp.1-16.

Wang, X., Zhou, S., Bu, X., Ni, C., Xie, G. and Peng, Y. 2021. Investigation on interaction behavior between coarse and fine particles in the coal flotation using focused beam reflectance measurement (FBRM) and particle video microscope (PVM). *Separation Science and Technology*. **56**(8), pp.1418-1480.

Wasmer, K., Le-Quang, T., Meylan, B. and Shevchik, S.A. 2019. *In situ* quality monitoring in AM using acoustic emission: a reinforcement learning approach. *Journal of Materials Engineering and Performance*. **28**(1), pp.666-672.

Weser, R., Woeckel, S., Wessely, B., Steinmann, U., Babick, F. and Stintz, M. 2014. Ultrasonic backscattering method for *in situ* characterisation of concentrated dispersions. *Powder technology*. **268**(1), pp.177-190.

Wiescher, M. and Manukyan, K. 2022. *Scientific Analysis of Cultural Heritage Objects*. California: Morgan and Claypool Publishers.

Wiklund, J. and M. Stading. 2008. Application of in-line ultrasound Doppler-based UVP-PD rheometry method to concentrated model and industrial suspensions. *Flow Measurement and Instrumentation.* **19**(1), pp.171-179.

Williams, J.J., Bell, P.S., Humphery, J.D., Hardcastle, P.J. and Thorne, P.D. 2003. New approach to measurement of sediment processes in a tidal inlet. *Continental Shelf Research*. **23**(14-15), pp. 1239-1254. Doi: 10.1016/S0278-4343(03)00127-4.

Williams, R.A., Xie, C.G., Bragg, R. and Amarsinghe, W.P.K. 1990. Experimental techniques for monitoring sedimentation in optically opaque suspensions. *Colloids and Surfaces*. **43**(1), pp.1-32.

Wilson, G.W. and Hay, A.E. 2015. Acoustic backscatter inversion for suspended sediment concentration and size: A new approach using statistical inverse theory. *Continental Shelf Research.* **106**(1), pp.130-139.

Wilson, K. and Briens, L. 2022. Investigation of passive acoustic emissions during power mixing in a V-blender. *Powder Technology.* **408**(1).

Wu, X. H. and Moin, P. 2008. A direct numerical simulation study on the mean velocity characteristics in turbulent pipe flow. *Journal of Fluid Mechanics*. **608**, pp.81-112.

Wypych, G. 2016. *Handbook of Fillers.* USA: Elsevier Science.

Xu, L., Ni, L., Zeng, F. and Wu, S. 2020. Tetranitrile-anthracene as a probe for fluorescence detection of viscosity in fluid drinks via aggregation induced emission. *Analyst*. **145**(3), pp.844-850. Doi: 10.1039/C9AN02157D.

Yam, B.J.Y., Le, D.J., Do, N.H., Nguyen, P.T.T., Thai, Q.B., Phan-Thien, N. and Duong, H.M. 2020. Recycling of magnesium waste into magnesium hydroxide aerogels. *Journal of Environmental Chemical Engineering.* **8**(5).

Yang, H., Kim, J.H. and Kim, K.J. 2019. Study of the crystallisation rates of β- and ϵ-form HNIW in in-situ Raman spectroscopy and FBRM. *Propellants, explosives, pyrotechnics.* **45**(3), pp.422-430.

Young, D.F., Munson, B.R. and Okiishi, T.H. and Huebsch, W.W. 2010. *A brief introduction to fluid mechanics.* New Jersey: Wiley.

Young, R.A., Merrill, J.T., Clarke, T.L., Proni, J.R. 1982. Acoustic profiling of suspended sediments in the marine bottom boundary layer. *Geophys. Res Lett.* **9**(3), pp.175-188.

Yu, Y., Safari, A., Niu, X., Drinkwater, B. and Horoshenkov, K.V. 2021. Acoustic and ultrasonic techniques for defect detection and condition monitoring in water and sewerage pipes: A review. *Applied Acoustics.* **183**(1).

Zagarola, M. V. and Smits, A. J. 1998. Mean-flow scaling of turbulent pipe flow. *Journal of Fluid Mechanics*. **373**(1), pp.33-79.

Zeiss. 2022. *Research Microscopy Solutions.* [Online]. [Accessed 27 October 2022]. Available from: https://www.zeiss.com/microscopy/int/products/scanning-electron-microscopes/evo.html

Zhang, Y., Kieft, B., Hobson, B.W., Raanan, B.Y., Urmy, S.S., Pitz, K.J., Preston, C.M., Roman, B., Benoit-Bird, K.J., Birch, J.M., Chavez, F.P. and Scholin, C.A. 2020. Persistent sampling of vertically migrating biological layers by an autonomous underwater vehicle within the beam of a seabed-mounted echosounder. *IEEE Journal of oceanic engineering.* **46**(2), pp.497-508.

Zhu, B. 2020. *In Situ* Analysis of Lactose Crystal in Solution through Slurry Flow Cell X-Ray Diffraction. *Crystal Research and Technology*. **55**(6).

Zhu, K., Chen, X., Qu, M., Yang, D., Hu, J. and Xie, J. 2021. Non-Contact Ultrasonic Flow Measurement for Small Pipes Based on AlN Piezoelectric Micromachined Ultrasonic Transducer Arrays. *Journal of Microelectromechanical Systems*. **PP**(99), pp.1-8.

11. ESM

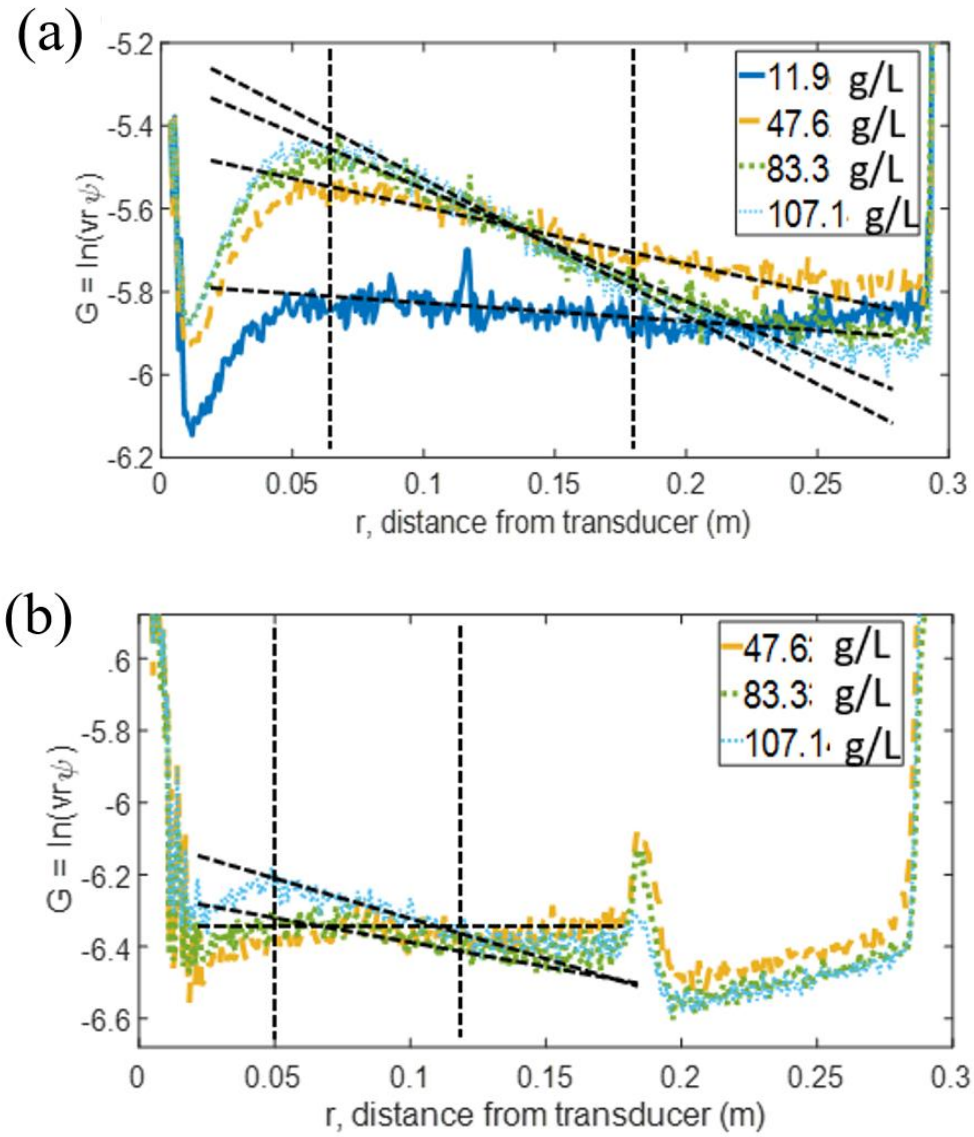

Figure A.1 G function profiles of silica glass beads with a d_{50} of 48 µm utilising a 2 MHz transducer in an (a) in situ and (b) remote placement.

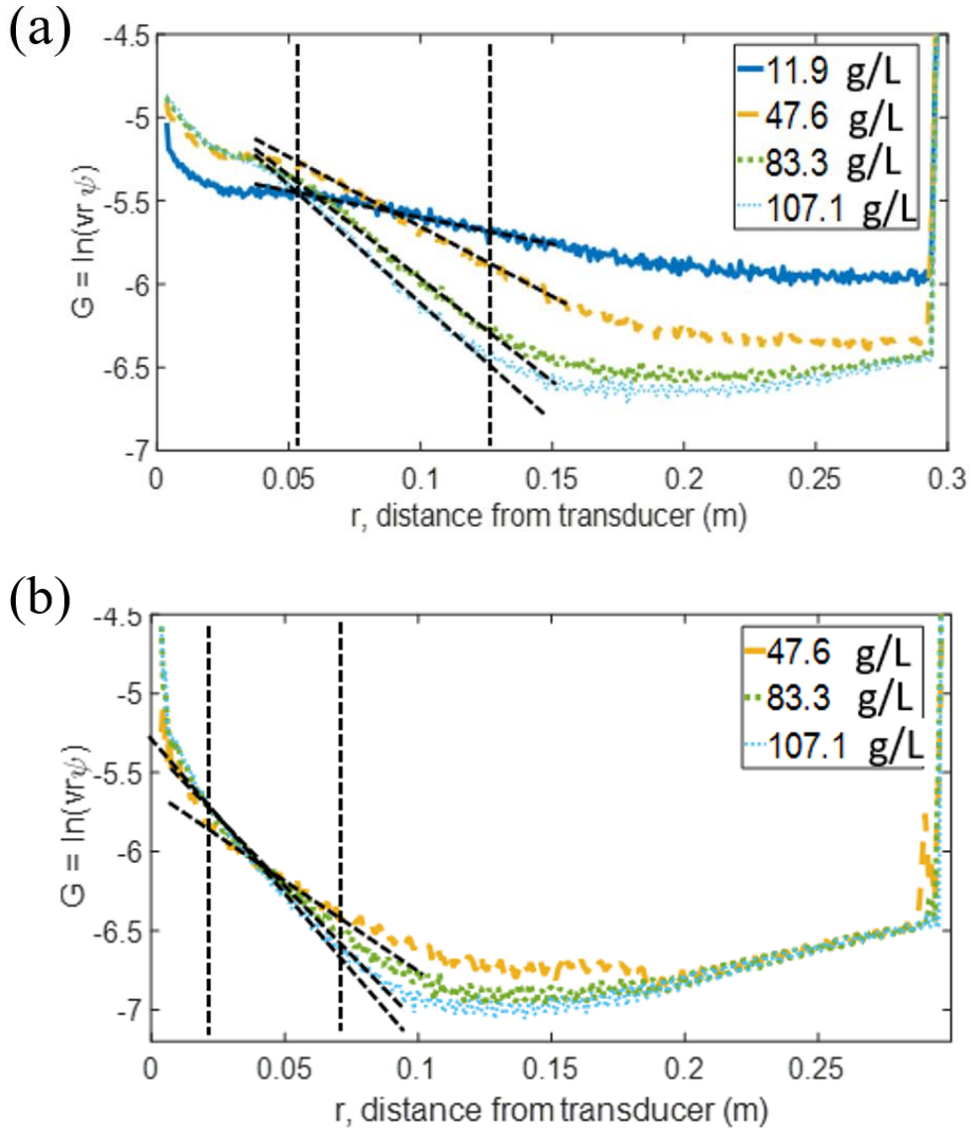

Figure A.2 G function profiles of silica glass beads with a d50 of 48 µm utilising a 4 MHz transducer in an (a) in situ and (b) remote placement.

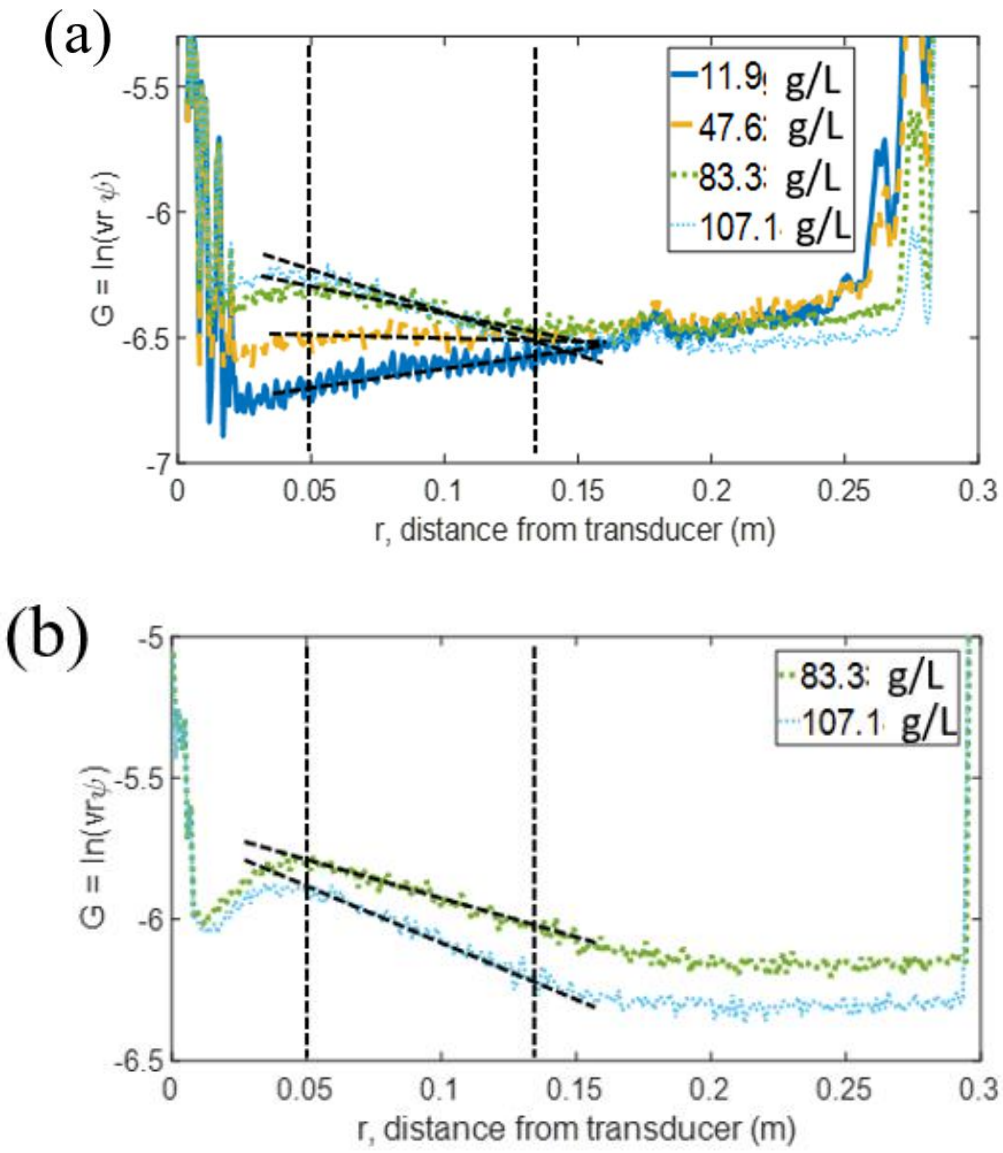

Figure A.3 G function profiles of silica glass beads with a d50 of 36 µm utilising a 2 MHz transducer in an (a) in situ and (b) remote placement.

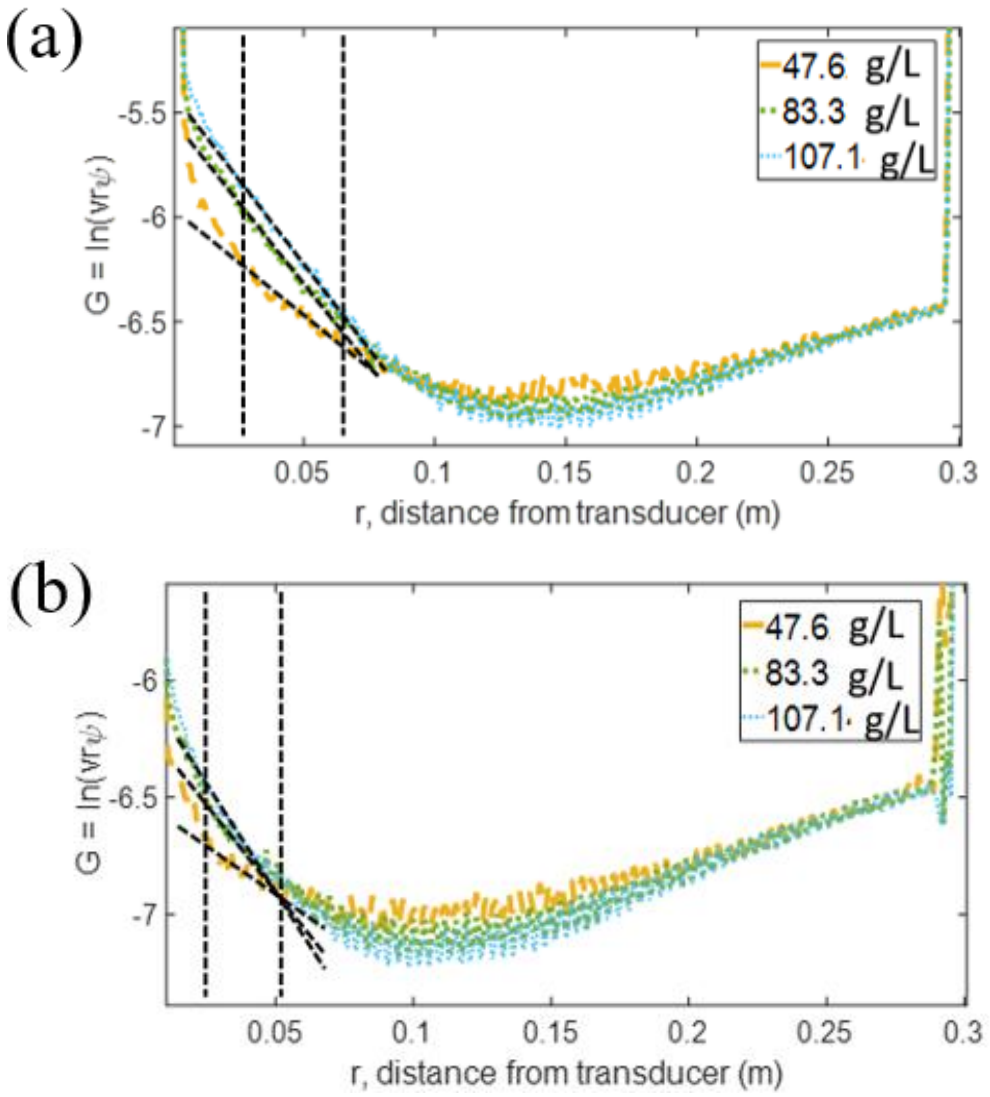

Figure A.4 G function profiles of silica glass beads with a d50 of 36 µm utilising a 4 MHz transducer in an (c) in situ and (d) remote placement.

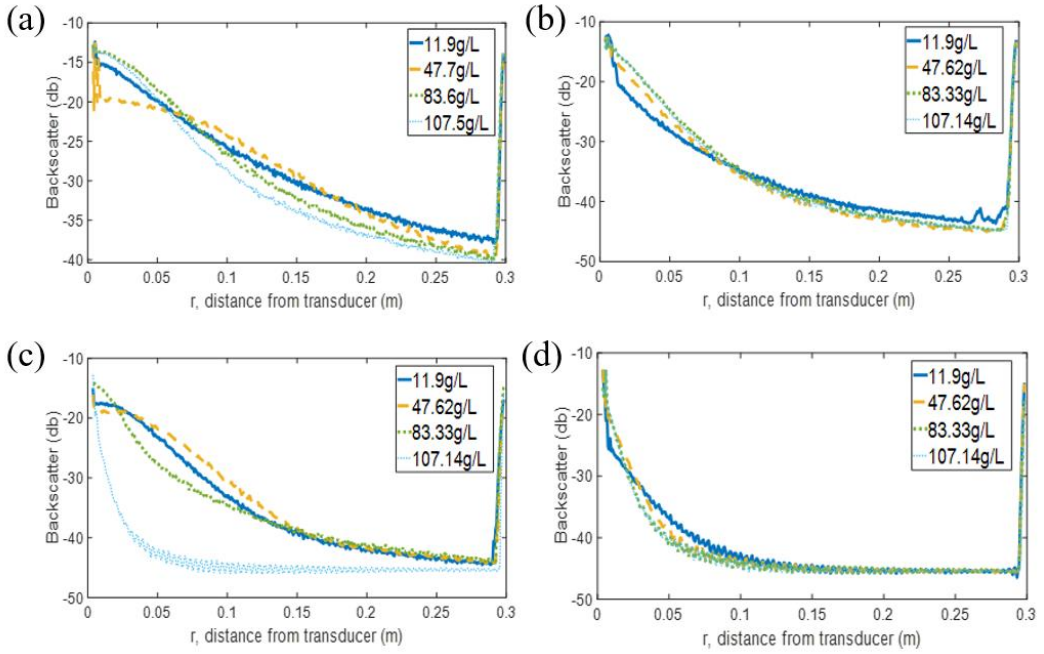

Figure A.5 Backscatter profiles of silica glass beads of d_{50} 170 µm utilising an (a) in situ 2 MHz probe, (b) remote 2 MHz probe, (c) in situ 4 MHz probe and an (d) remote 4 MHz probe.

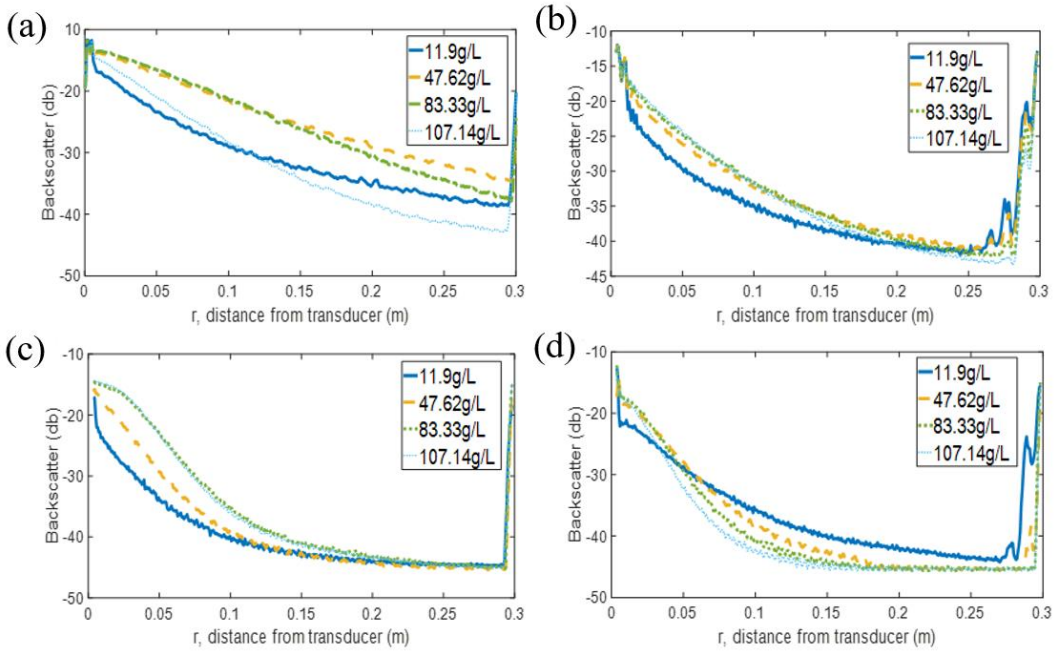

Figure A 6 Backscatter profiles of silica glass beads of d50 82 µm utilising an (a) in situ 2 MHz probe, (b) remote 2 MHz probe, (c) in situ 4 MHz probe and an (d) remote 4 MHz probe.

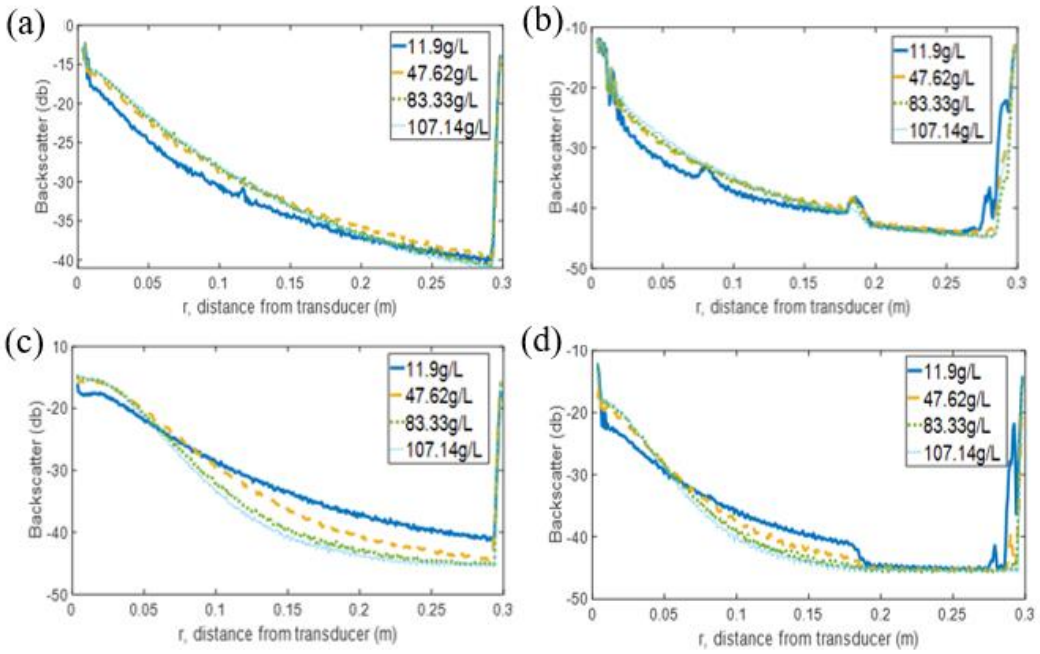

Figure A.7 Backscatter profiles of silica glass beads of d50 48 µm utilising an (a) in situ 2 MHz probe, (b) remote 2 MHz probe, (c) in situ 4 MHz probe and an (d) remote 4 MHz probe.

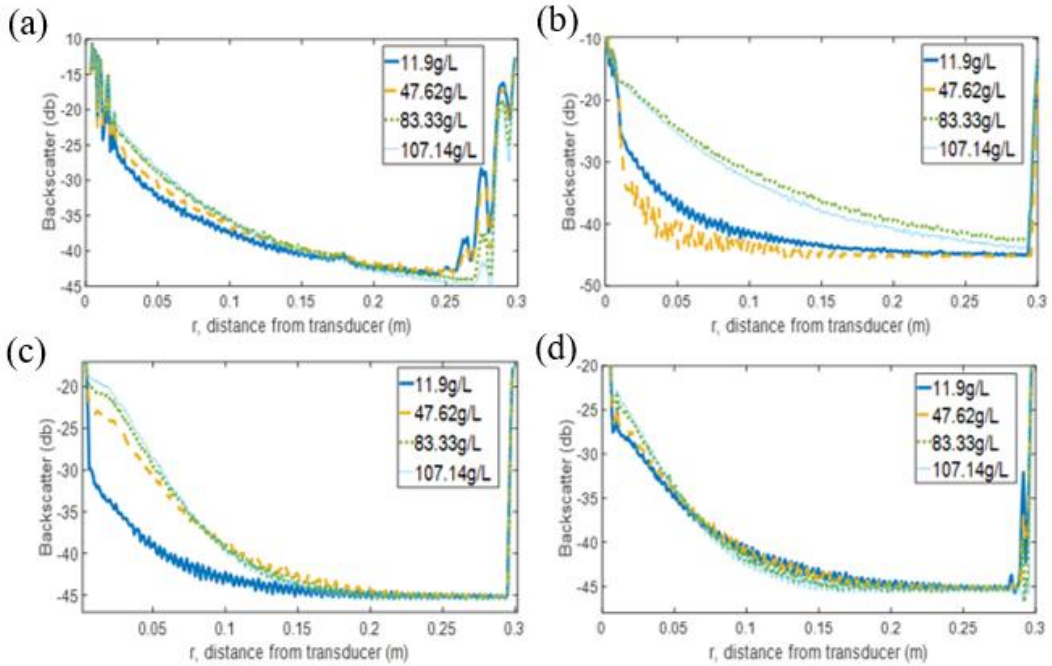

Figure A 8 Backscatter profiles of silica glass beads of d50 36 µm utilising an (a) in situ 2 MHz probe, (b) remote 2 MHz probe, (c) in situ 4 MHz probe and an (d) remote 4 MHz probe.

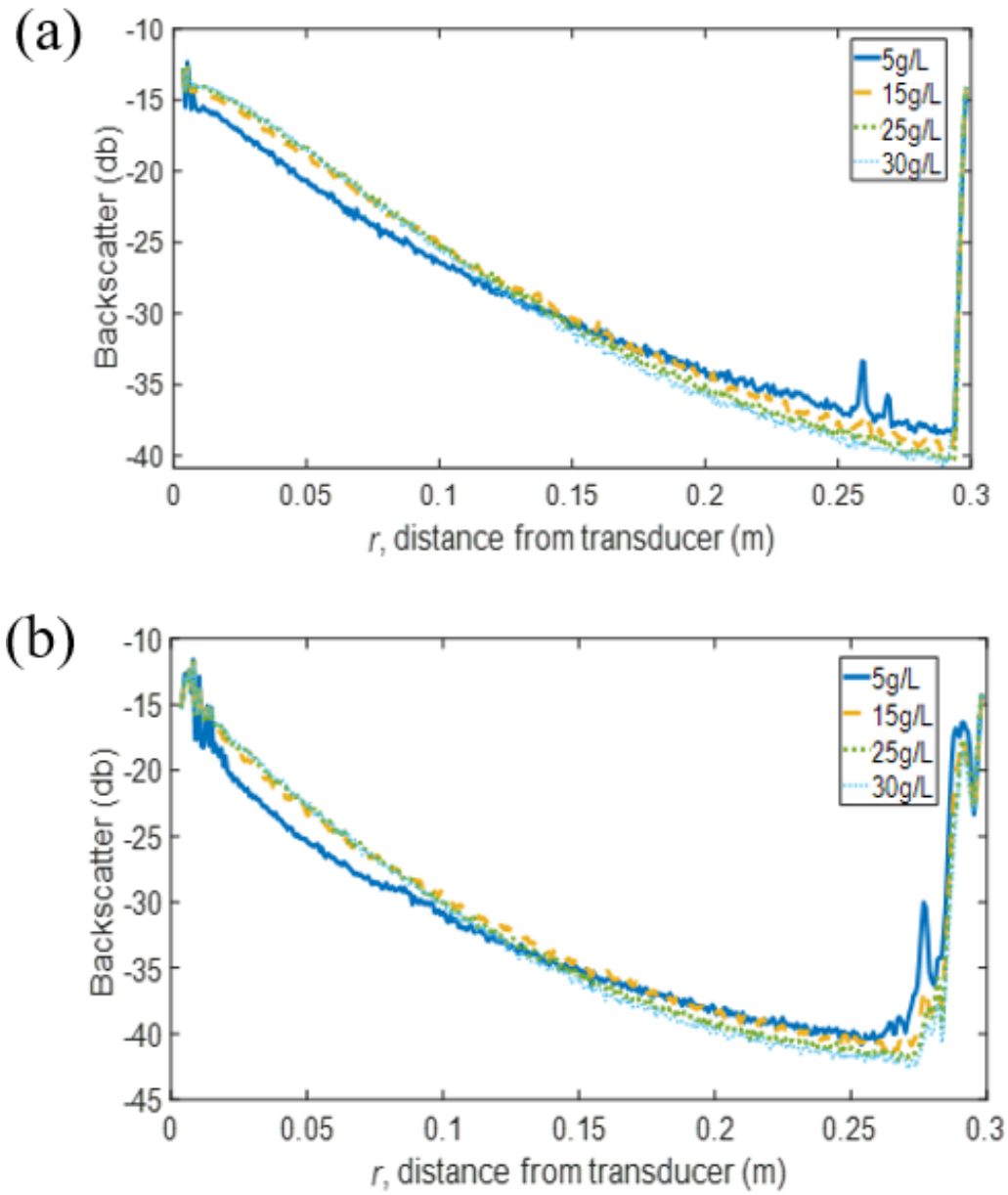

Figure A.9 Backscatter profiles of silica glass beads of d50 170 µm with a lower concentration range from 5 – 30 g/L utilising an (a) in situ 2 MHz probe and (b) a remote 2 MHz probe.

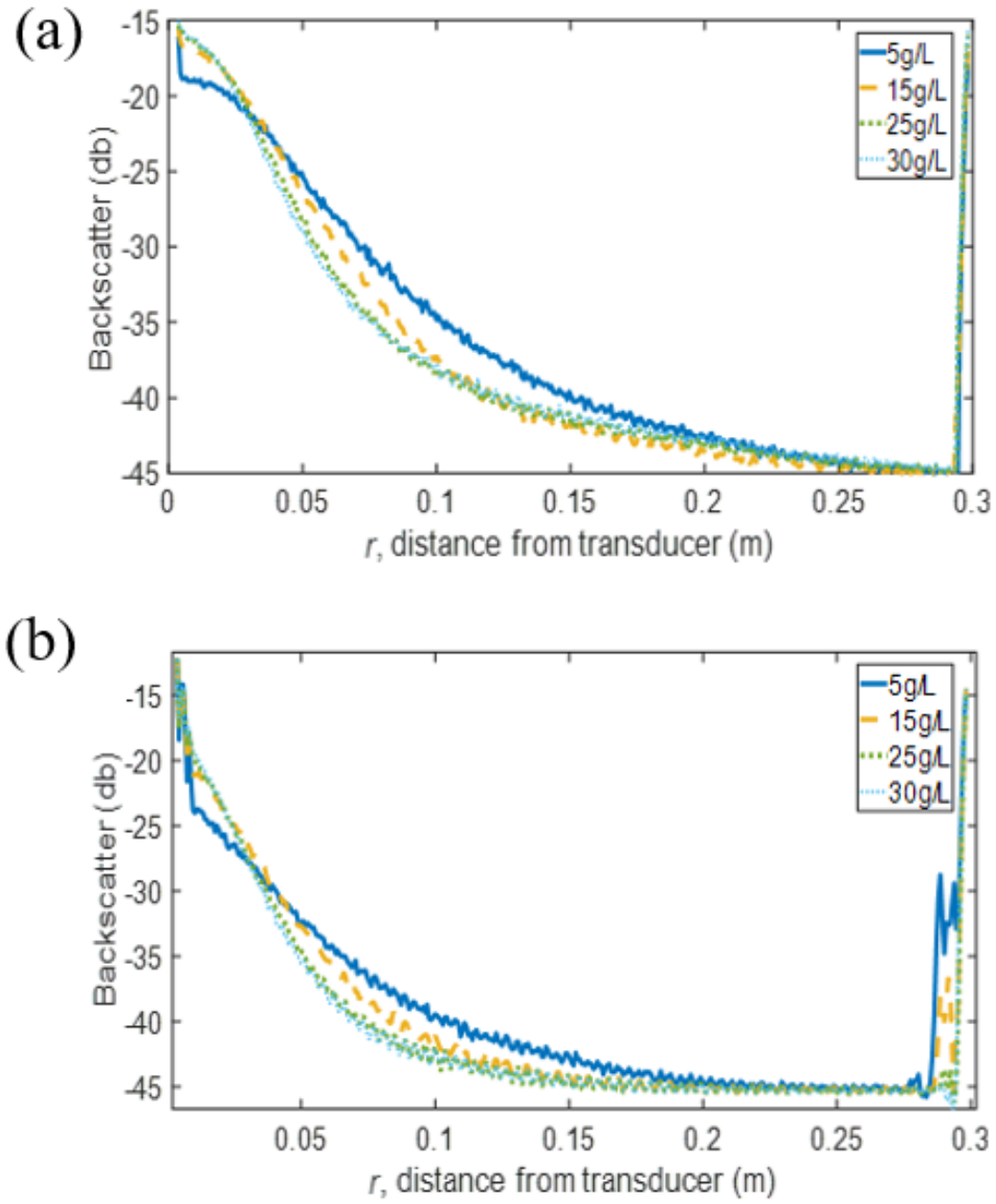

Figure A.10 Backscatter profiles of silica glass beads of d50 170 µm with a lower concentration range from 5 – 30 g/L utilising an (a) in situ 4 MHz probe and a (b) remote 4 MHz probe

Table A.1 dG/dr of silica glass bead suspensions utilising 2 MHz and 4 MHz transducers in situ and remotely

Transducer Frequency and Placement	dG/dr of glass beads with a d_{50} of:			
	170 µm	82 µm	48 µm	36 µm
2 MHz *in situ*	-0.11x + 0.04	-0.05x + 0.45	-0.03x - 0.23	-0.06x + 2.59
2 MHz remote	-0.14x - 0.24	-0.04x + 1.76	-0.03x + 1.98	-0.07x + 4.39
4 MHz *in situ*	-0.33x - 2.91	-0.18x + 4.90	-0.14x - 2.05	-0.07x - 5.48
4 MHz remote	-0.51x - 22.36	-0.17x - 2.80	-0.15x - 0.63	-0.07x - 9.41

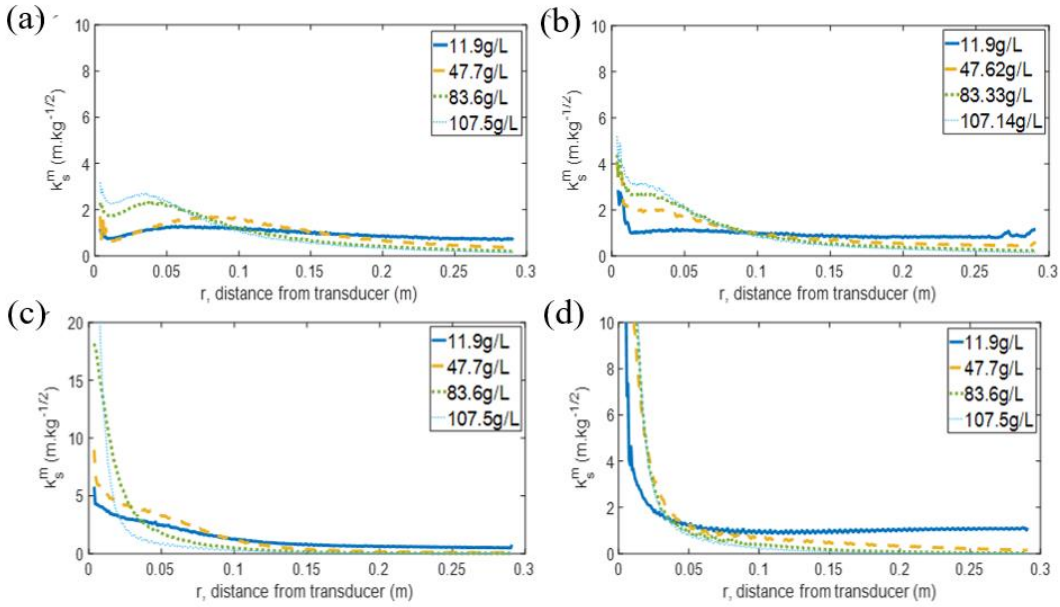

Figure A.11 k_s^m profiles of silica glass beads of d50 170 µm utilising an (a) in situ 2 MHz probe, (b) remote 2 MHz probe, (c) in situ 4 MHz probe and an (d) remote 4 MHz probe.

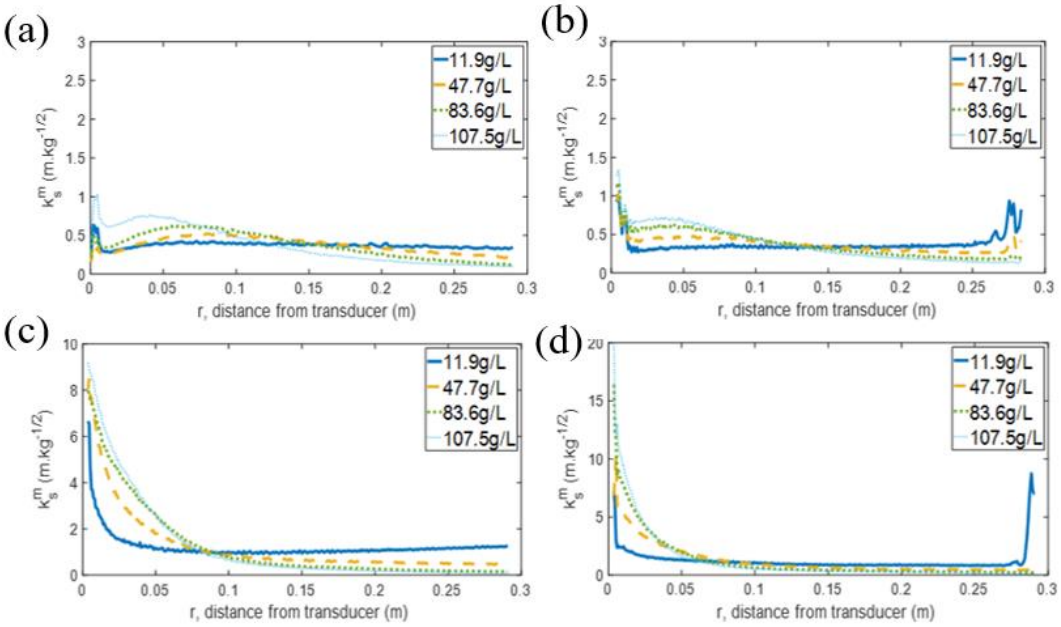

Figure A.12 k_s^m profiles of silica glass beads of d50 82 µm utilising an (a) in situ 2 MHz probe, (b) remote 2 MHz probe, (c) in situ 4 MHz probe and an (d) remote 4 MHz probe.

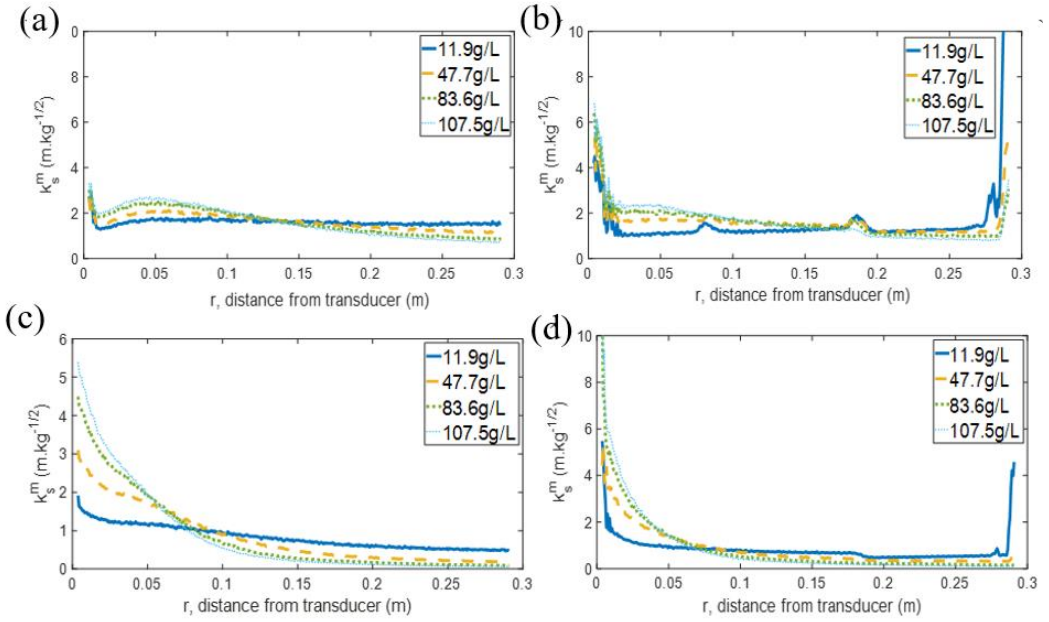

Figure A.13 k_s^m profiles of silica glass beads of d50 48 µm utilising an (a) in situ 2 MHz probe, (b) remote 2 MHz probe, (c) in situ 4 MHz probe and an (d) remote 4 MHz probe.

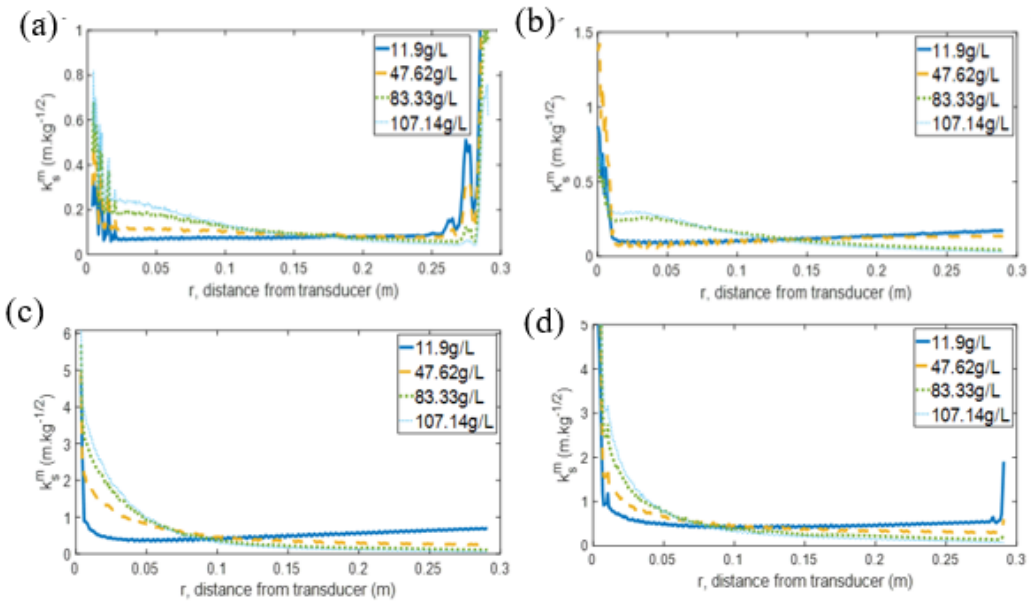

Figure A.14 k_s^m profiles of silica glass beads of d50 36 µm utilising an (a) in situ 2 MHz probe, (b) remote 2 MHz probe, (c) in situ 4 MHz probe and an (d) remote 4 MHz probe.

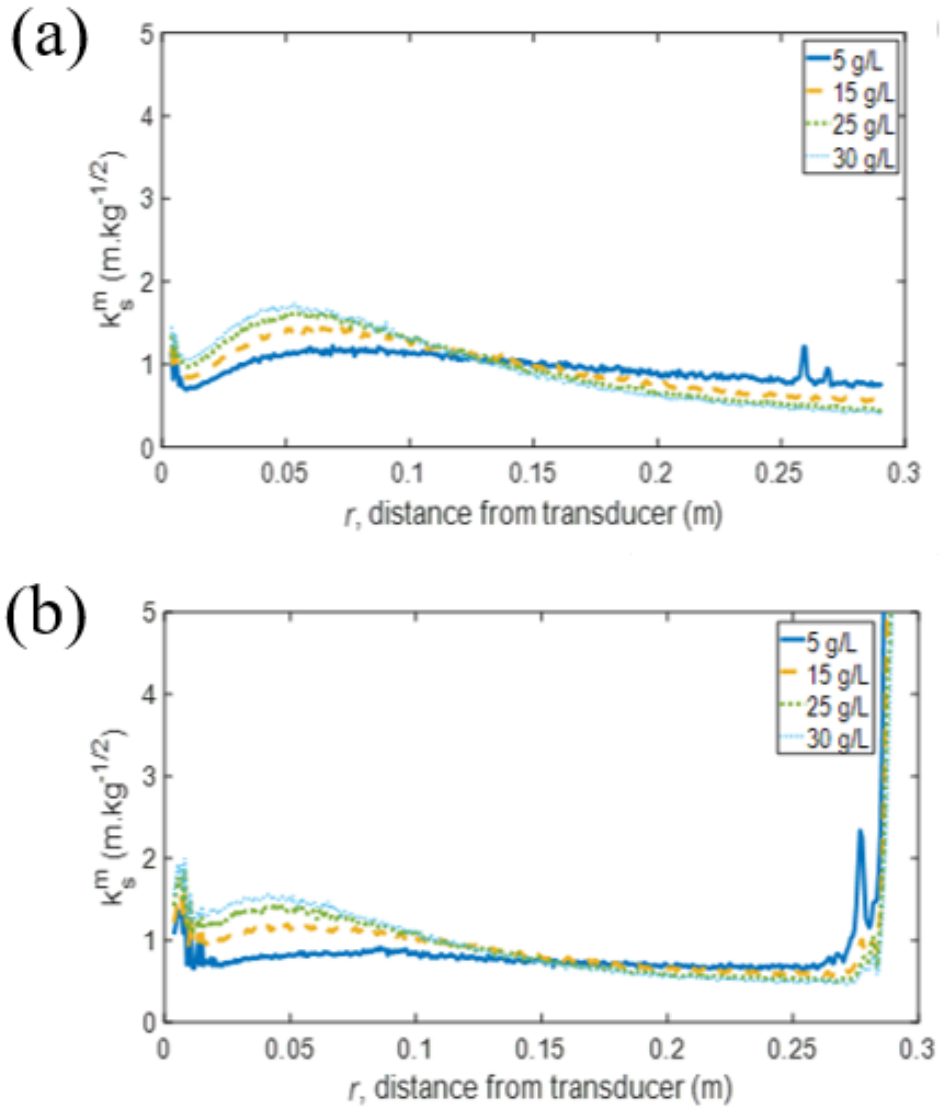

Figure A.15 k_s^m profiles of silica glass beads of d50 170 µm using a lower concentration range of 5 – 30 g/L utilising an (a) in situ 2 MHz probe and (b) remote 2 MHz probe

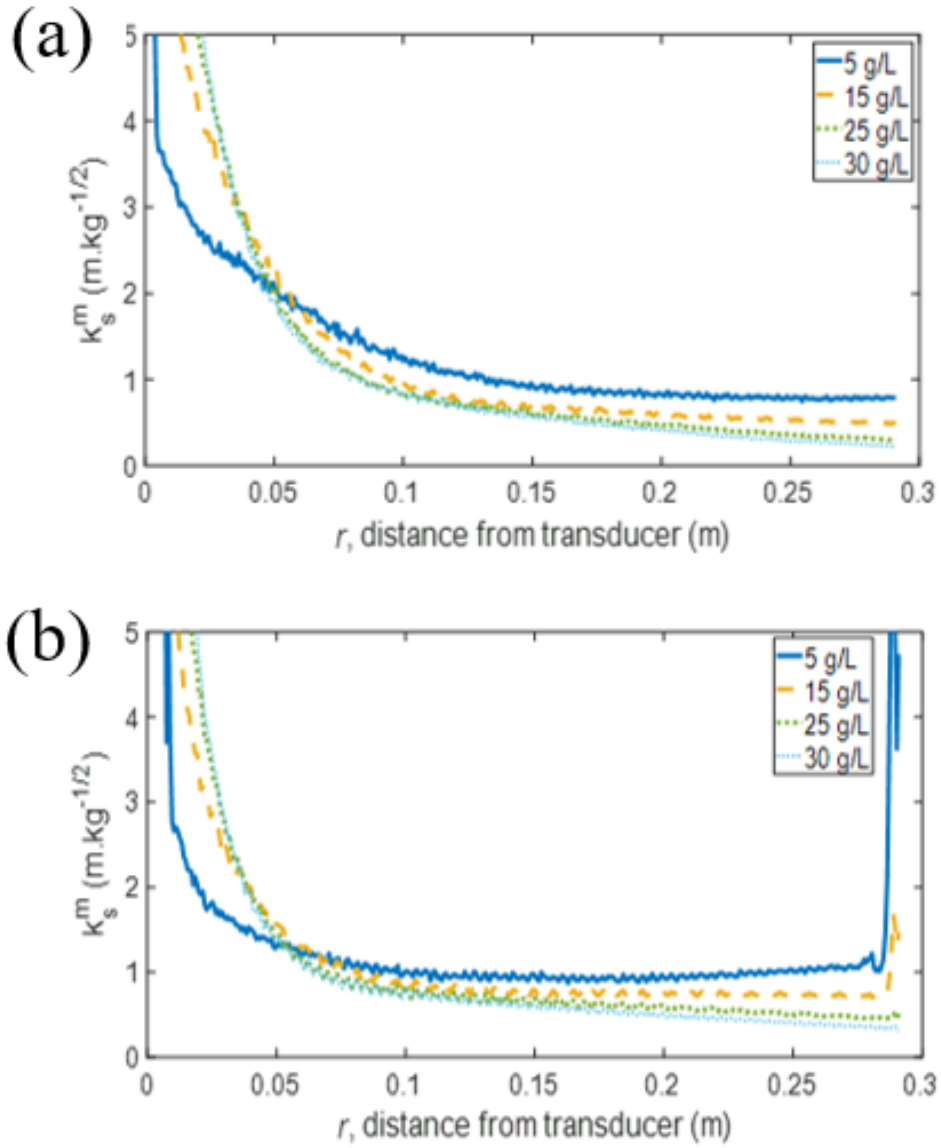

Figure A.16 k_s^m profiles of silica glass beads of d50 170 µm using a lower concentration range of 5 – 30 g/L utilising an (a) in situ 4 MHz probe and a (b) remote 4 MHz probe

Table A.2 k_s^m for silica glass beads of d_{50} 170 µm using a 2 and 4 MHz frequency transducer for a concentration range of 5 – 30 g/L

Transducer Frequency (MHz)	Silica Glass Bead d_{50}	Sediment backscatter constant k_s^m (m.kg$^{-0.5}$)
2 MHz	170 µm	0.89
4 MHz		0.96

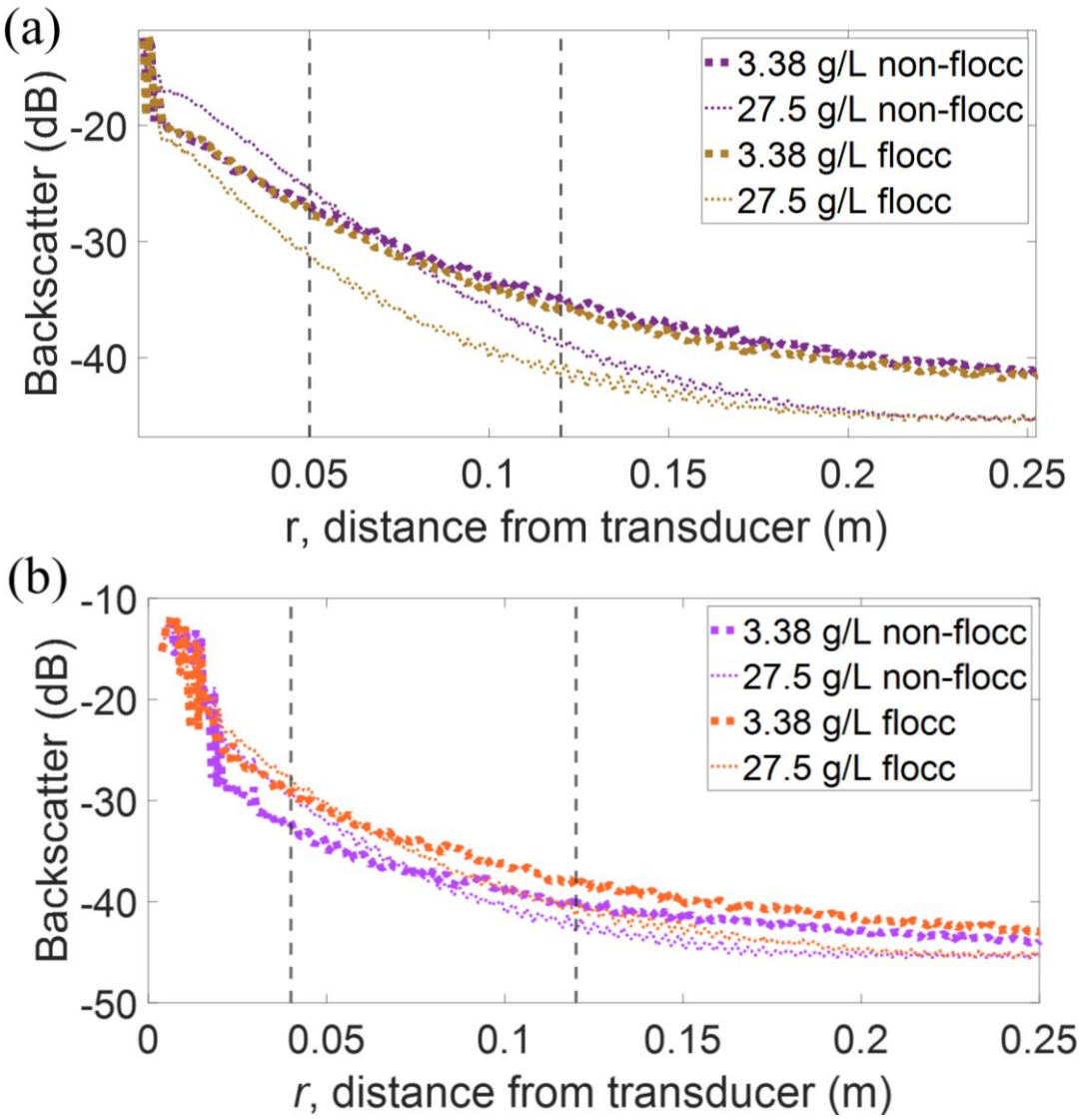

Figure A.17 Backscatter profiles for the flocculated calcium carbonate system using an (a) in situ transducer and a (b) remote transducer.

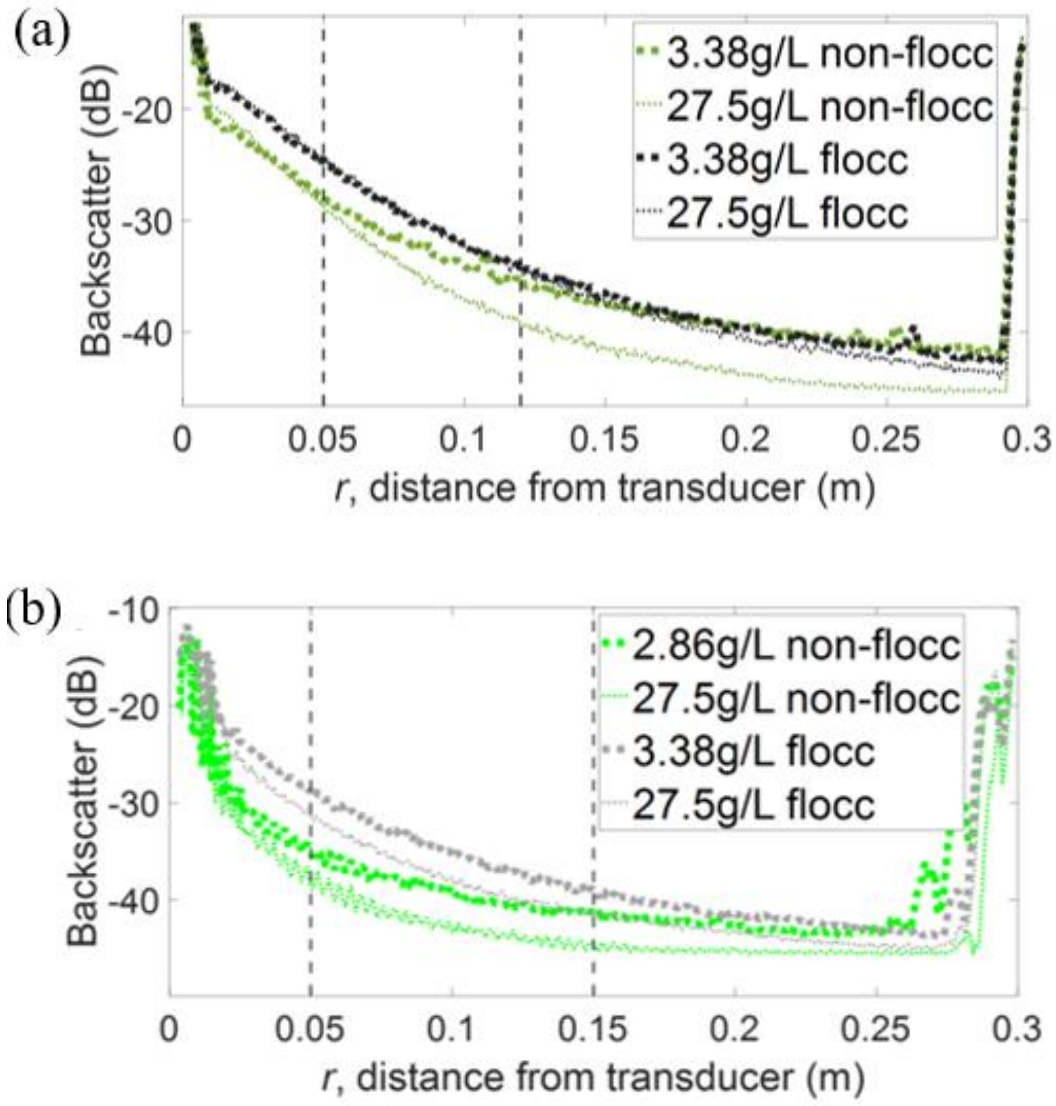

Figure A.18 Backscatter profiles for the flocculated magnesium hydroxide system using an (a) in situ transducer and a (b) remote transducer.

Table A.3 dG/dr of flocculated and non-flocculated suspensions of magnesium hydroxide and calcium carbonate utilising 2 MHz and 4 MHz transducers in situ and remotely

Transducer Placement for 2 MHz probe	Suspension Environment	d*G*/d*r* of Mineral Suspensions of: Calcium Carbonate	Magnesium Hydroxide
In Situ	Non-flocculated	-0.37x - 0.02	-0.17x + 0.44
Remote		-0.41x + 4.12	-0.14x + 4.16
In Situ	Flocculated	-0.18x - 0.89	-0.03x - 3.47
Remote		-0.20x +1.05	-0.02x - 0.57

11.1 Conference Papers

S.T. Hussain, T.N. Hunter, J. Peakall, H. Rice and M. Barnes
Remote Analysis of Complex Mineral Suspensions in Engineered Pipelines: Utilising Underwater Acoustic Backscatter Systems
Published in: Waste Management Symposium 2022, March 2022
DOI:

S.T. Hussain, T.N. Hunter, J. Peakall and M. Barnes
Characterising Flocculated Suspensions with an Ultrasonic Velocity Profiler in Backscatter Mode
Published in: IEEE International Ultrasonics Symposium (IUS) 2021, September 2021
DOI: 10.1109/IUS52206.2021.9593613

S.T. Hussain, T.N. Hunter, J. Peakall and M. Barnes
Simultaneous velocity and concentration profiling of nuclear waste suspensions in pipe-flow, using ultrasonic doppler and backscatter analysis.
Published in: 181st Meeting of the Acoustic Society of America, January 2021
DOI: 10.1121/2.0001525

S.T. Hussain, T.N. Hunter, J. Peakall and M. Barnes

Utilisation of underwater acoustic backscatter systems to characterise nuclear waste suspensions remotely.

Published in: Proceedings of meetings on acoustics Acoustical Society of America, October 2020

DOI: 10.1121/2.0001303